METHODS IN CELL BIOLOGY

VOLUME 22

THREE-DIMENSIONAL ULTRASTRUCTURE IN BIOLOGY

EDITED BY

JAMES N. TURNER

Prepared under the Auspices of the American Society for Cell Biology

METHODS IN CELL BIOLOGY

VOLUME 22

Three-Dimensional Ultrastructure in Biology

Advisory Board



Keith R. Porter (*Chairman*)

Elizabeth D. Hay
T. C. Hsu
Dan Mazia
George E. Palade
George D. Pappas
Jean-Paul Revel
David Sabatini

METHODS IN CELL BIOLOGY

Prepared under the Auspices of the American Society for Cell Biology

VOLUME 22

Three-Dimensional Ultrastructure in Biology

Edited by

JAMES N. TURNER

DIVISION OF LABORATORIES AND RESEARCH
NEW YORK STATE DEPARTMENT OF HEALTH
ALBANY, NEW YORK



1981

ACADEMIC PRESS

A Subsidiary of Harcourt Brace Jovanovich, Publishers

New York London Toronto Sydney San Francisco

COPYRIGHT © 1981, BY ACADEMIC PRESS, INC.
ALL RIGHTS RESERVED.
NO PART OF THIS PUBLICATION MAY BE REPRODUCED OR TRANSMITTED IN ANY FORM OR BY ANY MEANS, ELECTRONIC OR MECHANICAL, INCLUDING PHOTOCOPY, RECORDING, OR ANY INFORMATION STORAGE AND RETRIEVAL SYSTEM, WITHOUT PERMISSION IN WRITING FROM THE PUBLISHER.

ACADEMIC PRESS, INC.
111 Fifth Avenue, New York, New York 10003

United Kingdom Edition published by
ACADEMIC PRESS, INC. (LONDON) LTD.
24/28 Oval Road, London NW1 7DX

LIBRARY OF CONGRESS CATALOG CARD NUMBER: 64-14220

ISBN 0-12-564122-2

PRINTED IN THE UNITED STATES OF AMERICA

81 82 83 84 9 8 7 6 5 4 3 2 1

CONTENTS

LIST OF CONTRIBUTORS xi

PREFACE xiii

PART I. QUALITATIVE METHODS OF STEREO IMAGING

1. *Introduction to Stereo Imaging*
James N. Turner

I. Introduction 1
II. Production of the Stereo Effect 4
III. Display of Stereo Micrographs 7
References 10

2. *Theory of Stereopsis*
Murray Vernon King

I. Studies on Mechanisms of Stereopsis 13
II. Visual Cues That Induce Depth Perception 16
III. Limits on Allowable Parallax, Magnification Disparity, and Brightness Disparity 17
IV. Variation within the Population of Stereo Perception 20
V. Simultaneous Processing of Stereo and Color Information 21
VI. Stereo Perception of Transparent versus Opaque Objects 23
VII. Consequences of Binocular Vision in the Presentation of Micrographs 24
References 30

3. *Stages and Stereo-Pair Recording*
James N. Turner

I. Introduction 33
II. Specimen Tilting Method 35
III. Fixed-Tilt and Rotation Method 46
IV. Summary 49
References 50

4. *Stereomicroscopy of Whole Cells*
Keith R. Porter and Mark E. Stearns

I. Introduction 53
II. Background 55
III. Methods Currently in Use 55
IV. The Stereo Image of Whole Cells 56
V. Experimental Applications of Stereo Technology 59
VI. Properties of Differentiated Cell Systems 63
VII. Relating Whole-Cell to Thin-Section Images 64
VIII. Unique Applications of Stereo Techniques 66
IX. Alternative Analytical Approaches 70
X. Conclusions 73
References 74

5. *Stereoscopic Electron Microscopy of Chromosomes*
Hans Ris

I. Introduction 77
II. Methods 78
III. Levels of Organization in Chromosomes 82
References 95

6. *Preparing Biological Samples for Stereomicroscopy by the Quick-Freeze, Deep-Etch, Rotary-Replication Technique*
John Heuser

I. Introduction 97
II. Methods 98
III. Results 104
IV. Summary and Conclusions 121
References 121

7. *Dense Tissue and Special Stains*
Eichi Yamada and Harunori Ishikawa

I. Introduction 123
II. High-Voltage Electron Microscopy of Neutron and Glia Cells after Impregnation by the Golgi Method 124
III. High-Voltage Electron Microscopy of Biological Membranes after Selective Staining 127
IV. Membranous Systems in Striated Muscles 131
V. Membranous Organelles in Neurons 142
References 143

8. *Mock Stereo*
Murray Vernon King

I. Definition and Scope of Mock-Stereo Displays 147
II. Types of Image Disparities That Can Profitably Be Treated by Mock Stereo: Discussion and Examples 148
III. Simultaneous Handling of Positional and Color Information in Mock Stereo 149
IV. Applications of Mock Stereo in Electron Microscopy 150
V. Some Examples of Unintentional Mock Stereo 152
References 153

PART II. QUANTITATIVE METHODS APPLIED TO STEREO IMAGING

9. *Theory*
Sanjib K. Ghosh

I. Introduction 155
II. Coordinate Systems and Transformation 157
III. Projections and Distortions 163
IV. Stereo Model and Orientation 169
V. Calibration of the Electron Microscopy 173
References 176

10. *Hardware and Methods*
Sanjib K. Ghosh

I. Measuring Instruments 178
II. Accuracy and Reliability 185
III. The Digital Terrain Model and Computer Mapping 190
References 192

11. *Application to Single Specimens*
Sanjib K. Ghosh

I. Applications of the Scanning Electron Microscope 194
II. Applications of the Transmission Electron Microscope 195
III. Combining SEM and TEM Information 197
References 198

PART III. QUANTITATIVE THREE-DIMENSIONAL RECONSTRUCTION

12. *Introduction*
Joachim Frank

I. Quantitive Methods of Three-Dimensional Reconstruction in Electron Microscopy 199
II. Fourier Methods of Reconstruction 202
III. Direct-Space Methods of Reconstruction 209
IV. Alignment of Projections 211
References 212

13. *Thick and Thin Serial Sectioning for the Three-Dimensional Reconstruction of Biological Ultrastructure*
Conly L. Rieder

I. Introduction 215
II. Choosing an Appropriate Section Thickness for Serial Reconstruction 221
III. Serial Sectioning 226
IV. Three-Dimensional Reconstruction from Serial Sections 238
References 247

14. *Three-Dimensional Reconstruction of Membrane Protein Crystals*
Stephen D. Fuller

I. Introduction 251
II. Two-Dimensional Crystals 253
III. Preliminary Analysis of Crystals 261
IV. Technique of Three-Dimensional Reconstruction 262
V. Biochemical Results 283
References 294

15. *Visualization of Virus Structure in Three Dimensions*
Alasdair C. Steven

I. Introduction 298
II. Cryomicroscopy of Virus Particles 300
III. Advent and Application of the Scanning Transmission Electron Microscope 300
IV. Three-Dimensional Reconstruction of Virus Particles 304
V. Image Processing of Two-Dimensional Surface Lattices 308
VI. Electron Microscopy and Virus Crystallography 316
VII. Concluding Discussion 319
References 321

16. *Three-Dimensional Reconstruction of Single Molecules*
Joachim Frank

I. Introduction 325
II. Some General Problems 329
III. Reconstruction of Individual Molecules 331
IV. Reconstruction of Averaged Molecules 335
V. Concluding Remarks 341
References 342

INDEX 345

CONTENTS OF RECENT VOLUMES 349

This Page Intentionally Left Blank

LIST OF CONTRIBUTORS

Numbers in parentheses indicate the pages on which the authors' contributions begin.

JOACHIM FRANK, Division of Laboratories and Research, New York State Department of Health, Albany, New York 12201 (199, 325)

STEPHEN D. FULLER, Institute of Molecular Biology, University of Oregon, Eugene, Oregon 97403 (251)

SANJIB K. GHOSH, Department of Photogrammetry, Laval University, Québec G1K 7P4, P.Q., Canada (155, 177, 193)

JOHN HEUSER, Department of Physiology and Biophysics, Washington University School of Medicine, St. Louis, Missouri 63110 (97)

HARUNORI ISHIKAWA, Department of Anatomy, Faculty of Medicine, University of Tokyo, Tokyo 113, Japan (123)

MURRAY VERNON KING, Division of Laboratories and Research, New York State Department of Health, Albany, New York 12201 (13, 147)

KEITH R. PORTER, Department of Molecular, Cellular, and Developmental Biology, University of Colorado, Boulder, Colorado 80309 (53)

CONLY L. RIEDER,[1] Laboratory of Molecular Biology, University of Wisconsin, Madison, Wisconsin 53706 (215)

HANS RIS, Department of Zoology, University of Wisconsin, Madison, Wisconsin 53706 (77)

MARK E. STEARNS, Department of Molecular, Cellular, and Developmental Biology, University of Colorado, Boulder, Colorado 80309 (53)

ALASDAIR C. STEVEN, Laboratory of Physical Biology, National Institute of Arthritis, Metabolism, and Digestive Diseases, National Institutes of Health, Bethesda, Maryland 20205 (297)

JAMES N. TURNER, Division of Laboratories and Research, New York State Department of Health, Albany, New York 12201 (1, 33)

EICHI YAMADA, Department of Anatomy, Faculty of Medicine, University of Tokyo, Tokyo 113, Japan (123)

[1] *Present address:* Electron Optics Laboratory, Division of Laboratories and Research (Ultrastructure Analysis), New York State Department of Health, Empire State Plaza, Albany, New York 12201.

This Page Intentionally Left Blank

PREFACE

The electron microscope has had a great impact on our understanding of the structure and function of biological systems. The knowledge obtained to date has been derived from qualitative two-dimensional analyses with relatively few three-dimensional or quantitative studies. To extend this understanding, however, it is necessary to adopt quantitative techniques and to analyze the structure in all three dimensions.

The use of image processing methods and high-voltage electron microscopes (HVEMs), a combination which has already greatly facilitated such analyses, should become a particularly powerful tool in the future. Image processing utilizes computer methods to extract information from electron micrographs and to analyze that information. The HVEM is having an increasing impact on the analysis of biological ultrastructure because it makes available three-dimensional information from thick specimens. Although HVEMs are costly facilities and can only be justified by a community of users, the information they provide is essential and unobtainable from other methods.

Work from four HVEM sites is presented in this text. Two of these are funded by the National Institutes of Health, Division of Biotechnology Resources, and are located in the Department of Molecular, Cellular, and Developmental Biology, University of Colorado, Boulder, and the Department of Zoology, University of Wisconsin, Madison. Dr. H. Ris is in charge of the Madison facility and Dr. K. R. Porter supervises the Boulder site. These facilities are available to qualified workers by contacting Dr. Suzanne Stimler, of the Division of Biotechnology Resources at NIH. The third HVEM is funded by New York State and is located in the Division of Laboratories and Research, New York State Department of Health, Albany. It is available to qualified users by contacting Dr. D. F. Parsons, the supervisor of the site. The fourth is funded for both biological and physical science users by the Japanese government, Ministry of Education, Science, and Culture, and is located at the University of Tokyo.

The purpose of the present volume is to provide a basis for the expanded use of three-dimensional analysis, to review the present state of the art, and to predict future trends and applications. The first section concentrates on qualitative stereo imaging and discusses recording, display, interpretation, and application of stereo methods. The second section provides a detailed basis for the quantitative technique of stereo imaging by photogrammetric methods. Of necessity this section is somewhat mathematical, but its intent is to provide the necessary background for workers not presently using photogrammetric methods. The final section stresses three-dimensional reconstruction and image processing. It discusses serial sectioning and model building, as well as the numerical methods that are becoming widely used due to their power for analysis of electron micrographs.

I would like to extend my thanks to the contributing authors for their hard work and to the American Society for Cell Biology, particularly its publications committee and Dr. A. Zimmerman. Special gratitude is owed to Dr. Keith Porter, who recommended the venture to the Society on my behalf, and to the staff at Academic Press. Connie deserves thanks for her encouragement, editing, proofreading, and typing. Thanks are lastly due to Todd and Nicholas, from whom time was taken to accomplish this project.

JAMES N. TURNER

METHODS IN CELL BIOLOGY

VOLUME 22

Three-Dimensional Ultrastructure in Biology

This Page Intentionally Left Blank

METHODS IN CELL BIOLOGY, VOLUME 22

Part I. Qualitative Methods of Stereo Imaging

Chapter 1

Introduction to Stereo Imaging

JAMES N. TURNER

Division of Laboratories and Research,
New York State Department of Health,
Albany, New York

I. Introduction 1
II. Production of the Stereo Effect 4
III. Display of Stereo Micrographs 7
A. Prints 8
B. Slides 8
C. Transparent versus Opaque Objects 9
References 10

I. Introduction

The extremely high resolving power of the electron microscope has greatly advanced the study and understanding of biological systems. The transmission electron microscope, or TEM, produces a projection image of the object that contains only two-dimensional information. This image is a faithful representation of the object only if the specimen is assumed to be infinitely thin. Since this condition does not apply to a real specimen, a sufficient approximation is obtained if the sample is thin compared with the dimensions of the details under study. For most biological applications over the past forty years, it has been possible either to select problems and samples that meet this criterion or to section the sample to make it satisfy the assumption. However, the number of problems requiring three-dimensional information for their solution is increasing rapidly.

Copyright © 1981 by Academic Press, Inc.
All rights of reproduction in any form reserved.
ISBN 0-12-564122-2

There are, in general, three methods of obtaining this information: (1) use of specimens whose thickness is greater than the dimensions of the structures of interest; (2) serial sectioning through the sample, producing a series of "thin" sections whose images are later integrated into a three-dimensional representation of the object; and (3) mathematical construction of a three-dimensional representation of the object from a series of micrographs recorded in a particular way. The second and third approaches are fully discussed in Part III on three-dimensional reconstruction in this volume and will not be treated here. The collection and analysis of data using the first approach are the subjects of Part I.

A specimen whose thickness is greater than the dimensions of the details being analyzed may contain structures positioned directly above each other (that is, having the same x and y, but different z coordinates). When such a sample is viewed in projection, the images of these structures will overlap, producing a confusing or even a misleading image. The simplest way to eliminate this confusion is to record stereo pairs of micrographs and to view the images stereoscopically. This re-establishes the three-dimensional positions of the structures within the samples.

Stereo pairs are generally recorded by tilting the specimen, relative to the beam, first in one direction and then in the opposite direction by an equal amount from the initial position. A micrograph is recorded in each tilt position. The micrographs are then mounted side by side, with the direction of the tilt axis being from top to bottom. A stereo image is produced by ensuring that each eye views only one micrograph, while the other eye views only the other micrograph. Details of the recording and viewing of stereo pairs are found later in this chapter and in Chapters 2 and 3.

The tilting of the sample between exposures generates parallax, which is defined as the distance between two points in one micrograph minus the distance between the same two points in the second micrograph. Points having the same z coordinate in the untilted position have no parallax and will not exhibit depth with respect to each other when the micrographs are viewed stereoscopically. In contrast, points having different z coordinates initially have nonzero parallax with respect to each other and will exhibit depth when the micrographs are viewed stereoscopically. Thus, images that overlap in a single projection can be separated in the z direction to allow a more accurate analysis of the structures of interest.

Stereo imaging has come in and out of fashion several times in the short history of electron microscopy, which has resulted in later investigators' rediscovering the principles and practices of earlier workers. Von Ardenne published the first stereo pairs recorded with an electron microscope in 1940 (von Ardenne, 1940a,b,c), imaging MgO crystals and air-dried bacteria. Eitel and Gotthardt (1940) made the first attempt at quantitative stereo, or photogrammetry, an approach discussed in detail in Part II of this volume, "Quantitative Methods

Applied to Stereo Imaging," by Ghosh. The parallax equation as applied to electron microscopy was derived by both von Müller (1942) and Gotthardt (1942). Heidenreich and Matheson (1944) also derived this equation and, in addition, a second expression describing the resolution attainable in the z direction from a stereo pair. They used these expressions to measure metal film thickness and to plot parallax versus height difference (Δz) for a range of stereo tilt angles. These authors also constructed a contour-mapping and parallax-measuring device.

Biological objects have frequently been studied by stereo electron microscopy, and some of the earlier papers will be mentioned here. However, references on nonbiological studies will not be discussed unless they demonstrate a basic principle that is helpful for imaging biological objects. Bacteria were an object of early interest for von Ardenne (1940a,b,c) and for Marton (1944), but their images provided little biological information. Von Müller (1942) used stereo imaging to build a three-dimensional model of the structure of a diatom skeleton. Richards and Anderson (1942) used stereo imaging to study the trachea of several species of insects, and Anderson and Richards (1942) demonstrated the basis for insect structural colors. Replicas of surfaces were viewed stereoscopically by Heidenreich (1943) and by Heidenreich and Mathèson (1944), who also did quantitative analysis on the surface structures. (Stereo imaging of replicas will be discussed in detail by Heuser in Chapter 6 in this volume.) Little (1958a,b) combined stereo electron microscopy and x-ray diffraction data to study dental enamel and the development of dental caries. Williams and Kallmann (1955) used stereo imaging to help interpret single and serial sections, and they combined shadowing with stereo to demonstrate that beam irradiation extensively removed material from epoxy sections. (King discusses another application of stereo to the study of beam damage in Chapter 8 in this volume.) Shalla *et al.* (1964), using stereo imaging to study the penetration of stain into epoxy sections, demonstrated that the stain did not penetrate a thin plastic film on the section surface. Kelly (1966) used stereo imaging of thin sections to study the relationship of tonofilaments, desmosomes, and hemidesmosomes, and he proposed a model for their structural relationship. A similar study (Kelly, 1967) of the structure of skeletal muscle produced a model of the z band. Willis (1972) and Gray and Willis (1968) studied stereo imaging in considerable detail, especially as applied to membranes.

However, the most productive of the earlier workers in biological stereo electron microscopy was T. F. Anderson. Beginning with his observations of insects (Anderson and Richards, 1942; Richards and Anderson, 1942), he studied a wide range of biological objects and discussed most if not all of the principles of stereo recording and display used by many workers today. He published a number of stereo studies on *Escherichia coli,* and the attachment of bacteriophage on this bacteria, with their resultant infection (Anderson, 1952, 1953a-d; Anderson and

Oster, 1956; Anderson *et al.*, 1957). He also published stereo images of virus particles (Anderson, 1952, 1953a-c, 1956), human red blood cells (Anderson, 1950, 1951, 1953d, 1956), paramecium (Anderson, 1952; Anderson *et al.*, 1964), and normal and carcinomatous epidermal cells (Coman and Anderson, 1955). In addition, he published a paper on the resolution of stereo imaging (Anderson, 1957) and a detailed section on stereo imaging and display in a review article on electron microscopy of microorganisms (Anderson, 1966).

In spite of the obvious success of these studies in demonstrating three-dimensional relationships of biological structures, stereo electron microscopy has not been widely utilized. This is probably due to the overshadowing success of ultrathin-sectioning procedures. Sections are routinely cut so thin that for most purposes they are considered to be "infinitely" thin; that is, either the section thickness is much smaller than the details under study, or they are sufficiently separated that image overlap is not a significant problem. However, the increasing need to understand objects in three dimensions has led to the use of high-voltage electron microscopes (HVEMs) for three-dimensional analysis of objects, which are a significant fraction of a micron or greater in thickness. [See Glauert (1974) and King *et al.* (1980) for reviews of the application of the HVEM to biology.] The depth of field of the HVEM is sufficiently large that images of thick sections are in focus through their entire thickness, and therefore the image information overlaps in a single projection. Thus, stereo imaging is vital to HVEM work, and interest in and use of this technique have increased dramatically with the application of the HVEM to biological problems.

Although stereo imaging is convenient and readily available, the three-dimensional techniques discussed in the final chapters of this volume need to be applied to HVEM images to utilize fully the information available. An alternative approach is to intentionally limit the image information by special staining (see Yamada and Ishikawa, Chapter 7 in this volume). Another potential limitation of HVEM is that the depth of field is finite. If the section thickness approaches or exceeds the depth of field, decreased resolution may be observed and wrongly be assumed to be due to lack of penetrating power of the electrons. The depth of field is dependent on the objective and condenser apertures; if specimens 1.5 μm thick or thicker are used, the depth of field must be sufficient to image the entire specimen. Such very thick specimens are not discussed in this volume.

II. Production of the Stereo Effect

A stereo effect is achieved when two micrographs recorded with different orientations of the specimen with respect to the electron beam are viewed simultaneously. The most common method of producing this difference in orientation is to tilt the specimen, changing the angle between the beam and the specimen

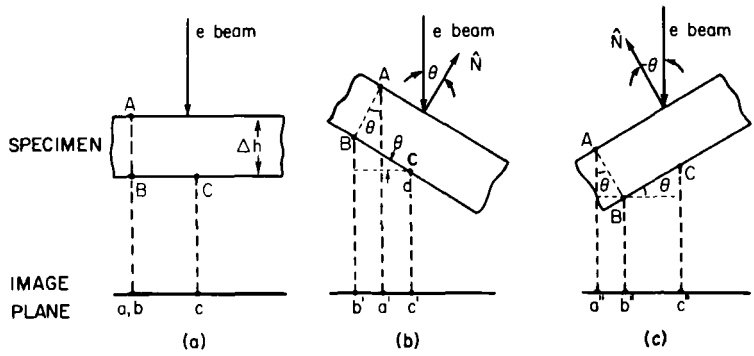


FIG. 1. Geometry of a specimen in tilted and untilted orientations. The positions relative to each other and to the incident electron beam of three points A, B, and C in the specimen and their corresponding image points a, b, and c are shown. Specimen (a) in untilted orientation; (b) in the $+\theta$ tilted orientation (at which the first micrograph of the stereo pair is recorded); and (c) in the $-\theta$ tilted orientation (at which the second micrograph of the stereo pair is recorded). $\hat{N}$ represents the unit vector normal to the top surface of the specimen.

detail, or, more precisely, the specimen normal. Figure 1 shows a specimen in the untilted position, and in the tilted positions for the recording of a stereo pair. The specimen is a section with details of interest on both the top (point A) and bottom surfaces (points B and C). From Fig. 1, an expression can be derived relating the specimen thickness, Δh; the total viewing magnification, M_T; the stereo tilt angle, θ; and the parallax, P. If we assume parallel projection, the image points a, b, and c correspond to the specimen points A, B, and C, where A and B define a line normal to the specimen's top surface. The angle between the specimen normal, $\hat{N}$, and the incident beam, defined here as θ, is zero for the untilted orientation, $+\theta$ for one micrograph of the stereo pair, and $-\theta$ for the second micrograph of the pair. The parallax corresponding to the object points A and C is equal to the linear distance between the corresponding image points in one micrograph of the stereo pair minus the corresponding distance in the second micrograph. Referring to Fig. 1, we have

$$P = a'c' - a''c'' \tag{1}$$

The distance $a'c'$ is given by the expression

$$a'c' = b'c' - b'a'$$

Since

$$b'c' = M_T BC \cos\theta \tag{2}$$

and

$$b'a' = M_T \Delta h \sin\theta \tag{3}$$

we obtain

$$a'c' = (BC \cos \theta - \Delta h \sin \theta)M_T$$

and $a''c''$ is given by

$$a''c'' = (BC \cos \theta + \Delta h \sin \theta)M_T$$

Thus, $a'c' - a''c''$ is given by

$$a'c' - a''c'' = 2\Delta h \sin \theta \, M_T \tag{4}$$

where M_T represents the total magnification at which the stereo pair will later be viewed (the microscope magnification times the magnification of the viewer).

Equation (4) is the basic expression for stereo electron microscopy, derived by von Müller (1942) and by Gotthardt (1942). The expression can be rearranged to predict the optimum tilt angle, given a knowledge of the total magnification and the specimen thickness:

$$\theta = \sin^{-1} P/(2M_T \Delta h) \tag{5}$$

Because the magnification of the electron microscope is usually a known quantity, as is the magnification of the stereo viewer to be used in observing the stereo pair, the value of M_T is known. In addition, the thickness of the specimen can usually be estimated. For sections, an estimate based on the interference colors observed on the microtome water bath is sufficient. The value for P is a function of the human visual system, so the value for optimum observation varies from individual to individual (see King, Chapter 2 in this volume). In practice, the range of perceptible parallax is 3.0–5.0 mm (Hudson and Makin, 1970). This author, following the recommendation of Hudson and Makin (1970), has set P equal to 3.5 mm.

Hudson and Makin also plotted tilt angle versus magnification for a series of specimen thicknesses. Their tilt angle, also denoted as θ, is twice the value of the θ designated in Eqs. (1)–(5) and defined in Fig. 1. The Hudson and Makin plots are for the total angular separation between the two specimen orientations of the stereo pair, the angle designated in this volume as the stereo angle, S. Thus, with the Hudson and Makin plots, the specimen should be tilted in the plus and minus directions only half the amount read off the vertical axis of the graph. Beeston (1973) pointed this out and replotted the curves for the stereo tilt angle as defined here. Thus, the angle read from Beeston's (1973) curves is the value of the tilt angle in the plus or minus direction from the initial position. This angle, shown in Fig. 1 as θ, is designated as the stereo tilt angle.

Equation (5) is an approximation based on the assumption of parallel projection. Although this assumption rarely is strictly correct, it is sufficient for qualitative observation of stereo pairs. The error due to the beam's formation of an

image by perspective projection has been pointed out by a number of workers (see Chapter 2 for a general discussion, and Part II of this volume for a detailed discussion and references).

III. Display of Stereo Micrographs

The advantage of stereo imaging can be easily lost if the micrographs are not mounted, aligned, masked, and trimmed with care. The two micrographs should be trimmed or masked so that no details appear in one, but not in the other. This establishes the stereo window (Anderson, 1966; Mohr and Wray, 1975, 1976), which defines the three-dimensional field of view and provides a sharp definition of its edge. Otherwise a blurred edge will make the images hard to fuse, causing eyestrain in the observer as well as loss of information.

The two micrographs must also be accurately aligned with respect to each other in the x and y directions, with the parallax direction from left to right, corresponding to the positions of the human eyes. Any y (vertical) displacement makes the pair hard to fuse, so corresponding images of the same detail must be on a horizontal line.

The observed depth in a stereo image can make objects appear either to recede away from or to come up toward the observer. This effect, which is governed primarily by the choice of which micrograph is presented to which eye, is usually reversible by interchanging the micrograph-eye combination (Anderson, 1966). If the object has distinct edges and is fully within the stereo window, the micrographs are generally best positioned so that the object appears to be coming up toward the observer, much like looking at a glass on a table top. This orientation works well for whole-cell or chromosome mounts. If, however, the object detail is limited by the stereo window, the micrographs are better oriented as if the observer were viewing a scene through a window. In this way, the stereo window appears to cut off the image detail, similar to a normal window limiting an outdoor scene viewed in everyday life. If the stereo window is placed behind the image, the details appear to end abruptly, as if one were looking at a transparent cube of material. Thus, sectioned material is usually best presented with the stereo window in front. Both types of presentation are discussed in later chapters, and the reader may wish to attempt to reverse some of them by interchanging the micrograph-eye combination. This reversibility is a highly individual effect and is sometimes prevented by strong visual clues. Good examples of nonreversibility are Haanstra's (1966) Figs. 6 and 7. For general references, see Thomas *et al.* (1974), Boyde (1974), Mohr and Wray (1976), Ledbetter *et al.* (1977), and Peachey (1978).

A. Prints

There are two common methods for presentation of photographically printed stereo images. The most frequently used is to mount the prints side by side, with the parallax axis horizontal. If the pair is to be viewed with the unaided eye or with a pocket viewer having two lenses spaced at the observer's interocular distance, the prints must be mounted with their centers ~65 mm apart (Peachey, 1978). (Some publishers specify 62.5 mm.) This spacing results in a total figure width of ~130 mm, which is easy to print horizontally on a standard page and is also easy to fuse visually. The vertical dimension, perpendicular to the parallax direction, should be approximately equal to the width of a single micrograph, or ~65 mm, for comfortable viewing.

If the prints are to be viewed with a folding-mirror stereoscope, which is merely an optical device for enlarging the effective interocular distance, the print size can vary considerably, and large prints are easily handled. However, the total viewing magnification—that is, microscope magnification × printing magnification × viewer magnification—cannot be larger than the value of M_T used in Eq. (5) to calculate the stereo tilt angle at which the original negatives were recorded. Values four times as large are often usable, but eight times is difficult. However, the eye-brain combination is amazingly adaptable in its integrative capacity, which allows stereo images to be viewed over a wide range of the recording and viewing parameters.

The second most common method of presenting stereo prints is by the anaglyph method, which uses color to distinguish the two images of the stereo pair. One image is printed in one color, and the second image is printed over the first in a different color. The resultant print is viewed with color filters (one over each eye), which are matched so that they transmit only one color and one image. Ledbetter *et al.* (1977) give a detailed description of the photographic process and the necessary filters. Other workers have also used anaglyphic methods, and some have used different colors (see, for example, Haanstra, 1966; Nemanic, 1972, 1974; Howell, 1975).

A third, less common method is the Nesch vertical system described by Nemanic (1974), in which the prints are mounted one above the other, but with the parallax direction still horizontal. A pair of prisms mounted on a transparent holder optically deflects the image of one print to one eye and the image of the other print to the second eye. This method allows almost any size print to be used with a simple and portable optical device and thus is particularly good for poster displays.

B. Slides

Stereo slides are usually projected either with polarized light or with the color anaglyphic system. In the first method the two slides are prealigned, illuminated

by individual polarized-light sources, and projected through individual lenses onto a screen. The two illumination systems are polarized at right angles to each other. The observer wears glasses with a polarizer over each eye, and because the plane of polarization of either polarizer coincides with the plane of polarization of the polarizers in the dual illumination system of the projector, each eye receives one and only one of the images constituting the stereo pair. Either a silver or a lenticular screen must be used to prevent depolarization of the projected light. This projection system can be used with a commercial dual-system stereo projector (Anderson, 1966; Thomas and Lentz, 1972; Thomas *et al.*, 1974) or with two conventional projectors (Peachey, 1978; and Heuser, this text). Alignment of the stereo pair is critical, as for the stereo prints discussed above. Mohr and Wray (1975, 1976), Peachey (1978), Fotino (1979), and Heuser (Chapter 6 in this volume) discuss this in detail.

The anaglyphic procedure requires that the two images be photographically reproduced on the same color transparency, with one color used for each image. The single transparency is then projected onto any type of screen with a standard projector. The observer views the image through color-matched glasses. This method is described in detail by Ledbetter *et al.* (1977), Nemanic (1972, 1974), and Howell (1975).

C. Transparent versus Opaque Objects

Most objects viewed in the TEM are transparent in that they are penetrable by the electron beam. Some object details may overlap, but they do not totally obscure each other. Objects of this type are not generally encountered in everyday life, where an observer receives his stereo training and experience. Stereo pairs taken in the TEM have the advantage of producing the stereo effect entirely by parallax, thereby eliminating sources of false depth impression. However, since stereo images of this type represent a volume and not merely surfaces of opaque objects obscuring other objects behind them, they lack perspective information present in most scenes observed in everyday life.

On the other hand, scanning electron microscope (SEM) images have strong perspective as well as shadowing effects because the SEM images a surface and not a volume. Thus, SEM images resemble scenes viewed in everyday life; single SEM images give the illusion of depth information due to the strong visual clues created by perspective and shadowing. However, this mono-image impression of depth can often be misleading, and stereo is necessary to visualize the true surface structure. An analogous situation occurs in TEM samples that are heavily shadowed, such as replicas of surfaces. Because of the large differences in electron scattering of shadowed and nonshadowed areas, the strong visual clues present a pseudo-stereo appearance. Heuser discusses this in more detail in Chapter 6.

References

Anderson, T. F. (1950). *J. Appl. Phys.* **21,** 724.

Anderson, T. F. (1951). *Trans. N.Y. Acad. Sci.* [2] **13,** 130-134.

Anderson, T. F. (1952). *Am. Nat.* **86,** 91-99.

Anderson, T. F. (1953a). *Cold Spring Harbor Symp. Quant. Biol.* **18,** 197-203.

Anderson, T. F. (1953b). *Ann. Inst. Pasteur, Paris* **84,** 1-10.

Anderson, T. F. (1953c). *Proc. Int. Conf. Electron Microsc. 1st, 1950* pp. 567-576.

Anderson, T. F. (1953d). *Proc. Int. Conf. Electron Microsc., 1st, 1950* pp. 577-585.

Anderson, T. F. (1956). *Proc. Int. Conf. Electron Microsc., 3rd, 1954* pp. 122-129.

Anderson, T. F. (1957). *Bull. Microsc. Appl.* **7,** 21-23.

Anderson, T. F. (1966). *Phys. Tech. Biol. Res.* **3A,** 319-387.

Anderson, T. F., and Oster, C. F. (1956) *Proc. Int. Conf. Electron Microsc., 3rd, 1954* pp. 333-335.

Anderson, T. F., and Richards, A. G. (1942). *J. Appl. Phys.* **13,** 748-758.

Anderson, T. F., Wollman, E. L., and Jacob, F. (1957). *Ann. Inst. Pasteur, Paris* **93,** 450-453.

Anderson, T. F., Preer, J. R., Preer, J. B., and Bray, M. (1964). *J. Microsc. (Paris)* **3,** 395-402.

Beeston, B. E. P. (1973). *J. Microsc. (Oxford)* **98,** 402-416.

Boyde, A. (1974). *In* "Scanning Electron Microscopy" (by O. C. Wells), pp. 277-307. McGraw-Hill, New York.

Coman, D. R., and Anderson, T. F. (1955). *Cancer Res.* **15,** 541-543.

Eitel, W., and Gotthardt, E. (1940). *Naturwissenschaften* **28,** 367.

Fotino, M. (1979). *Proc. 37th Annu. Meet. Electron Microsc. Soc. Am.* pp. 604-605.

Glauert, A. M. (1974). *J. Cell Biol.* **63,** 717-748.

Gotthardt, E. (1942). *Z. Phy.* **118,** 714-417.

Gray, E. G., and Willis, R. A. (1968). *J. Cell Sci.* **3,** 309-326.

Haanstra, H. B. (1966). *Philips Tech. Rev.* **27,** 231-237.

Heidenreich, R. D. (1943). *J. Appl. Phys.* **14,** 312-320.

Heidenreich, R. D., and Matheson, L. A. (1944). *J. Apply. Phys.* **15,** 423-435.

Howell, P. G. T. (1975). *In* "Scanning Electron Microscopy/1975" (O. Johari, ed.), pp. 697-706. IIT Res. Inst., Chicago, Illinois.

Hudson, B., and Makin, M. J. (1970). *J. Phys. E* **3,** 311.

Kelly, D. E. (1966). *J. Cell Biol.* **38,** 51-72.

Kelly, D. E. (1967). *J. Cell Biol.* **34,** 827-840.

King, M. V., Parsons, D. F., Turner, J. N., Chang, B. B., and Ratkowski, A. J. (1980). *Cell Biophys.* **2,** 1-98.

Ledbetter, M. C., Geisbusch, W. J., McKinney, W. R., and Woods, P. S. (1977). *EMSA Bull.* **7,** No. 2, 9-15.

Little, K. (1958a). *J. Microsc. (Oxford)* **78,** 53-47.

Little, K. (1958b). *J. Microsc. (Oxford)* **78,** 58-66.

Marton, L. (1944). *J. Appl. Phys.* **15,** 726-727.

Mohr, D., and Wray, G. (1975). *Proc. 33rd Annu. Meet. Electron Microse. Soc. Am.* pp. 668-669.

Mohr, D., and Wray, G. (1976). *Ultramicroscopy* **1,** 181-186.

Nemanic, M. (1972). *Proc. 30 Annu. Electron Microse. Soc. Am.* pp. 412-413.

Nemanic, M. (1974). *In* "Principles and Techniques of Scanning Electron Microscopy" (M. A. Hayat, ed.), Vol. 1, pp. 135-148. Van Nostrand-Reinhold, Princeton, New Jersey.

Peachey, L. D. (1978). *EMSA Bull.* **8,** No. 1, 15-21.

Richards, A. G., and Anderson, T. F. (1942). *J. N. Y. Entomol. Soc.* **50,** 147-167.

Shalla, T. A., Carroll, T. W., and DeZoeten, G. A. (1964). *Stain Technol.* **39,** 257-265.

Thomas, L. E., and Lentz, S. (1972). *EMSA Bull.* **2,** No. 2, 10-15.

Thomas, L. E., Lentz, S., and Fisher, R. M. (1974). *In* "High Voltage Electron Microscopy" (P. R. Swann, C. J. Humphreys, and M. J. Goringe, eds.), pp. 255–259. Academic Press, New York.
von Ardenne, M. (1940a). "Electronen-Ubermikroskopie." Springer-Verlag, Berlin and New York.
von Ardenne, M. (1940b). *Naturwissenschaften* **28,** 248–252.
von Ardenne, M. (1940c). *Z. Phys.* **115,** 339–368.
von Müller, H. O. (1942). *Kolloid-Z.* **99,** 6–28.
Williams, R. C., and Kallmann, F. (1955). *J. Biophys. Biochem. Cytol.* **1,** 301–314.
Willis, R. A. (1972). Ph.D. Thesis, Cambridge University, Cambridge, England.

This Page Intentionally Left Blank

METHODS IN CELL BIOLOGY, VOLUME 22

Chapter 2

Theory of Stereopsis

MURRAY VERNON KING

Division of Laboratories and Research,
New York State Department of Health,
Albany, New York

I. Studies on Mechanisms of Stereopsis 13
II. Visual Cues That Induce Depth Perception 16
III. Limits on Allowable Parallax, Magnification Disparity, and Brightness Disparity . 17
IV. Variation within the Population of Stereo Perception 20
V. Simultaneous Processing of Stereo and Color Information 21
VI. Stereo Perception of Transparent versus Opaque Objects 23
VII. Consequences of Binocular Vision in the Presentation of Micrographs 24
A. Choice of Stereo Angle in Electron Microscopy 24
B. Special Situations in the High-Voltage Electron Microscope 25
C. Special Situations in the Scanning Electron Microscope 26
D. Role of the Pocket Stereo Viewer 27
E. Consequences of Neglect of Good Stereo Mounting Technique 29
F. Summarized Recommendations 29
References 30

I. Studies on Mechanisms of Stereopsis

We shall use the term stereopsis in the broad sense of three-dimensional vision of objects and scenes without further restriction of meaning. The existing knowledge of the mechanisms of human stereopsis is of interest to the electron microscopist as a body of information that can guide the design of experiments involving stereo imaging to gain optimal interpretability of spatial information by the observer. While refraining from a total overview of this field of research, we shall touch on several topics of greatest interest to electron microscopists and list some of the most pertinent monographs and articles.

Copyright © 1981 by Academic Press, Inc.
All rights of reproduction in any form reserved.
ISBN 0-12-564122-2

Two monographs on stereopsis are especially to be recommended. The monograph of Julesz (1971) has collected and discussed the results of a wide range of studies designed to reveal the mechanism of the depth-perception faculty of the human brain and offers a model that in turn has stimulated many studies. The monograph of Valyus (1962) has outlined much of the information of practical and theoretical importance on the depth-perception system and has treated many applications.

The monographs of Carr (1966), Ittelson (1960), and Ogle (1950) have treated a range of aspects of the theory of stereopsis, and the monographs on stereoscopic photography of Judge (1950), Linssen (1952), and McKay (1951) also provide theoretical background for their treatment of the topic. Willis (1971) has discussed a variety of topics in the theory of stereopsis especially pertinent to electron microscopy.

Among the original articles that have appeared on various topics concerned with stereopsis since the publication of the monographs of Valyus and Julesz, we list here, by categories, some of special interest:

Accommodation and depth perception: Harkness (1978).

Brain structure and mechanisms of stereopsis: Bishop (1979), Blakemore (1979), Clarke *et al.* (1979), Fischer and Poggio (1979), Pettigrew (1979), Poggio (1979), Ramachandran *et al.* (1977), Zeki (1979).

Color perception and stereopsis: Gregory (1979), Ikeda and Sagawa (1979), Nakashima and Ikeda (1978), Ramachandran and Gregory (1978), Ramachandran and Sriram (1972), Russell (1979).

Conference reports on stereopsis: Pettigrew (1978), Robertson (1978).

Development of depth perception: Yonas *et al.* (1978).

Disorders of stereopsis: Blake and Cormack (1979), Cowey and Porter (1979), Larson (1978), Reinecke (1979), Ruddock and Waterfield (1978).

Models of stereopsis and scene analysis: Marr (1977), Marr and Nishihara (1978), Marr and Poggio (1976, 1979), Nelson (1975, 1977), Sutherland (1979), Trehub (1978), von der Heydt *et al.* (1977).

Motion and depth perception: Anstis (1977), Fox *et al.* (1978), Fremlin (1972), Ramachandran (1975), Regan *et al.* (1979), Regan and Beverley (1979), Shepard and Judd (1976), Ullman (1979).

Psychological experiments on depth perception: Blake and Camisa (1978), Cohn and Lasley (1976), Fox *et al.* (1977), Pepper *et al.* (1978), Ramachandran (1976), Semmlow and Wetzel (1979), Skrandies *et al.* (1979), Tilton (1978), Williams and Weisstein (1978).

Texture and depth perception: Braddick (1979), Burt *et al.* (1978), Kidd *et al.* (1979), Kulikowski (1978), Legge (1979), Mayhew and Frisby (1976), Ramachandran *et al.* (1973).

The view of the stereoptic mechanism that has emerged is one of a cerebral system for analyzing spatial information by integrating a wide variety of both binocular and monocular cues existing in the images seen by the two eyes. Its most potent source of depth cues is the disparity of positions of details (parallax) in the two images, although many other features such as perspective and motion of objects in the scene also contribute greatly (to be discussed in Section II). Interestingly, the impression of depth in a scene remains similar in character, regardless of the type of cues that the visual system extracts to generate it.

The role of left-right positional disparities will be central to much of our discussion, both because of the intrinsically large part they play in stereopsis and because they constitute the only type of depth information present in many electron microscopic situations, especially in the viewing of micrographs of tissue sections taken in the transmission electron microscope. We must point out that left-right image disparities of various types play a multiple role in contributing not only to depth perception but also to other perceptual phenomena such as recognition of luster and direction of illumination of objects. They can also impede stereopsis by leading to suppression of one image to favor the other, or to binocular rivalry, in which vision of the two retinal images alternates.

Familiar contours of objects, although undoubtedly contributing to stereopsis, are not at all necessary to it. This feature is of value in allowing depth perception of a wide range of unfamiliar objects, and it has been brilliantly demonstrated by the experiments of Julesz (1964, 1971). He has constructed pairs of random-dot patterns in which neither image yields any depth impression singly, although the pattern yields a striking impression of depth when viewed as a stereo pair. These studies have constituted the major proof that full depth perception can be generated by parallax alone.

A feature of stereopsis, which Julesz (1971) calls *global stereopsis,* is that the visual system always attempts to organize the perceived scene into *objects,* which amount to a consistent set of continuous, opaque surfaces with only local discontinuities. Surfaces are perceived as transparent only when no such interpretation can be made. However, our familiarity with transparent objects shows that the latter situation is far from rare in everyday experience.

The notion of the human visual system as possessing an image-processing computing network for extracting depth information has gained in attractiveness from the studies of Marr and Poggio (1976, 1979). They have devised a computer program for extracting depth information from random-dot stereograms by simulating the global-stereopsis feature of the visual system. Their program successfully solves the problem of false targets (false matching of points in the right and left images) and can analyze scenes of increasing complexity with results correlating with those of a human observer. Some salient features of the program are used to infer a model of the visual system. These include the

important role of a dynamic memory (which the authors call the 2½-D sketch) in which partial matches are stored, together with an active role of simulated vergence movements in creating matches.

II. Visual Cues That Induce Depth Perception

The range of highly varied cues that can induce depth perception while one views natural scenes includes the following:

1. Positional disparities between left and right images (parallax).
2. Motion of objects in the scene.
3. Linear perspective (apparent convergence of parallel lines).
4. Aerial perspective (progressive loss of contrast with distance caused by scattering of light by the atmosphere).
5. Obscuration of contours of remote objects by closer objects.
6. Light and shade (which allow inferences concerning the relations between shapes of objects and the illumination).
7. Shape of objects.
8. Size of objects.
9. Color (the so-called advancing and receding colors).
10. Brightness of objects (also involved with inferences about the illumination).
11. Position in the field (the lower field in a natural scene is assumed to be the foreground).
12. Accommodation of the lens of the eye (focusing on near and distant objects).
13. Vergence movements (convergence and divergence) of the eyes.

Since parallax is always the major factor and in many applications the only factor figuring in stereo electron microscopy, the most effective exploitation of this factor has been the key to design of effective stereo methods in electron microscopy. In viewing such objects as tissue sections in the electron microscope, parallax obtained by tilting the specimen between micrographs reveals authentic depth information, whereas intrusion of other effects only distracts. An example of a false impression yielded by collateral depth cues (Mohr and Wray, 1976) is that of a highly electron-dense object lying behind a more transparent detail in a section. Since the image of the dark object obscures that of the lighter object, it is falsely perceived as lying in front.

Yet the vividness of depth effects arising from nonparallax sources can often approach that arising from parallax, especially when depth perception stems from motion. Anstis (1977) has indeed speculated that the stereoscopic sense has

evolved biologically from the brain mechanism for motion detection. Motion effects have been exploited successfully in television computer displays of structural models of molecules to impart a vivid sense of depth to the observer (Katz and Levinthal, 1972). However, motion has not yet been tested as an auxiliary tool for revealing three-dimensional information in electron micrographs. Perhaps this could be done by recording an extended tilt series of a specimen in the electron microscope and displaying it as a motion picture while alternately running through the series in forward and reverse order to create the illusion that the object is being oscillated in the field of view.

Cues from shading and shape exist in micrographs taken of shadowed specimens or those taken in the scanning electron microscope. They lend an impression of depth to these micrographs, even in monocular viewing. On occasion this impression is illusory, because the stereo effect arising from shading dominates the entire scene. Thus, stereo viewing of shadowed, freeze-etched replicas (Hess and Allen, 1978; see also Heuser, Chapter 6 in this volume) reveals an accurate impression of the great depth of these specimens as the fracture plane jumps from one membrane surface to the next, whereas monocular viewing offers only an impression of shallow relief.

Since the aim of stereo electron micrography is to decipher the overlapped structural information in electron micrographs of specimens having some depth, it is pertinent to consider this technique as a special case of the general problem of pattern recognition. The electron microscopist's task is to make comprehensible an image when viewed as a three-dimensional scene that eludes interpretation in two-dimensional projection. Toward this aim, it is expedient to supplement the optimization of the stereo technique proper with other aids to pattern recognition that involve physical or chemical insertion of reference points into the specimen. Special staining methods can be used as a tool for decorating minority constituents of a tissue with electron-dense deposits (Yamada and Ishikawa, Chapter 7 in this volume; Yamada *et al.*, 1976; Peachey, 1978). Such markers in the field provide a strong aid in organizing the pattern to be deciphered, in facilitating stereo fusion by the observer, and in offering reference points for appreciating the spatial relationships of the remaining, undecorated tissue constituents.

III. Limits on Allowable Parallax, Magnification Disparity, and Brightness Disparity

The maximum parallax in stereo pairs that will allow fusion accompanied by depth perception is governed by some remarkable features of the visual system. Panum (1858) showed that the two retinal images fuse into a single perceived image under quite general conditions when corresponding points in the retinal

images are brought within a disk subtending an angle of 6′ (termed *Panum's fusional area*). Yet at a normal reading distance of 250 mm, that amounts to a shift of only about 0.44 mm, whereas much larger disparities are actually handled easily. Some of the phenomena that allow this are discussed by Julesz (1971) in summarizing the results obtained by various investigators. The key feature is that, when corresponding points have once been brought within Panum's fusional area, subsequent movements of the eyes over considerably larger angles fail to split the perceived image into two. When breakaway finally occurs, then the images must be returned within the fusional limit for stereopsis to resume. This feature allows an observer successively to examine features at different depths in a scene without losing single vision of the features first examined.

The limiting angular disparities for breakaway and refusion prove to depend critically on the character of the object being examined and on their direction relative to the vector joining the observer's eyes, which we take as the horizontal axis. For random-dot stereograms, breakaway occurred only at a horizontal angular disparity Δx of 2°, whereas refusion occurred at Panum's classical limit of 6′. In contrast, patterns of vertical line targets showed breakaway at 65′ disparity and refusion at 42′ disparity. Kulikowski (1978) has demonstrated that the limit of single vision in stereopsis depends on the contour sharpness by comparing sinusoidal with square-wave gratings. Burt *et al.* (1978) have similarly shown with random-dot stereograms that the stereoptic range is proportional to the coarseness of the texture. These phenomena help to explain why the presence of a few well-spaced details of high contrast in a stereo pair always facilitates stereopsis of the rest of the scene.

Experiments on the corresponding allowable vertical disparity Δy showed breakaway at 20′ and refusion at 6′ disparity. Interestingly, Δy disparities within the fusion limit do not normally contribute to depth perception as Δx disparities do. They are often ignored, especially if confined to local details, although they can give rise to some unusual perceptual phenomena not easily explained by simple geometric analysis of stereopsis (Ogle, 1950).

Vertical disparities are of concern in the problems of viewing misaligned stereo pairs, in which vertical as well as horizontal shifts of image details are expected. Vertical disparities can also arise if the two images are taken at slightly different magnifications, or in recording of mock-stereo pairs (see Chapter 8). Julesz (1971) states that the maximum difference in magnification allowable in a stereo pair is in the vicinity of 15%, but the limit depends considerably on the type of image being viewed. He has illustrated this with stereo pairs showing this disparity in magnification, some of which can be easily fused and others not at all. The visual impression that these stereograms yield when fused is a general tilt of the field that arises from the Δx disparities, while the visual system ignores the corresponding Δy disparities.

The limit on the allowable vertical disparity Δy is an important factor in stereo electron microscopy because most electron microscopes produce rotated images. Thus, the direction of the tilt axis is often not obvious in stereo micrographs, unlike stereo pairs of natural scenes. This can give rise to errors in orienting the paired images in mounting.

Another phenomenon is pertinent to the viewing of electron microscopic stereo pairs and especially of mock-stereo images (see Chapter 8). Many types of images (but not random-dot stereograms) show a phenomenon in which excessive disparities cause the object to be perceived as double, although it is still perceived as existing in depth [Julesz, 1971, pp. 23, 145, 150; see also Braddick (1979) on the dissociation of stereopsis and single vision]. This phenomenon, termed *patent stereopsis,* allows depth perception to be preserved when corresponding details in the two images differ considerably in shape. Mayhew and Frisby (1976) have shown that stereopsis can be obtained that involves only the coarse features of a stereo pair while the fine texture is completely rivalrous. This phenomenon is important in combating the effects of graininess and image distortion in electron microscopy, especially at high primary magnifications or high enlargements. Aschenbrenner (1954) has pointed out that this feature of stereo vision allows detection of details in stereo aerial photographs that cannot be seen in either of the images singly.

In the light of the estimates of the disparity limit for stereopsis, we note that Hudson and Makin (1970) suggest a maximum allowable parallax of 5 mm in prints to be viewed at a 250-mm distance, while adopting a preferred parallax of 3.5 mm as a basis for designing charts for choosing the optimal stereo angle for pairs taken in the electron microscope. The latter parallax amounts to a subtended angle of 0.80°, which is well within the breakaway limit for random-dot stereograms. Adoption of an angle near the limit generally yields the maximal number of separately discernible image planes in the stereo display (see Section IV). Thus, when taking micrographs of ultrathin specimens, one can employ enormous stereo angles to boost the stereoscopic effect and to attain resolution in depth of the maximum number of specimen planes.

Peachey (1978) has adopted a limiting parallax of 5% of the picture width, which amounts to 3 mm in stereo pairs of prints 60 mm wide.

A different situation exists whenever one wants to display a specimen as a stereo pair in a way that will preserve the natural ratio of perceived depth to perceived dimensions in the scene. This procedure, which is called *orthostereoscopy,* has been discussed in detail by Valyus (1962, pp. 376-385) and also by Hyzer (1978). It involves matching the ratios of the scales in the viewing space of the observer to those existing in the object space during the original preparation of the stereo views. This ensures that the depth information conveyed by perspective and by vergence movements coincides with that conveyed by parallax.

Ideally, the lenses in the stereoscope should have focal lengths that make the depth information conveyed by accommodation coincide as well. As Valyus points out, orthostereoscopy can be achieved under the conditions of viewing in a common stereoscope, but when stereo images are displayed by projection on a screen, at most one spectator in the audience can view them orthostereoscopically, while all others will receive a view distorted in its ratios between the depth dimension and the lateral dimensions.

The effects of brightness disparity can be quite striking; they depend greatly on whether the disparities exist globally over the field or in local areas. In viewing natural scenes, local brightness disparities between the retinal images are major cues for inferring luster of objects and direction of illumination (Valyus, 1962, pp. 53-54). Overall field brightness disparities have been of considerable interest in giving rise to striking optical illusions in viewing moving objects (the Pulfrich phenomenon: see Julesz, 1971, pp. 252-255).

Generally, both vertical positional disparities and brightness disparities should be minimized as distractions in the preparation of stereo electron micrographs. Caution is needed, not only to identify the direction of the tilt axis in the micrographs, but also to ensure that the two images of the stereo pair represent material taken at a comparable level of beam damage, using equal exposures. Owing to the inevitable alteration of biological specimens in the beam, either both exposures should be taken within a radiation threshold that has been judged to be allowable, or the beam should be played on the specimen until charring is complete before taking the exposures.

In contrast, the mock-stereo methods (discussed in Chapter 8) are based on deliberate production of brightness and positional disparities (both Δx and Δy).

IV. Variation within the Population of Stereo Perception

Stereoscopic acuity can be defined as the minimum angular parallax that an individual can discern. This ability varies widely, both among the population and among different viewing situations for a given person. Valyus (1962, pp. 42-45) has treated the subject and presented a series of graphs. One of these shows the distribution of stereoscopic acuity for a sample of 106 subjects. Interestingly, although stereoscopic acuity is often assumed to be about 30″ of angle, most of the subjects performed much better, with a mode of about 5″ and a median of about 10″. The distribution shows a long tail representing a minority of relatively stereo-blind observers. He also presents graphs of the variation of stereoscopic acuity for a single observer as functions of the illumination intensity, brightness of the object, and observation time. Acuity falls off steeply with dim illumina-

tion, faint object, or brief observation time. The optimal range of object brightness was from 0.41 to 38 candela/m^2, with acuity falling off on either side.

Valyus proceeds to relate stereoscopic acuity to the threshold distance Δd_0 between planes barely distinguishable in depth, and derives the equation

$$\Delta d_0 = d^2 \cdot \Delta\theta_0/(b - d \cdot \Delta S_0)$$

Here d is the viewing range of the object, b is the interocular spacing, and ΔS_0 is the stereoscopic acuity. If we assume $b = 65$ mm and $\Delta S_0 = 10'' = 4.85 \times 10^{-5}$ radian, we find that stereopsis is lost for objects farther than 1340 meters, whereas at a normal reading distance of 250 mm, planes spaced only 47 μm apart can be distinguished in depth.

Yonas *et al.* (1978) have shown that depth perception normally develops in infants between 22 and 26 weeks of age.

Stereo blindness has been discussed by Blake and Cormack (1979), Larson (1978), Reinecke (1979), and Ruddock and Waterfield (1978). In discussing public-health aspects of stereopsis, Larson has touched on occupational problems of defective stereopsis, causes of and tests for stereo blindness, and methods of improving stereopsis. Interestingly, he points out that stereopsis plays a substantial role in night vision, since stereoscopic acuity does not fall off as rapidly in dim illumination as visual acuity does.

V. Simultaneous Processing of Stereo and Color Information

The effectiveness of combining stereo and color information in a single display is revealed by the success of the common method of displaying stereoscopic pictures as anaglyphs, in which the image seen by one eye is printed in red and that seen by the other in green in overlapping positions. The scene is viewed with a red color filter over one eye and a green filter over the other, so that each eye sees only one image of the pair. [See Ledbetter *et al.* (1977) for a discussion of anaglyphic display of electron micrographs.] A similar technique is that of Padawer (1973), who inserts a light-colored filter over one lens of a stereo viewer in order to color-code the two images to facilitate alignment.

The observed phenomena become more complicated and somewhat contradictory when color disparities become an integral part of the paired scenes, rather than a coding aid for appreciating the parallax disparities. Studies by Ramachandran and his associates have revealed some of this complexity. Ramachandran and Sriram (1972) showed that random-dot stereograms can yield stereopsis in spite of binocular color rivalry caused by presenting a pattern printed in red to one eye and one in green to the other. The fused field looked alternately red or

green rather than fusing to yellow. This contrasts strikingly with the impression that most observers report from viewing anaglyphs, where the fused field looks white or pale yellow. Yet the results of Ramachandran and Sriram indicate that stereopsis persists even in the presence of color rivalry, whereby they postulate separate channels for stereo and color information.

The present author has repeated one of the experiments of Ramachandran and Sriram of inspecting black/white random-dot stereograms with a stereo viewer with a red filter over one lens and a green filter over the other; the results confirm the persistence of binocular rivalry, even long after stereopsis is achieved. Interestingly, one observer reported shifting areas of fused color (white) within the random-dot area, which soon reverted to red or green; the other saw a stable fused color (yellow) only in the surround, as Ramachandran and Sriram had reported.

Ramachandran *et al.* (1973) reported success in gaining stereopsis when an intensity contour was presented to one eye while a texture or color contour was presented to the other eye, and postulated a common processing center for texture, color, and intensity information. However, Ramachandran and Gregory (1978) have reported that the perception of motion in a bicolor display disappears when the two colors are made isoluminant. They view this as indicating that pure color information cannot be processed by the brain's motion detector. Also, Gregory (1979) reports that depth perception is lost at isoluminance. Nevertheless, Russell (1979) has presented evidence that depth perception can arise from disparities in the red-green channel.

Julesz (1971, pp. 30, 75) has discussed the wide range of ability of different observers to fuse different colors presented to the two eyes, and cited the case of von Helmholtz (1909), who could not perceive color fusion, although von Helmholtz had reviewed much of the early literature on binocular color mixture. Julesz (1971, p. 75) points out that the anaglyph technique successfully avoids the onset of binocular color rivalry and offers the experience of binocular color mixing to those who otherwise cannot experience it.

Nakashima and Ikeda (1978) and Ikeda and Sagawa (1979) have studied the limits of binocular color fusion and found that the wavelengths of the light presented to the two eyes must not differ unduly. This observation directly contradicts the success of the anaglyph technique, in which widely differing colors are obligatory in order to allow printing with two pigments that reflect light passed selectively by the two color filters. Their experience also contrasts with the success of the present author with the mock-stereo-color technique (see Chapter 8), although it fits with the results of Ramachandran and Sriram (1972). Perhaps this contrast shows a predominant role of the intensity patterns seen by the two eyes. Studies of the character of patterns that will induce binocular color fusion would be of great interest in clarifying the question of how far color-fusion methods can be pushed for the normal observer.

VI. Stereo Perception of Transparent versus Opaque Objects

A consequence of the model of global stereopsis of Julesz (1971) that has been discussed further by Nelson (1975) is that the visual system weights the odds in favor of perceiving scenes as consisting of opaque surfaces. Details are perceived as being embedded in depth in a transparent matrix only when the visual system can find no interpretation of the scene consistent with opaque surfaces.

However, a salient feature that distinguishes stereo pairs taken in a transmission electron microscope (TEM) from most natural scenes and from the bulk of test scenes designed for psychological studies of stereopsis is that the images of objects examined in the TEM consist of parallel projections of specimen details overlapping in depth, instead of lying on opaque surfaces that obscure more remote details. That is, we must view TEM specimens as transparent objects that suffer from the added problem that the details are not even confined to a small set of planes, but are distributed throughout the depth of the specimen.

An essential advantage of stereo recording, especially in examining the thicker sections that are allowed by the high-voltage electron microscope (HVEM), is that depth perception often successfully deciphers spatial relationships of overlapped specimen details, in spite of the preference of the human visual system for opaque scenes. Yet limits exist on the amount of overlapped information that the stereoptic mechanism can handle, especially when details are not confined to a small set of planes. Studies to ascertain these limits would be of great practical value in guiding the design of experiments in stereo electron microscopy.

An elementary illustration of the power of stereopsis in simplifying perception of a transparent scene is that two skew lines are both seen as continuous and not intersecting. The facility of tracing skew lines is an important feature in grasping the course of filaments in stereo micrographs of cells. Spatial distributions of granular aggregates are also correctly perceived up to a certain limiting overlap.

Although no critical experiments have been done on the maximum amount of stereo information that can be correctly interpreted in an experimentally devised transparent scene, it is interesting to examine a few of the stereograms of Julesz (1971) that give the illusion of transparency. Most of his random-dot stereograms yield a quite solid impression of patterns printed on a set of opaque planes, yet his Fig. 5.7-1 (1971, pp. 167, 343) shows a set of dots interspersed among three seemingly transparent planes. His Fig. 6.3-2 (1971, pp. 201, 348) shows dots lying on two intersecting transparent ellipsoidal surfaces—a situation not unlike that observed in some electron micrographs. In both of these stereograms the dots lying on the different surfaces are closely intermingled in a way that prevents their being perceived as belonging to a single corrugated surface. Julesz points out that considerable time must be taken to achieve stereopsis with the latter figure, in close parallel with the persistence often required in viewing stereo electron micrographs containing densely overlapped details.

Problems of this type in stereo electron microscopy give special emphasis to techniques that enhance the contrast of minority constituents of cells and tissues, such as enzyme cytochemistry, immunocytochemistry, and other selective staining techniques (see Yamada and Ishikawa, Chapter 7 in this volume; Yamada *et al.*, 1976; Peachey, 1978).

The situation is quite different in stereo electron microscopic examination of shadowed replicas (Heuser, Chapter 6 in this volume) and in stereo scanning electron microscopy (Porter and Stearns, Chapter 4 in this volume). Here, even when objects are transparent or semitransparent in the electron-optical sense, significant specimen details are commonly confined to a single curved surface without overlap. Thus, the visual system accepts the image as representing an opaque object.

VII. Consequences of Binocular Vision in the Presentation of Micrographs

A. Choice of Stereo Angle in Electron Microscopy

The design of stereo electron micrographs involves choosing the optimal stereo angle that would yield stereo pairs from which depth information can be most readily extracted. Increase of parallax to the maximum consistent with stereo fusion allows the visual system to distinguish as many planes in depth as possible. Yet it is also advantageous to create a scene of natural appearance that resembles the original object in proportions between the depth and lateral dimensions. Unless scaling criteria are met, these demands are mutually contradictory. Most often in electron microscopy it pays to allow deliberate stretching of the depth dimension in the interest of enhancing the observer's grasp of mutual depth relations of details.

If, nevertheless, we wish to apply orthostereoscopy, we face another interfering factor in that the object is imaged in the electron microscope as though viewed from a distance equal to the focal length of the objective lens. The focal length of a typical transmission electron microscope (TEM) exceeds the specimen thickness by a factor of 10^4 or more. In such a viewing situation, stereopsis hardly comes into play. Moreover, each micrograph amounts effectively to an orthographic rather than a perspective projection of the specimen.

Therefore, we cannot impose true orthostereoscopic scaling in stereo transmission electron microscopy. The most that we can do is to choose a combination of working parameters that will allow optimal depth discrimination while maintaining an optimal proportion between the lateral and depth scales of distance. Since the latter can be adjusted by varying the viewing distance in the stereoscope (as

will be explained in Section VII,D), the best policy seems to be to adopt the stereo angle that yields the desired maximum parallax without concern for orthostereoscopy. Then the stereo viewer (or mirror stereoscope) bears the entire burden of adjusting the perceived proportions of the depth and lateral scales. One can also adjust the convergence of the eyes by shifting the micrographs to yield a natural viewing situation that minimizes eyestrain, either in the initial mounting, or at any time when viewing separate 8 × 10-inch prints in the mirror stereoscope.

In stereo electron microscopy, as in other electron microscopic situations, a choice of primary magnification to optimize the trade-off between adequate resolution of significant details and sampling of an adequate area of the specimen takes precedence over any stereoscopic considerations. Therefore, the choice of stereo angle becomes the key factor in optimizing the range of parallax in the image. As mentioned, the charts of Hudson and Makin (1970) for quick determination of the appropriate stereo angle were based on an optimal parallax of 3.5 mm in images to be viewed at a distance of 250 mm. Inasmuch as Hudson and Makin employed aberrant terminology that could cause confusion (they used *tilt angle* in the sense that we have adopted for *stereo angle*), Beeston (1973) has redrawn Hudson and Makin's graph in terms of the stereo tilt angle, while adding separate magnification scales for use with the pocket stereo viewer and with the mirror stereoscope. Peachey (1978) proposed a maximum parallax of 5% of the picture width and presented a table of optimal tilt angles based on it.

Part of the confusion about recommended maximum parallaxes stems from the fact that different authors have based their recommendations on different viewing situations. Perhaps the best rule might be to follow Beeston in adopting an optimal angular parallax of 14 milliradians (0.80°) and then choosing the optimal stereo angle with a specific viewing situation in mind. This angle will differ for micrographs intended for viewing with a pocket stereo viewer or a mirror stereoscope, or by an observer employing no optical aids.

A further factor that can influence the choice of optimal stereo angle is the complexity of the images to be fused. Simpler images allow wider angles. For example, micrographs taken in the scanning electron microscope (SEM) or those taken in the TEM from shadowed replicas do not possess the complication of overlap of transparent details in depth. Also, micrographs taken at very high magnifications are generally simpler in the character of the details that they present.

B. Special Situations in the High-Voltage Electron Microscope

Stereo electron micrographs taken in the high-voltage electron microscope (HVEM) are noted for their wealth of overlapping detail occasioned by the large specimen thicknesses (up to 3 μm) that the HVEM allows. In the HVEM, stereo

methods become the normal, routine way to take micrographs, rather than an occasional tool. Stereo fusion is harder to obtain with these micrographs, so that more attention must be paid to optimizing the parallax range as well as other features such as the stereo window. Both Beeston (1973) and Peachey (1978) have offered a range of suggestions.

In a few situations in the HVEM, orthostereoscopic scaling gains in value. An example is a set of stereo views taken from an extended tilt series by juxtaposing successive views as stereo pairs. Orthostereoscopic scaling then ensures consistency of apparent dimensions of details throughout the series. Here, also, further studies on optimization of viewing conditions would be valuable.

C. Special Situations in the Scanning Electron Microscope

Stereo display of images taken in the scanning electron microscope (SEM) faces a number of features that sharply distinguish the situation from that in the TEM. The SEM treats objects as being opaque, so that SEM pairs resemble normal scenes in providing easier fusion. However, the choice of right and left images becomes much more important in order to avoid depth reversal. At the same time, the SEM is not a parallel projection system (Howell and Boyde, 1972; see also Chapter 1 in this volume), but yields perspective views. Unlike the TEM, whose depth of field vastly exceeds the thickness of specimens, it has a depth of focus that can be varied and is often shorter than the depth of the scene.

Thus, the problem of interpreting stereo scanning electron micrographs is eased by the opacity of the scene, while depth cues from occlusion and perspective begin to play a role. Yet, stereo scanning electron micrographs contain other cues, such as the high level of shading of objects that yield depth impressions possibly conflicting with the valid cues of parallax, perspective, and occlusion. Shading of SEM images varies with the imaging mode (secondary electron, backscattering, x-ray) and depends on the physical details of how each of these images is generated. Since the shading generated by these mechanisms seldom simulates well the shading of a natural scene under directional illumination, strong but often inconsistent impressions of the direction of illumination arise in SEM pictures that can interfere with appreciation of depth relations. Greater attention to the proper choice of stereo window and of the ratio of the depth and lateral scales may help to minimize these distractions.

Transmission electron micrographs of shadowed specimens resemble scanning electron micrographs in that they appear opaque (Heuser, Chapter 6 in this volume; see also Section VI of this chapter), although they differ in most of the other discussed features. Especially, the process of shadowing creates a distribution of light and shade that more closely resembles a normal scene under directional illumination than is normally shown by scanning electron micrographs. A major pitfall remains in the tendency of this play of light and shade to dominate

the entire scene. This accounts for the markedly differing depth impressions that an observer gains from monocular versus stereo examination of micrographs of shadowed freeze-fractured replicas (Section II, this chapter). Again, careful attention to the stereo window is important, whereas concern with orthostereoscopy hinges largely on how important a natural ratio of the depth and lateral scales is for the scientific purposes of the stereo display.

D. Role of the Pocket Stereo Viewer

Some problems of technique of stereo electron microscopy hinge more on the nature of stereo vision than on the microscope. The best use of the pocket stereo viewer is an example. The initial assessment of stereo electron micrographs is most commonly made with a pocket stereo viewer. Even when they are later enlarged for detailed study in a mirror stereoscope, micrographs are usually judged first by examining either the original negatives or contact prints in a pocket viewer. Therefore, the effect of the design of this simple instrument on the visual impression that the observer perceives merits discussion. The pocket viewer possesses some potentialities in enhancing the observer's perception of stereo pairs beyond its commonly assumed function of facilitating stereo examination for observers who have difficulty in crossing their eyes.

The most common design of viewers has a frame that allows adjustment of the spacing between the lenses in a range of about 55–75 mm, with a fixed height of the lenses above the plane of the paper. One viewer in the possession of the present author has two lenses of focal length 126.5 mm mounted at a distance 114.9 mm above the plane of the paper. However, a viewer from a different supplier has lenses of focal length 113.8 mm mounted 113.6 mm above the paper. This difference illustrates the considerable variation in the optics of these instruments.

The relationship between the viewing distance from lenses to pictures and the focal length of lenses proves to have a strong effect on the observer's subjective impression of the mean distance of the perceived images. In turn, this strongly affects the perceived ratio of the distance scales in the depth and lateral dimensions, because the visual system interprets *relative angular parallax* of details in the left and right retinal images in terms of a judgment of the distance to the object.

The possible factors that could govern the perceived mean distance of a stereo display viewed through lenses include the physical distance of the plane of the virtual images of the stereo pair from the plane of the lenses, together with the spacing between the two views as mounted, and the spacing between the lenses of the viewer. Brief experimentation shows that the latter two factors have practically no effect on the perceived mean distance of the scene. Adjustments by

lateral shift of the two pictures or of the lenses greatly affect the comfort of using the stereo viewer—eyestrain is minimal when the images are viewed at a convergence that matches the perceived distance of the images while the lenses are spaced to minimize optical distortions. Yet, the judged distance to the scene is affected little if at all by these adjustments.

Experiments with shifting the pictures *toward and away from* the lenses suggest that the visual system accepts the optically defined distance to the virtual images of the stereo pair as being the mean distance of the display only when the former remains relatively short (within a few meters). This judgment stems primarily from motion parallax generated by head movements and perhaps to some extent from accommodation of the lenses of the eyes. However, as one shifts the pictures closer to the focal plane of the lenses, the virtual images recede to infinity. An unreal viewing situation is created, in which the perceived angular parallax can have no physical meaning. Now, experiment shows that the visual system follows its usual rule of making the best of a muddle—creating a consistent percept from inconsistent cues. When the virtual images are made to recede beyond a certain distance, the *perceived images no longer seem to recede*. Until this point has been reached, the perceived depth range of the stereo image seems to increase along with the perceived mean distance. Then it ceases to elongate when the recession of the virtual images is no longer perceived as such.

Thus, the perceived ratio of the scales of depth and lateral dimensions reaches a plateau at a certain viewing distance, and then the scene looks deepest. This viewing distance differs greatly from the one at which the visual system can distinguish the greatest number of planes in depth, which lies much closer to the observer. The question of the optimal viewing distance of a stereo viewer that a particular observer will accept as yielding the best stereo view remains completely open. It would seem that many stereo electron micrographs, although rich in depth information, do not nearly exhaust the capabilities of stereoscopic acuity of the normal observer for close-range viewing. It may not be necessary to position the stereo pair in a plane that yields virtual images near the normal reading distance from the eyes (250 mm) so as to make available the maximum number of distinguishable planes. Rather, viewing at a greater distance may serve better by enhancing the apparent total depth of the scene. The fact that one of the tested commercial pocket stereo viewers yields images at about four times the normal reading distance suggests that the observers find such an arrangement quite acceptable. Further studies of the optimal relation between focal length and viewing distance in pocket stereo viewers would be most valuable in order to optimize these simple devices.

Many of the factors that figure in pocket stereo viewers apply as well to mirror stereoscopes, but with the advantage that the latter instruments allow adjustment of the convergence of the eyes, the alignment of the stereo pair, and the focus of the eyepieces. Projection of stereo images for viewing by an audience faces additional problems. Orthostereoscopic scaling is out of the question.

E. Consequences of Neglect of Good Stereo Mounting Technique

The concept of the stereo window, which has been discussed by Mohr and Wray (1976) and by Peachey (1978), is of considerable value in creating effective displays. Discussion will be confined here to some examples in which violation of good technique in published micrographs has yielded illustrations that lose force because they tax the observer's capability for stereo fusion.

The paper of Hess and Allen (1978) offers examples of stereo displays that are difficult to examine, owing to neglect of the stereo-window principle, although otherwise presenting high-quality micrographs. They discuss in detail the importance of the choice of right- and left-hand images in mounting stereo pairs of shadowed freeze-fractured replicas to avoid inversion of front–back relationships. Yet they neglect the equally important question of the stereo window, and present micrographs having parallaxes of features with respect to the borders ranging up to 14 mm. An example is shown in their Fig. 12, which resists fusion!

Another common error in mounting stereo pairs lies in mounting the pair too far apart for convenient examination in a stereo viewer. The normal interocular spacing is 65 mm, but stereo viewers are built for adjustment around this value. Accordingly, pairs mounted on centers from 60 to 65 mm apart prove most convenient. In contrast, Coleman *et al.* (1978) have presented a series of stereo pairs at spacings from 76 to 78 mm. Although such displays usually resist fusing in a pocket stereo viewer, a trick may lead to success. One bends the center of the page between the images upward into a loop to bring the images within range for easy stereo fusion. When one has gained fusion, one then straightens the paper gradually. This often enables an observer to diverge his eyes by surprisingly great angles, and leads to ready fusion of images that would otherwise take several minutes of heavy staring at to achieve the same result.

F. Summarized Recommendations

1. *Stereo considerations should not govern the choice of the primary magnification in most electron microscopic techniques.* In most techniques and instruments (transparent versus opaque specimens, TEM, HVEM), the key purpose in the choice of magnification is to permit taking a scientifically meaningful sample of specimen details. Only in instruments such as the SEM that operate by perspective projection is the interplay between primary magnification and optimal stereo display an important consideration.

2. *The optimal stereo angle relating the images of a stereo pair is normally the value that makes maximal use of the depth-perception faculty while preserving fusion.* The choice of angle depends mostly on the character of the images being recorded. For images containing much overlapped detail (HVEM), it should yield a maximum parallax of 14 milliradians (0.80°) in the adopted viewing situation; higher values are allowed for simpler images or those that can be visualized as opaque surfaces (SEM, shadowed replicas).

3. *Good stereo mounting technique demands attention both to creating an effective stereo window and to spacing the images correctly.* Stereo micrographs for publication will probably be examined with a pocket stereo viewer by many readers. The micrographs should be submitted for publication exactly in the desired format for printing, as many journals are prepared to reproduce them on a 1:1 scale. They must be mounted on centers 60-65 mm apart with the edges carefully cropped to create a correctly positioned stereo window.

4. *The instruments employed to examine stereo pairs have potentialities for adjusting the perceived proportions between the depth and lateral distance scales that merit greater attention.* With the pocket stereo viewer, this adjustment can be made most simply by shimming up either the stereo pair or the viewer, whereas mirror stereoscopes are normally provided with means for focusing the eyepieces. Application of this technique should allow optimization of the observer's appreciation of depth relations, and may enable at least an approximation to orthostereoscopy whenever the latter is desirable.

5. *Aids to the observer in appreciating the ratio between the perceived lateral and depth distance scales may prove effective.* Since the norm in stereo electron microscopy is deliberate distortion of this ratio, any aid to the observer in appreciating this relationship should improve the interpretability of the stereo scene. Such an aid could be a fiducial figure introduced into both images of the stereo pair in the form of a stereo drawing of a cube or of a triaxial cross having specified dimensions, so that the fiducial figure will undergo the same distortions of perceived distance scales during stereo viewing as do the details of the image pair.

REFERENCES

Anstis, S. M. (1977). *J. Opt. Soc. Am.* **67,** 1399.
Aschenbrenner, C. M. (1954). *Photogramm. Eng.* **20,** 398-401.
Beeston, B. E. P. (1973). *J. Microsc. (Oxford)* **98,** 402-416.
Bishop, P. O. (1979). *Proc. R. Soc. London, Ser. B* **204,** 415-434.
Blake, R., and Camisa, J. (1978). *Science* **200,** 1497-1499.
Blake, R., and Cormack, R. H. (1979). *Science* **203,** 274-275.
Blakemore, C. (1979). *Proc. R. Soc. London, Ser. B* **204,** 477-484.
Braddick, O. J. (1979). *Proc. R. Soc. London, Ser. B* **204,** 503-512.
Burt, P., Sperling, G., and Julesz, B. (1978). *J. Opt. Soc. Am.* **68,** 1365.
Carr, H. A. (1966). "An Introduction to Space Perception." Hafner, New York.
Clarke, P. G. H., Ramachandran, V. S., and Whitteridge, D. (1979). *Proc. R. Soc. London, Ser. B* **204,** 455-465.
Cohn, T. E., and Lasley, D. J. (1976). *Science* **192,** 561-563.
Coleman, S. E., Duggan, J., Aldrich, H. C., and Hackett, R. L. (1978). *Micron* **9,** 127-132.
Cowey, A., and Porter, J. (1979). *Proc. R. Soc. London, Ser. B* **204,** 399-407.
Fischer, B., and Poggio, G. F. (1979). *Proc. R. Soc. London, Ser. B* **204,** 409-414.
Fox, R., Lehmkuhle, S. W., and Bush, R. C. (1977). *Science* **197,** 79-81.

Fox, R., Lehmkuhle, S., and Leguire, L. E. (1978). *Vision Res.* **18,** 1189-1192.
Fremlin, J. H. (1972). *Nature (London)* **238,** 406-407.
Gregory, R. L. (1979). *Proc. R. Soc. London, Ser. B* **204,** 467-476.
Harkness, L. (1978). *New Sci.* **80,** 773-775.
Hess, W. M., and Allen, J. V. (1978). *Norelco Rep.* **25,** No. 2, 26-33.
Howell, P. G. T., and Boyde, A. (1972). *In* "Scanning Electron Microscopy/1972" (O. Johari and I. Corvin, eds.), pp. 233-240. IIT Res. Inst., Chicago, Illinois.
Hudson, B., and Makin, M. J. (1970). *J. Phys. E* **3,** 311.
Hyzer, W. G. (1978). *Opt. Eng.* **17,** SR96-SR98.
Ikeda, M., and Sagawa, K. (1979). *J. Opt. Soc. Am.* **69,** 316-321.
Ittelson, W. H. (1960). "Visual Space Perception." Springer-Verlag, Berlin and New York.
Judge, A. W. (1950). "Stereographic Photography. Its Application to Science, Industry and Education." Chapman & Hall, London.
Julesz, B. (1964). *Science* **145,** 356-362.
Julesz, B. (1971). "Foundations of Cyclopean Perception." Univ. of Chicago Press, Chicago, Illinois.
Katz, L., and Levinthal, C. (1972). *Annu. Rev. Biophys. Bioeng.* **1,** 465-504.
Kidd, A. L., Frisby, J. P., and Mayhew, J. E. W. (1979). *Nature (London)* **280,** 829-832.
Kulikowski, J. J. (1978). *Nature (London)* **275,** 126-127.
Larson, W. L. (1978). *Can. J. Optometry* **40,** 75-79.
Ledbetter, M. C., Geisbusch, W. J., McKinney, W. R., and Woods, P. S. (1977). *EMSA Bull.* **7,** No. 2, 9-13.
Legge, G. E. (1979). *J. Opt. Soc. Am.* **69,** 838-847.
Linssen, E. F. (1952). "Stereo-Photography in Practice." Fountain Press, London.
McKay, H. C. (1951). "Three-Dimensional Photography. Principles of Stereoscopy." American Photography, Book Dept., Minneapolis, Minnesota.
Marr, D. (1977). *Proc. R. Soc. London, Ser. B* **197,** 441-475.
Marr, D., and Nishihara, H. K. (1978). *Proc. R. Soc. London, Ser. B* **200,** 269-294.
Marr, D., and Poggio, T. (1976). *Science* **194,** 283-287.
Marr, D., and Poggio, T. (1979). *Proc. R. Soc. London, Ser. B* **204,** 301-328.
Mayhew, J. E. W., and Frisby, J. P. (1976). *Nature (London)* **264,** 53-56.
Mohr, D., and Wray, G. (1976). *Ultramicroscopy* **1,** 181-186.
Nakashima, Y., and Ikeda, M. (1978). *J. Opt. Soc. Am.* **68,** 1438.
Nelson, J. I. (1975). *J. Theor. Biol.* **49,** 1-88.
Nelson, J. I. (1977). *J. Theor. Biol.* **66,** 203-266.
Ogle, K. N. (1950). "Researches in Binocular Vision." Saunders, Philadelphia, Pennsylvania.
Padawer, J. (1973). *Experientia* **29,** 1586-1587.
Panum, P. L. (1858). "Physiologische Untersuchungen über das Sehen mit zwei Augen." Schwers, Kiel.
Peachey, L. D. (1978). *EMSA Bull.* **8,** No. 1, 15-21.
Pepper, R. L., Cole, R. E., Merritt, J. O., and Smith, D. C. (1978). *Opt. Eng.* **17,** 411-415.
Pettigrew, J. (1978). *Nature (London)* **273,** 9-11.
Pettigrew, J. D. (1979). *Proc. R. Soc. London, Ser. B* **204,** 435-454.
Poggio, G. F. (1979). *Trends NeuroSci. (Pers. Ed.)* **2,** 199-201.
Ramachandran, V. S. (1975). *Nature (London)* **256,** 122-123.
Ramachandran, V. S. (1976) *Nature (London)* **262,** 382-384.
Ramachandran, V. S., and Gregory, R. L. (1978). *Nature (London)* **275,** 55-56.
Ramachandran, V. S., and Sriram, S. (1972). *Nature (London)* **237,** 347-348.
Ramachandran, V. S., Madhusudhan Rao, V., and Vidyasagar, T. R. (1973). *Nature (London)* **242,** 412-414.

Ramachandran, V. S., Clarke, P. G. H., and Whitteridge, D. (1977). *Nature (London)* **268,** 333-335.
Regan, D., and Beverley, K. I. (1979). *Science* **205,** 311-313.
Regan, D., Beverley, K. I., and Cynader, M. (1979). *Proc. R. Soc. London, Ser. B* **204,** 485-501.
Reinecke, R. D. (1979). *N. Engl. J. Med.* **300,** 1139-1141.
Robertson, M. (1978). *New Sci.* **78,** 437-439.
Ruddock, K. H., and Waterfield, V. A. (1978). *Neurosci. Lett.* **8,** 93-98.
Russell, P. W. (1979). *Vision Res.* **19,** 831-834.
Semmlow, J., and Wetzel, P. (1979). *J. Opt. Soc. Am.* **69,** 639-645.
Shepard, R. N., and Judd, S. A. (1976). *Science* **191,** 952-954.
Skrandies, W., Lindenmaier, C., and Lehmann, D. (1979). *Experientia* **35,** 927.
Sutherland, N. S. (1979). *Nature (London)* **278,** 395-398.
Tilton, H. B. (1978). *J. Opt. Soc. Am.* **68,** 1420.
Trehub, A. (1978). *J. Theor. Biol.* **71,** 479-486.
Ullman, S. (1979). *Proc. R. Soc. London, Ser. B* **203,** 405-426.
Valyus, N. A. (1962). "Stereoskopiya." Izd. Akad. Nauk SSSR, Moscow (Engl. transl., "Stereoscopy." Focal Press, London and New York, 1966; page number citations are for the English text).
von der Heydt, R., Adorjani, C., and Hänny, P. (1977). *Experientia* **33,** 786.
von Helmholtz, H. (1909). "Handbuch der physiologischen Optik," 3rd ed. Voss, Leipzig (Engl. transl., "Helmholtz's Treatise on Physiological Optics." Dover, New York, 1924).
Williams, A., and Weisstein, N. (1978). *J. Opt. Soc. Am.* **68,** 1365.
Willis, R. A. (1971). Ph.D. Thesis, University College, University of London.
Yamada, E., Mizuhira, V., Kurosumi, K., and Nagano, T., eds. (1976). "Recent Progress in Electron Microscopy of Cells and Tissues." University Park Press, Baltimore, Maryland.
Yonas, A., Cleaves, W. T., and Pettersen, L. (1978). *Science* **200,** 77-79.
Zeki, S. M. (1979). *Proc. R. Soc. London, Ser. B* **204,** 379-397.

Chapter 3

Stages and Stereo-Pair Recording

JAMES N. TURNER

Division of Laboratories and Research,
New York State Department of Health,
Albany, New York

I. Introduction 33
II. Specimen Tilting Method 35
A. Selection of the Optimum Stereo Tilt Angle 35
B. Transmission Electron Microscopes 37
C. Scanning Electron Microscopes 42
D. Vector Analysis of Stage Motion 45
III. Fixed-Tilt and Rotation Method 46
IV. Summary 49
References 50

I. Introduction

The recording and subsequent viewing of the two micrographs of a stereo pair require the specimen and the electron beam to be oriented relative to each other in such a way that parallax is produced. This can be accomplished either by changing the specimen position while holding the beam fixed, or by tilting the beam while holding the specimen fixed. Both methods have been tried, but specimen manipulation is presently the most commonly used, for, in general, it is easier to move the specimen than it is to move the illumination.

Von Ardenne (1940a,b,c) developed two methods of stereo recording. One was the standard method of tilting the specimen by rotating its holder in the specimen translation stage. The second employed an asymmetric condenser aperture, which splits the electron beam into two beams incident on the specimen and separated by an angle equal to the stereo angle. The beams give rise to two images, which are projected by a dual projector system. The final images of the

Copyright © 1981 by Academic Press, Inc.
All rights of reproduction in any form reserved.
ISBN 0-12-564122-2

stereo pair are formed simultaneously and side by side on the viewing screen or the photographic emulsion.

Marton and Schiff (1941) proposed a system of beam tilt for recording stereo pairs. Von Müller (1942) used both specimen and beam tilts, although in his design the entire condenser system was tilted by the stereo tilt angle to each side of vertical. Anderson (1942) suggested that the stereo tilt angle be selected to yield the desired three-dimensional impression and pointed out that its value would depend on specimen thickness. He also stated that the entire thickness of the specimen is in focus and that parallel rather than perspective projection applies in transmission electron microscopy (TEM). Von Müller (1942) and Gotthardt (1942) both derived the parallax equation for parallel projection in TEM. Kinder (1946) used a specially designed condenser system to produce a two-beam illumination system with the beams separated by the stereo angle. The images were projected side by side in the final image plane. Von Rühle (1949) used specimen tilt with z control, in an attempt to compensate for the vertical motion that results from tilting.

The tilted-beam and split-beam methods involve use of the off-axis position of the objective and projector lenses. This results in serious image degradation, especially for large stereo tilt angles. These methods can be used, however, for the small stereo tilt angles required at high magnifications. High-quality beam deflection systems are available, and accurate small-angle deflections could relieve the accuracy constraints on the specimen tilting stage. In addition, deflection systems are easy to make eucentric. The more recent literature will be discussed later in this chapter, and in other chapters where applicable.

Two direct-viewing methods have also been developed. The Elektros microscope developed by Gertrude Rempfer uses a system that deflects the beam alternately to each of the two angles corresponding to the conditions necessary for stereo recording. The two images obtained can be viewed side by side through a pocket stereo viewer. In the other viewing scheme the images are superimposed on the screen and viewed through a stereo light microscope, which is modified to interrupt the optical system for one eye at a time in synchrony with the deflection system (G. Rempfer, private communication).

Similar direct stereo-viewing systems have been developed for the scanning electron microscope (SEM). Again, the beam is deflected to produce parallax by changing the incident angle on the specimen. The ability to produce an image that is renewable at television scan rates, and the rastered nature of the image, can be exploited in the viewing system. Two television screens can be used with a stereo viewer, so that one image of the stereo pair is displayed on each screen. A single screen can also be used with a split display, or a color television display can be used with an anaglyphic viewer. In the latter system, one image of the stereo pair is displayed in green, and the other in red. These methods are thoroughly discussed by Chatfield (1978).

II. Specimen Tilting Method

The most commonly employed method of stereo recording in both the TEM and the SEM is to tilt the specimen relative to the optical axis, using the specimen stage. Although a stage with a single-tilt axis is sufficient to record stereo pairs, it may not always allow the specimen to be oriented for optimal observation of the detail of interest. Beeston (1973) pointed out the importance of pretilting the specimen for such optimization. Since the microscopist usually has no control over the orientation of the specimen on the grid, pretilting may require complete freedom of specimen movement relative to the beam. This necessitates a double-tilt stage or a single-tilt and rotation stage whose rotation axis is perpendicular to the specimen.

In general, it is best to select the simplest stage (that is, the one with the fewest motions) that is compatible with the problem being studied. Each additional motion or degree of freedom adds complexity of design, maintenance, and operation—all of which often adversely affect the attainable resolution. The stage should be designed to prevent image motion in the x, y, and z directions when the specimen is tilted or rotated. Such a stage is referred to as "eucentric" if the specimen can be oriented in any position relative to the beam. In an "axis-centered" stage, a single-tilt motion does not affect the translational or vertical position of the stage (and therefore the specimen). These terms are often interchanged or used inconsistently. A "goniometer" stage is defined by Valdré and Goringe (1971) as a tilting stage in which an angular position is directly measurable with an accuracy of at least $\pm 0.1°$. Unfortunately, the term goniometer is often used incorrectly to mean a positioning or tilting device with the specimen at the center of a sphere, preventing translation as a function of tilting. In electron microscopy this would be termed eucentric, as discussed above.

A. Selection of the Optimum Stereo Tilt Angle

When stereo pairs are recorded by the specimen-tilting method, the specimen is tilted in one direction by a certain angle (referred to here as the stereo tilt angle) and the first micrograph is recorded. The sample is then tilted by the same angular displacement past the initial position in the opposite direction, and the second micrograph of the stereo pair is recorded. The total angular separation between the two recording positions is defined as the stereo angle(s). The value of the stereo tilt angle can be calculated from the parallax equation (discussed below).

Any study should be begun by using the stereo tilt angle calculated from the parallax equation. This is especially true if the microscopist has a good estimate of the height change in the specimen, as is true for most TEM samples. Thick-

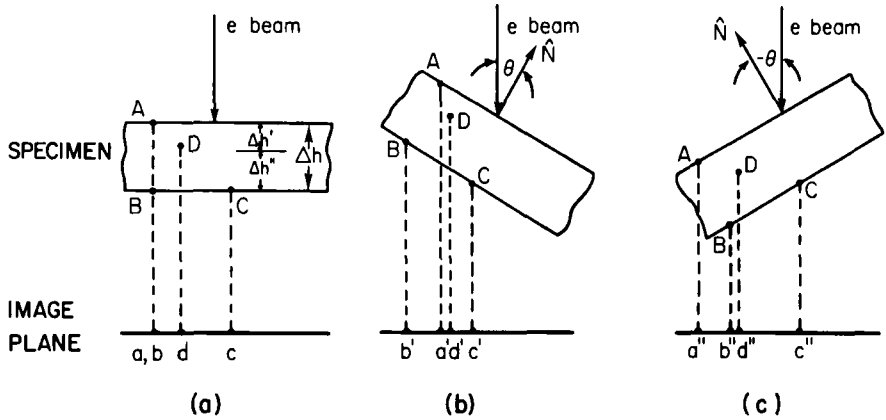


FIG. 1. Geometry of a specimen in the tilted and untilted orientations. The relative positions of four points in the specimen, and their corresponding image points, relative to each other and to the incident electron beam, are shown. Specimen (a) in untilted orientation; (b) in the $+\theta$ tilted orientation (at which the first micrograph of the stereo pair is recorded); (c) in the $-\theta$ tilted orientation (at which the second micrograph of the stereo pair is recorded). $\hat{N}$ represents the unit vector normal to the top surface of the specimen. The parallax between images of points A and D is less than that between the points D and C, owing to the relative vertical positions of the three points.

ness can be estimated for sectioned material from the advance of the microtome, and from the characteristic interference colors generated by epoxy sections. Estimates for whole mounts may be more difficult and generally are based on the microscopist's knowledge of the specimen from previous experiments. Height changes in replicas, particularly in freeze-fractured replicas, are very difficult to estimate, as few clues are available. SEM specimens, like whole mounts, usually require some prior knowledge about the specimen, although Blödorn (1978) points out that the height change can be estimated by observing the lens current required to just focus the highest and lowest points in the field.

Insertion of the estimated height change in the parallax equation yields the optimum stereo tilt angle for observing image points separated by that height change. However, the details of interest may lie not at the extremes of the specimen height variation but in planes *within* the specimen. Such points would be imaged with less than the optimum stereo effect. This condition is shown in Fig. 1 and Eq. (1):

$$P_{AD} = 2M_T \, \Delta h' \sin \theta \tag{1}$$

where P_{AD} is the parallax of the image of point A with respect to the image of point D.

$$P_{DC} = 2M_T \, \Delta h'' \sin \theta \tag{2}$$

$$P_{AC} = 2M_T \, \Delta h \sin \theta \tag{3}$$

Since for any stereo pair M_T and θ are the same for all points, the apparent vertical separation between image points viewed in stereo decreases directly with their vertical separation in the object. This can be appreciated by measuring the parallax of the image points in Fig. 1 with a scale. The parallax is the absolute value of the difference of the image distances in the two tilted images (for example, $P_{AD} = |a''d'' - a'd'|$). Thus, if the details of interest lie *within* the specimen, a larger stereo tilt angle may be desired to increase the stereo impression and the vertical discrimination between them. This can be particularly effective for sectioned material of low overall specimen density or for selectively stained specimens. The embedding medium, which provides the estimate of Δh, is usually not observed in the stereo image, owing to its low contrast. Thus, the Δh of the particular details of interest determine the scene field so that larger angles may be permitted. However, if the specimen density is high, other image details may bound the stereo scene field, making the stereo pair hard to fuse when larger stereo tilt angles are used.

If angles larger than those predicted by the parallax equation [Eq. (5) in Chapter 1 of this volume] are used, the resultant stereo pair may be difficult to fuse. This is particularly true if the angle exceeds the predicted angle for the maximum height changes in the specimen and if P exceeds 5 mm, the maximum observable parallax (Hudson and Makin, 1970). Prior knowledge of the dimensions of the specimen is thus very important, and the best practical approach is trial and error, beginning with the parallax equation.

B. Transmission Electron Microscopes

Specimen stages employed in the TEM are of two general types—top-entry and side-entry. Top-entry stages have two components, an x-y translation mechanism, mounted on top of the upper objective pole piece, and a removable specimen cartridge, which fits into this device. The specimen cartridge extends through the upper pole piece bore, positioning the sample in the lens gap in the high-strength region of the magnetic field. This design has extreme mechanical stability because (1) the specimen cartridge seats into the x-y translation mechanism on a conical surface, which results in good contact between the two components; (2) the x-y translation mechanism is massive and thus tends to be mechanically stable; (3) the critical mechanical distances within the stage are short, thus minimizing the effect of vibration; and (4) the volume above the upper pole piece available for the stage mechanism is relatively large, which allows mechanical designs to be easier. The major disadvantages of top-entry stages are the difficulty of specimen tilting, which must be done by very small linkages through the bore of the upper pole piece, and the extreme difficulty of making these stages eucentric or axis-centered.

In a side-entry stage the specimen is introduced through the column of the

microscope, along a direction perpendicular to the beam axis, by means of a long rod. The specimen is generally mounted between the pole pieces of the objective lens, in the region of high magnetic field strength. This type of stage also has two basic components, the x-y translation device and the specimen rod. The major advantage of the side-entry stage is that the specimen rod provides a degree of specimen tilting as well as access to the specimen region for other manipulations, such as rotation. The major disadvantages are that vibration is transmitted by the long specimen rod and that the stage must fit in a small volume between the objective pole pieces, which makes manipulation difficult. The vibration is a particular problem for high-voltage electron microscopes because the rods are especially long (approximately 30 cm). One solution is to detach the tip of the rod that holds the specimen in the x-y translation mechanism (Thalen *et al.*, 1970; Sansom, 1974). This shortens the lever arm over which vibration can act and thus decreases specimen movement. However, it also eliminates the rod as a transmitter of mechanical motion to tilt or rotate the specimen. Another solution is to decouple the rod with respect to vibration, while still providing a rotationally strong connection (Turner and Ratkowski, 1980). This dampens vibration while maintaining the capability of tilting the specimen about the rod's long axis.

Good reviews of stage mechanisms and the problems inherent in the various designs are presented by Valdŕe and Goringe (1971), Sansom (1974), Lange (1976), and Swann (1979).

Figure 2 shows the gimbaled arrangement used in most top-entry double-tilt stages. The double gimbal and linkages 1 through 4 must fit through and be translated within the bore of the upper pole piece. However, to achieve high resolution, this bore diameter must be as small as possible, typically a few millimeters (Bursill *et al.*, 1979). The specimen is tilted about the θ axis by working linkages 1 and 2 against each other. This rotates the inner ring on an axle that mounts it to the middle ring. The ϕ tilt is achieved by working linkages 3 and 4 against each other, producing rotation on the axle that mounts the middle ring to the outer one. Despite the complex linkages, an angular accuracy of $\pm 0.1°$ is achievable (Valdŕe and Goringe, 1971), and the tilt mechanism is extremely stable mechanically (Bursill *et al.*, 1979). Because the x-y translation is above and outside the gimbals, the stage is noneucentric. However, Merli and Valdŕe (1971) made a stage of this type eucentric by adding a lifting or z motion parallel to the optical axis. The specimen motion is very complex, since the required z motion is dependent on x, y, θ, and ϕ. Siemens has attempted to produce such a stage and to control its motion by a microprocessor (D. Willasch, private communication, 1979), but no results are available.

A typical side-entry double-tilt design is shown in Fig. 3 (Swann, 1972, 1979; Allinson and Kisch, 1972). The θ tilt is achieved by rotating the rod about its long axis, and the ϕ tilt by rotating a cradle holding the specimen about an axis perpendicular to the rod. This mechanism is also noneucentric, and transmission

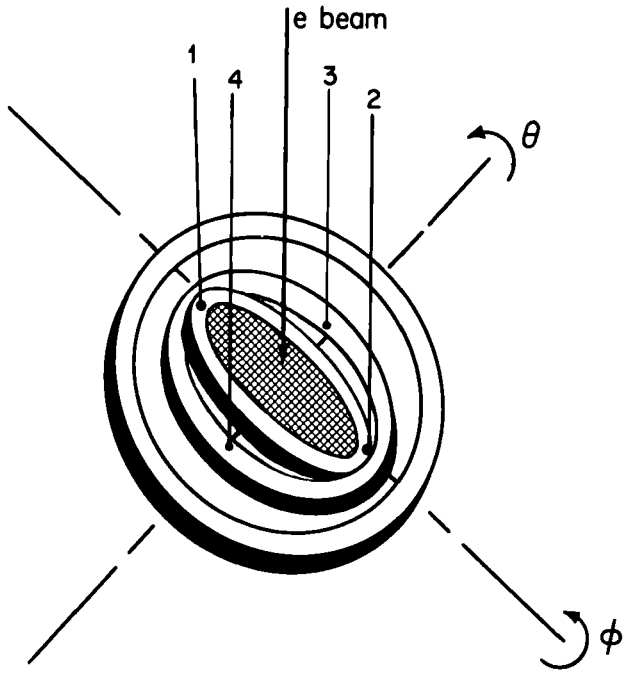


FIG. 2. The typical top-entry double-tilt stage design. The specimen is mounted on the innermost ring, which is attached to the middle ring by a gimbal along the axis. Linkages 1 and 2 allow the inner ring to be rotated about the gimbal axis, producing the tilt θ. The middle ring is similarly attached to the outer ring, and the ϕ tilt is produced by linkages 3 and 4. The mechanism is neither axis-centered nor eucentric and can usually be rotated about the optical axis, which is parallel to the linkages shown.

of vibration through its long, solid rod can decrease the image resolution. Both the top-entry double-tilt design of Fig. 2 and the side-entry double-tilt design of Fig. 3 allow complete freedom of motion in orienting the specimen with respect to the electron beam. In the top-entry design, the θ and ϕ tilts usually have the same angular range, but in the side-entry design the ϕ tilt can be considerably greater than the θ tilt, owing to the small size of the specimen cradle.

The side-entry specimen rod can provide access to the specimen cradle for rotating the specimen. Figure 4 shows a typical design for which the θ single tilt is achieved by rotation about the rod's long axis, and the specimen is rotated by pulling or releasing a spring-loaded metal tape or wire that is wound around the specimen cradle. The cradle is trapped along the rod axis by the spring, which pulls it against two sapphire posts or bearings. The specimen rotation axis is always coincident with the specimen normal, and, since the rotation mechanism is inside the rod, the specimen rotation axis rotates with θ. This important

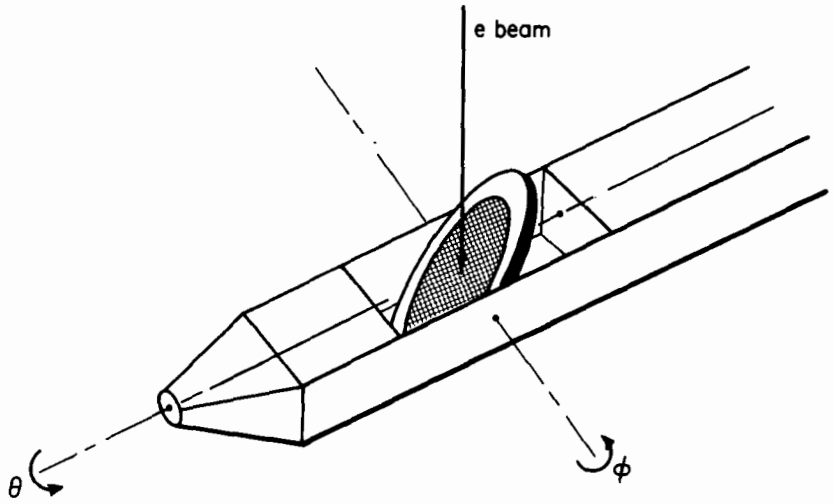


FIG. 3. Typical design for a side-entry double-tilt stage. The specimen is mounted in a cradle, which is gimbaled to the specimen rod, establishing the ϕ axis. The specimen is tilted by rotation about this axis. Rotation about the θ axis, which is the long axis of the specimen rod, produces the second specimen tilt. The tilt axes are not independent; that is, the orientation of the ϕ axis relative to the optical axis changes as a function of θ. The figure shows the case where $\theta = 0$, $\phi \neq 0$, and the electron beam is incident on the center of the specimen; that is, the stage is translationally centered.

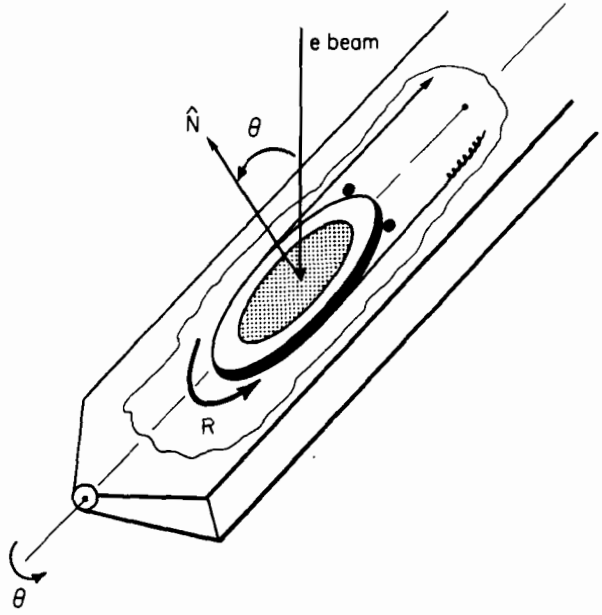


FIG. 4. Typical design for a side-entry single-tilt stage with rotation. The specimen is mounted in a cradle that is trapped on top and bottom in the specimen rod (cutaway view). A spring-loaded tape traps the cradle against two pins; the cradle is rotated with respect to the pins. When the tape is pulled from outside the microscope, the specimen rotation is always about the specimen normal, $\hat{N}$. The tilt motion is accomplished by rotation about the long axis of the specimen rod. The rotation axis ($\hat{N}$) changes orientation with respect to the optic axis as a function of θ. The position of the incident electron beam is shown for a centered stage.

capability allows the specimen to be observed from a different orientation as it is rotated (provided that $\theta \neq 0$). Rotation about the optical axis, a feature of many top-entry stages, does not offer this different perspective for observing the specimen (see Section IV of this chapter for a more detailed discussion).

The θ tilt in a single-tilt side-entry rod can be made axis-centered, preventing the specimen detail under observation from translating as a function of tilt (Rakels *et al.*, 1968; Browning, 1974; Lange, 1976). However, a second motion (additional tilt or a rotation) is very difficult to make axis-centered. Thus, there are few truly eucentric stages, whereas axis-centered stages are relatively common. In recording stereo pairs, an axis-centered stage eliminates refocusing between the exposures, which could cause magnification changes and image rotation. The image detail of interest remains in the same position relative to the viewing screen and recording film as the specimen is tilted.

When one is recording the micrographs of a stereo pair, the orientation of the tilt axis must be known with respect to the viewing screen, the photographic film, and the image details of interest. This knowledge is essential for alignment of the micrographs for proper stereo fusion. The lenses of most high-voltage electron microscopes are ganged so that the image does not rotate as the magnification is changed. Thus, the microscopist always knows the orientation of the tilt axis or axes with respect to the micrograph. Most conventional voltage instruments do not have this capability.

Figure 5 shows schematically the importance of pretilting details of interest in thick sections. The two parallel disks are randomly oriented in (a), and the projected image does not separate their respective images. Tilting about one axis results in the orientation and projected image shown in (b). The image is still overlapped, however, and thus is unclear. Tilting about a second axis perpendicular to the first orients the two disks parallel to the electron beam, producing an image free from overlap. A stereo pair could be recorded with (c) as the initial position to produce a stereo image clearly showing the disks viewed edge on. Figure 5 points up the usefulness of pretilting to orient details of interest optimally with respect to the electron beam, and it makes clear the need for a stage with two degrees of freedom: either a double-tilt stage, or a single-tilt and rotation stage. Figure 6 shows two stereo pairs of the same area of a 0.5-μm section of a desmosome from a squamous cell carcinoma tumor. The top pair was taken without pretilting ($\theta_0 = \phi_0 = 0°$) and gives little indication of a desmosome near the center of the field of view. The lower pair, however, was pretilted for optimal orientation of this desmosome, which is now clearly visible. These two stereo pairs demonstrate the importance of positioning optimally the sample with respect to the beam before recording the stereo pair. A stage of the type shown in Fig. 3 was used to record the stereo pairs.

A stage with two degrees of freedom for tilting the specimen relative to the beam can also be used to view the sample and record stereo pairs from different

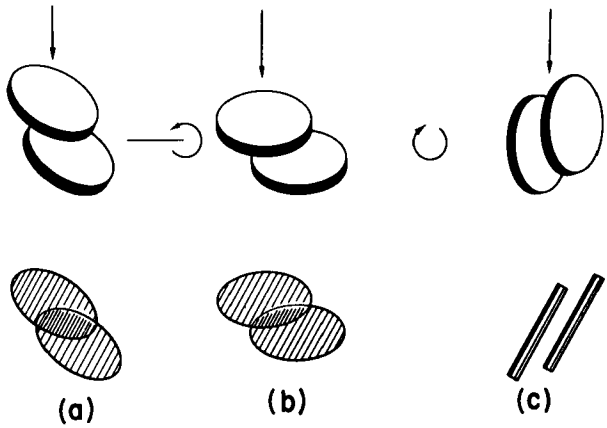


FIG. 5. Pretilting with a double-tilt stage. (a) Untilted orientation for two disks whose projections overlap, resulting in a confused image; (b) tilted orientation produced by rotating (a) about an axis in the plane of the paper; (c) optimized orientation produced by rotating (b) about an axis normal to the plane of the paper. A stereo pair can be recorded about this optimized orientation by tilting the specimen to $\pm\theta$ in addition to the pretilts used to orient the specimen.

perspectives. Figure 7 shows two stereo pairs recorded from two different perspectives, such that the tilt axes are perpendicular to each other. Information about the shape of the membrane surfaces near the ends of desmosome is present in one pair, but not in the other. The shape of the surface marked by the arrow in the upper stereo pair is more clearly seen in the lower pair, and the microvillus-like projection marked in the lower pair is seen differently in relation to nearby surfaces. (The membrane surfaces may be somewhat difficult to visualize, as membranes do not stand out strongly in stereo because they are thin and do not scatter electrons as strongly as other nearby structures.) The two pairs are rotated relative to each other so that the parallax axis corresponds to the direction of the eye separation. This figure may require careful study by the reader, especially if his or her stereo-viewing experience is limited, and use of a pocket viewer is advisable. These stereo pairs were recorded by using a double-tilt stage of the type shown in Fig. 3.

C. Scanning Electron Microscopes

The SEM produces an image with apparent three-dimensionality, the result of perspective plus the fact that the object is solid and only its surface is imaged. This impression can be misleading. However, true stereo imaging can provide an accurate presentation of the three-dimensional structure of the object's surface. The parameters and their relationships for the recording of stereo images in the SEM are exactly the same as in the TEM. However, there is the added complica-

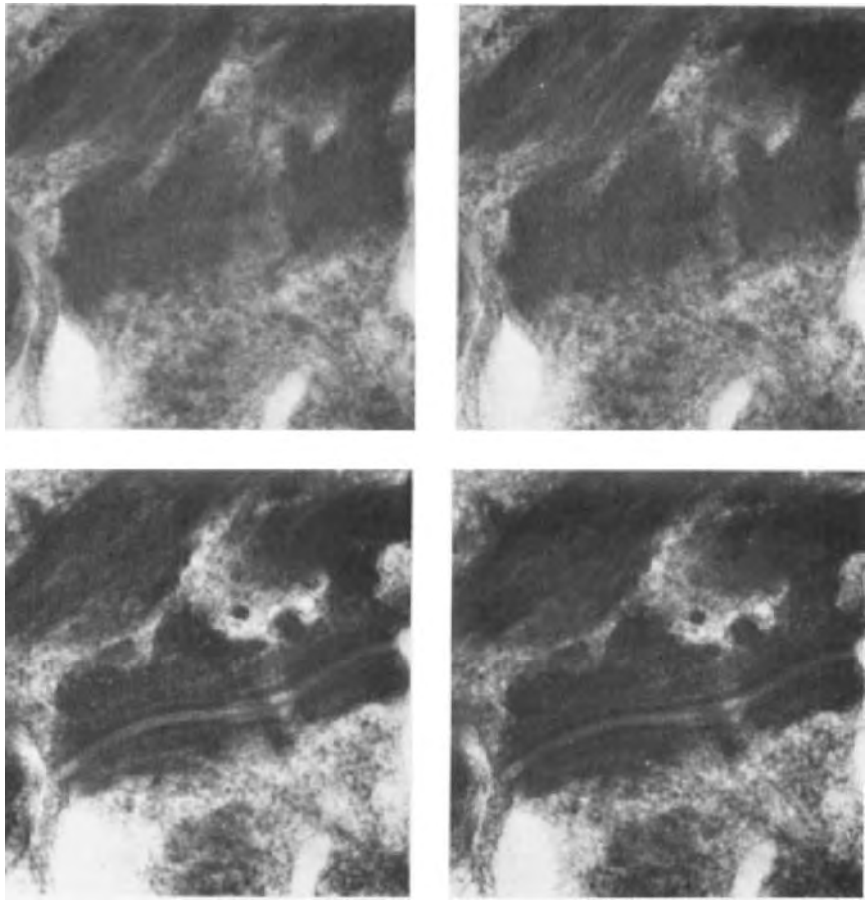


FIG. 6. Two stereo pairs showing the same area of a 0.5-μm section of a squamous cell carcinoma recorded at 1.0 MeV and 40,000× magnification. The upper pair was recorded by tilting $\theta = \pm 2^0$ about the horizontal ($\theta_0 = \phi_0 = 0$) position. The lower pair was recorded by tilting $\theta = \pm 2^0$ about a pretilted position ($\theta_0 = -13°$, $\phi_0 = 34°$), which was determined by direct observation; θ and ϕ are as defined in Fig. 3.

tion in the SEM that the height of the surface structure is less well known than is the thickness in the TEM. If the Δh can be estimated from any outside information or experience, it can be substituted into the parallax equation to calculate the stereo tilt angle. Another approach is to estimate the maximum height change in the field of view by first focusing above the specimen, gradually decreasing the lens current, and then noting the value of the current when both the highest and lowest areas first come into focus. This current change can be translated into a height change for the particular SEM being used.

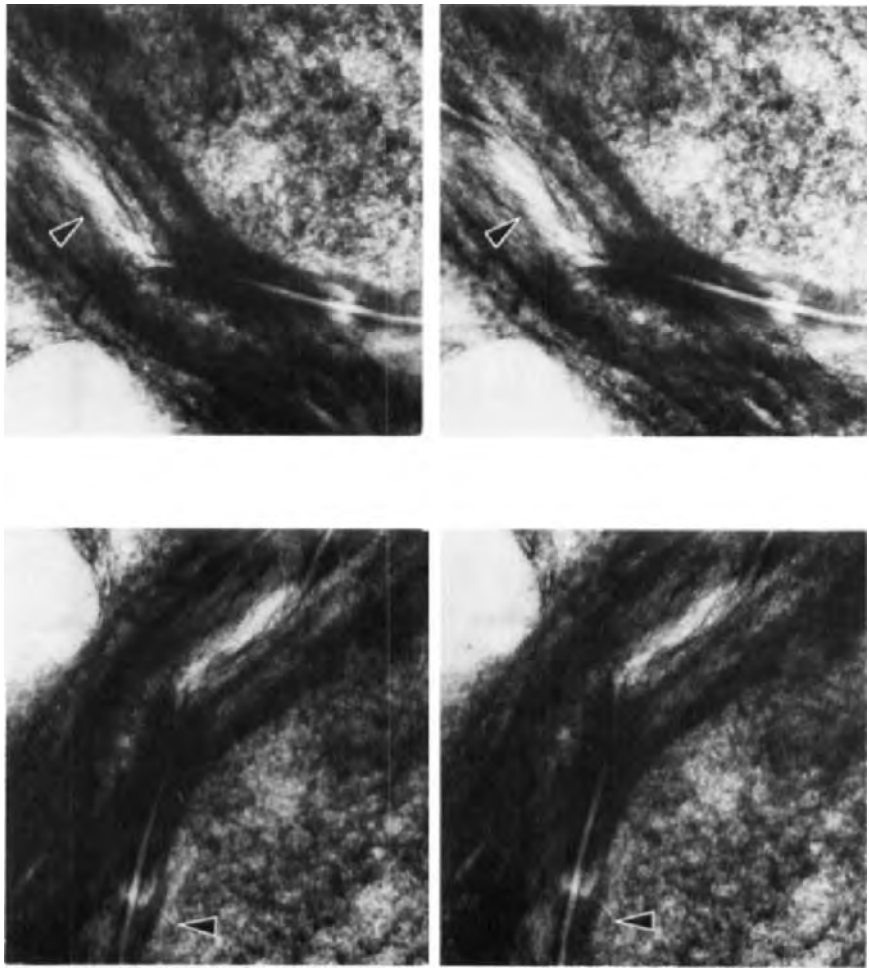


FIG. 7. Two stereo pairs showing the region of a desmosome from the same sample as in Fig. 6. The upper pair was recorded by tilting the specimen $\theta = \pm 2°$ with $\phi = 0$, and the lower pair was recorded by tilting $\phi = \pm 2°$ with $\theta = 0$. The micrographs were recorded at 1.0 MeV and 32,000× magnification; θ and ϕ are as defined Fig. 3.

After the stereo tilt angle based on the estimated Δh has been calculated, it may be helpful to record a through-tilt series of micrographs, starting at an angle greater than the calculated angle, and recording micrographs at several equally spaced angular positions until the sample is oriented in the opposite direction and at an angle equal to the initial one. Examination of the respective pairs will yield a better estimate of the optimum angle.

Figure 8 is a schematic representation of a double-tilt rotation stage for an

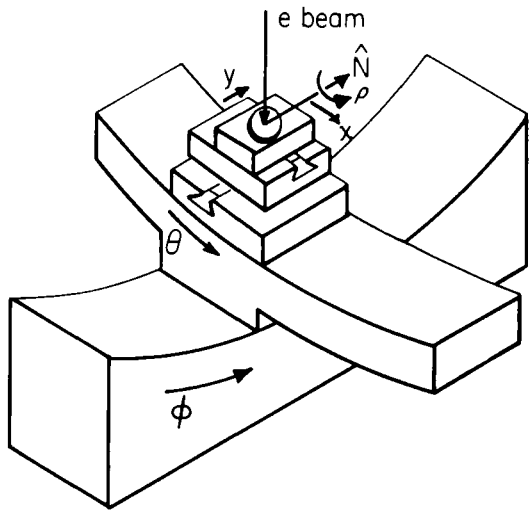


FIG. 8. Schematic representation of a eucentric double-tilt stage with rotation for an SEM. The x-y translation stage is within the double-tilt arcs that produce the θ and ϕ tilts, making these tilts eucentric. The rotation indicated by the angle ρ, however, is not eucentric.

SEM. Because the SEM specimen chamber is beneath the optical column, the stage mechanism can be much larger and thus considerably easier to design and build than in the TEM. The tilt angles θ and ϕ are achieved by moving a stage block along an arc. Since the x-y translations are located inside the θ and ϕ arcs, the stage is eucentric. The specimen can also be rotated about an axis parallel to its normal unit vector by either a eucentric or non-eucentric motion. Not all SEM stages are capable of all these motions, and not all are eucentric. The double-tilt or single-tilt stage with rotation can provide complete freedom of specimen positioning, as discussed above for TEM. This allows optimum pretilting and azimuthal positioning of the parallax axis in any direction.

Although specimen tilting is the most common method of stereo recording in the SEM, an alternative (discussed below) is to rotate the specimen about its normal vector when one or both of the tilt angles are not equal to zero.

D. Vector Analysis of Stage Motion

Vector analysis applied to specimen stage motion is a classical mechanical method of expressing mathematically the motion of the stage that allows the exact position of the sample in three-dimensional space to be determined and predicted for any conditions. This determination is essential for good quantitative results, as discussed in detail by Ghosh in this volume. It is helpful for qualitative work as well, because it allows the sample to be positioned in any pretilt orienta-

tion for stereo recording. It also permits the microscopist to select any desired parallax direction relative to the photographic film (Turner *et al.*, 1978), a useful capability for optimizing observation of particular details. For an example of an object photographed from two different directions or perspectives, see Fig. 7. In this case the directions corresponded to the two tilt axes of the double-tilt stage, but the parallax axis could be placed along any azimuthal direction by using the vector analysis approach.

If the specimen has highly ordered structures in a particular direction, such as fibers or muscle filaments, a detailed vector analysis would allow the parallax axis to be placed either parallel or perpendicular to the long axis of the structure, independent of the specimen's orientation on the grid. Sykes (1979) pointed out that such analysis can be used to position selected crystallographic orientations relative to the beam direction. Periodic biological ojects such as virus crystals could benefit similarly. Details of this type of analysis and a complete listing of references are given by Ghosh in this volume.

III. Fixed-Tilt and Rotation Method

In addition to simple tilting methods, image parallax can be generated by first tilting the specimen and then recording the micrographs of the stereo pair at two different rotational positions. In the SEM the axis of rotation is perpendicular to the top surface of the specimen stub (see Fig. 8), whereas in the TEM it is perpendicular to the plane of the specimen-supporting grid (see Fig. 4). (It should be noted that rotation about the optical axis of the microscope does not produce parallax, even if the specimen is tilted.) This tilt and rotation method was explored in detail by Blödorn and Lange (1976), Blödorn (1978), and Burkhardt (1978), who made an analysis of the specimen motion and tabulated the angular settings for the SEM (see also Boyde, 1974). Ledbetter *et al.* (1977), who also give a table of these settings, pointed out that the method is equally applicable to the TEM by inclusion of the parallax equation in the equations of motion.

The geometry of the method for the TEM is shown in Figs. 4 and 9. Figure 4 shows the design of the tilt and rotation specimen holder, and Fig. 9a shows a specimen that has been tilted by rotating the specimen rod about its long axis. This rotation, labeled θ in Fig. 4, is termed ν in Fig. 9 for consistency with the notation in Blödorn (1978) and Burkhardt (1978). Points A and B are object points on the top surface of the specimen, and C is on the bottom surface. Their corresponding image points are labeled a, b, and c. Figure 9b shows the sample rotated about the optical axis, which is represented as the direction of the electron, or e, beam. From comparison of the relationship of the image points a, b, and c in Fig. 9a to a', b', and c' in (b), it is clear that the identical triangle is

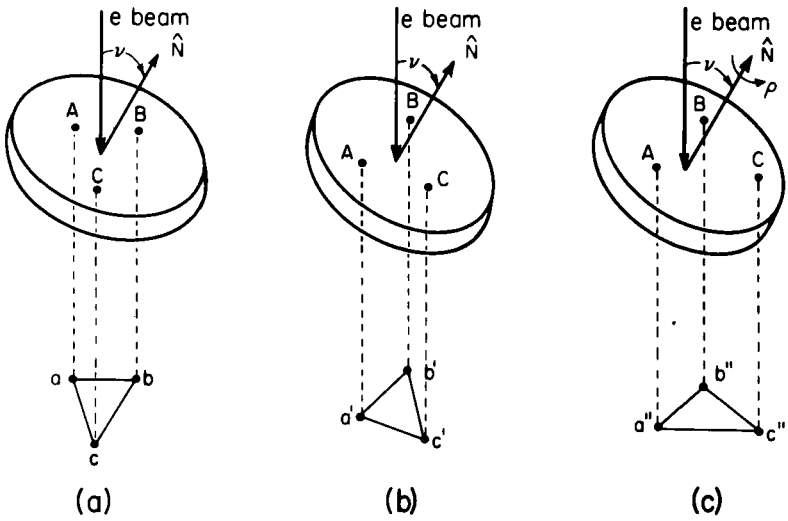


FIG. 9. Schematic demonstration that parallax is not generated when a sample is rotated about the electron beam but is generated when a tilted sample is rotated about its normal. Points A and B are on the top surface of the sample, and C is on the bottom surface. (a) Sample tilted about the θ axis; (b) rotation of (a) about the electron beam; (c) rotation of (a) about the specimen normal. The lower-case letters represent the projected image points of their corresponding objects points.

formed. In (b), although the triangle is rotated about the optical axis, no new information is present compared with (a). Thus, no parallax was generated by this rotation.

Figure 9c shows the same sample, but now rotated about an axis perpendicular to the specimen's top and bottom surfaces. In this case, the triangle $a''b''c''$ is significantly different from the triangles abc and $a'b'c'$. The distance $a''b''$ is the same as ab, because A and B are in the same tilted plane perpendicular to the rotation axis. However, the distance $a''c''$ and $b''c''$ are not equal to their corresponding distances ac and bc. Thus, comparison of (a) and (c) shows that parallax has been generated between image points lying in different planes perpendicular to the rotation axis. Although image formation by this method in the SEM is more difficult to present schematically, the arguments above hold equally well.

Ledbetter *et al.* (1977) and Blödorn (1978) give expressions relating the angles defined in Fig. 6. The expression derived by Blödorn is given below in the original notation:

$$\sin \gamma/2 = \sin \rho/2 \cdot \sin \nu \tag{4}$$

where γ is the stereo angle, S, or 2 θ by the previous definitions in Chapter 1 of this volume; ρ is the total rotation between the recording positions of a stereo

pair; and ν is the angle by which the specimen is tilted. Since

$$\sin \gamma/2 = P/2\Delta h M_T \tag{5}$$

substitution of Eq. (5) into Eq. (4) produces an expression for ρ in terms of experimentally defined parameters:

$$\sin \rho/2 = P/2\Delta M_T \cdot 1/\sin \nu \tag{6}$$

To record stereo pairs by this method, the microscopist must first decide whether Eq. (4) or Eq. (6) is to be used for calculating the rotational angle. This decision is based on a knowledge of Δh. If no information regarding Δh is available, Eq. (4) must be used. A second decision is then the choice of value for the stereo angle γ. Ledbetter *et al.* (1977) used a stereo angle of 7°; Blödorn (1978), referring to this angle as the convergence angle, calculated a table for angles of 5°, 10°, 15°, and 20°. Next, a tilt angle must be selected, and any convenient value will allow ρ to be calculated. The stereo micrographs are then recorded at rotations of $\pm\rho/2$ about the specimen normal. The best practical procedure is to calculate a table of values of $\rho/2$ for various values of γ and ν, and then to use those combinations that produce the best results for the particular specimen and instrument.

If some estimate of Δh can be made, however, Eq. (6) should be used to calculate $\rho/2$ after the selection of total viewing magnification and tilt angle. The parallax value should be between 3.0 and 5.0 mm, with 3.5 mm being a good

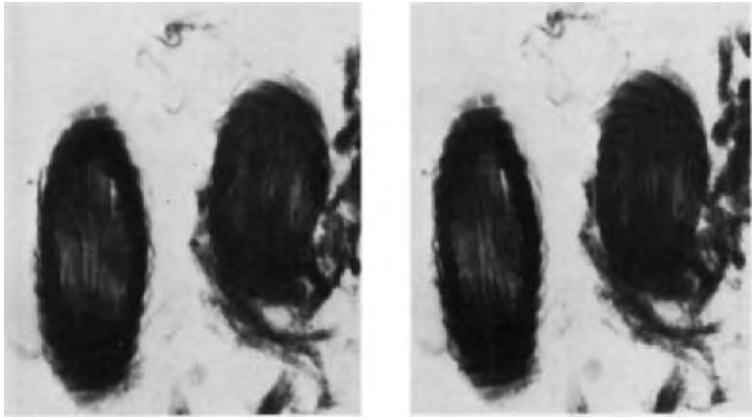


FIG. 10. Stereo pair of a 0.25-μm section of bovine sperm recorded for P = 3.0 mm, ν = 30°, $\rho/2$ = 54°, and γ = 48°, and displayed with $\kappa/2$ = 50°. A rotation single-tilt holder with a Philip EM 300 goniometer stage was used at an accelerating potential of 100 keV and 14,800× magnification. Micrographs courtesy of Michael Marko, Division of Laboratories and Research, New York State Department of Health.

starting point (Hudson and Makin, 1970). Again, a tabulation of the angles and an adjustment of the parameters by trial and error are both helpful.

This method is most easily applied with a stage whose rotational motion is eucentric. Use of a noneucentric stage necessitates either changing the z axis to maintain focus, or refocusing, with its inherent errors.

Rotation-generated parallax produces an effective tilt axis whose orientation with respect to the micrograph is dependent on ρ and ν. Thus, for optimum stereo viewing the micrographs must be rotated in opposite directions by the angle $\kappa/2$ given by the expression $\tan \kappa/2 = \tan \rho/2 \cdot \cos \nu$. Figure 10 shows a stereo pair of bull sperm tails recorded by this method. Blödorn (1978), while using this method, ignored the effect of the stereo window, which makes viewing of his stereo pair difficult.

IV. Summary

Because of the enormous integrative capacity of the human eye-brain combination, good-quality stereo pairs can be viewed over relatively large variations of recording and viewing conditions. However, a stereo study should be begun with the simplest specimen-tilting stage and with as much control as possible over the parameters. The parallax equation should be used to calculate the stereo tilt angle for recording the stereo pairs. After the initial stereo pairs have been viewed, the stereo tilt angle can be increased or decreased, depending on whether the image detail should be more or less separated in the z direction. It is also often helpful to record a series of stereo pairs for stereo tilt angles larger and smaller than the calculated one and then to optimize the angle after comparison of the various pairs. After experience has been gained for a particular type of specimen using a single tilt for orientation, pretilting and double tilting can be used to improve visualization of the details of interest. If the specimen has highly ordered detail, a particular alignment of the parallax axis with respect to the direction of anisotropy may also be beneficial.

When possible, a eucentric or at least an axis-centered stage should be used to enhance the ease and the accuracy with which stereo pairs are recorded. A noneucentric stage motion can introduce several errors that make qualitative stereo imaging inconvenient and quantitative stereo imaging difficult (see the chapters by Ghosh in this volume). The most common problem introduced by a noneucentric stage is the change in height when the sample is tilted. To focus the image at the two specimen positions, a change in the objective lens current is required, which can change the magnification and rotate one image relative to the other. These errors may hamper orientation of the stereo pair for optimum fusion.

However, Julesz (1971) has determined that a 10% difference in magnification between the images of a stereo pair does not impede fusion for most viewers, and, since the resultant image rotation is usually small, it can be compensated for by rotating the micrographs while viewing them in stereo. For a comprehensive treatment of the influence of various positional parameters, see Garrod and Nankivell (1958), Wells (1960), Nankivell (1963), Gray and Willis (1968), and Ghosh in this volume. Gray and Willis (1968) also discuss the problems associated with the stereo imaging of membrane systems in biological objects.

To optimally orient the sample for recording and the micrographs for stereo viewing, the position of the tilt axis or axes relative to the microscope viewing screen must be known. The image on the final viewing screen of most conventional-voltage TEMs rotates as the magnification is varied, which can produce confusion about the position of the tilt and parallax axes relative to the specimen detail. This often makes the later viewing of stereo pairs difficult, owing to the orientation of the parallax axis with respect to the micrographs. However, high-voltage electron microscopes, which rely heavily on stereo imaging, generally have rotation-free projection systems, in part to avoid such problems. Thus, the orientations of the tilt and parallax axes relative to the instrument and to the micrographs are always known.

ACKNOWLEDGMENTS

Michael Marko of the Electron Optics Laboratory of the Division of Laboratories and Research, of the New York State Department of Health, prepared the samples used for this work and recorded the stereo pair in Fig. 10. His help is greatly appreciated as is that of Dr. A. J. Rutkowski and D. Barnard, who maintain our HVEM. Communications with Drs. T. F. Anderson and M. von Ardenne were very helpful, and their assistance is appreciated.

REFERENCES

Allinson, D. L., and Kisch, E. (1972). *J. Phys. E* **5,** 205-207.

Anderson, T. F. (1942). *Adv. Colloid Sci.* **3,** 353-390.

Beeston, B. E. P. (1973). *J. Microsc. (Oxford)* **98,** 402-416.

Blödorn, J. (1978). *In* "Scanning Electron Microscopy/1978" (O. Johari, ed.), pp. 283-388. SEM Inc., AMF O'Hare, Illinois.

Blödorn, J., and Lange, R. H. (1976). "Mikro 76." Royal Microscopical Society, Oxford.

Boyde, A. (1974). *In* "Scanning Electron Microscopy" (O. C. Wells, ed.), pp. 277-307. McGraw-Hill, New York.

Browning, G. (1974). *In* "High Voltage Electron Microscopy" (P. R. Swann, C. J. Humphreys, and M. J. Goringe, eds.), pp. 121-123. Academic Press, New York.

Burkhardt, R. (1978). *Optik* **50,** 279-296.

Bursill, L. A., Spargo, A. E. C., Wentworth, D., and Wood, G. (1979). *J. Appl. Cryst.* **12,** 279-286.

Chatfield, E. J. (1978). *In* "Principles and Techniques of Scanning Electron Microscopy." (M. A. Hayat, ed.), Vol. 6, pp. 47-88. Van Nostrand-Reinhold, Princeton, New Jersey.

Garrod, R. I., and Nankivell, J. F. (1958). *Br. J. Appl. Phys.* **9,** 214-218.

Gotthardt, E. (1942). *Z. Phys.* **118,** 714-717.

Gray, E. G., and Willis, R. A. (1968). *J. Cell Sci.* **3,** 309-326.

Hudson, B., and Makin, M. J. (1970). *J. Phys. E* **3,** 311.

Julesz, B. (1971). "Foundations of Cyclopean Perception." Univ. of Chicago Press, Chicago, Illinois.

Kinder, E. (1946). *Naturwissenschaften* **33,** 367.

Lange, R. H. (1976). *In* "Principles and Techniques of Electron Microscopy" (M. A. Hayat, ed.), Vol. 6, pp. 241-270. Van Nostrand-Reinhold, New Jersey.

Ledbetter, M. C., Geisbusch, W. J., McKinney, W. R., and Woods, P. S. (1977). *EMSA Bull.* **7,** No. 2, 9-15.

Marton, L., and Schiff, L. J. (1941). *J. Appl. Phys.* **12,** 759-765.

Merli, P. G., and Valdfe (1971). *Electron Microsc., Proc. Int. Cong., 7th, 1970* Vol. II, pp. 589-590.

Nankivell, J. F. (1963). *Optik* **20,** 171-198.

Rakels, C. J., Teimeijer, J. C., and Witteveen, K. W. (1968). *Philips Tech. Rev.* **39,** 307-386.

Sansom, H. C. (1974). "Side Entry Specimen Stage for the EM7 One Million volt Electron Microscope," AERE-Rep. No. R7868. United Kingdom Atomic Energy Authority, Harwell, England.

Swann, P. R. (1972). *Inst. Phys. Conf. Ser.* **14,** 322-323.

Swann, P. R. (1979). *Krist. Tech.* **14,** 1235-1243.

Sykes, L. J. (1979). *Proc. 37th Annu. Meet. Electron Microsc. Soc. Am.*, pp. 602-603.

Thalen, J., Spoelstra, J., van Breeman, J. F. L., and Mellema, J. E. (1970). *J. Phys. E* **3,** 499-500.

Turner, J. N., and Ratkowski, A. J. (1980). *Proc. 38th Annu. Meet. Electron Microsc. Soc. Am.* (submitted for publication).

Turner, J. N., Chang, B. B., Ratkowski, A. J., and Parsons, D. F. (1978). *Electron Microse., Proc. Int. Congr., 9th, 1978*, p. 670.

Valdfe, U., and Goringe, M. J. (1971). *In* "Electron Microscopy in Material Science" (U. Valdré, ed.), pp. 208-235. Academic Press, New York.

von Ardenne, M. (1940a). "Elektronen-Ubermikroskopie." Springer-Verlag, Berlin and New York.

von Ardenne, M. (1940b). *Naturwissenschaften* **28,** 248-252.

von Ardenne, M. (1940c). *Z. Phys.* **115,** 339-368.

von Müller, H. O. (1942). *Kolloid-Z.* **99,** 6-28.

von Rühel, R. (1949). *Optik* **5,** 534-548.

Wells, O. C. (1960). *Br. J. Appl. Phys.* **11,** 199-201.

This Page Intentionally Left Blank

Chapter 4

Stereomicroscopy of Whole Cells

KEITH R. PORTER AND MARK E. STEARNS

Department of Molecular, Cellular and Developmental Biology,
University of Colorado,
Boulder, Colorado

I. Introduction 53
II. Background 55
III. Methods Currently in Use 55
IV. The Stereo Image of Whole Cells 56
V. Experimental Applications of Stereo Technology 59
A. Cell Structure and Behavior 59
B. Cation Effects on Cells 62
C. Drug Effects on Cells 62
D. Hormone Effects on Cells 63
VI. Properties of Differentiated Cell Systems 63
VII. Relating Whole-Cell to Thin-Section Images 64
VIII. Unique Applications of Stereo Techniques 66
IX. Alternative Analytical Approaches 70
X. Conclusions 73
References 74

I. Introduction

Over the past thirty-five years, electron microscopy of thin sections and centrifugal fractionation have contributed greatly to our understanding of cells. From the very limited knowledge available in 1945, we have moved rapidly to a vast amount of information on cell morphology and function that fills numerous compendia. This information encompasses not only whole cells but also cell organelles and structural elements such as mitochondria and microtubules. We have come to appreciate that the thin section represents a very small fragment of the cell, and that fractions derived from homogenized cells may not be represen-

Copyright © 1981 by Academic Press, Inc.
All rights of reproduction in any form reserved.
ISBN 0-12-564122-2

tative of what was present and functional in the intact unit. Thus, techniques now being introduced are used to make increasingly serious attempts to derive high-resolution information from intact whole cells or, at the very least, from thick sections of cells. These include imaging with high-energy electron beams, stereo viewing for three-dimensional observation, and selective staining of complex systems such as the Golgi to increase their electron-scattering properties and segregate them more positively from their surroundings. It is here, especially, that stereo viewing serves to prevent errors in interpretations that normally stem from two-dimensional images of thin sections or even from reconstructions from serial sections.

Stereo viewing, although widely employed in scanning electron microscopy (SEM), has been infrequently used in transmission electron microscopy (TEM). The main reason is that the small depth dimension of these sections, as well as the consequent good resolutions provided by the conventional electron microscope (TEM), have invalidated any extensive use of stereo microscopy. With the introduction of high-voltage electron microscopy (HVEM) for biological research, however, it is now possible to penetrate specimens much thicker than 100 nm and still obtain high resolution images of structure and even the three-dimensional disposition of enzymes and other specific proteins. Here, in particular, the increased information in thicker sections has made stereo images mandatory for properly resolving the three-dimensional details of integral structural components. We have thus reached the stage where we can move forward from an informative period in cell biology devoted to thin-section cytology and cell fractionation and begin to view at superb resolutions the organization and properties of both whole cells and tissues in the depth perspective.

This development seems very desirable, for there are several reasons to believe that the normal functioning cell depends on an organized distribution of organelles, systems, and structural components. After all, cells show polarities and a nonrandom distribution of parts. They are well known to possess forms that are in some instances highly asymmetric and unstable. They have, moreover, a sense of size and wholeness, which is there to be satisfied in any regeneration of a lost part. These are hardly the properties that one expects of a homogeneous cytosol or a "bag of enzymes." They describe, rather, the probable existence of a precisely structured unit extending from cell center to cell periphery—a unit that involves cytoskeletal microtubules and filaments, all contained in a gelatinous matrix that somehow knows and determines the disposition of the better-known organelles and systems. To collect information on this unit, the investigator needs to do less homogenizing and sectioning and more microscopy of the whole, intact unit. For this purpose the thinly spread cultured cell is a fairly ideal specimen. And the capability of the high-voltage microscope in providing images (in stereo) of even the thicker parts of these cells makes structural information of the intact unit available in three dimensions for the first time.

This chapter will give the reader an introduction to the techniques of specimen

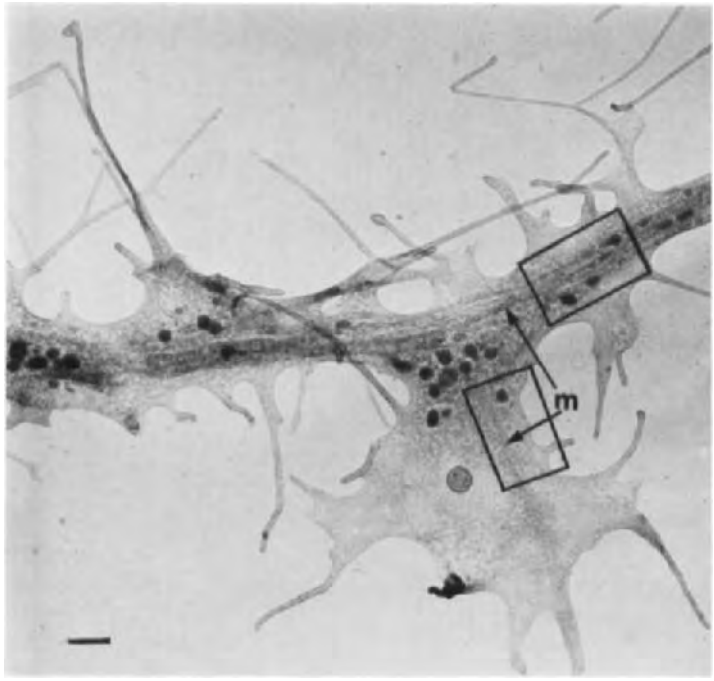
preparation and the various potentials of the stereo approach. As with most methods, this one has its limitations, and these, as well, will be given some attention.

II. Background

The first attempt to look at cultured cells by electron microscopy was made by Porter *et al.* (1945). The cells were grown on Formvar-coated cover-glasses, fixed in vapors of OsO_4, and transferred to grids with small pieces of the Formvar peeled away manually from the coverglass. They were then dried in air. The resulting cellular images varied in content as well as quality with the duration of exposure to OsO_4. Left for as long as 12–18 hours, the cells contained only membrane-limited structures, but it was from such images that one obtained the earliest characterizations of the endoplasmic reticulum (ER) (Porter and Kallman, 1953, Porter, 1953). The cisternae were clearly visible because the cytoplasmic ground substance (CGS) or matrix had been removed. Except for the manipulation of the film and cells on to the grid, the procedure was simple. However, the problems inherent in growing cells *in vitro* in this early period, not to mention the problems of maintaining a functioning electron microscope, served at the time to discourage the widespread use of this technique.

III. Methods Currently in Use

The current methods are both simpler and more effective. In the first place, cultured cells of a wide variety are now available for continuous culture under highly controlled conditions. Methods involving the trypsinization of differentiated tissues (or differentiating tissues from embryos) can provide primary cultures of almost any cell type. The preparation of these for microscopy is now achieved more simply by plating them on gold grids coated with Formvar and carbon. After fixation in 3% glutaraldehyde, the cells on the grids are dehydrated through increasing concentrations of alcohol and then transferred from anhydrous ethanol to liquid anhydrous CO_2 in a pressure chamber (bomb). Here the liquid CO_2 gradually replaces the ethanol and is eventually taken through the critical point (34°C) for drying (Anderson, 1951). Unexposed to the surface tension of air–water interphase, the cells emerge from the bomb with all parts in their original three-dimensional configuration (Figs. 1 and 2). A chapter in *Practical Tissue Culture Applications* (Wolosewick and Porter, 1979a) describes in greater detail the preparation of cultured cells for transmission electron microscopy.



FIGS. 1-3. HVEM pictures showing part of a neurite of a cultured neuroblastoma (C1300) cell. Cells were induced to form spreading lamellipodia with 1 m*M* Mg^{2+} for 10 minutes at 37°C following starvation in Mg^{2+}-free Hank's buffer.

FIG. 1. Low-power view to illustrate that axons contain central microtubule bundles (m) along which organelles are localized. A microtubule bundle is seen extending into the lamellar region of the axon. High-magnification stereo views of the thin (<μm) and thick (<1.5 μm) areas outlined are depicted in Figs. 2 and 3. Bar = 1 μm. Magnification 6200×.

IV. The Stereo Image of Whole Cells

Whole cells can be viewed in conventional TEMs (Buckley, 1975). However, for consistent high-resolution work, most investigators have found the 1000-kV microscope the instrument of choice (Buckley and Porter, 1973, 1975; Buckley, 1974). Image improvements provided by the HVEM are evident in the final resolution and in the ability of high-energy electrons to penetrate thick regions of cells (Figs. 1-3). This is especially obvious in stereo views. Figure 3 is a view of part of the thick central region of a forming nerve axon of a neuroblastoma cell; it

is included to illustrate this point. The reader is advised to compare the two-dimensional impression of Fig. 3a with the improved quality of the stereo image of Figs. 3a and 3b combined. In the thicker regions toward the cell center, the CGS takes on a dense, flocculent appearance in single micrographs. In stereo, however, it is clear that the structural organization of various cytoskeletal elements can actually be resolved (Figs. 3a and 3b).

From studies of this nature, one can visualize minute elements of the cytoplasm made up of microtubules, microfilaments, and the associated ground substance or matrix. In high-magnification images, viewed stereoscopically (Fig. 2), the CGS presents itself as a three-dimensional lattice composed primarily of slender strands ranging from 4 to 10 nm in diameter. These have been called microtrabeculae, and the structure they form, a microtrabecular lattice (MTL).

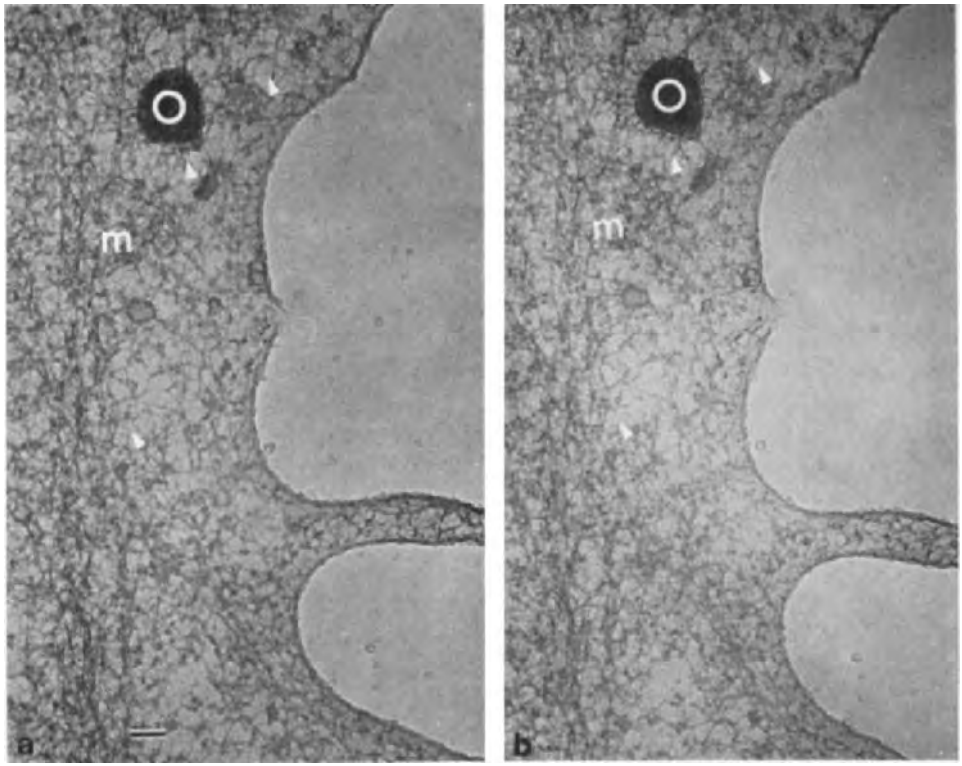


FIG. 2. The microtubule bundle is suspended in a three-dimensional lattice of anastomosing microtrabecular fibers (arrowheads). The lattice is seen to form a cytoskeletal matrix that is continuous with the subplasmalemmal surface and with the surfaces of the organelles (O). Stereo angle (S) = 12°. Bar = 0.1 μm. Magnification 40,000×.

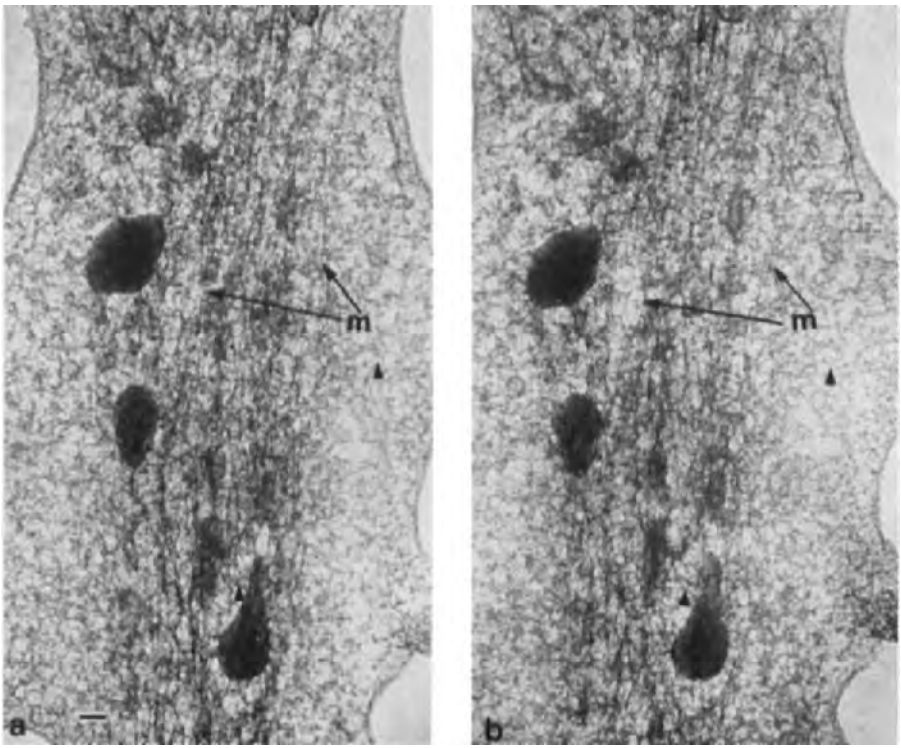


FIG. 3. A thick region of the axon. Stereo images enable one to visualize the three-dimensional interrelationship of microtubules (m), microtrabeculae (arrowheads), and cell organelles. The lattice is seen to form a continuous matrix extending from the cell membrane to interconnect the surfaces of suspended microtubules and organelles. Channels consisting of microtubules and lattice material appear to function in organelle transport along axons. Stereo angle (S) = 12°. Bar = 0.1 μm. Magnification 35,000×.

This system of microtrabeculae is continuous throughout the cell; it divides the cytoplasm into a "protein-rich" polymerized phase and an excluded "water-rich" fluid phase (Porter *et al.*, 1979a). The better-known formed structures, such as the polysomes, microfilaments, microtubules, and cisternae of the ER, are contained in and are part of the protein-rich phase. Thus, the products of protein synthesis in growing and differentiating cells become part of the protein-rich phase. This could account for a nonrandom distribution of tubulin essential to the patterned assembly of microtubules or of actin (De Mey *et al.*, 1980), and of myosin and α-actinin in the localized assembly of myofibrils (see Figs. 9 and 10). The structure, as depicted, would be expected to give to the CGS its gelatinous consistency and to restrain contained organelles from showing Brownian motion in living cells. It is reasonable to proceed from this view to the concept of the cytoplasm as part of a continuous organized structure or cytoplast,

an idea that is supported as well by numerous observations on the unit behavior displayed by the cytoplast and the ER in cell motion and during mitosis and cytokinesis. At the same time, the apparent capacity of the microtrabeculae to shorten and elongate locally seems, on the basis of available evidence, to provide the motive force required for intracellular motion. In this connection, there is good reason to believe that the saltatory transport of organelles in nerve fibers is dependent on the contracting and expanding properties of anastomosing microtrabecular fibers associated with the microtubule bundles (see Figs. 1-3) (Stearns, 1980; Ellisman and Porter, 1980).

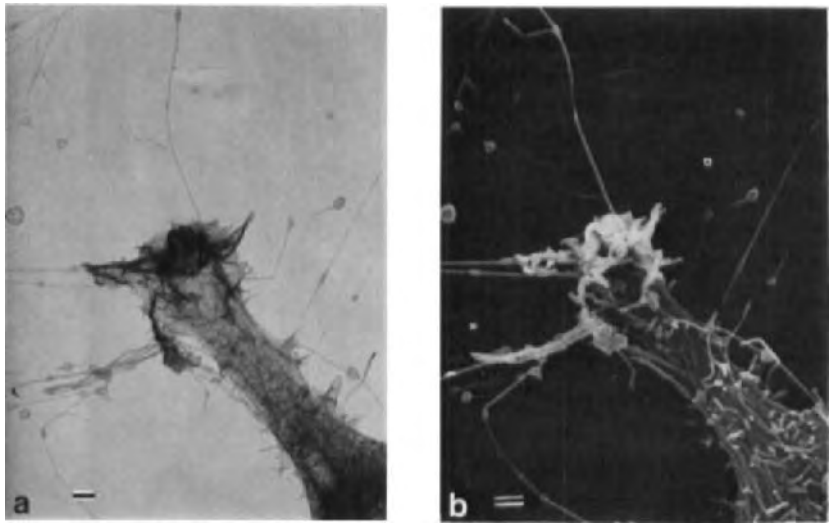
These are examples of the new concepts concerning important cell phenomena that have grown out of stereo images of whole cells.

One should always keep in mind the possibility that artifacts will be produced in the preparation of whole cells for electron microscopy. In a published study of this possibility, Wolosewick and Porter (1979b) varied the fixative and the method of fixation (freeze-substitution versus direct application of the fixative to the cells) and showed that the lattice structure was consistently present. In earlier papers, Buckley (1975) and Wessells *et al.* (1973) discussed the likelihood of the appearance of artifacts in some detail. They pointed out that subplasmalemmal filament networks are normally observed in thin-section studies (for example, studies of nerve axons by Yamada *et al.*, 1971) and that they bear a close resemblance to microtrabecular meshworks preserved in fixed critical-point-dried cells. Therefore, in agreement with the evidence already available in the literature, they correctly surmised that the cytoplasmic ground substance exists as an organized lattice and is not the artifactual product of fixation procedures.

V. Experimental Applications of Stereo Technology

A. Cell Structure and Behavior

The applications of stereomicroscopy of whole cells are expanding rapidly and will doubtless take on greater significance when more high-voltage microscopes become available. It is feasible, for instance, to analyze the internal architecture of whole cells (Figs. 4 and 5) and then metal-coat the same cell to view the external membrane surface in stereo SEM (see Figs. 5a and 5b). The correlative information made available by this approach will help to define precisely the influence that changes in cytoskeletal components can exert on the external cell surface morphology (for example, in microvilli, ruffles) during cell spreading and elongation. This approach has already been successfully applied to follow virus propagation, maturation, and release from host cell systems (Fonte and Porter, 1974). The same methods will also be useful in analyzing the ultrastructural basis for endocytosis, especially where it involves selective uptake by clathrin-coated pits and vesicles. The capping process in cells and the involvement of the subsurface lattice also lend themselves to this approach.



FIGS. 4-6. HVEM and SEM pictures of Mg^{2+}-induced ruffles of a normal rat kidney cell.

FIG. 4. Low-magnification HVEM and scanning views of a forming lamellipodia. The ruffling has occurred in response to 1 m*M* Mg^{2+} following the starvation of cells in Mg^{2+}-free Hank's buffer. Bar = 1 μm. Magnification 3600×.

Even though in its earliest phases of use, the technique has contributed many valuable observations on the responses of cells, in terms of fine structure, to a number of environmental conditions (temperature, tonicity) and to drugs known to influence the assembly or disassembly of cytoskeletal elements, such as colchicine and cytochalasin. With whole cells and stereo imaging, one can record the holistic responses of cells and relate the observed changes to structural features at the level of 2.0–5.0 nm.

For example, when cultured cells are chilled to 4°C over a period of 2–3 hours, they tend to withdraw their thin margins and round up. Only slender filopodia persist to mark the location of the cell margins. Microtubules disassemble in most occurrences, and it has been assumed that this collapse of a cytoskeletal component is responsible for the change in cell shape. Actually, the microtubules depolymerize within minutes, whereas the shape change takes much longer. Examination of the thinner margins of the chilled cells reveals a major change in the microtrabecular lattice. It essentially collapses by 2–3 hours into small masses of deformed microtrabeculae and clusters of polysomes. Other trabeculae associate in sheets and merge with the cytoplasmic cortex. And the water-rich phase of the CGS becomes an enlarged void in which the vesicular fragments of the ER and lysosomes may move in Brownian motion. Cells returned to incubator temperatures (37°C) immediately (within 5 minutes) extend their margins

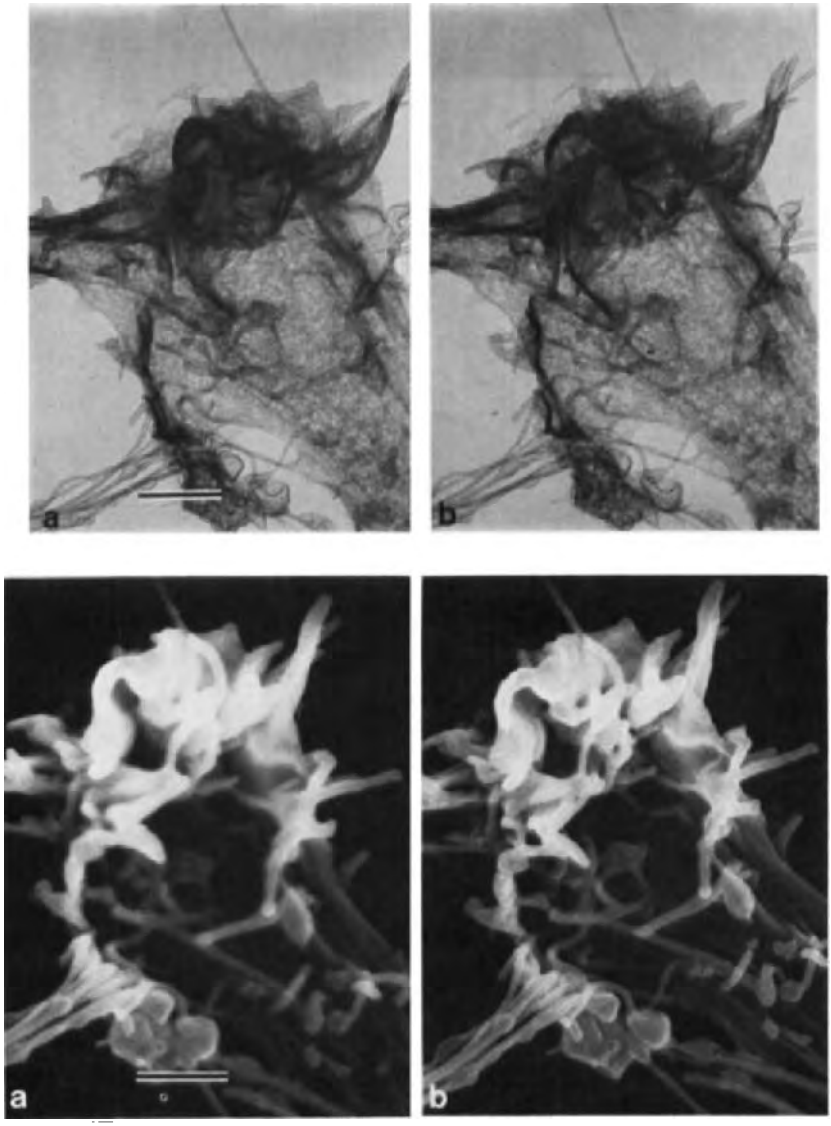


FIG. 5. HVEM picture of Mg^{2+}-induced ruffles of a normal rat kidney cell. Stereo view showing a thin margin of the lamellipodia. The cytoplasmic ground substance comprises an organized microtrabecular lattice and the lattice is seen to extend as a continuous structural element in forming filopodia. In general, this image gives information about organizational properties of the ultrastructural components responsible for cell shape. To ascertain the corresponding properties of the cell surface, cells were coated with gold and viewed by SEM. Stereo angle (S) = 12°. Bar = 1 μm. Magnification 11,200×.

FIG. 6. Stereo SEM view showing that the cytoplasmic membrane is retained intact. Numerous projections of the forming ruffle are highly visible. Note that the cell cytoskeleton discerned in HVEM images closely corresponds in distribution to the cell shape seen in SEM. Stereo angle (S) = 9°. Bar = 1 μm. Magnification 11,200×.

through a restructuring of the lattice, and this occurs without the immediate involvement of microtubules. Thus, a dramatically rapid change in the three-dimensional structure of the MTL can be observed as it relates to changes in cell shape. This information could not readily be derived from thin sections without great effort and uncertainty (Wolosewick and Porter, 1979b).

B. Cation Effects on Cells

Equally rapid and striking changes occur in response to the presence or absence of divalent cations. Cells exposed for as little as 3 minutes to a medium devoid of Mg^{2+} withdraw rapidly to a rounded form as the lattice, ordinarily finely divided, becomes coarse by comparison. Returned to a balanced salt solution, including 1 m*M* Mg^{2+}, the cells begin at once to respread (3 minutes) and display prominent ruffling (Figs. 4–6) or, in neurons, to form rapidly lamellipodia at their advancing edges (Figs. 1–3). From preparations of such cells, it is possible to obtain high-resolution images, which depict a return of the MTL to its normal morphology. Although the explanation for these rapid changes is not immediately evident, the collapse of the lattice and its recovery suggest an involvement of Mg^{2+}-dependent ATPases and the utilization of metabolic energy in the maintenance of the finely divided form (the normal form) of the MTL.

C. Drug Effects on Cells

It is obvious from the above examples, and especially from the experiments with divalent cations, that stereo viewing of whole cells is an invaluable aid in studies of cytoskeletal involvement in cell motility. One could design systems of gradients that would induce chemotactic responses (cyclicAMP-dictyostelium) or construct systems of surface ridges along and over which cells could migrate preferentially, and then examine the associated configurations of skeletal structures (Albrecht-Buehler, 1979).

Cell responses to a number of drugs such as cytochalasin B and Taxol (or colchicine or nocodazole) offer attractive opportunities for observing fine structural changes associated with the gross form changes that the treated cells display.

The response of normal rat kidney cells (NRK) and chick epithelial cells when exposed to 20 μM dihydrocytochalasin B (H_2CB) has been explored by Fonte *et al.* (1978). As expected from previous studies of this nature (Gerschenbaum *et al.*, 1974), the cells promptly lose their stress fibers (microfilament bundles) and adopt an arborized form. Concomitantly, the MTL transforms from the finely dispersed normal form to a lattice of thickened trabeculae (5–30 nm in diameter), and these are coextensive with numerous pimple-like mounds of greatly thickened trabeculae. The apparently unaffected microtubules persist in the numerous branches of the cells. This morphology continues until the H_2CB is with-

drawn, after which the MTL returns to its accustomed form as the margins of the cell move out to fill in the spaces between the slender pseudopodia of the arborized form. Although one can only speculate on what is happening in this extraordinary response and recovery, it is anticipated that the approach and the excellent resolutions provided by the HVEM will eventually give some valuable clues as to the involvement of the MTL in the shaping of cells, especially when labeled antibodies are available for observing actin distribution in EM images (see below).

D. Hormone Effects on Cells

One should in time derive insight into normal cell behavior from the fact that several kinds of cells that are the normal targets of hormones can display *in vitro* a response to hormones that is remarkably similar to that induced by H_2CB. Just as in the above example, stress fibers disappear, and the cell margins withdraw and thicken except along branches or arborizations in which microtubules persist. Such striking morphological changes have been described in ovarian granulosa cells exposed to follicle-stimulating hormone (FSH) (Lawrence *et al.*, 1979), in osteoblasts treated with parathyroid hormone (Miller *et al.*, 1976), and in human thyroid cells subjected to *in vitro* concentrations (10 μg/ml) of thyroid-stimulating hormone (TSH). Similar effects are also evoked when adrenocortical cells are exposed to adrenocorticotropin (ACTH) (Sato *et al.*, 1970). In each instance it has been reported that the hormone induces an increase in cyclic AMP (cAMP), especially when potentiated with theophylline. And the effects of TSH and FSH are mimicked by the addition of 1 m*M* dibutyryl cAMP plus 1 m*M* theophylline. Again, stereo viewing at relatively high magnifications (50,000×) gives evidence of distinct changes in the form and dimensions of the MTL. That cAMP is the mediator in these dynamic reorganizations of the cytoplasmic ground substance, and in the stabilization and assembly of microtubules, seems perfectly clear (Westermark and Porter, 1980). But it is not so evident that cAMP always expresses itself in the same way. For example, in chromatophores (see below) the addition of cAMP to the environment induces the cell to undergo a dispersing action and a restructuring of the lattice from the collapsed form in pigment aggregation. This effect perhaps mimics the longer term effects of TSH on thyroid cells in which the cells respread after arborization.

VI. Properties of Differentiated Cell Systems

Many of the observations on the structure and responses of cells to external factors have been made on cell lines that are relatively undifferentiated and are capable of continuous proliferation. Comparisons between neoplastic and non-neoplastic cells as they appear in culture are less valuable because of this. It is

important to show, in this context, that differentiated, nonproliferating cells can be brought to the stage of the electron microscope and profitably examined as whole units by stereomicroscopy. They perform as differentiated cells when appropriately stimulated.

A case in point is represented by chromatophores of fish and other forms, which may be isolated from other cells of the tissue by collagenase digestion (Byers and Porter, 1977; Luby and Porter, 1980). When allowed to spread on coated gold grids, they are available for experimental observations on the mechanism of pigment transport. When exposed to epinephrine or to membrane-depolarizing concentrations of K^+, they aggregate their pigment. Although this happens very rapidly, stages in the process can be captured by glutaraldehyde fixation. In the dispersed cell, the pigment is contained in a sparsely represented MTL. It is evident in stereo images of such preparations that all granules are connected by slender trabeculae to other granules or to microtubules and the cytoplasmic cortex. During aggregation this morphology changes dramatically; the trabeculae shorten, and the whole centrally based lattice contracts, carrying the pigment with it. The balance of the lattice moves with the microtubules into close association with the cell cortex. In pigment dispersion the lattice is restructured; that is, it re-expands from the contracted state, carrying the pigment in a radial direction defined by a frame of microtubules. This process is ATP-dependent and can be initiated by dibutyryl cAMP applied exogenously or by such inhibitors of phosphodiesterase as caffeine or theophylline. Luby and Porter (1980) have collected evidence by HVEM stereo that the elongation of the trabeculae in lattice restructuring is specifically inhibited by such metabolic inhibitors as DNP, KCN, and oligomycin.

Yet another way to study differentiated cells involves the use of very thick sections—as thick as 5 μm. Good results from this approach depend on the selective staining of the system of interest, such as the ER (the sarcoplasmic reticulum of muscle: Peachey and Eisenberg, 1978) or the Golgi complex, and access to a high-voltage microscope (Favard and Carasso, 1973). Since this method is beyond the scope of this chapter and is discussed elsewhere in this volume (see Yamada and Ishikawa, Chapter 7), we shall not dwell on it here, except to say that it is potentially a very valuable approach, especially for observations at low magnifications of the three-dimensional organization of selected systems within cells. The methods for achieving selective staining could be expanded, and when applied in experimental or comparative cytology they should yield valuable observations.

VII. Relating Whole-Cell to Thin-Section Images

One question that has grown out of HVEM examination of whole cells concerns the fairly obvious discrepancy between the structure of the CGS as seen in thin-section and whole-cell microscopy. In thin sections of cultured cells one

would expect to see fragments of microtrabeculae and occasionally complete strands running as bridges between the better-known formed structure. What one does see are very fine strands (3.0 nm) and images of what is best described as fluffy material associated with surfaces and with polysomes. If one assumes that the whole-cell image would provide an holistic impression of what is seen in thin-section images of epoxy-embedded cells (and there is no good reason to question this), then one must conclude that something is lost in the embedding or that the epoxy and part of the MTL both scatter electrons to the extent that the trabeculae are difficult to visualize. For several reasons the latter seems to be the most accurate interpretation. It is known that to see the well-known cell components in sections from epoxy blocks one must stain with uranyl and lead, whereas in the whole cells no stain is required because there is no embedding matrix in the cells. To test this hypothesis, tissues and isolated cells have been fixed in the

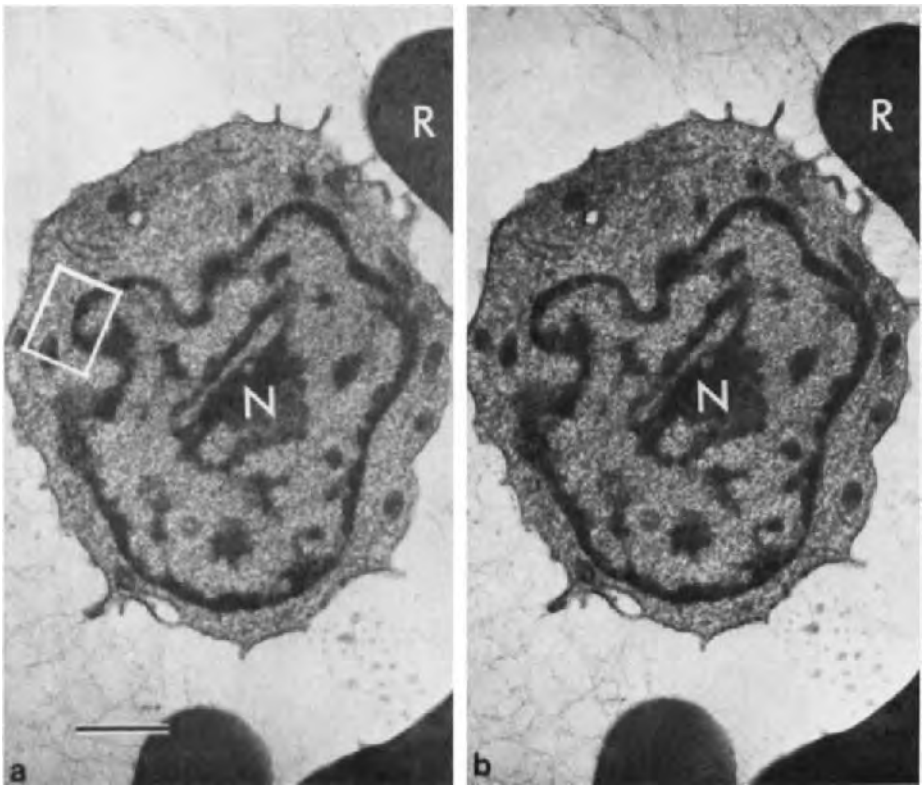


FIG. 7. Stereo views of a human lymphocyte prepared by PEG sectioning methods. The cell is unstained except for brief osmification. The increased density of organelles (membranes, mitochondria, nucleus) makes them easy to discern from the surrounding cytoskeletal matrix. The nucleus (N) heterochromatin is especially dense. A red blood cell (R) is seen to be devoid of any obvious microtrabecular lattice. Stereo angle (S) = 20°. Bar = 1 μm. Magnification 11,300×. Figure supplied courtesy of John Guatelli.

usual way and eventually embedded in polyethylene glycol (PEG). Subsequently, and after the embedded cell is sectioned, the PEG is dissolved from the sections with H_2O (or alcohol) and the section is dried from liquid CO_2. This provides a thick (0.25–0.5 μm) section, which has the major attributes of the whole cultured cell without being a whole cell. The stereo micrographs (Figs. 7 and 8) depict for the CGS the same microtrabecular lattice as is found in images of the whole cell (see Figs. 1–3). The dimensions and the volume ratios of trabeculae to intertrabecular space are different, but that is to be expected, since differentiated cells normally contain less H_2O.

This suggests, at the very least, that the conventional thin-section image does not tell the whole story. If, after the thick section has been cut from the PEG and the PEG has been water-extracted, the section is embedded in epoxy, thin-sectioned, and stained, the conventional thin-section image emerges. Experiments with this procedure are in their earliest stages, but enough has been done to justify these comments (see Figs. 7 and 8).

VIII. Unique Applications of Stereo Techniques

Significant contributions toward our complete understanding of cellular differentiation are possible from high-resolution investigations of changes in the CGS during the morphogenesis of cytoskeletal components. We have chosen for this purpose to examine in whole myoblasts the emergence of myofibrils. Previous studies using thin sections of muscle tissues undergoing differentiation have followed the appearance first of microtubules, then Z bands and thin actin filaments, and, finally, the thick myosin filaments in an ordered pattern relative to the thin microfilaments (Warren and Porter, 1969; Toselli and Pepe, 1968). Such observations have failed to relate these events to the whole cell and have given neither a reasonable explanation for the parallel order of the myofibrils nor any clues as to how the muscle proteins might be synthesized where they are needed for fibril assembly. What exists is a continuous system that might tie together these seemingly disparate events. To look for answers to these questions, Porter *et al.* (1979b) have cultured myoblasts from chick embryo heart tissue, following the methods of De Haan (1967). When populations of pulsating myoblasts were present on the coated gold finder grids, they were fixed in the usual manner for critical-point drying and high-voltage microscopy. The location of contracting cells on the grids was recorded to make it easier to find them in the high-voltage microscope after fixation and processing.

Stereo viewing of these cells reveals the usual space-filling lattice that has been observed in other cells and described elsewhere. In addition to this ground substance, the myoblasts contain, as expected, a number of myofibrils. Frequently, one end (the proximal end, relative to the cell center) of these will

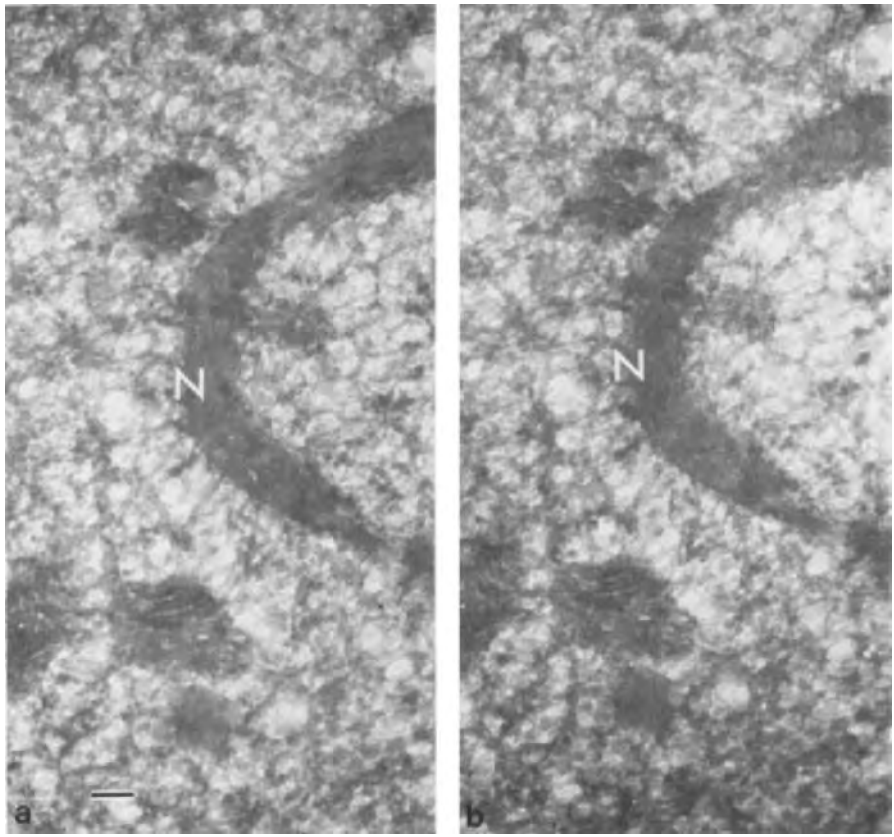


FIG. 8. High-magnification stereo view of part of a cell similar to that outlined in Fig. 7a. The Peg-sectioned specimen (0.25 μm thick) has retained the basic three-dimensional properties of the cytoskeletal matrix seen in whole mounted cells. The anastomosing trabecular fibers are continuous with the membrane surface of the nuclear envelope (N). The nucleus appears to contain a lattice structure similar to that seen in the cytoplasm. Stereo angle (S) = 20°. Bar = 0.1 μm. Magnification 53,000×. Figure supplied courtesy of John Guatelli.

appear fully differentiated, whereas the other end is obviously in an early stage of assembly. Intermediate stages are evident in between the two extremes (see Figs. 9 and 10). It is consequently possible to observe, in three dimensions, the relation of Z bands and actin filaments to the MTL during the differentiation of the fibril. First, it is evident that all elements of the myofibril are continuous structurally with the surrounding trabeculae and that the myofibril is essentially a local differentiation of the lattice. The actin filaments are seen to emerge from the MTL as a fusion of elongated trabeculae very loosely associated with the adjacent myofibril. Sometimes the association is evident only in its parallel orientation. As a rule, however, such filamentous structures have one end in

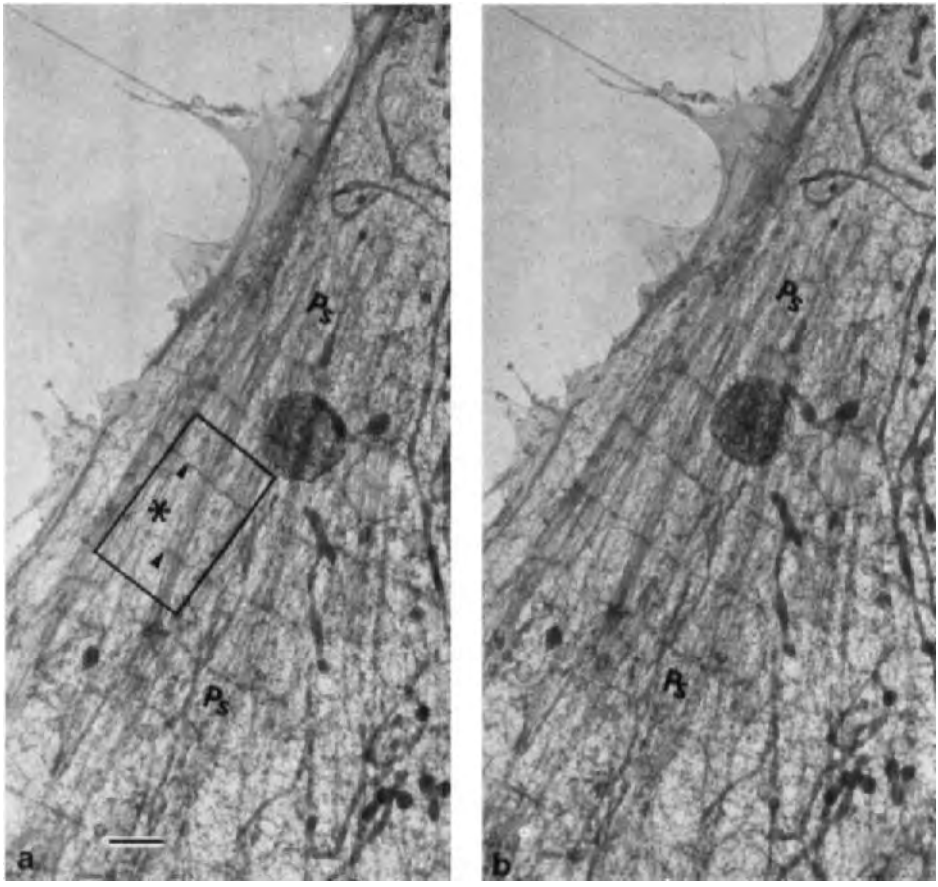


FIG. 9. Stereo image showing part of a developing myoblast cultured from 12-day-old chick heart. The myofibrils, here, are thin and mostly located next to the lower cortex of the cytoplast. They consist of very fine filaments, probably actin. The microtrabeculae of the surrounding ground substance are long, slender filaments often seen oriented parallel to adjacent fibrils (*) and studded with polysomes (PS). At the Z band, the trabeculae are less linear and have their long dimensions oriented normal to the axis of the fibril. In this form they extend across the spaces between the fibrils (arrowheads). Stereo angle (S) = 15°. Bar = 1 μm. Magnification 6500×.

continuity with a forming Z band. The microtrabeculae intimately linked with Z-band formation are obviously short and broad compared with those coextensive with the actin filaments. It is also evident that polysomes are clustered in trabeculae adjacent to the forming filaments and bands of the sarcomere. Presumably, this association, which is difficult to quantitate, provides for the differential synthesis of the proteins (actin and α-actinin) normally required for building the early myofibril. The implications of this observation are obvious: messenger RNA for muscle proteins seems to be distributed nonrandomly in the

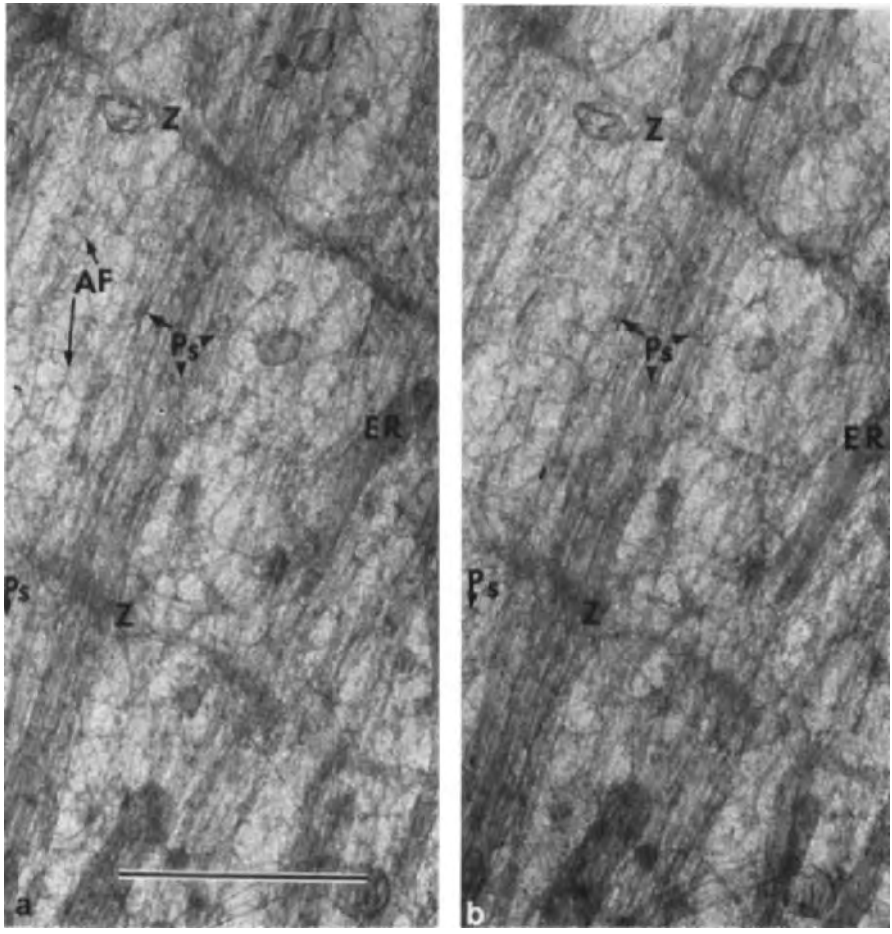


FIG. 10. Enlargement of the area in the small rectangle in Fig. 9. This stereo pair shows the relationship between the earliest assembled myofibril and associated cytoplasmic ground substance in which actin myofilaments are assembling. In areas between the myofibrils (AF), the microtrabeculae consist mostly of long filamentous units (diameter of 12.5 nm), which in some instances run the full length of the sarcomere. Where they are in contact, they form bundles that insert into the Z bands at their ends. Here, the trabeculae are relatively short and have their long axis oriented normal to the axis of the fibrils. Some vesicles (ER) are present. Free polysomes (Ps) are evident, especially at the ends of forming fibrils where the demand for muscle proteins is greatest. Stereo angle (S) = 12°. Bar = 1 μm. Magnification 33,400×.

structured ground substance of the myoblast, and its translation is locally controlled to give a graded growth and differentiation of the myofibril. The potential of this system and this approach for understanding the process of cellular differentiation will not escape the students of such phenomena. Once more, we find in such investigations an important role for stereomicroscopy of whole cells.

IX. Alternative Analytical Approaches

Having observed the structural features of the CGS in whole cells, the investigator logically begins to ask questions about the composition of the observed structures and how the components are distributed. For example, is the distribution of actin confined to microfilament bundles (stress fibers), and is tubulin for tubule assembly distributed randomly throughout the ground substance, or localized in channels? Black and Lasek (1979) have demonstrated actin and tubulin proteins to be transported at distinctly different rates in neurons. The exciting possibility is that separate microtubule and microfilament channels might exist, with each functioning in the transport of separate proteins. Different properties of the two types of transport channels could then account for differences in rates of transport.

Questions of this kind can be explored with apparent profit by techniques that examine whole cells at EM resolutions.

In studies that began several years ago, a few investigators undertook to extract cells with detergents of various potencies to determine which of the formed filaments might resist solubilization by detergents and what might be the composition and source of the extractable components (Brown *et al.*, 1976; Lenk *et al.*, 1977). The results are very interesting in showing that microfilaments (actin) and intermediate filaments resisted extraction, whereas numerous other soluble components could be removed. The extracts, examined by the techniques of gel electrophoresis, were remarkable in showing the presence of numerous proteins, of which only a few could be identified. Refinements in the extraction procedure, as subsequently introduced by Lenk *et al.* (1977) and by the Osborn and Weber group (1977), left intact the cytoskeletal filaments including the microtubules. Application of stereomicroscopy to these remnants has helped to define the three-dimensional relationships, and particularly the connections between the more detergent-resistent filaments (microfilaments, intermediate filaments, and microtubules). Such images (Fig. 11) clearly illustrate, as well, that the MTL has been extracted in very large part (Schliwa, 1980). In some places, especially in the cell margins, the fine lattice of actin filaments (identified by HMM decoration) would seem to represent the MTL that was previously there. This suggests that microfilaments of actin may, quite generally, be a central component of the microtrabeculae. As analysis of the detergent extracts continues by gel electrophoresis, it should be possible to characterize in greater detail the molecular composition of the detergent-sensitive MTL components.

Another approach that involves the use of labeled antibodies to localize specific proteins used as antigens promises compositional information at much higher resolutions than those provided by extraction studies. Thus far, peroxidase, ferritin, and colloidal gold have found particular favor as markers.

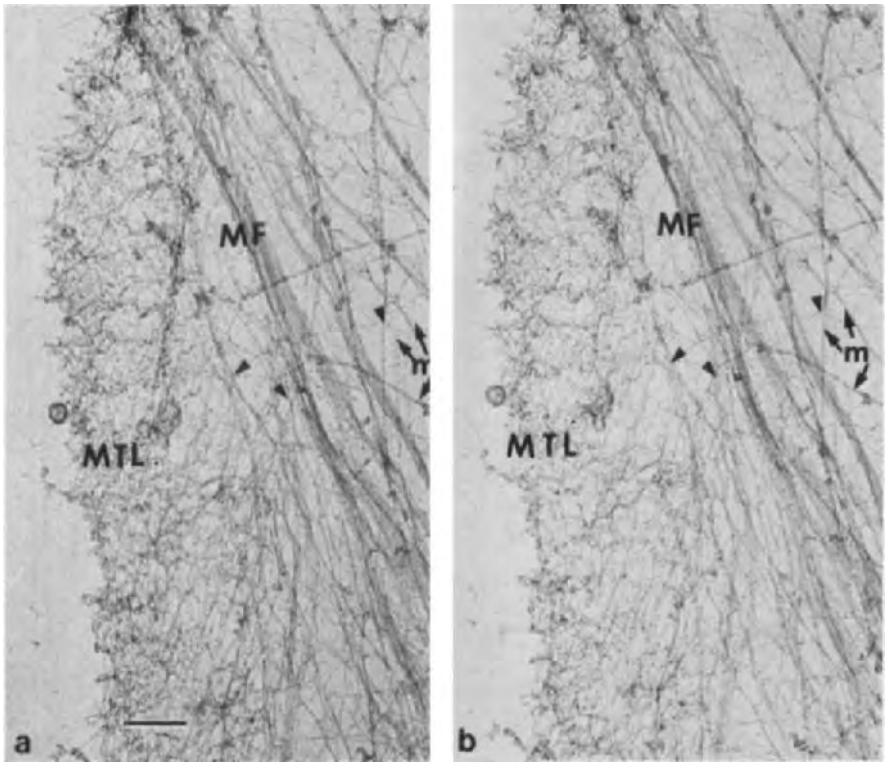


FIG. 11. Detergent cytoskeleton showing a chick fibroblast cell margin. The microtubules (m), the actin-microfilament bundles (MF), and much of the actin-rich microtrabecular lattice (MTL) in the thin margins have resisted extraction. The lattice has retained some aspects of its three-dimensional organization. In stereo, remnant cross-linking trabeculae (arrowheads) are seen interconnecting the surfaces of microtubules and microfilament bundles. Stereo angle (S) = 18°. Bar = 1 μm. Magnification 10,700×. Micrograph courtesy of Dr. Manfred Schliwa.

Admittedly, getting the labeled antibodies into the cell presents problems. Agents such as detergents, that will open the membrane, seem prone to damage and aggregate the underlying structures. Webster *et al.* (1978) have utilized immunoferritin identification of actin- and tubulin-containing structures to visualize the three-dimensional distribution of cytoskeletal elements in 80-kV stereo micrographs of detergent-treated animal cells. The results are interesting in that actin antibody can decorate both microfilament bundles and at least some of the filamentous elements of the microtrabecular lattice. Thus, it is possible by this technique and stereo viewing to track microfilaments and determine how they interact with other filamentous elements of the CGS. Similar results with peroxidase-antiperoxidase antibodies coupled to antitubulin have been obtained

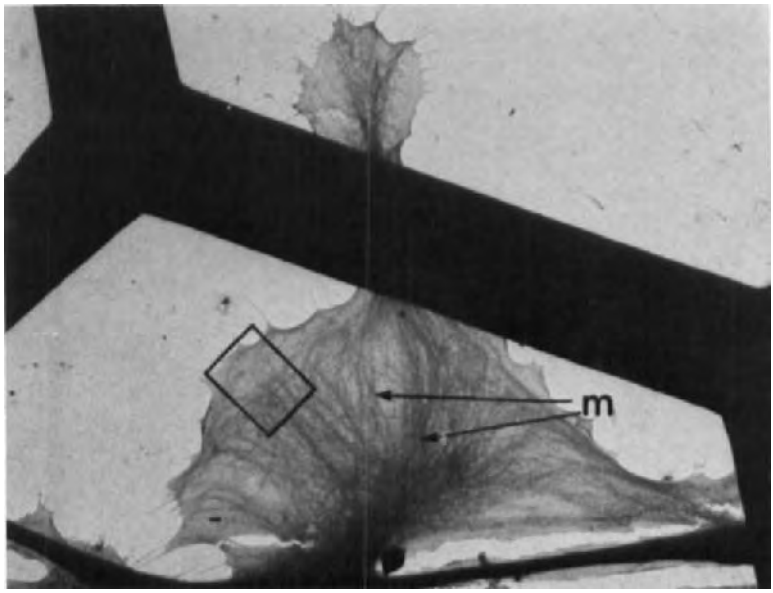


FIG. 12. HVEM view of a PtK_2 cell stained with tubulin antibodies by the PAP-immunoperoxidase method of Sternberger (1979). Numerous microtubules (m) are seen emanating from the centrosomal region of the cytoskeletons. Bar = 1 μm. Magnification 1700×. Figure kindly supplied by Dr. Jan De Mey.

by Jan De Mey and associates. In collaborative studies with our laboratory, they have been able to stain selectively microtubule networks in whole critical-point-dried cells prepared for HVEM (Figs. 12 and 13). High-magnification stereo images of these cells (Fig. 13) reveal that tubulin-containing components make up at least part of the lattice material associated with and cross-linking suspended microtubules. This suggests that tubulin proteins may be localized in channels for the purposes of transport (see above discussion) and assembly in developing cell systems.

In future studies using immunochemical techniques, it is anticipated that these staining methods can be used in conjunction with PEG sectioning procedures. This approach will permit dissection of the cytoskeleton components important for development and differentiation of both cells and tissues. For example, to improve the quality of HVEM images in studies of lymphocyte differentiation, cells can be treated with multivalent anti-IgM antibodies coupled with hemocyanin surface markers. In such work, it should also be possible to label preferentially (that is, with anti-actin) the internal cytoskeletal elements responsible for changes in cell surface shape.

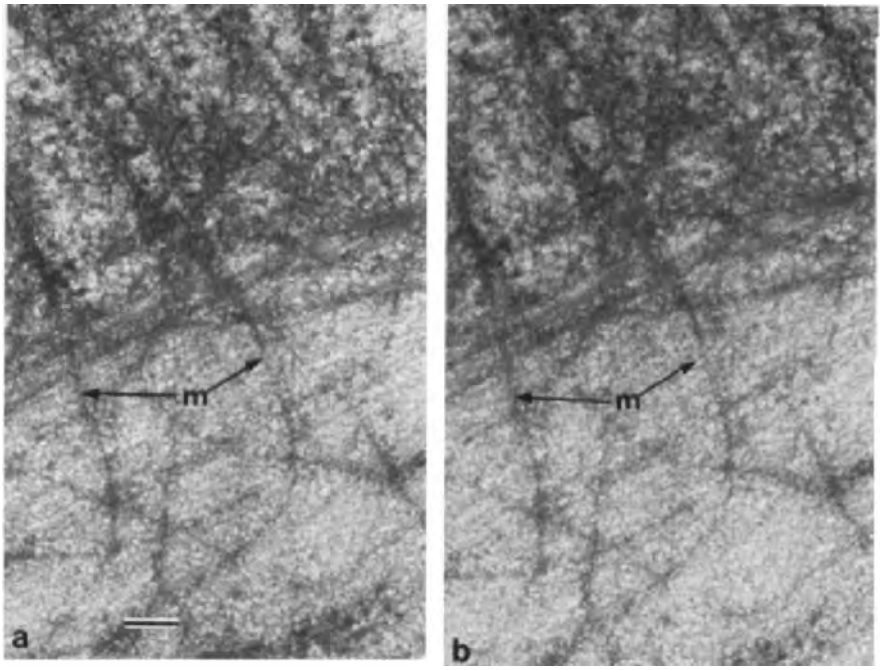


FIG. 13. Enlargement of the part of the cell outlined in Fig. 12. The stereo picture reveals that the peroxidase-antiperoxidase-labeled strands are microtubules (m). The microtrabeculae of the lattice are lightly, but nonuniformly, stained. A uniform density of label is seen on trabeculae (presumably tubulin-rich) coating the surfaces of microtubules. Stereo angle (S) = 20°. Bar = 1 μm. Magnification 6800×. Figure kindly supplied by Dr. Jan De Mey.

X. Conclusions

This article has outlined some of the important principles and applications of stereomicroscopy to the study of whole cells. The major achievements have come from HVEM investigations of specimens prepared by critical-point drying, in combination with stereo-viewing techniques. By utilizing these three-dimensional imaging techniques, it is possible to determine intimate interrelationships between cell behavior and the distribution of organelles and cell structural components. The high resolution of images obtained has especially enabled the visualization of intricate cytoplasmic elements important in cell operations as diverse as the shaping of cells and the regulation of protein distribution. This progress, made in the infancy of HVEM stereomicroscopy, encourages one to expect much greater achievements in the immediate future.

ACKNOWLEDGMENTS

We wish to thank Karen Anderson for excellent technical assistance and Joyce Albersheim for help in the preparation and typing of the manuscript.

REFERENCES

Albrecht-Buehler, G. (1979). *J. Cell Biol.* **80,** 53-60.
Anderson, T. F. (1951). *Trans. N.Y. Acad. Sci.* [2] **13,** 130-134.
Black, M. M., and Lasek, R. J. (1979). *Brain Res.* **171,** 401-413.
Brown, S., Levinson, W., and Spudich, J. A. (1976). *J. Supramol. Struct.* **5,** 119-130.
Buckley, I. K. (1974). *Tissue & Cell* **6,** 1-20.
Buckley, I. K. (1975). *Tissue & Cell* **7,** (1), 51-72.
Buckley, I. K., and Porter, K. R. (1973). *J. Cell Biol.* **59,** 37a.
Buckley, I. K., and Porter, K. R. (1975). *J. Microsc. (Oxford)* **104,** 107-120.
Byers, H. R., and Porter, K. R. (1977). *J. Cell Biol.* **75,** 541-558.
De Haan, R. L. (1967). *Dev. Biol.* **16,** 216-249.
De Mey, J., Wolosewick, J. J., De Brabander, M., Geuens, G., Joniau, M., and Porter, K. R. (1980). *In* "Cell Movement and Neoplasia" (M. De Brabander *et al.*, eds.), pp. 21-28. Pergamon, Oxford.
Ellisman, M. H., and Porter, K. R. (1980). *J. Cell Biol.* **87,** 464-479.
Favard, P., and Carasso, N. (1973). *J. Microsc. (Oxford)* **97,** 59-81.
Fonte, V. G., and Porter, K. R. (1974). *In* "Scanning Electron Microscopy," Part III, pp. 827-834. IIT Res. Inst., Chicago, Illinois.
Fonte, V. G., Anderson, K. L., Wolosewick, J. J., and Porter, K. R. (1978). *J. Cell Biol.* **79,** No. 2, 74a.
Gerschenbaum, M. R., Shay, J. W., and Porter, K. R. (1974). *In* "Scanning Electron Microscopy," Part III, pp. 589-596. IIT Res. Inst., Chicago, Illinois.
Lawrence, T. S., Ginzberg, R. D., Gilula, N. B., and Beers, W. H. (1979). *J. Cell Biol.* **80,** 21-36.
Lenk, R., Ransom, L., Kaufmann, Y., and Penman, S. (1977). *Cell* **10,** 67-78.
Luby, K. J., and Porter, K. R. (1980). *Cell* **21,** 13-23.
Miller, S. S., Wolff, A. M., and Arnaud, C. D. (1976). *Science* **192,** 1340-1343.
Osborn, M., and Weber, K. (1977). *Exp. Cell Res.* **106,** 339-349.
Peachey, L. D., and Eisenberg, B. R. (1978). *Biophys. J.* **22,** No. 2, 145-154.
Porter, K. R. (1953). *J. Exp. Med.* **97,** 727-750.
Porter, K. R., and Kallman, F. (1953). *Exp. Cell Res.* **4,** 127-141.
Porter, K. R., Claude, A., and Fullam, E. F. (1945). *J. Exp. Med.* **81,** 233-246.
Porter, K. R., Byers, H. R., and Ellisman, M. H. (1979a). *In* "The Neurosciences: Fourth Study Program" (F. O. Schmitt and F. G. Worden, eds.), pp. 703-722. MIT Press, Cambridge, Massachusetts.
Porter, K. R., Fleming, J., and Wray, G. (1979b). *J. Cell Biol.* **83,** 46a.
Sato, G., August-Tocco, G., and Posner, M. (1970). *Recent Prog. Horm. Res.* **26,** 539-546.
Schliwa, M. (1980). *Proc. 38th Annu. Meet. Electron Microsc. Soc. Am.* pp. 814-817.
Stearns, M. E. (1981). *J. Cell Biol.* (in press).
Sternberger, L. A. (1979). "Immunocytochemistry," 2nd ed., Wiley, New York.
Toselli, P. A., and Pepe, F. (1968). *J. Cell Biol.* **37,** 445-481.
Warren, R. H., and Porter, K. R. (1969). *Am. J. Anat.* **124,** 1-30.

Webster, R. E., Henderson, D., Osborn, M., and Weber, K. (1978). *Proc. Natl. Acad. Sci. U.S.A.* **75** (11), 5511-5515.

Wessells, N. K., Spooner, B. S., and Ludueña, M. A. (1973). *Ciba Found. Symp.* **14** (new ser.), 53-82.

Westermark, B., and Porter, K. R. (1980). *J. Cell Biol.* (in press).

Wolosewick, J. J., and Porter, K. R. (1979a). *In* "Practical Tissue Culture Applications" (K. Maramorosch and H. Hirumi, eds.), pp. 59-85. Academic Press, New York.

Wolosewick, J. J., and Porter, K. R. (1979b). *J. Cell Biol.* **82,** 114-139.

Yamada, K. M., Spooner, B. S., and Wessells, N. K. (1971). *J. Cell Biol.* **49,** 614-635.

This Page Intentionally Left Blank

METHODS IN CELL BIOLOGY, VOLUME 22

Chapter 5

Stereoscopic Electron Microscopy of Chromosomes

HANS RIS

Department of Zoology,
University of Wisconsin,
Madison, Wisconsin

I. Introduction 77
II. Methods 78
A. The 20-Nm Chromatin Fiber 78
B. Polytene Chromosomes 79
C. Mitotic Chromosomes 79
D. Kinetochore 80
E. Heterochromatin, C Bands, Giemsa Bands 81
F. Stereophotography 82
III. Levels of Organization in Chromosomes 82
A. The 20-Nm Chromatin Fiber 83
B. Polytene Chromosomes and Interphase Chromomeres 83
C. Mitotic Chromosomes 85
D. Kinetochore Organization in Mammals 90
E. Heterochromatin 95
References 95

I. Introduction

For most biological specimens, resolution is at best about 2 nm because of radiation damage by the imaging electrons (Glaeser, 1975). Chromatic aberration of the electromagnetic lenses imposes additional limitations except where the specimen thickness is less than 20 nm. In the past, this has restricted electron microscopy of cells and tissues to ultrathin sections, and the images obtained have been essentially two-dimensional. With relatively open structures or when

Copyright © 1981 by Academic Press, Inc.
All rights of reproduction in any form reserved.
ISBN 0-12-564122-2

maximum resolution is not essential, satisfactory images can be obtained at 100 kV with sections up to 100 or 150 nm thick. Interpretation becomes difficult, however, as specimen thickness increases, owing to overlapping of structures. Stereomicroscopy greatly improves the situation by separating structures according to their position in the vertical axis. Most 100-kV instruments are equipped with tilt stages, but stereophotography has rarely been used because with thin sections the three-dimensional effect is limited. Some examples are the stereo micrographs of lampbrush chromosomes (Lafontaine and Ris, 1958), of isolated metaphase chromosomes (Stubblefield and Wray, 1971), and of interphase chromatin in sections (Hyde, 1964).

The availability of the high-voltage electron microscope (HVEM) in recent years has greatly expanded the applications of stereomicroscopy. At 1 million volts a resolution of 2 nm can be obtained in 1-μm-thick sections of dense tissues (Fotino, 1975). Thus, the general limit set by beam damage can be achieved even with whole mitotic chromosomes.

Recent studies on the higher order structure of chromosomes suggest that stereomicroscopy at 1 MeV is at present the most useful method of obtaining information on the complex three-dimensional structure of chromosomes (Ris and Korenberg, 1979). The tilt stage of the AEI EM-7 at the HVEM facility at the University of Wisconsin, Madison, can, in addition to single stereo pictures, provide a through-tilt series over a range of 90° that contains many stereo views of a structure from different angles.

Reconstruction from serial thin sections, on the other hand, has not been successful with chromosomes. Even slight distortions due to the sectioning process make it impossible to match corresponding chromatin fiber profiles from one section to another. Computer-assisted reconstruction of cross sections using a large number of projections obtained from a through-tilt series of micrographs has been attempted with isolated metaphase chromosomes (Bahr *et al.*, 1979). To date, however, there is no evidence that the resolution necessary to reconstruct chromosomes from electron micrographs can be achieved with this technique.

II. Methods

The methods used in our laboratory to prepare chromatin and chromosomes for electron microscopy have already been reviewed (Ris, 1978a). The methods used for the examples presented in this chapter are summarized in this section.

A. The 20-Nm Chromatin Fiber

This fiber is the basic unit of inactive chromatin. It is most easily prepared from nuclei in which all transcription is turned off (for example, erythrocytes of

vertebrates). A drop of cell suspension is applied to a clean water surface from a glass rod or pipette (a black, Teflon-coated trough is most convenient). The chromatin fibers are suspended in the hypophase from a protein surface film and can be picked up by touching a grid covered with a carbon-coated Formvar film to the surface. They are fixed in 4% aqueous paraformaldehyde. The native 20-nm fiber is a supercoil of the closely packed string of nucleosomes stabilized by Ca^{2+} (Ris and Korenberg, 1979). Brief treatment with a chelating agent (for example, 5 m*M* sodium citrate for 10 seconds) before fixation slightly opens this coil and makes it more obvious. After fixation, the fibers are embedded in a drop of 2% uranyl acetate, which dries down into a layer about 100 nm thick. This method avoids organic solvents, provides some protection against beam damage, and gives excellent contrast.

B. Polytene Chromosomes

Polytene chromosomes can be isolated from dipteran larval tissue by squashing in 50% acetic acid between a slide and a coverslip. This process is facilitated by fixation in methanol-acetic acid (3 : 1); aldehyde fixatives tend to make this more difficult. Ethanol-acetic acid fixation extracts some chromatin proteins, but the 20-nm fiber remains distinct, although somewhat thinner (Ris, 1978a). The chromosomes can be transferred to a grid without distortion (Ris, 1961). The coverslip is removed with a razor blade after freezing in liquid nitrogen. The slide is thawed in distilled water, stained in 1% aqueous uranyl acetate for 5 minutes, rinsed in two changes of 50% ethanol, and dehydrated through 70%, 80%, 95%, and absolute ethanol. After soaking for 5 minutes in amyl acetate, the slide is wiped dry except for the area with specimens, and rapidly covered with 2% Parlodion. It is important that the material never dry during the entire process. When the Parlodion film has hardened, the slide can be searched with a phase microscope and a suitable area selected and marked with a diamond object marker by making a circle around it (2.5 mm in diameter). Under a dissecting microscope, this circle is covered with water, and the disk with the specimen embedded in it is carefully stripped from the glass and transported to the surface. It can then be picked up on a 75-mesh grid covered with a 0.5% Formvar film. When dry, the grid is immersed overnight in amyl acetate to remove the Parlodion and then critical-point-dried (Anderson, 1956). A thin layer of carbon can be evaporated on the underside of the grid to stabilize the film.

C. Mitotic Chromosomes

1. Spreading of Metaphase Cells on a Water Surface

Mitotic chromosomes are most easily obtained from colcemid-arrested cultured cells. They can be separated from the cells by spreading them on a water

surface, by breaking the cells mechanically in a variety of isolation media, or by squashing after methanol-acetic acid fixation. For spreading on a trough, the cells are swollen in hypotonic medium [75 m*M* KCl, or a growth medium diluted with H_2O (1 : 1)] and centrifuged. Part of the pellet is then touched to a clean water surface. A grid is touched to the surface, floated on 4% paraformaldehyde in H_2O, stained briefly in 1% uranyl acetate, dehydrated in ethanol, and critical-point-dried through liquid CO_2 (Anderson, 1956).

2. Mechanical Isolation of Chromosomes

Chromosomes free of contamination are easily obtained with the pH 6.7 procedure of Wray and Stubblefield (1970). Colcemid-arrested metaphase cells are mechanically broken by syringing through a 22-gauge needle in an isolation medium containing 0.1 m*M* Pipes buffer (pH 6.7), 0.5 m*M* $CaCl_2$, and 1 *M* hexylene glycol. A drop of the suspension is placed on a grid, and the grid is suspended on 4% paraformaldehyde, followed by staining with 1% uranyl acetate, dehydration in ethanol, and drying with the CO_2 critical-point procedure (Anderson, 1956). Alternatively, a drop of the chromosome suspension can be spread on a clean water surface and processed as described above.

3. Squashing in Acetic Acid

A third method consists in fixing chromosomes within the cells and isolating them by the squashing procedure. Chromosomes fixed *in situ* are extremely compact, and it is informative to swell them by treating the colcemid-arrested metaphase cells with hypotonic media. The cells are suspended for 10–20 minutes in 75 m*M* KCl or in hypotonic phosphate buffer, fixed in methanol-acetic acid (3 : 1), squashed in 50% acetic acid between a slide and a coverslip, and transferred to a Formvar-covered grid as described for polytene chromosomes. Free chromosomes are also obtained if the fixed cells are suspended in 50% acetic acid and syringed through a 22-gauge needle. A drop of this suspension is placed on a fenestrated Formvar-carbon film. Metaphase chromosomes suspended over a hole in the film appear to be minimally distorted.

D. Kinetochore

1. Microtubule-Chromosome Attachment in Whole Mounts

Mouse chromosomes are used (A9 cell lines) because the centromere is easily located at one end, marked by the prominent centric heterochromatin. Cells are synchronized by growing them in 10 m*M* thymidine in medium for 12 hours followed by 0.06 gm of colcemid per milliliter in medium for 8 hours. Mitotic

cells are shaken off, washed in fresh medium twice, and left at 37°C for 45 minutes for spindle microtubules to re-form. Hypotonic treatment and spreading on water depolymerize microtubules. Microtubules are stabilized by using D_2O for the hypotonic pretreatment (10 minutes in 75 m*M* KCl in D_2O) and as the hypophase for spreading (Inoué and Sato, 1967; Burkholder *et al.*, 1972). Chromosomes are picked up by touching a Formvar-carbon-coated grid to the surface, fixed in 2% paraformaldehyde, stained in 1% uranyl acetate, dehydrated in ethanol, and dried with the CO_2 critical-point procedure (Anderson, 1956).

2. Microtubule-Chromosome Attachment in Sections

Mouse (A9) and Chinese hamster (CHO) metaphase cells are obtained as described in the preceding section. Several pretreatments are used to swell chromosomes and yet preserve microtubules:

a. 10 minutes, 75 m*M* KCl in D_2O. This treatment preserves the disk structure of the kinetochore with microtubules attached to the outer dense disk. The chromosomes consist of 20-nm fibers.

b. 10 minutes, 50 m*M* KCl in D_2O. The disk structure is no longer present, but microtubules are attached to randomly dispersed 20-nm chromatin fibers in the centromere region.

c. 10 minutes, 1 m*M* $MgCl_2$, 1 m*M* EGTA, in D_2O. The chromosomes consist of somewhat irregular, partially aggregated 50-nm fibers. The outer kinetochore disk with attached microtubules is well preserved.

d. CHO metaphase cells are partially lysed in 10 m*M* Pipes buffer (pH 7.0) containing 0.5 m*M* $MgCl_2$, 2 m*M* EGTA, 1 m*M* GTP, and 0.5% Triton X-100. No disk structure is visible; microtubules are attached to a condensed mass of 10-nm chromatin fibers.

The cells are centrifuged, fixed in 2% glutaraldehyde in 1 m*M* Pipes buffer (pH 7.0) with (*a*, *b*), or without (*c*, *d*) postfixation in 1% OsO_4, or in 2% glutaraldehyde in lysis medium (*d*). Sections 0.25 μm thick (Epon-araldite) are stained in 7% uranyl Mg acetate for 4 hours at 50°C followed by Reynold's lead citrate for 20 minutes.

E. Heterochromatin, C Bands, Giemsa Bands

Extraction of very lysine-rich histones (H1) from metaphase chromosomes differentiates between C bands, Giemsa bands, and euchromatin (Ris and Korenberg, 1979).

Mouse A9 metaphase chromosomes are isolated in Wray-Stubblefield buffer by syringing through a 22-gauge needle, spread on a clean water surface, and picked up on Formvar-carbon-coated grids. The grids are floated on 0.6 *M* NaCl at 4°C for 15 minutes and then fixed in 4% paraformaldehyde, stained in 1% uranyl acetate, and critical-point-dried (Anderson, 1956).

F. Stereophotography

All photographs shown here were obtained at 1 MeV with the AEI EM-7 high-voltage electron microscope at the University of Wisconsin facility at Madison, Wisconsin. This instrument has an axis-centered tilt stage with a ±45° tilt from the horizontal and a 360° rotation of the specimen grid. In the EM-7 the projector currents are designed so that at magnifications above 4000× no image rotation occurs. Thus, the image on the film is in the same orientation as the specimen, and the tilt axis corresponds to the long axis of the negative. For optimum stereo vision, the parallel or lateral displacement of equivalent points in the two images must be within defined limits. Since this depends on the specimen thickness as well as on final magnification of the image, the stereo angle is determined by these variables. A convenient nomogram from which the stereo angle can be obtained for the final magnification and specimen thickness used has been published by Hudson and Makin (1970). It is often informative to take a through-tilt series at intervals of the appropriate stereo angle. When the prints are correctly mounted side by side, a series of stereo views from different angles is obtained. For comfortable stereo viewing, the mounting of the prints is important. For whole mounts it appears most pleasing if the structure is seen as if it were sitting on a table. This is accomplished by adjusting the lateral separation of the two images so that the apparent level of the Formvar film corresponds to the plane of the "window"—that is, the limiting edges of the photograph. This is done by trimming either the left or right edge of the two pictures so that corresponding structures situated on the Formvar film are at the same distance from the edge. The other vertical edge defining the total width of the picture is determined by the interocular distance, which is about 6.5 cm. The horizontal edges of the two prints must be equidistant from corresponding points on the Formvar film of the two images.

For sections, it appears more pleasing if they are viewed as if through a window with the closer surface in the plane of the "window." To obtain this effect, several conspicuous structures in the upper surface of the section are selected. The correct left edge in both images is made equidistant from the corresponding selected points in the two pictures. The right vertical edge is then trimmed to give a 6.5-cm width to each photograph.

III. Levels of Organization in Chromosomes

Chromosomes reveal a distinct hierarchy of structures, which achieve an increasing condensation or packing of the exceedingly long DNA double helix that forms the backbone of each chromatid (reviewed in Ris and Korenberg, 1979). The first such level of packing is represented by the nucleosomes, where specific

arrays of the four core histones compact the DNA sevenfold into a string of closely packed nucleosomes, a fiber 10 nm in diameter. In inactive chromatin, this fiber is supercoiled into a helix 20–30 nm thick. The very lysine-rich histones and calcium ions are necessary to maintain this superstructure.

A. The 20-Nm Chromatin Fiber

Figure 1 shows the supercoil in the 20-nm fibers released from erythrocyte nuclei of the newt *Notophthalmus viridescens* by spreading on a water surface. In this nucleus, all chromatin is transcriptionally inactive and is in the form of 20-nm fibers.

B. Polytene Chromosomes and Interphase Chromomeres

The next higher order of packing is most clearly seen in polytene chromosomes of dipteran larvae. These chromosomes are formed through many cycles of replication without separation of daughter chromosomes. The chromatids

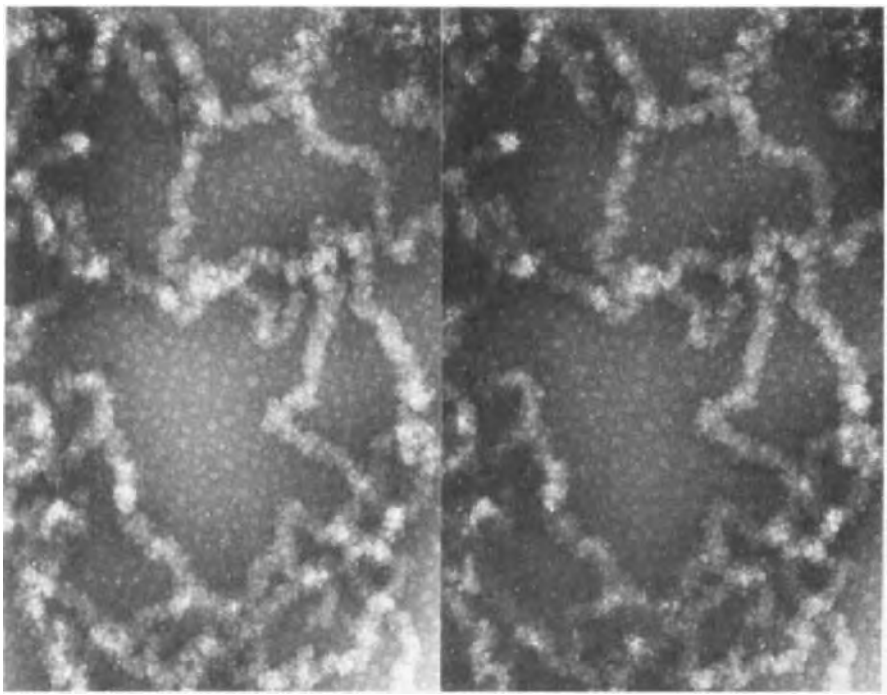


FIG. 1. Chromatin fibers (20 nm) from erythrocyte nuclei of the newt *Notophthalmus viridescens*, negatively stained (Methods, A). The 20-nm fiber is a helical supercoil of the 10-nm fiber; the 10-nm fiber consists of closely packed nucleosomes. Nucleosomes are visible in the lower right-hand corner. 1 MeV, $S = 20°$, magnification 110,000×.

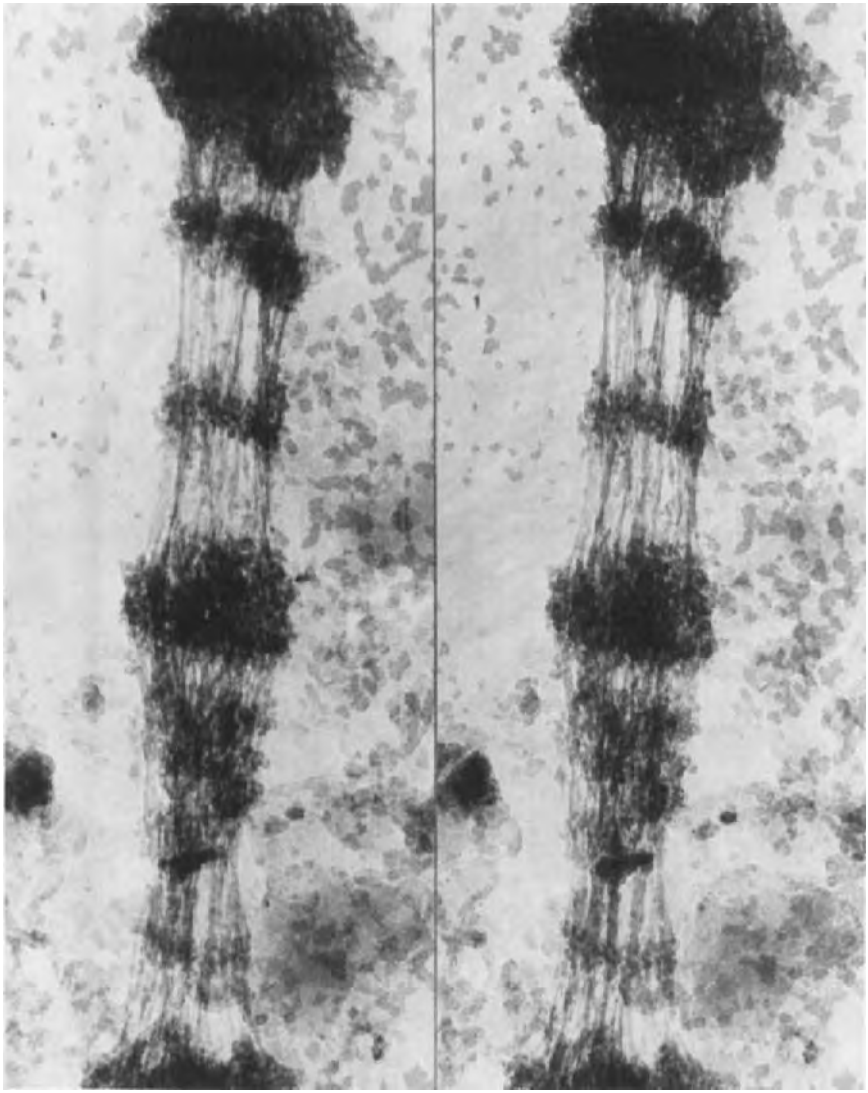


FIG. 2. Polytene chromosome from a fat cell of *Drosophila melanogaster*. Methanol-acetic acid squash (Methods, B). The 20-nm fibers are more or less straight in interbands and irregularly compacted in the chromomeres forming the bands. 1 MeV, $S = 10°$, magnification 40,000×. From Ris (1976). Copyright 1976 by Intertal, International Publishing Co., Ltd., Givatayim, Israel.

remain closely packed and in perfect registry. The most interesting feature of these chromosomes is the specific pattern of crossbands of varying thickness. These bands are known to correspond to specific gene loci. Figure 2 shows a

region of a polytene chromosome from a fat cell of *Drosophila melanogaster*, which contains between 20 and 30 chromatids. Each chromatid consists of a 20-nm fiber that is more or less straight in interbands but tightly folded in bands. The compacted region is known as *interphase chromomere*. What causes this compaction of a specific segment of the 20-nm fiber is as yet unknown. It has been suggested that specific nonhistone proteins clamp a certain DNA region into a loop, which, when associated with histones, becomes compacted into a chromomere (Benyajati and Worcel, 1976).

C. Mitotic Chromosomes

During mitosis, chromosomes become highly condensed into compact, rod-like structures, which can be moved about on the mitotic spindle without getting tangled. Prophase chromosomes cannot be isolated, and *in situ* pictures are

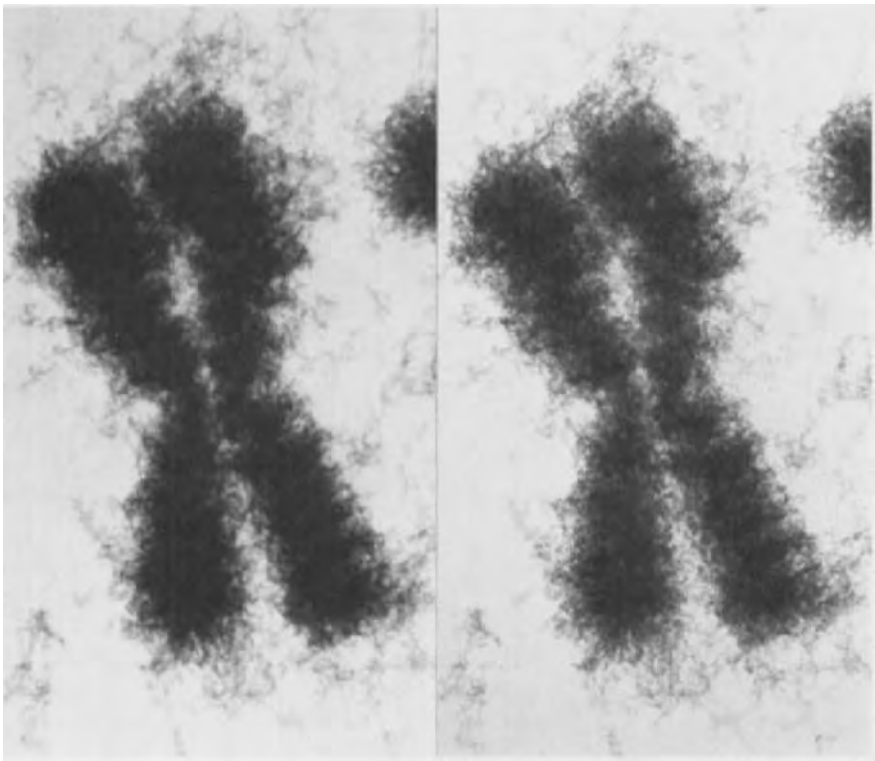


FIG. 3. Metaphase chromosome from a Chinese hamster ovary (CHO) cell culture. Hypotonic phosphate buffer, methanol-acetic acid squash (Methods, C-3). 1 MeV, $S = 10°$, magnification 15,000×. From Ris (1978b). Copyright 1978 Microscopical Society of Canada, Toronto, Canada.

confusing because the chromosomes are enmeshed in a fibrous nuclear matrix (Wunderlich and Herlan, 1977). Therefore, information on mitotic condensation is derived mainly from studies of metaphase chromosomes. In untreated cells, metaphase chromosomes are generally so compact that no substructure is visible. Therefore, various pretreatments have been used to swell chromosomes and make their detailed structure more apparent. Results to date suggest that there is a definite hierarchy of organization in metaphase chromosomes and that its preservation is highly dependent on the methods of preparation. On the light microscope level, it has been established that metaphase chromosomes consist of a helically coiled thread 100–200 nm thick (the chromonema). In some organisms this coil is visible in living cells (Bajer, 1966). Generally, however, pretreatment of cells with hypotonic salt solutions is necessary to open up the structure and make the coil visible (Ohnuki, 1968).

In preparations for electron microscopy, the coiled chromonema is visible only if the chromosomes are fixed *in situ* after hypotonic treatment of cells. Figure 3 shows a metaphase chromosome from a Chinese hamster CHO cell after pretreatment in hypotonic phosphate buffer (pH 7.0), fixation in methanol-acetic acid, and squashing in 50% acetic acid (Methods, C-3). In the lower right chromatid, the direction of the coil is right-handed. In the upper right chromatid next to the centromere, the direction is left-handed. Most chromatin fibers pro-

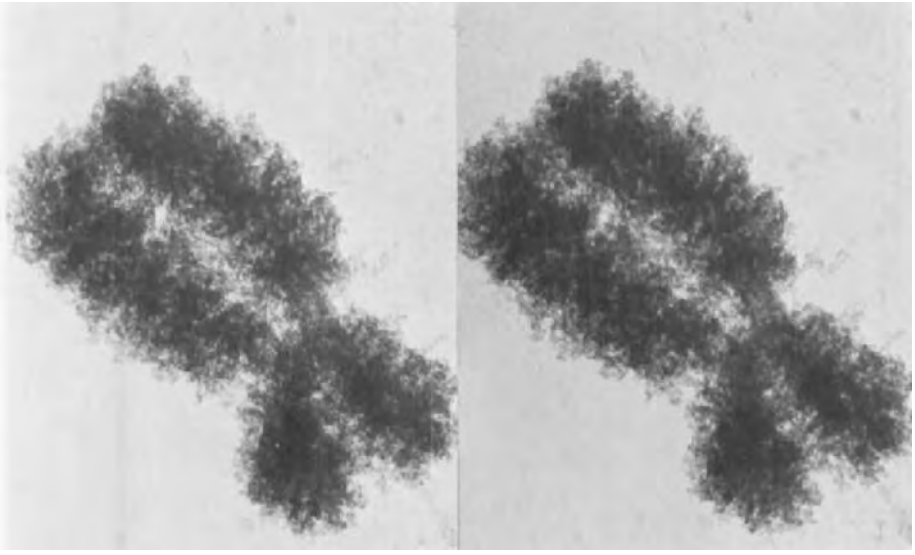


FIG. 4. Metaphase chromosome from a Chinese hamster ovary (CHO) cell culture, 75 m*M* KCl, methanol-acetic (3:1), syringed in 50% acetic acid (Methods, C-3). 1 MeV, $S = 10°$, magnification 20,000×. From Ris (1976). Copyright 1976 by Intertal International Publishing Co., Ltd., Givatayim, Israel.

truding from the edges are 20 nm thick. Figure 4 represents a CHO metaphase chromosome prepared identically, except that after fixation the chromosomes were isolated by syringing and then were placed directly on a Formvar-carbon-coated grid. With this method there is less distortion of peripheral chromatin fibers. They are mostly about 50 nm thick and appear to be supercoiled 20-nm fibers. Figure 5 shows a chromosome that was isolated by syringing in Wray-Stubblefield medium and then placed on a Formvar-carbon-coated grid (Methods, C-2). The component fiber is 50 nm thick, and gyres of the chromonema helix are preserved (arrow).

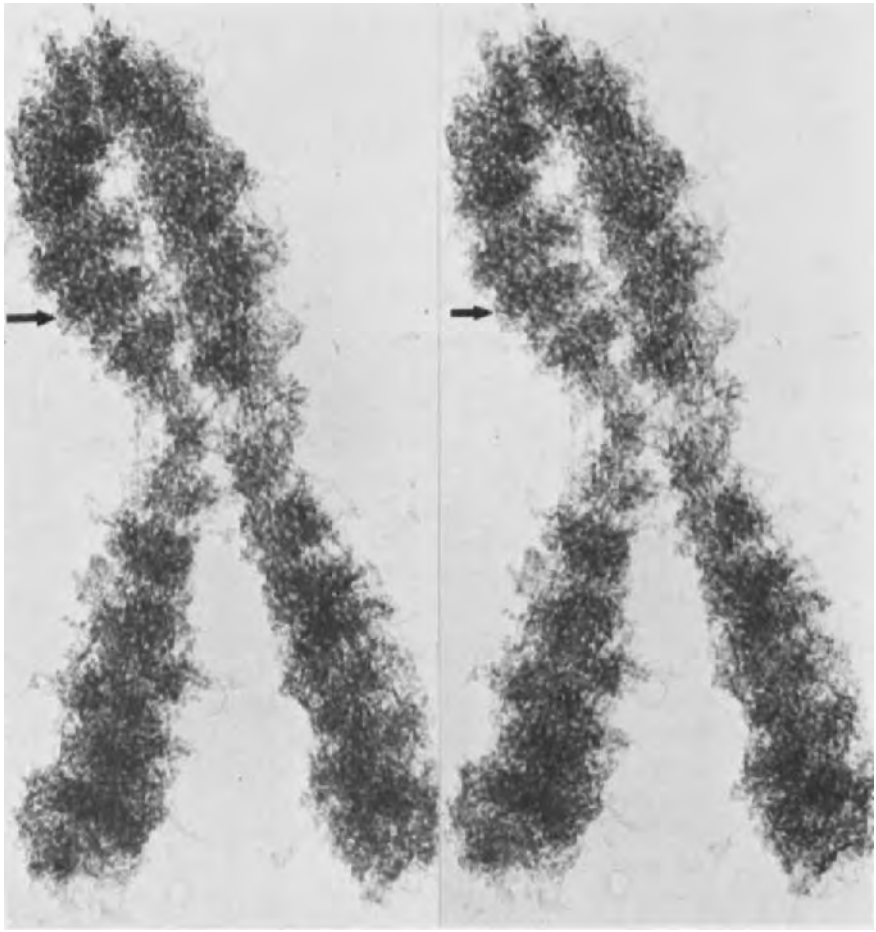


FIG. 5. Metaphase chromosome from a Chinese hamster ovary (CHO) cell culture, 75 *mM* KCl, Wray-Stubblefield medium, methanol-acetic acid squash (Methods, C-2). 1 MeV, $S = 10°$, magnification 20,000×.

Quite different images are obtained by the popular method of spreading the metaphase cells on a water surface (Methods, C-1) (Dupraw, 1970; Bahr, 1975). The chromonema helix is not visible, and the chromatids look like a jumble of irregularly looping 20-nm fibers. A similar appearance is produced if chromosomes isolated in Wray-Stubblefield buffer are placed in 0.1 m*M* Pipes buffer. The change from 50-nm to 20-nm fibers is reversible; after being returned to the 0.5 m*M* $CaCl_2$, the chromosome again uniformly consists of 50-nm fibers, as in Fig. 5. Since chromosomes fixed *in situ* show 50-nm fibers, we must conclude that in chromosomes spread on water the 50-nm supercoil has unraveled.

From the preparations discussed so far, it is not obvious how the 50-nm fiber is arranged in the coiled chromonema. Experiments by Laemmli and collaborators (1978) provide a clue. If histones are extracted from isolated chromosomes and the chromosomes are spread with cytochrome c, one finds in the core of each chromatid an irregular fibrous meshwork from which a large number of DNA loops project. The coarse, fibrous material consists mainly of nonhistine pro-

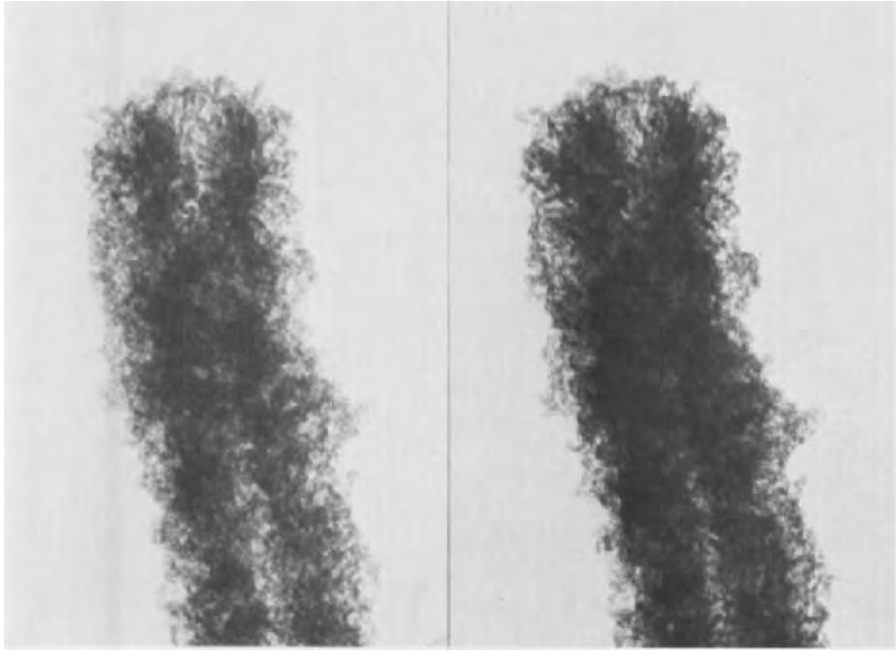


FIG. 6. Metaphase chromosome from a Chinese hamster ovary (CHO) cell culture. Methanol-acetic acid (3: 1), syringed in 50% acetic acid (Methods, C-3). Part of the chromosome is suspended over a hole in the Formvar support film. Note loops of 20-nm fibers projecting from the denser chromonema axis. 1 MeV, $S = 10°$, magnification 25,000×. From Ris (1978b). Copyright 1978, Microscopical Society of Canada, Toronto.

tein bound to a small fraction of DNA. After critical-point drying of similarly treated chromosomes, the dense core of chromatids consists of short segments of thicker fibers that are tightly packed in heterochromatin and in segments that seem to correspond to G bands (Ris, 1978b). This suggests that the denser core of chromatids is formed by regions along the chromatid fiber where nonhistone proteins stabilize a higher order configuration. These regions perhaps correspond to the "clamps" that arrange specific segments of DNA into chromomere-sized loops. In mitotic chromosomes, these "clamps" would form the helically coiled "core" of chromatids from which the DNA loops project. In the presence of histones these loops are 20 nm or 50 nm thick, depending on the ionic composition of the medium (Ris, 1978b). The core and loop structure is apparent in whole mounts of isolated chromsomes (Fig. 6), and in thick sections through metaphase chromosomes. The loops are 20 nm thick if the chromosomes are swollen in 75 m*M* KCl (Fig. 7), but 50 nm thick when isolated in Wray-Stubblefield medium (Fig. 8).

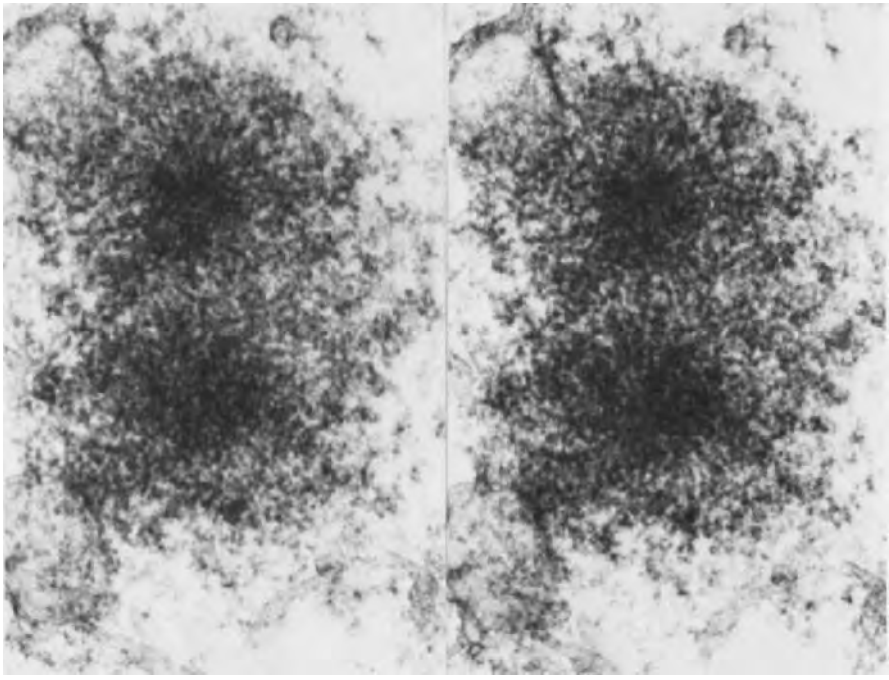


FIG. 7. Cross section (0.25 μm) of a metaphase chromosome, mouse A9 cell culture. Cells treated with 75 m*M* KCl for 10 minutes before fixation with 2.5% glutaraldehyde in 1 m*M* Pipes buffer (pH 7.0) followed by 1% OsO_4 in H_2O. Stain: 7.5% uranyl magnesium acetate in water, 4 hours at 50°C followed by Reynold's lead citrate. 1 MeV, $S = 10°$, magnification 40,000×.

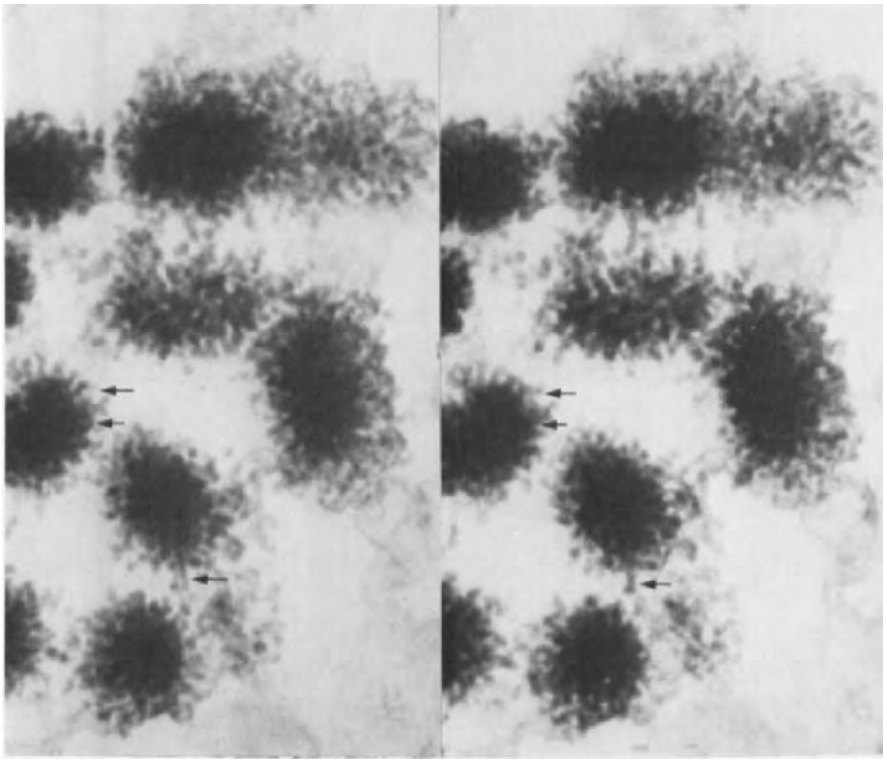


FIG. 8. Section of metaphase chromosomes from a Chinese hamster ovary (CHO) cell culture (0.25 μm). Cells suspended in Wray-Stubblefield isolation medium (pH 6.7), fixed and stained as in Fig. 7. The chromatin fibers are 50 nm thick and appear to project as loops from the denser core of chromatids (arrows). 1 MeV, S = 16°, magnification 20,000×.

D. Kinetochore Organization in Mammals

In mammals a structural differentiation of the kinetochore appears during mitosis and links chromosomes to chromosomal microtubules of the spindle. It has been described as a triple-layered disk consisting of an inner and outer electron opaque layer separated by a less dense region (Roos, 1973). Microtubules are attached to the outer layer. We have used stereoscopic electron microscopy at 1 MeV after various prefixation treatments to study the relationship between microtubules, kinetochore structure, and chromatin fibers (Ris and Witt, 1981). The kinetochore disk has so far been seen only in sections. It has not been preserved in isolated chromosomes or in chromosomes spread on a water surface. With the intent of using microtubules as a marker for the kinetochore, we spread colcemid-arrested metaphase cells after recovery of spindle mi-

crotubules, on D_2O, which stabilized the microtubules at a low ionic strength (Inoué and Sato, 1967; Burkholder *et al.*, 1972). In such preparations, microtubules are seen attached to 20-nm chromatin fibers in the centromere region, but no disk structure is ever seen (Fig. 9). At the arrow, one can see a microtubule attached to a chromatin fiber loop coming from the region just below the centric heterochromatin. This suggests that in acrocentric mouse chromosomes the centric heterochromatin corresponds to a heterochromatic short arm with the centromere located just inside of it. The disk organization is not necessary for microtubule–chromatin association, since microtubules are attached to 20-nm chromatin fibers directly, as has also been described in yeast (Peterson and Ris, 1976). Since microtubules attach to the outer dense disk when fixed without pretreatment, we must assume that chromatin fibers are present there. Perhaps this disk is formed by a special arrangement of chromatin fibers looping out from the centromere region. This arrangement would not be preserved at low ionic strength—for

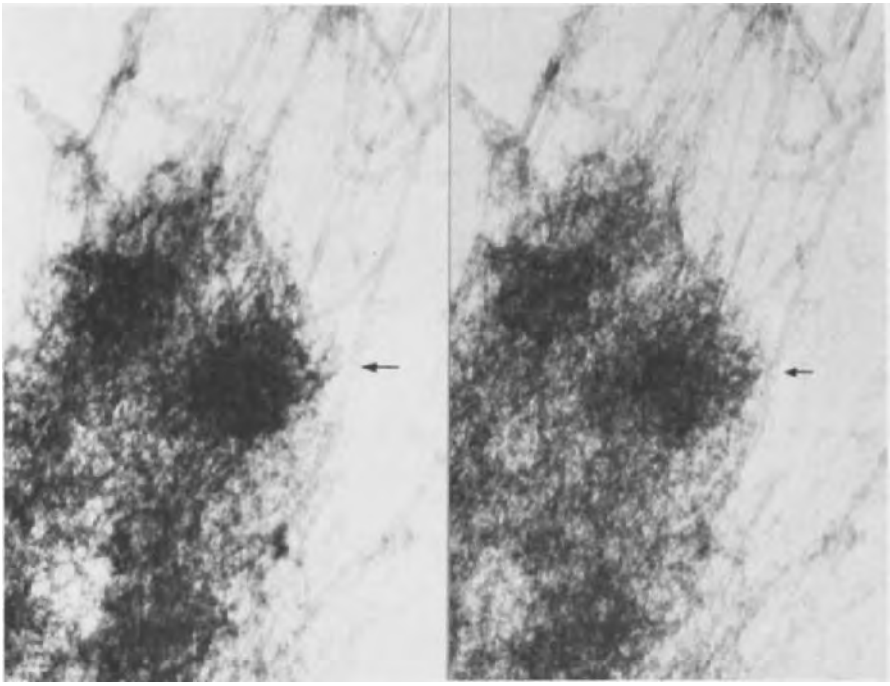


FIG. 9. Whole mount of metaphase chromosome from mouse A9 cell culture (centromere end). After recovery from colcemid in medium (Methods, D-1) the cells were suspended in 75 m*M* KCl in D_2O for 10 minutes and spread on D_2O. No kinetochore disks are present, but microtubules (smooth contours) are found attached to 20-nm chromatin fibers (knobby contours). One microtubule is attached to a chromatin fiber loop that issues from the region behind the centromeric heterochromatin (arrow). 1 MeV, $S = 7°$, magnification 50,000×. From Ris and Witt (1981).

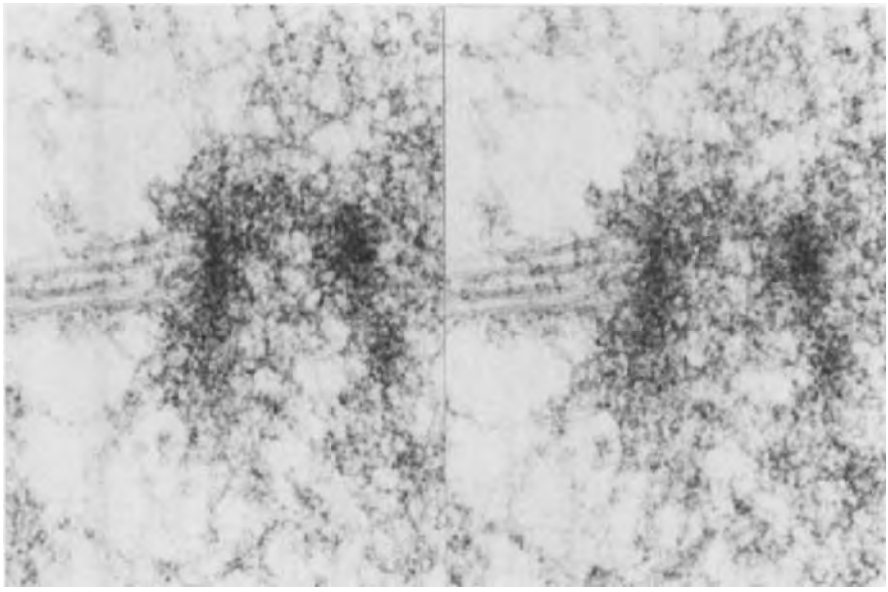


FIG. 10. Section (0.25 μm) of centromere regions in the two chromatids of a metaphase chromosome from a Chinese hamster ovary (CHO) cell culture. The cells were partially lysed in 10 m*M* Pipes buffer (pH 7.0) containing $MgCl_2$, EDTA, and Triton X-100 (Methods, D-2-d). No disk structure is present, but microtubules attach directly to twisted chromatin fibers. 1 MeV, $S = 20°$, magnification 40,000×. From Ris and Witt (1981).

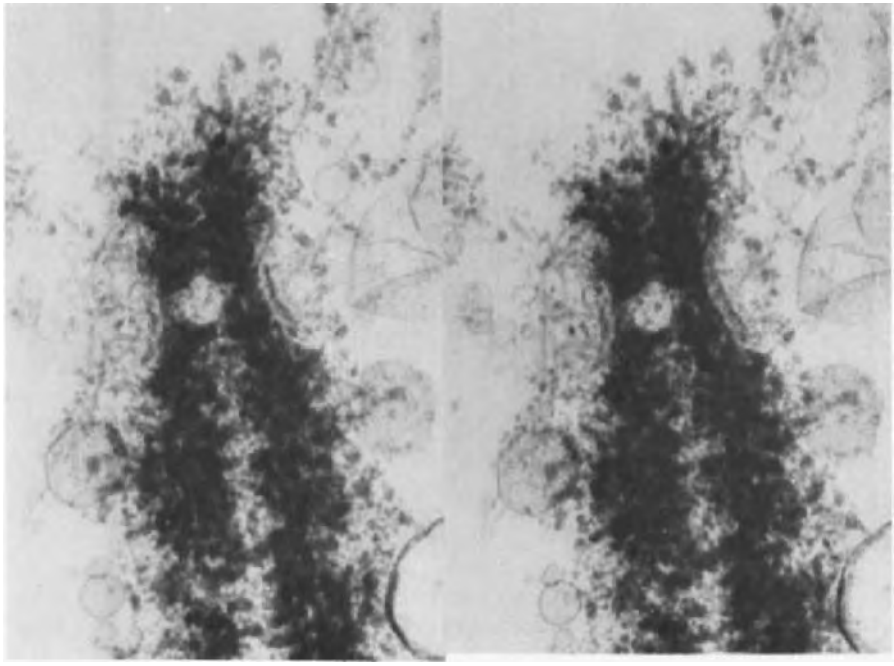


FIG. 11. Section (0.25 μm) of metaphase chromosome from a Chinese hamster ovary (CHO) cell culture. Prefixation treatment with EGTA and $MgCl_2$ in D_2O (Methods, D-2-c), fixation in 2.5% glutaraldehyde in 1 m*M* Pipes buffer (pH 7.0). The kinetochore disk is composed of 20-nm chromatin fibers to which microtubules are attached. The apparent disk structure is due to overlapping chromatin fibers, which here run obliquely downward in the plane of the "disk." 1 MeV, $S = 11°$, magnification 30,000×. From Ris and Witt (1981).

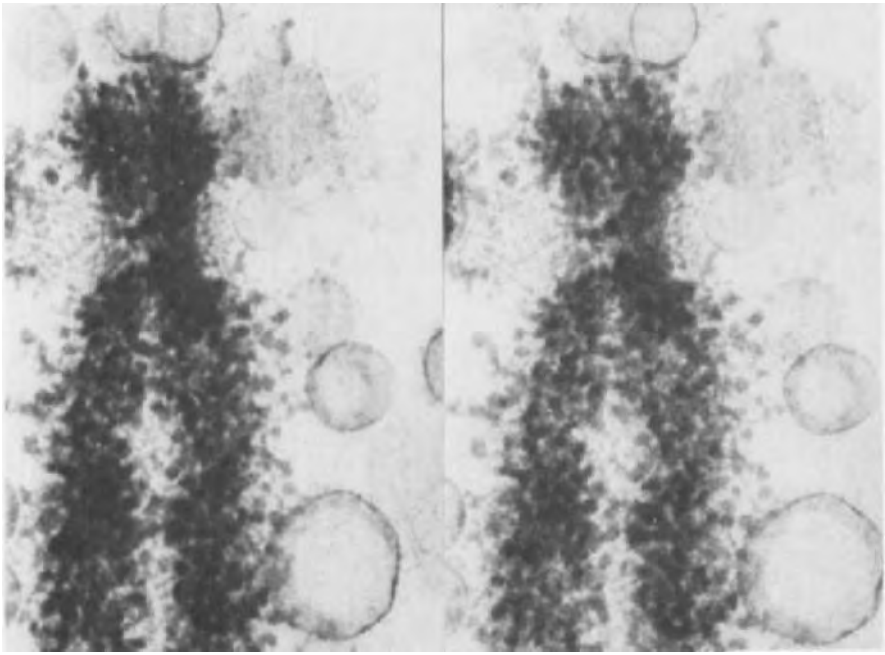


FIG. 12. Section the same as in Fig. 11. The chromosome is tilted so that the kinetochore disk is seen obliquely from the side. The 20-nm chromatin fibers making up the disk are here seen coming from the inner centromere chromatin. 1 MeV, $S = 11°$, magnification 30,000×.

example, after spreading on D_2O. This hypothesis is supported by the study of sections after various prefixation treatments. Figure 10 represents the centromere regions of a CHO chromosome in a cell partially lysed as described under Methods, D-2-d. No disk structure is preserved under these conditions (10 m*M* Pipes buffer), but microtubules are seen ending within the 0.25-μm section on randomly oriented chromatin fibers. Similar pictures are obtained when cells are treated before fixation with either 50 m*M* or 75 m*M* KCl in D_2O. In 50 m*M* KCl, the disk is absent and the microtubules end directly on dispersed chromatin fibers, as in Fig. 10. After 75 m*M* KCl, however, the normal disk structure is preserved. Direct evidence that the outer disk is formed from chromatin fibers is presented in Fig. 11 and 12. These chromosomes were pretreated with EGTA and $MgCl_2$ in D_2O (Methods, D-2-c). Under these conditions, the chromatin consists of somewhat irregular 50-nm fibers, except in the outer kinetochore disk, which consists of 20-nm fibers looping out from the centromere chromatin. Microtubules are attached to these 20-nm fibers. In Fig. 11, the stage is tilted so that we have a perfect cross-sectional profile of the kinetochore disks on both chromatids. In Fig. 12, which represents the same chromosome in an adjacent section, the stage was tilted to get an oblique view of the kinetochore disk. Stereoscopic viewing of

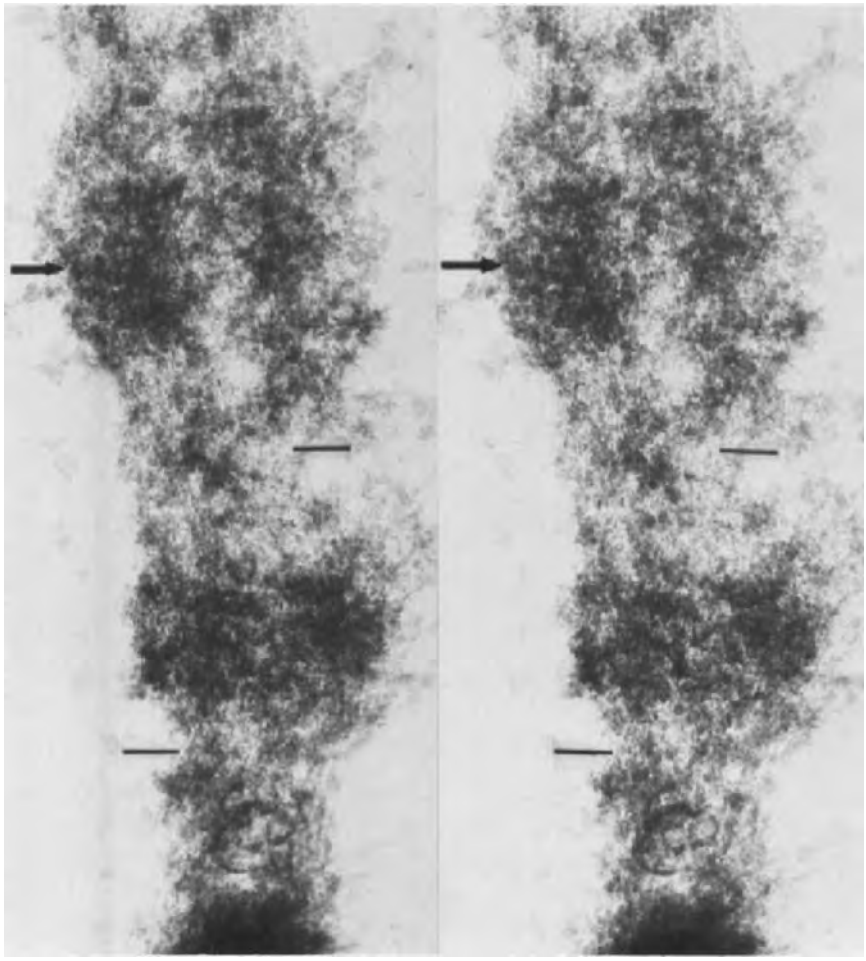


FIG. 13. Whole mount of the centric heterochromatin of a metacentric mouse chromosome (A9 cell line) after extraction with 0.6 *M* NaCl (Methods, E). The C-banding seen here is due to the differential effect of 0.6 *M* NaCl on heterochromatin and euchromatin. In the euchromatin the fibers are unraveled into a string of nucleosomes (thin arrow). In the heterochromatin the fibers remain compacted (thick arrow). 1 MeV, $S = 4°$, magnification 40,000×. From Ris and Korenberg (1979).

Fig. 11 shows that the outer disk is not a solid disk at all but is due to superposition of sections through 20-nm fibers. On the left, these fibers run obliquely downward; on the right they form short arcs. Microtubules end on some of these fibers (left kinetochore). In Fig. 12, the outer disk is seen obliquely, showing the 20-nm fibers and connections into the centromere chromatin (right kinetochore). This study, which is still in process, has led to a new concept of the mammalian kinetochore. It suggests that specific regions of the chromatid fiber in the cen-

tromere region loop out to be arranged into a disk-like structure. Microtubules are attached to the chromatin fibers on these segments.

E. Heterochromatin

Ris and Korenberg (1979) have shown that extraction of H1 histones from isolated metaphase chromosomes produces a different structure in the heterochromatin of C bands and G bands as compared with euchromatin. In euchromatic regions, the chromatin fiber is unraveled into a string of nucleosomes, whereas in heterochromatin, the chromatin remains compacted. Figure 13 shows the centric heterochromatin in a metacentric chromosome of the mouse A9 cell line after extraction of very lysine-rich histones (Methods, E). In the C bands, the chromatin remains compacted, apparently in closely packed segments about 50 nm long and 50 nm thick (thick arrow). In the light bands, the chromatin is unraveled into strings of nucleosomes (thin arrow).

ACKNOWLEDGMENTS

This study was supported by a research career program award (K-6-GM21,948) and research grant (GM 04738) from the National Institutes of Health. The High-Voltage Electron Microscope Facility is supported by a grant from the Research Resources Division, National Institutes of Health (RR 570).

REFERENCES

Anderson, T. F. (1956). *Phys. Tech. Biol. Res.* **3,** 198-240.

Bahr, G. F. (1975). *Fed. Proc., Fed. Am. Soc. Exp. Biol.* **34,** 2209-2217.

Bahr, G. F., Boccia, J. A., Engler, W. F., Robb, R. A., Jurkevich, I., and Petty, A. F. (1979). *Ultramicroscopy* **4,** 45-53.

Bajer, A. (1966). *In* "Probleme der biologischen Reproduction" (P. Sitte, ed.), pp. 91-119. Springer-Verlag, Berlin and New York.

Benyajati, C., and Worcel, A. (1976). *Cell* **9,** 393-407.

Burkholder, G. D., Okada, T. A., and Comings, D. E. (1972). *Exp. Cell Res.* **75,** 497-511.

Dupraw, E. J. (1970). "DNA and Chromosomes." Holt, New York.

Fotino, M. (1975). *In* "Microscopie électronique à haute tension" (B. Jouffrey and P. Favard, eds.), pp. 361-364. Soc. Fr. Microsc. Electron., Paris.

Glaeser, R. (1975). *In* "Physical Aspects of Electron Microscopy and Microbeam Analysis" (B. M. Siegel and D. R. Beaman, eds.), pp. 205-229. Wiley, New York.

Hudson, B., and Makin, M. J. (1970). *J. Phys. E* **3,** 311.

Hyde, B. B. (1964). *In* "The Nucleohistones" (J. Bonner and P.O.P. Ts'o, eds.), pp. 163-166. Holden-Day, San Francisco, California.

Inoué, S., and Sato, H. (1967). *J. Gen. Physiol.* **50,** Suppl., 259-288.

Laemmli, U. K., Cheng, S. M., Adolph, K. W., Paulson, J. R., Brown, J. A., and Baumbach, W. R. (1978). *Cold Spring Harbor Symp., Quant. Biol.* **42,** 351-360.

Lafontaine, J. G., and Ris, H. (1958). *J. Biophys. Biochem. Cytol.* **4,** 99-106.
Ohnuki, Y. (1968). *Chromosoma* **25,** 401-428.
Peterson, J., and Ris, H. (1976). *J. Cell Sci.* **22,** 219-242.
Ris, H. (1961). *Can. J. Genet. Cytol.* **3,** 95-120.
Ris, H. (1976). *Proc. Eur. Congr. Electron Microsc., 6th, 1976* Vol. II, pp. 21-25.
Ris, H. (1978a). *Methods Cell Biol.* **18,** 229-246.
Ris, H. (1978b). *Electron Microsc., Proc. Int. Congr., 9th, 1978* Vol. III, pp. 545-556.
Ris, H., and Korenberg, J. (1979). *Cell Biol.* **2,** 267-361.
Ris, H., and Witt, P. L. (1981). Structure of the mammalian kinetochore. *Chromosoma* (in press).
Roos, U. P. (1973). *Chromosoma* **41,** 195-220.
Stubblefield, E., and Wray, W. (1971). *Chromosoma* **32,** 262-294.
Wray, W., and Stubblefield, E. (1970). *Exp. Cell Res.* **59,** 469-478.
Wunderlich, F., and Herlan, G. (1977). *J. Cell Biol.* **73,** 271-278.

Chapter 6

Preparing Biological Samples for Stereomicroscopy by the Quick-Freeze, Deep-Etch, Rotary-Replication Technique

JOHN HEUSER

Department of Physiology and Biophysics,
Washington University School of Medicine,
St. Louis, Missouri

I. Introduction 97
II. Methods 98
A. Freeze-Etching 98
B. Replication 98
C. Photography 99
D. Stereo Projection 100
III. Results 104
A. Membrane Surfaces 104
B. Cell Interiors 108
C. Freeze-Dried Tissue Culture Cells 112
D. Biochemical Fractions 119
IV. Summary and Conclusions 121
References 121

I. Introduction

This chapter presents the details of a method of preparing tissue for stereo viewing which has not been widely adopted yet, but which we think is the best way currently available for visualizing the overall macromolecular organization of the cell. It very effectively bridges the gap between thin-section and freeze-fracture views. It is not capable of enough resolution to reveal actual molecular structure, but it is able to resolve individual protein-protein interactions such as occur in

Copyright © 1981 by Academic Press, Inc.
All rights of reproduction in any form reserved.
ISBN 0-12-564122-2

biopolymers and in antigen-antibody or ligand-receptor interactions. It has the advantage that no chemical fixatives or dehydrants are used; instead, tissues are frozen directly from the living state. Since they are frozen quickly enough to minimize damage from ice crystals, they are amenable to freeze-drying, which in turn minimizes damage from surface tension forces, much as does critical-point drying. It thus preserves a remarkable degree of three-dimensionality. After freeze-drying, the tissues are replicated with platinum and viewed with a transmission electron microscope at conventional voltages. Stereoscopic images obtained with the standard tilt stages available on such electron microscopes provide novel and informative views of cell structure, especially cytoplasmic filaments, extracellular coats, and various membrane differentiations. Results of this new technique have been presented in a number of recent publications (Heuser, 1978, 1980; Heuser and Salpeter, 1979; Friend and Heuser, 1979; Chandler and Heuser, 1980; Klymkowsky *et al.*, 1980). Details of this method are discussed below, and representative stereo views of freeze-dried samples are then presented.

II. Methods

A. Freeze-Etching

Tissues are frozen by pressing them against pure copper cooled to less than 20°K. Details of the machine we have designed to do this have been published elsewhere (Heuser *et al.*, 1976, 1979). The machine flattens the tissue, and produces a thin—less than 10 μm thick—layer of extremely good freezing, in which ice crystals are too small to obscure overall macromolecular organization. Frozen tissue is transferred directly from this freezing machine to a Balzer's vacuum evaporator where its well-frozen surface is scraped clean, and in places slightly freeze-fractured with the relatively accurate cryomicrotome available commercially in these units. Because the tissue is in a vacuum, it can then be freeze-dried by warming it to −90°C. In less than 5 minutes, about ¼ μm of water will have etched away from the scraped surface, leaving behind the nonaqueous components of the cell, more or less where they were during life—that is, with minimal displacement by ice crystals and minimal collapse during freeze-drying.

B. Replication

The exposed domains are next replicated by depositing a thin film of metal onto their surfaces by standard evaporation techniques. As has become the tradition in freeze-fracture techniques (Moor *et al.*, 1961; Steere, 1973), the metal is

usually a platinum–carbon mixture, which has been volatilized by electron bombardment. Platinum–carbon is chosen because it forms films that are low in granularity and are chemically stable (Bradley, 1958). However, as will be shown below, the granularity of these films is still the major factor limiting the overall resolution of the method.

Ordinarily in freeze-fracture, the platinum is deposited from a fixed angle of about 45° onto a stationary sample, thus creating a "shadow casting" of its surface, on which elevated objects obtain a deposit of metal on one side and cast long "shadows" with no metal on the other (Moor *et al.*, 1961). However, the shadows created by this form of replication become too severe when applied to deep-etched or completely freeze-dried material, because their surfaces are so rough. With such material, a more informative image can be obtained by rotating the sample as the platinum is applied, thereby producing a more radially symmetric deposit of metal, which highlights the surface elevations in a visually pleasing manner. This technique was originally developed to improve the imaging of intramembrane particles (Margaritis *et al.*, 1977), but it works well for deep-etched material also.

C. Photography

After the traditional unidirectional form of platinum deposition (Williams and Wykoff, 1944), it is most informative to study negative images of the resultant replicas, as has been advocated for years by Steere (1973). In the negatives, the deposited metal looks white, since it was originally an electron-dense deposit that scattered electrons and looked black in the electron microscope, and the absence of platinum in the shadows or the background looks black, as would be expected of a true shadow. This, in itself, produces a strong sense of three-dimensionality, since we are accustomed to viewing objects that cast dark shadows in the setting sun. The alternative of viewing replicas in positive contrast, in which platinum looks black and shadows look white, has been adopted in freeze fracture, and has led to the tradition of mounting micrographs upside down, with the shadowing angle coming from below, in order to give a pseudo-sense of three-dimensionality by making the black deposits of platinum look like shadows (Moor *et al.*, 1961). We find that this does not work when one is displaying unidirectionally applied replicas of deeply contoured material, because the large white shadows cast by elevated areas of the sample then look like snowdrifts or, worse, like tears in the replica.

Surprisingly, rotary-applied replicas are also easier to interpret in negative image than they are in the electron microscope. This is because the platinum is deposited from a very low angle, so a great deal of the etched surface is still hidden in the shadows of neighboring structures. When these unreplicated areas are blank white, the replica looks thin and flat. In the photographic negative,

however, they look like a nice black background, and the replicated areas look as if they are highlighted with a gentle, diffuse "moonlight." Indeed, the image quality in such negatives is exactly like that obtained with a standard secondary electron mode of imaging in the scanning electron microscope, where objects look highlighted because of the greater emissivity of their edges.

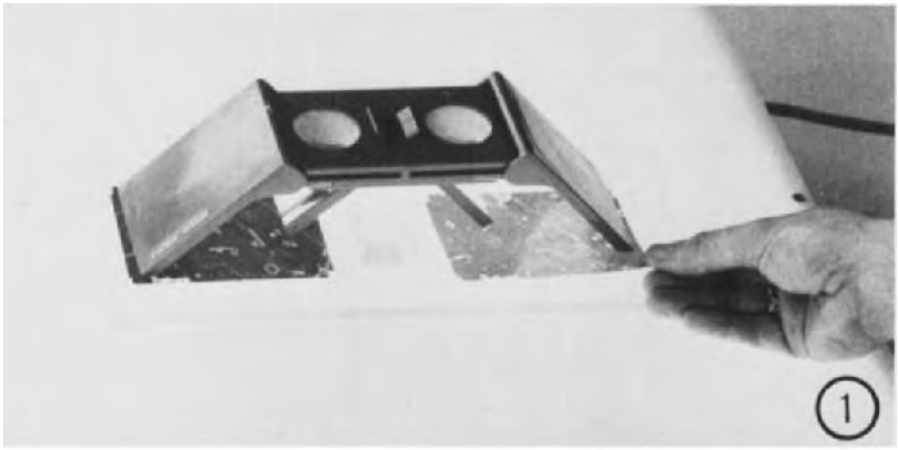
We have found no photographic reversal technique can maintain the tonal quality of the original negatives. All techniques involve an increase in contrast and a disappointing loss of the gray scale inherent in the original image. Thus, whenever possible, we *project* the original negatives, with all the risk of loss or damage that is entailed. The next section describes how we carry out such projection.

When it is necessary to make photographic prints of the replicas, as for this chapter, we then contact-print the original electron microscope negative onto another piece of Kodak 4489 electron microscope film, which we intentionally overexpose and underdevelop in order to hold down contrast. This second contact negative is then mounted in the enlarger and printed on flat grades of Agfa rapid print paper.

D. Stereo Projection

Before we discuss the results obtainable with this new method of tissue preparation and viewing, it may be helpful to describe in some detail the exact method we use to display stereo views of electron microscope negatives to ourselves in the laboratory and to others in lectures. This method grew out of the frustration experienced by lecturers and audiences alike when stereo presentations were given at national meetings, and the relative success of Steere's presentation at an ASCB conference in 1977 (Steere *et al.*, 1979). He displayed stereo views of freeze-fractured replicas by projection through a dual overhead projector of his own design, which was manufactured for him by the Buhl Optical Company of Pittsburgh, Pennsylvania. His projector avoided the problem of alignment inherent in simultaneous projection of two 2 × 2-inch slides through two independent Kodak Carousel® projectors and achieved the visual clarity obtainable only with 3¼ × 4-inch slides. [See Steere (1973) for more information on his use of stereoscopy in freeze-fracture.]

The method we use is built around Steere's 3¼ × 4-inch overhead projector. Stereo pairs of electron micrographs are taken by the usual method of sample-tilt inside the electron microscope. These 3¼ × 4-inch negatives are first inspected and then triaged by viewing them side by side on a light box with a Wild pocket mirror stereoscope (Fig. 1). This is the cheapest and simplest of the mirror stereoscopes, yet it permits separation of the negatives beyond the 60-mm intraocular distance, so the negatives do not need to be overlapped, and it provides a field of view just about the size of a 3¼ × 4-inch negative. While on the light



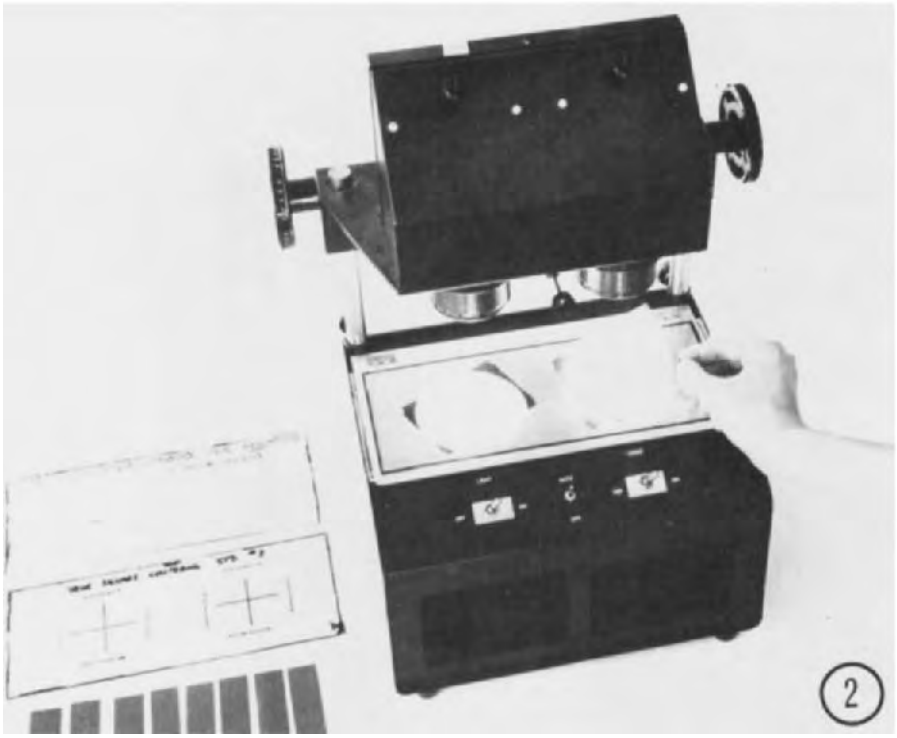


FIG. 1. Wild TSP-1 pocket stereoscope used for initial triaging of stereo pairs of negatives.

FIG. 2. The Steere overhead stereo projection (manufactured by Buhl Optical Company) used to orient and mount stereo pairs on 6 × 12-inch plastic sheets.

box, each pair is separated into left and right negatives in order to make the image look as if the replica is being viewed from the front, rather than through its backside. At this point, pairs that look interesting enough for mounting and projection are chosen.

The next step is to attach these chosen pairs to a single piece of Lexan® polycarbonate plastic in the proper orientation for projection. To do this, we use the Steere overhead projector (Fig. 2). The slide carrier of this projector was rebuilt to accommodate 6 × 12-inch pieces of 10-mil Lexan polycarbonate sheeting, and to hold them in a precisely reproducible position and orientation. Since this is an overhead projector, the plastic lies horizontal so that the stereo pairs of negatives can be laid on top of it and be oriented in each of the two channels until exact register is accomplished.

As this is done, the negatives are also rotated until the original tilt axis between them is aligned precisely vertical. Since the final projected image in most electron microscopes rotates as the magnification is changed, the final tilt for each different magnification must be determined beforehand. We found it easiest to make a transparent underlay for the slide carrier on the overhead projector, which has inscribed on it the exact orientation that the negatives should have at each magnification.

Next, once the correct tilt and register have been achieved, the negatives are attached to the plastic with Scotch tape. Then bare or uninteresting areas are masked off by attaching thin strips of black paper around the edges with more Scotch tape. All this is done *without* viewing the pairs in stereo. Finally, they are ready for projection through crossed polarizers and viewing with the standard stereo glasses. With this overhead projector, stereos not only can be studied in the laboratory, but also can be projected for small groups and seminars. Its limitations are a considerable degree of flare, which is unavoidable with the optics of an overhead projector, and an annoying transmission of heat to the negatives, which makes them gradually warp. This is due to the compact design of its condensers, which do not have enough room for adequate heat filters and cooling fans.

For larger lectures, especially those in conventional halls, the limitations of the Steere projector were restrictive enough to encourage us to build our own stereo projector. This was accomplished by welding together two of the old 3¼ × 4-inch Delineascope® lantern slide projectors (Fig. 3). Placed side by side, these projectors are spaced just right to project the same Lexan-mounted pairs used in the Steere projector, and all that need be done is to construct a suitable slide carrier that will bridge the two. In practice we chose to increase the brightness of the projected image by modifying the projectors to accommodate 1200-watt light bulbs, rather than the usual 750-watt bulbs. This required installation of six extra heat filters, to prevent melting of the negatives, and two extra fans to cool the high-candlepower light bulbs and all the heat filters, which otherwise had an alarming tendency to explode during a lecture.

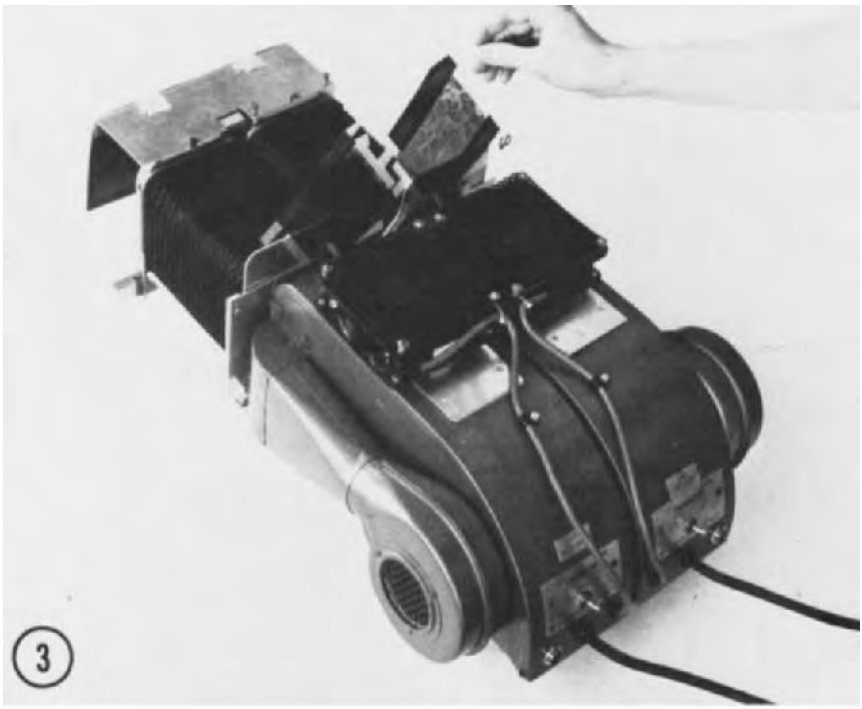




FIG. 3. Homemade dual Delineascope 3¼ × 4-inch lantern slide projectors used to project the mounted and masked stereo pairs of negatives.

FIG. 4. Stereo projection pointer, designed to give a visual impression of one arrow moving in third dimension.

To complete the dramatic effect, this projector was designed to contain the power supplies of two low-voltage projection pointers, which are hand-held side by side and also projected through cross polarizers (Fig. 4). The holder for these pointers was designed to allow the lecturer to vary the lateral position of the two polarized arrows that are projected, thereby creating the visual impression that one arrow is moving in the third dimension, down into the valleys and up onto the peaks of the stereo image.

III. Results

A. Membrane Surfaces

Figure 5 shows the evolution of this technique—from the initial freeze-fractured image on the left; through the interjection of deep etching before replication, in the center; and finally, on the right, the introduction of rotary replication instead of the traditional unidirectional shadow-casting. Each of the three fields shown contains an invagination of the plasma membrane at the surface of a chemically excitable electric cell in the torpedo fish. Freeze-fracture alone reveals only the fracture face of the membrane, speckled with a relatively low concentration of intramembrane particles. The cross-fractured cytoplasm below and the extracellular space above look relatively smooth and structureless. Deep etching (center plate) removes some water from these areas and leaves behind discrete filaments in the cytoplasm and a veil-like material in the extracellular space. More important, it exposes the true inner and outer surfaces of the invaginated membrane. The inner surface, below, is contacted by filaments but does not display any reflection of the intramembrane particles seen on the E fracture face in the left plate. The outer surface is seen at the mouth of the trumpet, behind the extracellular veil, which is the cell's basal lamina. Finally, on the right, rotary shadowing removes the harsh shadows and highlights the cytoplasmic filaments and extracellular lamina. Also, rotary shadowing highlights the surface structure of the membrane itself.

Details of this surface cannot be seen clearly in this figure, but can be seen in Fig. 6, which is a more optimal exposure of the true outer surface of this membrane. Here, the basal lamina was mostly scraped away during the fracturing, leaving only the netlike veil on the left. Stereo viewing demonstrates that this veil lies above the membrane surface and extends down into the circular invagination at the bottom of the field. Stereo viewing also demonstrates quite clearly that the membrane itself was fractured through on the right and that the

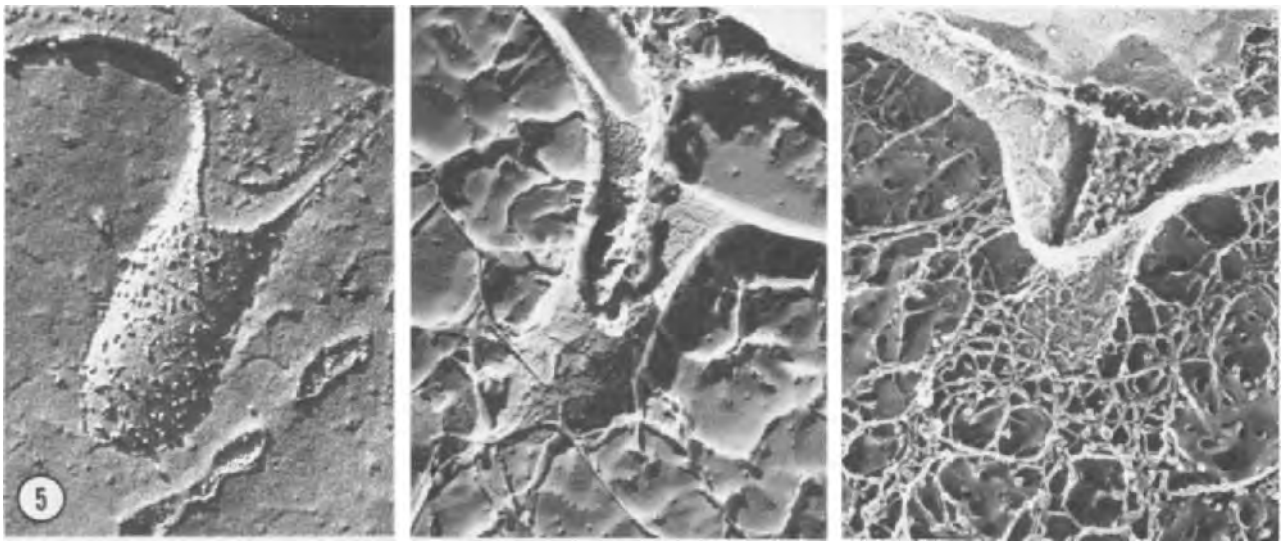


FIG. 5. Three views of plasma membrane invaginations, showing evolution of the method from freeze-fracture (left), to deep etching (center), to rotary platinum deposition (right). All magnifications approximately 55,000×. Reprinted from Heuser and Salpeter (1979), with permission.

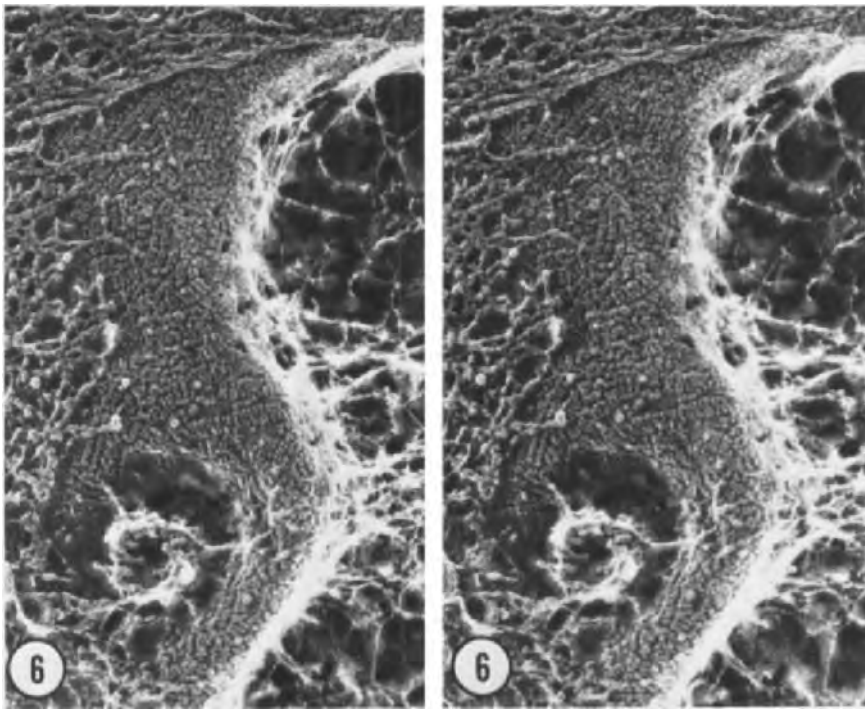


FIG. 6. Deep-etched exposure of the true outer surface of postsynaptic membrane in the electric organ synapse of the torpedo fish. Magnification 65,000×.

coarse network of filaments on the far right lies underneath the membrane, in the cell cytoplasm. Higher magnification of this field (Fig. 7) shows that the membrane surface is covered with small protrusions, individually 8-9 nm in diameter. These protrusions group together into twos and fours, especially "molar"-like fours, which in places line up into rows two "molars" abreast. They are thought to represent the heads of the acetylcholine receptor molecules that characterize this membrane. They had been seen before by negative stain, but their size, elevation, and tendency to crystallize had not been appreciated before they were seen by the present method (cf. Heuser and Salpeter, 1979).

At this point it is worth repeating that the sense of three-dimensionality present even in a flat view such as that shown in Fig. 7 is due to the photographic reversal step used here. The result is that platinum looks white and appears to highlight elevated structures. The original replica is much harder to interpret in the electron microscope, because then platinum is black and the background is white. Figure 8 shows the same field as in Figs. 6 and 7, but printed in positive contrast, the way it looks in the electron microscope. One must be very familiar with looking at metal replicas in order to gain information from them.



FIG. 7. High magnification of membrane surface shown in Fig. 6, to illustrate the receptor molecules that cluster and line up in this membrane. Magnification 175,000×. Reprinted from Heuser and Salpeter (1979), with permission.

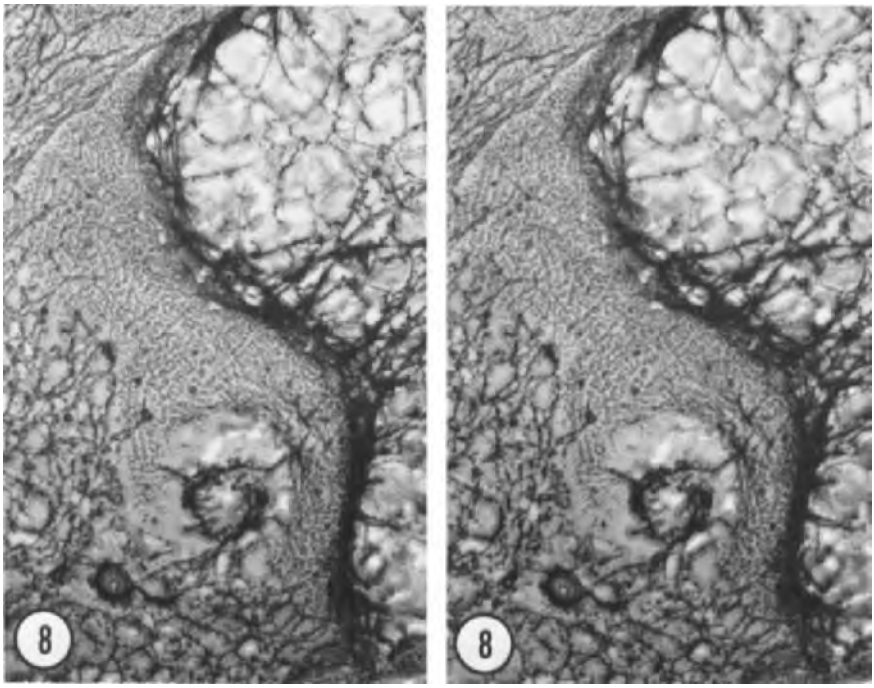


FIG. 8. Stereo view of the same field as in Figs. 6 and 7, printed in positive contrast, with platinum black, as it actually looks in the electron microscope. Magnification 60,000×. Reprinted from Heuser and Salpeter (1979), with permission.

B. Cell Interiors

The second advantage of the present method, besides the opportunity to view membrane surfaces, is that it can simultaneously reveal interior cellular structures in a way very much like thin sectioning. Figure 9 shows a junction between a nerve and a muscle cell that has been cross-fractured and then deep-etched. The dark convolution in the center is a fold in the muscle plasma membrane; the muscle is below, and its long filaments can just barely be seen. Most impressive about the three-dimensional view of the field is the barbed basal lamina that bisects the narrow extracellular cleft between the muscle and the nerve terminal (which lies above and can be recognized by its complement of spherical synaptic vesicles). Owing to the narrowness of the cleft, and the low angle of platinum deposition, one cannot see down in this cleft very far; the three-dimensional depth is not much greater than that in a normal thin section. But because the *surfaces* of structures are seen and because they look *solid* after being coated with metal, they appear quite dramatic when viewed stereoscopically. The ob-

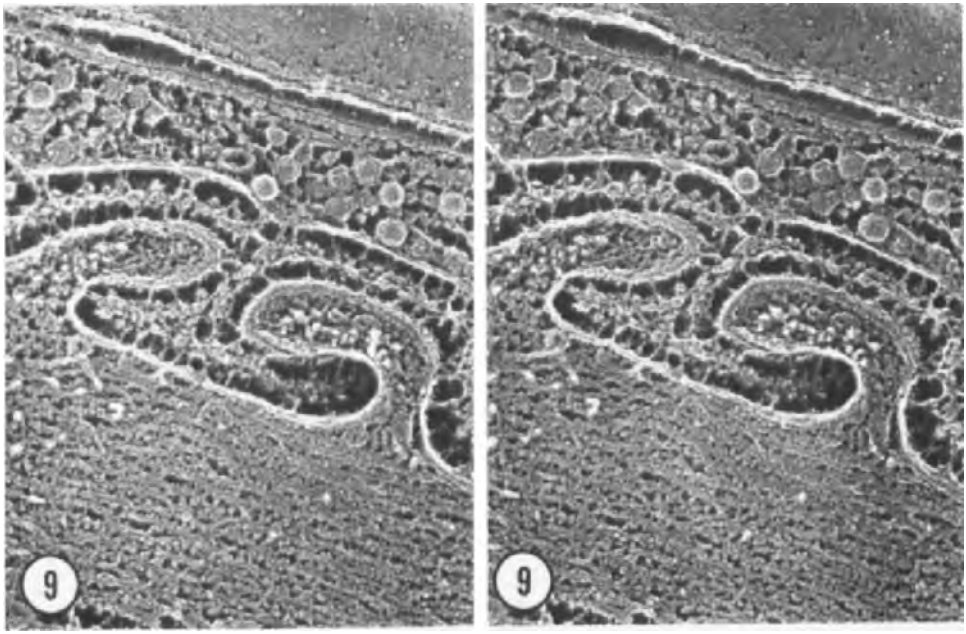


FIG. 9. Cross-fractured and deep-etched neuromuscular junction, with vesicle-laden nerve above and muscle cytoplasm below the dark, convoluted synaptic cleft. Magnification 80,000×.

server can immediately understand how such structures are put together. Here, for example, one can see how the basal lamina attaches by delicate wisps to the pre- and postsynaptic membranes of the neuromuscular junction.

Although this technique can thus bridge freeze-fracture and thin sectioning, it runs into one major difficulty when it is applied to studies of the cell interior. This problem is shown in Fig. 10, which is a broader field of the inside of a nerve terminal, with three sausage-like mitochondria above and a hoard of small, spherical synaptic vesicles below. In such a view it would be interesting to see the surfaces of these internal structures and to see how they relate to each other and to the filamentous systems found in other regions of the cell. Unfortunately, the organelles are so tightly packed and so much unetchable material surrounds them that nothing but fracture faces can be seen. As soon as such views were obtained, it was clear that something had to be done to *clear out* the unetchable material in the background of the cytoplasm. So far, we have explored three different ways to do this.

The first method is illustrated in Fig. 11. Here, a synapse in the electric organ of the torpedo fish was "blown up" by brief immersion in distilled water before quick freezing. This exposed the membrane organelles in the oval nerve terminal (above) and the cytoplasmic filaments within the postsynaptic cell (below). Pre-

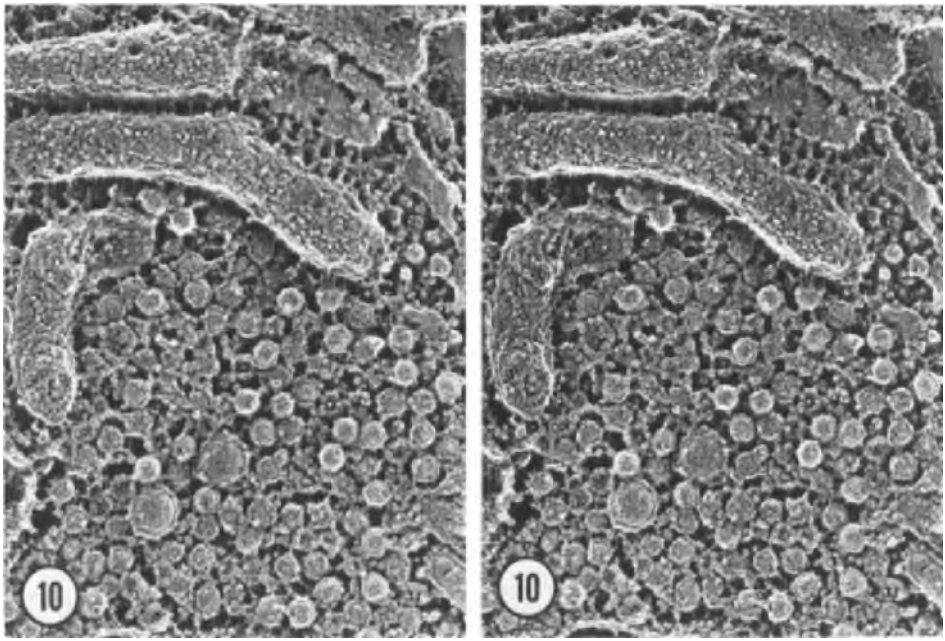


FIG. 10. Deep-etched view of the inside of a motor nerver terminal, showing three mitochondria at the top and a hoard of synpatic vesicles below. Magnification 80,000×.

sumably the distilled water shock-ruptured the cells in some other area than that shown here, thereby releasing the soluble components of the cytoplasm—including proteins and salts—which would otherwise have been left behind after deep etching and would have filled in the spaces between the cytoplasmic organelles. Figure 12 shows an adjacent field from the same "shocked" preparation, with a nerve terminal in the center that was not fractured open. This field displays more optimally the inside of the postsynaptic membrane and the web of filaments that attach to it. By viewing it in stereo, one can recognize that the postsynaptic membrane forms three invaginations, which extend away from the dark, crescent-shaped synaptic cleft in three different directions. The cytoplasmic filaments appear to embrace these invaginations and give them support. Figure 13 is a higher magnification of such an area, which shows more clearly the web that underlies this membrane and surrounds its invaginations, such as the one in the lower right-hand corner of the field. At the top of this picture, the fracture plane passed obliquely across the synaptic cleft; after etching, one sees sequentially the nerve terminal fracture face, the true outer surface of the nerve, then the extracellular cleft with its basal lamina, and finally a bit of the fracture face of the postsynaptic membrane (the wedge-shaped area dotted with white

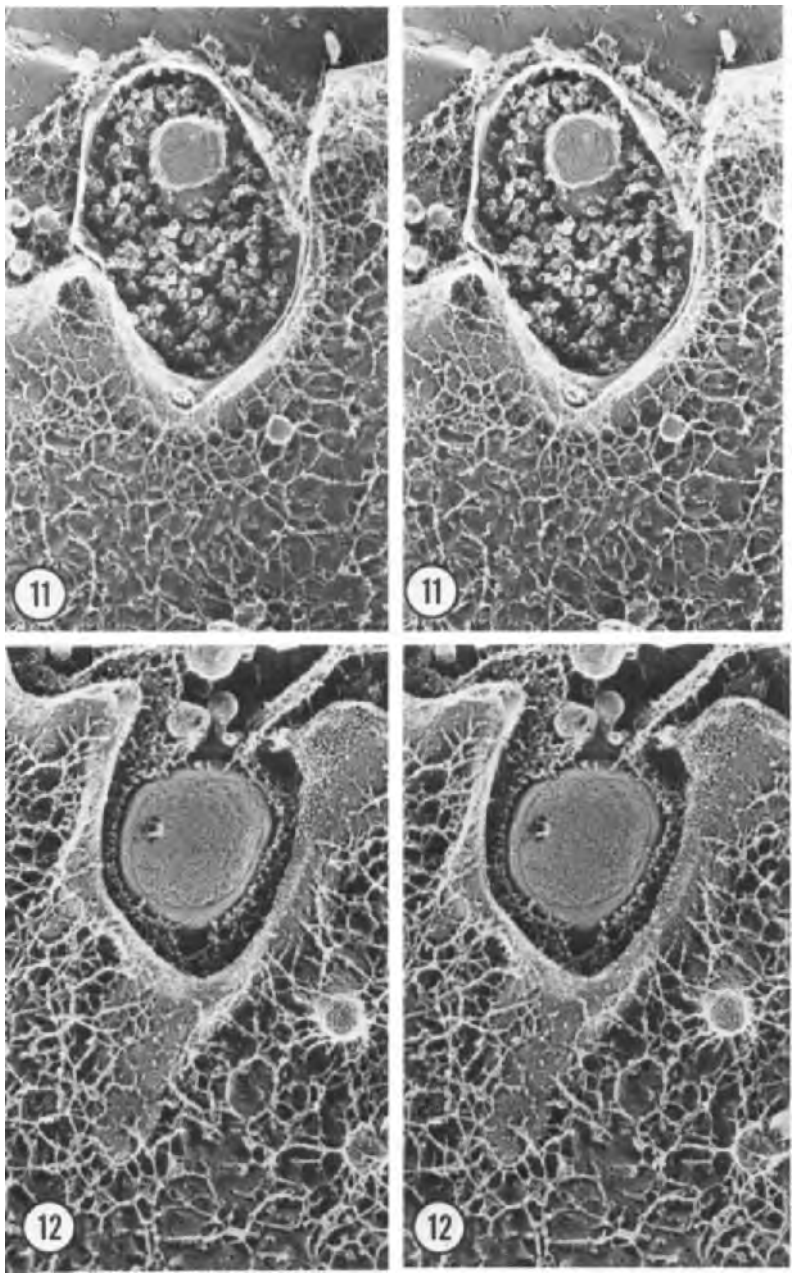


FIG. 11. Fractured and deep-etched view of nerve-electrocyte synapse from the torpedo fish. Tissue was washed by exposure to distilled water for a minute before quick-freezing. Magnification 14,000×.

FIG. 12. Synapse prepared as in Fig. 11, in which the cytoplasmic web beneath the postsynaptic membrane is particularly clear. Magnification 22,000×.

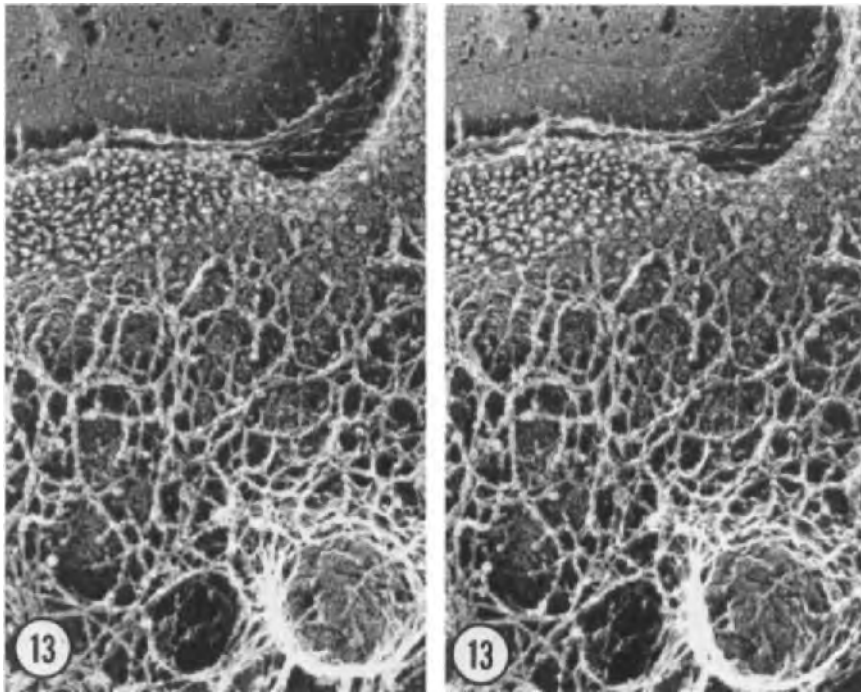


FIG. 13. High magnification of the submembranous web seen in Fig. 12. This is the true inner surface of the same membrane seen in Fig. 6 and 7. Magnification 60,000×. Reprinted from Heuser and Salpeter (1979), with permission.

bumps), before coming out to the true inner surfaces of this membrane and the cytoplasmic membrane web.

C. Freeze-Dried Tissue Culture Cells

The discovery of the submembranous web at the torpedo synapse led us into a broader study of cytoplasmic filaments with the collaboration of M. Kirschner, R. Cooke, T. Pollard, and their co-workers. At first, we began to fracture and deep-etch purified gels of actin, and we were struck by how similar they looked to the postsynaptic web just described. Then we began a study of the cell cytoskeleton, which is the insoluble residue of actin and intermediate filaments left behind after a living cell is exposed to concentrated detergent and its plasma membrane is dissolved away. For the study of cytoskeletons, our technique had to be modified to permit quick freezing of tissue culture cells on coverglasses. Such cells are so flat that they would be hard to hit by freeze-fracturing, but once their membrane had been removed, their interiors could be exposed simply by

freeze-drying the coverslips completely. This meant leaving them at −90°C *in vacuo* for 1 hour, in contrast to the 3- to 5-minute etch used after freeze-fracturing in all the above examples. Such freeze-dried cytoskeletons displayed a wealth of information about how filaments are organized in the cell. Figure 14, for example, shows a high magnification of one of the "stress fibers" that crisscross the cytoplasm of mature, flattened-out fibroblasts. It is known from light microscopic immunocytochemistry that stress fibers are rich in actin. Our high-magnification views of freeze-dried cytoskeletons reveal these actin filaments directly, and stereo viewing shows how they are woven together to form the stress fibers. Note that on close inspection each individual filament appears to be cross-banded. The repeat here is 5.5 nm, which is what would be expected for actin, since it is a double helix of 5.5-nm actin monomers. Surprisingly, the helix

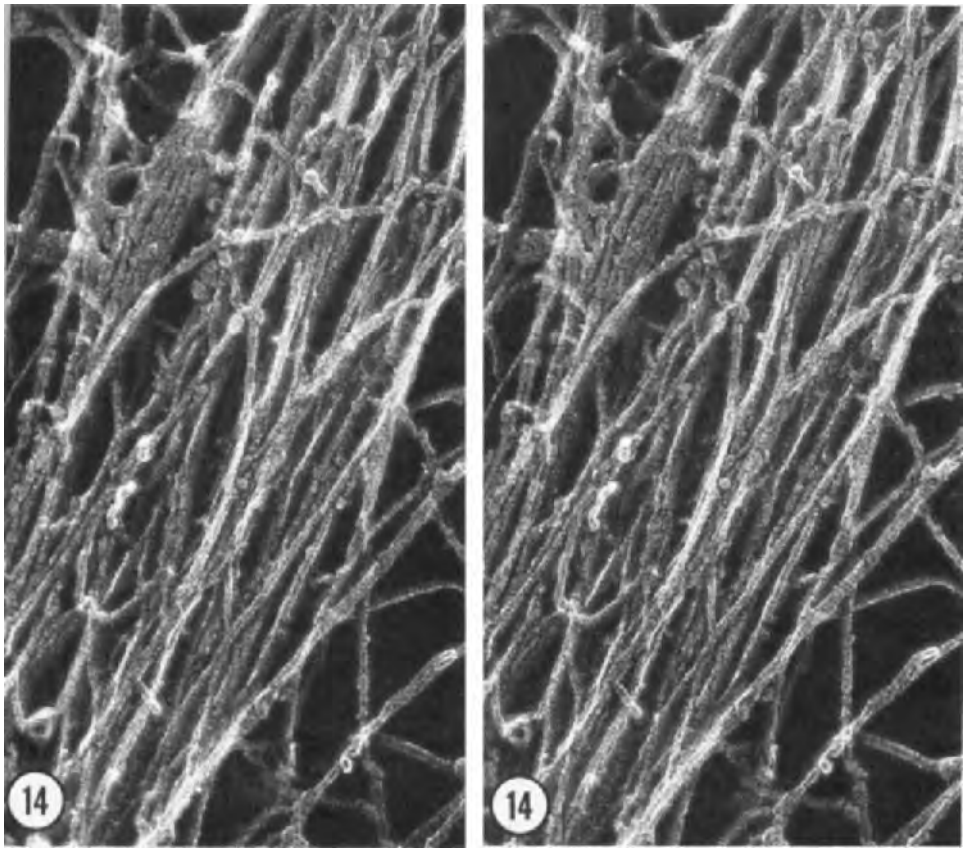


FIG. 14. High magnification of a "stress fiber" bundle of actin filaments in a freeze-dried fibroblast cytoskeleton. Magnification 200,000×. Reprinted from Heuser and Kirschner (1980), with permission.

is not apparent in freeze-dried actin, the way it is in negatively stained actin. We cannot explain this, but can only add that S-1 decoration of such stress fibers converts each actin filament into a beautiful helical "rope" much the way it forms "arrowheads" on actin seen in thin section.

Further study of freeze-dried cytoskeletons and purified cytoplasmic proteins demonstrated that the resolution in platinum replicas formed by rotary deposition was good enough to discriminate actin filaments from intermediate filaments, and to recognize microtubules by their characteristic construction. Figure 15 shows a field of purified microtubules, some of which have been cracked open

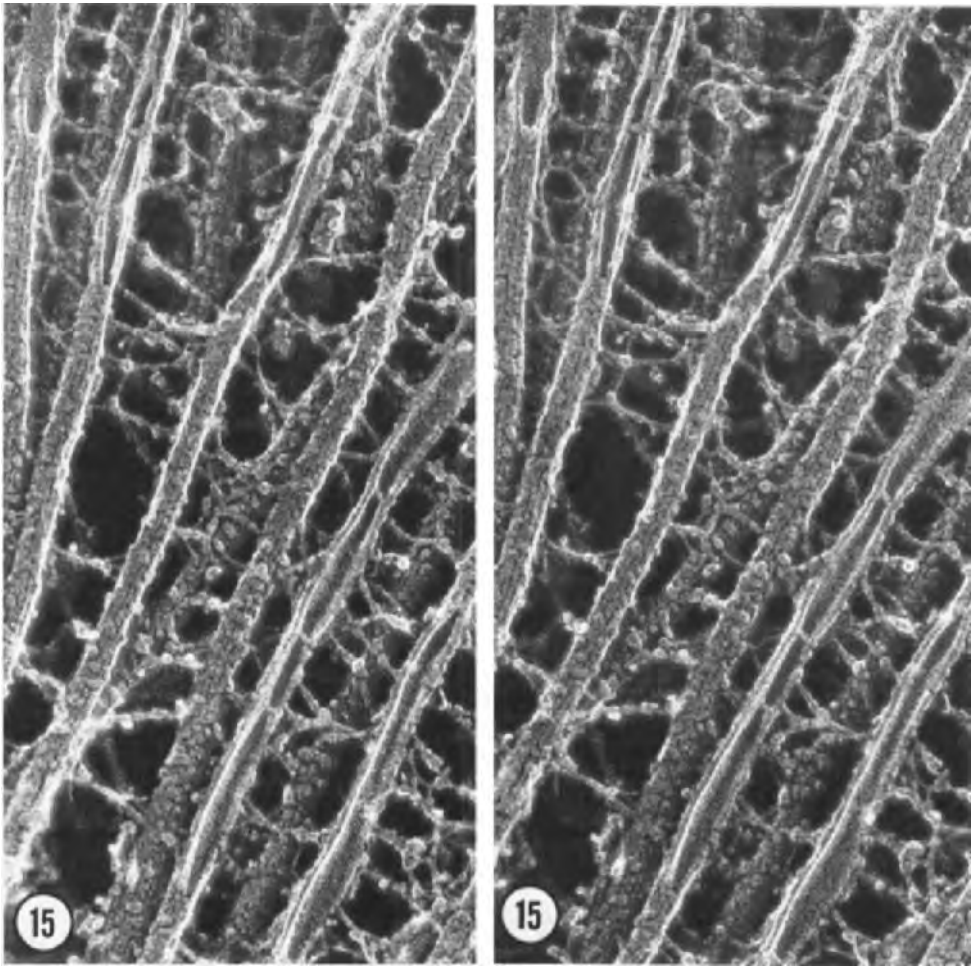
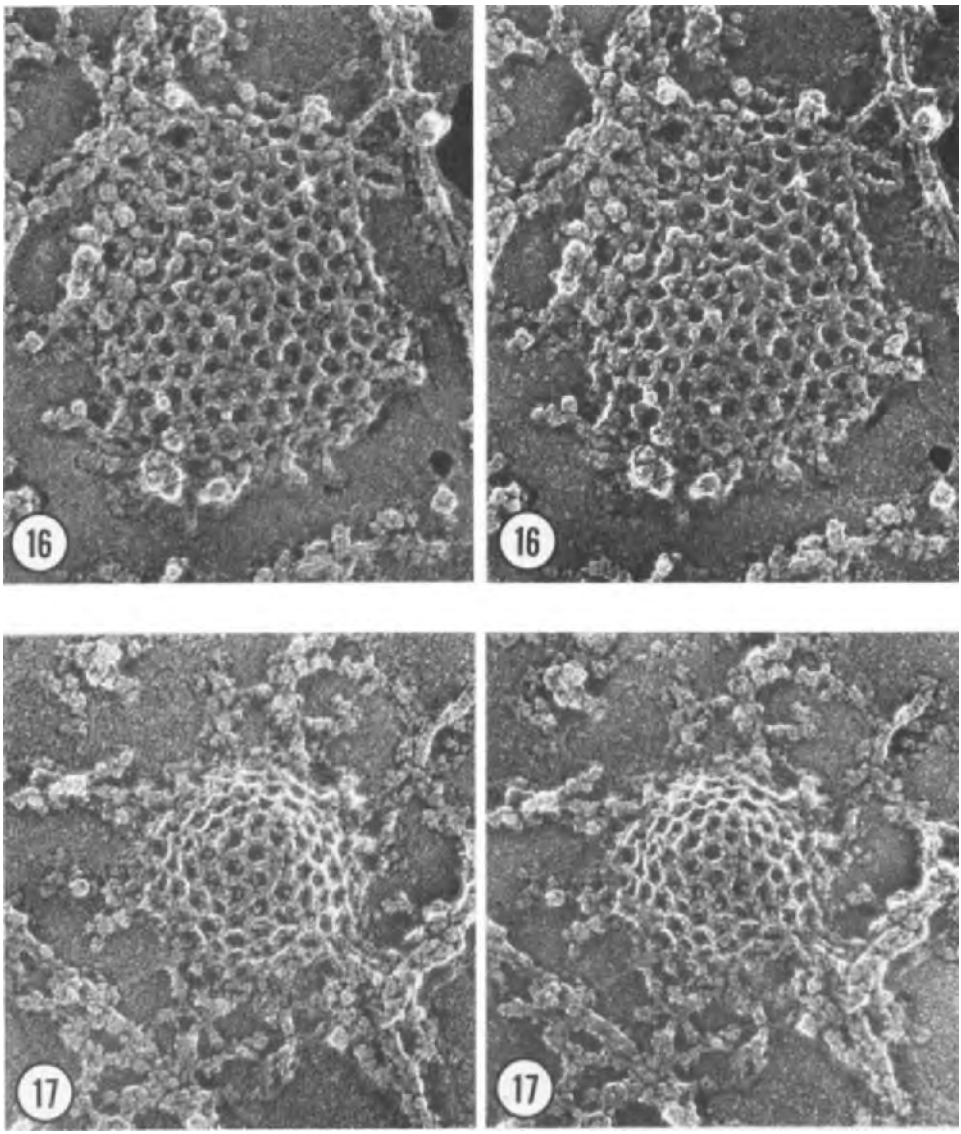


FIG. 15. High magnification of purified and repolymerized microtubules plus MAPs, fractured so that the interior three-start helix (repeat: 4 nm) is visible in some tubules. Magnification 200,000×. Reprinted from Heuser and Kirschner (1980), with permission.

during fracturing to display oblique internal striations, which repeat every 4 nm. These striations represent the characteristic three-start helix—one of the patterns that emerge when tubulin monomers polymerize into microtubules. Their 4-nm repeat displays the limit of resolution of the platinum replication technique as we



FIGS. 16 and 17. Two views of the polygonal "coat" that condense against the inside of the plasma membrane at sites of adsorptive endocytosis, here from freeze-fractured and deep-etched mouse fibroblasts. Magnification 130,000×. Reprinted from Heuser (1980), with permission.

now do it. There is considerable hope for improvement here, since the resolution of the microscope is at least an order of magnitude better.

A third way to open up the cell and wash out soluble components—one that does not destroy membranes the way that detergent extraction does, and does not expose the cell interior to distilled water the way that hypotonic shock does—is to physically scrape the cell open while it is still alive (cf. Vacquier, 1975; Clarke *et al.*, 1975; Boyles and Bainton, 1979). When this is done in an isotonic solution of KCl that contains a physiological level of $MgCl_2$ and enough EGTA to keep calcium as low as it must have been inside the living cell, then the cell fragments look quite good. Particularly useful is the opportunity to view membranes and filaments at the same time. The first surprise that emerged from such samples was the structure of "coated pits" that are involved in adsorptive endocytosis (Figs. 16 and 17). These are differentiations of the plasma membrane, at which a cytoplasmic material condenses into a small patch on the inside of the membrane, following which this region curves up and pinches off. Platinum replicas of these differentiations in fibroblasts illustrate that the patch of cytoplasmic material forms a hexagonal mesh of 7-nm-thick struts (Fig. 16), and that this honeycomb begins to look like a geodesic dome as the membrane curves up (Fig. 17).

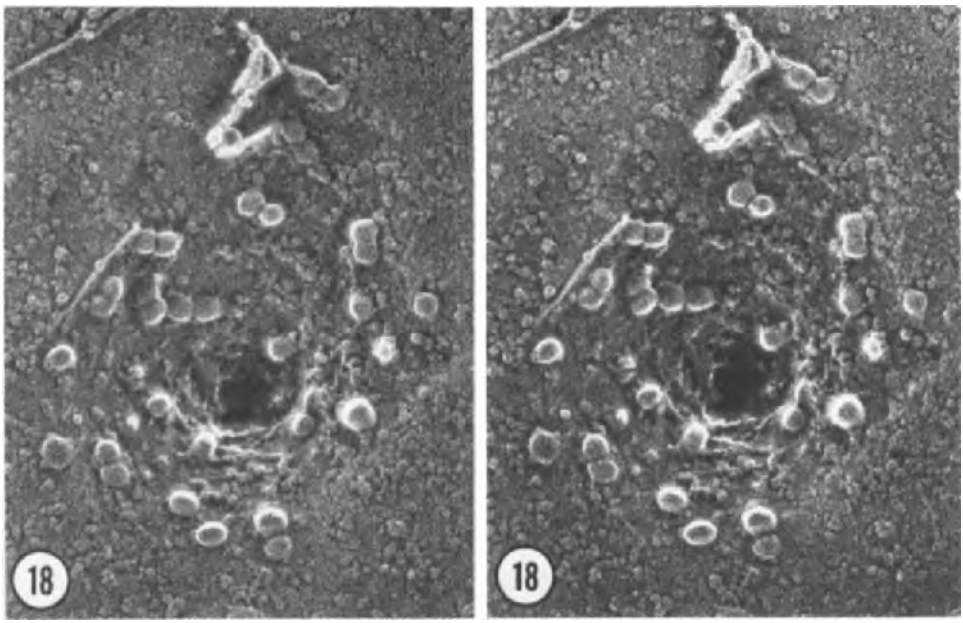


FIG. 18. The outside of an endocytotic pit, laden with 25-nm droplets of low-density lipoprotein, from a cultured fibroblast quick-frozen and freeze-dried. Magnification 110,000×. Reprinted from Heuser (1980), with permission.

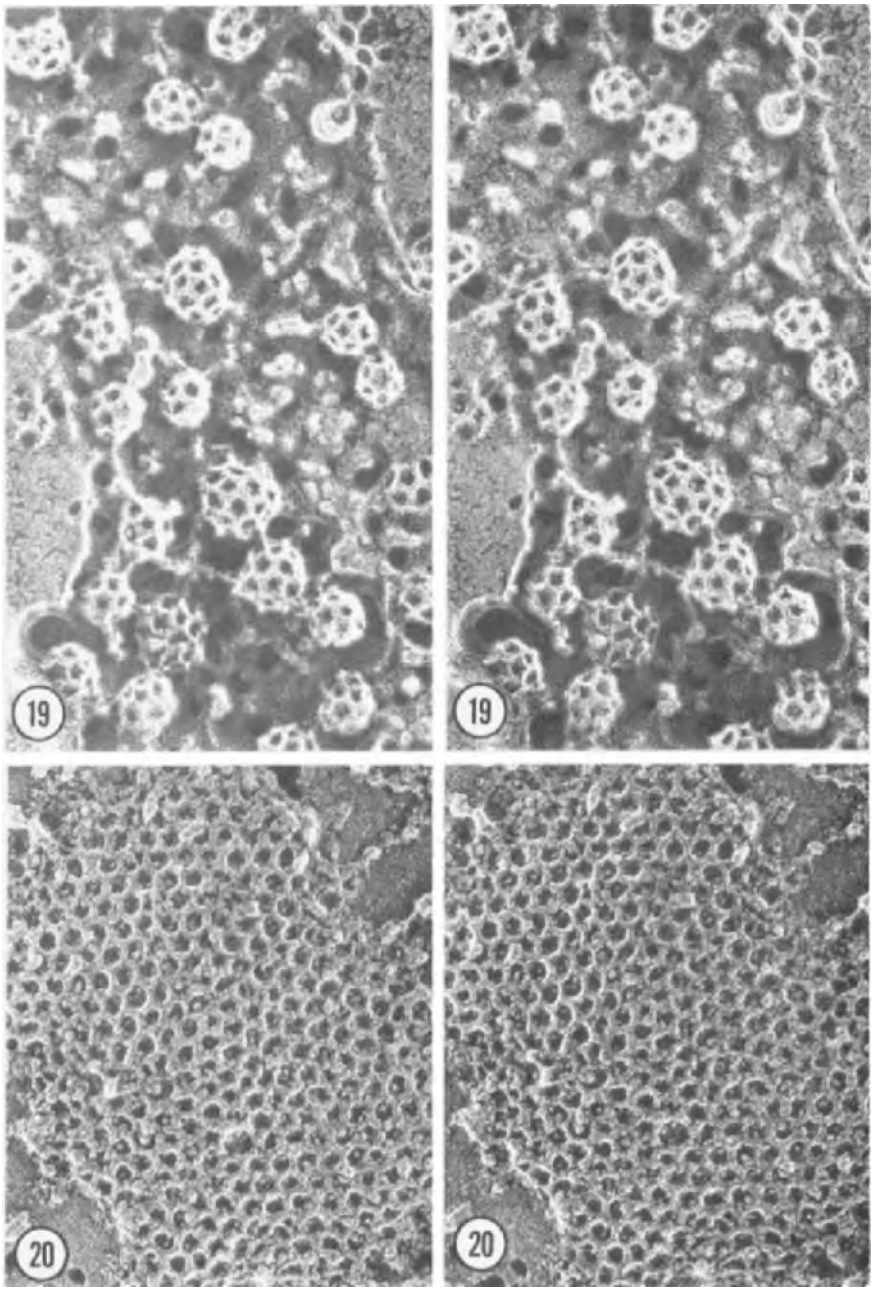


FIG. 19. Coated vesicles isolated from pig brain and purified on a density gradient. The method of tissue preparation advocated here is particularly effective for visualizing such biochemical fractions. Magnification 140,000×. Reprinted from Heuser (1980), with permission.

FIG. 20. Large field of hexagons at the site of incipient endocytosis, which displays a few pentagonal dislocations at sites where it has begun to curve inward (arrows). Magnification 130,000×. Reprinted from Heuser (1980), with permission.

What is occurring on the cell surface while this internal change is taking place can be seen by simply freeze-drying whole fibroblasts without ever scraping them open or removing them from the culture dish. Thus exposed, the cell surface reveals a plethora of circular depressions, just the same size as the patches of basketworks seen on the inside of their membranes (Fig. 18). Not surprisingly, these depressions are speckled with 25- to 30-nm droplets that look just like low-density lipoprotein (LDL), one of the proteins that these cells are known to take up by adsorptive endocytosis. The clustering of LDL molecules in these depressions is thought to result from the cross-linking of LDL receptors to the underlying basketworks (Goldstein *et al.*, 1979).

Earlier investigators studying the structure of coated vesicles isolated from brain, such as those shown in Fig. 19, appreciated that the coat was a basketwork composed of hexagons and pentagons (Kanaseki and Kadota, 1969; Crowther *et al.*, 1976). But what they could not see, because they had available only negative-staining and thin-sectioning techniques, was the broad fields of poly-

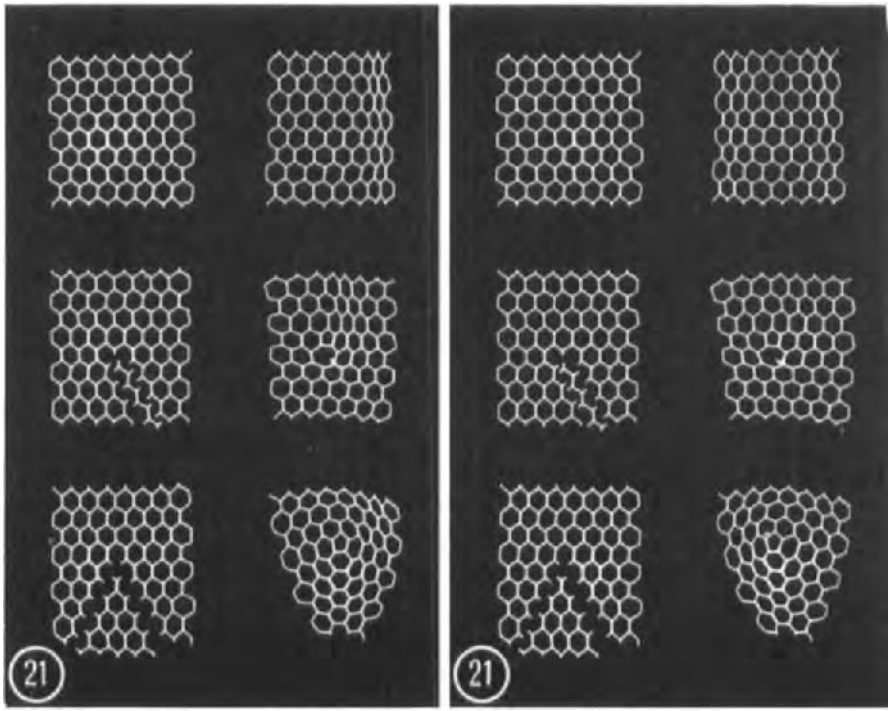


FIG. 21. Stereo views of chicken wire models illustrating how coat rearrangement could power endocytosis. Bonds could break to form five to seven dislocations with a slight degree of curvature (center) and progress to pure pentagonal insertion with greater curvature (bottom). Reprinted from Heuser (1980), with permission.

gons that form on the inside of the plasma membrane before the vesicles pinch off (Fig. 20). When these are viewed by stereo-microscopy of platinum replicas, again the resolution is good enough to see variations in the 30-nm polygons that constitute the network. Viewing a large number of these structures, and correlating their composition of five-, six-, and seven-sided polygons with their degree of curvature as assessed by stereo-microscopy, we have a clue as to how the membrane curvature could be brought about (cf. Heuser, 1980). A chicken wire model of one possible sequence is shown in Fig. 21, which illustrates how progressive breakage of bonds and reannealing could lead, first, to juxtaposition of five- and seven-sided rings at points of moderate curvature, and then to isolated five-sided rings at points of more extreme (spherical) curvature.

These, then, are three ways of opening up the cell and exposing internal structures to the freeze-drying, platinum replication technique. We are currently exploring a number of variations in these approaches (including, for example, a brief exposure to plasma membrane-specific detergents, such as saponin, during the initial moments of fixation with formaldehyde; cf. Ohtsuki *et al.*, 1978) in an effort to inflict minimal damage to the cell but still wash out its complement of soluble cytoplasmic proteins.

D. Biochemical Fractions

Finally, it should be apparent from Figs. 15 and 19 that the deep-etch, rotary-replication technique is particularly suitable for looking at isolated cell organelles prepared by homogenization and differential centrifugation. In this situation, there is no problem with the density of packing or with other surrounding obscurations, and the surfaces of structures are revealed with unsurpassed clarity. Figure 22 shows, for example, small vesicular fragments of the type of postsynaptic membrane shown in Figs. 6–8, fragments prepared by classical cell fractionation techniques (Cohen *et al.*, 1972; Reed *et al.*, 1975).

Here the surface replication technique is an ideal way to observe the vesicles, to assess their purity, and to study variations in their complement of receptor molecules. For example, the sequence in Fig. 22 shows the effects of treating such postsynaptic membrane vesicles with a dilute protease. At the top is a typical untreated vesicle. Receptors appear to be randomly arranged or irregularly aggregated, unlike the crystalline pattern seen in the intact membrane. (This is thought to be due to removal during fractionation of an associated protein, which maintains the crystalline pattern.) In the center is a vesicle showing the first effects of protease: Receptors appear to have clustered into tight groups, so that the vesicle is beginning to look like a raspberry. At the bottom is a vesicle showing the final outcome of this tendency of the receptors to cluster. Presumably because the molecules are wedge-shaped and have fat heads, the clusters evaginate and eventually pinch off the main body of the vesicle, leaving it

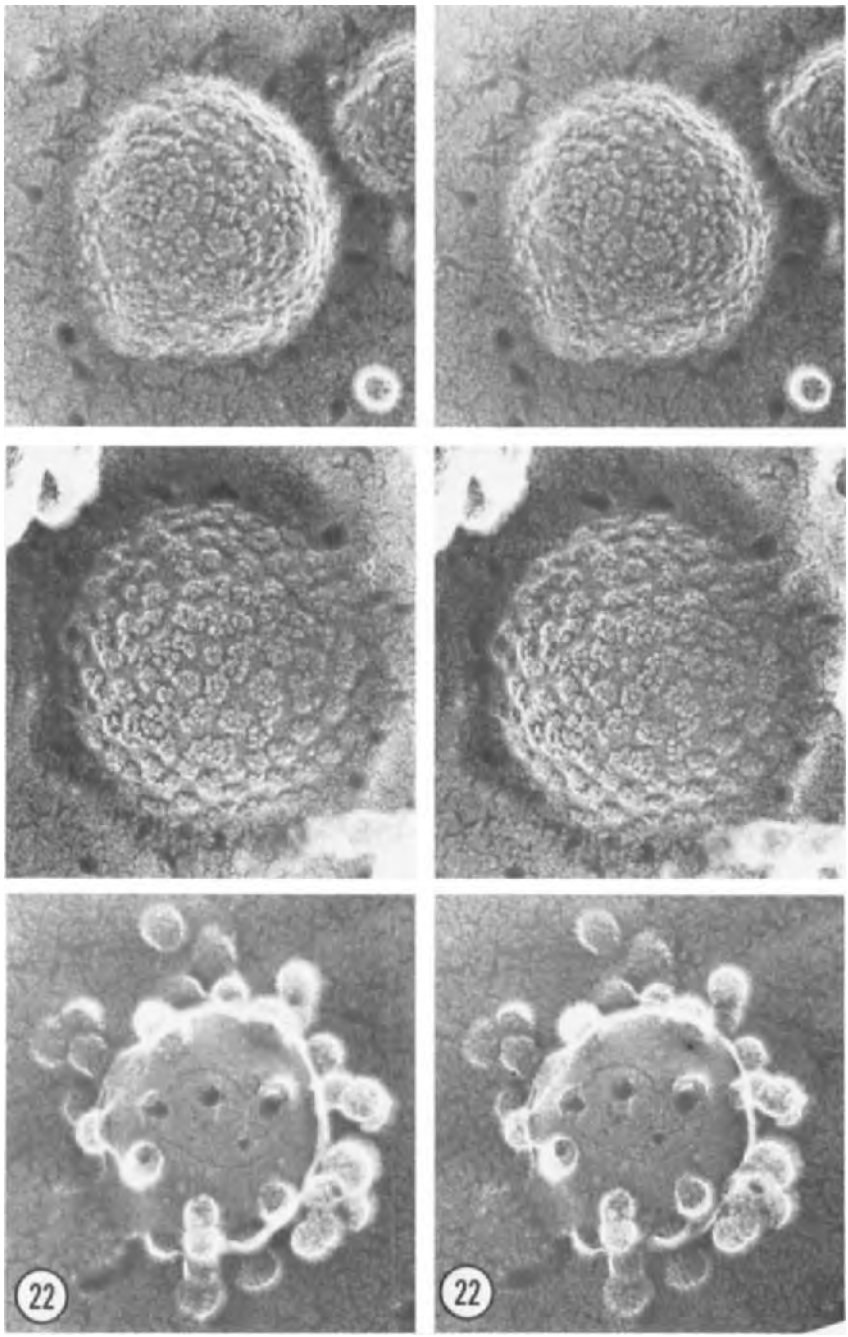


FIG. 22. Deep-etched exposure of a purified fraction of postsynaptic membrane vesicles, before (top) and after exposure to protease (center and bottom). This treatment causes the receptors to cluster and pinch off, as described in the text. Stereo viewing illustrates this phenomenon most dramatically. Magnification 120,000×. Reprinted from Klymkowsky *et al.* (1980), with permission.

smooth and devoid of receptors (cf. Klymkowsky *et al.*, 1980). Stereo viewing of such replicas illustrates this budding process most dramatically.

IV. Summary and Conclusions

Stereomicroscopy offers a unique opportunity when applied to metal replicas, particularly rotary-deposited replicas of freeze-dried biological materials. The sense of depth obtained by the classical shadow-casting method of metal application is mostly lost in rotary replicas, but depth is recaptured by viewing the replicas in stereo. Thus, harsh, obscuring shadows are eliminated without a loss of information. Moreover, the depth retained in freeze-dried samples is so great that stereo-viewing techniques are needed to appreciate them fully. Surface replicas do not absolutely require stereo, the way that high-voltage electron microscopy does. This is because the structures on metal replicas are almost completely opaque, whereas in high-voltage electron microscopy they are translucent and thus subject to becoming superimposed on one another. Nevertheless, stereo viewing of replicas can greatly increase the viewer's appreciation and discriminative awareness of the three-dimensional organization inherent in all kinds of biological structures.

Acknowledgments

Thanks to Louise Evans and Frank McKeon for excellent technical assistance, to Marc Kirschner and Margaret Lopata for providing fibroblasts, and to Lou Reichardt for providing the coated vesicle fraction. This work was supported by grants from the Muscular Dystrophy Association of America and the United States Public Health Service.

Special thanks also to Jim Wall, Senior Mechanician in the Department of Physiology, University of California School of Medicine, San Francisco, for his help with the design and construction of the freezing machine, projectors, etc., used in this study.

References

Boyles, J., and Bainton, D. F. (1979). Changing patterns of plasma membrane-associated filaments during the initial phases of polymorphonuclear leukocyte adherence. *J. Cell Biol.* **82,** 347-368.

Bradley, D. E. (1958). Simultaneous evaporation of platinum and carbon for possible use in high-resolution shadow-casting for the electron microscope. *Nature (London)* **181,** 875.

Chandler, D. E., and Heuser, J. E. (1980). The vitelline layer of the sea urchin egg and its modification during sterilization: A freeze fracture study using quick freezing and deep etching. *J. Cell Biol.* (in press).

Clarke, M., Schatten, G., Mazia, D., and Spudich, J. A. (1975). Visualization of actin fibers associated with the cell membrane in amoebae of *Dictyostelium discoideum*. *Proc. Natl. Acad. Sci. U.S.A.* **72,** 1758-1762.

Cohen, J. B., Weber, M., Huchet, M., and Changeux, J.-P. (1972). Purification from *Torpedo marmorata* electric tissue of membrane fragments particularly rich in cholinergic receptor. *FEBS Lett.* **26,** 43-47.

Crowther, R. A., Finch, J. T., and Pearse, B. M. F. (1976). On the structure of coated vesicles. *J. Mol. Biol.* **103,** 785-798.

Friend, D. S., and Heuser, J. E. (1979). Organized particle arrays on the outer mitochondrial membrane of rapidly frozen sperm. *J. Cell Biol.* **83,** 271a.

Goldstein, J. L., Anderson, R. G. W., and Brown, M. S. (1979). Coated pits, coated vesicles, and receptor-mediated endocytosis. *Nature (London)* **279,** 679-685.

Heuser, J. E. (1978). Membrane surfaces viewed by transmission EM of tissues of quick-frozen, deep etched and rotary replicated: A simple alternative to high-resolution scanning EM. *J. Cell Biol.* **79,** 224a.

Heuser, J. E. (1980). 3-D visualization of coated vesicle formation in fibroblasts. *J. Cell Biol.* (in press).

Heuser, J. E., and Kirschner, M. W. (1980). Filament organization resolved in platinum replicas of freeze-dried cytoskeletons. *J. Cell Biol.* (in press).

Heuser, J. E., Reese, T. S., and Landis, D. M. D. (1976). Preservation of synaptic structure by rapid freezing. *Cold Spring Harbor Symp. Quant. Biol.* **40,** 14-24.

Heuser, J. E., Reese, T. S., Dennis, M. J., Jan, Y., Jan, L., and Evans, L. (1979). Synaptic vesicle exocytosis captured by quick freezing and correlated with quantal transmitter release. *J. Cell Biol.* **81,** 275-300.

Heuser, J. E., and Salpeter, S. R. (1979). Organization of acetylcholine receptors in quick-frozen, deep etched and rotary replicated torpedo postsynaptic membrane. *J. Cell Biol.* **82,** 150-173.

Kanaseki, T., and Kadota, K. (1969). The "vesicle in a basket." *J. Cell Biol.* **42,** 202-220.

Klymkowsky, M., Heuser, J. E., and Stroud, R. (1980). Protease effects on the structure of acetylcholine receptor membranes from *Torpedo californica* electroplaques. *J. Cell Biol.* (in press).

Margaritis, L. H., Elgasaeter, A., and Branton, D. (1977). Rotary replication for freeze-etching. *J. Cell Biol.* **72,** 47-56.

Moor, H., Mühlethaler, K., Waldner, H., and Frey-Wyssling, A. (1961). A new freezing-ultramicrotome. *J. Biophys. Biochem. Cytol.* **10,** 1.

Ohtsuki, R. M., Manzi, R. M., Palade, G. E., and Jamieson, J. D. (1978). Entry of macromolecular tracers into cells fixed with low concentrations of aldehydes. *Biol. Cell.* **31,** 119-126.

Reed, K., Vandlen, R., Bode, J., Duguid, J., and Raftery, M. A. (1975). Characterization of AcChR rich and AcChE-rich membrane particles from *Torpedo californica* electroplaques. *Arch. Biochem. Biophys.* **167,** 138-144.

Steere, R. L. (1973). Preparation of high-resolution freeze-etch, freeze-fracture, frozen-surface, and freeze-dried replicas in a single freeze-etch module, and the use of stereo electron microscopy to obtain maximum information from them. *In* "Freeze-etching Techniques and Applications" (E. Benedetti and P. Favard, eds.), Chapter 18, pp. 223-255. Soc. Fr. Microsc. Electron., Paris.

Steere, R. L., Erbe, E. F., and Moseley, J. M. (1979). Controlled contamination of freeze-fractured specimens. *In* "Freeze Fracture: Methods, Artifacts, and Interpretations" (J. E. Rash and C. S. Hudson, eds.), pp. 99-109. Raven, New York.

Vacquier, V. D. (1975). The isolation of intact cortical granules from sea urchin eggs: Calcium ions trigger granule discharge. *Dev. Biol.* **43,** 62-74.

Williams, R. C., and Wyckoff, R. W. G. (1944). The thickness of electron microscopic objects. *J. Appl. Phys.* **15,** 712.

METHODS IN CELL BIOLOGY, VOLUME 22

Chapter 7

Dense Tissue and Special Stains

EICHI YAMADA AND HARUNORI ISHIKAWA

Department of Anatomy,
Faculty of Medicine,
University of Tokyo,
Tokyo, Japan

I. Introduction 123
II. High-Voltage Electron Microscopy of Neuron and Glia Cells after Impregnation by the Golgi Method 124
III. High-Voltage Electron Microscopy of Biological Membranes after Selective Staining 127
A. The Golgi Apparatus 127
B. Other Biological Membranes 130
IV. Membranous Systems in Striated Muscles 131
A. Application of Selective Staining 131
B. The T-System in Skeletal Muscle 134
C. The T-System in Cardiac Muscle 141
V. Membranous Organelles in Neurons 142
References 143

I. Introduction

One method of three-dimensional analysis of cellular fine structure at the electron microscope level is to make serial thin sections and reconstruct certain structures by superimposition of their electron micrographs (see Rieder, Chapter 13 of this volume). It is often difficult to follow the structure from one section to the next, however, especially when it is delicate and complicated. In this respect, high-voltage electron microscopy of thick sections has the advantage of revealing the three-dimensional cellular fine structure within the range of the section thickness when one observes the electron micrographs of the stereo pair. At the same time, this technique has a disadvantage, since all the structures found within the section are clearly focused and are superimposed, obscuring structural detail and

Copyright © 1981 by Academic Press, Inc.
All rights of reproduction in any form reserved.
ISBN 0-12-564122-2

making analysis difficult. This drawback becomes more serious when the structures are more densely packed and smaller in size.

One way of overcoming this difficulty is to increase the contrast of certain structures within the cell selectively by various techniques and then observe them in the high-voltage electron microscope. Novikoff *et al.* (1971) and Favard *et al.* (1971), for example, applied this method to visualize the three-dimensional structure of the Golgi apparatus by increasing its contrast selectively with osmification or an enzyme cytochemical reaction. Similar studies have followed, and we too have applied this procedure to analyze the infoldings of renal epitheliocytes and the T-tubules of cardiac myocytes by introducing the electron-dense molecular tracer into the extracellular space (Yamada and Ishikawa, 1972). The literature up to 1974 relating to this subject has been reviewed by Glauert (1974). In this chapter we present some of our own data concerning the selective staining method combined with high-voltage electron microscopy to analyze the three-dimensional structure within dense tissue.

II. High-Voltage Electron Microscopy of Neuron and Glia Cells after Impregnation by the Golgi Method

The Golgi impregnation technique is an excellent method of revealing the three-dimensional morphology of neurons and glia cells; it has been used extensively by light microscopists to explore the organization of the central nervous system (see Ramón y Cajal, 1955). For unknown reasons, this technique impregnates a small percentage of cells that constitute the nervous tissues; when stained, a whole cell, including its soma and processes, is entirely impregnated. This characteristic is convenient for analysis of complicated dense tissues such as those found in the central nervous system.

In contrast to light microscopy, electron microscopy of Golgi impregnated tissue has the advantage of revealing both impregnated and impregnated cells at the same time in greater detail. Thus, we can easily analyze the synaptic connection between these particular cells. Actually, Stell (1967) was the first to show the connection between horizontal and visual cells in goldfish retinas by observing thin sections of impregnated, resin-embedded specimens. Since then, the technique has been much improved, especially as it became clear that impregnation was possible even after fixation by buffered glutaraldehyde (Boycott *et al.*, 1978). High-voltage electron microscopy of the Golgi preparation was first performed by Chan-Palay and Palay (1972a,b). They used the Golgi rapid method on aldehyde-perfused cerebellum and observed 0.25- to 5-μm sections in the 0.8- to 1-MeV electron microscope. They claimed that the study enables one to make

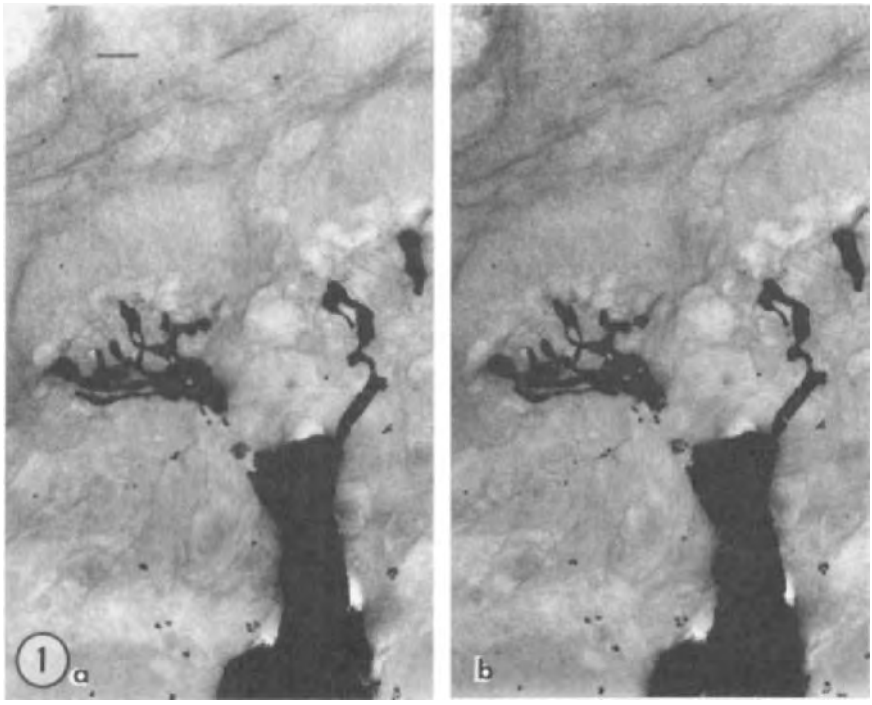


FIG. 1. Stereo pair of electron micrographs of snake retina (*Elaphe climacophora*) prepared by the rapid Golgi method. An impregnated bipolar cell sends out branched dendrites, which terminate under the horizontal cell terminals at the cone feet. Unstained 1.5-μm section. 1 MeV. Tilting angles $\pm 7°$. Magnification 5200×.

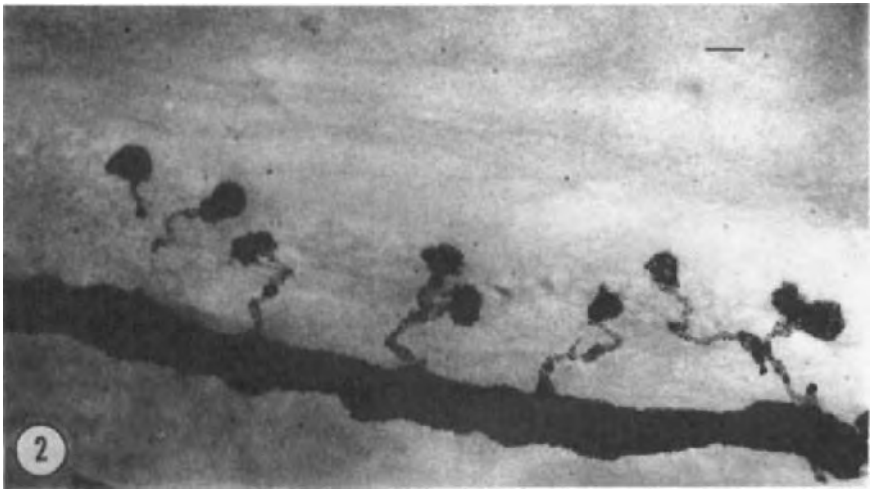


FIG. 2. Snake retina prepared by the rapid Golgi method. An impregnated horizontal cell axon sends out small side branches, each of which terminates by bulbous expansion in the cone foot. Unstained 1.5-μm section. 1 MeV. Magnification 4800×.

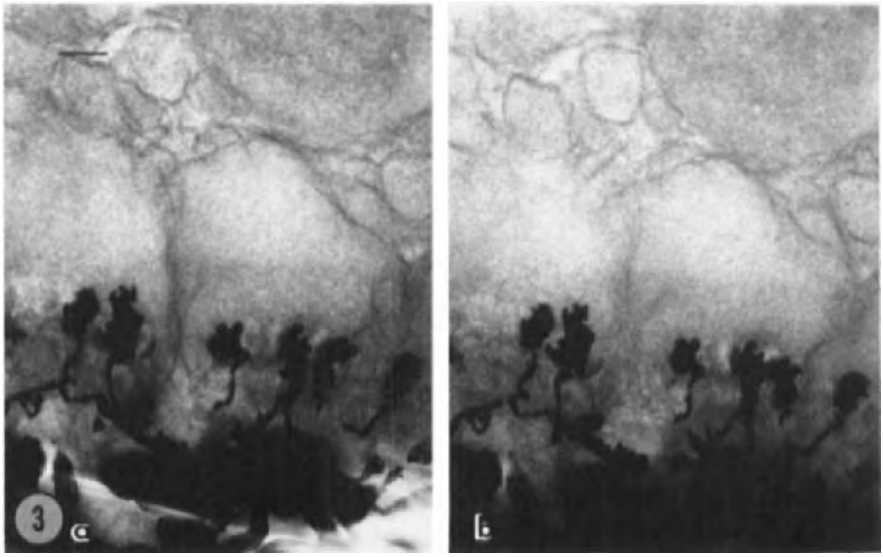


FIG. 3. Stereo pair of electron micrographs of snake retina prepared by the rapid Golgi method. Several horizontal cell processes synapse with the cone end-feet. Unstained 1.5-μm section. 1 MeV. Tilting angles $\pm 7°$. Magnification 5200×.

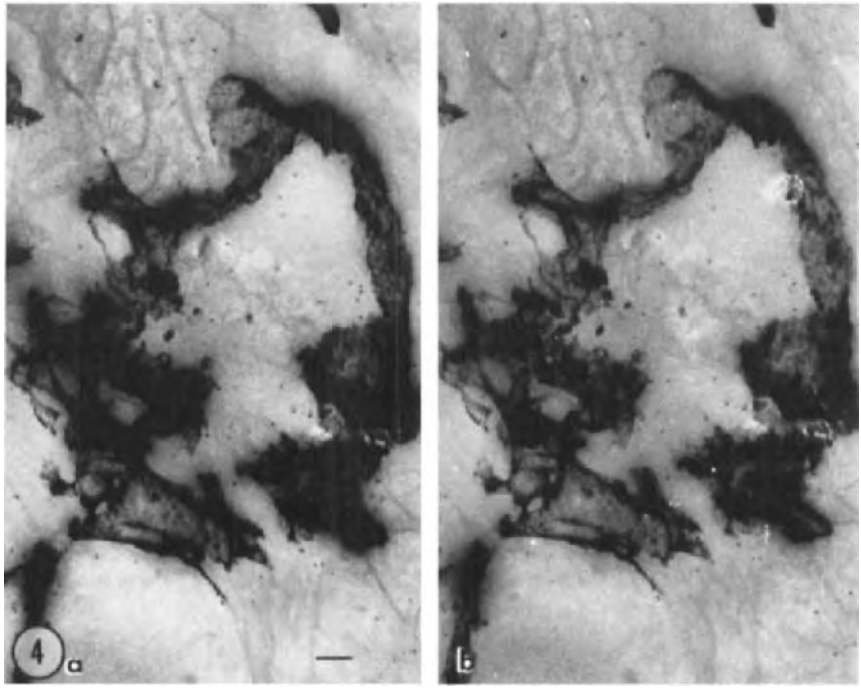


FIG. 4. Stereo pair of electron micrographs demonstrating a complicated sheet of cytoplasm of Müller cells in snake retina prepared by the rapid Golgi method. The cytoplasmic sheet covers the cone ending and fills the space between processes from bipolar and horizontal cells. Unstained 1.5-μm section. 1MeV. Tilting angles $\pm 7°$. Magnification 4800×.

an accurate estimate of the number of synapses effected by an axon along its course, information not obtainable either by light microscopy or by electron microscopy of thin sections. They also observed the protoplasmic astrocyte in the cerebellar cortex by high-voltage electron microscopy and demonstrated the veil-like processes or extremely thin sheets of cytoplasm expanding from the larger processes of the cells. Similar observations on the central nervous system and the retina were later reported by Hama *et al.* (1977, 1978) and by Hashimoto *et al.* (1977). High-voltage electron microscopy of the serial thick sections of the Golgi preparation is certainly a useful tool for analysing the cellular connection of neuronal elements, as was pointed out by Chan-Palay and Palay (1972b).

Several examples of retinal cells prepared by the rapid Golgi method and high-voltage electron microscopy are shown in Figs. 1–4.

III. High-Voltage Electron Microscopy of Biological Membranes after Selective Staining

A. The Golgi Apparatus

The fine structure of the Golgi apparatus was established by Dalton and Felix (1956) in the early phase of biological electron microscopy. It consists of vesicles, vacuoles, and stacks of flattened saccules or cisternae. However, the three-dimensional fine structure of the Golgi apparatus was not easily appreciated from the images of thin sections, although in the favorable tangential section through the Golgi stacks the fenestrated nature of the saccules could occasionally be observed. The use of selectively stained thick sections easily reveals this characteristic of the saccule. This technique was first introduced by Rambourg (1969), who stained thick sections (0.5–1 μm) with phosphotungstic acid and observed them in the 100-kV electron microscope. The following year (1970), Rambourg and Chrótien made similar observations on osmium-impregnated Golgi apparatus prepared according to the method of Friend and Murray (1965). Novikoff *et al.* (1971) made extensive observations of the Golgi apparatus utilizing 0.5- to 1-μm-thick sections stained by osmium impregnation or by lead precipitates representing enzyme activity of acid phosphatase, thiamine pyrophosphatase (TPPase), or nucleotide diphosphatase. In the same year, high-voltage electron microscopy was successfully applied to selectively stained Golgi apparatus by Carasso *et al.* (1971) and Favard *et al.* (1971). They used thick sections (up to 5 μm) and observed them in 1- to 2-MeV electron microscopes, after increasing contrast by osmium impregnation or acid phosphatase reaction.

In 1974, Rambourg *et al.* described the detailed three-dimensional structure of the Golgi apparatus in ganglion cells, Leydig cells, and Sertoli cells. Contrast

was achieved by the osmium impregnation technique, and sections were observed in the 1-MeV electron microscope. Favard and Carasso (1973) made a similar study on the epididymal and snail mucous gland cells.

As was first pointed out by Dalton and Felix (1956), the osmium treatment usually impregnates the outer or forming face of the Golgi apparatus. In other words, reduced osmium metal deposition is found in several of the outer saccules of Golgi lamellae. These saccules are revealed in the thick sections as an anastomosing network of highly irregular tubules, referred to as the "primary network" by Rambourg *et al.* (1974). On the other hand, acid phosphatase, TPPase, and nucleotide diphosphatase activities were exhibited as the deposition of lead on the inner aspect of the Golgi apparatus. Novikoff *et al.* (1971) found in the thick sections of ganglion cells that these saccules showing a TPPase-positive reaction formed a regular hexagonal network and were composed of the inner aspect of the Golgi apparatus, whereas acid phsophatase-positive saccules formed a less regular network with a flattened cisternal form and were located between the granular endoplasmic reticulum and the Golgi apparatus. Furthermore, the acid phosphatase-positive saccule was sometimes continuous with the tubular network and lysosomes; hence, Novikoff proposed the term GERL—the Golgi-associated ER (endoplasmic reticulum) from which the lysosomes arise.

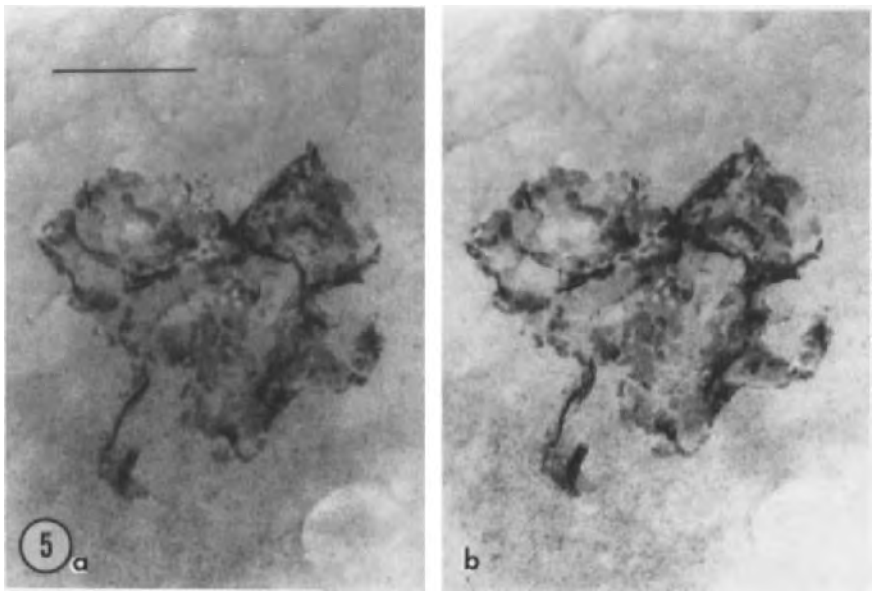


FIG. 5. Stereo pair of electron micrographs of a myelocyte in mouse bone marrow. Glutaraldehyde-fixed tissue was incubated in TPPase medium. The positive area appears as a tubular network and a cisternal sheet. Unstained 1.5-μm section. 1 MeV. Tilting angles $\pm 7°$. Magnification 19,000×.

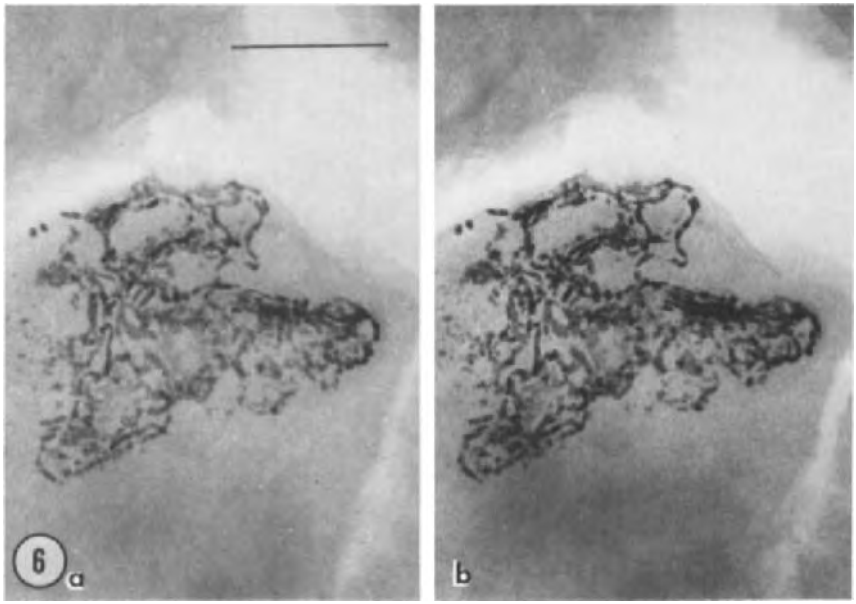


FIG. 6. Stereo pair of electron micrographs of myelocytes in mouse bone marrow incubated in TPPase medium. The TPPase-positive structure is seen as a tubular network, a portion of which is very close to the cell surface. Unstained 1.5-μm section. 1 MeV. Tilting angles $\pm 7°$. Magnification 21,000×.

However, acid phosphatase activity is also demonstrated in the several saccules of the inner Golgi stack. Therefore, it seems to be more reasonable to regard GERL as a portion of the Golgi apparatus (Mayahara *et al.*, 1978). In any case, the relationship between the OsO_4-impregnated portion and the enzyme-positive area has not been clarified.

Rambourg (1977) has demonstrated that the maturing face of the Golgi apparatus is heavily stained by the periodic acid–silver methenamine technique for glycoprotein. He further demonstrated that the whole Golgi apparatus could be stained by his double impregnation technique, using uranyl acetate followed by lead and copper. He observed that the apparatus consists of a central region composed of smaller tubules in a tight network, and a peripheral region composed of larger tubules in a wider meshwork.

In our experiment, mouse bone marrow was fixed with 3% glutaraldehyde in cacodylate buffer, then washed and incubated in the TPPase medium according to the method of Novikoff and Goldfisher (1961). Thick sections (1.5-3 μm) were cut, and unstained sections were observed in the high-voltage electron microscope (1 MeV).

As shown in Figs. 5 and 6, TPPase-positive tubules form a regular network,

and this network in turn forms a twisted and continuous sheet. In some areas, especially in Fig. 5, the flattened cisternae can be recognized. Here, the whole structure resembles a cylindrical vase.

B. Other Biological Membranes

To visualize the three-dimensional aspect of the intracellular compartment derived from the cell surface, Favard *et al.* (1971) used thorium dioxide, ingested by endocytosis. Yamada and Ishikawa (1972, 1976) introduced ruthenium red and horseradish peroxidase as a molecular tracer into the extracellular space and succeeded in demonstrating the three-dimensional architecture of T-tubules of cardiac myocytes, and lateral infoldings of a renal epitheliocyte (Fig. 7) in the high-voltage electron microscope.

The contrast in the ER can be increased by enzyme cytochemistry—for example, by glucose-6-phosphatase activity (Favard and Carasso, 1973). Also,

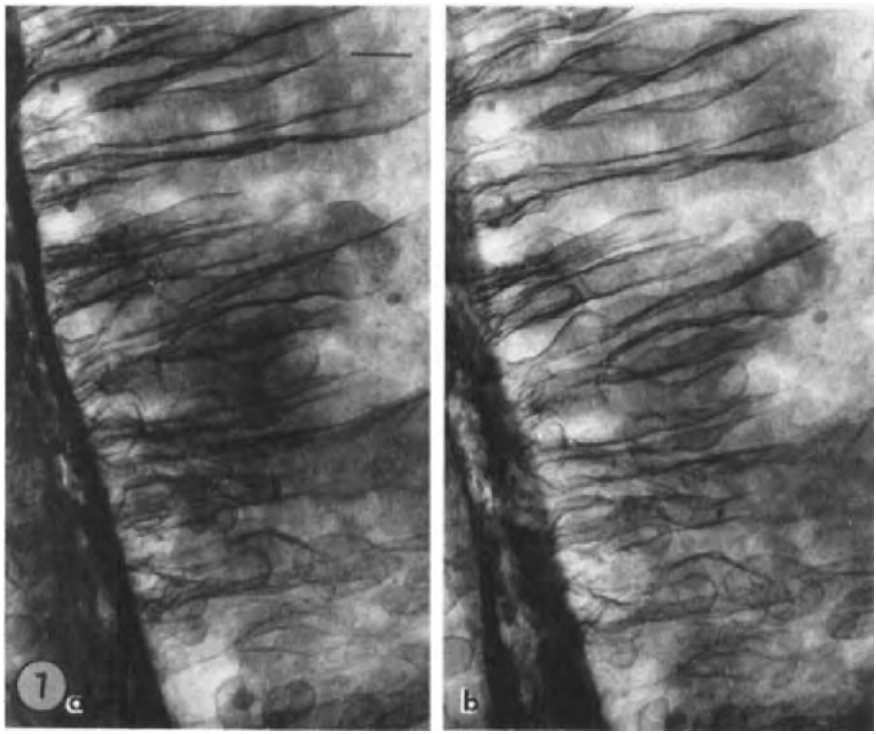


FIG. 7. Stereo pair of electron micrographs of a proximal tubule epitheliocyte of mouse kidney. The extracellular space was stained by ruthenium red, and the lateral infoldings of the cell are clearly demonstrated. Large mitochondria are seen along the infoldings. Unstained 3-μm section. 1 MeV. Tilting angle $\pm 10°$. Magnification 7800×.

mitochondria and the ER occasionally exhibit reactivity with OsO_4; their contrast can be increased by the osmium impregnation method similar to that used for the Golgi apparatus (Favard and Carasso, 1973), which, therefore, was utilized to reveal their arrangement in three dimensions. Thiéry and Rambourg (1976) reported a new staining technique for various cell organelles, which enables one to observe them in good contrast in the high-voltage electron microscope. Glutaraldehyde-fixed tissues were treated in uranyl acetate solution and post-stained in a double lead and copper citrate solution. Then the tissues were finally incubated in unbuffered OsO_4. By varying the pH of the uranyl acetate solution, selective impregnation of the Golgi apparatus, the ER, the cell surface, and the mitochondria was achieved.

Waugh and his co-workers (1974) reported a technique by which the sarcoplasmic reticulum is selectively and heavily stained. In their method, glutaraldehyde-fixed muscle was immersed in Tris buffer containing 3,3′-diaminobenzidine tetrahydrochloride (DAB) and hydrogen peroxide. The tissue was then post-fixed in a potassium ferrocyanide–osmium tetroxide mixture. Later, however, Forbes *et al.* (1977) found that the staining effect was produced by post-fixation in osmium–ferrocyanide solution after the tissue was fixed in an aldehyde solution containing calcium but lacking phosphate. They also found that the tissue fixed in the aldehyde solution containing phosphate or lacking calcium produced heavy staining of the extracellular space, including the T-tubule system. When applying this technique to other tissues, we noticed that the staining was not confined to the sarcoplasmic reticulum but occurred also in the ER of diverse cell types. The mechanism for tissue staining by the osmium–ferrocyanide mixture was proposed by White *et al.* (1979).

IV. Membranous Systems in Striated Muscles

A. Application of Selective Staining

Striated muscle cells contain two distinct interfibrillar membranous systems—the sarcoplasmic reticulum (SR) and the T-system. The SR is the specialized smooth ER that surrounds the myofibril. The T-system tubule extends transversely into the cell from its surface, and hence it is considered to be part of the sarcolemma. Both systems are believed to provide the morphological basis of excitation–contraction coupling. Thus, the three-dimensional distribution and the degree of development of these membranous systems seem to be closely related to the physiological properties such as the speed of contraction (Peachey, 1966).

High-voltage electron microscopy of thick sections combined with selective

staining has been successfully applied to the three-dimensional visualization of the SR in skeletal muscles (Bailey and Peachey, 1975a) and in cardiac muscles (Waugh *et al.*, 1974; Sommer and Waugh, 1976), and of the T-system in skeletal muscles (Bailey and Peachey, 1975b; Eisenberg and Peachey, 1975; Ishikawa and Tsukita, 1977) and in cardiac muscles (Yamada and Ishikawa, 1976). These studies prove that selective staining is the most helpful approach to the three-dimensional analysis of the T-system and SR, since this method can avoid the superimposed image of the myofibril, which would otherwise obscure the structure of interest.

The principle of selective staining for the T-system is to fill or stain the extracellular space with molecular tracers. Selective stains or tracers successfully used are horseradish peroxidase, lanthanum, ruthenium red, and diaminobenzidine. Since the result is not always uniform within the tissue samples or reproducible among preparations, one should choose the method that produces the desired result.

1. Horseradish Peroxidase

Fresh muscle tissues are soaked in horseradish peroxidase dissolved in physiological saline (Eisenberg and Eisenberg, 1968). For small animals, this solution is injected twice, each time with the same amount, at 20-minute intervals. Five minutes after the second injections, the animal is sacrificed (Yamada and Ishikawa, 1976). Muscle tissues are fixed in 2% paraformaldehyde-2.5% glutaraldehyde in 0.1 *M* sodium cacodylate buffer (pH 7.2) for 2 hours. Tissues of several fascicles are rinsed in the Tris-HCl buffer (pH 7.8) and incubated for cytochemistry according to the method described by Graham and Karnovsky (1966). Incubation continues for 30-60 minutes, which is long enough to get a substantial quantity of the reaction product. Specimens are then post-fixed in 1% OsO_4 in cacodylate buffer for 1 hour.

2. Lanthanum

Selective staining of the T-system with lanthanum nitrate is carried out basically according to the method of Revel and Karnovsky (1967). Lanthanum nitrate is added to the fixatives, aldehyde and OsO_4. The modification* we used is as follows. Muscles are fixed by perfusion or immersion with 2% formaldehyde-2.5% glutaraldehyde in 0.1 *M* sodium cacodylate buffer (pH 7.2) for 20-30 minutes, and then rinsed in the same buffer for more than 3 hours. Small pieces

*This modification was kindly suggested by Dr. K. Oguchi, Shinshu University.

of tissue are post-fixed for 2 hours by constant agitation with 1.3% OsO_4 in *s*-collidine buffer, pH 7.3, to which lanthanum nitrate is added to make 3% immediately before use. For agitation, we use a small air pump to which sample vials are attached.

Lanthanum was also used to fill the SR in mouse diaphragms in combination with Alcian blue and potassium ferrocyanide (Waugh *et al.*, 1973).

3. Ruthenium Red

Ruthenium red also can stain or fill the T-system, as was first demonstrated by Luft (1971). Muscle tissues are fixed by perfusion or immersion with 3% glutaraldehyde in 0.1 *M* sodium cacodylate buffer (ph 7.4) containing 500 ppm of ruthenium red. Tissues are post-fixed for 2 hours with 1% OsO_4, again containing ruthenium red.

4. Diaminobenzidine-Ferrocyanide

This method was originally developed by Waugh *et al.* (1974) to stain the SR in the cardiac muscles, and later it was found to be applicable to the SR in skeletal muscles (Bailey and Peachey, 1975a; Forbes *et al.*, 1977). With minor modifications, the method can be used to selectively stain the T-system in skeletal and cardiac muscles (Ishikawa and Tsukita, 1977), and also to stain membranous organelles such as the smooth ER and mitochondria in neurons (Tsukita and Ishikawa, 1976), and the SR in smooth muscles (Forbes *et al.*, 1977).

In our modification (Tsukita and Ishikawa, 1976), muscle tissues are fixed by perfusion or immersion with 2% formaldehyde-2.5% glutaraldehyde in 0.1 *M* sodium cacodylate buffer (pH 7.3) for 2 hours at room temperature and rinsed in 10% sucrose in the same buffer overnight at 4°C. After a brief wash with 0.05 *M* Tris-HCl buffer (pH 7.6,), small pieces of the tissue are incubated with 0.05% 3,3'-diaminobenzidine tetrachloride and 0.01% H_2O_2 in Tris-HCl buffer (adjusted to a final pH 7.6) for 2 hours at room temperature, and then fixed again in the same aldehyde fixative overnight at 4°C. The post-fixation is performed in 2% OsO_4 in cacodylate buffer (pH 7.3) containing 0.8% potassium ferrocyanide for 2 hours at 4°C.

After selective staining and fixation, tissues are dehydrated in ethanol and embedded in Epon. Thick sections of 0.5–3 μm are cut on ultramicrotome with glass knives and, without post-staining, are examined in a high-voltage electron microscope. Pairs of electron micrographs of the same field are taken by tilting the specimen stage at $\pm 8°$. The stereo pairs of printed micrographs are viewed under a stereoscope.

B. The T-System in Skeletal Muscle

The T-system in the mouse diaphragm was studied by use of the DAB-ferrocyanide method (Ishikawa and Tsukita, 1977). By the modified method, the T-system was consistently stained without any staining of the SR or mitochondria. It is interesting to note that, in the modification by Forbes *et al.* (1977), the SR staining in skeletal muscle usually is inseparable from the T-system filling, although filling of the T-system may occur in the absence of SR staining (see also Forbes and Sperelakis, 1977; Sybers and Gann, 1975).

High-voltage electron micrographs of 1- to 3-μm-thick sections provided information on the overall distribution and extent of development of the T-system (Fig. 8). Furthermore, stereo pairs of the printed micrographs gave clear-cut three-dimensional images of the T-system better in longitudinal sections than in transverse sections of muscle cells (Fig. 9). In mature muscles, the T-tubules were seen running transversely around the myofibrils at the level of the A-I junction to form planes of continuous networks. At the cell surface, the T-tubules

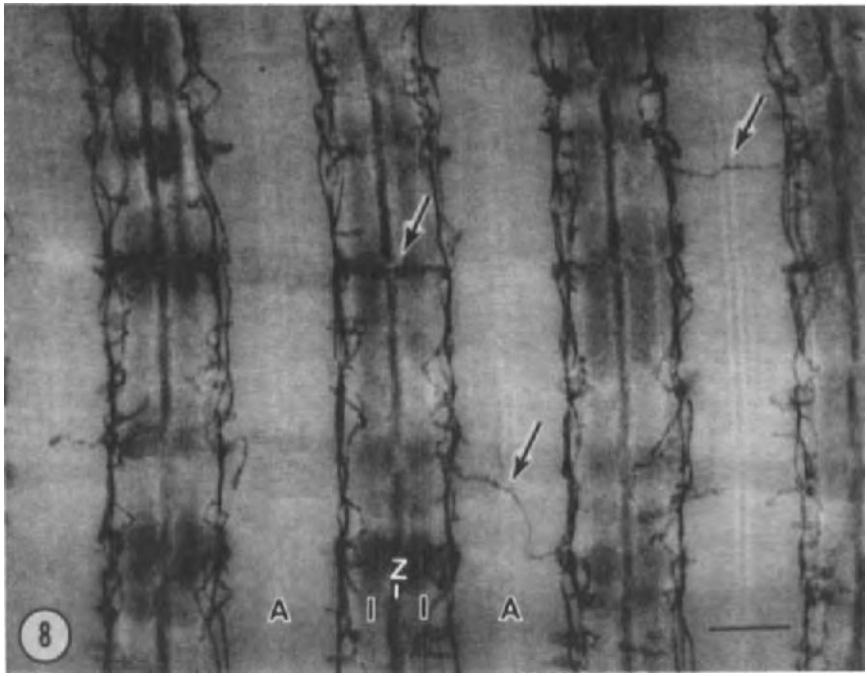


FIG. 8. High-voltage electron micrograph of part of a longitudinally sectioned muscle fiber from the adult mouse diaphragm. Note the regular pattern of the T-system distribution at the level of the A-I junction. Longitudinal T-tubules connecting adjacent planes of the T-system network are occasionally seen (arrows). A, A band; I, I band; Z, Z disk. Diaminobenzidine-ferrocyanide staining. Section 2 μm thick. Magnification 11,000×.

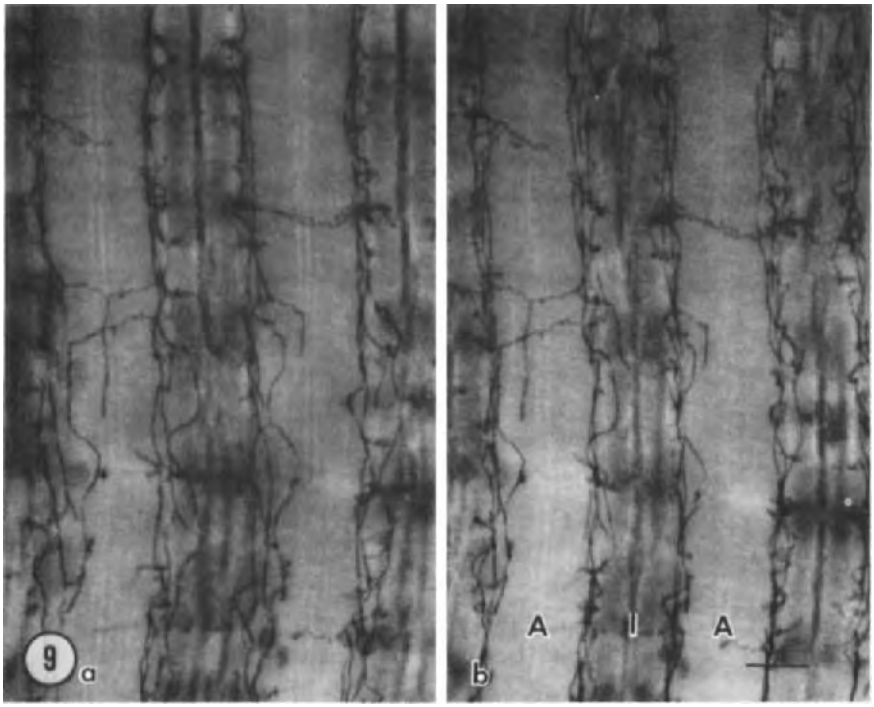


FIG. 9. Stereo pair of high-voltage electron micrographs of a longitudinally sectioned muscle fiber from the adult mouse diaphragm. The three-dimensional image of T-system tubules can be clearly obtained from the stereo pair, which were taken at tilting angles of ±8°. A, A band; I, I band. Diaminobenzidine-ferrocyanide staining. Section 2 μm thick. Magnification 8600 ×.

were connected with the sarcolemma via a series of caveolar units and were not as regularly spaced as was generally expected. The greater part of the T-tubule was seen as a flattened tubule reflecting the triadic portion. There were longitudinal T-tubules connecting two adjacent planes of the networks, which occurred more often at the I-band level than at the A-band level (Figs. 8 and 9). The longitudinal T-tubules were conspicuous between two adjacent myofibrils where their cross-striations were shifted or dislocated from each other. The T-tubules often traversed the gaps, suggesting that these dislocations occur naturally, and are not due solely to artifacts that appear during fixation. Such dislocations seen in longitudinal sections were shown to reflect the helicoidal arrangement of the sarcomeres from reconstruction of thick serial transverse sections of frog sartorius muscle cells stained for the T-system with horseradish peroxidase (Peachey, 1975; Peachey and Eisenberg, 1978). The T-tubules occasionally extend short blind-ended tubules along their course. Some differences in the form and distribution of the T-system were observed between red and white muscle

fibers (cells) in this muscle. In red fibers, the T-system was less regularly distributed and was twisted in its course, with more longitudinal T-tubules than are found in white fibers. The course of the T-tubules was severely disturbed by the mitochondrial aggregates and lipid droplets.

The observations on the T-system in DAB-ferrocyanide preparations were consistent with those made after lanthanum staining.

In postnatal development of mouse diaphragms, the T-system was less in quantity and irregular in distribution. The T-system in newborn muscles had not yet formed any particular planes of networks, frequently taking longitudinal courses (Fig. 10a). Nevertheless, flattened cisternae were seen along the T-tubules, preferentially at the level of the A-I junction reflecting the portions of the triadic structure. The T-tubules followed a twisted course, showing a beaded configuration along the tubule, except in the area of flattened cisternae. Furthermore, sections 2-3 μm thick clearly showed that the T-tubules tended to align at the level of the A-I junction (Fig. 10b). As development proceeded, the T-system became more regularly arranged in register with respect to the cross-striations of the myofibril.

It is interesting to compare these findings with Veratti's light microscopic observations (Veratti, 1961). His reticular structure indeed corresponds to the T-system as demonstrated by high-voltage electron microscopy. Clearly, his metal impregnation can be included in selective staining for the T-system. It is surprising to see how precisely the distribution pattern of Veratti's reticular structure in mouse muscles coincides with that of the T-system that we observed.

In our experience, to stain the T-system in chick skeletal muscles, DAB-ferrocyanide was less effective than lanthanum nitrate, for unknown reasons. Therefore, we used lanthanum staining to study the development of the T-system in chick skeletal muscles with two different speeds of contraction: anterior latissimus dorsi (ALD) as a slow muscle, and posterior latissimus dorsi (PLD) as a fast muscle (Ishikawa *et al.*, 1977).

In 17-day chick embryos, ALD revealed a quite dense distribution of the T-system in thick sections, whereas in thin sections only scattered profiles of T-tubules were seen (Fig. 11). The T-tubules were very irregular in distribution and followed a predominantly longitudinal course to the cell axis. There was no definite position of T-tubule openings on the cell surface with respect to the level of myofibril cross-striations. Packed networks of the T-tubules were occasionally found (Fig. 12). The T-system in PLD was far less developed than that in ALD, with otherwise similar patterns of distribution. This delayed proliferation of the T-system seems to correlate with the delayed development in the fiber diameter and the myofibril in PLD. The T-system in PLD developed progressively until the time of hatching. At hatching, ALD and PLD showed no appreciable difference in quantity and distribution of the T-system. Although most of the

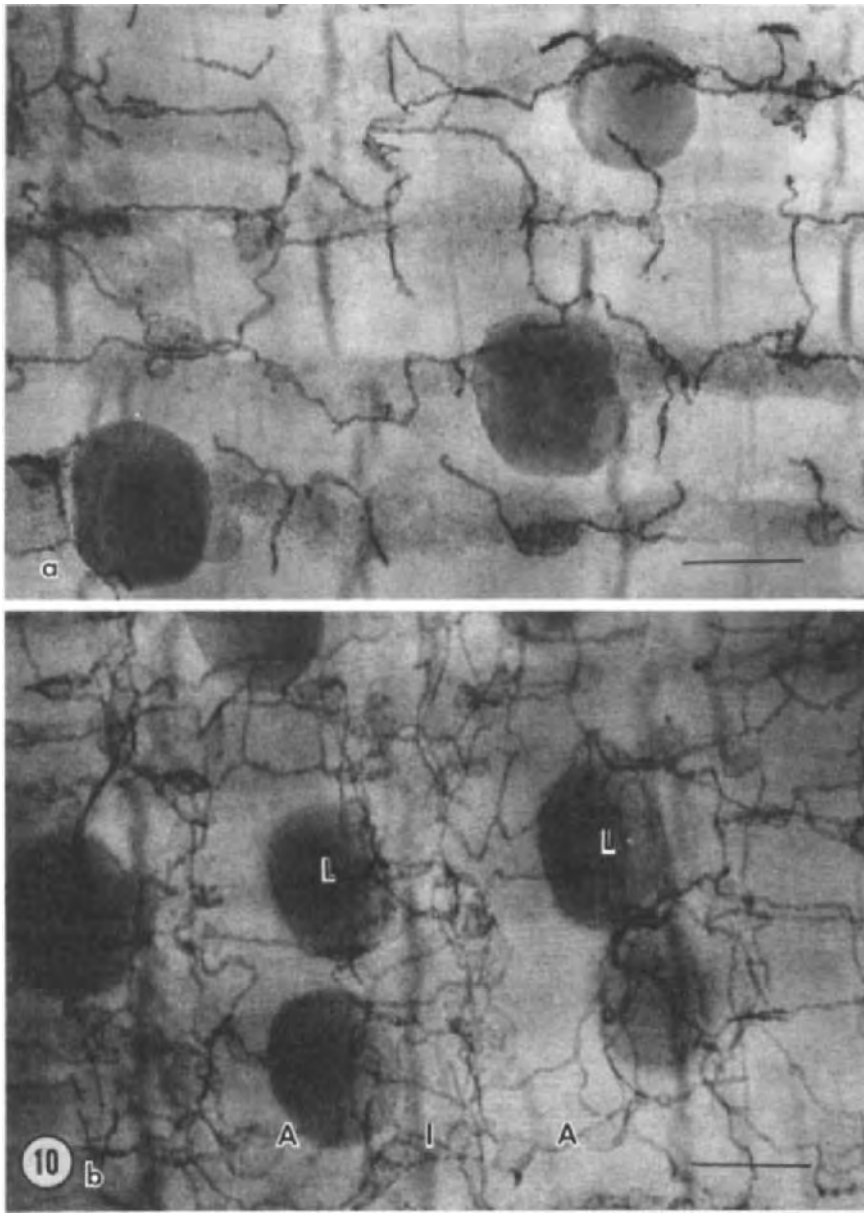
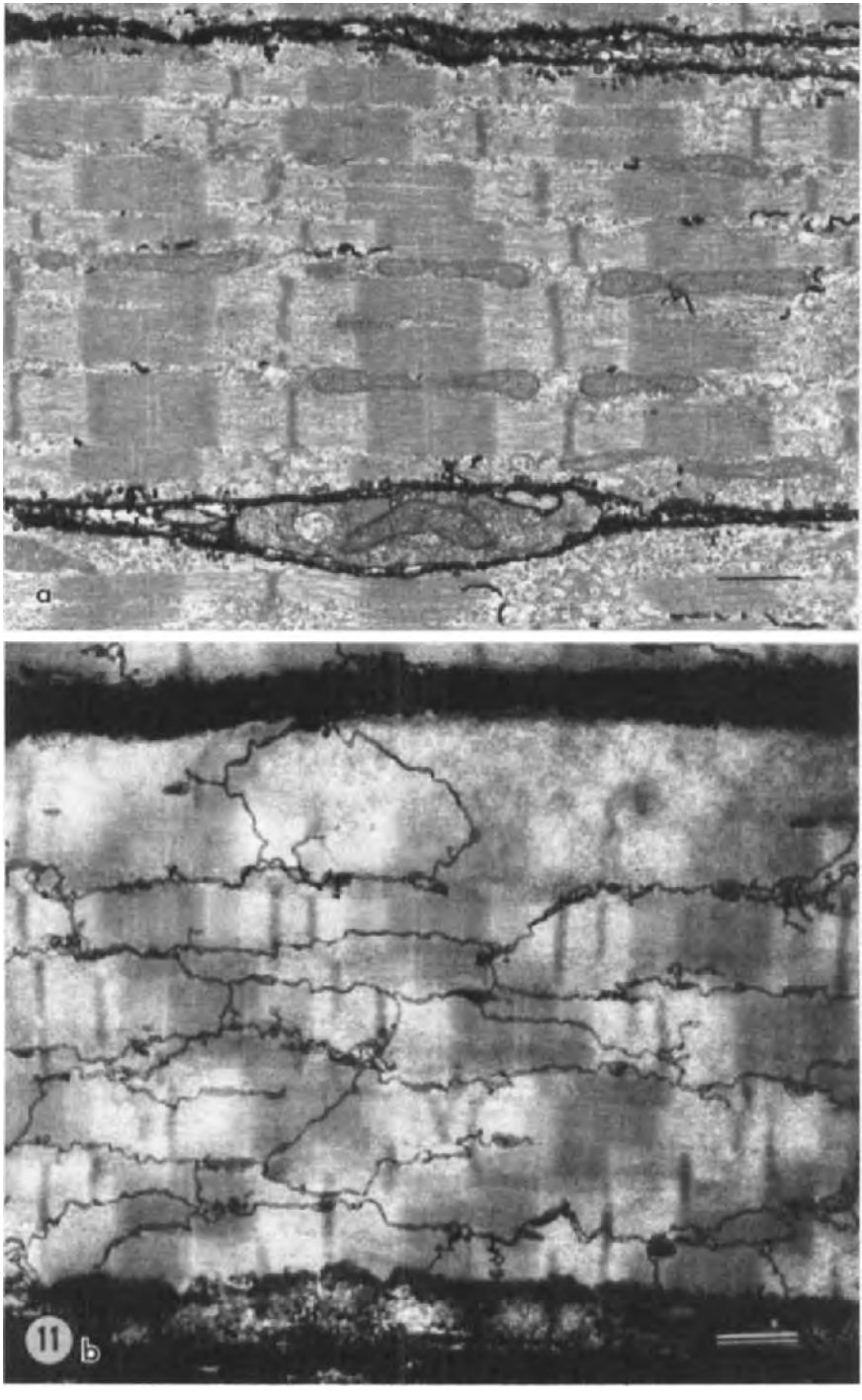


FIG. 10. High-voltage electron micrographs of longitudinally sectioned muscle fibers from a newborn mouse diaphragm. (a) Section 1 μm thick (b) Section 3 μm thick. In the 1-μm-thick section the T-system is irregularly distributed, with less quantity. In the 3-μm-thick section, however, the T-tubules tend to be arranged at the level of the A-I junction. A, A band; I, I band; L, lipid droplet. Diaminobenzidine-ferrocyanide staining. Magnification 16,000×.


a
11
b

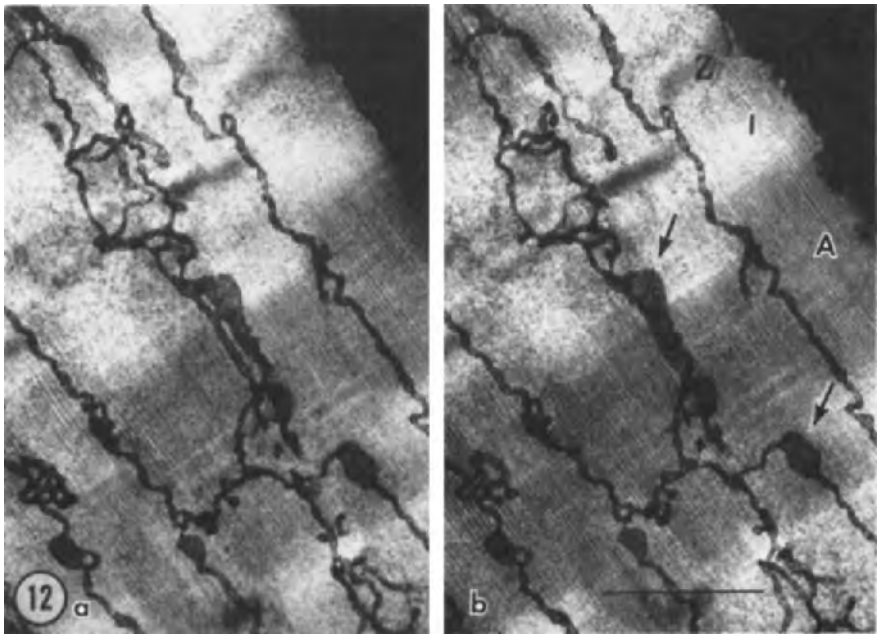


FIG. 12. Stereo pair of high-voltage electron micrographs of a longitudinally sectioned muscle fiber from the ALD of a 17-day chick embryo. The T-system predominantly takes a longitudinal and twisted course. Flattened cisternae are formed along the T-tubules (arrows). Packed networks of the T-tubules are occasionally seen. A, A band; I, I band; Z, Z disk. Lanthanum staining. Section 1 μm thick. Tilting angles $\pm 8°$. Magnification 22,000×.

tubules were still longitudinally oriented, some transverse tubules were seen to extend from longitudinal tubules at the level of the A–I junction. The T-tubules in both muscles followed a twisted course, with an occasional occurrence of flattened cisternae (see Figs. 12 and 13). At 1–2 weeks after hatching, a dramatic difference appeared in the distribution and course of the T-system between ALD and PLD. In ALD the T-system never attained a regular distribution (Fig. 13a), whereas in PLD the T-system progressively developed in quantity and regularity of distribution, taking its course transversely at the level of the A–I junction (Fig. 13b).

FIG. 11. Longitudinally sectioned muscle fibers from ALD muscle of a 17-day chick embryo. (a) *Thin section, 100-KV electron microscope.* (b) *Section 1 μm thick, 1-MeV electron microscope.* In the thick section the T-system is densely distributed, with a predominantly longitudinal course, whereas in the thin section only scattered profiles of the T-tubules are seen. Note the sites of the T-tubule openings into the extracellular space in the thick section. Lanthanum staining. Magnification 11,000×.

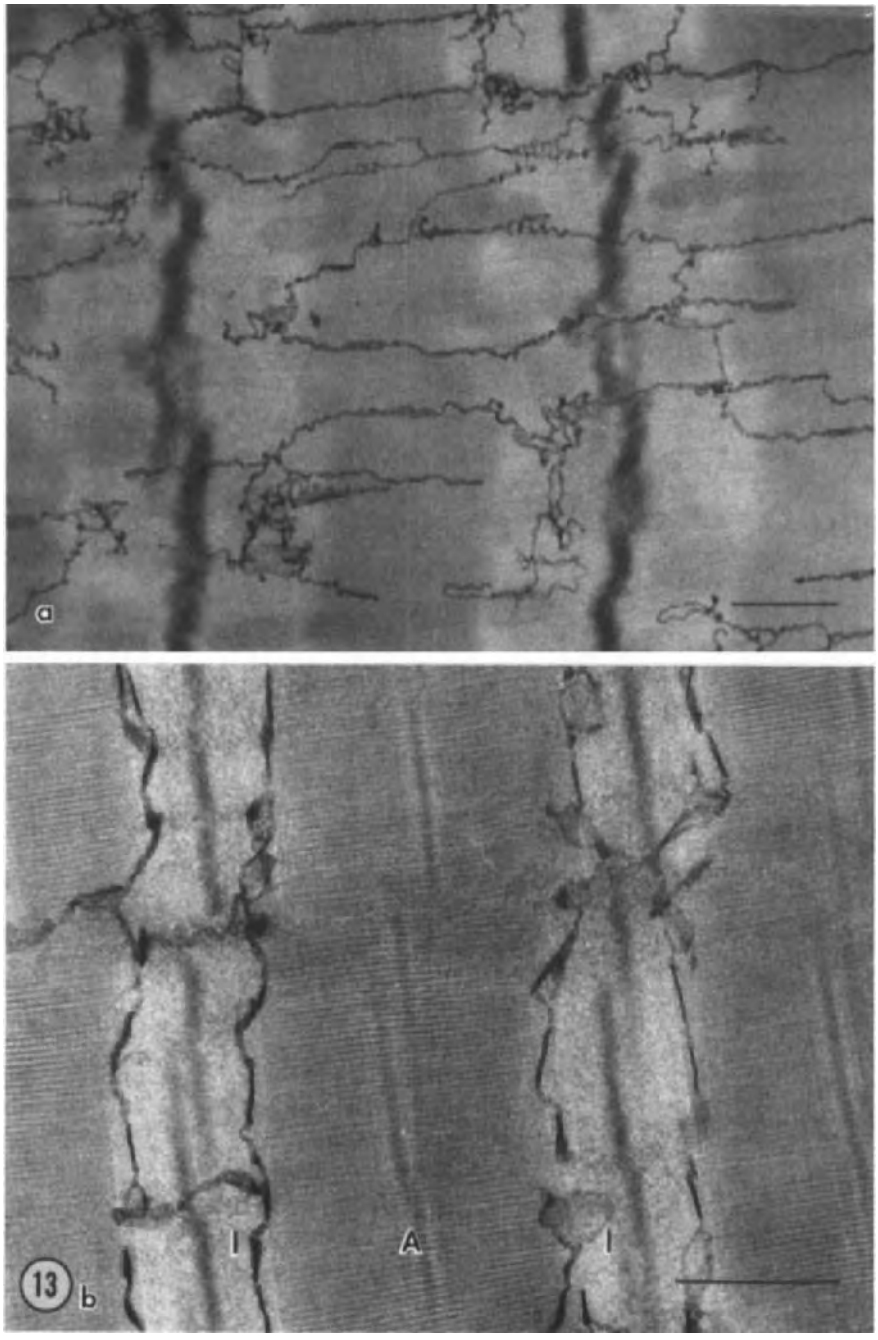


FIG. 13. High-voltage electron micrographs of longitudinally sectioned muscle fibers from two different chicken muscles. (a) ALD muscle from a two-month-old chicken. (b) PLD muscle from an adult chicken. In ALD the T-system is not regularly arranged (a), whereas in PLD it shows a regular distribution, taking a transverse course at the level of the A-I junction (b). A, A band; I, I band. Lanthanum staining. Section 1 μm thick. (a) Magnification 14,000×; (b) Magnification 22,000×.

C. The T-System in Cardiac Muscle

The T-system in the mouse cardiac muscle was selectively stained by either horseradish peroxidase cytochemistry (Yamada and Ishikawa, 1976) or the DAB-ferrocyanide method (Ishikawa and Tsukita, 1977). High-voltage electron microscopy of thick sections of such stained materials yielded not only information on the overall distribution and extent of development, but also three-dimensional images of the T-system. The results were identical in the two different staining preparations. The T-system in mouse cardiac (ventricular) cells was usually seen as larger tubules than in skeletal muscle cells. The T-tubules ran preferentially at the level of the Z disk, where they formed planes of loose networks (Fig. 14). However, the cardiac T-systems of the mouse do not possess such a uniform size along their entire length nor regular positioning at the level of the Z disk as has been generally believed. The T-tubules often formed locally dilated cisternae as well as narrow beaded tubules similar in size to those of skeletal muscles. Such an irregularity in size and course of the mature cardiac T-system can be explained by the mode of T-system formation. It is proposed that the T-tubules are formed in postnatal development by sarcolemmal invagina-

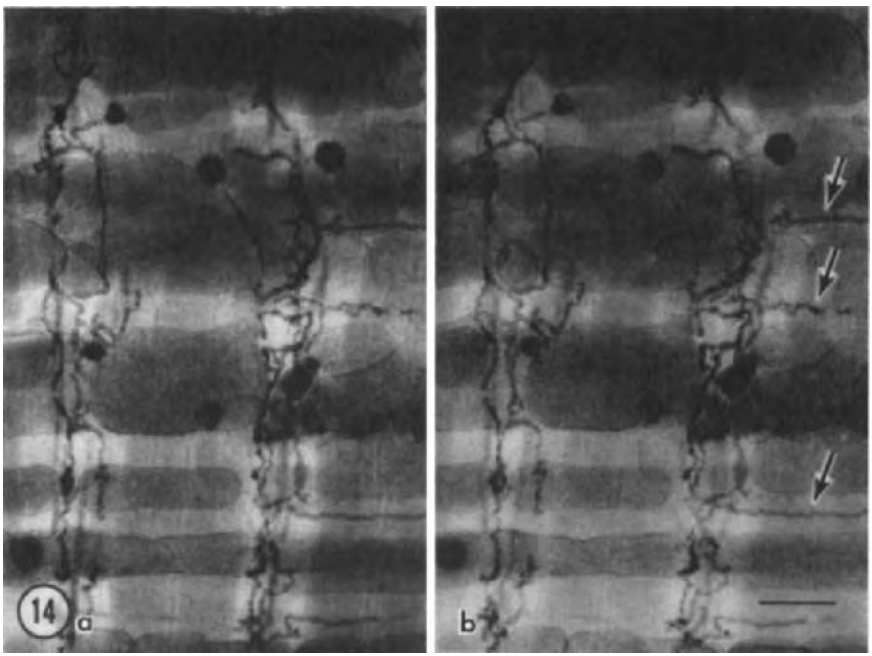


FIG. 14. Stereo pair of high-voltage electron micrographs of a longitudinally sectioned cardiac muscle cell from an adult mouse. The T-system is seen running transversely at the level of the Z disk with frequent occurrence of longitudinal T-tubules (arrows). Narrow beaded segments are formed along the T-tubules. Diaminobenzidine-ferrocyanide staining. Section 1 μm thick. Tilting angles $\pm 8°$. Magnification 10,000×.

tion as narrow tubules (Ishikawa and Yamada, 1975) in a manner basically similar to the formation of the T-system in skeletal muscles (Ezerman and Ishikawa, 1967; Ishikawa, 1968). It may be possible that some of the T-tubules, if they are small in size and not accompanied by the basement membrane with irregular courses, are overlooked or even misinterpreted as the part of the SR. Our three-dimensional analysis with thick sections confirms the previous thin-section observations that the T-system has branches and takes a connecting longitudinal course between adjacent, transversely oriented tubules (Forssmann and Girardier, 1966; Fawcett and McNutt, 1969; Sperelakis and Rubis, 1971). The T-system network varies in the degree of its packing and can form complex labyrinths (Forbes and Sperelakis, 1973, 1977; Ishikawa and Yamada, 1975).

V. Membranous Organelles in Neurons

An exact understanding of the three-dimensional distribution of the smooth endoplasmic reticulum (SER) in axons is needed to elucidate the involvement of SER in axonal transport. Selective staining with DAB-ferrocyanide for SER was used to visualize its distribution within 0.5- to 1-μm-thick sections of mouse and frog peripheral nerves in high-voltage electron microscopy (Tsukita and Ishikawa, 1976). A similar approach was made in a study of the axonal SER by using a metal impregnation (Droz *et al.*, 1975). In our preparations, SER and mitochondria in myelinated axons of mouse sciatic and phrenic nerves were stained in good contrast, whereas fibrous elements such as microtubules and neurofilaments were not clearly imaged (Tsukita and Ishikawa, 1976). The rough-surfaced ER and Golgi membranes in nerve cell bodies and the synaptic vesicles and presynaptic membranes in terminal boutons were also stained.

In thin sections, the SER in axons appeared as scattered pieces of slender tubules, often seen running longitudinally through the axons, with occasional branching. In thick sections, however, the SER was by no means small in amount. Furthermore, stereo pairs of high-voltage electron micrographs of thick sections revealed that almost all the SER elements were anastomosed with each other to form a continuous three-dimensional network (Fig. 15). The network was polarized; the SER tubules tended to run parallel to the axon. Thus, the three-dimensional organization of the SER was better visualized in the longitudinal section of the axons. In the motor axons, the SER showed more developed and delicate networks near their terminal boutons. At the node of Ranvier, the SER tubules were closely packed together into several parallel bundles and appeared to converge from the internodal part of the node, where the axon was considerably reduced in diameter. There were few isolated SER fragments and vesicles in the internodal part, whereas free vesicles were more frequently ob-

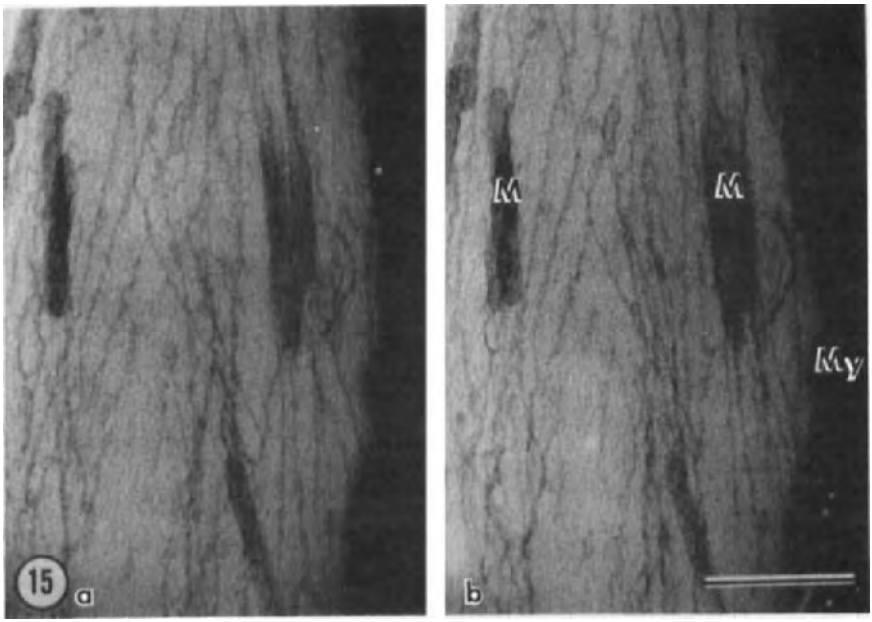


FIG. 15. Stereo pair of high-voltage electron micrographs of a longitudinally sectioned myelinated axon (internodal region) from the frog sciatic nerve. The SER is seen as a continuous network of longitudinally running, narrow tubules. M, mitochondria, My, myelinated sheath. Diaminobenzidine-ferrocyanide staining. Section 1 μm thick. Tilting angles $\pm 8°$. Magnification 20,000×.

served at the node. In an experimental blockage of axonal transport, the membranous organelles were shown to accumulate dramatically in thick, selectively stained sections (Tsukita and Ishikawa, 1980).

Similar selective staining for SER was achieved with potassium oxalate (H. Ishikawa and S. Tsukita, unpublished data). Nerves were fixed with 2.5% glutaraldehyde in sodium cacodylate buffer (pH 7.4) followed by 1% OsO_4 containing potassium oxalate in both fixatives according to the method of Popescu *et al.* (1974).

REFERENCES

Bailey, C. H., and Peachey, L. D. (1975a). *Proc. 33rd Annu. Meet. Electron Microsc. Soc. Am.* pp. 552-553.

Bailey, C. H., and Peachey, L. D. (1975b). *Proc. 33rd Annu. Meet. Electron Microsc. Soc. Am.* pp. 554-555.

Boycott, B. B., Peichl, L., and Wässle, H. (1978). *Proc. R. Soc. London, B Ser.* **203,** 225-245.

Carasso, N., Ovtracht, L., and Favard, P. (1971). *C. R. Hebd. Seances Acad. Sci., Ser. D* **273,** 876-879.

Carasso, N., Favard, P., Mentré, P., and Poux, N. (1974). *Proc. Int. Conf. HVEM, 3rd 1974* pp. 414-418.
Chan-Palay, V., and Palay, S. L. (1972a). *Z. Anat. Entwicklungsgesch.* **137,** 125-152.
Chan-Palay, V., and Palay, S. L. (1972b). *Z. Anat. Entwicklungsgesch.* **138,** 1-19.
Dalton, A. J. and Felix, M. D. (1956). *J. Biophys. Biochem. Cytol.* **2,** Suppl., 79-84.
Droz, B., Rambourg, A., and Koenig, H. L. (1975). *Brain Res.* **93,** 1-13.
Eisenberg, B. R., and Eisenberg, R. S. (1968). *J. Cell Biol.* **39,** 451-467.
Eisenberg, B. R., and Peachey, L. D. (1975). *Proc. 33rd Annu. Meet. Electron Microsc. Soc. Am.* pp. 550-551.
Ezerman, E. B., and Ishikawa, H. (1967). *J. Cell Biol.* **35,** 405-420.
Favard, P., and Carasso, N. (1973). *J. Microsc. (Oxford)* **97,** 59-81.
Favard, P., Ovtracht, L., and Carasso, N. (1971). *J. Microsc. (Paris)* **12,** 301-316.
Fawcett, D. W., and McNutt, N. S. (1969). *J. Cell Biol.* **42,** 1-45.
Forbes, M. S., and Sperelakis, N. (1973). *J. Cell Biol.* **56,** 865-869.
Forbes, M. S., and Sperelakis, N. (1977). *J. Ultrastruct. Res.* **58,** 50-65.
Forbes, M. S., Plantholt, B. A., and Sperelakis, N. (1977). *J. Ultrastruct. Res.* **60,** 306-327.
Forsmann, W. G., and Girrardier, L. (1966). *Z. Zellforsch. Mikrosk. Anat.* **72,** 249-275.
Friend, D. S., and Murray, M. J. (1965). *Am. J. Anat.* **117,** 135-150.
Glauert, A. M. (1974). *J. Cell Biol.* **63,** 717-748.
Graham, R. C., and Karnovsky, M. J. (1966). *J. Histochem. Cytochem.* **14,** 291-302.
Hama, K., Hirosawa, K., and Kosaka, T. (1977). *Proc. Int. Conf. HVEM, Proc. 1977,* pp. 333-338.
Hama, K., Mizukawa, A., and Kosaka, T. (1978). *Sens. Process* **2,** 296-299.
Hashimoto, P. H., Gotow, T., Tada, K., and Shimizu, N. (1977). *Proc. Int. Conf. HVEM, 5th, 1977* pp. 355-358.
Ishikawa, H. (1968). *J. Cell Biol.* **38,** 51-55.
Ishikawa, H., and Tsukita, S. (1977). *Proc. Int. Conf. HVEM, Proc. 1977* pp. 359-362.
Ishikawa, H., and Yamada, E. (1975). *In* "Developmental and Physiological Correlates of Cardiac Muscle" (M. Lieberman and T. Sano, eds.), pp. 21-35. Raven, New York.
Ishikawa, H., Tsukita, S., and Ueno, H. (1977). *Proc. Annu. Meet. Muscular Dystrophy Res. Group* pp. 18-19.
Luft, J. H. (1971). *Anat. Rec.* **171,** 369-416.
Mayahara, H., Ishikawa, T., Ogawa, K., and Chang, J. P. (1978). *Acta Histochem. Cytochem.* **11,** 239-251.
Novikoff, A., and Goldfisher, S. (1961) *Proc. Natl. Acad. Sci. U.S.A.* **47,** 802.
Novikoff, P. M., Novikoff, A. B., Quintana, N., and Hauw, J.-J. (1971). *J. Cell Biol.* **50,** 859-886.
Peachey, L. D. (1966). *Ann. N. Y. Acad. Sci.* **137,** 1025-1037.
Peachey, L. D. (1975). *In* "The Basic Neuroscience" (D. W. Dower, ed.), pp. 81-89. Raven, New York.
Peachey, L. D., and Eisenberg, B. R. (1978). *Biophys. J.* **22,** 145-154.
Popescu, L. M., Diculescu, I., Zelck, V., and Ionescu, N. (1974). *Cell Tissue Res.* **154,** 357-378.
Rambourg, A. (1969). *C.R. Hebd. Seances Acad. Sci., Ser. D* **269,** 2125-2127.
Rambourg, A. (1977). *Proc. Int. Conf. HVEM, 5th, 1977* pp. 327-331.
Rambourg, A., and Chrétien, M. (1970). *C.R. Hebd. Seances Acad. Sci., Ser. D* **270,** 981-983.
Rambourg, A., Clermont, Y., and Marraud, A. (1974). *Am. J. Anat.* **140,** 27-46.
Ramón y Cajal, S. (1955). "Histologie du système nerveux de l'homme et des vertébrés." Instituto Ramón y Cajal, Madrid.
Revel, J. P., and Karnovsky, M. J. (1967). *J. Cell Biol.* **33,** C7-C12.
Sommer, J. R., and Waugh, R. A. (1976). *Am. J. Pathol.* **82,** 192-232.
Sperelakis, N., and Rubio, K. (1971). *J. Mol. Cell. Cardiol.* **2,** 211-220.

Stell, W. K. (1967). *Am. J. Anat.* **121,** 401-424.

Sybers, H. D., and Gann, M. K. (1975). *Proc. 33rd Annu. Meet. Electron Microsc. Soc. Am.* pp. 359-360.

Thiéry, G. (1973). *J. Microsc. (Paris)* **17,** 101a.

Thiéry, G., and Rambourg, A. (1976). *J. Microsc. Biol. Cell.* **26,** 103-106.

Tsukita, S., and Ishikawa, H. (1976). *J. Electron Microsc.* **25,** 141-149.

Tsukita, S., and Ishikawa, H. (1980). *J. Cell Biol.* **84,** 513-530.

Veratti, E. (1961). *J. Biophys. Biochem. Cytol.* **10,** Suppl., 1-59.

Waugh, R. A., Spray, T. L., and Sommer, J. R. (1973). *J. Cell Biol.* **59,** 254-260.

Waugh, R. A., Sommer, J. R., and Peachey, L. D. (1974). *Circulation* **50,** III-139.

White, D. L., Mazurkierwicz, J. E., and Barrnett, R. J. (1979). *J. Histochem. Cytochem.* **27,** 1084-1091.

Yamada, E., and Ishikawa, H. (1972). *Proc. 30th Annu. Meet. Electron Microsc. Soc. Am.* pp. 480-481.

Yamada, E., and Ishikawa, H. (1976). *In* "Recent Progress in Electron Microscopy of Cell and Tissues" (E. Yamada, V. Mizuhira, K. Kurosumi, and T. Nagano, eds.), pp. 354-362. University Park Press, Baltimore, Maryland.

This Page Intentionally Left Blank

METHODS IN CELL BIOLOGY, VOLUME 22

Chapter 8

Mock Stereo

MURRAY VERNON KING

Division of Laboratories and Research,
New York State Department of Health,
Albany, New York

I. Definition and Scope of Mock-Stereo Displays 147
II. Types of Image Disparities That Can Profitably Be Treated by Mock Stereo: Discussion and Examples 148
III. Simultaneous Handling of Positional and Color Information in Mock Stereo . . . 149
IV. Applications of Mock Stereo in Electron Microscopy 150
V. Some Examples of Unintentional Mock Stereo 152
References 153

I. Definition and Scope of Mock-Stereo Displays

A mock-stereo display is one that generates depth perception from parallax information arising from sources other than a shift of vantage point. Such displays have at times proved effective in various fields of study including electron microscopy; therefore it is interesting to examine the conditions under which such displays can prove advantageous.

Mock-stereo displays can include (1) before-and-after pictures of a scene in which some details have become shifted by motion or distortion of objects; (2) comparisons to establish identity or equivalence of objects in two scenes; and (3) image pairs in which the shifts in placement of details arise from image processing.

In view of the variety of ways in which one can create mock-stereo pairs, these pairs will often differ from normal stereo displays in exhibiting vertical Δy disparities of size comparable to the horizontal Δx disparities. The success of this type of display will depend substantially on limiting the vertical disparities to a range that allows the visual system to ignore them while maintaining stereoscopic

Copyright © 1981 by Academic Press, Inc.
All rights of reproduction in any form reserved.
ISBN 0-12-564122-2

fusion. The author's experience suggests that the allowable limits on vertical disparities are rather ample.

A bonus of the mock-stereo method is that one can view a pair and then rotate both members and view them again so as to interchange the horizontal and vertical disparities and thus examine both sets of disparities individually in succession.

II. Types of Image Disparities That Can Profitably Be Treated by Mock Stereo: Discussion and Examples

A criterion for selecting types of images as candidates for mock-stereo treatment is that this method should offer advantages over other modes of display in enhancing recognizability of features. Some factors that favor mock-stereo display are as follows:

1. Ease of generation. Often it suffices merely to select two pictures out of a set and examine them in a stereo viewer, while the skill resides in choice of object, timing, and careful control of the direction of view.

2. Amenability to detection. This is perhaps the major factor for selecting objects for mock stereo. The problem is that the pair should show adequate horizontal disparities that yield an interpretable pattern of false relief while vertical disparities remain within the allowable limit. The optimal ratio of maximum parallax to picture width is not yet known for mock stereo, but we should expect it to be somewhat smaller than the proposed ratios (see Chapter 2) for normal stereo pairs because of the distracting effect of the vertical disparities. Image features that help in normal stereo such as contrasty details with well-defined contours should help also in mock stereo.

3. Image quality. The images should be of sufficient quality so that presentation of two copies of the same scene to the two eyes yields a strictly flat impression. Otherwise false inferences can be drawn.

4. Opportunities of presenting disparities via two channels. Mock-stereo methods gain another advantage when we wish to display two different types of disparities in an image pair simultaneously to the observer. One of the types can be assigned to the mock-stereo channel by displaying it as horizontal parallax, and the other, for example, to the color channel (see Section III). Section IV will discuss an application of this technique to electron microscopy.

Some examples from outside the field of electron microscopy illustrate the scope of the mock-stereo method. Cutler (1956) has discussed a method in which a stereo display is generated by electronic processing of range information obtained by radar. Sawchuk (1978) has developed a technique of creating stereo pairs from a single monocular image by digital image processing. This technique

generates depth information from various features extracted from the scene, including pixel brightness, edge information, texture, and multispectral information. Mock-stereo images thus generated are proposed as an aid for enhanced pattern recognition without trying to reproduce reality. Interestingly, Sawchuk's mock-stereo pairs generated by analyzing pixel brightness in a single image can hardly be distinguished from normal stereo pairs of the same objects, whereas those generated by edge extraction possess a quite unreal appearance in which detectability of edges has been massively enhanced.

Some of the monographs on stereoscopic methods have described applications of mock stereo. Linssen (1952, p. 226) discusses applications of the stereo comparator for detection of counterfeiting and other forensic applications in which the specimen in question and an authentic standard are treated as a stereo pair. He also discusses treatment of time-lapse pairs by mock stereo for detecting motion, especially in biological light microscopy, and cites some cinematographic studies of fiber swelling as examples of studies that could have benefited by the viewing of successive frames in mock stereo. Judge (1950) has also discussed the application of mock stereo to motion studies, with special stress on a stereo adaptation of the blink microscope in astronomy for detecting the motion of celestial objects. Valyus (1962, p. 289) has discussed the application of mock stereo for detecting forgery of documents and art objects; he points out that this method can even be applied to objects possessing relief, such as medals. He indicates, however, that the method fails in distinguishing counterfeit currency because the deviations in printing of authentic currency suffice to give an impression of depth.

In view of the current interest in analysis of aerial images in resource studies (see Section V), another potential application of mock stereo is in detecting erosion by aerial photographs taken from the same vantage point at different times. Since shifts of shadows could yield distracting impressions, the photographs should be taken at the same time of day on different days to minimize shifts of shadows, or, even better, at the same time on the same calendar day in successive years. Conversely, since shadows often represent the only moving details in an otherwise motionless landscape, one could invert this principle to create a striking demonstration of mock stereo by taking time-lapse pictures of a landscape over a portion of the day and displaying selected pairs in stereo. The shadows would then stand out in relief in a scene that otherwise looks flat.

III. Simultaneous Handling of Positional and Color Information in Mock Stereo

Chapter 2 has discussed the evidence for independence of the stereo and color channels in human vision. Its application to mock stereo consists in the opportunity of presenting two types of image disparities simultaneously to the visual

system as a global view. One does this by generating two images that contain disparities in color as well as in positions of details so that disparity information is conveyed by both channels. One can either view mock-stereo images that possess local brightness disparities through filters of contrasting color, or directly color the pictures in such a way as to convert disparities in brightness or other features into color disparities. The advantage is that the visual system tends to ignore small brightness disparities between the right and left images, while interpreting only major brightness disparities as information on luster and direction of illumination. However, even small color disparities are directly noticeable.

Studies on binocular color fusion (see Chapter 2) suggest limits on the maximum allowable color contrast, but the evidence is much more confused than in the case of the maximum allowable parallax. Studies by our group (see Section IV below) have indicated quite ample limits when the objects are typical electron micrographs, perhaps because of their wealth of detail that promotes fusion. Even presentation of one image in red and the other in green allows color fusion, with conversion of brightness disparities into red/green disparities. The choice of colors for this type of display has not yet been optimized. Whenever color fusion fails, however, a simple remedy is to choose filters of two colors lying closer together in the color scale.

Perhaps the combination of color disparity with mock stereo (which can be called *mock-stereo color*) comes most fully into its own with the application of Sawchuk's (1978) methods of digital image processing, with procedures added to generate the needed color displays. In addition to offering a versatile tool for image processing, such a system may provide the best way to determine the optimal levels of parallax and of color disparity for efficient pattern recognition in this type of display.

IV. Applications of Mock Stereo in Electron Microscopy

Our group has found an effective application of mock stereo in electron microscopy in assessing the character of artifacts caused by radiation damage in micrographs of normal tissue sections (King and Parsons, 1976, 1978, 1979). Distortions of sections of embedded tissues caused by charring in the electron beam were revealed by taking a low-fluence micrograph of a chosen area, then allowing the beam to play on a fraction of this area for a timed long interval, and finally taking a second low-fluence micrograph of the original specimen area. The micrographs were viewed as a mock-stereo pair to reveal the distortions in the plane of the section as a visual impression of false relief. Charring of only a fraction of the picture area allowed comparison in the same picture of heavily

damaged and minimally damaged material. Taking a series of pairs with increasing electron fluences in the damaged area offered a rapid, global view of the onset of radiation damage that could otherwise be gained only by laborious point-by-point comparison of the before-and-after micrographs.

The overall lateral shrinkage of the damaged area was revealed as an impression that this area was tilted out of the specimen plane. A further impression that the organelles in this area had become distributed throughout some depth suggested that the shifts in these bodies during charring of the embedment are not uniform, perhaps because the course of the charring is affected by the presence of the tissue.

Mock stereo was supplemented by placing a red and green filter over the lenses of the stereo viewer. This aided in making evident the brightness disparities between the two images caused by the thinning of the plastic embedment upon charring. While viewing, one first saw a fine-grained color rivalry (alternation of perceived color), but this rivalry faded out as stereopsis was achieved to leave a general disparity in color tone between the charred and uncharred areas. This suggests that stereopsis in this type of image succeeds in suppressing binocular color rivalry.

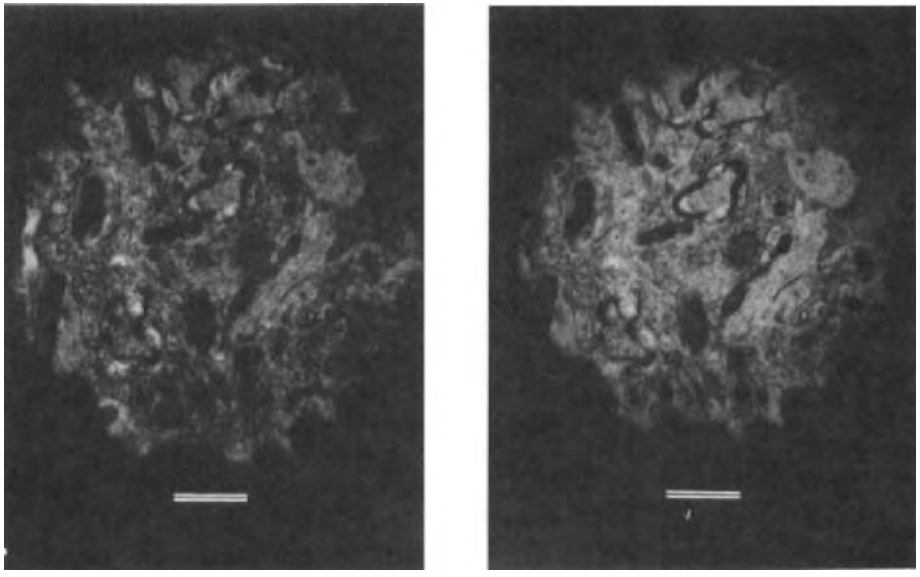


FIG. 1. Mock-stereo pair illustrating radiation damage in a thin section of feline cerebral cortex embedded in Epon and stained with uranyl and lead. Bar = 1 μm. The central area in the right-hand image (about half the total diameter) has been damaged by a fluence of about 1500 C/m^2 of 80-keV electrons. Examination with a pocket stereo viewer with a red filter over one lens and a green filter over the other reveals both the false relief and false color effects occasioned by radiation damage. Adapted from King and Parsons (1978), with permission from the *Journal of Microscopy*.

The mock-stereo effect proved most vivid when the original negatives were examined in this way. Mock-stereo examination of contact prints showed essentially the same features but with loss of some fine detail. However, high-contrast prints showed a compensatory gain in mock-stereo-color examination. When made with careful exposure control, they presented enhanced gray-scale disparities leading to greater color contrast. Stereo projection for demonstration to a large audience entailed considerable loss in both stereo and color effects, although both were still distinct. The stereo effects can be seen even in xerographic copies of the micrographs, although the color effects are lost in the xerographic noise.

Figure 1 shows an example of a mock-stereo pair, illustrating radiation damage in a thin section of feline cerebral cortex. The left-hand image was taken with a fluence on the specimen of 24 C/m^2. The central area in the right-hand image has been damaged by a fluence of about 1500 C/m^2, while the periphery has received only 47 C/m^2, with an acceleration potential of 80 kV. The described effects can be examined in either mock stereo or mock-stereo color.

A promising field for further application of both mock-stereo and mock-stereo-color techniques is in tracing changes in specimens during electron microscopic *in situ* experiments in materials science or biology. A further application of these techniques might be made in comparing pairs of images of specimens of protein molecules, viruses, and fibers for overall resemblance, either as done on the original electron images or after image processing.

V. Some Examples of Unintentional Mock Stereo

Mock-stereo examination of image pairs that were never intended for this type of display is often facilitated by the common practice of printing illustrations side by side in journals and monographs at about the right spacing for examination with a pocket stereo viewer. Then mock-stereo or even better, mock-stereo-color examination, will allow the observer to obtain a global view of the disparities in placement and brightness of details in the two images, and thus to gain a new glance at the presented information.

An outstanding example is the cover of the Spring 1979 issue of *EMSA Bulletin*, which shows six micrographs of uranium atoms on a carbon film displayed in false color as taken by Isaacson *et al.* (1979) in the high-resolution scanning transmission electron microscope. The micrographs show successive stages in the migration of uranium atoms over the surface of the carbon. The left-right pairs are spaced too far apart for comfortable viewing with a pocket stereo viewer, but they can easily be brought within range by folding the middle of the page. Then mock-stereo examination reveals a vivid impression of depth

arising from the horizontal components of the displacements of the features. The false color seems to aid in gaining stereopsis, while the vertical shifts and distortions of figures between the compared images somewhat retard but do not prevent stereopsis. Once gained, the illusion of depth is quite striking.

Some other examples give disappointing results in mock stereo alone, but quite vivid impressions in mock-stereo color. An example is Fig. 2 in an article by Millard and Arvesen (1973) on detection of oil slicks by taking images of the scene with horizontally and vertically polarized light. The lack of an impression of depth upon mock-stereo viewing suggests that, not only were the two cameras separated by a distance negligible in comparison with the distance to the scene, but also the photographs were taken simultaneously. Thus, only brightness disparities are evident.

Another example is an article by Jackson *et al.* (1978) on analysis of infrared aerial photographs by false color processing. Some of their comparison pictures (Fig. 3C, D, and E) are printed in a convenient format for stereo viewing and should be examined without color filters. When thus viewed, they show vivid color disparities but no appreciable depth effect. Interestingly, the present author perceives binocular color rivalry between images C and D, but color fusion between D and E, in spite of the greater color disparity of the latter pair. Inasmuch as Jackson *et al.* obtained their comparison pictures by image processing from a single original, no parallax is expected.

A further example from the same journal issue is an article by Colwell (1978) on interpreting vegetation resources in images taken from orbiting spacecraft. He applied a battery of techniques including both false color and true stereo. Figures 4A–F are printed conveniently for stereo viewing of pairs. They show large black/white disparities highly visible in mock-stereo-color examination, although no depth effect is evident except in the arrows attached to the photographs. Again the disparities are practically exclusively in brightness, not in parallax.

We recommend as a sport the hunting of further examples of this type.

ACKNOWLEDGMENTS

The work from which Fig. 1 is derived was supported by grants No. RR 00754 and RR 01088 awarded by the Division of Research Resources of the National Institutes of Health, United States Public Health Service, Department of Health, Education and Welfare.

REFERENCES

Colwell, R. N. (1978). *J. Appl. Photogr. Eng.* **4**, 107–117.

Cutler, C. C. (1956). U. S. Airforce Report No. 24269/K, pp. 98–102.

Isaacson, M., Utlaut, M., Ohtsuki, M., Crewe, A., and Kopf, D. (1979). *EMSA Bull.* **9**, No. 1, front cover.

Jackson, H. R., Wallen, V. R., and Downer, J. F. (1978). *J. Appl. Photogr. Eng.* **4,** 101-106.
Judge, A. W. (1950). "Stereoscopic Photography. Its Application to Science, Industry and Education." Chapman & Hall, London.
King, M. V., and Parsons, D. F. (1976). *Proc. 34th Annu. Meet. Electron Microsc. Soc. Am.* pp. 580-581.
King, M. V., and Parsons, D. F. (1978). *J. Microsc. (Oxford)* **113,** 301-305.
King, M. V., and Parsons, D. F. (1979). *Biophys. J.* **25,** 282a (Abstr. W-AM-F12).
Linssen, E. F. (1952). "Stereo-Photography in Practice." Fountain Press, London.
Millard, J. P., and Arvesen, J. C. (1973). *Science* **180,** 1170-1171.
Sawchuk, A. A. (1978). *Appl. Opt.* **17,** 3869-3873.
Valyus, N. A. (1962). "Stereoskopiya." Izd. Akad. Nauk SSSR, Moscow (Engl. transl., "Stereoscopy." Focal Press, London and New York, 1966; page number citations are for the English text).

Part II. Quantitative Methods Applied to Stereo Imaging

Chapter 9

Theory

SANJIB K. GHOSH

Department of Photogrammetry,
Laval University,
Québec, P. Q., Canada

I. Introduction 155
II. Coordinate Systems and Transformation 157
A. The Photo-Coordinate System (x, y) 157
B. The Model-Coordinate System (X', Y', Z') 158
C. The Object-Coordinate System (X, Y, Z) 159
D. Transformation of Coordinates 160
III. Projections and Distortions 163
A. Parallel Projection 163
B. Perspective Projection 165
C. Distortions 166
IV. Stereo Model and Orientation 169
V. Calibration of the Electron Microscope 173
References 176

I. Introduction

The term "quantitative" refers to precise dimensional measurements made to obtain *direct* information on the object being measured (relative to its size and shape), or *derived* information (for example, changing parameters such as velocity and area; statistical parameters, such as area distribution and standard deviation; or other associated parameters, such as stress and force). This discussion will be limited to the "direct" part, the rest being considered beyond the scope of our present treatise.

Copyright © 1981 by Academic Press, Inc.
All rights of reproduction in any form reserved.
ISBN 0-12-564122-2

Except by chance, a value obtained from a measurement is never exactly true. Furthermore, although many authors (mainly theoretical scientist-engineers) use the two words "measurement" and "observation" interchangeably, a subtle difference exists between them.* In the context of both terms, however, the following fundamental considerations are imperative:

1. Measurements are almost always made with either simple or complex instruments or with the aid of physical phenomena (breaking up of cells, periods of time, etc.). Associated with these are the operators (human observers), with their individual characteristics.
2. Measurements must be referred to the corresponding standards with which direct or indirect comparisons are to be made. Associated with them are the corresponding dimensions and their units.
3. The numerical data obtained from the observation process represent the measurements. The data indicate the circumstances and conditions under which the measurements were made.
4. The process of measurement involves a physical operation. Often several more operations are implied, however, such as preparation (setting up and calibration of the system), pointing, and comparing.
5. Measurements are generally the means to other ends (even within the instrument; for example, angles and distances are measured to obtain locations, areas, etc.), giving *derived data,* obtained directly or indirectly.
6. Such derived data are based on *theoretical concepts,* which may be expressed by "mathematical models" based on physical laws. The possibility remains, however, that such concepts are not fully understood or established.

A physical situation or a set of events can be expressed through the abstract symbolic language of mathematics. Symbolic expressions, known as *mathematical models,* provide the theoretical background, but they have no scientific value until and unless they have been adequately validated. Scientific validation is an open-ended course. The "model" becomes established when it has been tested successfully for repeated applications. Otherwise, depending on the degree of failure, it stands to be modified or even rejected.

In practical applications of a mathematical model, the expression should describe the situation as exactly as possible. It should also be simple enough to provide solutions without undue difficulties. These two requirements are not always compatible. Thus, one often compromises with the mathematical model to obtain useful results, knowing that these results may not be exact. Fur-

**Measurement* (Eisenhart, 1969) is the assignment of numbers to objects to represent the relations existing among them with respect to particular properties. In a quantitative sense, one does not measure an object but rather its dimensional properties—length, volume, etc. *Observation* refers to both the operational process and its outcome, particularly with regard to the associated "adjustment" procedure.

thermore, it is often convenient to apply several equations sequentially, as this approach is generally simple, is convenient for detecting operational blunders, and is applicable by the user with judgment, depending on the degree of exactness necessary to that specific application. However, any sequential approach also implies primary, secondary, tertiary, etc., effects of importance.

Mathematical models are composed of two parts: (1) the *functional* model, which describes the deterministic properties of the physical situation being considered. For precise quantitative work, usually a static (time-independent) situation is assumed. Dynamic mensuration problems are beyond the scope of this discussion. (2) The *stochastic* model, which describes and defines the nondeterministic or probabilistic (stochastic) properties of the involved variables that represent the measurements. These models are subject to statistical evaluations, which can offer ways of estimating the quality of the work.

Our discussion will cover basically the functional model, with adequate consideration of the associated stochastic state. For interesting ideas on stochastic models and corresponding principles of "adjustment computations," the reader will benefit from various books (e.g., Hamilton, 1964; Hirvonen, 1971; Mikhail, 1976).

II. Coordinate Systems and Transformation

A coordinate system is one of reference for defining points or objects in a specified space by means of distances and/or angles. The reference can be made with regard to designed axes, planes, or surfaces (Ghosh, 1979). In electron microscopy, however, only the *rectangular* systems are useful. They can be either two-dimensional, where points are defined by linear distances from two mutually perpendicular axes in a plane, or three-dimensional, where points are located with reference to three mutually perpendicular planes in a solid. Further, a coordinate system can be used with respect to a photo (micrograph), a stereo model, or the corresponding object. Accordingly, one refers to photo-, model-, or object-coordinate systems. These systems can be related to one another through transformation of coordinates.

A. The Photo-Coordinate System (x, y)

The process of measuring two-dimensional photo-coordinates requires a reference system established with a set of marks that can be observed on each photograph and that would maintain a fixed relationship to the imaging system—for example, the recording CRT in a scanning electron microscope (SEM). In the ideal situation, there would be at least four such marks at the extremities of the

photo format. An excellent solution would be to have a set of grid marks etched on the CRT surface (in SEM) or on a fixed glass plate (in the transmission electron microscope, TEM) that could be sharply focused by the registering camera. Since the manufacturers have made no such provision, it is usually up to the user to furnish such necessary *fiducial marks*. Ghosh (1975) describes one set of marks made by using epoxy steel fillers on the camera frame. In a right-handed system of coordinates, the fiducial center is the origin (see Fig. 1), and the marks provide the x, y references in which the x axis is customarily considered along the base line (direction of tilt, or the angle of convergence, also known as the parallactic angle). The fiducial center (analogous to the *principal point* in conventional photogrammetry, $0'$ in Fig. 1) has the coordinates x_0, y_0. Any image point (p) on the photo, in this system, is defined by $x = x' - x_0$ and $y = y' - y_0$, with x', y' being the observed values. The photo rotation (κ) is around the normal to the photo plane at the fiducial center (that is, around the principal electron axis) in a counterclockwise direction (analogous to κ rotation around the camera axis in conventional photogrammetry). It may be pertinent in some cases to have fiducial marks in the corners of the image format. This would correspond to a rotation and translations, in x and y directions, of the image point coordinates, as will be obvious. The variation in the use of a photo negative is also illustrated in Fig. 1.

B. The Model-Coordinate System (X', Y', Z')

The model-coordinate system refers to the stereoscopic model, established analogically at a stereo instrument, or mathematically by means of a computer or calculator. This coordinate system is three-dimensional, orthogonal, and right-handed (see Fig. 2). The location of the origin and the orientation of the system may be arbitrary, depending on the convenience of the use of the EM data. In practice, the X' direction coincides with the base line or the direction of tilt used in creating the stereo model. The model rotations—ω around the X' axis, ϕ

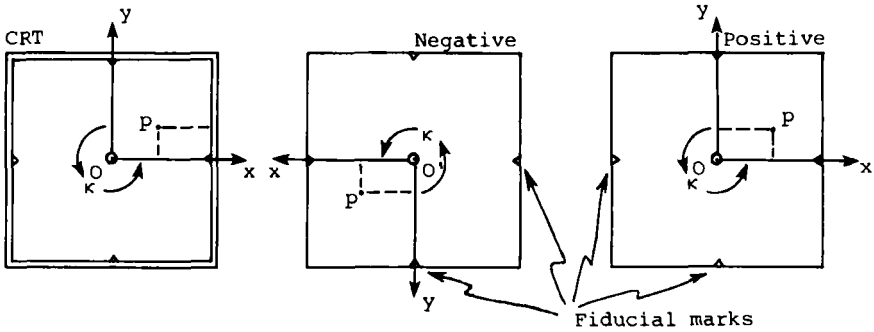


FIG. 1. Photo-coordinate system.

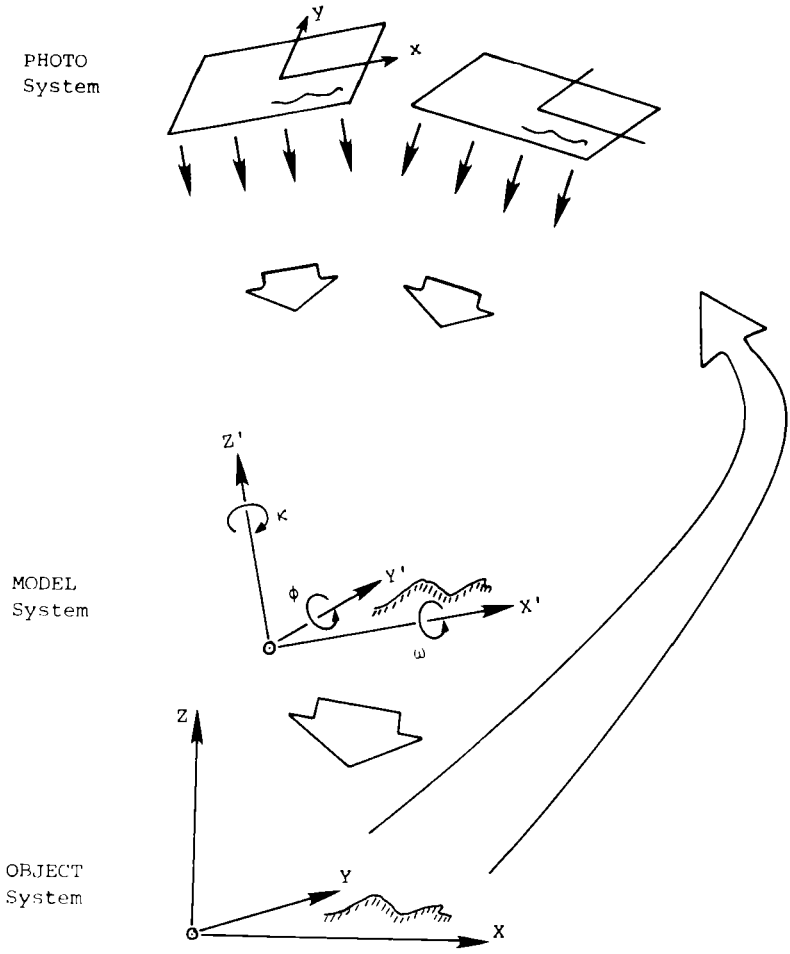


FIG. 2. Various coordinate systems involved in electron micrography.

around Y' axis, and κ around the Z' axis—are counterclockwise when viewed along the particular axis into the origin. Depending on the specific circumstance, ω or ϕ would correspond to the tilt angle θ used in creating a stereo pair. The model may be considered as a stage intermediate between the object and the corresponding micrographs, and this is where the quantitative data are obtained. However, the model data need to be related finally to the object.

C. The Object-Coordinate System (X, Y, Z)

The object-coordinate system is the final three-dimensional system of reference to the object. It is also right-handed and orthogonal. Depending on the

specific application, the choice of the origin or the orientation of the system can be arbitrary (see Fig. 2).

D. Transformation of Coordinates

It is often necessary to establish a relationship between coordinate systems in order to relate points of one system to points of the other. There are numerous methods of transformation for quantitative applications (Ghosh, 1979). It may mean a simple change in location and orientation, which involves no change in the shape or size of the transferred body, or a complex one, which implies a change in both shape and size. For the purpose of efficient quantitative work with EM, a *general three-dimensional* or similarity transformation is very effective. It basically considers only changes in location, orientation, and size, yet it is adaptable to considerations of minor changes in shape. This transformation is symbolized as follows:

$$X = kM^{\mathrm{T}}\bar{X} + X_0 \tag{1}$$

where

$X = [X\ Y\ Z]^{\mathrm{T}}$ coordinates after transformation;
$\bar{X} = [\bar{X}\ \bar{Y}\ \bar{Z}]^{\mathrm{T}}$ coordinates before transformation;
$X_0 = [X_0\ Y_0\ Z_0]^{\mathrm{T}}$ vector of three shifts indicating the X, Y, Z coordinates of the origin of the $\bar{X}$, $\bar{Y}$, $\bar{Z}$ system;
M = an orthogonal three-angle rotation matrix, consisting of three sequential rotations;
k = a scale factor.

Considering the rotations sequentially—ω around $\bar{X}$ (primary rotation), ϕ around $\bar{Y}$ (secondary rotation), and κ around $\bar{Z}$ (tertiary rotation)—their effects are expressed by the rotation matrices

$$M_\omega = \begin{bmatrix} 1 & 0 & 0 \\ 0 & \cos\omega & \sin\omega \\ 0 & -\sin\omega & \cos\omega \end{bmatrix} \qquad M_\phi = \begin{bmatrix} \cos\phi & 0 & -\sin\phi \\ 0 & 1 & 0 \\ \sin\phi & 0 & \cos\phi \end{bmatrix}$$

$$M_\kappa = \begin{bmatrix} \cos\kappa & \sin\kappa & 0 \\ -\sin\kappa & \cos\kappa & 0 \\ 0 & 0 & 1 \end{bmatrix}$$

The final effect of all three rotations is then expressed by the rotation matrix M as used in Eq. (1), M^{T} being its transpose:

$$M = M_\omega \cdot M_\phi \cdot M_\kappa. \tag{2}$$

The elements of this rotation matrix can be expressed in various ways:

$$M^{\mathrm{T}} = \begin{bmatrix} m_{11} & m_{21} & m_{31} \\ m_{12} & m_{22} & m_{32} \\ m_{13} & m_{23} & m_{33} \end{bmatrix}$$

$$= \begin{bmatrix} \cos\phi\cos\kappa & -\cos\phi\sin\kappa & \sin\phi \\ \cos\omega\sin\kappa + \sin\omega\sin\phi\cos\kappa & \cos\omega\cos\kappa - \sin\omega\sin\phi\sin\kappa & -\sin\omega\cos\phi \\ \sin\omega\sin\kappa - \cos\omega\sin\phi\cos\kappa & \sin\omega\cos\kappa + \cos\omega\sin\phi\sin\kappa & \cos\omega\cos\phi \end{bmatrix} \tag{3}$$

Also, the orientation matrix M can be expressed in terms of the direction cosines relating to the angles between the corresponding axes in the two systems, X, Y, Z and $\bar{X}, \bar{Y}, \bar{Z}$:

$$M^{\mathrm{T}} = \begin{bmatrix} \cos X\bar{X} & \cos Y\bar{X} & \cos Z\bar{X} \\ \cos X\bar{Y} & \cos Y\bar{Y} & \cos Z\bar{Y} \\ \cos X\bar{Z} & \cos Y\bar{Z} & \cos Z\bar{Z} \end{bmatrix} \tag{4}$$

The general transformation expressed by Eq. (1) assumes that the scale in the three-dimensional space is the same in all directions. It has, however, been noticed by many workers that in electron micrography different scales may exist along different directions. This condition causes geometric *affinity* and a corresponding variation in the shape of the object as registered on the micrographs or as observed or measured in the stereo model (Ghosh, 1975). In such cases the problem can be alleviated, if not totally removed, in most applications with Eq. (1), modified by using $k = 1$ and

$$\bar{X} = [k_{\bar{X}}\bar{X}\ k_{\bar{Y}}\bar{Y}\ k_{\bar{Z}}\bar{Z}]^T \tag{5}$$

where $k_{\bar{X}}$, $k_{\bar{Y}}$, and $k_{\bar{Z}}$ are the respective scale factors along the $\bar{X}$, $\bar{Y}$, and $\bar{Z}$ axes.

In the practical utilization of such a transformation method, it is often convenient to proceed in a sequential pattern with intermediate steps as illustrated in Fig. 3 with regard to establishing the relationship between the object and corresponding micrograph coordinates. These steps can be performed in the reverse mode—that is, from a micrograph to the object.

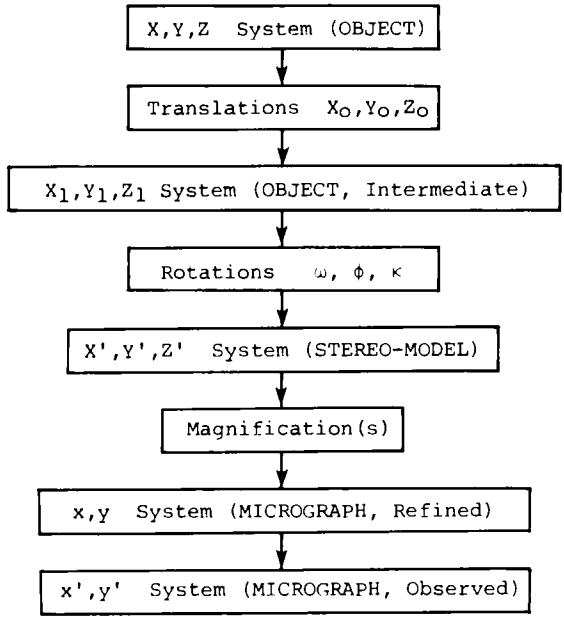


FIG. 3. Scheme of sequential steps in transformation from object to micrograph.

POLYNOMIAL TRANSFORMATION

Sometimes, in view of propagated errors or systematic deformations in a photo or a stereo model, a polynomial transformation is more efficient. Depending on the most appropriate or adequate mathematical model, one may use polynomials of various types (Ghosh, 1979). The general polynomials in three dimensions are given in Eqs. (6):

$$\begin{aligned} X &= a_0 + a_1\bar{X} + a_2\bar{Y} + a_3\bar{Z} + a_4\bar{X}^2 + a_5\bar{Y}^2 + a_6\bar{Z}^2 + a_7\bar{X}\bar{Y} \\ &\quad + a_8\bar{Y}\bar{Z} + a_9\bar{Z}\bar{X} + a_{10}\bar{X}\bar{Y}^2 + a_{11}\bar{X}^2\bar{Z} + a_{12}\bar{X}\bar{Z}^2 + \ldots \\ Y &= b_0 + b_1\bar{X} + b_2\bar{Y} + b_3\bar{Z} + b_4\bar{X}^2 + b_5\bar{Y}^2 + b_6\bar{Z}^2 + b_7\bar{X}\bar{Y} \\ &\quad + b_8\bar{Y}\bar{Z} + b_9\bar{Z}\bar{X} + b_{10}\bar{X}\bar{Y}^2 + b_{11}\bar{X}^2\bar{Y} + b_{12}\bar{X}\bar{Z}^2 + \ldots \\ Z &= c_0 + c_1\bar{X} + c_2\bar{Y} + c_3\bar{Z} + c_4\bar{X}^2 + c_5\bar{Y}^2 + c_6\bar{Z}^2 + c_7\bar{X}\bar{Y} \\ &\quad + c_8\bar{Y}\bar{Z} + c_9\bar{Z}\bar{X} + c_{10}\bar{X}\bar{Y}^2 + c_{11}\bar{X}^2\bar{Y} + c_{12}\bar{X}\bar{Z}^2 + \cdots \end{aligned} \tag{6}$$

The number of terms used in specific applications will depend on the degree of required refinement and limitations of the computer/calculator. Note that in Eqs. (6) the a's, b's, and c's are certain constants. In actuality, these may be composed of nonlinear trigonometric or other functions. Therefore, the polynomials are not conformal, and they should be used only in cases where the rotation angles are very small. Such polynomials may not provide information on actual

physical parameters involved in the system. They are, nonetheless, extremely helpful in performing the necessary numerical transformations, as well as in evaluating the quality of the utilized data.

III. Projections and Distortions

A photograph or micrograph may be regarded as a projected record of information. It can also be considered to be three-dimensional (x, y, z), where the third dimension (z) is a constant ($-C$). By using Eq. (1), one can establish the projective relationship between the photograph and the object through three equations as represented in Eq. (7) (see Fig. 4 also):

$$\begin{bmatrix} x \\ y \\ -C \end{bmatrix} = k \begin{bmatrix} m_{11} & m_{12} & m_{13} \\ m_{21} & m_{22} & m_{23} \\ m_{31} & m_{32} & m_{33} \end{bmatrix} \begin{bmatrix} X - X_0 \\ Y - Y_0 \\ Z - Z_0 \end{bmatrix} \tag{7}$$

If the resulting first and second equations are divided by the third, one obtains the following equations:

$$\begin{aligned} x &= -C \frac{(X - X_0)m_{11} + (Y - Y_0)m_{12} + (Z - Z_0)m_{13}}{(X - X_0)m_{31} + (Y - Y_0)m_{32} + (Z - Z_0)m_{33}} \\ y &= -C \frac{(X - X_0)m_{21} + (Y - Y_0)m_{22} + (Z - Z_0)m_{23}}{(X - X_0)m_{31} + (Y - Y_0)m_{32} + (Z - Z_0)m_{33}} \end{aligned} \tag{8}$$

Equations (8) ensure that the location vectors for the point (P) with respect to the perspective center in the object and the photo spaces are collinear. Thus, these equations are known in photogrammetric literature as *collinearity equations*. They are free from the scale factor (k) and are useful in many applications. In view of the possible affinity (different scale or magnification along different axes) in the micrograph, however, one simple way of modifying them is to consider two different projection constants, C_x and C_y, for the respective equations.

A. Parallel Projection

Because of the extremely small objects and extremely large magnifications involved, an electron micrograph has an extremely small field angle of projec-

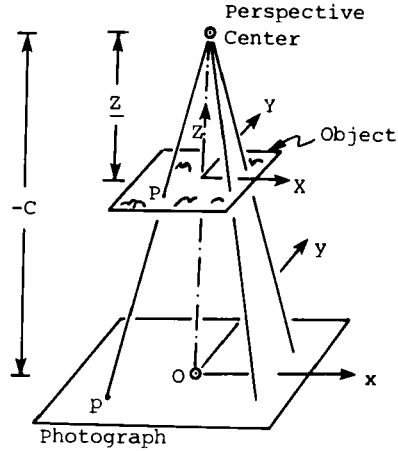


FIG. 4. Perspective projection and collinearity condition.

tion, which for the sake of simplification can be viewed as a parallel (or near-parallel) projection (see Fig. 5). The parallel projection system can be expressed by

$$\begin{bmatrix} x \\ y \\ 0 \end{bmatrix} = \begin{bmatrix} K_1 & 0 & 0 \\ 0 & K_2 & 0 \\ 0 & 0 & 0 \end{bmatrix} \begin{bmatrix} X_R \\ Y_R \\ Z_R \end{bmatrix} \tag{9}$$

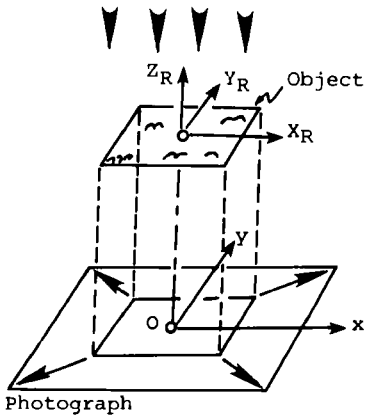


FIG. 5. Parallel projection with magnification.

where x, y are the photo coordinates: K_1, K_2 are the scale factors along the X_R, Y_R directions, respectively; and X_R, Y_R, Z_R are the object-space coordinates (after rotations).

As a result of rotations and translations to a selected origin, the last term in Eq. (9) becomes

$$\begin{bmatrix} X_R \\ Y_R \\ Z_R \end{bmatrix} = M \begin{bmatrix} X - X_0 \\ Y - Y_0 \\ Z - Z_0 \end{bmatrix} \tag{10}$$

where X_0, Y_0, Z_0 are the coordinates of the selected origin in the object system, and M is the orientation matrix.

If the height datum (level reference) is defined by setting $Z_0 = 0$, after substitutions and simplifications (Ghosh, 1979) one obtains the following projective equations for parallel projection:

$$\begin{aligned} x &= K_1(X - X_0)(c\phi c\kappa + s\omega s\phi s\kappa) + K_1(Y - Y_0)c\omega s\kappa \\ &\quad + K_1Z(s\omega c\phi s\kappa - s\phi c\kappa) \\ y &= K_2(X - X_0)(s\omega s\phi s\kappa - c\phi s\kappa) + K_2(Y - Y_0)c\omega c\kappa \\ &\quad + K_2Z(s\phi s\kappa + s\omega c\phi c\kappa) \end{aligned} \tag{11}$$

where prefixes c and s indicate cosine and sine functions, respectively, of the rotation angles as indicated.

B. Perspective Projection

The principal features of the perspective projection are a perspective center and finite projection distance(s) (see Fig. 4). With reference to our previous discussions, the following relationships are pertinent:

$$x = X_R\,[C_x/(\underline{Z} - Z_R)] \qquad \text{and} \qquad y = Y_R\,[C_y/(\underline{Z} - Z_R)] \tag{12}$$

where $\underline{Z}$ is the projection distance to the reference datum of the object, and the other terms are as previously defined.

By substituting the expansion for Z_R from Eq. (10) in Eqs. (12), after rearranging we obtain

$$\begin{aligned} x &= \frac{(C_x/\underline{Z})\,X_R}{1 + (1/\underline{Z})\{(X - X_0)c\omega s\phi - (Y - Y_0)s\omega + (Z - Z_0)c\omega c\phi\}} \\ y &= \frac{(C_y/\underline{Z})\,Y_R}{1 + (1/\underline{Z})\{(X - X_0)c\omega s\phi - (Y - Y_0)s\omega + (Z - Z_0)c\omega c\phi\}} \end{aligned} \tag{13}$$

It is quite appropriate to substitute K_1 for $C_x/\underline{Z}$ and K_2 for $C_y/\underline{Z}$. Also, since the second term in the denominator is smaller than unity, the expression can be expanded in a series $(1/\{1 - q\} = 1 + q + q^2 + q^3 + \ldots)$. This gives the final expressions for the perspective projection case:

$$\begin{aligned} x &= K_1 X_R \{1 + \nabla + \nabla^2 + \ldots\} \\ y &= K_2 Y_R \{1 + \nabla + \nabla^2 + \ldots\} \end{aligned} \tag{14}$$

where ∇ represents the second term in the denominators of Eqs. (13). For details of this derivation and the validity of the various approximations, see Nagaraja (1974).

C. Distortions

It is practical and convenient in the case of electron micrography to consider the parallel projection as regular and normal. One may consider the deviations from parallel projection as *distortions*. The various distortions as mathematically modeled are given below in the order of their relative magnitudes [established from research studies reported by Nordberg (1972), Maune (1973), Ghosh and Nagaraja (1976), and Ghosh and El Ghazali (1977)]. See Fig. 6 for their patterns.

1. Perspective Distortion

Perspective distortion defines the difference between the perspective and parallel projections. One may note that the first terms of Eqs. (14) constitute Eq. (9). This gives

$$\begin{aligned} x_{\text{parallel}} &= x_{\text{pers}} - x_{\text{pers}} \{\nabla + \nabla^2 + \ldots\} \\ y_{\text{parallel}} &= y_{\text{pers}} - y_{\text{pers}} \{\nabla + \nabla^2 + \ldots\} \end{aligned} \tag{15}$$

The representative values of ∇, ∇^2, etc., will have to be obtained from calibration studies on the specific imaging system.

2. Radial Distortion

Radial distortion is conventionally considered, with regard to the fiducial center or principal point of the micrograph, to be either positive (in the outward direction) or negative (in the inward direction). As in conventional photogrammetry, it is expressed by a polynomial:

$$\Delta r = k_0 r + k_1 r^3 + k_2 r^5 + \ldots \tag{16}$$

where r is the radial image point distance from the photo center, and the k's are certain constants. The first term (k_0), however, is equivalent to a scale factor and, in a sequential application of corrections, can be considered to be contained in the terms K_1 or K_2.

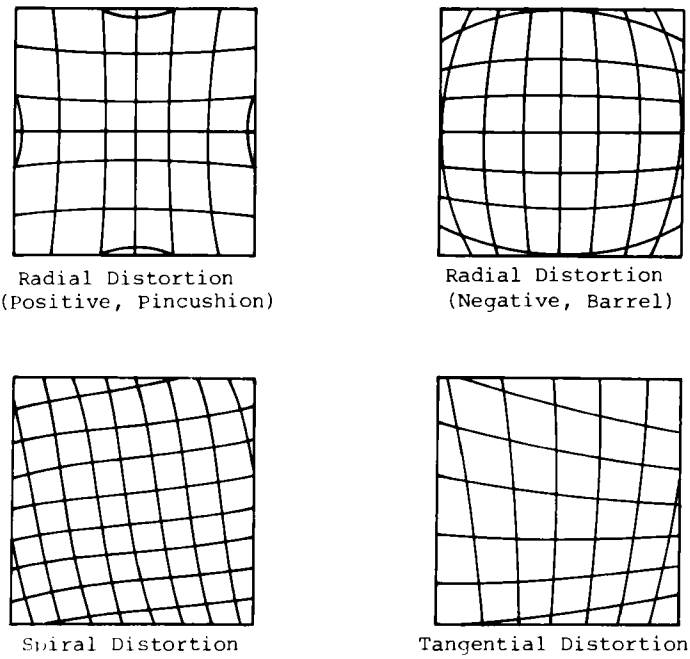


FIG. 6. Some distortion patterns in electron micrography.

It has been found from actual studies that terms of 5 and higher order in r can be neglected in normal applications. For the x and y components of this type of distortion, therefore, one obtains

$$\begin{aligned} \Delta x &= \Delta r(x/r) = k_1 r^3(x/r) = k_1(x^3 + xy^2) = D_1 x^3 + D_2 xy^2 \\ \Delta y &= \Delta r(y/r) = k_1 r^3(y/r) = k_1(x^2 y + y^3) = D_3 y^3 + D_4 x^2 y \end{aligned} \tag{17}$$

where the D's are certain constants, which may be obtained through calibration.

3. SPIRAL DISTORTION

The spiral or rotational twist of the electron beam, according to Klemperer and Barnett (1971), can be expressed by

$$\Delta d = C(y_0'/y)r^3 \tag{18}$$

where Δd is the displacement of the ray lateral to the radial direction on the micrograph, C is the spiral distortion coefficient, y_0'/y is the magnification, and r is the radial distance of the point from the principal electron axis.

Magnification being already contained in the K factors, a substitution, $S = C(y_0'/y)$, may be pertinent. Furthermore, consideration of possible affinity will give two values of S—S_1 and S_2—for the x and y directions, respectively. Then one obtains

$$\Delta x = S_1(y/r)r^3 = S_1(x^2y + y^3)$$
$$\Delta y = S_2(x/r)r^3 = S_2(x^3 + xy^2) \qquad (19)$$

where S_1 and S_2 may be called the spiral constants.

This distortion pattern existing in the micrograph should not be confused with systematic rotation of the entire beam, which takes place by changing the magnification. Such rotations can be of rather large magnitudes (see Fig. 7). As long as the same magnification is used for data acquisition, however, such a systematic rotation, being contained in transformation, has no adverse effect on mensuration.

4. Tangential Distortion

Only Maune (1973) has modeled this pattern of distortion after that of a conventional photogrammetric camera lens effect and obtained satisfactory results. Others (e.g., Nagaraja, 1974), however, have found that this type of distortion can be effectively accommodated in the mathematical model for spiral distortion. Because the effect of tangential distortion is small and often negligible, and the mathematical model is somewhat lengthy, it is not presented here. The interested reader may obtain ideas from the *Manual of Photogrammetry* published by the American Society of Photogrammetry.

The degree of stability of the EM system has a significant influence on distortion. The reliability of the mathematical models, therefore, would depend on the calibration and evaluation of the specific imaging system performed under specific working conditions. The degree of refinement attainable by considering such distortions is illustrated in Table I.

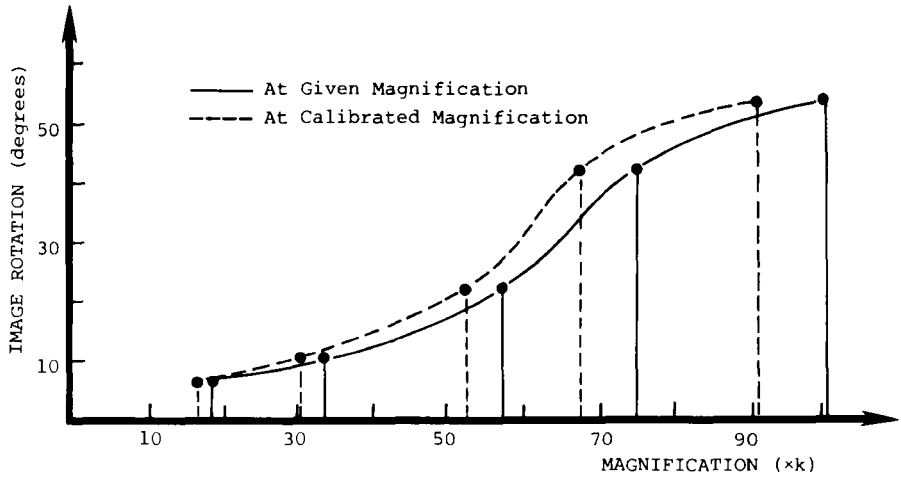


FIG. 7. Average angles of rotation for magnifications in one TEM. Example from research reported by Ghosh and El Ghazali (1977).

TABLE I

STANDARD DEVIATION OF POINT LOCATIONS FROM ONE EXPERIMENTAL SAMPLE CALIBRATION OF A SEM WITH CALIBRATION GRID MICROGRAPHS AT 5000X AND BASED ON FIFTY POINTS RANDOMLY DISTRIBUTED OVER THE ENTIRE FORMAT

Uncorrected for any distortion	±300 nm
Corrected for only scale affinity	±110 nm
Corrected for all distortions	±23 nm

IV. Stereo Model and Orientation

If two corrected photos are available of the same object with different orientations of the imaging system (or object/specimen tilt angles), then a stereo model replica of the object can be constructed by means of spatial intersection of conjugate rays, which give X, Y, Z coordinates of all object points. In conventional photogrammetry, camera or photo orientations are defined by "exterior" orientation elements consisting of translations along, and rotations about, the X, Y, and Z axes. In EM photogrammetry, however, there is no "exterior space," and the orientations of the stage plate become of prime importance.

The stage plate containing the object in both TEM and SEM has, generally, four elements of movement: (1) tilt, uniaxial, around the Y axis, which corresponds to the ϕ tilt in conventional photogrammetry and eventually yields the stereo angle S, better known in photogrammetry literature as the parallactic angle or angle of convergence; (2) rotation about the general direction of the principal electron axis, which corresponds to the κ rotation in conventional photogrammetry; (3) X translation, which corresponds to the Bx element in conventional photogrammetry, contributing to or complementing the "base" of the stereo model; and (4) Y translation, which corresponds to the By element in conventional photogammetry, analogous to the Y parallax, or lack of correspondence in the Y direction, for the entire photo. Peculiar to various EM's, however, there are limitations in each of these elements.

The spatial intersection of conjugate rays is performed by a procedure of *relative orientation* (Ghosh, 1972, 1979), which ensures the condition of coplanarity of the three vectors—the two conjugate rays and the base. Relative orientation with EM photos becomes extremely simple if, for generating the second micrograph, one uses only the elements of tilt and the associated x translation. Therefore, it is necessary that the micrographs be appropriately "oriented" by using the fiducial marks, analogically on the measuring instrument or computationally at a calculator with a two-dimensional transformation.

The stereo model replica of the object obtained after relative orientation

requires another operation, *absolute orientation,* before meaningful three-dimensional data can be extracted. In computational approaches, this is performed by using the three-dimensional transformation equations. In analogical or instrumental approaches, it is done in two steps: (1) scale correction (or scaling), by making measurements against dimensions of known values—as, for example, replica grids or other "standards"; and (2) tilting, rotating, and translating the model to fit the coordinate system in which the final mensural data are acquired (Ghosh, 1972, 1979).

The orientations and acquisition of data are greatly facilitated if the first micrograph is taken with a tilt angle amounting to half of the stereo angle (that is, $\theta = \frac{1}{2}S$), and the second micrograph is taken with the same tilt angle in the opposite direction ($\theta' = -\theta$). The pretilt, if any (θ_0), would then contribute to the tilting of the stereo model—that is, leveling of the height datum as necessary in the absolute orientation. Orientation theories and practices are discussed in detail in numerous books on photogrammetry (see, e.g., Ghosh, 1979).

If we assume parallel projection, the generation of three-dimensional data of a point P in the stereo model, with regard to reference point A (see Fig. 8), will be given by Eqs. (20):

$$\begin{aligned} Z' &= \Delta p \frac{1}{2 \sin \theta} = (x' - x'') \frac{1}{2} \operatorname{cosec} \frac{S}{2} \\ X' &= x' \sec \theta - Z' \tan \theta \\ Y' &= y' = y'' \end{aligned} \tag{20}$$

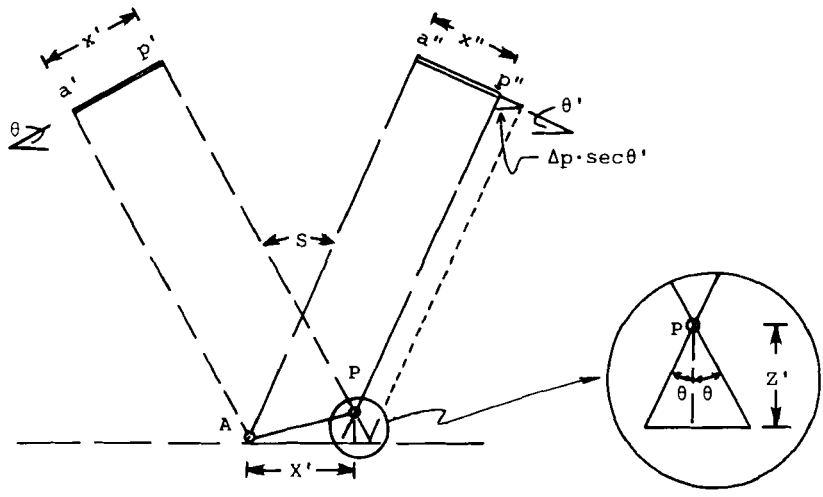


FIG. 8. Geometry of intersection with parallel projection.

where x', y' are the photo coordinates with regard to the reference, A, in the first (left) photo; x'', y'' are the photo coordinates with regard to the same reference, A, in the second (right) photo; and $\Delta p = x' - x''$ is the parallax difference between the observed point, P, and the reference, A.

It may be noted that the second term in the expression for X', $(Z' \tan \theta)$, may be negligible in practice in view of the small tilt angle and small height difference. Furthermore, considering calibrated magnifications, M_x and M_y in x and y directions, respectively, on the micrographs, we can express Eqs. (20) as follows:

$$\begin{bmatrix} X' \\ Y' \\ Z' \end{bmatrix} = \begin{bmatrix} \sec \theta/M_x & 0 & 0 \\ 0 & 1/M_y & 0 \\ 0 & 0 & \operatorname{cosec} \theta/2M_x \end{bmatrix} \begin{bmatrix} x' \\ y' \\ \Delta p \end{bmatrix} \tag{21}$$

The final data in the object space are then subject to a simple transformation from the X', Y', Z' system into the X,Y,Z system. Often, however, this step may not be necessary.

With regard to the accuracy of the mensural data, one must consider several points:

1. Scale repeatability of the micrographs, which can be assessed by measuring the same distances in multiple micrographs taken under the same operational conditions and settings. From these measurements, the range of scale variations for the specific imaging system can be established. One research study (Ghosh *et al.*, 1978) indicated as much as $\pm 1.17\%$ for one SEM and $\pm 2.07\%$ for one TEM as the average ranges. Such values must be obtained empirically.

2. The mensuration capability of the measuring instrument, or its accuracy in locating a point in planimetry on single micrographs or in stereo space of the model. Empirical studies in this regard would indicate the optimum value of the total system. An example, reported by Ghosh and El Ghazali (1977), is illustrated in Fig. 9; the corresponding data are given in Table II. Note that the pointing accuracy is also a function of the type of point observed. The data in Table II refer to grid intersection points measured in a Zeiss PSK Stereocomparator. The same comparator, when used to locate the centers of carbon-black spheroids in 18,000× TEM micrographs, had a standard pointing accuracy between a maximum of ± 0.72 nm and a minimum of ± 0.22 nm. The stereoscopic pointing accuracy depends, apart from the inherent capabilities of the imaging and measuring instruments, on the parallactic angle (relating to the strength of the geometry of intersection). As an example, with a parallactic angle of 10°, by using TEM stereomicrographs of 18,000× magnification at a Wild A7 Auto-

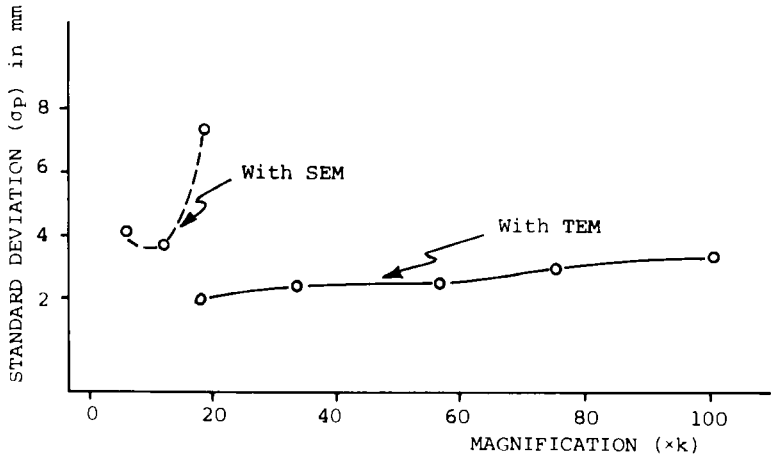


FIG. 9. Standard pointing accuracy in planimetry for various magnifications at two specific EM instruments. Examples from research reported by Ghosh and El Ghazali (1977).

graph, the pointing accuracy in height of locating the centers of carbon-black spheroids was ±0.89 nm.

3. The influence of the parallactic angle on the quality of intersection of the conjugate rays. The best intersection, theoretically, is when the angle is 90°. Very large angles create stereo gaps and mapping problems, however, and very small angles give unreliable heights. It has been found from extensive research (Ghosh and El Ghazali, 1977) that a parallactic angle between 8° and 20° generally gives acceptable results, the optimum being usually between 10° and 15°.

TABLE II

EXAMPLES OF STANDARD PLANIMETRIC POINTING ACCURACIES ON ELECTRON MICROGRAPHS

Magnification (k ×)			
Nominal	Calibrated	Standard pointing accuracy (nm)	Instruments
6	6.238	±4.18	SEM + PSK[a]
12	11.118	±3.59	SEM + PSK
18	16.952	±7.36	SEM + PSK
18	16.821	±1.96	TEM + PSK
33	30.236	±2.30	TEM + PSK
57	52.632	±2.51	TEM + PSK
75	68.307	±3.01	TEM + PSK
100	90.777	±3.26	TEM + PSK

[a] PSK is the precision stereocomparator made by Carl Zeiss, West Germany.

V. Calibration of the Electron Microscope

Calibration is a refined form of measurement (Eisenhart, 1969) for the purpose of evaluating the performance of the working system (that is, the man-material-equipment-technique combination). It is better done by assigning numbers to specific elements or parameters with statistically sound expressions for their systematic errors and precisions. To characterize the process, the scientist-engineer first establishes specifications indicating permissible ranges or variations and, next, a state of statistical control. There are, however, some difficulties that one must try to overcome or eliminate:

1. The working system may be sensitive to factors other than the desired input (the micrographs in our case). The system, unfortunately, may produce outputs with errors contributed by factors in which one is not interested. It is necessary, therefore, to calibrate the system under circumstances that are reasonably representative of the working conditions under which the calibration results will be applied.
2. Acceptable "standards" should be established against which both the input and the output are to be judged. Such standards may not be available for direct use and are often assumed or generated; their dependability would then rest on the guidelines of assumption and the application setup. Nevertheless, in all cases one should use a reference standard of proven stability with acceptable repeatability of the working system in mind.
3. The working system may not be appropriately "stable" and may fail to give the same output for repeated applications. This implies that the results of calibration should remain within the permissible range over the time period for which such results are applied. Two strong assumptions are made—that the factors causing the outputs to be in error are randomly active, and that they are not correlated to one another. With multiple observation data, the difference of the individual values from the mean (or accepted as correct) value would help one calculate the standard deviation of the observations. There is, however, always a constant difference between the input and the mean value of the output, known as *bias*. Furthermore, *precision,* indicating the scattering of the output values, measures the ability of the working system to give the same output for repeated applications of a given input. The standard deviation would indicate the *accuracy* with which the outputs can be related to the input.

With regard to the EM systems in use, the following parameters are considered essential in the mensural (geometric) calibration:

1. The locations of the fiducial marks, relative to each other, in the micrograph.
2. The magnification with the consideration of affinity, when known to exist.

3. All distortion parameters in consideration of the mathematical model(s) to define the systematic deviations of points in the micrograph from their ideal locations.

4. All tilt and rotation angles and translation elements related to each micrograph separately.

The number of parameters necessary for a practical solution can be reduced by using some well-planned manipulations during the multiple micrographing of the "standard," as well as by limiting the scope of the mathematical model(s) that define the distortions and the degree of refinement necessary. There is always the possibility, however, of encountering "critical geometry" involving physical-mathematical correlation between certain parameters without uncoupling which no meaningful solution is possible.

The best available "standards" are carbon replicas made from master diffraction gratings. Since these are two-dimensional, certain configurations of convergent photography can be used to "generate" the third dimension (see Fig. 10, and Ghosh, 1975). Such a setup and utilization of the procedure of "self-calibration" have been highly successful in these calibrations. In some cases it may be advisable to use the known or derived parameters directly or indirectly according to their comparative reliabilities. This is done by utilizing the constraints of *a priori* "weights" for the respective parameters (Ghosh, 1979).

The collinearity equations (see Section III of this chapter) provide the basis for such analytical calibration schemes. Equations (8) are augmented to best describe the geometry of an EM system (considering effective distortions):

$$
\begin{aligned}
&x_{ij} + D_1\, x_{ij}^3 + D_2\, x_{ij}\, y_{ij}^2 + S_1(x_{ij}^2\, y_{ij} + y_{ij}^3) \\
&= -C_x \frac{(X_j - X_{0_i})m_{11_i} + (Y_j - Y_{0_i})m_{12_i} + (Z_j - Z_{0_i})m_{13_i}}{(X_j - X_{0_i})m_{31_i} + (Y_j - Y_{0_i})m_{32_i} + (Z_j - Z_{0_i})m_{33_i}} \\
&y_{ij} + D_3\, y_{ij}^3 + D_4\, x_{ij}^2\, y_{ij} + S_2(x_{ij}^3 + x_{ij}\, y_{ij}^2) \qquad (22) \\
&= -C_y \frac{(X_j - X_{0_i})m_{21_i} + (Y_j - Y_{0_i})m_{22_i} + (Z_j - Z_{0_i})m_{23_i}}{(X_j - X_{0_i})m_{31_i} + (Y_j - Y_{0_i})m_{32_i} + (Z_j - Z_{0_i})m_{33_i}}
\end{aligned}
$$

where the 0 subscript refers to the perspective center, the i subscript refers to the photograph, and the j subscript refers to the object point. The remaining subscripts have been referred to in the preceding sections. (Note: The C's, D's, and S's are common to all points and photos used.)

With a convergent configuration of multiple photos as indicated in Fig. 10, one finds three types of unknown parameters:

1. Eight parameters (C_x, C_y, D_1, D_2, D_3, D_4, S_1, and S_2) common to all points and photos.

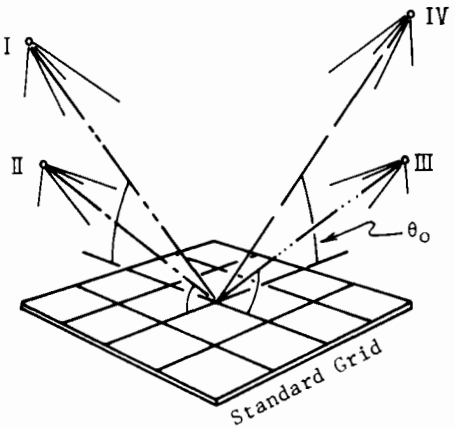


FIG. 10. Convergent configuration of micrographs by using one tilt angle (θ_0 or ϕ_0) and four rotations (κ).

2. Two parameters (Z_0 and tilt angle, θ, the latter interpreted as ω or ϕ, as the case may be) common to each tilt used.

3. Three parameters (κ, X_0, and Y_0, which are unique to each photo.

A calibration would involve a minimum of two photographs (at, say, 0° and 180° rotations) for each of one or more tilts. For example, with two tilt angles and four rotations, there are $8 + (2 \times 2) + (4 \times 2 \times 3) = 36$ calibration parameters. This indicates the necessity of a calculator or computer of adequate capability. For many applications, however, consideration of radial, tangential, or spiral distortions may not be necessary. Appropriate reduction of the parameters and utilization of an adequate number of "control" points in a sufficient number of photos should then be considered.

The final solution requires the formation of "observation equations," which express the relationship between the observations, the values of parameters, the errors in observations, the errors in the parameters, and the errors in the satisfaction of a particular mathematical model. Equations (22), being nonlinear, are to be "linearized" by a "Taylor expansion" to obtain such an observation equation in this case. The number of terms required in this expansion would depend upon the accuracy required or the number of iterations permissible. The linearization is about the measured quantities x_{ij} and y_{ij} and initial approximate values of the unknown parameters. If all linearized equations are collected, they may be written in matrix notations, concisely stated (see Ghosh, 1979, Chapter 9):

$$\bar{V} + \bar{B}\bar{\delta} + \bar{\epsilon} = \bar{0} \tag{23}$$

where $\bar{V}$ is the vector of residuals; $\bar{B}$ is the matrix of the partial derivatives of the function, Eqs. (22) with respect to the parameters and the object points (grid

coordinates); $\bar{\delta}$ is the vector of corrections or alterations to the parameters and object point coordinates; and $\bar{\epsilon}$ is the discrepancy vector, $\bar{0}$ being the null matrix.

Considering a weight matrix, $\bar{W}$, of observations, by applying the principles of *least squares*, the contributions of all observations are added to what are called *normal equations*. Least squares obtains its name from minimizing the sum of the squares of the weighted residuals of all observations—that is, by minimizing $\bar{V}'\bar{W}\bar{V}$. The normal equations in compact symbolic form are

$$\bar{N}\bar{\delta} + \bar{U} = \bar{0} \tag{24}$$

From this, one finds the solution, the correction vector:

$$\bar{\delta} = -\bar{N}^{-1}\bar{U}. \tag{25}$$

In these, $\bar{N} = \bar{B}^T\bar{W}\bar{B}$ and $\bar{U} = \bar{B}^T\bar{W}\bar{\epsilon}$. For interesting ideas on adjustment computations, see Hirvonen (1971) or Mikhail (1976).

References

Eisenhart, C. (1969). *Natl. Bur. Stand. (U.S.), Spec. Publ.* **300,** Vol. 1.

Ghosh, S. K. (1972). "Theory of Stereophotogrammetry," 2nd ed., Ohio State University Bookstores, Columbus.

Ghosh, S. K. (1975). *Photogrammetria* **31,** 91-114.

Ghosh, S. K. (1979). "Analytical Photogrammetry." Pergamon, Oxford.

Ghosh, S. K., and El Ghazali, M. S. (1977). "Stereo Electron Micrographic Studies of Carbon Black," Initial Report on the OSU Res. Found. Proj. No. 784507. Ohio State University, Columbus.

Ghosh, S. K., and Nagaraja, H. (1976). *Photogramm. Eng. Remote Sens.* **42,** 649-657.

Ghosh, S. K., El Ghazali, M. S., Deviney, M. L., and Mercer, H. N. (1978). *In* "Three Dimensional Mapping by Combining Transmission and Scanning Electron Microscopes," Int. Soc. Photogrammetry Commission V Rep. (K. Torlegard, ed.), pp. 1-10.

Hamilton, W. C. (1964). "Statistics in Physical Science—Estimation, Hypothesis Testing and Least Squares." Ronald, New York.

Hirvonen, R. H. (1971). "Adjustment by Least Squares in Geodesy and Photogrammetry." Frederick Ungar Publ. Co., New York.

Klemperer, O., and Barnett, M. E. (1971). "Electron Optics," 3rd ed. Cambridge Univ. Press, London and New York.

Maune, D. F. (1973). Photogrammetric self-calibration of a scanning electron microscope. Ph.D. Dissertation, Ohio State University, Columbus.

Mikhail, E. M. (1976). "Observations and Least Squares." IEP-A Dun-Donnelley Publisher, New York.

Nagaraja, H. (1974). Application studies of scanning electron microscopes photographs for micromeasurements and 3-D mapping. Ph.D. dissertation, Ohio State University, Columbus.

Nordberg, J. A. (1972). A procedure for photogrammetric calibration of EMs. M.Sc. Thesis, Ohio State University, Columbus.

Chapter 10

Hardware and Methods

SANJIB K. GHOSH

Department of Photogrammetry,
Laval University,
Québec, P.Q., Canada

I. Measuring Instruments 178
A. Analogical Types (Representative) 178
B. Analytical Types (Representative) 182
II. Accuracy and Reliability 185
A. Standard Deviation 186
B. Mapping Accuracy 187
C. Contouring 188
D. Stability and Repeatability 189
III. The Digital Terrain Model and Computer Mapping 190
References 192

In extracting quantitative data, the primary requirement of instrumentation is to obtain coordinates, either two-dimensional (x, y of photo image points) or three-dimension (X, Y, Z of model points), with the supplementary requirement of a facility for continuous plotting. The two principal approaches are analogical and analytical. The former involves double-projection optical-mechanical analog systems in which replicas of objects are created for the acquisition of data. In the latter, computer-interfaced comparators are used to derive the required data computationally. Each approach has three basic components: (1) the viewing system; (2) the measuring system, including the orientation mechanisms; and (3) the readout and recording system. The acquired data, after possible corrections and manipulations, may be directly displayed graphically, with a mechanical analog plotter, or handled digitally, leading to computer mapping.

Copyright © 1981 by Academic Press, Inc.
All rights of reproduction in any form reserved.
ISBN 0-12-564122-2

I. Measuring Instruments

Because imaging systems in the electron microscope have parallel or very nearly parallel projection, at least at high magnifications, and because most conventional photogrammetric instruments have perspective projections (optical or mechanical), the two systems are greatly incompatible. The primary effect of combining the two will be a significant affinity in the stereo model affecting the Z coordinate as compared with the X and Y. One way of alleviating this problem is to consider an appropriate scale factor for the heights (Z) of points and to utilize developed (ad hoc) nomograms for continuous mapping of features, as was done by Oshima *et al.* (1970) working at a Wild A7 Autograph. Another approach would be to modify such a stereo plotter for EM applications. This approach, however, would create extreme problems with the optical projection type of instrument. A rather successful modification of a mechanical projection type of instrument (the Wild B9 Aviograph) has been reported by Wood (1972). The third possibility—that of using approximate instruments (that is, those of the camera lucida type, but without rigorous perspective projection) in obtaining and overall three-dimensional model—is not really suited to the production of large volumes of quantitative data (Boyde, 1968). The fourth possibility, utilizing instruments with the capability of correcting the final deformed model (such as the Zeiss Stereotope), has been successfully demonstrated by Ghosh (1971). Such an instrument, interfaced with a computer and a plotter, gives an analytical plotting system well suited to EM applications. The only other possibility would be a specialized instrument made specifically for EM applications, such as the EMPD (see below), albeit with its inherent mechanical and optical limitations. A precision analytical plotter, although somewhat beyond the reach of the average user because of its high cost, seems to be the ultimate in EM instrumentation. Ideas on these systems are given below.

A. Analogical Types (Representative)

1. Instruments Specifically for EM Measurements

The EMPD (Electron Micrograph Plotting Device), Model 2, is a good example of an EM measuring device (Fig. 1). First discussed by Boyde and Ross (1975), this instrument was developed by Cartographic Engineering Ltd., Salisbury, United Kingdom, and marketed in the United States by Commonwealth Scientific Corporation, Alexandria, Virginia. The design philosophy includes the two basic assumptions that a simple optical-mechanical solution is adequately

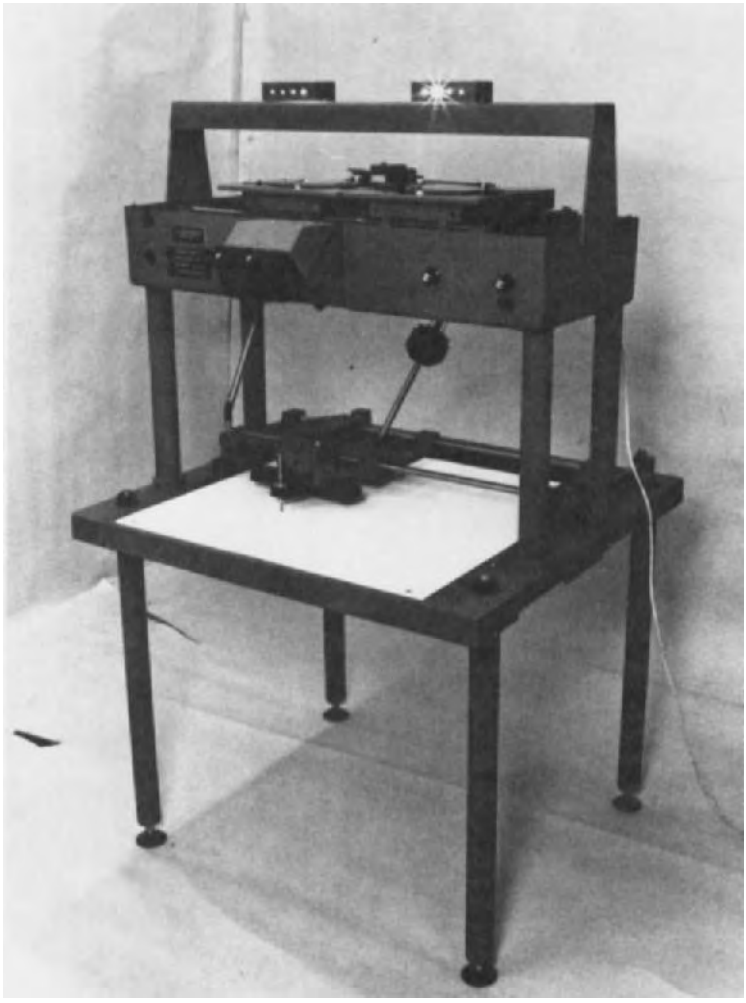


FIG. 1. Electron Micrograph Plotting Device (EMPD), Model 2. Courtesy of the Commonwealth Scientific Corporation, Alexandria, Virginia.

efficient, and that distortion-free photographs are available. Based on a parallel projection system, with the same magnification in each of the stereo pair, the instrument is designed so that the scale variation in the photo, assumed to be due to tilt only, is rectified by using a cylindrical lens to cause a corrective anamorphic change. The intersection geometry works on *scale-corrected parallax* (Δp) such that, if one chooses the left-side photograph as the map plane (datum for measuring heights), the right-side photograph is foreshortened by $\cos\theta$ so that

$\Delta p = x' \cdot \cos \theta - x''$ [note analogy from Eq. (21) of Chapter 9]. This gives the following expression for height:

$$Z'_{\text{left}} = \Delta P/(\sin \theta \, M_x) \tag{1}$$

The free-hand plotting motion is coordinated with the movement in the model of the floating mark, similar to standard photogrammetric plotters. With a drawing/plotting pantograph, plotting is possible in an enlarged scale. This instrument has the capability of plotting profiles plus the facility for selecting the profile anywhere on the model and in any direction. It can handle photographs of formats up to 100 × 125 mm.

2. Standard Photogrammetric Stereo Instruments

The Wild A10 Autograph, manufactured and marketed by Wild Heerbrugg Ltd., Heerbrugg, Switzerland, is a universal precision instrument designed for the extraction and plotting of three-dimensional data from overlapping photographs (see Fig. 2). The two projectors holding the photographs can be oriented at will. It can also be used as a stereo- or monocomparator. The Wild A10 can accommodate all sizes and forms of negatives and diapositives on films or plates up to 23 × 23 cm. Focal lengths of between 85 and 308 mm can be set continuously with an accuracy of 0.01 mm. Spatial control of the measuring mark is done by two handwheels for X and Y movements, and a footdisk for Z movements. The viewing system has interchangeable eyepieces of various magnifications, and the binocular is adjustable to individual requirements. All linear



FIG. 2. Wild A10 Autograph. Courtesy of Wild Heerbrugg Ltd., Heerbrugg, Switzerland.

measurements can be made with a precision of 0.01 mm, and all rotation elements can be set with a precision of 1^c (one centesimal minute). Any standard photogrammetric operation is possible with this instrument, which is also extremely stable. With auxiliary equipment, additional profiling, printing of coordinates, etc., are possible, also with very high precision. With interfaced digitizers, this instrument would develop a tremendous automated cartographic capability with the DTM (digital terrain modeling) technique. All these features contribute to this instrument's substantial adaptability to various demands and applications with EM data.

Since parallel projection is involved in the micrograph geometry, it is highly desirable that one sets the largest possible principal distance (focal length) when working at such an instrument. The perspectivity of the instrument effects a model deformation, which gives primarily falsified heights. The height of a point P in the stereo model with regard to a reference point A (see Fig. 8 of Chapter 9) is given by (from any standard book on photogrammetry)

$$Z' = \frac{B f(P_1 - P_2)}{P_1 P_2 M} = \frac{B f \Delta p}{P_1 P_2 M} \tag{2}$$

where B is the base setting, f is the focal length, P_1 and P_2 are the parallaxes at points A and P, respectively, Δp being the parallax difference, and M is the magnification.

The parallaxes of the two points can be regarded as known or fixed quantities. The base and focal length (B and f), on the other hand, quantities of no physical significance in parallel geometry can be chosen arbitrarily in view of the stereo angle (S). One can infer that, with proper choice of B and f, the height difference can be reduced to zero. This inference is true if one is interested in only two points in the object. In three-dimensional continuous mapping, however, one is faced with the inevitable deformation in height, which can be kept within certain bounds by proper use of Eq. (2). If the base and focal length are chosen rather arbitrarily, in some cases the height exaggeration will be uncontrollable. To avoid this situation, it is advisable to establish the relationship between Z'_{parallel} and $Z'_{\text{perspective}}$ for the specific values used for B and f [by considering Eqs. (20) of Chapter 9 and Eq. (2) above; see also Oshima *et al.*, 1970].

In this light, it is suggested that for the typical sample, when such a stereo instrument is used, a table should be prepared showing the relationships (in terms of numerical values) among the four parameters P_1, P_2, Z'_{para}, and Z'_{pers} for the particular B and f combination. From these relationships, a correction graph can be constructed by plotting Z'_{para} against Z'_{pers}. This graph can be used in practice, or the relationship can be programmed, for all mapping jobs with the same base-focal length setting in the same instrument.

Slight corrections are required in the X' and Y' coordinates, as will be appar-

ent. In most cases with no lateral tilt, however, Y' does not change, and owing to the low parallactic angle, one can consider unit value for the cosine function in X'. Thus, both X' and Y' can be taken directly from, for example, the left-side micrograph (the magnification being considered). This will be more profound if the stereo micrographs are taken with the left one being vertical (that is, zero tilt) and the right one with the desired tilt (equivalent to the desired stereo angle). This approach will tilt the datum for the Z' values, however. For most applications, the datum is arbitrary and will not be any cause for concern, as there is no unique or natural datum. See Boyde and Ross (1975) for an interesting discussion on the choice of datum plane.

B. Analytical Types (Representative)

1. Standard Analytical Plotters

An analytical plotter consists of a precision *stereocomparator and coordinatograph* interfaced with an *electronic digital computer* plus other auxiliary devices as may be necessary (see the system schematic in Fig. 3). These plotters are capable of solving a wide variety of photogrammetric problems. Many analogical operation-related solutions, such as relative and absolute orientations,

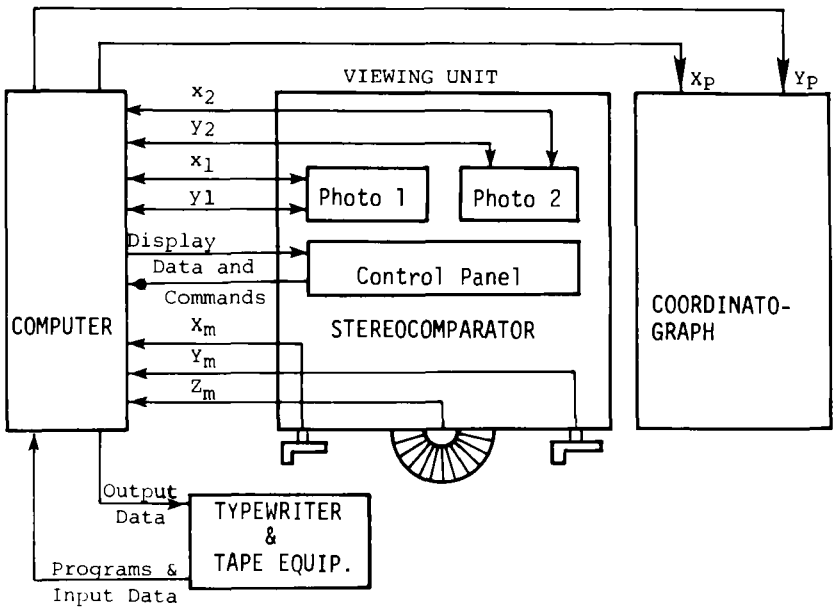


FIG. 3. Schematic diagram of a typical analytical plotter.

continuous mapping, and profiling, are possible in such instruments, apart from their being used as stereo- or monocomparators. A good example of a commercially available analytical plotter is the AP/C-3T, manufactured by the OMI S.p.A. of Rome, Italy, and marketed in the United States by the OMI Corporation of America, Alexandria, Virginia (Fig. 4). The instrument operates by solving analytical equations based on the observation data on the photo coordinates, the stored information, and the mathematical model relating the problem. Outputs from the comparator–computer combination activate servomotors to drive the plotting device (pencil or scriber) at the coordinatograph, which gives the graphical plotted information. Separately, digital information can be recorded or displayed automatically via the typewriter, tape, or card punching equipment. The adaptability of the analytical plotter to various problems, its various geometric patterns and the rapid accomplishment of such tasks are its primary assets.

With appropriate programming, the following tasks (and more) can be routinely performed at the instrument:

1. Interior orientation, involving consideration of appropriate projection, distortions, and dynamic corrections (if any) in each photograph.
2. Relative orientation of the stereo pair.
3. Absolute orientation of the stereo model.
4. Cartographic presentation of the data at the plotting table (coordinatograph), including the drawing of profiles in any direction.
5. Recording and storing of digital information.
6. Obtaining various derived information such as area, volume, and perimeter.

2. Simple Analytical Plotters

Analytical plotters with limited scopes have recently appeared on the market. The APPS-IV (manufactured by Ideas, Inc., Beltsville, Maryland, and marketed by Autometric, Inc., Arlington, Virginia) and the Zeiss Stereocord G2 (developed and marketed by Carl Zeiss, Oberkochen, West Germany) are two outstanding examples of this type of instrument that are remarkably suited for EM applications. In view of their few limitations, they are comparatively low priced and yet reasonably precise for most applications. The Stereocord G2 (illustrated with all its components in Fig. 5) is a modified Zeiss Stereotope, the analog mechanical computers having been replaced by an electronic desk calculator (for example, Hewlett-Packard Model 9830). The instrument has linear encoders on x, y, Δx, and Δy (the photo coordinates and the two parallaxes at a point) motions. These measurement values are digitized with the aid of a commercial pulse generator in conjunction with a counter (DIREC-1) and an interface



FIG. 4. Analytical plotter AP/C-3T. Courtesy of the OMI Corporation of America, Alexandria, Virginia.



FIG. 5. Stereocord G2. Courtesy of Carl Zeiss, Oberkochen, West Germany.

system. All numerical data for each stereo pair are stored on a magnetic tape cassette together with the calculator program required for data reduction. The stereotope part is used as a stereo viewer. All data reduction is performed automatically by the calculator, and the three-dimensional coordinates can be printed and displayed. When a plotter (for example, Hewlett-Packard Model 9872A, for multiple color plotting) is connected, it becomes a complete analytical plotter. One such instrument system has been used with success in plotting more than two thousand SEM and TEM stereo models (Ghosh *et al.*, 1978). This system was found to be about ten times as fast in its acquisition of three-dimensional data, although somewhat poorer (by about 50%) in accuracy, as a precision analogical stereo plotter like the Wild A10 Autograph.

II. Accuracy and Reliability

Technological, circumstantial, and economic factors interact in a complicated fashion in the design and successful conclusion of any project. Since this volume emphasizes the technical aspects only, the socioeconomic aspects will not be discussed. Some fundamental, important technical considerations are necessary in designing or evaluating any project relating to the extraction of quantitative data.

To an EM user, comparative or relative results from different specimens are more important than absolute accuracy. The variability between specimens sometimes far outweighs the importance of certain inaccuracies in individual results, which leads to a general reluctance to consider these accuracy-related aspects. Nevertheless, they are important considerations and are presented here for that reason.

Standard accuracy specifications and testing criteria are usually established for standard jobs. Topographical mapping is one good example of such work.

A. Standard Deviation

There is general agreement on the desirability of using "standard deviation" (or "error") or "root-mean-square error" to express accuracy directly or indirectly. Depending on the circumstances, however, the concept must be considered in terms of the following five possibilities in EM applications, for which the following notation is used ("i" refers to individual observations):

$t_1, t_2, \ldots, t_n$	observations; n is the number of measurements;
$x, y, z, \ldots$	unknowns; u is the number of unknowns;
$v_i = x - t_i$	corrections in direct observations;
$v_i = f(x, y, z, \ldots) - t_i$	corrections where unknowns are related by functions (linear or nonlinear);
$m_x, m_y, m_z, \ldots$	standard errors (deviations) of unknowns;
m and m_0	standard errors of one observation and one observation of unit weight, respectively;
p	weight of one measurement.

Possibility 1. Adjustment of Direct Observations of Identical Accuracy

In this case, $p = 1$; $x = (1/n)(t_1 + t_2 + \cdots + t_n) = [t]/n$ and $[v] = 0$ are assumed. These give, from basic statistical principles,

$$m = \pm\sqrt{[vv]/(n-1)} \qquad \text{and} \qquad m_x = \pm m/\sqrt{n} \tag{3}$$

Possibility 2. Adjustment of Direct Observations of Different Accuracy

In this case, one assumes

$$p = m_0^2/m_i^2; \qquad [vp] = 0$$

and

$$x = \frac{t_1p_1 + t_2p_2 + \cdots + t_np_n}{p_1 + p_2 + \cdots + p_n} = [tp]/[p]$$

These give

$$m_0 = \pm\sqrt{[vvp]/(n-1)} \qquad m_i = \pm m_0/\sqrt{P_i} \qquad m_x = \pm m_0/\sqrt{[p]} \tag{4}$$

Possibility 3. Adjustment of Linear Functions (in View of the Law of Error Propagation)

One assumes $x = a_1t_1 + a_2t_2 + \cdots + a_nt_n$, the a's being certain constants. These give

$$m_x^2 = a_1^2m_1^2 + a_2^2m_2^2 + \cdots + a_n^2m_n^2 \tag{5}$$

Possibility 4. Adjustment of Nonlinear Functions (in View of the Law of Error Propagation)

One assumes $x = f(t_1, t_2, \cdots, t_n)$. This gives

$$m_x^2 = \left(\frac{\partial f}{\partial t_1}\right)^2 m_1^2 + \left(\frac{\partial f}{\partial t_2}\right)^2 m_2^2 + \cdots + \left(\frac{\partial f}{\partial t_n}\right)^2 m_n^2 \tag{6}$$

Possibility 5. Adjustment of Intermediate Observations (in View of the Law of Error Propagation)

The original error equation can be set up in the form

$$T_i + v_i = f_i(x, y, z, \cdots) \qquad \text{with weights, } p_i = m_0^2/m_i^2$$

Next, approximate values of the unknowns can be introduced: $x = x_0 + dx$; $y = y_0 + dy$; etc. Consequently, the approximate function values can be computed:

$$f_i(x_0, y_0, z_0, \cdots)$$

Then the error equations can be written in absolute terms:

$$-t_i = -\{T_i - f_i(x_0, y_0, z_0, \cdots)\}$$

The transformed error equations can then be set in the following form:

$$v_i \cdot \sqrt{p_i} = a_i\sqrt{p_i}\,dx + b_i\sqrt{p_i}\,dy + c_i\sqrt{p_i}\,dz + \cdots - t_i\sqrt{p_i} \tag{7}$$

where the coefficients are $a_i = (\partial f_i/\partial x)_0$; $b_i = (\partial f_i/\partial y)_0$; $c_i = (\partial f_i/\partial z)_0$, etc. The changes (corrections), dx, dy, dz, etc., are computed from the "normal equations" set after Eq. (7). The standard deviations (errors) are given by

$$m_0 = \pm\sqrt{[vvp]/(n-u)} \qquad \text{and} \qquad m_x = m_0\sqrt{q_{xx}}$$
$$m_y = m_0\sqrt{q_{yy}} \qquad m_z = m_0\sqrt{q_{zz}} \qquad \text{etc.} \tag{8}$$

where the q's are the weight reciprocals (from variances).

Discussion of the law of error propagation, the principles of least squares, the formation and solution of normal equations, etc., can be found in standard books [e.g., Hirvonen (1971) or Mikhail (1976)].

B. Mapping Accuracy

There is widespread agreement for separating planimetry (by combining X and Y coordinates) from height (Z coordinate). There is, however, a continuing debate

whether the planimetric accuracy should be expressed in terms of univariate or bivariate (consisting of two variables, X and Y) data.

In keeping with common practice in mapping, the *linear standard error* for the X coordinate is

$$\sigma_X = \left\{ \frac{\sum_{i=1}^{n} (\Delta X_i)^2}{n-1} \right\}^{1/2} \tag{9}$$

where ΔX_i are the coordinate discrepancies between accepted (as true or absolutely correct—for example, from calibrated grid observation data) and mapped positions at each test point; and n is the total number of points used for checking. Similarly, linear standard errors for the Y and Z coordinates are obtainable. It is also debatable whether n or $n-1$ should be used in the denominator of Eq. (9). For large values of n, however, the difference is not significant.

Next, the *planimetric standard error* (σ_P^2) is expressed by

$$\sigma_P^2 = \sigma_X^2 + \sigma_Y^2 \tag{10}$$

Some prefer to use the *two-dimensional* (*circular*) *standard error* in such cases. This is the error in a quantity defined by two random variables, with the basic assumption that planimetric errors are expected (in continuous mapping) with equal probability in any direction and with equal magnitude, which is a very popular concept with many practitioners. The circular standard error (σ_c) is related to σ_p as shown in Eq. (11).

$$\sigma_c = \sigma_p / \sqrt{2} \tag{11}$$

For interesting ideas in this regard, see Thompson and Rosenfield (1971).

C. Contouring

The permissible minimum contour interval should be related to the obtainable accuracy in height. A relationship widely used in the world of mapping is

$$\sigma_Z = 0.3\, C \tag{12}$$

where σ_Z is the standard error in Z obtainable from the working system, and C is the permissible minimum contour interval.

Note: The factor 0.3 in Eq. (12) is based on the fundamental assumption that, with normal distribution of errors, spot heights as derived by interpolation from contour lines are expected to be in error by more than σ_Z at not more than 10% of the points. Further discussion on contouring is given by Richardus (1973). A very logical question still remains concerning whether correct statistical theory is applied in using this factor. The practitioner, however, may have other strong reasons for selecting a specific contour interval.

D. Stability and Repeatability

Stability and repeatability are two interrelated words often used to express the same meaning. In assessing a complex system (such as three-dimensional EM mapping), Leipholz (1970) postulates that first an "unperturbed state" of the system be specified. Next, a perturbation is applied by repeating the same study but changing only the specific "element" or "parameter" being evaluated. Certain statistical measures and tests will characterize the state of the system. Alternatively, without changing the elements or parameters, the system can be evaluated in terms of the output under repeated performances.

Stability tests on parameters (or elements) in EM systems indicate that, with the usual consideration that 90% of the checked items should pass a test, even at the significance level of 0.02, the parameters (photogrammetric mensuration-related elements) are statistically stable (Maune, 1973; Nagaraja, 1974; El Ghazali, 1978).

Repeatability tests on X, Y, and Z coordinates generally indicate results consistent with those obtained after the parameters have been tested (El Ghazali, 1978). These results appear to be even better, usually being statistically stable at a significance level of 0.01 for all three coordinates.

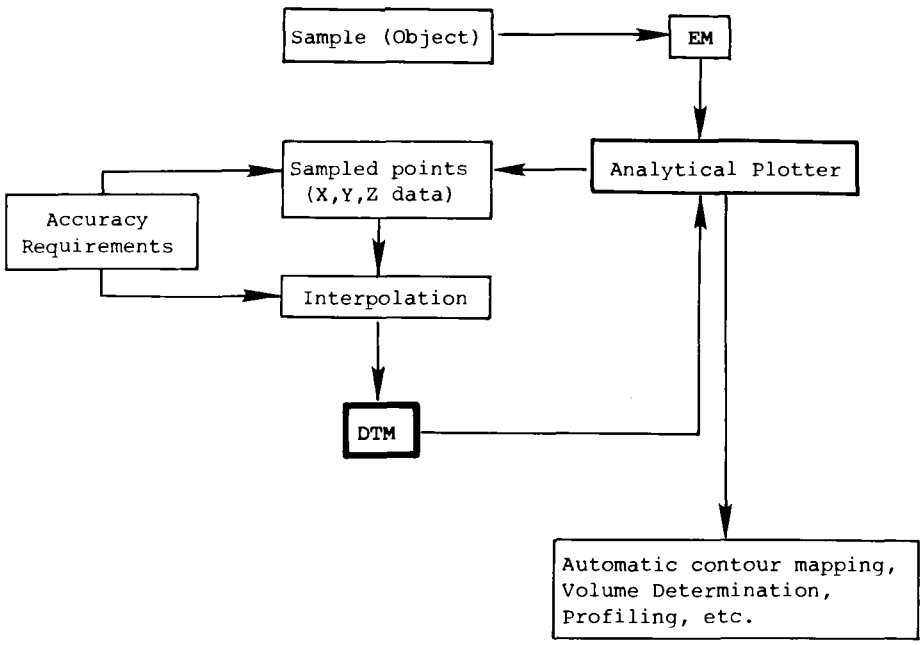


FIG. 6. Role of DTM with regard to an analytical plotter.

III. The Digital Terrain Model and Computer Mapping

A digital terrain model (DTM) is a numerical description of the surface of an object in terms of the X, Y, and Z coordinates of points on the surface. This is usually done with an ordered array of numbers, which can be based on measured and derived (by interpolation) coordinates of discrete points on the surface. The

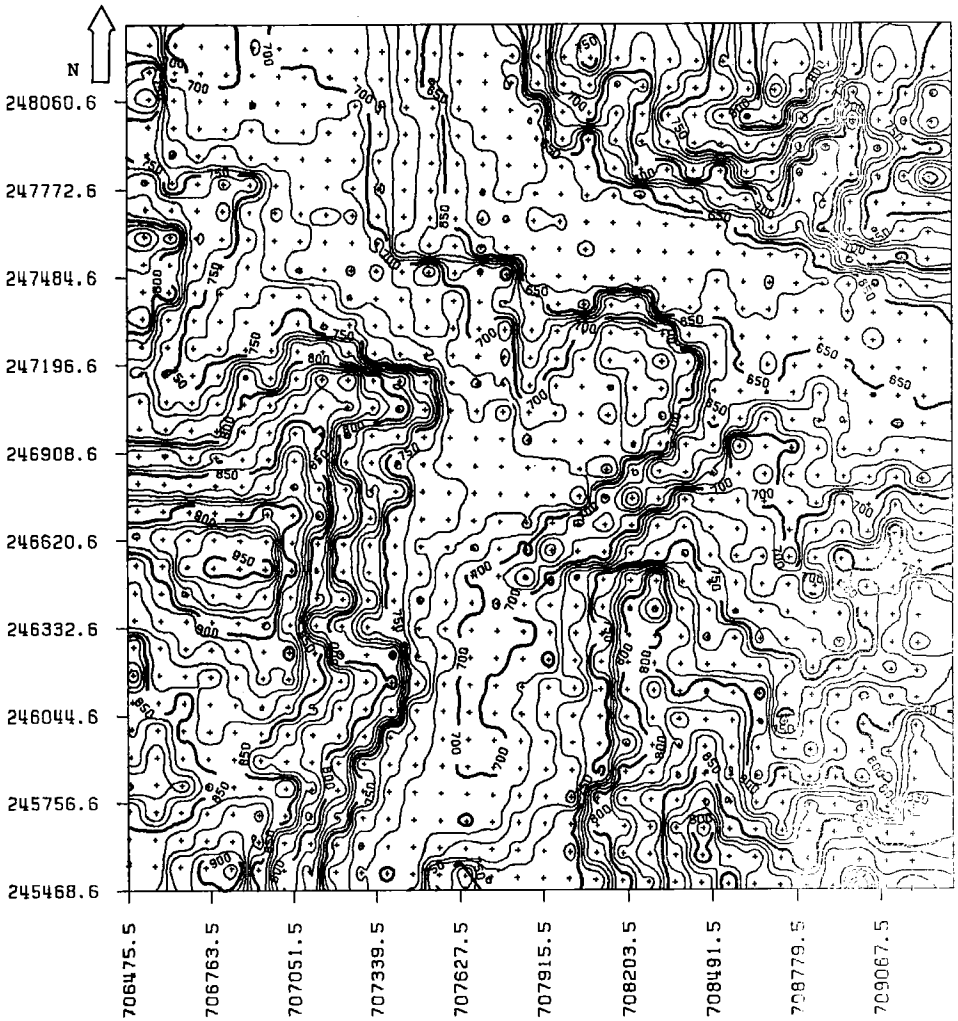


FIG. 7. Contour plot at a Versatec Plotter; automated interpolation from a photogrammetrically generated DTM. Area, Laufen, Switzerland; contour interval, 10 meters; graticule values in meters. Adapted from Adigüzel (1979).

derived data depend on the directly measured data based on actual observations, and the corresponding interpolation rules. The DTM concept has been widely used in many applications since its inception at the Massachusetts Institute of Technology (Miller and Laflamme, 1958).

Any work involving DTM has two essential phases: (1) *data sampling* (acquisition), and (2) *data interpolation* (processing). Both require a considerable amount of *data storage and management capabilities,* the efficient handling of which requires the use of high-speed computers.

There is also an understanding in the scientific community that DTM data have much more value than simple mapping applications. Computer-controlled cartographic operations have enhanced such applications in recent years. One major benefit is the ability to store the data for use on a real-time basis or for instantaneous statistical or other analyses. In this regard, the use of DTM with an analytical plotter offers tremendous potentials. Figure 6 describes such a system in schematic form. One application of computer mapping with EM data at an analytical plotter has been reported in Ghosh and El Ghazali (1979). Furthermore, modern technology is so advanced that computer mapping with DTM

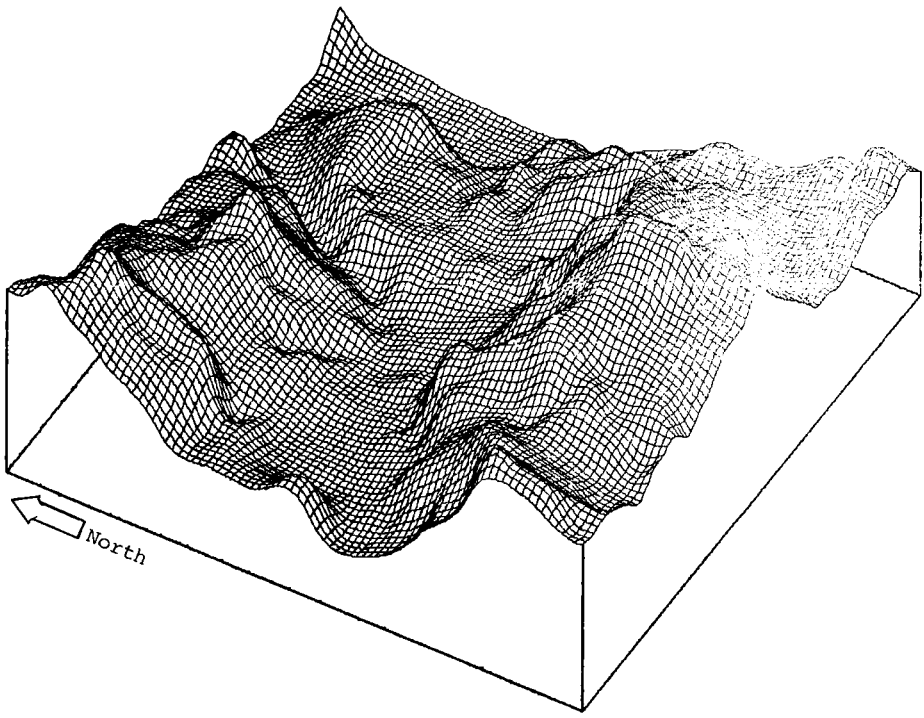


FIG. 8. Perspective representation by computer graphics of area shown in Fig. 7. Viewing tilt, 45°; rotation of block, 60°. Adapted from Adigüzel (1979).

data and corresponding perspective diagramming is routinely possible, examples of which are given in Figs. 7 and 8. Adigüzel (1979) and Ayeni (1976) have presented interesting ideas on various aspects and applications of DTM. For further discussion of interpolation techniques, see Schut (1977).

The DTM approach also offers many possibilities for qualitative and quantitative studies of dynamic objects by way of "differential mapping"—that is, the mapping of an object surface relative to itself in view of changes in time and space or relative to another object with which it may bear some physical and dimensional relationships.

References

Adigüzel, M. (1979). Digital terrain models and their applications to perspective diagramming and contouring. M.Sc. Thesis, Ohio State University, Columbus.

Ayeni, O. (1976). Considerations for automated DTM's with applications in differential photo mapping. Ph.D. Dissertation, Ohio State University, Columbus.

Boyde, A. (1968). *Beitr. Elektronenmikrosk. Direktabbildung von Oberflachen* **1**, 94-106.

Boyde, A., and Ross, H. F. (1975). *Photogramm. Rec.* **8**, 408-457.

El Ghazali, M. S. (1978). Some photogrammetric investigations of scanning and transmission electron micrography and their applications. Ph.D. Dissertation, Ohio State University, Columbus.

Ghosh, S. K. (1971). *Photogramm. Eng.* **31**, 187-191.

Ghosh, S. K., and El Ghazali, M. S. (1979). "Application of Digital Terrain Models (DTM) to Carbon Black Aggregates," OSU Geodetic Sci. Rep. No. 283. Ohio State University, Columbus.

Ghosh, S. K., El Ghazali, M. S., Deviney, M. L., and Mercer, H. N. (1978). *In* "Three Dimensional Mapping by Combining Transmission and Scanning Electron Microscopes," Int. Soc. Photogrammetry Commission V Rep. (K. Torlegard, ed.), pp. 1-10.

Hirvonen, R. H. (1971). "Adjustment by Least Squares in Geodesy and Photogrammetry." Frederick Ungar Publishing, New York.

Leipholz, H. (1970). "Stability Theory." Academic Press, New York.

Maune, D. F. (1973). Photogrammetric self-calibration of a scanning electron microscope. Ph.D. Dissertation, Ohio State University, Columbus.

Mikhail, E. M. (1976). "Observations and Least Squares." IEP-A Dun-Donnelley Publisher, New York.

Miller, C. L., and Laflamme, R. A. (1958). "Digital Terrain Model System Manual," Mass. H.P.S. 1 (13). Massachusetts Department of Public Works and US Bureau of Public Roads, Boston.

Nagaraja, H. (1974). Application studies of scanning electron microscope photographs for micromeasurements and 3-D mapping. Ph.D. Dissertation, Ohio State University, Columbus.

Oshima, T., Kimoto, S., and Suganuma, T. (1970). *Photogramm. Eng.* **36**, 874-879.

Richardus, P. (1973). *Photogrammetria* **29**, 81-107.

Schut, G. H. (1977). "Review of Interpolation Methods for DTM." Archives of the International Society for Photogrammetry, Helsinki Congress, Helsinki, Finland.

Thompson, M. M., and Rosenfield, G. H. (1971). *Surv. Mapping* **31**, 57-64.

Wood, R. (1972). *Photogramm. Rec.* **7**, 454-465.

Chapter 11

Application to Single Specimens

SANJIB K. GHOSH

Department of Photogrammetry,
Laval University,
Québec, P.Q., Canada

I. Applications of the Scanning Electron Microscope 194
II. Applications of the Transmission Electron Microscope 195
III. Combining SEM and TEM Information 197
References 198

The idea of using the transmission electron microscope (TEM) for stereoscopic measurements of specimen features occurred at an early stage in its development (Helmcke, 1954). The TEM was believed to provide an essentially parallel projection, at least when used at high magnifications. Very simple geometric relationships yielded satisfactory results, particularly when the specimens were tilted symmetrically between two attitudes. In such cases, analogical-graphical mapping of planimetry and a separate solution for heights determined by means of a simple parallax equation [see Eq. (20) in Chapter 9] would suffice.

The first photogrammetric work with the scanning electron microscope (SEM) did not consider the solutions to be significantly different from those obtained with the TEM. It was soon recognized (Wells, 1960), however, that the projection is evidently perspective, at least at very low magnification ranges, where the micrographs are the sharpest, and the error arises through the use of false assumptions in the projection.

Since the TEM and the SEM offer different types of information, it is appropriate to discuss their applications to single specimens in separate sections. On the other hand, in certain specimens an amalgamation of data from both yields information that cannot be obtained with any other system. That aspect will be discussed in the third section of this chapter.

Copyright © 1981 by Academic Press, Inc.
All rights of reproduction in any form reserved.
ISBN 0-12-564122-2

I. Applications of the Scanning Electron Microscope

In the SEM, the focused beam impinges upon the surface of the specimen. The electron radiation is used for two synchronous scanning beams, one sweeping over the surface of the specimen, and a corresponding second one over a cathode ray tube (CRT), which is recorded with a camera. The micrograph thus obtained shows the surface features of the specimen. Comparatively low resolution (~6 nm) and the absence of subsurface features are the two primary characteristics of SEM micrographs.

Many SEM users find it convenient to use cameras capable of recording the specimen almost instantaneously (for example, a Polaroid Land camera). These cameras are designed for photographing CRT displays at 1:1 or lower scales. The total magnification, however, always refers to the image recorded finally by the camera. Therefore, three-dimensional mapping cannot always be referred to the scale of the visual (CRT) display. Furthermore, with the polaroid type of camera, although paper prints may be very convenient, for high-precision mapping one should insist on glass plates or film. Two major considerations lead to this recommendation. First, paper as the emulsion carrier is seldom adequately stable dimensionally. Second, most of the precision photogrammetric measuring instruments are designed for transparencies.

As was indicated in Section IV of Chapter 9, resolution of the SEM system plays a major role in three-dimensional mapping. A resolution of 6 nm, for example, with a magnification of 10,000× corresponds to 0.06 mm on the micrograph. The measuring instrument having a standard error of less than 0.06 mm on the photo should then be considered as adequate. Higher magnification would tend to result in unsharp images. Lower magnification would give sharp photos but would demand precision instruments, a stable photo base, etc. Therefore, depending on the SEM and the measuring instrument, an optimum magnification (in view of the desired accuracy) must be decided upon.

The following working steps are necessary for three-dimensional mapping with SEM micrographs:

1. Determination of the optimum magnification and parallactic angle.
2. Consideration of the distortions in the micrographs, and the method and extent of their elimination.
3. Consideration of the mathematical model(s) with regard to the specific instrument, the magnification, and the degree of refinement desired.
4. Obtaining the necessary pair of micrographs at the SEM.
5. Performing the orientations (relative and absolute) at the stereo plotting instrument.
6. Obtaining three-dimensional data and/or graphical-cartographic presentation of the data.
7. Obtaining other necessary derived data.

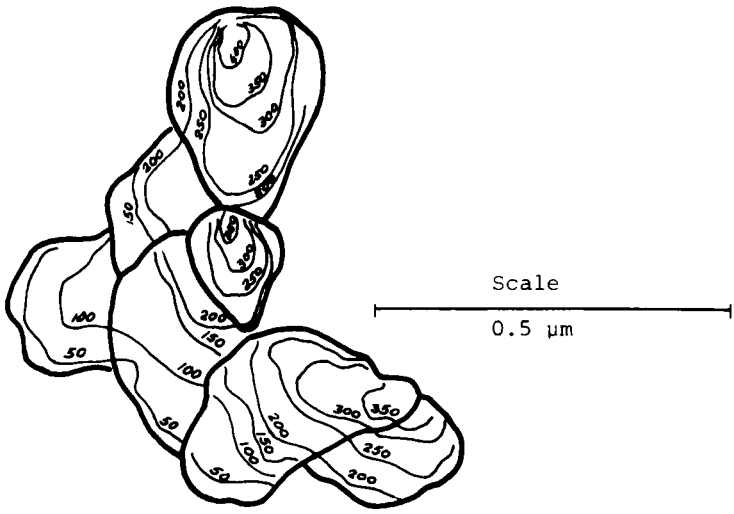


FIG. 1. Contour map of an aggregate of carbon black with a SEM micrograph pair at the Wild A7 Autograph. Technical data: scale of micrographs 12k×; scale of stereo model 27k×; scale of contour map 108k× (note scale change due to reproduction). stereo angle (S) 15°; pretilt (left photo) −7°30′; contour intervals 50 nm. The thick lines indicate grouping of particles for specific investigations.

An example of a contour map plotted at a Wild A7 stereo plotter with a pair of SEM micrographs is illustrated in Fig. 1. In using an instrument with perspective projection for such high-magnification micrographs, there is bound to be an appreciable scale error in the Z coordinate as compared with the X and Y coordinates, which has to be accounted for. Accordingly, the height values must be appropriately corrected for use in scaling as well as in contouring.

II. Applications of the Transmission Electron Microscope

In the TEM, the image is formed by the electromagnetic lens; it is a measure of the scattering power of each point as the electron beam passes in the specimen, which is an ultrathin section. The image is magnified and can be displayed on a fluorescent screen. To obtain a micrograph, however, the beam is transmitted through the specimen, defocused below the specimen, and projected onto a photographic emulsion surface. High resolution (~0.3nm) and loss of surface features are two typical characteristics of TEM micrographs. Of course, if three-dimensional data of the subject are to be obtained, it must be no larger than the thickness of the specimen slice. This serious limitation does not apply to the SEM.

Basic photogrammetric considerations concerning optimum magnification, op-

timum stereo angle, and the working steps are the same as for the SEM application. Since the TEM has a much better resolution than the SEM, however, stereo plotting from TEM micrographs offers minimal problems when compared with plotting from SEM micrographs.

Figure 2 illustrates the cartographic representation of the same carbon black aggregate as was shown in Fig. 1 at the same Wild A7 Autograph with a pair of TEM micrographs. Depending on the specimen, contour mapping in the true sense of the term may be impossible, as in this case where the particles in TEM stereo appear as disks without features on their surfaces. However, determination of the height of specific points or levels poses no problem.

Since TEM micrographs provide no background, orientations of the stereo model by using points outside the specimen (in view of interpolation) may puzzle an uninitiated photogrammetrist. This difficulty can be circumvented by using points at or near the perimeter of the sample. In the same context, one must select a specific point as the height datum (zero height). In Fig.2, the number 1 refers to such a point, being at the edge of the lowest particle of the aggregate.

The problem of appreciable scale error in the Z coordinates when one is using a perspective projection type of instrument exists in this case also. Appropriate corrections are therefore necessary. Without due consideration of such affinity in the stereo model, the necessary rotations of the model may not be adequately

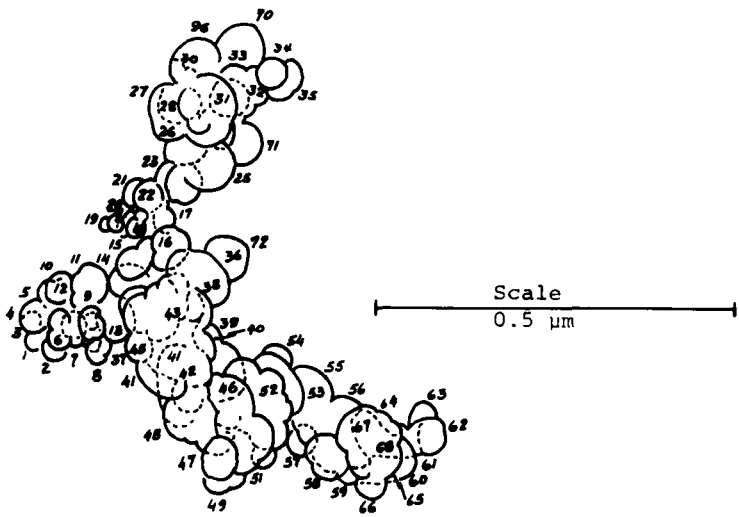


FIG. 2. Cartographic representation of an aggregate of carbon black (the same as in Fig.1) with TEM micrograph pair at the Wild A7 Autograph. Technical data: scale of micrographs 18k×; scale of stereo model 36k×; scale of plotting 108k× (Note scale change due to reproduction). stereo angle (S) 15°; pretilt (left photo) −7°30′. The numbers are for reference to a list of heights, which is not reproduced here. The broken lines indicate segments of perimeter lines below other particles and yet are visible in stereo, owing to the nature of the TEM.

correct, and the final three-dimensional data may reveal, albeit mistakenly, unusual deformations, adjustment of which may not be that easy.

III. Combining SEM and TEM Information

Amalgamation of three-dimensional information obtained from the SEM and the TEM on the same sample would certainly result in the best possible representation of the sample. It involves superposing the data from one stereo model onto the other. It can be done conveniently either at the stage of the stereo model or at the stage of graphical plotting. It also assumes the same absolute orientation of the two models at the stage of amalgamation.

The two imaging systems being different, such orientation requires careful planning for the extraction of the three-dimensional data. When an empirical graphical display of the data is desired, it is best done at the stage of final plotting. One such example is given in Fig.3, where the data from Figs. 1 and 2 are combined. In this case, after initial trials, in view of the desired scientific investigations, scale considerations for the various working steps were established as in Fig.4. Most of the stereo-plotting precision instruments have the capability of such flexibility. Accurate and absolute orientation of the stereo models in such applications is imperative. There should be also distinctly identifiable points common to the two models on which such amalgamations are to be

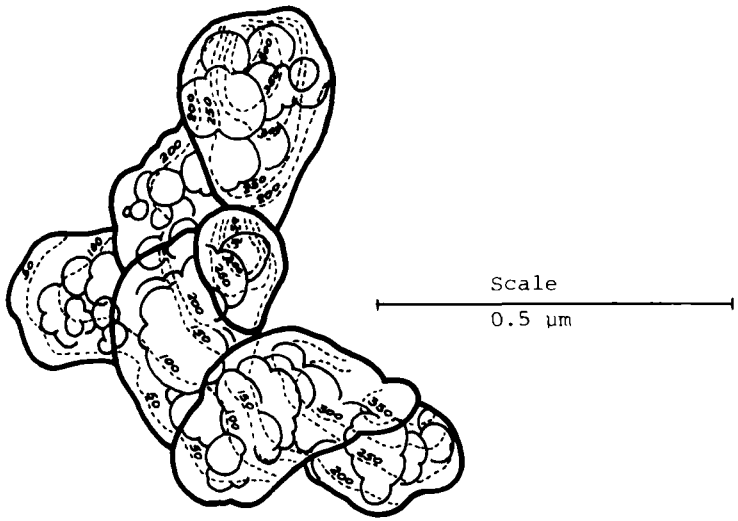


FIG. 3. Combination of TEM and SEM plots (from Figs. 1 and 2). (*Note:* The broken lines indicate the contours at the surface of the sample; the rest are as described in the respective figures.)

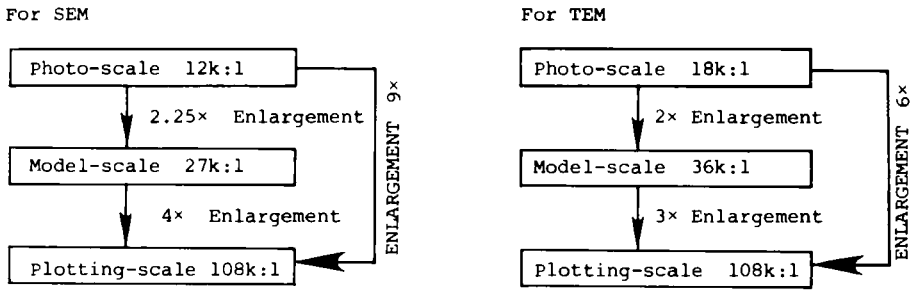


FIG. 4. Scale considerations at various working steps.

based. Assuming that the individual models are free from deformations, one would require only three widely distributed points on the sample. With more points, however, a better fit is expected, the degree of reliability depending on the number, distribution, and accuracy of locating such points.

If there is the capability of digital terrain modeling, such superposition is better done at the stereo model. Scaling, rotating, and translating one model with respect to the other are then operations that are better performed with a high-speed computer. An interfaced plotter will then complete the job of displaying the desired information.

REFERENCES

Helmcke, J. G. (1954). *Optik* **11**, 201-225.
Wells, O. C. (1960). *Br. J. Appl. Phys.* **11**, 199-201.

METHODS IN CELL BIOLOGY, VOLUME 22

Part III. Quantitative Three-Dimensional Reconstruction

Chapter 12

Introduction

JOACHIM FRANK

Division of Laboratories and Research,
New York State Department of Health,
Albany, New York

I. Quantitative Methods of Three-Dimensional Reconstruction in Electron Microscopy 199
II. Fourier Methods of Reconstruction 202
A. Fourier Representation of an Image 202
B. Fourier Representation of a Three-Dimensional Object 204
C. The Projection Theorem, and the Principles of Three-Dimensional Reconstruction 205
D. Five Different Terms of Resolution 208
III. Direct-Space Methods of Reconstruction 209
IV. Alignment of Projections 211
A. Use of Fourier Transform Phases 211
B. Center of Gravity 212
C. Cross-Correlation 212
References 212

I. Quantitative Methods of Three-Dimensional Reconstruction in Electron Microscopy

Some of the previous chapters deal with semiquantitative methods of combining and interpreting three-dimensional information about biological ultrastructure. Stereoscopy, for instance, produces a three-dimensional mental image of the object studied (see Chapter 2 by King in this volume), but fails to give an unambiguous map containing a point-for-point account of the object's three-dimensional density. Although the features of the mental image can to some

Copyright © 1981 by Academic Press, Inc.
All rights of reproduction in any form reserved.
ISBN 0-12-564122-2

extent be communicated between one observer and another, they do not lend themselves to a quantitative, reproducible characterization of the object.

The methods to be discussed in the following chapters have the goal of rendering a faithful, quantitative three-dimensional model of the ultrastructure. In serial section reconstruction (see Chapter 13), the object is dissected into a series of successive slices for investigation with the conventional-voltage or high-voltage transmission electron microscope. Micrographs of these slices, or their representations in the computer, are subsequently stacked together into a three-dimensional representation of the object, with fiducial marks being used to bring consecutive micrographs into register.

As an alternative to serial section reconstruction, reconstruction of a biological object from a series of projections is feasible in experimental situations where the object is fully penetrated by the beam and where the optical density in the electron micrograph can be quantitatively related to the object's mass density. This requirement limits the object thickness to a few hundred angstroms for a conventional-voltage electron microscope. However, the high-voltage electron microscope allows thicknesses of up to 3 μm to be used, making possible the reconstruction of thick tissue sections from projections (Johnson, 1975).

The three-dimensional reconstruction of an object from projections is based on a quantitative model describing the relationship between object and image. For many electron microscopic applications in the medium-resolution range, the electron micrograph can be interpreted as a shadowgraph of the object's mass density distribution. The predominant mechanism for image formation is the absorption of electrons by scattering outside the objective aperture. This absorption, as a function of mass thickness, follows an exponential law (Hall, 1953). Since the optical density of the micrograph is proportional to the electron intensity over a wide range, the projected mass density is proportional to the logarithm of the optical density. Linearization of this functional relationship is possible if only a small argument range is being used.

A more complicated situation arises in the high-resolution range, where the electron microscopic phase contrast comes into play. In the same way as phase-contrast light microscopy, the shift of the electron wave by the object produces additional image contrast through a mechanism of constructive interference with the unscattered wave. For image details of a given size, the amount of phase contrast and its polarity depend, in a complicated way, on the size of additional phase shifts produced by wave aberrations and defocusing of the objective lens (Thon, 1965). The resulting image may be a severely distorted representation of the object's projection. Electron micrographs containing significant high-resolution ($<$2.0 nm) information require a correction (e.g., Erickson and Klug, 1971), which must be applied before the three-dimensional reconstruction is carried out.

The mathematical basis for reconstruction of a three-dimensional density dis-

tribution from its projections, which had been known as early as 1917 (Radon, 1917), found its first successful application in the reconstruction of the bacteriophage T4 phage tail (DeRosier and Klug, 1968). Subsequent development of the mathematical and computational techniques extended the field of application to spherical virus particles (Crowther, 1971) and to molecular assemblies with two-dimensional order (Henderson and Unwin, 1975; see also Chapter 14 of this volume), thus establishing three-dimensional reconstruction as a powerful method in molecular-structure research (e.g., reviews by Crowther and Klug, 1975; Mellema, 1980).

There are two approaches to three-dimensional reconstruction from a tilt series: (1) The Fourier method (DeRosier and Klug, 1968) is based on the Fourier projection theorem, which relates the Fourier transforms of the projections to the Fourier transform of the three-dimensional object density. (2) The real-space methods (e.g., ART, Gordon *et al.*, 1970) are based on the direct-space relationship between projections and object density. Subsequent sections of this chapter will give an introduction to the concept of the Fourier transform and an outline of the two approaches.

Because of the mathematical tractability and the immediate physical interpretation of the Fourier transform in terms of the object's scattering, only the Fourier method of reconstruction has gained practical importance in electron microscopic structural research. However, the reconstruction of thick mounted cell sections from high-voltage electron microscope images (Johnson, 1975; Frank *et al.*, 1980), which is closely related to medical tomography, is likely to be a field of application for the real-space methods. The computational convenience of these methods becomes important when large volumes of data must be handled.

Owing to the design of the electron microscope and to the small dimensions of the specimen support, the tilt angle is limited to a maximum range of about $\pm 60°$. This limitation poses serious problems in the effort to retrieve the complete information on the three-dimensional structure. The information gap produced by the angular limitation may be filled in either one of the following ways. (1) For objects with helical or point-group symmetry, the views in the inaccessible range can be generated from views in the accessible range by symmetry operations. For certain helical objects, a single view provides sufficient information to compute the three-dimensional density (DeRosier and Klug, 1968). To give another example, a single view of a virus particle with icosahedral symmetry generates 59 symmetry-related views (Crowther, 1971). (2) For objects without helical or point-group symmetry, which present different views on the specimen grid, the micrographs from a single-tilt series contain overlapping ranges of views that may be combined to span the entire 180° range. The situation arises because the objects can be deposited on the grid in large numbers. Unwin (1977) was able to combine the normal view of the ribosome tetramer crystal with the edge-on view to obtain a full span of three-dimensional data.

If neither of these situations applies,* one can attempt to maximize the information yield in the angular range available. Here the design of the goniometer stage becomes important: Double-tilt stages are generally preferable to single-axis tilt stages, because they allow the maximum tilting angle to be accessed in all azimuthal directions (conical-collection geometry). However, for objects that occur in random azimuthal positions on the specimen grid—for example, single molecules (Frank *et al.*, 1978) or patches of a crystal (Henderson and Unwin, 1975)—a single-axis tilt stage will yield data equivalent to those obtained by conical collection from a fixed object.

II. Fourier Methods of Reconstruction

A. Fourier Representation of an Image

Because of the important role of Fourier techniques in three-dimensional reconstruction, this section will give a brief introduction to the Fourier representation of images, avoiding all mathematical formulations. For a detailed introduction, more extensive reviews (Mellema, 1980) or standard textbooks on Fourier theory should be consulted (Bracewell, 1965; Goodman, 1968).

Figure 1a shows the averaged axial projection of a negatively stained cytochrome oxidase crystal as obtained by Goldfarb *et al.* (1979). This image was constructed by summing a number of two-dimensional sine waves (Fig. 1b) with different spatial frequencies (number of full cycles of the sine wave per unit length), directions, amplitudes, and phases (positions of the wave with respect to the image origin). Any image can be represented by a series of two-dimensional sine waves. The number of different sine waves needed depends on the image size and on the size of the smallest significant detail in the image (resolution distance).

The sine wave can be ordered into a two-dimensional scheme according to the size of the components of their spatial frequency vectors: 1 cycle per unit length in x direction and 0 cycle in y direction would be denoted by (1, 0), 3 cycles in x direction and 2 cycles in y direction would be denoted by (3, 2), etc. To have a complete record of the information needed in the sine-wave representation of the image, one must write down, for each point of the scheme, the amplitude and the phase shift of the corresponding sine wave. This scheme is the *Fourier transform*

*Single molecules presenting different views owing to their different orientations on the grid may be unequally affected by the staining and drying process. Data from differently oriented molecules may therefore be inconsistent.

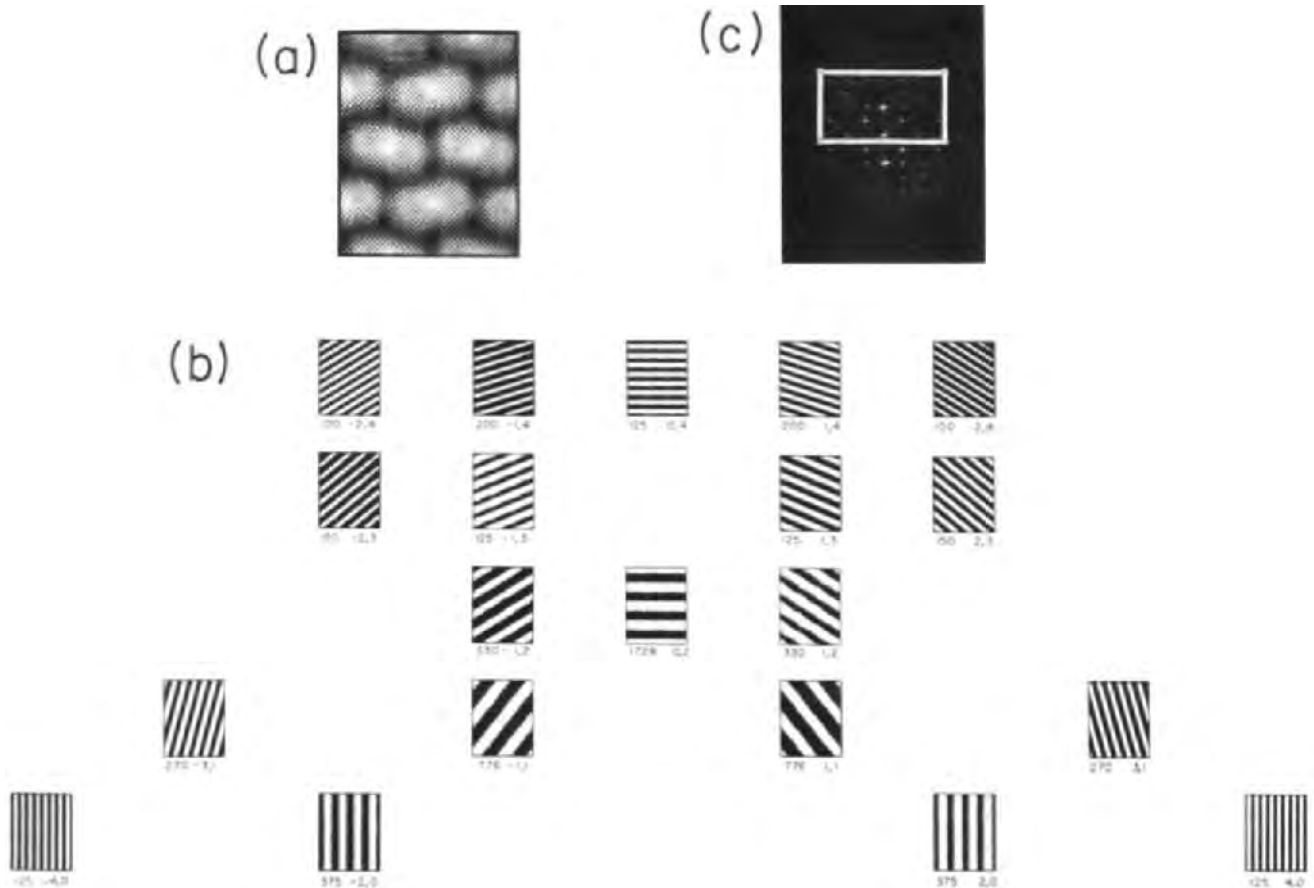


FIG. 1. Construction of a projection of a cytochrome oxidase crystal from two-dimensional sine waves. The image (a) can be generated by superposition of the sine waves in (b) using the weights indicated. The sine waves have been arranged and indexed according to the positions of the corresponding reflections in the Fourier transform (c).

or *Fourier expansion* of the image.* The Fourier transform is an alternative mathematical representation of the image density. This representation frequently simplifies the theoretical and computational analysis of images for several reasons:

1. The Fourier transform can be interpreted in terms of the scattering of the object.
2. The influence of instrument aberrations can be formulated in a much simpler way than in the direct-space representation.
3. Signal and noise portions of the image appear separated in the Fourier transform when the image of a repeating structure is analyzed. The noise portion can, therefore, be filtered out from the transform by use of an appropriate mask.

If the image consists of a two-dimensionally repeating pattern, then obviously only sine waves that fit into the lattice describing the repeating positions will be needed for the representation. These waves will have spatial frequencies that are multiples of the basic spatial frequencies of the repeating pattern. The Fourier transform thus consists of sharp peaks arranged on a regular lattice (Fig. 1c), one for each sine wave.

There are fast computer algorithms for computation of the Fourier transform (forward transformation) of an image represented by a rectangular array of optical density readings, as well as for computation of an image from its Fourier transform (inverse transformation or Fourier synthesis) (Cooley and Tukey, 1965). Special implementations of the algorithm allow the use of small computers even for large images that do not fit into the core memory.

B. Fourier Representation of a Three-Dimensional Object

In the previous section it was shown that two-dimensional images can be represented by a series of two-dimensional sine waves. Similarly, three-dimensional density distributions can be represented by a series of three-dimensional sine waves. These are more difficult to visualize but are constructed in full analogy to the two-dimensional waves. A sine wave with the spatial frequency components $x^* = 0$, $y^* = 0$, $z^* = 1$, denoted by (0, 0, 1), would perform 1 full cycle per unit length in the z direction (parallel to the electron beam). Since the x and y components are 0, the value of the wave would depend only on z. To take another example, a sine wave indexed (1, 1, 1) would change fastest in the diagonal direction of the three-dimensional coordinate system.

*Instead of sine waves with amplitudes and phases, the usual Fourier representation employs the related complex exponential function with complex coefficients. However, this difference does not impair an understanding of the main concepts to be presented here.

Again, the waves can be ordered according to their indices, but now a three-dimensional scheme is needed to present the amplitude and phase of each wave—the *three-dimensional Fourier transform*. It is common to refer to the scheme, with its three coordinate axes and its potentially infinite extension, as the Fourier space.

Owing to physical limitations of the image-forming instrument, only details above a certain size or resolution distance will be present in the image. In terms of the sine-wave representation, this means that high-indexed sine waves, which change more frequently than a certain limiting number of cycles per unit length, do not contribute to the object. The three-dimensional Fourier transform of the object as measured in the electron microscope therefore has a finite extension, allowing it to be enclosed by a "sphere of resolution."

Several different terms of resolution, which should not be confused with one another, must be dealt with in any treatment of three-dimensional reconstruction from micrographs of biological objects. A separate section of this chapter is devoted to an explanation of the various terms.

It is sufficient for the reconstruction of the three-dimensional object density that the Fourier transform is known within the sphere of resolution. This means that only a limited number of Fourier transform values must be measured, since the Fourier transform does not change abruptly within a spatial frequency range that is inversely proportional to the linear dimension of the object. A large object therefore requires a fine grid in Fourier space on whose points the measurements must be provided, whereas a small object requires only a coarse grid.

C. The Projection Theorem, and the Principles of Three-Dimensional Reconstruction

Directly accessible by measurement are two-dimensional projections of the object. The basis for the Fourier approach to reconstruction is the Fourier projection theorem. It provides a recipe for measurement of the three-dimensional Fourier transform of an object from the two-dimensional Fourier transforms of its projections.

This theorem states: The Fourier transform of the object's projection in a given direction is equal to a central section (normal to the direction of projection) of the object's three-dimensional Fourier transform. This means, in particular, that the $z^* = 0$ section of the three-dimensional Fourier transform of an object is identical to the Fourier transform of its axial (untilted) projection. Thus, each different view of the object generates a different Fourier plane filled with data. If the object could be tilted in all possible directions with respect to the beam, the entire three-dimensional Fourier transform would be covered by data lying on two-dimensional planes that intersect the origin in different directions. To obtain a valid model of the object, however, one must furnish the values of the Fourier

transform on a regular grid. This can be a three-dimensional cartesian or a cylindrical coordinate system, the latter being more appropriate for objects with helical symmetry (Fig. 2). Interpolation and functional-expansion schemes have been devised for computing the regular grid values from the measured values of the Fourier transform.

As mentioned above, only a limited angular range can be accessed by the electron microscope goniometer. Because of the projection theorem, this means that a certain region within the limiting sphere of resolution of the three-dimensional Fourier transform cannot be filled with data unless the object possesses symmetries. In the single-axis tilt experiment the region is shaped like two opposed wedges of an orange, whereas in a tilt series obtained with a double-tilt stage the region has the shape of a double cone. These gaps cause severe artifacts in the reconstructed object model. To analyze the nature of the artifacts and to assess the performance of the reconstruction scheme, one must consider the reconstruction of a single object point. The tilting experiment and the subsequent synthesis provide a representation of the point in three dimensions, the so-called point-spread function. Owing to the resolution limitations of the electron microscope, the best representation to be expected from a reconstruction experiment is a blurred sphere, and this only if views from all directions are available. The limitation of the angular range means that no information is present on the extension of the object in directions close to the direction of the electron beam in the microscope. The point-spread function is blurred in this direction and has a "sputter" appearance; that is, it shows small regions of high density with alternating sign radiating from the center. The model computation (Fig. 3) by Hoppe

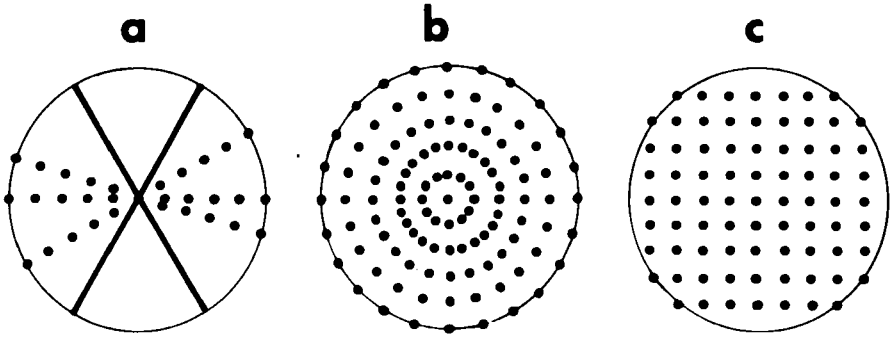


FIG. 2. Three different Fourier sampling geometries. (a) Fourier sampling points on a plane normal to the tilting axis, as obtained by measurements. Each micrograph, sampled on a square grid and then Fourier-transformed, contributes a central, one-dimensional section with equispaced Fourier coefficients. The resolution range is limited by a circle. The range devoid of projection measurements is due to physical limitations of the tilt stage. (b) Fourier sampling grid on a plane normal to the axis of a cylindrical coordinate system. (c) Regular Fourier sampling grid on a plane of a three-dimensional cartesian coordinate system.

and Grill (1977) shows such a function obtained with a very high resolution currently not achieved in the electron microscope. The oscillations of the point-spread function are due to the abrupt cutoff of information in Fourier space.

To assess the performance of a three-dimensional reconstruction procedure for

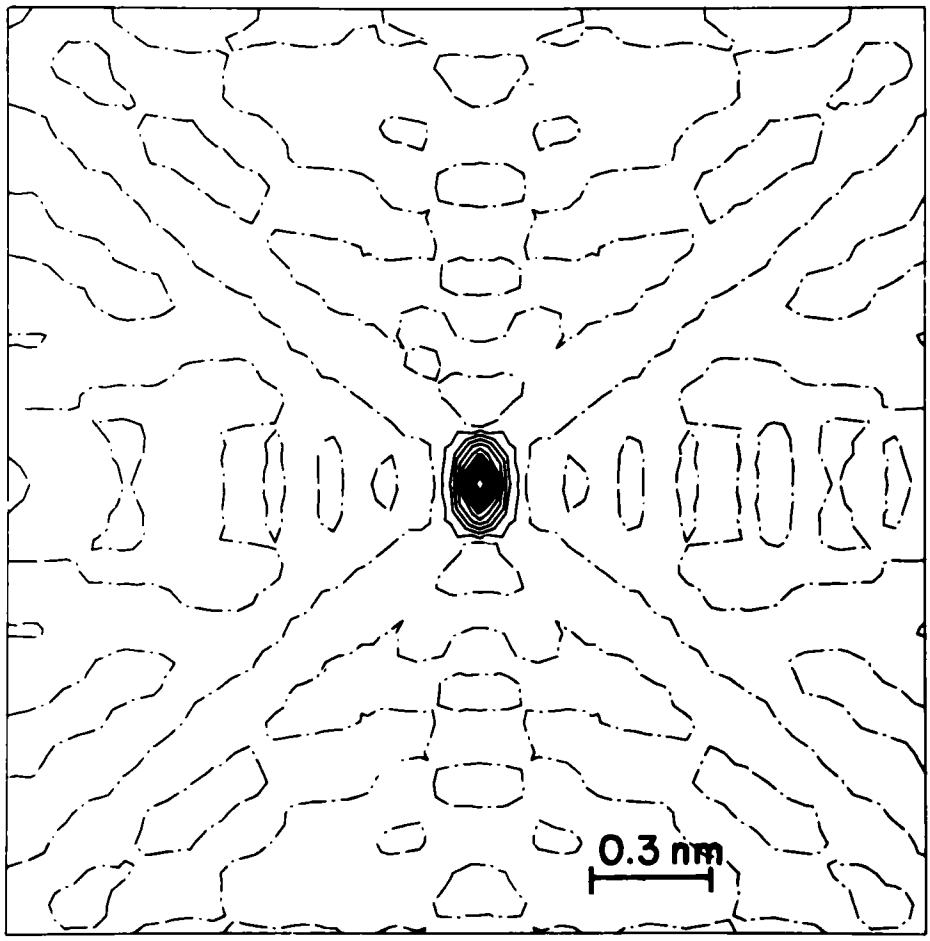


FIG. 3. Contour map of a point-spread function characterizing the three-dimensional reconstruction of a single object point. In this example, a conical tilting geometry is assumed, with a maximum tilting angle of 50° and a resolution of $(0.15\ \text{nm})^{-1}$. The half-broken contour lines indicate zero values of the point-spread function. The central maximum appears elongated in the direction of the angular gap. At some distance from the center, a pattern of side maxima appears in four areas separated by radial streaks. Although the resolution assumed in this model is not realistic, the general character of the artifacts due to the angular limitation becomes evident from the map. From Hoppe and Grill (1977), courtesy of the authors and North-Holland Publishing Company, Amsterdam, The Netherlands.

an arbitrary object, one must consider the object as being composed of density points with different weights. Theoretically, the reconstructed object density is built up from a superposition of point-spread functions, each weighted by the value of the corresponding object point. Since the point-spread function is blurred and streaked in the direction of the missing cone, all pronounced object details will have that appearance—notably edges, sharp discontinuities, and localized density maxima. These artifacts may be so severe in some cases as to make the result uninterpretable in terms of a physical structure. Whether the result is of adequate quality depends on the amount of a priori information available and on the particular circumstances (resolution, size of the angular gap, number of views, etc.). The purple membrane protein (Henderson and Unwin, 1975) presents a fortunate situation; the seven strands of the molecule run almost perpendicular to the membrane, so that the most significant information on the relative positions of the strands is shown in the view range accessible by tilting.

The problem of three-dimensional reconstruction from an incomplete range of views has been the subject of a number of investigations (Klug and Crowther, 1972; Oppenheim, 1975; Bates *et al.*, 1975; Tam *et al.*, 1979). For an entirely noise-free situation it would be possible, owing to the mathematical properties of the Fourier transform, to compute the data in the angular gap from the data in the accessible range if a sufficient number of views were available. However, Klug and Crowther (1972) showed that even the slightest amount of noise makes the solution of the equation system employed unstable. An interesting approach by Oppenheim (1975) and Tam *et al.* (1979) combines some a priori knowledge about the overall shape of the object with the existing measurements by using an iterative scheme of computation. This method could be particularly useful when applied to the reconstruction of single molecules (Chapter 16).

D. Five Different Terms of Resolution

Electron-optical resolution. It was mentioned that there is a resolution limitation that is intrinsic to the physical nature of the object and to measurement in the electron microscope. Atomic resolution is achieved only in special instruments and under special experimental conditions. Normally the imaging in the electron microscope limits the resolution to a value between 0.3 and 1.0 nm. Several factors affect the practical performance of a conventional transmission electron microscope, among them energy spread, illumination divergence, defocus setting, and degree of compensation for axial astigmatism. This resolution figure, however, indicates nothing about the resolution achieved for biologically significant detail under the given set of preparative conditions.

Resolution limit due to stain. When staining is used to provide the electron microscopic contrast, the granularity of the stain prevents visualization of dis-

tances smaller than about 2.0 nm. The exact figure depends on the type of stain used, and figures between 1.5 and 2.5 nm are reported in the literature.

Resolution limit due to disorder. Most three-dimensional reconstruction techniques make use of the ordered arrangement of the object in two or three dimensions. Deviations from perfect order by random rotations or translations will result in a resolution limitation that may be more severe than the limitation due to stain. Crystallographic theory takes this effect into account by introduction of the so-called temperature factor.

Sampling resolution. When the reconstruction is being carried out, the image data must be represented by an array of samples lying on a regular grid. The resolution of sampling must be such that no additional resolution loss occurs. According to the Whittaker-Shannon theorem, the sampling distance should be at least half the size of the smallest image detail to be represented. Optical diffraction analysis is helpful in the decision on a safe sampling distance. For a crystalline object, the size of the Fourier transform containing significant information is apparent from the extent of the regular diffraction pattern.

Computational resolution cutoff. Finally, the appearance of the reconstructed object's density distribution is determined by the cutoff radius in the Fourier synthesis. If this cutoff allows the passage of Fourier coefficients that are beyond the structurally significant resolution limit (that is, 2.0 nm for stained specimens), the details in the reconstructed object model will not necessarily reflect reproducible properties of the object. It is, therefore, normal practice to choose a cutoff that corresponds to the limiting resolution. For a discussion of this question, see Baumeister and Hahn (1975) and Hoppe *et al.* (1975).

III. Direct-Space Methods of Reconstruction

Unlike the Fourier methods, the direct-space methods make direct use of the mathematical relationship between the object density and its projections obtained with the electron beam. This relationship is very simple to formulate if one considers the projecting beam as being composed of equidistant, parallel rays that intersect the object represented by measurements on a three-dimensional sampling grid (Fig. 4). The projection of each ray is obtained by summing the values of the object along the ray. For a single-tilt axis the reconstruction problem is simplified, since only the relationship between a two-dimensional section and its one-dimensional projection must be considered. This is the geometry usually assumed in theoretical treatments of the subject.

Gordon *et al.*'s (1970) Algebraic Reconstruction Technique (ART) is an iterative method that starts with a random object model and successively attempts to satisfy the projection relation for the different viewing angles. This is done, for

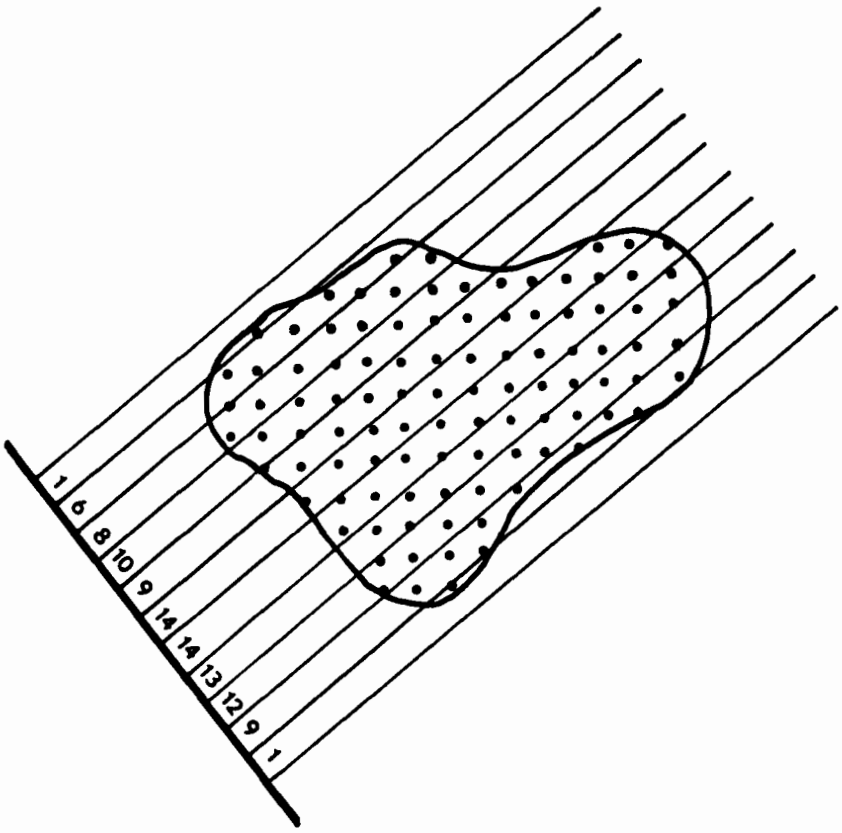


FIG. 4. Schematic illustration of the back-projection algorithm used in iterative direct-space methods of reconstruction. The scheme illustrates the relationship between a slice of the object (lying perpendicular to the tilting axis) and the corresponding projection strip of one of the micrographs of the tilt series. At any stage of the iterative scheme an estimate of the object is represented by samples on a square grid. The estimate is successively corrected to match the different strips of the tilt series. The correction to be applied to each sample in a ray is obtained by comparing the ray sum with the actual projection measurement.

each ray, by correcting the values of all points contained in the ray according to the difference between the current ray sum and the experimental projection measurement. Model computations using this algorithm typically show a semiconvergent behavior: The error between the reconstructed object and the true object decreases steadily for a certain number of iterations until a (nonzero) minimum is attained. Further iterations beyond this point only increase the error again.

Since the ART method was originally proposed for electron microscopic application, numerous variations of the algorithm, which differ in computational efficiency, stability in the presence of noise, and fidelity of reconstruction, have

been suggested. The motivation for this exploration came from the rapid development of medical tomography. For a review of the various schemes, the reader is referred to Gordon and Herman (1974).

Probably the fastest direct method of reconstruction is the modified back-projection method (Gilbert, 1972), in which the object is synthesized, without iteration, by direct superposition of rays back-projected from the measured projection data (see Fig. 4). The mathematical analysis shows that, for the resulting reconstruction to be valid, the measured projection data must be convoluted with a modifying function that has the effect, in terms of the Fourier representation of the projection, of emphasizing the high spatial frequencies.

The great advantages of all direct-space methods are that they are easy to implement on small computers and they are relatively fast compared with Fourier methods. Both the time factor and the hardware requirements are important considerations in tomographic applications. The disadvantage of these methods is that they do not allow one to understand or predict, other than by model computations, the artifacts resulting from an incomplete range of views. In addition, compensation for instrument aberrations and filtration of periodic structures, both of which are easily feasible in Fourier space, lead to unintelligible expressions in real space.

Within the realm of electron microscopic applications, the task of reconstructing thick tissue sections viewed in the high-voltage microscope comes closest to the task of reconstructing body sections in medical tomography. Both have in common the large data volume, an absence of serious instrument aberrations at the resqlution level used, and an absence of periodic structures in experiments of practical interest. The main difference between the two fields of application is created by the limitation due to the electron microscopic tilt stage, which causes the reconstruction of a thick section to be always much poorer in the direction normal to the surface than in the planes parallel to it.

IV. Alignment of Projections

For three-dimensional reconstruction, the relative position of all projections with respect to each other must be known with high accuracy.

A. Use of Fourier Transform Phases

In crystalline specimens (Henderson and Unwin, 1975) the structural information is concentrated in the reciprocal lattice points of the Fourier transform. The phase of each reflection can be interpreted in terms of the position of the corresponding two-dimensional sine wave with respect to the image (see Section II,A). To align two neighboring projections, one basically must compare the

phases of corresponding reflections for different lateral shifts. The best match is achieved where the overall phase error is minimized.

Owing to the Fourier projection theorem, the Fourier transforms of two projections always have a line in common, even for large differences in angle. By matching the phases along these common lines, different views of particles with point-group symmetry can be related to one another (Crowther, 1971). Three-dimensional reconstruction of single molecules without symmetries, however, necessitates a search for other methods of alignment.

B. Center of Gravity

It can easily be shown that the center of gravity of each projection coincides with the projected volume's center of gravity. Although this simple principle could be used for aligning projections, it is too inaccurate for determination of molecular structure. The main cause of this inaccuracy is the contribution of unrelated surrounding structures to the center-of-gravity determination. The center of gravity shifts around its true position, depending on the accuracy of the subjective definition of the particle boundary (Hoppe *et al.*, 1976). Moreover, the method fails entirely when applied to low-dose images in which the particle boundary is barely perceptible (e.g., Goldfarb and Frank, 1978).

C. Cross-Correlation

Two-dimensional cross-correlation functions may be used as a general tool for alignment of electron microscopic images represented in digital form (Frank, 1973, 1980). Briefly, the cross-correlation function of two images is obtained in the following way: For different relative shifts between the images, the products of image elements facing each other are summed. The result, as a function of the shift vector, is the two-dimensional cross-correlation function. It assumes high values for shift vectors that produce a match between identical or similar motifs occurring in both images.

Hunsmann *et al.* (1972) reported that even for relatively large tilting increments (up to 20°) the common information in two different views is sufficient to give a detectable cross-correlation signal. Hoppe *et al.* (1974, 1976) have subsequently implemented alignment by cross-correlation in the reconstruction of individual molecules. Frank *et al.* (1980) used this method to align the images of a HVEM tilt series of a mitochondrion for the purpose of reconstruction.

References

Bates, R. H. T., Lewitt, R. M., Peters, T. M., and Smith, P. R. (1975). "Image Processing for 2-D and 3-D Reconstruction from Projections, Stanford 1975," Tech. Dig. WA2-1.

Baumeister, W., and Hahn, M. (1975). *Hoppe-Seyler's Z. Physiol. Chem.* **356,** 1313-1316.
Bracewell, R. N. (1965). "The Fourier Transform and its Applications." McGraw-Hill, New York.
Cooley, J. W., and Tukey, J. W. (1965). *Math. Comput.* **19,** 297-301.
Crowther, R. A. (1971). *Philos. Trans. R. Soc. London, Ser. B* **261,** 221-230.
Crowther, R. A., and Klug, A. (1975). *Annu. Rev. Biochem.* **44,** 161-182.
DeRosier, D. J., and Klug, A. (1968). *Nature (London)* **217,** 130-134.
Erickson, H. P., and Klug, A. (1971). *Philos. Trans. R. Soc. London, Ser. B* **261,** 105-118.
Frank, J. (1973). *In* "Advanced Techniques in Biological Electron Microscopy" (J. K. Koehler, ed.), pp. 215-274. Springer-Verlag, Berlin and New York.
Frank, J. (1980). *In* "Computer Processing of Electron Microscope Images" (P. W. Hawkes, ed.), pp. 187-222. Springer-Verlag, Berlin and New York.
Frank, J., Goldfarb, W., Eisenberg, D., and Baker, T. S. (1978). *Ultramicroscopy* **3,** 283-290.
Frank, J., Turner, J. N., Marko, M., Asmus, K., and Parsons, D. F. (1980). *Proc. 38th Annu. Meet. Electron Microsc. Soc. Am.* pp. 46-47.
Gilbert, P. F. C. (1972). *Proc. R. Soc. London, Ser. B.* **182,** 89-102.
Goldfarb, W., and Frank, J. (1978). *Electron Microsc., Proc. Int. Congr., 9th, 1978* Vol. II, pp. 22-23.
Goldfarb, W., Frank, J., Kessel, M., Hsung, J. C., Kim, C. H., and King, T. E. (1979). *In* "Cytochrome Oxidase" (T. E. King *et al.*, eds.), pp. 161-167. Elsevier/North-Holland Biomedical Press, Amsterdam.
Goodman, J. W. (1968). "Introduction to Fourier Optics." McGraw-Hill, New York.
Gordon, R., and Herman, G. T. (1974). *Int. Rev. Cytol.* **38,** 111-151.
Gordon, R., Bender, R., and Herman, G. T. (1970). *J. Theor. Biol.* **29,** 471-481.
Hall, C. E. (1953). "Introduction to Electron Microscopy," Chapter 9. McGraw-Hill, New York.
Henderson, R., and Unwin, P. N. T. (1975). *Nature (London)* **257,** 28-32.
Hoppe, W., and Grill, B. (1977). *Ultramicroscopy* **2,** 153-168.
Hoppe, W., Gassmann, J., Hunsmann, N., Schramm, H. J., and Sturm, M. (1974). *Hoppe-Seyler's Z. Physiol. Chem.* **355,** 1483-1487.
Hoppe, W., Gassmann, J., Hunsmann, N., Schramm, H. J., and Sturm, M. (1975). *Hoppe-Seyler's Z. Physiol. Chem.* **356,** 1317-1320.
Hoppe, W., Schramm, H. J., Sturm, M., Hunsmann, N., and Gassmann, J. (1976). *Z. Naturforsch. Teil A* **31,** 645-655.
Hunsmann, N., Bussler, P., and Hoppe, W. (1972). *Inst. Phys. Conf. Ser.* **14,** 654-655.
Johnson, D. E. (1975). *Proc. 33rd Annu. Meet. Electron Microsc. Soc. Am.* pp. 292-293.
Klug, A., and Crowther, R. A. (1972). *Nature (London)* **238,** 435-440.
Mellema, J. E. (1980). *In* "Computer Processing of Electron Microscope Images" (P. W. Hawkes, ed.), pp. 89-126. Springer-Verlag, Berlin and New York.
Oppenheim, B. E. (1975). "Image Processing for 2-D and 3-D Reconstruction from Projections," Stanford, 1975, Tech. Dig. WA1-1.
Radon, J. (1917). *Ber. Saechs. Akad. Wiss. Leipzig., Math. Phys. Kl.* **69,** 262.
Tam, K.-C., Perez-Mendez, V., and McDonald, B. (1979). *IEEE Trans. Nucl. Sci.* **ns-26,** 2797-2805.
Thon, F. (1965). *Z. Naturforsch., Teil A* **20,** 154-155.
Unwin, P. N. T. (1977). *Nature (London)* **269,** 118-122.

This Page Intentionally Left Blank

Chapter 13

Thick and Thin Serial Sectioning for the Three-Dimensional Reconstruction of Biological Ultrastructure

CONLY L. RIEDER*

Laboratory of Molecular Biology,
University of Wisconsin,
Madison, Wisconsin

I. Introduction 215
A. Background 215
B. When Is Three-Dimensional Ultrastructural Information Required? 217
C. Methods Currently Available for Obtaining Three-Dimensional Ultrastructural Information 217
II. Choosing an Appropriate Section Thickness for Serial Reconstruction 221
III. Serial Sectioning 226
A. Block Trimming 226
B. Block Alignment 230
C. Sectioning 233
D. Mounting Serial Sections onto Specimen Support Grids 233
E. Estimating Section Thickness 236
IV. Three-Dimensional Reconstruction from Serial Sections 238
A. The Problem of Continuity between Adjacent Sections 238
B. Methods Used in Three-Dimensional Reconstruction 241
References 247

I. Introduction

A. Background

In the past, high-resolution three-dimensional information concerning the structure of cells and cell interactions was obtained primarily through reconstruc-

*Present address: Electron Optics Laboratory, Division of Laboratories and Research (Ultrastructure Analysis), New York State Department of Health, Empire State Plaza, Albany, New York. 12201

Copyright © 1981 by Academic Press, Inc.
All rights of reproduction in any form reserved.
ISBN 0-12-564122-2

tion of a three-dimensional model from a series of ultrathin serial sections. This is a technically difficult and often laborious task with many inherent problems, the most severe of which is reconstructing the correct three-deminsional structure of the area of interest by precisely aligning each section in all three axes (see reviews of Ware and Lopresti, 1975; Gaunt and Gaunt, 1978).

The ability of the high-voltage electron microscope (HVEM) to produce high-resolution stereo (that is, three-dimensional) images of thick (0.25–10 μm) biological specimens (see reviews of Favard and Carasso, 1972; Hama, 1973, 1976; Glauert, 1974, 1979) promises to eliminate many of the problems encountered in building models from serial thin sections. Indeed, according to Glauert (1974), "this restoration of the third dimension in the appreciation of biological organization has been the major contribution of the HVEM so far." When viewed with a HVEM, however, all the structural details within the thickness of a conventionally stained preparation are brought into focus as a superimposed image. This overlapping of cell constituents, in whole mounts of cells or in sections thicker than 0.5–1.0 μm, often hides and obscures the structure(s) of interest, even when viewed in stereo (Yamada and Ishikawa, 1972; Scott and Guillery, 1974). The problem of constituent overlap can, in some cases, be eliminated by selectively staining the structure of interest *in situ* (Glauert, 1974, 1979). However, the usefulness of this technique is currently restricted by the limited number of select staining procedures applicable to electron microscopy.

If a cell or cell constituent cannot be selectively stained or prepared as a whole mount, and if it is too large to be totally included with a section of practical thickness, then its three-dimensional structure must be reconstructed from serial sections (Peachey, 1975). Of course, the use of thick in lieu of thin serial sections often facilitates three-dimensional reconstruction, since significantly fewer sections are needed to reconstruct an object of a given size (Glauert, 1974; Peachey, 1975). However, many of the techniques involved in and the problems inherent to reconstructing the third dimension from serial thin sections are also applicable to reconstruction from thicker sections. In addition, many structures (especially those smaller structures limited by a membrane—for example, a synapse or mitochondrion) are still best reconstructed from serial sections 0.25 μm thick or less, since the structure of an object may be hidden or obscured if a significant portion of its volume is included within a single section (Peachey, 1958, 1975; Scott and Guillery, 1974; Paulin, 1975a).

The purpose of this chapter is to discuss (1) under what circumstances three-dimensional information concerning the structure of cell and cell constituents is needed; (2) when it is necessary to obtain such information by reconstruction from serial sections; (3) when to use thick sections or thin sections for reconstruction; (4) some of the methods used to obtain serial thick or thin sections from embedded material; and (5) some of the techniques involved in and difficulties associated with the reconstruction of a three-dimensional model from serial thin

and thick sections. It is hoped that the information presented here may provide the reader with insight concerning how best to approach a particular biological problem in which three-dimensional ultrastructural information is required.

B. When Is Three-Dimensional Ultrastructural Information Required?

Under many circumstances the two-dimensional information obtained from observing numerous nonserial thin sections may be quite adequate. This is often the case when the experimental protocol calls for comparing the gross effects of various treatments on components that make up a sizable volume of the cell or tissue (for example, nuclei, mitochondrion, myofibrils). However, three-dimensional ultrastructural information is required when it is necessary (1) to be able to precisely correlate the structure of a specific region of a cell with a previously recorded light microscopic event (as in correlative light and electron microscopy; see, e.g., Buckley, 1974; Rattner and Berns, 1976; Rieder and Bajer, 1977; Heath and Dunn, 1978); (2) to determine the exact number of cell components (Paulin, 1975b, 1977; Haskins, 1976; Murray and Davies, 1979), their correct structure (Paulin, 1975b, 1977; Sattler and Staehelin, 1976; Koukl *et al.*, 1977; Peachey and Eisenberg, 1978), and the spatial relationships between them (Keddie and Barajas, 1969; Cox and Juniper, 1972; Peachey and Eisenberg, 1978; Crang and Pechak, 1978; Murray and Davies, 1979); and (3) to elucidate the structure of cell-to-cell relationships and interactions (Sjöstrand, 1958, 1974, 1978; Karlsson *et al.*, 1966; Macagno *et al.*, 1973).

C. Methods Currently Available for Obtaining Three-Dimensional Ultrastructural Information

Three-dimensional information concerning the structure and interaction of cells or cell constituents may currently be obtained by one or more of the following methods, listed in order of their desirability.

1. By Viewing Whole-Mount Preparations in Stereo

Many isolated cells (Buckley and Porter, 1973, 1975; Brecher, 1975; Wolosewick and Porter, 1976a,b, 1979) or parts of cells (for example, the mitotic spindle—McIntosh *et al.*, 1979a; chromosomes—Ris, 1978; Ris and Korenberg, 1979) can be directly observed in their entirety after fixation and critical-point drying by whole-mount stereomicroscopy. These studies have provided valuable information on the mechanism of cell motility and on the three-dimensional structure and organization of cell constituents.

Unfortunately, however, whole-mount microscopy is amenable only to a few select cell types that can be isolated and grown on Formvar-coated grids, or to those organelles that have an appreciable dimension and can be isolated intact. Thus, at the present time it is not possible to observe in whole-mount preparations the internal structural features of those cells fixed *in situ*, nor the interactions between those cells (for example, neurons) that are buried in a mass of surrounding tissue. To gain specific three-dimensional information concerning the structure and interaction of cells within a tissue or an organ, such cells or cell components must either be totally included in a single section of a practical thickness (see below), or be reconstructed from conventionally stained serial thick or thin sections.

2. By Viewing Single Thick Sections in Stereo

a. Conventionally Stained Sections. Porter and Hama (1968) were the first to demonstrate that high-contrast images and good resolution could be obtained by high-voltage electron microscopy of conventionally stained (uranyl acetate and lead citrate) thick (0.5–1.0 μm) sections of biological material. Soon afterward, Nagata *et al.* (1969; see also Ris, 1969; Hama and Porter, 1969; Hama and Nagata, 1970) reported that three-dimensional structural information could be obtained from such thick sections by photographing and viewing them in stereo.

Since then, numerous investigators have used stereo pairs from nonserial thick sections to investigate the three-dimensional structure of a variety of materials. For example, Glauert and Mayo (1972) examined thick (0.5–1.0 μm) sections of connective tissue cells in stereo and obtained three-dimensional information concerning the interrelationships of membrane systems. At the same time, Cox and Juniper (1972) used stereo pairs taken from single thick (0.5–1.0 μm) sections to study cell wall structure and deposition in celery. They were able to observe the three-dimensional architecture of the cellulose microfibril skeleton of the wall and the organization of the plasma membrane. These authors note that HVEM of thick sections allows for observing membranes in diagonal and face views that would be impossible in ultrathin sections (see, however, Scott and Guillery, 1974). Subsequently, Paulin (1974) used stereomicroscopy of thick sections (0.25 μm) to study both the spatial distribution of flagellar subpellicular microtubules and the mitochondrial–kinetoplast complex in trypanosomes. Similarly, Heath and Dunn (1978) have used correlative light and high-voltage stereomicroscopy of single thick sections to study the three-dimensional relationship between the microfilament system and substratum contacts in chick heart fibroblasts.

Stereo viewing of a single thick section can, therefore, provide three-dimensional information concerning the structural arrangement of cell compo-

nents. When viewed with a HVEM, however, all the structural details within the thickness of a conventionally stained section are brought into focus as a superimposed image. Unfortunately, this overlapping of cell constituents in sections thicker than 0.5-1.0 μm often hides or obscures the structure of complicated cell components, even when viewed in stereo (Nagata *et al.*, 1969; Yamada and Ishikawa, 1972; Scott and Guillery, 1974). The confusion arising from specimen overlap is a serious problem and can be overcome only by either choosing a section thickness "in accordance with the degree of complication of the structure to be observed" (Nagata *et al.*, 1969) or by selectively staining the structure of interest (see below).

b. Selectively Stained Sections. The problem of overlapping structures can in some cases be eliminated by selectively staining the structure *in situ* (Favard and Carasso, 1972; Glauert, 1974, 1979). It is then embedded, thick-sectioned (1-10.0 μm), and photographed in stereo with a HVEM. With this method, three-dimensional structural information has been obtained concerning the transverse system in striated muscle (Peachey and Franzini-Armstrong, 1977; Peachey and Eisenberg, 1978), ganglia and connectives in the leech nervous system (Couteaux *et al.*, 1975), the Golgi apparatus in Sertoli, Leydig, and ganglion nerve cells (Rambourg *et al.*, 1972, 1974), and the endoplasmic reticulum in developing seeds of *Vicia faba* (Harris, 1979).

Unfortunately, the limited number of selective staining procedures applicable to electron microscopy restricts the usefulness of this technique. Furthermore, even though selective staining may provide three-dimensional information concerning the organization of a specific cell or cell component, by its nature it provides very little information concerning the interaction and spatial relationships between the stained structure and the rest of the cell or tissue. Moveover, in some instances a selectively stained structure may be too large to be totally included within the section. If this is the case, its complete three-dimensional structure must still be deduced from serial sections (Peachey, 1975; Peachey and Eisenberg, 1978).

3. By Reconstruction from Thick or Thin Serial Sections

The three methods discussed above are advantageous in that they may directly provide the necessary three-dimensional ultrastructural information. However, as noted, each contains constraints that severely limit their usefulness. Three-dimensional information is frequently needed that cannot be obtained from either a whole-mount preparation or a thick section study of nonserial sections. Under these conditions, the necessary information can be obtained only by reconstruction from thick or thin serial sections. In fact, it is safe to conclude that extensive three-dimensional information concerning the structure and interaction of cells in dense tissues can be obtained only through reconstruction from serial sections.

For example, Macagno and Levinthal (1975; see also Macagno *et al.*, 1973) used 1500 serial thin sections to reconstruct the morphology and synaptic connectivity of various neurons in the optic ganglion of *Daphnia magna*. The size (150 microns in length) and complex nature of this ganglion is such that it cannot be viewed in whole mount or within a thick section. Sjöstrand (1974,1978) used up to 800 serial sections to study the complicated circuitry of a part of the outer plexiform layer in the rabbit retina. At present, this information can be obtained only through serial reconstruction. Similarly, Karlsson *et al.* (1966) used approximately 10,000 serial sections to reconstruct the distribution and topography of the different cell types that make up the frog muscle spindle. The size of the spindle (up to 700 microns in length) and its complicated cellular architecture eliminate the possibility of obtaining this information by any other means.

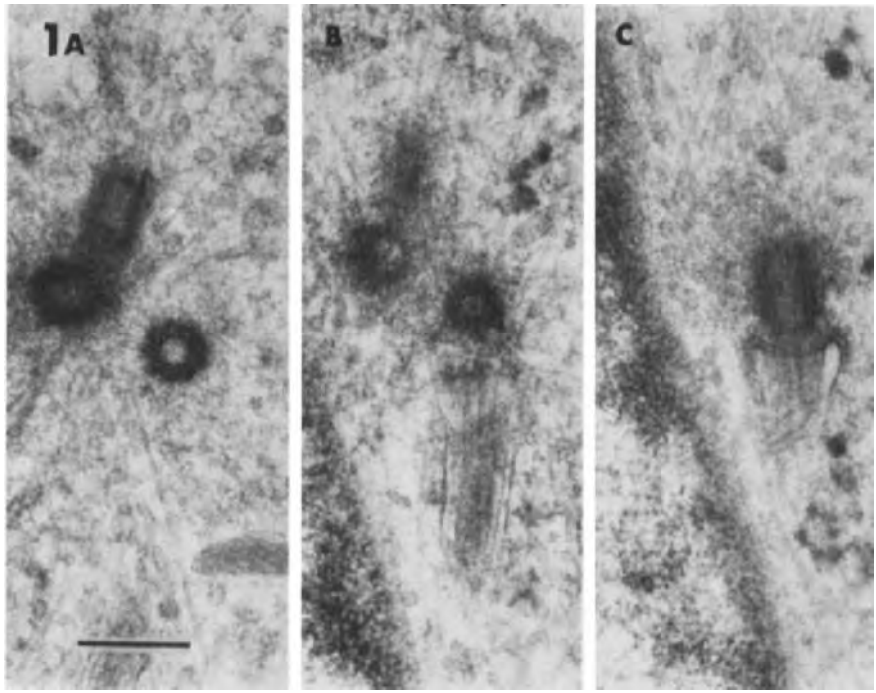


FIG. 1. Three 0.25-μm serial sections through the replicated centrioles of a late interphase cell from a subline of PtK_1. Many of the cells in an actively growing culture of this particular subline possess a single primary cilium, which is associated with one of the mitotic centrioles (C). In this example, serial sections were required not only to locate the centrioles within the cell, but also to determine how many of them possess a cilium. The conclusion that only one of the four centrioles is ciliated could not have been obtained by viewing the individual sections in (A), (B) (three nonciliated centrioles), or (C) (one ciliated centriole). Magnification 30,000×. Bar in (A) = 0.5 μm. From Rieder *et al.* (1979).

Thus, when three-dimensional information concerning the organization and structure of biological material cannot be obtained by stereo viewing of whole-mount preparations or individual thick sections, it must be obtained through reconstruction from serial sections. Furthermore, in addition to providing the basis for a method of gaining three-dimensional information, serial sections may also be required when it is necessary to be able to locate within a cell a single organelle or group of organelles that constitutes a small portion of the total cell volume (for example, a centriole duplex—see Fig. 1).

II. Choosing an Appropriate Section Thickness for Serial Reconstruction

The obvious advantage of using thick rather than thin serial sections is that fewer sections are needed to obtain the desired information. For example, Haskins (1976) has used two consecutive 0.5-μm-thick sections to determine the chromosomal number in the slime mold *Echinostelium minutum*. The same information could be obtained from the required ten to fifteen serial thin sections, but this would be much more laborious and complicated. Similarly, Sattler and Staehelin (1976) were able to reconstruct the entire oral cavity of *Tetrahymena* from seventeen 0.5-μm-thick serial sections. A similar reconstruction from thin sections would require building a model from 80–120 sections, a difficult and time-consuming operation.

Since the use of thick sections facilitates reconstruction, more cells or cell components can be reconstructed in the same time that it takes to complete a single reconstruction from thinner sections (Crang and Pechak, 1978). This increase in sample size provides additional data, which can be used to formulate a more reliable conclusion. In addition, reconstruction of a particular structure from thicker sections may give a more reliable three-dimensional model of the structure, since positional errors that arise during reconstruction (due to dislocations produced between adjacent sections during cutting—see Section IV,A) are minimized.

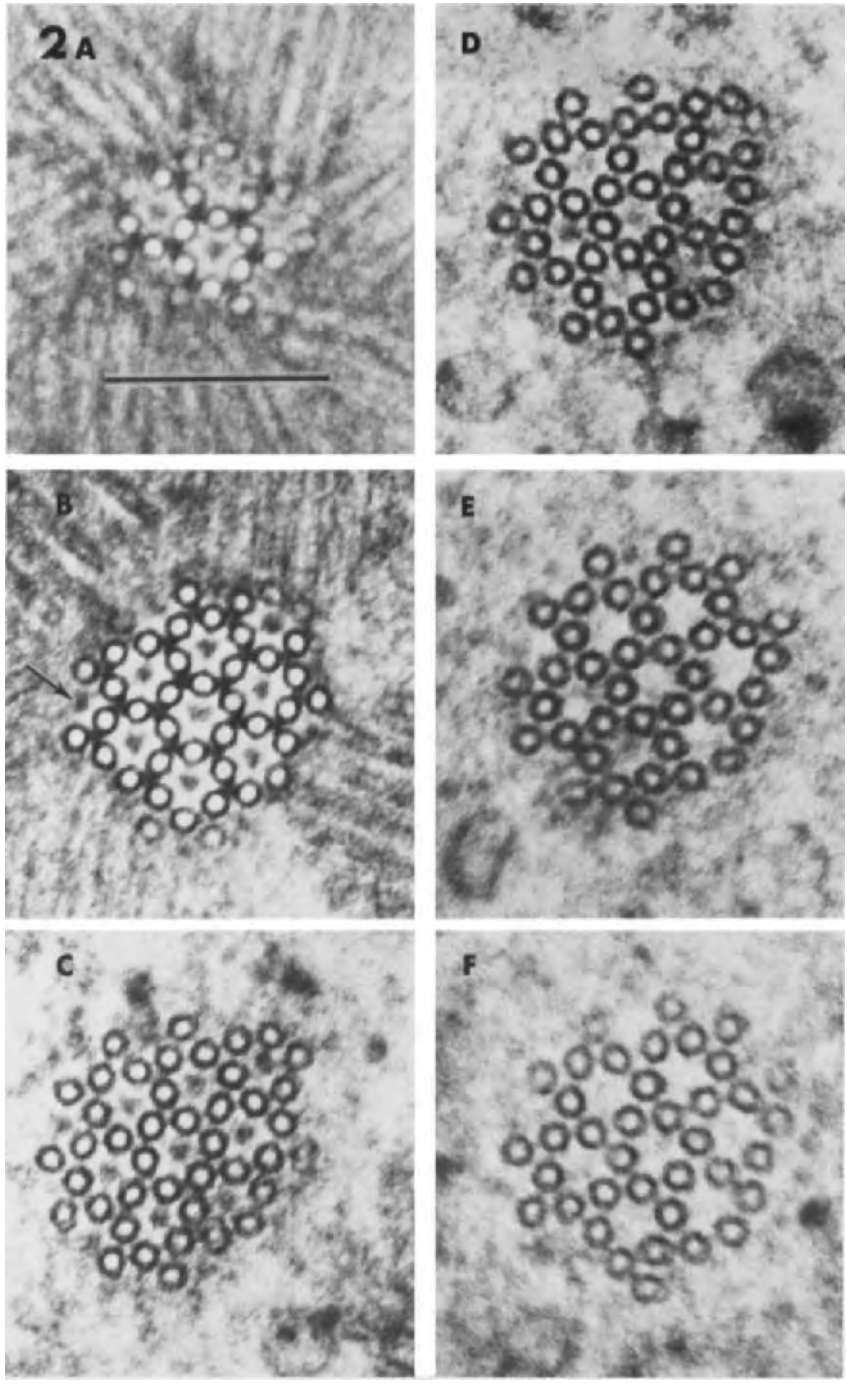
An additional advantage of using thick instead of thin serial sections is that structures may be visible in thick sections that go unnoticed in thin sections of the same material (Coss and Pickett-Heaps, 1974; Rieder, 1979a,b,c). For example, the author (1979a,b,c) has recently used serial thick sections to determine the distribution of two microtubule-associated components found within the axonemes of the centrohelidian *Raphidiophrys*. These two components are visible in thin sections but had gone unnoticed, owing to their location, amorphous nature, and lack of electron opacity. However, when the section thickness is increased to 0.25–0.50 μm, these structures are easily seen because of their

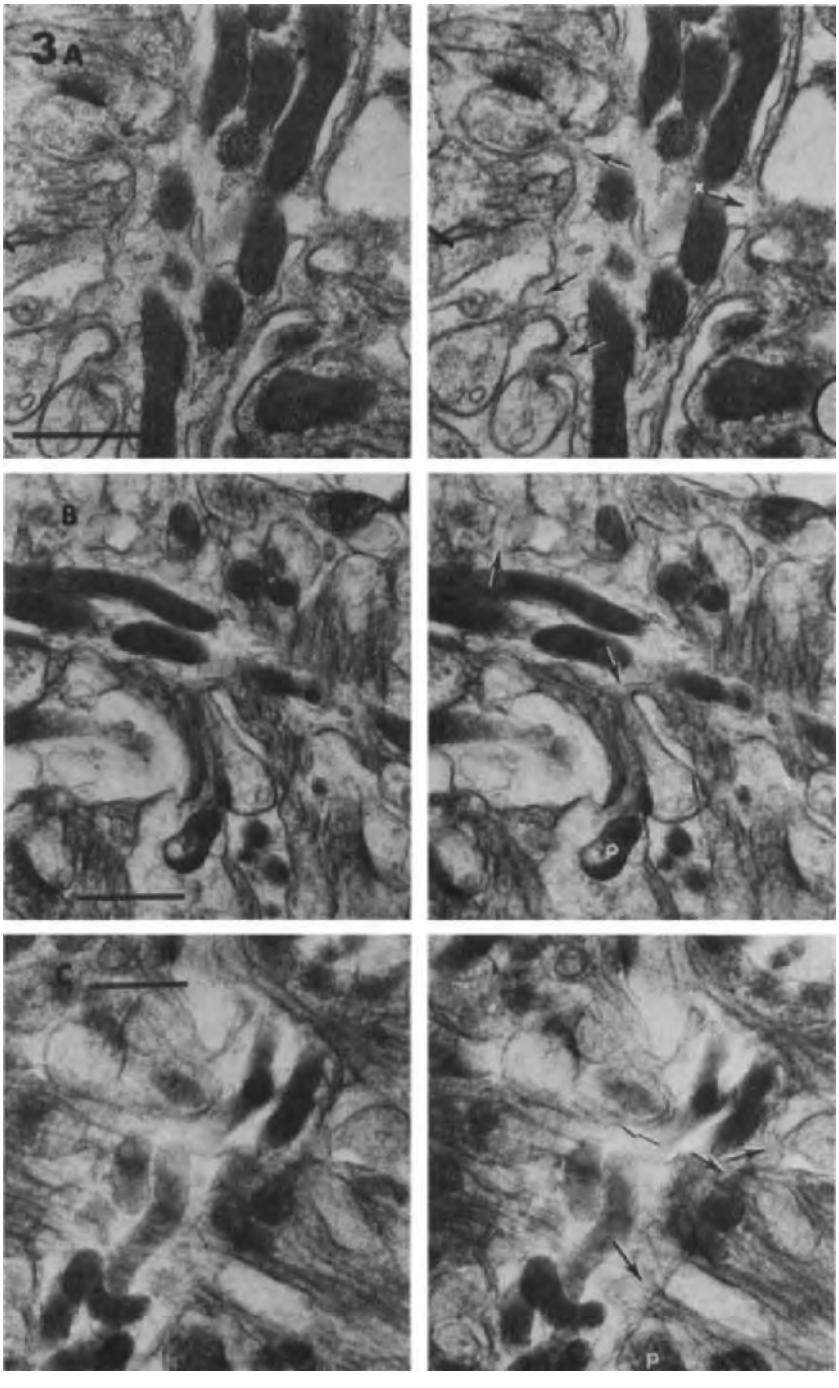
increased contrast. This increase in contrast may be attributed to the fact that more of the component is captured in the thicker sections (see Fig. 2). Similarly, stereo viewing of thick sections often reveals relationships between cell components that cannot be readily elucidated from thin sections. For example, Peterson and Ris (1976) used serial 0.25- to 1.0-μm sections to study the relationship between the diffuse chromatin and the mitotic spindle in the yeast *Saccharomyces cerevisiae*. They note that in thick sections these components can be followed without interruption over a greater distance. Stereo viewing of these sections allows for a more precise interpretation of the relationship between the chromatin fibers and the spindle microtubules, since the true chromatin–microtubule connections can be distinguished from apparent connections that arise when microtubules overlap chromatin.

Large, uncomplicated structures that are well defined (such as myelinated axon or a large vacuole) may be reconstructed from serial cross sections as thick as 5 μm (H. Ris, personal communication). However, three-dimensional reconstruction from serial sections (see Section IV) requires that the image obtained from each section be projected onto a two-dimensional surface. The three-dimensional information obtained by stereo viewing is, therefore, lost, and constituents that overlap within a thick section will appear superimposed when imaged onto a two-dimensional surface. This superimposition of structures often leads to ambiguities, especially when the size of the structure of interest is less than or equal to the thickness of the section, "since the reconstruction assumes uniformity of profile through the whole slice thickness" (Peachey, 1975).

This problem of constituent overlap was noted by Paulin (1975b, 1977) in his studies on the three-dimensional structure of the mitochondrion in Trypanosomatidae. He found that 0.5- to 1.0-μm-thick sections often contained delicate mitochondrial extensions, which lead "to possible ambiguities of interpretation" during reconstruction (Paulin, 1977). Paulin was able to eliminate this problem by simply making his reconstructions from thinner (0.25 μm) sections. A similar situation was encountered by Murray and Davies (1979) during their study on the three-dimensional reconstruction of the chromatin bodies in nuclei of mature erthrocytes from the newt. These authors attempted to use 0.5- to 1.0-μm-thick sections to reduce the number of sections required for the reconstruction. However, they were forced to use 0.25-micron sections, as

FIG. 2. Six 0.5-μm serial sections taken from the base of a cross-sectioned axoneme in the centrohelidian *Raphidiophrys*. The axonemes can be seen to consist of a patterned array of microtubules. These thick sections clearly reveal the presence of a single central rod within each hexagon of microtubules (white arrow in B), and an electron-opaque linkage material, which connects adjacent microtubules (A, B). Serial sections reveal that these two structures, which had gone unnoticed in thin section studies of the same material, are restricted to the base of the axoneme (A–C). It is thought that they play a role in forming and maintaining the characteristic axonemal microtubule pattern. Magnification 120,000×. Bar in (A) = 0.25 μm. From Rieder (1979c).


2A
D
B
E
C
F


3A
X
B
P
C
P

the thicker sections proved impractical, since "the details become ambiguous as a result of the two-dimensional nature of the projected image" (Murray and Davies, 1979). Scott and Guillery (1974) conducted a more thoroughly documented study on the problems that arise when thick sections are used. These authors studied synaptic relationships between neuronal processes in the brains of numerous mammals. They note that in thick sections ($\geq$0.50 μm) the borders between individual neuronal processes were obscured, since membranes that are viewed face-on are invisible. They attribute this to the low staining density of membranes relative to the density of the embedding media. More important, they found that those continuities that are obscured in sections thicker than 0.50 μm tend to be evident in thinner sections (0.1-0.25 μm) (see Fig. 3 and Section IV,A).

The overlapping of cell constituents, therefore, places constraints on section thickness. Indeed, many small and/or complex structures are still best reconstructed from serial sections 0.25 μm thick or less. For example, the general overall arrangement of microtubules within many diatom spindles can usually be deduced from serial cross or longitudinal thick (0.3-0.50 μm) sections (Tippit and Pickett-Heaps, 1977). However, reliable data concerning the length and distribution of microtubules within these spindles are best obtained by tracking crosssectioned microtubules through serial thin sections (McIntosh *et al.*, 1979a; Tippit *et al.*, 1978). Tracking errors may arise in thick sections when one microtubule terminates close (within one section thickness and in close register) to the beginning of another microtubule. The frequency of such errors is decreased when thinner sections are used. An additional example of a situation where thin sections would be preferable to thicker ones was previously mentioned; the ambiguities that arise when neuronal processes are reconstructed from thick sections are often eliminated by using thinner sections (Scott and Guillery, 1974). Similar difficulties can be expected in studying the interaction between membrane processes of adjacent cells in most types of dense tissues.

In general, serial sections that are 0.25 μm thick or less may be necessary to reliably reconstruct (1) the internal and external structure of small, membrane-bound organelles (for example, a mitochondrion or chloroplast), the volume of

FIG. 3. Stereo pairs of photomicrographs from sections showing spiny Purkinje cell dendrites and parallel axons. (A) A thin (silver) section; (B) a section approximately 0.4 μm thick; and (C) a section approximately 0.7 μm thick. The white arrows in (A) indicate several areas where the continuity between dendritic spines and stems can be seen. In (B) the dendritic spines appear to arise from the stems (white arrows). However, there is doubt about the cytoplasmic continuity of each spine. In (C) the stalks of the dendritic spines (arrows) cannot be followed into the dendritic stem with any degree of certainty. Note also that the apparent depth of the specimen in each stereo pair increases as a function of section thickness. P, synaptic knob formed by a parallel axon. Bar = 1.0 μm. Total tilt in (A) = 22°; in (B) = 23°; in (C) = 14°. From Scott and Guillery (1974). Used with permission of Chapman & Hall, Ltd.

which may be totally included within a thicker section; (2) the structure, interaction, and relationship between membrane processes of adjacent cells in dense tissue (synaptic processes, juxta-glomerular apparatus, etc.); and (3) large, complicated cell components composed of smaller, closely situated or overlapping elements (for example, the mitotic spindle).

The section thickness used to reconstruct a particular object will depend on the structural detail desired in the final reconstruction. Unfortunately, the present methods of serial reconstruction (see Section IV,B) assume that the profile of an object remains uniform throughout the thickness of the section. This means that "structural details of the order of or less than the slice thickness become ambiguous" (Peachey, 1975). It follows that, when a detailed reconstruction is desired, thinner sections must be used. The practical section thickness for a given reconstruction will, therefore, depend on the size and complexity of the structure to be reconstructed and on the detail desired in the reconstruction. If the recent literature is surveyed, it becomes evident that the great majority of serial reconstruction studies utilize sections between 0.1 and 0.5 μm thick. A good preliminary section thickness for most types of serial reconstruction studies should therefore be about 0.25 μm.

III. Serial Sectioning

The process of serial sectioning may be conveniently divided into two stages: the production of a long, straight ribbon of sections of a known thickness, and the mounting of this ribbon onto a specimen support grid so that wrinkles are avoided and none of the sections overlap each other. The production of a ribbon of serial sections, which will be discussed below, involves trimming and aligning an embedded block of material in a way that encourages the sections to adhere to each other as they are cut.

A. Block Trimming

Before sectioning, the block of polymerized plastic that contains the material of interest must be trimmed down to a size that is in accordance with the object of the study [for a thorough review on the trimming of specimen blocks, see Pease (1964) or Hayat (1970)]. Smaller block faces are advantageous in that they produce thinner ribbons, which contain more sections per unit of length, and more of these ribbons can be conveniently placed on a single grid. As noted by Pease (1964), the full series of sections should be mounted on as few grids as practical, since the probability of interrupting the series by film breakage or contamination increases when one is handling an excessive number of grids. In

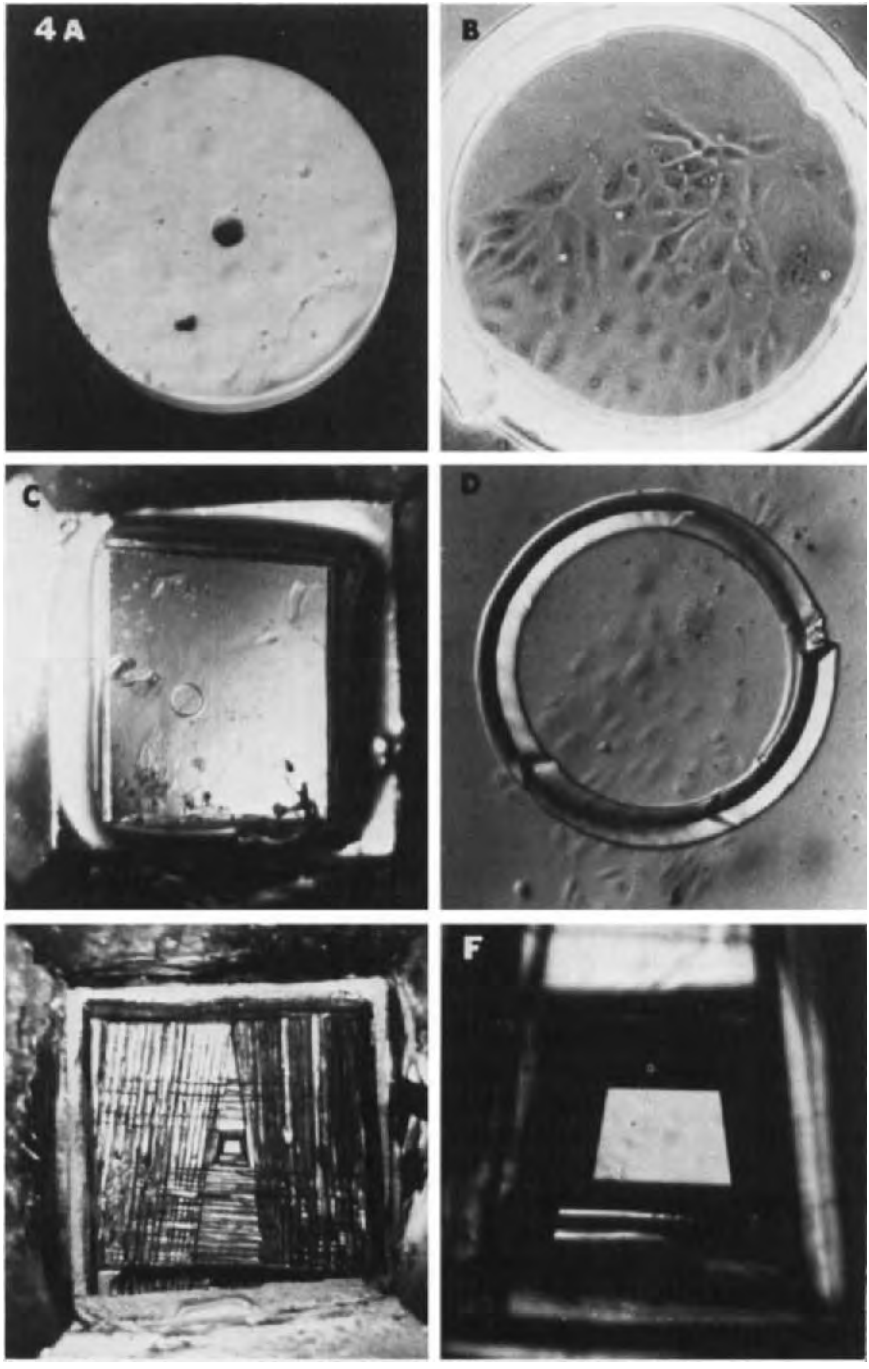
addition, a better quality of section is produced with a smaller block face, since section compression, which arises during cutting, is reduced (Hayat, 1970).

The block should be shaped by trimming it into a pyramid or trapezoid with a short vertical height. Such a shape furnishes support to the face of the block during sectioning (Gelber, 1957). If the block tip is excessively thin and long, it will vibrate during cutting and sections with chatter will be produced.

Trimming can usually be accomplished by making the cuts under a stereomicroscope with a clean, sharp razor blade (the author prefers GEM Super Stainless Steel single-edge blades). If the specimen or specimen area can be made visible under a stereomicroscope with reflected light, then it may be mounted in a Butler (1974) block trimmer (or a similar device) for freehand trimming. However, the successful trimming of many small specimens (that is, single cell within a flat embedded monolayer) requires that they be viewed under the stereomicroscope at very high magnifications. The intensity of reflected light at such magnifications is often too dim for this purpose. Under these circumstances the specimen(s) can often be viewed and trimmed by using transmitted light. The author has developed a simple device that may be rapidly constructed for this purpose (see Fig. 4). The bottom of a 60-mm glass Petri dish is filled with Silastic elastomer (or a suitable alternative), and an old Epon peg, onto which flat, embedded specimens are usually mounted, is pushed into the center of the Petri until it contacts the bottom. After the Silastic has polymerized, the Epon peg is removed. The Silastic-filled Petri will then contain a hole the size of a peg in its center through which light may be transmitted. A new peg on which a specimen is mounted is inserted specimen-up into the hole in the Silastic mold. The ensemble is then placed on a stereomicroscope stage and illuminated from the bottom. With this method, flat, embedded specimens can easily be observed at very high (50–100×) magnifications, especially if they have been stained prior (that is, en block—Hayat, 1970) or after (whole block—Nelson and Flaxman, 1972) embedding. The Silastic mold will hold the specimen peg motionless during trimming.

Since the production of long, straight ribbons of sections is crucial to serial work, it is mandatory that the sections adhere to each other as they are cut. This will usually be the case when the leading edge (that is, the edge that will make first contact with the knife) and the trailing edge of the block face are smooth, clean, and parallel to each other. This can be done, if necessary, by placing a roughly trimmed specimen block into a microtome and fine-trimming its leading and trailing edges with an old glass or diamond knife.

Experience indicates, however, that sections (especially thick sections) may sometimes fail to form ribbons no matter how clean, smooth, and straight the leading and trailing edges of the block are. When this occurs, the sections can be encouraged to adhere to each other by carefully coating the top and bottom facets


4A
B
C
D
F

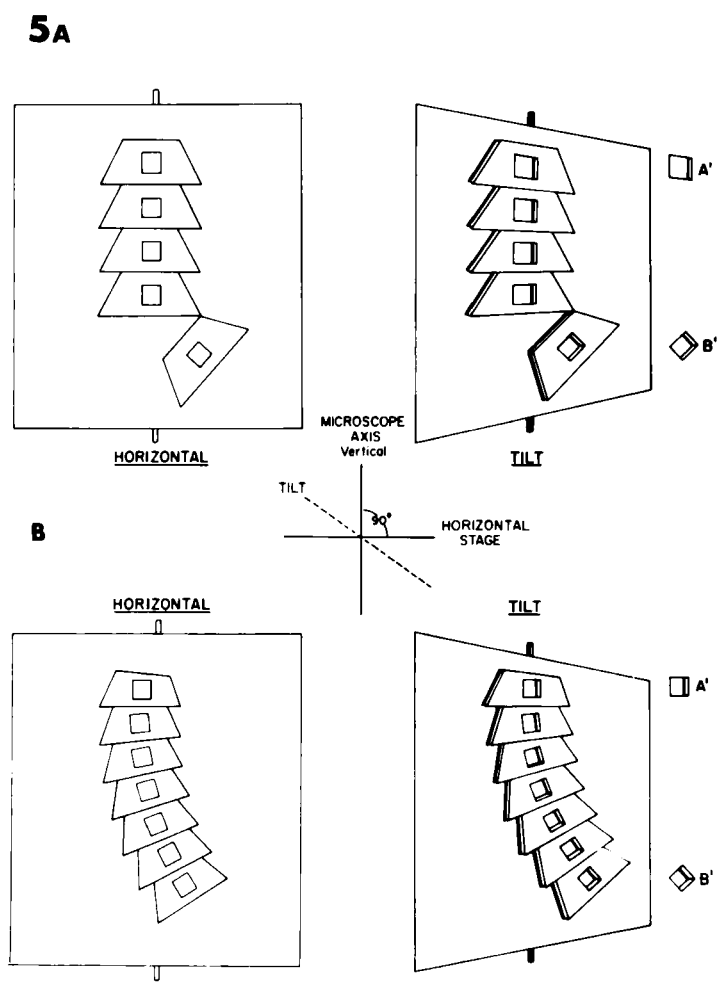


FIG. 5. Schematic drawing showing the change in perspective of a tilted specimen within a nonlinear ribbon of sections. In (A) the ribbon is linear with the exception of the first section, whereas in (B) the ribbon shows a gradual curvature. The effects of tilting in both (A) and (B) can be seen by comparing (A') and (B'), respectively. See text for details.

FIG. 4. This series of photomicrographs illustrates a method for trimming an embedded block of material using transmitted light (see text for details). The Silastic mold, into which a specimen block is inserted, is illustrated in (A). In (B) a metaphase PtK_1 cell is circled and photographed in phase contrast. The circled cell is then excised from the culture and mounted on an Epon peg (C). (D) shows a similarly mounted metaphase cell, under higher magnification, using a dissecting stereomicroscope and transmitted light. In (E) the block has been hand-trimmed into a trapezoid with the metaphase cell in the middle of the block (F).

of the block with Scotch tape adhesive dissolved in choloroform (Macagno *et al.*, 1973) or with printer's paste-up wax (Peachey and Eisenberg, 1978).

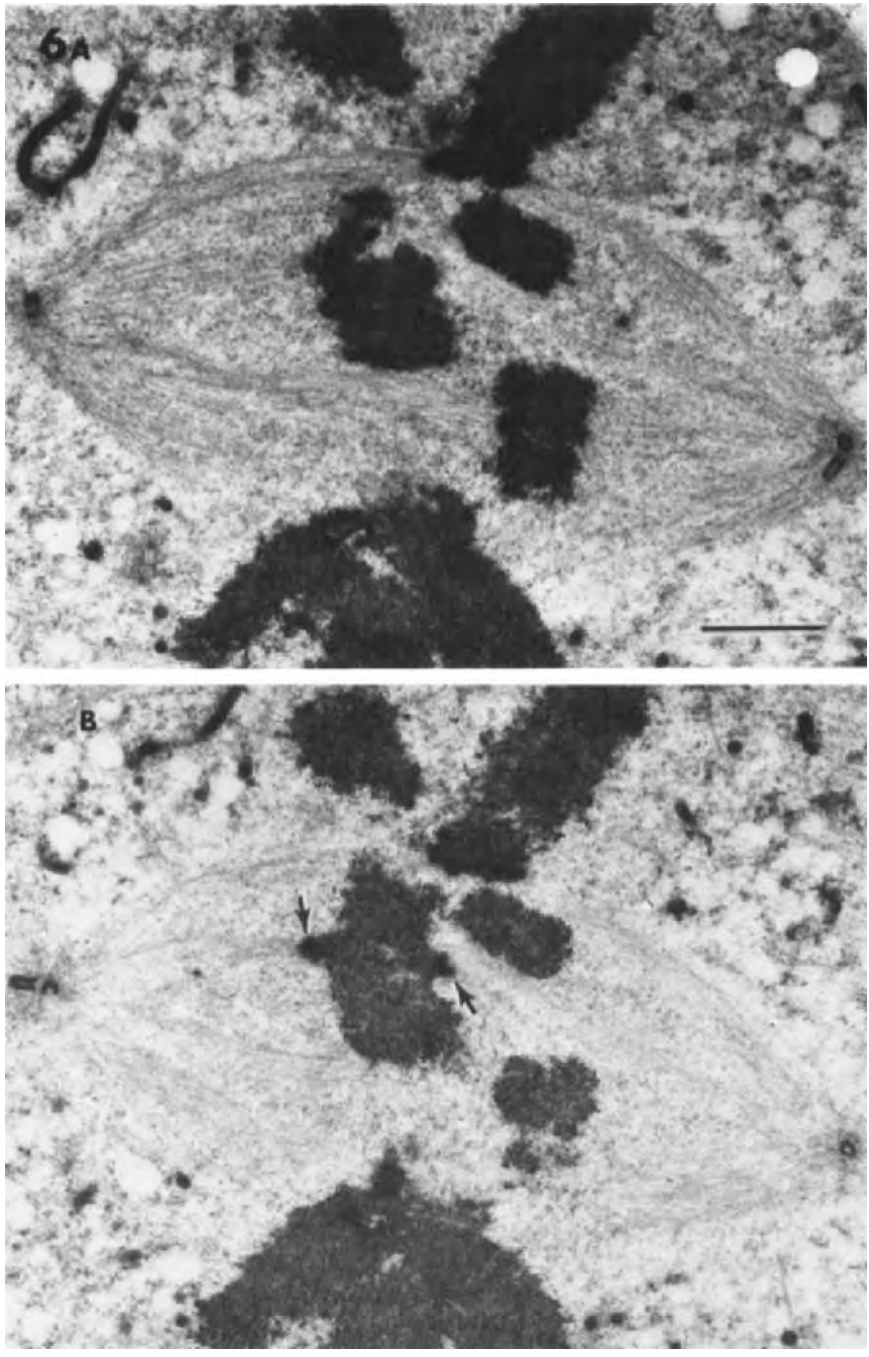
In order for a straight ribbon of sections to be formed, the leading and trailing edges of the block must be parallel to each other. Straight ribbons are especially important when one is reconstructing an object from serial thick sections. This arises from the considerations that HVEMs are equipped with tilt stages and that thick sections have an appreciable thickness. If the microscope stage is horizontal, then the specimen will always be photographed perpendicular to the plane of the section. Under these conditions, the point that a particular structure is viewed from will be determined by the plane in which it was sectioned; further, this viewpoint will be the same in all sections, regardless of how the sections are oriented on the grid. However, if the horizontal stage is tilted (for example, to orient a structure in perfect cross section), and if the ribbon is not absolutely straight, then the specimen will be rotated and subsequently will be viewed from a different perspective in each successive section (see Fig. 5). Depending on the size and nature of the specimen, this change in orientation may be subtle and easily overlooked.

This problem is of minor importance when one is photographing a structure in serial thin sections, since thin sections are essentially two-dimensional and are most often viewed in a horizontal plane. However, it becomes of major significance when one is photographing a structure in serial thick sections, if the sections are not aligned in a linear fashion. Under these circumstances, a consistent viewing orientation of the specimen can be maintained from section to section only by constantly reorienting the specimen around its vertical axis. This time-consuming and difficult process can be eliminated by ensuring consistent linearity within the ribbon.

B. Block Alignment

It is often necessary to be able to cut a complete section of desired thickness the first time the knife makes contact with the face of the specimen block. This is especially crucial (1) when a thick section (1.0-5.0 μm) has been re-embedded for subsequent serial thin sectioning (Schabtach and Parkening, 1974; Sigee,

FIG. 6. Two serial sections through a mitotic spindle of a metaphase PtK_1 cell. PtK_1 cells remain flat throughout division, and the longitudinal axis of the spindle is frequently parallel to the embedding substrate. By properly aligning the block face with the knife edge (see text), both poles of the spindle can be captured in a single section. This provides a clear view of the fusiform shape of the spindle and the interaction between its chromosomal, microtubular, and polar components. These two sections were cut using a 0.25-μm thickness setting on the microtome. The observation that section (B) appears to be thinner than section (A) illustrates the variability of section thickness along a ribbon (see Section III, E). Magnification 8000×. Bar in (A) = 2.0 μm. Picture in (B) is from Rieder (1979d).


6A
B

1976; Davidowitz *et al.*, 1976); (2) when the specimen(s) are entirely contained within the first few microns of the block (as in flat embedded monolayers of cultured cells used for selected cell or correlative light electron microscopic studies—see Brinkley *et al.*, 1967; Hopkins, 1979; Nicklas *et al.*, 1979); (3) when serial cross or longitudinal sections are needed from a flat embedded specimen oriented in such a manner that the plane of sectioning must remain perfectly parallel to the plane of the block face (for example, in order to capture in a single section both poles of a mitotic spindle—Fig. 6); or (4) when it is necessary to be able to start resectioning a block in the same plane and without a loss of sections, after removing it and subsequently reinserting it back into the microtome.

Gorycki (1965) was the first to describe a method that can be routinely used for precisely aligning the face of a block with a knife edge. He mounted a substage microscope mirror onto the base of a Porter-Blum knife holder and used it to reflect light from an overhead fluorescent lamp onto the front edge of the knife. When the specimen block was brought suitably close to the knife, the light reflected from the knife edge was imaged onto the block face. Gorycki found that the leading edge of the block could then be aligned with the knife edge by rotating the block until the knife edge was parallel to its reflected image on the block face. The block face could then be aligned to the cutting plane by "tilting the block until the image of the knife neither approaches nor recedes from it with an up and down movement of the block" (Gorycki, 1965).

Although there have been many minor modifications (see references in Wyatt, 1974; Gorycki, 1977) of Gorycki's original description, the great majority of these still use reflected light as a guide for alignment. In Gorycki's (1965) original alignment procedure, a good reflection for alignment could be achieved only when the lamp, mirror, knife face, block face, and stereomicroscope were properly positioned. This often takes a considerable amount of time. He has since described a method (Gorycki, 1977) for prealigning the above elements so that the only variable is the orientation of the block face itself. Prealignment of the components is performed by cutting sections from an old block (after which the block face will be perfectly aligned with the knife) and then aligning the components of the system to give the brightest possible knife edge reflection onto the undisturbed block face. When a new block is positioned in the microtome, it can be rapidly prealigned by positioning it so that the reflection of the knife edge on the block face is at its maxium intensity. The block can then be fine-aligned by minor adjustments as described above.

In practice, it may sometimes be difficult to obtain the proper lighting for aligning some specimen blocks, especially if the specimen block is translucent. The illumination around the specimen area can often be improved by simply painting the lower portion of the leading block facet with the white correction fluid commonly used to cover typing errors (Mollenhauer, 1976). The painted

surface reflects overhead light back into the specimen area of the block and thus facilitates knife-block alignment.

C. Sectioning

Serial sectioning is a procedure that is best approached after one has gained considerable practical experience in microtomy. For this reason, a detailed knowledge of sectioning techniques will be assumed, and only a few points relevant to obtaining serial thick or thin sections will be reviewed here. A thorough discussion of sectioning procedures can be found in Pease (1964; see also Glauert and Phillips, 1967; Hayat, 1970).

Serial sectioning requires that a properly trimmed specimen block be carefully aligned with the edge of a good glass or diamond knife. Although diamond knives are preferable for serial work (since they are less likely to dull during extensive sectioning or when cutting hard specimens), many thin serial sections can successfully be cut from softer tissues by using a good glass knife (for example, see Sjöstrand, 1974). However, glass knives should not be used for cutting serial thick sections since it has been shown that they often seriously damage the upper surface of the sections (Favard and Carasso, 1972). This damage can be minimized by using a good diamond knife.

As the sections are cut, they will float onto the surface of the trough and, under the proper conditions (see Section III,A), will form a ribbon. Once sectioning is started, it should be continued without interruption for as long as is practical (that is, until the specimen has been totally sectioned or until the trough contains as many sections as it will conveniently hold). Since the sections are compressed as they are cut, they must be expanded (or flattened) before they are mounted onto a specimen grid. Compression is generally relieved by exposing the sections to the vapors of organic solvents (chloroform, trichloroethylene, etc.). The author prefers the method introduced by Roberts (1970), whereby a heat pen is used to relative section compression. Heat eliminates the use of potentially harmful solvent vapors and relieves section compression as well as, or better than, organic solvents do.

As noted by Williams and Kallman (1955), the main difficulty in preparing serial sections for examination is not the microtomy "but rather in the mounting of ribbons of sections upon the specimen grids" (Williams and Kallman, 1955). This problem will be discussed in the next section.

D. Mounting Serial Sections onto Specimen Support Grids

Ribbons of serial sections must be mounted onto specimen support grids in such a way that they (1) can be viewed without obstruction, (2) remain unbroken

and wrinkle-free, and (3) do not overlap each other. As noted above, this can often be a more difficult process than obtaining the ribbon of sections.

Serial sections are viewed without obstruction by mounting them onto a specimen grid containing a single hole or slot. The optimum size of this hole or slot will depend on the width and length of the ribbons and on how many of them are to be placed on a single grid. For this reason, grids containing various size holes or slots can be purchased from most suppliers of electron microscopic accessories. In general, it is best to use the hole of smallest diameter that is practical for the study, since this will reduce the incidence of film breakage. Hayat (1970) notes that grids that contain a spherical hole may be preferred to those that contain a slot, since hole grids do not require as exact an orientation of the ribbon(s).

A ribbon of serial sections is mounted over a slot or hole in a grid by supporting it on a thin film of Formvar or a suitable alternative. Additional support and an increased stability under the electron beam can be obtained by coating the grid with a thin layer of evaporated carbon before or after mounting the sections. Thin sections can be mounted directly on a Formvar-carbon film (that is, a composite film—see Dowell, 1959; Bradley, 1967) prior to staining, since the stains rapidly penetrate the exposed surface of the sections. Alternatively, thin sections can be mounted on a Formvar film, stained, and subsequently coated with carbon. Thick sections, which require longer staining times, should be mounted only on a Formvar film prior to staining. This allows stain penetration from both sides of the section. After staining, the thick sections can be coated with a thin layer of carbon.

Many methods have been described for collecting and aligning ribbons of sections onto grids. In general, these methods can be divided into two groups: those in which a Formvar-coated grid is used to pick up the sections directly from the trough (the direct method), and those in which the ribbon(s) are first collected from the trough (using a wire loop, bent slot grid, etc.) and then mounted onto a grid (the multistep method).

1. Direct Methods

Early microtomists were sometimes successful in picking up ribbons of sections by hand directly from the trough, onto a Formvar-coated slot grid (Gelber, 1957; Dowell, 1959). This practice requires extremely steady hands and much patience. In addition, the low success rate and the problems encountered are such that this method should never be used for critical serial work. However, with the introduction of the "third hand" (Behnke and Rostgäard, 1964; see also Ward, 1972; Rostgäard, 1973), ribbons of flat serial sections can be routinely collected onto slot grids directly from the trough. In this method, a Formvar-coated slot grid is grasped in a pair of clean forceps so that the long axis of the slot is parallel

to the points of the forceps. The forceps are then mounted in a simple micromanipulator (the third hand), which is positioned near the rear of the knife trough. The micromanipulator is used to lower the grid slowly into the trough at a 45° angle so that the major axis of the slot is perpendicular to the knife edge. The grid is then slowly raised mechanically until the meniscus of the flotation fluid is just below the top of the slot in the grid. A ribbon of sections is then manipulated (with an eyelash) so that one end of the ribbon makes contact and adheres to the film at the meniscus between the film and the trough fluid. As the grid is slowly raised from the trough, the ribbon of sections is picked up by the film.

Using this method, the author has found that multiple parallel ribbons of sections can be collected on a single grid in the following way: A Formvar-coated slot grid is grasped in forceps so that the long axis of the slot is perpendicular to the points of the forceps. The grid is then placed in the trough in the manner described above. A series of ribbons is then positioned so that their long axis is parallel to the long axis of the slot. The first ribbon is then manipulated into position until it contacts and adheres to the Formvar film. The grid is slowly raised until the ribbon just disappears from the trough. At this point a second ribbon is positioned in the same manner, and the process is repeated. The number of ribbons that can be collected on a single grid is determined by the width of the ribbons and the width of the slot. If a ribbon bends or breaks as it is being picked up, it can be refloated onto the trough fluid by slowly resubmerging the grid. The process can then be repeated until the ribbon(s) are correctly positioned on the grid.

Ribbons of sections may also be directly mounted onto grids by a method described by Westfall (1961; see also Westfall and Healy, 1962). In this method, a narrow edge of Bakelite is glued to the knife about 1 mm below the cutting edge. After a ribbon of sections is cut, a grid is carefully slid below the ribbon so that it rests on the Bakelite shelf. The ribbon is then positioned over the grid. At this point, the water level in the trough is slowly lowered, thus dropping the ribbon onto the grid surface.

2. Multistep Methods

A widely used method for mounting ribbons of serial sections onto grids is based on a modification (Barnes and Chambers, 1961; see also Mazziotta *et al.*, 1973) of a procedure introduced by Gay and Anderson (1954; see also Sjöstrand, 1958). Sections are collected, as they float on the trough, onto a thin film of Formvar, which is supported by a wire loop. The loop is inserted into the trough at a 45°–90° angle, and the ribbon(s) are centered across its diameter. As the loop is slowly raised from the trough, the ribbon(s) adhere to the Formvar film. The Formvar-coated loop, which contains the sections, is then allowed to dry. A clean slot grid is then mounted on a peg of similar diameter. With the aid of a

good stereomicroscope, the ribbon(s) are carefully aligned over the slot in the grid. The loop is then lowered over the peg, thus attaching the Formvar film (with the adhering sections) to the grid. The Formvar film can then be coated with a thin layer of carbon after the sections have been stained.

A variety of methods have been introduced in which an uncoated slot grid is used for collecting and mounting the sections. In these procedures a clean slot grid, which has no support film, is positioned so that the slot is over the ribbon in the trough. The grid is then lowered until it contacts the fluid in the trough. When the grid is raised from the trough, the ribbon will be contained on the surface of the drop of water that adheres to the slot. The ribbon can then be mounted onto a second slot grid, which contains a composite film by the method of Galey and Nilsson (1966). Alternatively, the grid containing the suspended ribbon can be placed directly onto a Formvar film suspended over a ring (Wells, 1974) or an aluminum rack (Rowley and Moran, 1975). The advantage of these procedures is that the sections can be transferred directly to different staining and rinsing solutions before mounting. This eliminates the possibility of losing sections to broken films during staining and carbon-coating (Galey and Nilsson, 1966). In addition, this method can be used when it is necessary to treat sections with reagents (various acids, silver and sulfate solutions, etc.), which may have a deleterious effect on the metallic grid or support film. However, difficulties arise with these methods when one is attempting to mount more than one ribbon on a single grid.

A unique multistep procedure for handling and mounting a large number of serial sections has been described by Sjöstrand (1974). The knife trough is enlarged to accommodate a large number of ribbons. A rectangular frame, slightly smaller than the trough in dimensions, is then coated with a thick collodion film, which is in turn coated with a Formvar film. The frame is then placed on a shelf a few milimeters below the surface of the knife edge. When a large number of ribbons has been cut, the frame supporting the collodion-Formvar film is slowly raised until the ribbons contact the Formvar film. After drying, the ribbons are stained directly on the collodion-Formvar frame. The film is then cut into parts (one ribbon on each part), and each part is placed onto a Formvar-coated slot grid. After mounting, the collodion film is selectively dissolved away in amyl acetate. The end result is that the stained sections are sandwiched between two Formvar films.

E. Estimating Section Thickness

In order to construct a reliable three-dimensional model from serial sections (see Section IV), the structural information obtained from each section must be precisely aligned on the vertical axis. This necessitates obtaining an accurate estimation of the thickness of the sections (Peachey, 1958). It must be noted,

however, that sections undergo an instantaneous decrease in thickness (they are thinned) upon exposure to the electron beam (Hayat, 1970). Just how much a particular section will be thinned will depend on what type of embedding plastic it is composed of, the intensity of the beam, and how thick the section is. Favard and Carasso (1972) have noted that the "radiation-induced decrease in section thickness is more pronounced with an increase in the thickness of the original sections". Thus, whereas a thin (150–200 nm) Epon or Araldite section may lose 20–50% of its original thickness (Favard and Carasso, 1972; Zelander and Ekholm 1960), a 25-μm-thick section may lose up to 80% (Favard and Carasso, 1972). It is not known whether the decrease in section thickness is due to section sublimation (Hayat, 1970), or to a general shrinkage of the embedding polymer (Favard and Carasso, 1972).

An average section thickness, for thin or thick sections, can be calculated by simply determining how much of the block face has been cut and then dividing by the number of sections in the ribbon (Gunning and Hardham, 1977). This method was thought to be particularly useful for serial work, since it provides depth dimension information. However, it is limited by the fact that it provides no information concerning the average thickness of a ribbon of sections after exposure to the beam. A similar approach, which enables section thickness to be approximated after exposure to the beam, was noted by Barajas (1970; see also Stempak and Laurencin, 1976) in his serial section study of the juxta-glomerular apparatus. This author estimated section thickness by counting the number of sections required to go through the entire spherical cytoplasmic bodies of the proximal convoluted tubules.

The thickness of a 60- to 250-nm section can also be estimated from its interference color while it is floating in the trough (Hayat, 1970). However, estimates obtained in this manner are reliable only to within 10–20 nm (Peachey, 1958) and do not take into account section thinning by the beam. In addition, since each color represents a range of 30 nm, there can be considerable variation in section thickness along a ribbon, which will not be manifested as a change of interference color. This variation in section thickness can be detected and measured by interference microscopy (Zelander and Ekholm, 1960; Gunning and Hardham, 1977) which, in addition, allows one to determine the thickness of a section to within 1 nm (Gillis and Wibo, 1971). More important, interference microscopy can be used to determine the thickness of a section after examination in the electron microscope (Zelander and Ekholm, 1960).

Interference colors may also be used to roughly estimate the thickness of sections in the range of 0.25–1.0 μm (Locke and Krishan, 1971). However, after exposure to the beam, the thickness of such sections can be known only by either re-embedding and sectioning them perpendicular to their surface (Favard and Carasso, 1972) or by using photogrammetric methods (see below).

Thickness may also vary within a section. It may therefore be necessary to

determine a section's thickness at or near the structure to be studied after it has been exposed to the electron beam. Silverman *et al.* (1969) have developed a method, based on quantitative electron microscopy, that allows just such measurements. They stained and embedded the anion exchange resin Dowex and used it as a thickness standard for accurately measuring section thickness. This particular method is found to be reliable when the sections are between 2.5 and 100 nm thick.

Photogrammetric methods have also been used to estimate the thickness of sections that are thicker than 0.25 μm. Scott and Guillery (1974; see also Hama, 1976; Heath and Dunn, 1978) were able to obtain reliable estimates of the thickness of a section by using the "floating dot" technique described by Nakinvell (1963; see also Hudson and Makin, 1970). This method employs a mirror stereoscope that enables one to determine, from a stereo pair of photographs, the height (thickness) of a structure by making parallax measurements. To obtain an accurate determination of the section thickness, however, the parallax measurements must be made between a point situated on the top surface of the section and another point situated on the bottom surface of the same section. The advantage of this method is that it gives a reliable estimate of the thickness of a section after it has been exposed to the beam. It is, however, reliable only in those cases where the top and bottom edges of the section can be readily defined (Scott and Guillery, 1974).

IV. Three-Dimensional Reconstruction from Serial Sections

A. The Problem of Continuity between Adjacent Sections

In order to reconstruct the third dimension from serial sections, the information from each section must be correctly aligned in all three axes. Ideally, in correctly aligned sections, the continuity of all structures should be maintained between adjacent sections. In reality, however, adjacent sections frequently fail to exhibit the degree of continuity expected for an accurate reconstruction (Williams and Kallman, 1955; Sjöstrand, 1958; Peachey, 1958). This frequent failure of adjacent sections to match is thought to arise from one or more of the following sources: (1) Some of the tissue between sections is destroyed by the knife edge during sectioning (Williams and Kallman, 1955; Gelber, 1957; Bang and Bang, 1957); (2) sections within a ribbon often very in thickness (Sjöstrand, 1958; Peachey, 1958; Gunning and Hardham, 1977); (3) sections are unevenly compressed during cutting, and residual compression exists after section expansion (Bang and Bang, 1957; Sjöstrand, 1958; Peachey, 1958); (4) sections undergo a significant decrease in thickness upon exposure to the beam (see

Section III,E); and (5) good intrinsic or external reference structures or marks, which are necessary for proper section alignment, are often absent.

In a study on interpreting micrographs from serial sections, Williams and Kallman (1955) concluded that the failure of sections to match properly was due primarily to the removal of tissue between sections by the gouging or scraping action of the knife during microtomy. Later, Peachey (1958) suggested that the lack of continuity between adjacent sections, seen by Williams and Kallman, did not arise primarily from a loss of material but rather from "a lack of consideration of section thickness" (Peachey, 1958). Sjöstrand (1958) provided support for this view by noting that the continuity of membranes between adjacent sections was lost if there was a large variation in the individual section thickness along a ribbon. Under these circumstances, the lack of continuity of membranes between adjacent sections can be attributed to the fact that reconstruction relies on projected images, which "assumes uniformity of profile through the whole slice thickness" (Peachey, 1975; see also Section II). More recently, Gunning and Hardham (1977) compared the sum of the thickness of individual sections (as measured by interference microscopy) to the total amount of material removed from the block face, and concluded that the loss of material during cutting was "insignificant." Thus, the loss of material attributed to the scraping action of the knife during microtomy, which at one time was thought to be the primary reason for the lack of continuity between adjacent sections, is probably not a major causative factor for the failure of adjacent sections to match.

Similarly, although sections undergo a considerable amount of "thinning" in the beam (see Section III,E), it is unclear as to what extent this contributes to the lack of continuity between adjacent sections. The confusion arises primarily from the fact that it is currently unknown whether section thinning results from the loss of specimen and embedding material (that is, due to sublimation) or from an overall vertical shrinkage of the embedding polymer without a significant loss of specimen material. The situation is further confused by the observation of King and Parsons (1978) that the electron beam induces not only a thinning of the section but also a lateral displacement of specimen details. This in-plane distortion of specimen details results from the lateral shrinkage of the embedded specimen. There is, however, a threshold dose above which the specimen is stable.

The fact that many small areas within a cell, which contain good intrinsic reference marks, can often be reliably reconstructed suggests that sections of similar thickness along a ribbon undergo similar amounts of thinning and lateral shrinkage without a significant loss of specimen material. Furthermore, the detrimental influence on the reconstruction, which arises from the radiation-induced lateral displacement of specimen details, is most likely overshadowed by residual compression remaining in the section (see below). However, the radiation-induced in-plane shrinkage of the specimen may lead to an erroneous impression

as to the diameter of the structure. For similar reasons, the size of a structure (when measured by multiplying the number of sections necessary to complete its reconstruction) should, therefore, be calculated from the thickness of the sections *before* exposure to the beam. However, in order to maintain the proper relationship between the section thickness and its corresponding profile thickness during reconstruction (see Section IV,B), a reliable estimation of section thickness after exposure to the beam must also be obtained (see Section III,E).

A more important consideration as to why adjacent sections may fail to match undoubtedly arises from the residual compression that remains in the sections after they have been expanded. During microtomy, sections are compressed in a direction perpendicular to the leading and trailing edges of the block (Peachey, 1958). Since the degree of compression is related to the thickness of the section (Williams and Kallman, 1955; Hayat, 1970), the varying thickness of sections along a ribbon suggests that sections will show a variable amount of residual compression after expansion (Bang and Bang, 1957; Peachey, 1958; Sjöstrand, 1958). This residual compression cannot be eliminated and will result in the permanent distortion of the structure(s) to be reconstructed. A large variation in the compression of serial sections makes it extremely difficult to reconstruct large areas (Bang and Bang, 1957; Fuscaldo and Jones, 1959). According to Sjöstrand (1958), the variation in structural distortion (which arises from compression) must be smaller than the size of the smallest component to be included in the reconstruction for the reconstruction to be accurate. Peachey (1958) notes that the amount of distortion can be estimated by measuring the axial ratios of structures, which are presumed to be spherical before sectioning. Indeed, compression can be such a serious problem that, in constructing a three-dimensional model, the surfaces of the various components of the model must be filed smooth to "approximate the average position of the contours in the drawing" (Sjöstrand, 1958; see also Karlsson, 1966).

Without proper reference marks it is difficult to align serial sections without biasing the reconstruction by a preconceived conception as to how the structure should look (Sjöstrand, 1958; Peachey, 1975). Gaunt and Gaunt (1978) describe three types of reference marks; included, intrinsic, and best fit. Included reference marks, in which objects are positioned near the field to be reconstructed before sectioning, were frequently used in light microscopic serial reconstruction. Although it is technically feasible, there are at present no reports describing the use of included reference marks in positioning electron micrographs of serial sections (Gaunt and Gaunt, 1978). In some cases, one or more cell structures may be found within the area to be reconstructed, which can serve as appropriate reference marks. These intrinsic reference structures are usually constituents (plasma membrane, synaptic ribbon, nucleus, lipid drops, etc.), which can easily be followed from section to section (Sjöstrand, 1958; Koukl *et al.*, 1977). When large areas are to be reconstructed, however, the sections must be aligned by

using reference marks that are external to the area being reconstructed (that is, by the best-fit method). As noted by Gaunt and Gaunt (1978), these reference marks usually consist of either elements whose long axis is perpendicular to the plane of the section (axons, blood vesicles, membranes, etc.) or sharply delineated cell components (nuclei, mitochondrion, etc.). Under these circumstances, at least two (and preferably more) of these types of reference structures must be used to ensure a faithful reconstruction.

In reconstructing an area from serial thick sections, it is necessary to align the bottom of a reference structure in one section with the top of the same reference structure in the next consecutive section. This is facilitated if the reference structure is a linear element, the long axis of which is perfectly perpendicular to the plane of the section. However, if the reference structure traverses the thickness of the section at an angle, it will be necessary to establish which part of the structure lies on the surface of the section and which part is on the bottom. This can be done only by viewing the reference structure in stereo micrographs in two consecutive sections (Hama, 1976). During the reconstruction (see below) the bottom of the reference structure in one section can then be aligned with the surface of the same structure in the adjacent section.

B. Methods Used in Three-Dimensional Reconstruction

The procedures used in obtaining useful three-dimensional information from photomicrographs of serial sections have been reviewed (Ware and Lopresti, 1975; Gaunt and Gaunt, 1978), and only a brief description will be given here. The three-dimensional information contained in a series of serial thick or thin sections can be either displayed graphically in two dimensions, or used to build a solid model. In either case, to obtain an accurate reconstruction, reference structures must be used to ensure proper alignment between adjacent sections (see Section IV,A). In addition, the information from each section must also be carefully aligned in the vertical axis so that the total vertical thickness of the reconstruction is "proportional to the thickness of the layer of tissue represented" (Fuscaldo and Jones, 1959). This involves calculating the vertical space within the reconstruction that must be alloted to each section after it has been magnified to the desired level. For example, if an object or area is to be reconstructed from sections that average (after exposure to the beam—see Section III,E) 0.25 μm thick, at a final magnification of 20,000×, then the final thickness of each section in the reconstruction should be 5 mm (20,000 × 0.25 μm). In this example, the two-dimensional information obtained from each section must be spaced 5 mm apart in the vertical axis in order to achieve an accurate reconstruction. An additional consideration arises when thicker sections ($\geq$0.25 μm) are to be used for serial reconstruction. At present there is no satisfactory way of transposing the three-dimensional information obtained from a section,

by stereo viewing, onto a solid medium in a manner that maintains the three-dimensional relationship between cell constituents (however, see Section IV,B,1). Therefore, a satisfactory reconstruction can be achieved only by stacking, at an appropriate vertical distance, only that two-dimensional information contained within either the top or bottom surface of each section (as determined by stereo viewing). However, it must be noted that under these circumstances an accurate reconstruction will be obtained only if the profile of interest is uniform throughout the section thickness (Peachey, 1975). If this is not the case, then an accurate reconstruction can be achieved only by using thinner sections.

1. Graphic Methods

Bang and Bang (1957) described a simple procedure for graphically reconstructing the third dimension from serial electron micrographs. In this method, the structure(s) of interest in the first photomicrograph are carefully traced onto a sheet of transparent acetate plastic. The outlines of the structure(s) in each sequential section are then aligned and traced, with different colored pencils, onto the same sheet of paper. The result is a composite tracing of the structure(s) on a single sheet of paper with depth information coded by color. Procedures based on this method are frequently used to reconstruct the distribution (e.g., Rattner and Berns, 1976) and arrangement (e.g., Jensen and Bajer, 1973) of spindle microtubules during the various stages of mitosis (see Fig. 7). Depending on the nature of the material, the reconstruction can become quite confusing, especially if a large number of sections are displayed in this manner.

To eliminate some of this confusion by stereo viewing, Bang and Bang (1957) introduced a second method whereby the information contained in each micrograph is traced onto separate thin sheets of clear plastic. After the structures of interest are filled in with colored ink, the tracings are stacked in alignment at an appropriate (see Section IV,B) distance apart and illuminated from the end. This method, which is widely used in serial reconstruction (e.g., see Kubai and Ris, 1969; Barajas, 1970; Koukl *et al.*, 1977; Crang and Pechak, 1978), provides an effective way of stereoscopically visualizing particular structures within the reconstruction (see Fig. 8). Jordan and Saunders (1976) have modified the above procedure by using waterproof inks and clear acetate sheets. The sheets are supported by a frame that can be immersed in water and illuminated from below. This technique is particularly useful for displaying the enclosed structures. In addition, the use of suitable colors allows for the emphasis of selected components. The authors note that the information contained in up to sixty sections (depending on the nature of the material) can be easily visualized and that the reconstruction can be recorded by stereophotography.

In a similar manner, a three-dimensional image can also be reconstructed from up to ten serial thin sections by stacking lantern slides of negatives from consecu-

tive sections (Fuscaldo and Jones, 1959). In this procedure, the density at which the positive slides are printed is varied to produce a graded series in which the top section of the series is the least dense while the bottom section is the most dense. Consecutive transparencies are then aligned, glued together, and illuminated from below for stereophotography. A method similar to this has been used by Fuge (1974) to study the arrangement of microtubules during mitosis in *Tipulid* spermatocytes.

Dunn (1972) has described an additional method for graphically reconstructing serially sectioned structures, which is based on a procedure used by cartographers to convey topographical configurations. It is particularly suited for reconstructing the shape of areas or structures that are delineated by membranes. In this method, the photographs are arranged in a serial sequence, and the structural information from the first photograph is traced in its entirety onto a single piece of tracing paper. The same piece of tracing paper is then superimposed over the second serial micrograph. With the aid of a sheet of plastic that contains scribed lines, the tracing paper is staggered at an angle from the tracing of the previous section. When the structural information from the second micrograph is traced onto the paper, only those surfaces "in front" of the structures from the previous section will be shown. The angle and increment at which the tracing paper is moved between sections will determine, respectively, the angle and slope at which the surface is viewed. It is possible that this method of reconstruction could be slightly modified to retrieve some of the three-dimensional shape information which is lost when the image of a thick section is traced onto a two-dimensional surface. For example, a stereo pair of photographs from each thick section could be projected onto a single piece of tracing paper, and, with the aid of a stereo viewer, more than one contour line could then be drawn to portray the three-dimensional shape of each object on the section. The process could then be repeated, as described above, for each section. If only shape information is required, this approach may possibly provide a more accurate reconstruction by eliminating the "uniformity of profile" assumed by other methods of reconstruction.

Extensive serial reconstruction projects have recently been facilitated by the ability of computers to collect, store, and analyze data from a series of serial micrographs. The task of reconstruction can then be left to the computer, which will create a visual representation of the structure or area of interest on a graphic terminal (see the review by Ware and Lopresti, 1975). For example, Macagno *et al.* (1973; see also Levinthal and Ware, 1972; Levinthal *et al.*, 1974; Macagno and Levinthal, 1975) have used a computer to reconstruct the structure and development of neuronal connections in the optic system of *Daphnia magna*. The two-dimensional structural information obtained from 1500 thin serial sections through the optic ganglion was collected by a computer using a CARTOS (Computer-Aided Reconstruction by Tracing of Serial Sections) system de-

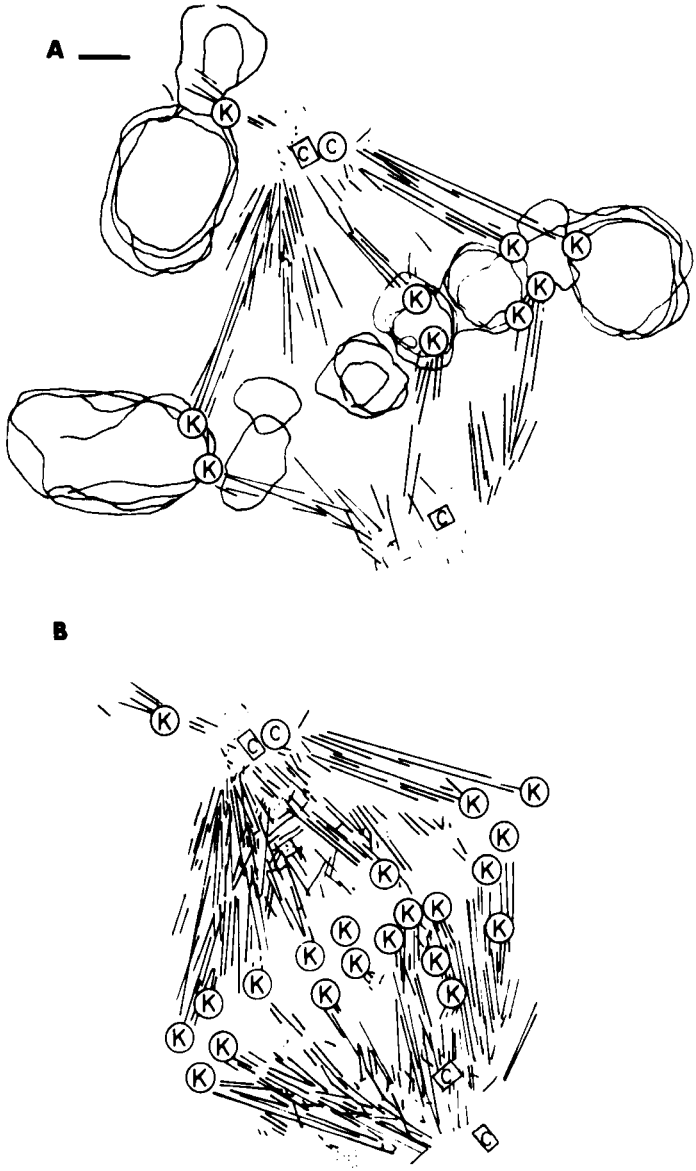


FIG. 7. A modification of a procedure introduced by Bang and Bang (1957—see text) was used to reconstruct the mitotic apparatus of a Chinese hamster ovary (CHO) cell recovering from colcemid arrest. Microtubules, chromosomes, centrioles, and kinetochores were traced, from micrographs of 0.25-μm-thick serial sections, onto plastic transparent sheets. The serial tracings were then superimposed, using the chromosomes as reference structures, to reconstruct the mitotic apparatus in two dimensions. Depth dimension information was computed from the number of intervening sections. In (A) the compiled tracings from four sections are shown. In (B) eighteen adjacent and alternate-adjacent sections, representing a total specimen thickness of 6.0 μm, are shown (chromosomal outlines were excluded for clarity). From the reconstruction, the spatial arrangement and relationship between kinetochores, microtubules, and centrioles can be determined. C = centriole, K = kinetochore. Magnification 8000×. Bar in (A) = 1.0 μm. Courtesy of Dr. P. Witt. University of Wisconsin.

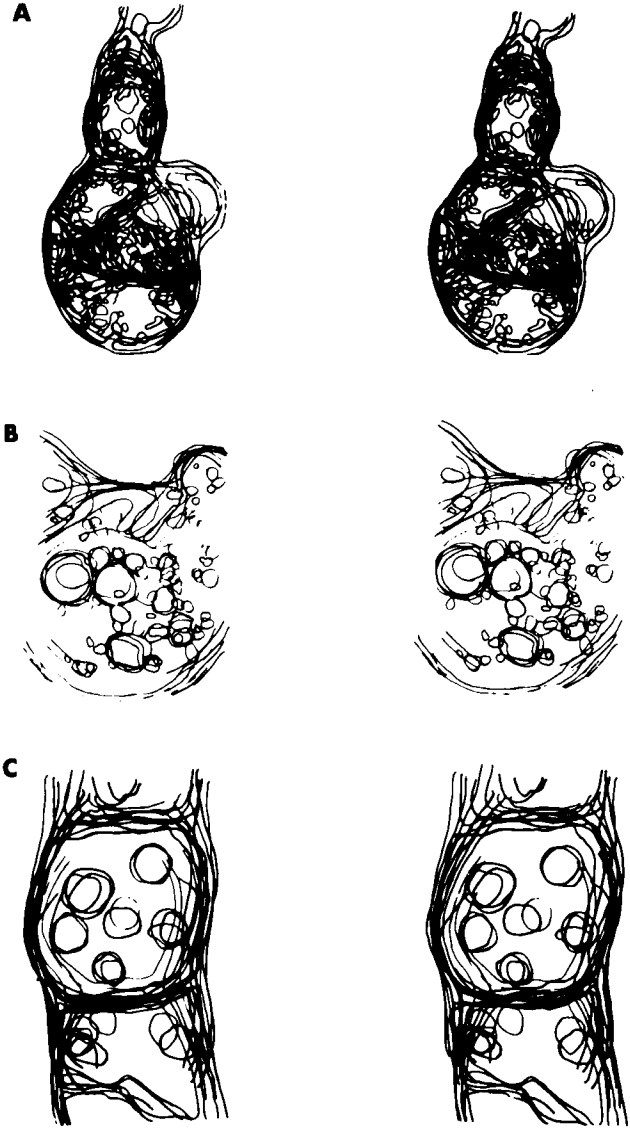


FIG. 8. Stereo pairs of the black yeast *A. pullulans* made from line drawing overlays of serial thick sections. These three reconstructions were made by tracing cell walls and either mitochondrion (A), vacuoles (B), or nuclei (C) onto clear acetate sheets with felt-tip pens. The sheets were then aligned and spaced vertically with cardboard spacers. Stereo pictures were made to facilitate the interpretation of cellular three-dimensional arrangement. In (A) five serial sections were used to reconstruct the arrangement of the mitochondrion within a total specimen thickness of 2.5 μm. The mitochondrion can be seen to be highly polymorphic and form a network around the cell periphery. In (B) five 0.5-μm-thick serial sections were used to reconstruct part of the vacuolar system. This reconstruction reveals that several large vacuoles are connected by smaller vacuolar canals at different levels within the cell. In (C) eight 0.5-μm-thick serial sections were used to reconstruct a total specimen thickness of approximately 4.0 μm. In this reconstruction, seven unconnected nuclei are present in the center of the cell. Stereo viewing indicates that the centermost profiles represent two nuclei in widely separated planes. Magnification in (A) 2100×; in (B) 5300×; in (C) 4200×. From Crang and Pechak (1978).

veloped by the authors. The computer was then used to analyze and assemble the data into a graphic three-dimensional reconstruction. With this system, these investigators were able to study the detailed structural organization of the various classes of nerve cells and fibers that compose the optic ganglion in *Daphnia*.

Peachey (1975) has developed a method for computer-aided reconstruction from thick sections. It uses a manual analog device to trace, in each serial section, those profiles to be reconstructed. The resulting coordinate data concerning the structure(s) of interest and associated reference structures are stored in a small digital computer. A larger digital computer is then used to process the information and to graphically display a three-dimensional reconstruction. However, the two-dimensional nature of the image that is traced from any one section leads to ambiguities if the structural detail desired is on the order of, or smaller than, the section thickness (see Section II,IV,B above). Under these circumstances, thinner sections must be used for reconstruction.

2. Solid Models

As an alternative to graphic reconstruction, a solid model can be built from the information contained in serial sections. Model building is particularly useful when it is necessary to obtain a three-dimensional view of the external surface and overall morphology of a particular component. In general, model building is accomplished in one of two ways. In the first method, the two-dimensional information from each section is traced onto individual acetate sheets as described by Bang and Bang (1957). These sheets are then aligned sequentially by the best-fit method (see Section IV,A), spaced vertically, and glued together (usually by flooding with acetone). The structure(s) of interest are then cut from the composite with a jeweler's saw, sanded smooth, and painted (e.g., see Sjöstrand, 1958; Paulin, 1975b, 1977).

In the second method the information from each section is projected and traced onto individual sheets of cardboard (e.g., Sotelo *et al.*, 1973; Koukl *et al.*, 1977), polystyrene (e.g., Pedler and Tilly, 1966; Karlsson, 1966; Sattler and Staehelin, 1976; Murray and Davies, 1979), or clear acetate (e.g., Keddie and Barajas, 1969; Kubai and Ris, 1969; Stempak and Laurenchin, 1976). The structures of interest are then cut from the sheets and stacked sequentially, using appropriate reference structures. The resultant model, which will have a "step-like" appearance, can be sanded smooth and painted to facilitate photography.

Regardless of how the model is built, the thickness of the substrate onto which the image of each section is projected must be equal to the product of the average section thickness and the final magnification of the reconstruction. In this manner the total vertical thickness of the reconstruction will be proportional to the actual thickness of the structure represented (see above).

ACKNOWLEDGMENTS

Support from the following sources is gratefully acknowledged. PHS Postdoctoral Training Grant GM 07194, PHS Grant 25062 to Dr. G. Borisy, and a NIH Research Grant RR 00570 to the AEI-EM7 High Voltage Electron Microscope Facility, University of Wisconsin, Madison, Wisconsin. I should also like to thank Drs. H. Ris, D. Neuberger, J. Pawley, and Ms. S. Nowogrodzki for their helpful assistance.

REFERENCES

Bang, B. G., and Bang, F. B. (1957). *J. Ultrastruct. Res.* **1,** 138-146.
Barajas, L. (1970). *J. Ultrastruct. Res.* **33,** 116-147.
Barnes, G. G., and Chambers, T. C. (1961). *J. Biophys. Biochem. Cytol.* **9,** 724-725.
Behnke, O., and Rostgäard, J. (1964). *Stain Technol.* **39,** 205-208.
Bradley, D. E. (1967). *In* "Techniques for Electron Microscopy" (D. Kay, ed.), pp. 58-74. Blackwell, Oxford.
Brecher, S. (1975). *Exp. Cell Res.* **96,** 303-310.
Brinkley, B. R., Murphy, P., and Richardson, L. C. (1967). *J. Cell Biol.* **35,** 279-283.
Buckley, I. K. (1974). *Tissue & Cell* **6,** 1-20.
Buckley, I. K., and Porter, K. R. (1973). *J. Cell Biol.* **59,** 37a.
Buckley, I. K., and Porter, K. R. (1975). *J. Microsc. (Oxford)* **104,** 107-120.
Butler, J. K. (1974). *Stain Technol.* **49,** 129-132.
Coss, R. A., and Pickett-Heaps, J. D. (1974). *J. Cell Biol.* **63,** 84-97.
Couteaux, R., Carasso, N., and Favard, P. (1975). *J. Microsc. (Paris)* **24,** 283-294.
Cox, G., and Juniper, B. (1972). *J. Microsc. (Oxford)* **97,** 29-40.
Crang, R. E., and Pechak, D. G. (1978). *Protoplasma* **96,** 225-234.
Davidowitz, J., Paghter, B. R., and Breinin, G. M. (1976). *Stain Technol.* **51,** 247-248.
Dowell, W. C. T. (1959). *J. Ultrastruct. Res.* **2,** 388-392.
Dunn, R. F. (1972). *J. Microsc. (Oxford)* **96,** 301-307.
Favard, P., and Carasso, N. (1972). *J. Microsc. (Oxford)* **97,** 59-81.
Fuge, H. (1974). *Chromosoma* **45,** 245-260.
Fuscaldo, K. E., and Jones, H. H. (1959). *J. Ultrastruct. Res.* **3,** 1-10.
Galey, F. R., and Nilsson, S. E. (1966). *J. Ultrastruct. Res.* **14,** 405-410.
Gaunt, W. A., and Gaunt, P. N. (1978). "Three Dimensional Reconstruction in Biology." University Park Press, Baltimore, Maryland.
Gay, H., and Anderson, T. F. (1954). *Science* **120,** 1071-1073.
Gelber, D. (1957). *J. Biophys. Biochem. Cytol.* **3,** 311-316.
Gillis, J. M., and Wibo, M. (1971). *J. Cell Biol.* **49,** 947-949.
Glauert, A. M. (1974). *J. Cell Biol.* **63,** 717-748.
Glauert, A. M. (1979). *J. Microsc. (Oxford)* **117,** 93-101.
Glauert, A. M., and Mayo, C. R. (1972). *J. Microsc. (Oxford)* **97,** 83-94.
Glauert, A. M., and Phillips, R. (1967). *In* "Techniques for Electron Microscopy" (D. Kay, ed.), pp. 213-253. Blackwell, Oxford.
Gorycki, M. A. (1965). *Stain Technol.* **40,** 265-267.
Gorycki, M. A. (1977). *Stain Technol.* **52,** 255-260.
Gunning, B. E. S., and Hardham, A. R. (1977). *J. Microsc. (Oxford)* **109,** 337-340.
Hama, K. (1973). *In* "Advanced Techniques in Biological Electron Microscopy" (J. K. Koehler, ed.), pp. 275-297. Springer Verlag, Berlin and New York.

Hama, K. (1976). *In* "Recent Progress in Electron Microscopy of Cells and Tissue" (E. Yamada, V. Mizuhira, K. Kurosumi, and T. Nagano, eds.), pp. 343-353. University Park Press, Baltimore, Maryland.
Hama, K., and Nagata, F. (1970). *J. Cell Biol.* **45,** 654-659.
Hama, K., and Porter, K. R. (1969). *J. Microsc. (Paris)* **8,** 149-158.
Harris, N. (1979). *Planta* **146,** 63-69.
Haskins, E. F. (1976). *Chromosoma* **56,** 95-100.
Hayat, M. A., ed. (1970). "Principles and Techniques of Electron Microscopy," Vol. 1. Van-Nostrand-Reinhold, Princeton, New Jersey.
Heath, J. P., and Dunn, G. S. (1978). *J. Cell Sci.* **29,** 197-212.
Hopkins, W. G. (1979). *J. Micros. (Oxford)* **115,** 107-109.
Hudson, B., and Makin, M. J. (1970). *J. Phys. E* **3,** 311.
Jensen, C., and Bajer, A. S. (1973). *Chromosoma* **44,** 73-80.
Jordan, E. G., and Saunders, A. M. (1976). *J. Micros. (Oxford)* **107,** 205-206.
Karlsson, U. (1966). *J. Ultrastruct. Res.* **16,** 482-509.
Karlsson, U., Andersson-Cedergren, E., and Ottoson, D. (1966). *J. Ultrastruct. Res.* **14,** 1-35.
Keddie, F. M., and Barajas, L. (1969). *J. Ultrastruct. Res.* **29,** 260-275.
King, M. V., and Parsons, D. F. (1978). *J. Microsc. (Oxford)* **113,** 301-305.
Koukl, J., Vorbeck, M. L., and Martin, A. P. (1977). *J. Ultrastruct. Res.* **61,** 158-165.
Kubai, D. F., and Ris, H. (1969). *J. Cell Biol.* **40,** 508-528.
Levinthal, C., and Ware, R. (1972). *Nature (London)* **236,** 207-210.
Levinthal, C., Macagno, E., and Tountas, C. (1974). *Fed. Proc., Fed. Am. Soc. Exp. Biol.* **33,** 2336-2340.
Locke, M., and Krishan, N. (1971). *J. Cell Biol.* **50,** 550-557.
Macagno, E., and Levinthal, C. (1975). *Proc. 33rd Annu. Meet. Electron Microsc. Soc. Am.* pp. 284-285.
Macagno, E., Lopresti, V., and Levinthal, C. (1973). *Proc. Natl. Acad. Sci. U.S.A.* **70,** 57-61.
McIntosh, J. R., McDonald, K. L., Edwards, M. K., and Boss, B. M. (1979a). *J. Cell Biol.* **83,** 428-442.
McIntosh, J. R., Sisken, J. E., and Chu, L. K. (1979b). *J. Ultrastruct. Res.* **66,** 40-52.
Mazziotta, J. C., Hamilton, B. C., and Fenner-Crisp, P. A. (1973). *Stain Technol.* **48,** 153-154.
Mollenhauer, H. H. (1976). *J. Microsc. (Oxford)* **107,** 203-204.
Murray, A. B., and Davies, H. G. (1979). *J. Cell Sci.* **35,** 59-66.
Nagata, F., Hama, K., and Porter, K. R. (1969). *J. Electronmicrosc.* **18,** 106-109.
Nankivell, J. F. (1963). *Optik. Z. Gesamte Geb. Lichtund Elektrononptik.* **20,** 171-198.
Nelson, B. K., and Flaxman, B. A. (1972). *J. Microsc. (Oxford)* **97,** 377-380.
Nicklas, R. B., Kubai, D. F., and Ris, H. (1979). *Chromosoma* **74,** 39-50.
Palay, S. L., and Chan-Palay, V. (1972). *J. Micros. (Oxford)* **97,** 41-47.
Paulin, J. J. (1974). *Proc. 32nd Annu. Meet. Electron Microsc. Soc. Am.* pp. 62-63.
Paulin, J. J. (1975a). *Proc. 33rd Annu. Meet. Electron Microsc. Soc. Am.* pp. 286-287.
Paulin, J. J. (1975b). *J. Cell Biol.* **66,** 404-413.
Paulin, J. J. (1977). *Exp. Parasitol.* **41,** 283-280.
Peachey, L. D. (1958). *J. Biophys. Biochem. Cytol.* **4,** 233-242.
Peachey, L. D. (1975). *Proc. 33rd Annu. Meet. Electron Microsc. Soc. Am.* pp. 288-289.
Peachey, L. D., and Eisenberg, B. R. (1978). *Biophys. J.* **22,** 145-154.
Peachey, L. D., and Franzini-Armstrong, C. (1977). *Proc. 35th Annu. Meet. Electron Microsc. Soc. Am.* pp. 570-571.
Pease, D. C. (1964). "Histological Techniques for Electron Microscopy." Academic Press, New York.
Pedler, C., and Tilly, R. (1966). *J. R. Microsc. Soc.* **86,** 189-197.

Peterson, J. B., and Ris, H. (1976). *J. Cell Sci.* **22,** 219-242.
Porter, K. R., and Hama, K. (1968). *J. Cell Biol.* **39,** 157a.
Rambourg, A., Marraud, A., and Chrétien, M. (1972). *J. Micros. (Oxford)* **97,** 49-57.
Rambourg, A., Clermont, Y., and Marraud, A. (1974). *Am. J. Anat.* **140,** 27-46.
Rattner, J. B., and Berns, M. W. (1976). *Cytobios* **15,** 37-43.
Rieder, C. L. (1979a). *Proc. 37th Annu. Meet. Electron Microsc. Soc. Am.* pp. 160-161.
Rieder, C. L. (1979b). *J. Cell Biol.* **83,** 333a.
Rieder, C. L. (1979c). *J. Cell Sci.* **40,** 215-234.
Rieder, C. L. (1979d). *J. Ultrastruct. Res.* **66,** 109-119.
Rieder, C. L., and Bajer, A. S. (1977). *Cytobios* **18,** 201-234.
Rieder, C. L., Jensen, C. G., and Jensen, L. S. (1979). *J. Ultrastruct. Res.* **68,** 173-185.
Ris, H. (1969). *J. Microsc. (Paris)* **8,** 761-766.
Ris, H. (1978). *Electron Microsc., Proc. Int. Cong. 9th, 1978* pp. 545-556.
Ris, H., and Korenberg, J. (1979). *Cell Biol.* **2,** 268-362.
Roberts, I. M. (1970). *J. Microsc. (Oxford)* **92,** 57-61.
Rostgäard, J. (1973). *Stain Technol.* **48,** 279-282.
Rowley, J. C., and Moran, D. T. (1975). *Ultramicroscopy* **1,** 151-155.
Sattler, C. A., and Staehelin, L. A. (1976). *Tissue & Cell* **8,** 1-18.
Schabtach, E., and Parkening, T. A. (1974). *J. Cell Biol.* **61,** 261-264.
Scott, G. L., and Guillery, R. W. (1974). *J. Neurocytol.* **3,** 567-590.
Sigee, D. C. (1976). *J. Micros. (Oxford)* **108,** 325-329.
Silverman, L., Schreiner, B., and Glick, D. (1969). *J. Cell Biol.* **40,** 768-772.
Sjöstrand, F. S. (1958). *J. Ultrastruct. Res.* **2,** 122-170.
Sjöstrand, F. S. (1974). *J. Ultrastruct. Res.* **49,** 60-156.
Sjöstrand, F. S. (1978). *J. Ultrastruct. Res.* **62,** 54-81.
Sotelo, J. R., Garcia, R. B., and Wettstein, R. (1973). *Chromosoma* **42,** 307-333.
Stempak, J., and Laurencin, M. (1976). *Am. J. Anat.* **145,** 261-282.
Tippit, D. H., and Pickett-Heaps, J. D. (1977). *J. Cell Biol.* **73,** 705-727.
Tippit, D. H., Schultz, D., and Pickett-Heaps, J. D. (1978). *J. Cell Biol.* **79,** 737-763.
Ward, R. T. (1972). *Stain Technol.* **47,** 257-260.
Ware, R. W., and Lopresti, V. (1975). *Int. Rev. Cytol.* **40,** 325-440.
Wells, B. (1974). *Micron* **5,** 79-81.
Westfall, J. A. (1961). *Stain Technol.* **36,** 36-37.
Westfall, J. A., and Healy, D. L. (1962). *Stain Technol.* **37,** 118-121.
Williams, R. C., and Kallman, F. (1955). *J. Biophys. Biochem. Cytol.* **1,** 301-314.
Wolosewick, J., and Porter, K. R. (1976a). *Am. J. Anat.* **147,** 303-324.
Wolosewick, J., and Porter, K. R. (1976b). *Am. J. Anat.* **149,** 197-226.
Wolosewick, J., and Porter, K. R. (1979). *J. Cell Biol.* **82,** 114-139.
Wyatt, J. H. (1974). *J. Microsc. (Oxford)* **101,** 207-210.
Yamada, E., and Ishikawa, H. (1972). *Proc. 30th Annu. Meet. Electron Microsc. Soc. Am.* pp. 480-481.
Zelander, T., and Ekholm, R. (1960). *J. Ultrastruct. Res.* **4,** 413-419.

This Page Intentionally Left Blank

Chapter 14

Three-Dimensional Reconstruction of Membrane Protein Crystals

STEPHEN D. FULLER

Institute of Molecular Biology,
University of Oregon,
Eugene, Oregon

I. Introduction 251
II. Two-Dimensional Crystals 253
A. Source 253
B. Structures of Crystals 255
III. Preliminary Analysis of Crystals 261
IV. Technique of Three-Dimensional Reconstruction 262
A. Conditions for Microscopy 266
B. Projection Analysis 271
C. Three-Dimensional Analysis 277
V. Biochemical Results 283
A. Cytochrome *c* Oxidase 283
B. Purple Membrane 290
C. Gap Junction 291
References 294

I. Introduction

Molecular biology aims at an understanding of biological systems in terms of the interactions of their molecular components. X-ray crystallography has contributed to this goal by determining the structures of biological molecules to atomic resolution. Electron microscopy has fulfilled a complementary role by revealing structure at the cellular and organellar level, and by providing a context in which the relevance of high-resolution structural information to the larger biological system is seen.

Copyright © 1981 by Academic Press, Inc.
All rights of reproduction in any form reserved.
ISBN 0-12-564122-2

X-ray crystallography is the best method for obtaining three-dimensional structural information when suitable crystals are available. Despite intense effort, three-dimensional crystals of intrinsic membrane proteins suitable for x-ray work have not yet been produced (for review, see Henderson, 1980). As a result, many details of membrane-based processes remain mysterious because so little structural information is available about the proteins involved. Three-dimensional reconstruction of two-dimensional crystals provides a source of structural conformation on intrinsic membrane proteins that is filling the gaps in our understanding of them. This technique has great potential, owing to the seemingly general tendency of these proteins to form two-dimensional crystals.

In the beginning, DeRosier and Klug (1968) first used computer processing of electron micrographs to reveal the structure of a helical virus assembly. This chapter will discuss the application of these Fourier processing techniques to crystals of membrane proteins. The work described has resulted in either low-resolution structures (2.0–3.0 nm) from negatively stained crystals, or high-resolution structures (0.7 nm or finer) from unstained, glucose- or metrizamide-embedded crystals. The structure observed at low resolution is the result of scattering from a number of domains whose relationship to protein subunits may be obscure. As a result, interpretation of the low-resolution structure in terms of biochemistry is often difficult. Despite this, the relation of the protein to the bilayer, the fraction of the protein exposed to the solvent, the orientation of features of the protein relative to the bilayer, and sometimes the relationship of these features to the function have been determined from the low-resolution structure. At higher resolution, secondary structure is often revealed.

The chapter begins with a discussion of the structures of some well-characterized two-dimensional crystals. This is followed by a brief section covering structural and biochemical techniques that complement the reconstruction technique. After a brief introduction to Fourier processing, the three-dimensional reconstruction technique is detailed. The technique is considered in three parts: first, the factors that limit resolution, and ways of overcoming them; second, the processing of a single view of a crystal and its interpretation; and, third, the piecing together of the single views to give a final three-dimensional structure. A review of the results produced by the combination of reconstruction with other techniques concludes the chapter.

Three-dimensional reconstruction has been applied to two-dimensional crystals of many biological molecules. Although the work is not considered explicitly, this chapter will serve as an introduction to crystal studies of ribosomes (Unwin, 1977), muscle proteins (Cohen *et al.*, 1972), viral proteins (Aebi *et al.*, 1973), bacterial cell walls (Stevens *et al.*, 1977), chromatin (Finch *et al.*, 1977), lipoproteins (Ohlendorf *et al.*, 1978), and others in which the Fourier reconstruction technique has been used.

II. Two-Dimensional Crystals

The techniques described in this chapter depend for success on the availability of suitable two-dimensional crystals. The quality of crystals is the primary factor limiting three-dimensional reconstruction as a structural tool.

A. Source

Some membrane proteins are found to be crystalline *in vivo*. The halophilic bacterium *Halobacterium halobium* assembles its light-driven proton pump bacteriorhodopsin into well-ordered two-dimensional crystals, the purple membrane on the surface (Oesterhelt and Stoeckenius, 1971; Blaurock and Stoeckenius, 1971). These arrays are isolated by lowering the salt content of the medium to dissociate the bacterium and by separating the crystalline purple membrane from cell debris on a sucrose gradient. Acetyl choline receptor (Ross *et al.*, 1977) and connexon, the protein of the gap junction (Zampighi and Unwin, 1979), are found as two-dimensional crystals in some tissues, although the isolation of these crystalline membranes is more difficult. Some biological assemblies, including viruses and microtubules, are ordered but not crystalline. This intrinsic order can be used to study these structures (Crowther and Klug, 1975; Smith *et al.*, 1976). More detailed information can sometimes be obtained by isolating the proteins and repolymerizing them as larger crystalline arrays that retain some or all of the symmetry of the original structure. The study of Mg^{2+}induced tubulin crystals and their relation to the microtubule structure is an elegant example of this approach (Amos and Baker, 1979; Crepeau *et al.*, 1978).

Most membrane proteins are not crystalline *in vivo*. For example, the mitochondrial inner membrane is not crystalline, but some of its proteins have been isolated as two-dimensional crystals. Two crystal forms of cytochrome *c* oxidase have been prepared by detergent treatment of mitochondria (Sun *et al.*, 1968; Seki *et al.*, 1970). Both preparations take advantage of the low solubility of the oxidase in detergents relative to other proteins in this membrane. Treating mitochondria with detergent extracts some lipid and the other proteins, leaving oxidase-enriched membranes that form crystals at the appropriate ionic strength and pH. Triton treatment produces lipid-rich $p22_12_1$ crystals (Henderson *et al.*, 1978), and deoxycholate treatment produces lipid-poor $p12_1$ crystals (Fuller *et al.*, 1979).

Crystals can also be formed from protein purified by more standard methods and reconstituted. The two oxidase crystal forms have been prepared from purified beef heart enzyme (Goldfarb *et al.*, 1979; S. D. Fuller, unpublished results). In addition, crystals of complex III from beef heart (Asai, 1978) and neurospora (Wingfield *et al.*, 1979) have been formed from the purified proteins after reconstitution.

TABLE I

Protein	Two-sided plane group	Related three-dimensional space group	Unit cell (nm)	Molecular weight of monomer (subunits)	Molecular association in crystal	Lipid: protein ratio	Crystal form *in vivo*	Type of crystal
Bacteriorhodopsin Blaurock and Stoeckenius (1971)	p3	P3	$a = b = 6.3$	26,000 (1)	Trimer	1:3	Yes	One-layered membranous
Michel *et al.* (1980)	$p22_12_1$	$P2_12_12$	5.76 × 7.35	26,000 (1)	Monomer		No	One-layered membranous
Connexon Zampighi and Unwin (1979)	p622	P622	$a = b = 8.5$	25,000–30,000 (2)	Hexamer	1:1	Yes	Two-layered membranous
Cytochrome *c* oxidase Henderson *et al.* (1977)	$p22_12_1$	$P2_12_12$	$a = 10.0$ $b = 12.5$	140,000 (7–10)	Dimer	0.3:1	No	Two-layered membranous
Fuller *et al.* (1979)	$p12_1$	$P2_1$	$a = 6.8$ $b = 17.4$	140,000 (7–10)	Monomer	0.1:1	No	Nonmembranous
Cytochrome *c* reductase Wingfield *et al.* (1979)	$p22_12_1$	$P2_12_12$	$a = 13.7$ $b = 17.4$	280,000 (10)	Dimer	0.6:1	No	One-layered membranous
Acetyl choline receptor Ross *et al.* (1977)	p1	P1	$a = 9.08$ $b = 9.10$ $\beta = 118$	380,000 (8)	Monomer		Yes	One-layered membranous

[a] This table includes only those intrinsic membrane proteins for which the two-sided plane group has been determined. The two-sided plane group nomenclature is described in Holser (1958).

B. Structures of Crystals

The intrinsic membrane protein crystals characterized so far fall into three classes: two-layered membranous, single-layered membranous, and nonmembranous (Table I).

1. Two-Layered Membranous Crystals

The $p22_12_1$ cytochrome *c* oxidase crystals have a lipid content high enough (0.3–0.4 mg/mg protein) to contain a bilayer (Henderson *et al.*, 1978). They show rounded vesicle-like edges, and, in a broken vesicle, crystallinity never extends beyond the overlap of the two sheets of the vesicle (Fig. 1A). The structure of the crystal (Fig. 1B) explains these observations. The $p22_12_1$ crystal is a collapsed vesicle. The interaction between the oxidase molecules in the two sheets of the vesicle holds the crystal together. The protein is a dimer in this crystal, and its orientation in the bilayer is opposite to the mitochondrial one. The

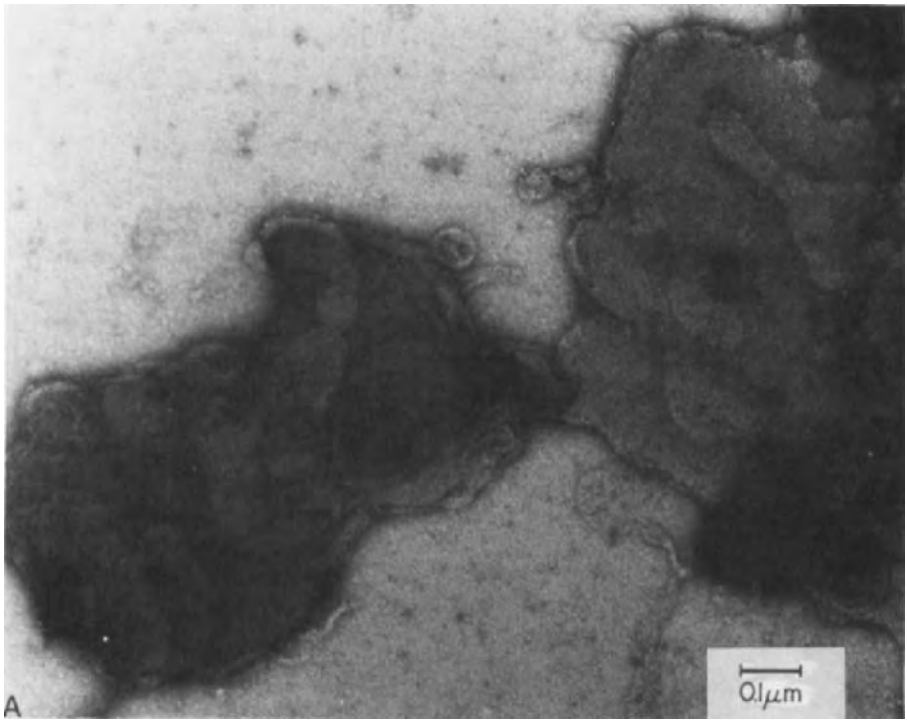


FIG. 1. Micrographs and packing of two-dimensional crystals. (A) Micrograph of $p22_12_1$ cytochrome *c* oxidase crystals negatively stained with uranyl acetate. The stacking of crystals and their rounded edges can be seen. Figure 1B-H follow on pp. 256-260.

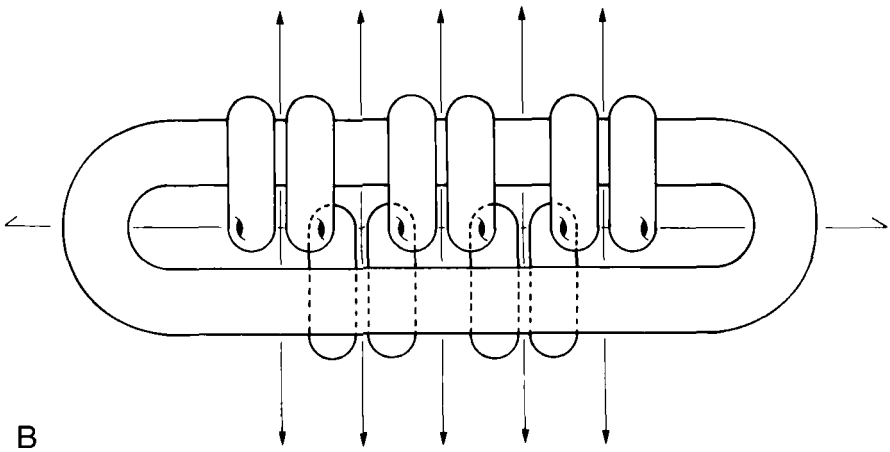


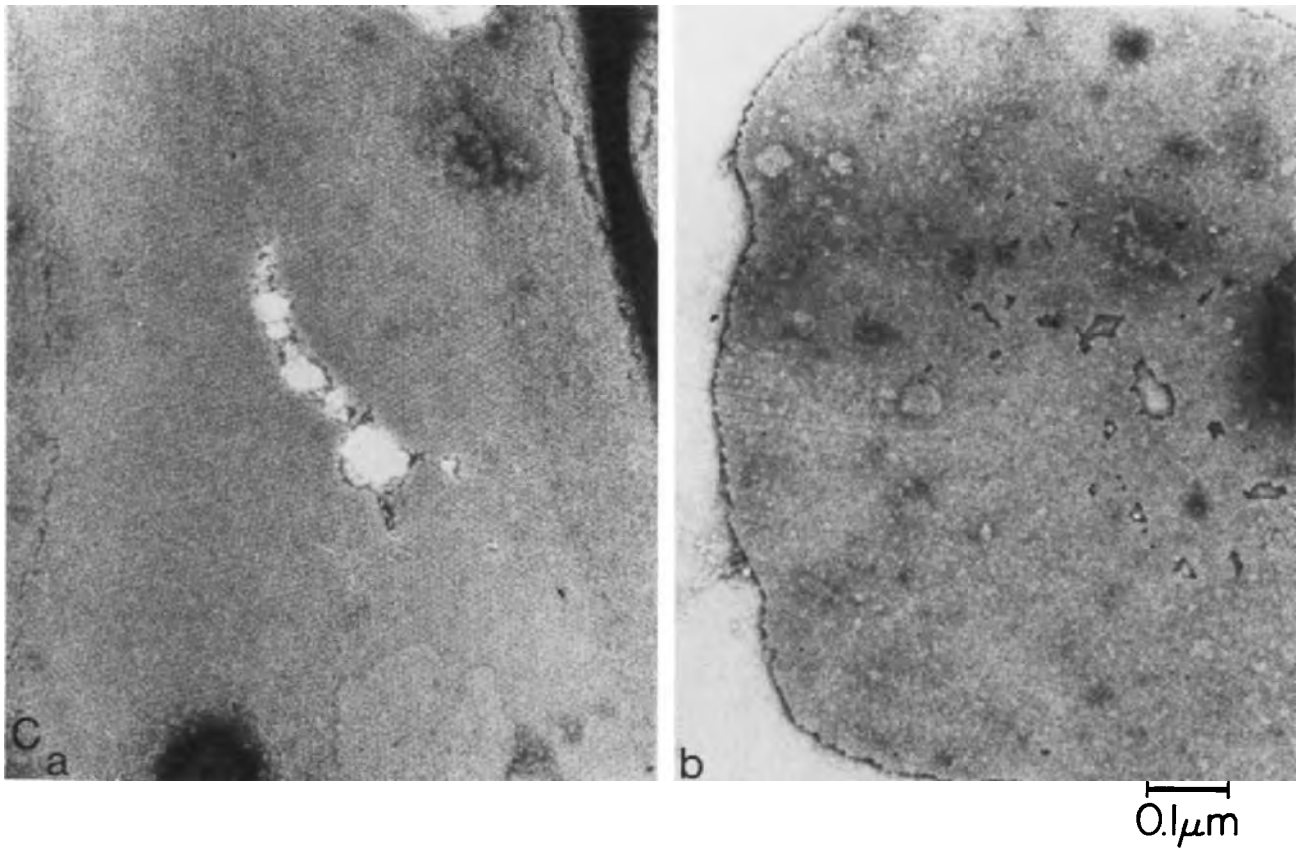
FIG. 1B. Diagram indicating the packing of cytochrome oxidase in the $p22_12_1$ crystals. The crystal is a collapsed vesicle in which the protein occurs as a dimer. The 10.0-nm (horizontal) × 12.5-nm (into page) unit cell contains two dimers. Vertical twofold axes (→) relate the monomers in each dimer. Twofold screw axes (◠ and —›) relate the dimers in the two membranes of the vesicle. The cytoplasmic (C) end of all the dimers is inside the vesicle. From Henderson *et al.* (1977), used with permission.

cytochrome *c* binding site (C) is within the vesicle, while the matrix end (M) is exterior to it. Ionic strength and pH changes disorder the crystal without destroying the membrane, suggesting that the crystal is held together by ionic interactions (Hayashi *et al.*, 1972). Another example of a two-layered crystal is the gap junction (Fig. 1C). The proteins, rather than intercalating as in $p22_12_1$ oxidase, about to form a channel (Fig. 1D) (Unwin and Zampighi, 1980).

2. One-Layered Membranous Crystals

The purple membrane protein bacteriorhodopsin is segregated in crystalline patches on the surface of its bacterium (Henderson, 1977). Upon isolation, the membrane remains a single crystalline sheet (Fig. 1E), indicating that the presence of a second membrane is unnecessary for crystallinity. Reconstituted bacteriorhodopsin spontaneously forms crystals, and their order is unaffected by ionic strength and pH over a wide range. This suggests that the crystal-forming interaction is within the membrane. All the protein molecules in the crystal are arranged in trimers and have the same orientation (Fig. 1F).

FIG. 1C. Micrographs of the A (open) form of gap junction (a) and the B (closed) form of gap junction (b) from rat hepatocyte. Both forms show p622 crystal symmetry. From Zampighi and Unwin (1979), used with permission.


a
b
0.1μm

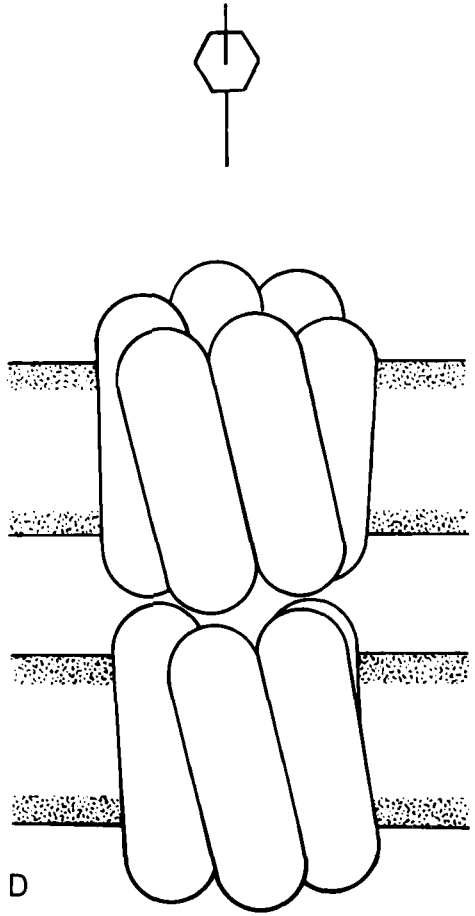
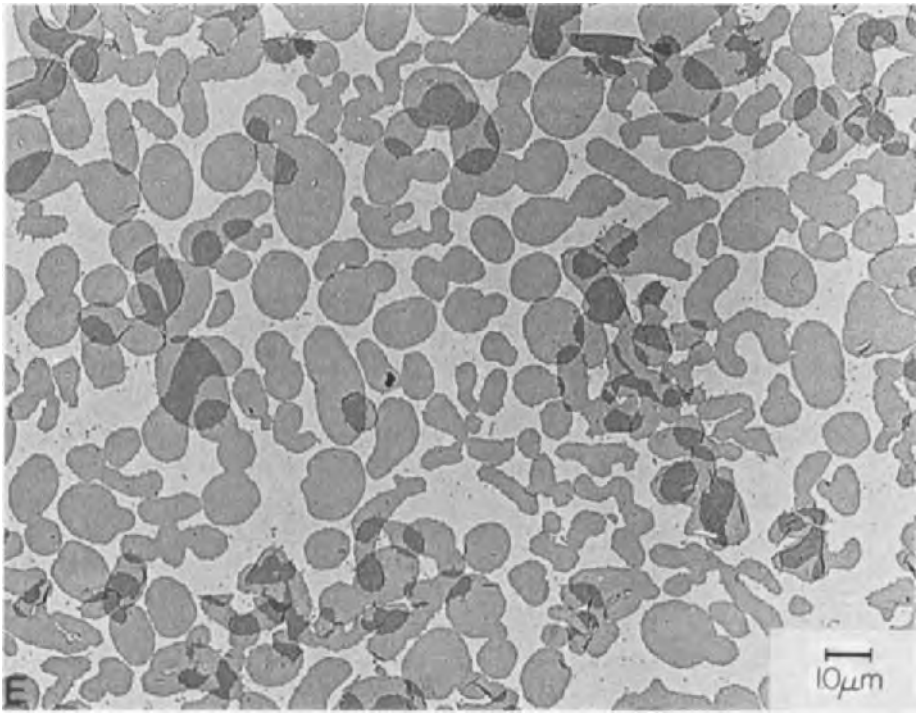


FIG. 1D. The symmetry of the connexon in p622 gap junction crystals. A sixfold symmetry axis passes vertically through the center of the connexon. The hexamers in the two membranes are related by twofold axes passing between them, perpendicular to the sixfold axis. The unit cell contains a single connexon and has axes $a = b = 8.5$ nm.

Two crystals formed from purified protein also are of the single-layered type. The ubiquinone-cytochrome *c* reductase from *Neurospora crassa* can be isolated as a Triton X-100 solubilized dimer by affinity chromatography. Reconstitution of this purified enzyme into lipid vesicles produces a $p22_12_1$ crystal in which dimers are in a single membrane but alternate in orientation (Wingfield *et al.*, 1979). A single-layered $p22_12_1$ crystal form of bacteriorhodopsin has been produced by the use of a positively charged anionic detergent (Michel *et al.*, 1980).

FIG. 1E. Low-magnification micrograph of isolated purple membranes.

FIG. 1F. The packing of bacteriorhodopsin in the p3 crystal of purple membrane. The protein is packed as trimers with a threefold axis perpendicular to the plane of the membrane. The unit cell contains a single trimer and has axes $a = b = 6.3$ nm. From Henderson (1975), used with permission.



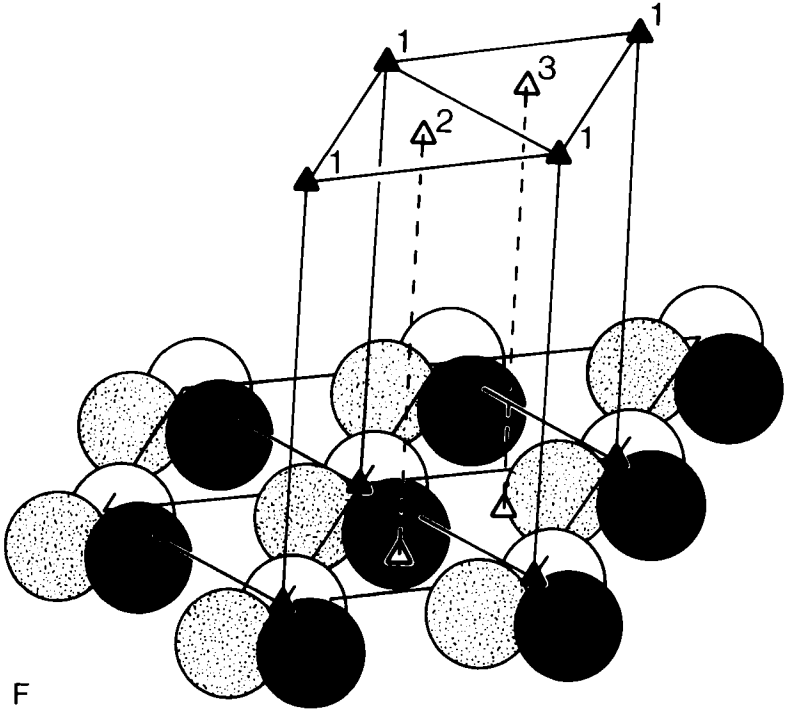


FIG. 1E and F.



FIG. 1G. Micrograph of $p12_1$ crystals of cytochrome *c* oxidase negatively stained with phosphotungstic acid.

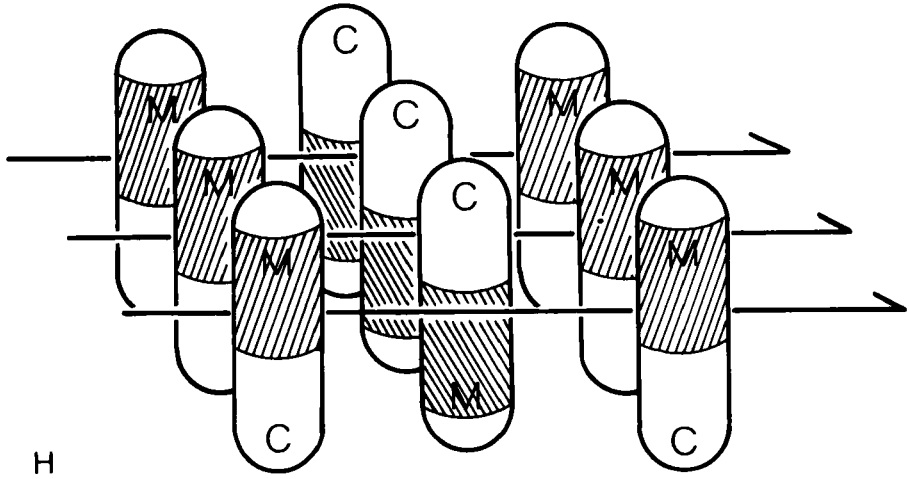


FIG. 1H. The packing of cytochrome *c* oxidase in $p12_1$ crystals. The unit cell contains two monomers related by a twofold screw axis so that both matrix (M) and cytoplasmic (C) ends of the protein are exposed on each side of the sheet. The dimensions of the unit cell are $a = 6.8$nm and $b = 17.4$ nm. The long axis is parallel to the screw axis. From Fuller *et al.* (1979), used with permission.

In the presence of this detergent (*N,N*-dodecyltrimethylammonium chloride), the $p22_12_1$ form is more stable than the p3 form.

3. Nonmembranous Crystals

The $p12_1$ crystal form of cytochrome *c* oxidase appears very different from the $p22_12_1$ form (Fuller *et al.*, 1979). The lipid content is so low (less than 0.2 mg/mg protein) that a bilayer cannot be present. The edges of the crystals are ragged, and single sheets are as well-ordered as stacked ones (Fig. 1G). The structure shows the origin of these differences (Fig. 1H). The enzyme is monomeric in this crystal, and no continuous membrane is present. The monomers touch at their hydrophobic regions within rows. Alternate rows fall in opposite orientations, such that hydrophobic regions cannot be in contact between rows. The difference between these two types of contact can be seen by lowering the pH, splitting the crystal into rows. The pH change seems to create an unfavorable ionic interaction between rows while leaving intact the hydrophobic interactions within rows.

III. Preliminary Analysis of Crystals

Two of the aims of biochemical studies on membrane protein crystals have been the characterization of their protein and lipid components, and the gaining of insight about their interactions within the crystal. Ambiguity in these studies often results from the heterogeneity of the crystalline preparations. Unless a preparation is homogeneous in protein composition and completely crystalline, biochemical techniques that measure the gross properties of the preparation, including gel electrophoresis, spectral analysis, and protein-to-lipid ratio measurements, need not indicate the crystal properties. An extreme example is that of the cytochrome *c* oxidase $p12_1$ crystals prepared with deoxycholate from mitochondria. Even the identity of the crystalline protein is in doubt, because only 40% of the preparation is cytochrome *c* oxidase (Fuller *et al.*, 1979). One way around this problem is the isolation of pure crystalline protein from the heterogeneous mixture. Preparations can be resolved on the basis of protein-to-lipid composition using isopycnic centrifugation. Crystals studied by this procedure (Goldfarb *et al.*, 1979; Fuller *et al.*, 1979; Wingfield *et al.*, 1979) are found in only a narrow segment of the gradient, indicating that they have a characteristic lipid-to-protein ratio. Unfortunately, noncrystalline protein is also found in this band.

A direct link is needed between biochemically identifiable components and the crystals themselves in heterogeneous preparations. Microscopically visualizable

labels provide this link. Examples include immunological labels (Frey *et al.*, 1978; Klymkowsky and Stroud, 1979) and specific chemical reagents with an electron-dense portion such as the avidin-ferritin-biotin system (Heitzman and Richards, 1974) and mercurial reagents (Stewart and Diakiw, 1978). Coupling specific labeling with the increased resolution made possible by reconstruction of an image of the crystal not only can identify components, but also can localize them in the structure (Aebi *et al.*, 1977; Frey *et al.*, 1978).

Other structural methods complement the reconstruction technique to give a more detailed picture of the structure. For example, the interpretation of the reconstruction results is easier if an independent determination of the thickness of the crystal is available. Several ways of estimating crystal thickness are possible. Shadowing from a fixed angle provides an estimate of the crystal thickness and a crude image of its surface. Thin sectioning also indicates the thickness of the crystal and the approximate density distribution through the structure when artifacts arising from fixation, dehydration, and embedding are minimized. The vagaries of positive staining and the superposition of many unit cells in a single section make the details of the image difficult to interpret. X-ray diffraction from stacked crystals provides a very reliable measurement of thickness and of the unit cell parameters of the crystal. The diffraction pattern can also show the presence and orientation of secondary structure features in the molecule (Henderson, 1975; Blaurock, 1975; Blaise *et al.*, 1978; Ross *et al.*, 1977). These can later be identified with features in the reconstruction.

IV. Technique of Three-Dimensional Reconstruction

Single biological molecules scatter electrons so poorly that resolution must be traded for image contrast to visualize them. In a micrograph taken of an unstained object with a low electron dose, the signal—the scattering from the biological molecule—is buried in the noise of the unscattered electrons. However, at high doses the molecule is destroyed by the impact of the electrons, producing an image of the remnants of the original structure. Contrast can be increased at the expense of resolution in other ways. For example, heavy metal negative staining increases the scattering from a specimen such as a protein by embedding it in a dense medium. The difference in density between the stain and the specimen is reflected in greater contrast in the image, but, because the stain does not coat the protein perfectly and denatures it (Unwin, 1975), only low-resolution information about the molecule is revealed. However, these problems can be bypassed by averaging processes. Images can be taken under conditions that preserve the protein, and subsequent averaging cancels out the noise while re-

TABLE II

h, K	$\lvert F\rvert$ measured	α measured	α shifted	α average	Phase error	$\lvert F\rvert$ average	$\lvert F\rvert$ error
−1, 0	393	165	185	162.5			
1, 0	393	190	170	177.5	15	393	0
−2, 0	202	180	170	165			
2, 0	215	170	180	175	10	209	6
−2, 2	235	−10	340	320			
2, 2	316	10	320	275	40	276	40
−2, 4	49	310	300	300			
2, 4	148	290	300	300	0	98	50
−1, 2	315	320	305	300			
1, 2	311	300	315	310	10	313	2
−1, 4	207	10	5	−5			
1, 4	177	340	345	335	20	192	0
−2, 1	172	130	120	125			
2, 1	178	300	310	315	10	175	3
−2, 3	136	160	150	165			
2, 3	159	290	300	315	30	147	12
−1, 1	469	20	150	15			
1, 1	458	190	195	195	0	46	0
−1, 5	109	40	35	55			
1, 5	127	250	255	275	40	118	9
−3, 0	131	90	75	0			
3, 0	96	−90	285	210	150	113	0
−3, 4	119	250	235	180			
3, 4	109	330	345	290	110	114	0
−2, 6	60	90	80	10			
2, 6	106	290	300	230	140	83	23
−1, 6	164	90	85	50			
1, 6	179	10	15	−20	170	172	8
02	467	180		180		467	
04	124	50		50		124	
06	189	280		280		189	
08	139	10		10		139	
01	2	240		240		22	
03	11	300		300		11	
05	22	260		260		22	
07	30	300		300		30	

[a] The phases (α) and amplitudes ($|F|$) are taken from a uranyl acetate negatively stained p12$_1$ crystal of cytochrome oxidase. Phases are given in degrees and are measured to ±5°. Before comparison, the measured phases were shifted by 20° using the formula $\alpha_{\text{shifted}} = \alpha_{\text{measured}} + h \cdot (\text{shift})$. Only half the reflections are shown, because the Fourier transform of any real density is symmetric about the origin (Friedel symmetry). As a result, the h, k reflection determines the values of the phase and amplitude of the $-h, -k$ reflection, regardless of the symmetry of the image.

inforcing the information from the protein. This procedure extracts the maximum information from the specimen.

The Fourier transform can be used to calculate the average structure of a molecule in a crystal in a direct way. The micrograph is scanned with a microdensitometer and the resultant array of densities transformed with a computer. As shown in Chapter 12, the transform displays the image broken into its spatial frequency components. The image components that repeat with the period of the crystal have phases and amplitudes at equally spaced points of the transform called reflections. The values of the phases and amplitudes of the reflections describe the repeating element of the crystal. In the $p12_1$ crystal of cytochrome *c*

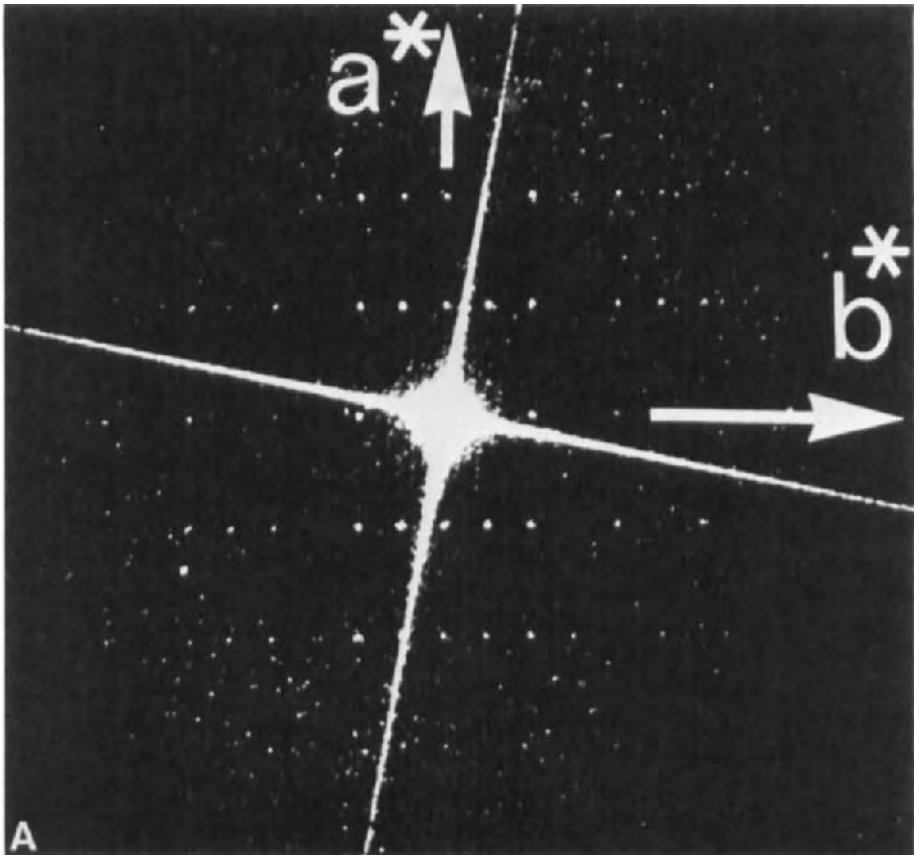


FIG. 2. Optical transform. (A) The optical transform of a minimum-dose micrograph of a $p12_1$ cytochrome *c* oxidase crystal negatively stained with uranyl acetate. From Fuller *et al.* (1979), used with permission. (B) The indexing of the pattern in (A). The crystallographic notation for negative indices ($\bar{r} = -r$) has been followed. The a^* axis (1/6.8 nm) is verticle, and the b^* axis (1/17.4 nm) is horizontal.

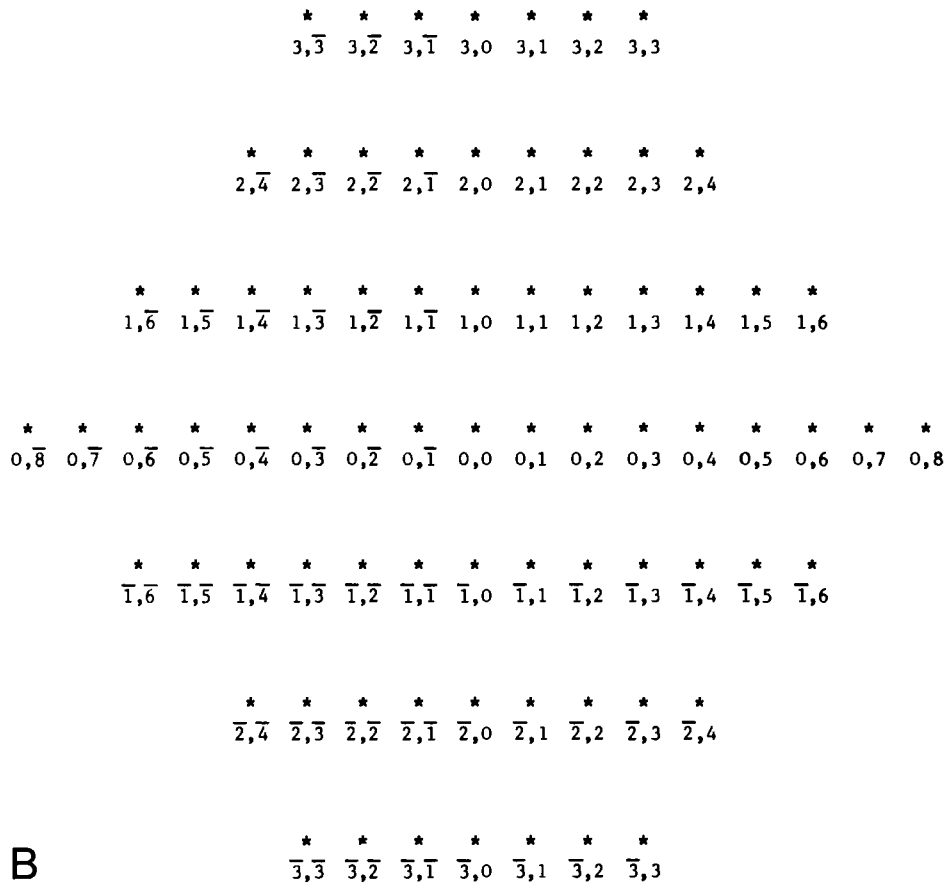


FIG. 2B.

oxidase, the repeating element or unit cell is 6.8 × 17.4 nm and contains two monomers of the protein (Fig. 1B). Table II and Fig. 2 show the transform of an image of this crystal. Reversing the process by back-transforming the phases and amplitudes of the reflections gives the repeating element of the image. This is called filtering, because only the repeated part of the image is reproduced. Noise occurring at other spatial frequencies is eliminated. The larger and better-ordered the crystal, the greater will be the number of elements averaged, and the greater the increase in signal over noise.

The amplitude of a reflection indicates the strength of that component in the image. If high-resolution reflections are present, the transform describes the average structure to high resolution. If the crystal is disordered so that the proteins in it have somewhat random positions or orientation, the average will be blurred and the transform will have weak high-resolution reflections.

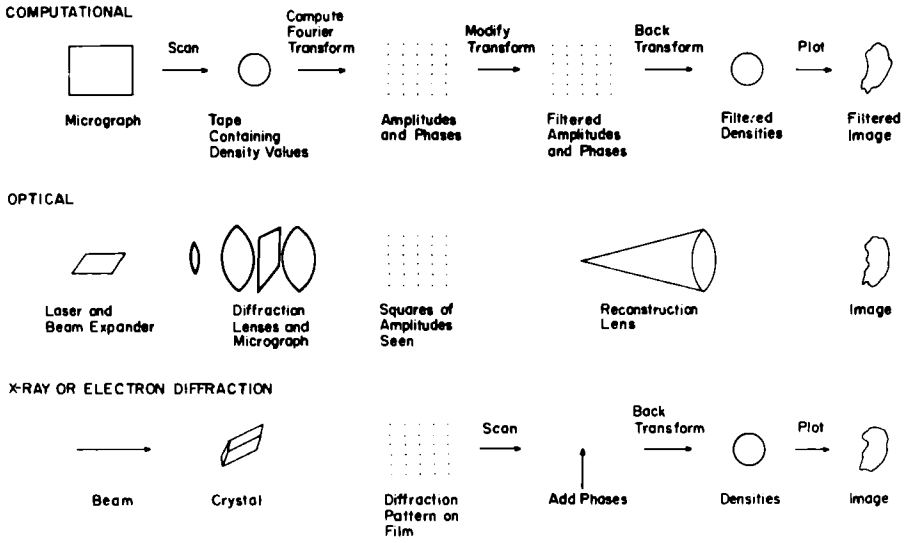


FIG. 3. Relation between the Fourier transform and diffraction. In all cases, both phases and amplitudes of the transform are needed to generate an image of the repeating unit. When the transform is computed from the density values directly, phases and amplitudes are obtained. The optical diffractometer displays the squares of the amplitudes of the transform of an image, the optical diffraction pattern. This pattern can be recorded on film, or a reconstruction lens can be used to re-form the image of the repeating unit after spatial filtering of the transform. In x-ray or electron diffraction, only the amplitudes of the diffraction pattern are accessible. Phases, determined separately, must be added to generate an image of the repeating unit.

The three stages in a three-dimensional reconstruction study of a crystal are (1) finding the best conditions for imaging, (2) calculating and interpreting the projection (the filtered image of a single view of the crystal), and (3) combining the views to obtain the three-dimensional structure. The transform is used throughout this procedure to evaluate images because it shows clearly how much and what quality of structural information is recorded in the image. The optical diffractometer (Fig. 3) is routinely used for preliminary evaluation because computation is both expensive and time-consuming. The diffraction pattern shows the squares of the amplitudes and hence the strength of the reflections in the transform (Klug and Berger, 1964; DeRosier and Klug, 1968).

A. Conditions for Microscopy

The information in a micrograph of a crystal is primarily limited by one of four effects: the beam dose, the environment of the crystal during microscopy, optical effects, and the intrinsic order of the crystal. The object of the initial step is to find conditions under which the order of the crystal is the factor limiting resolution. Once this limit has been reached, the use of more-sophisticated resolution-

preserving techniques is pointless. Only better crystals will yield high resolution with this reconstruction method. An alternative is the use of processing techniques that do not depend on the crystallinity of the specimen. These are described in Chapter 16.

1. Dose

High electron beam doses increase image contrast, but destroy the structure of the specimen (Issacson *et al.*, 1973; Stenn and Bahr, 1970). Unfortunately, an electron beam dose low enough to leave the structure unaffected produces little image contrast (Glaeser, 1973). The Fourier averaging techniques can separate the signal from the noise, allowing the use of very low electron doses to record micrographs. Unwin and Henderson (1975) took advantage of the large size and high order of purple membrane crystals to record low-dose images of unstained bacteriorhodopsin and catalase with a slightly modified Phillips EM301. To protect the crystal from radiation damage, a shutter was constructed, which, by rapidly translating the condenser aperture between two fixed positions, cut off or let through the electron beam. The position of the optic axis at low magnification was marked and the microscope aligned so that an object placed there would be in the center of the main viewing screen at high magnification. The deflectors were set so that the beam would move from the center of the main viewing screen at high magnification to an off-axis viewing screen when they were switched on. Finally, the setting of the condenser lens that gave the proper low dose exposure in 8 to 10 seconds was marked. Crystals were located at low magnification and centered on the marked optic axis. Focusing at the higher recording magnification was done with the beam contracted and deflected to the off-axis viewing screen. The shutter was then closed, the deflectors were turned off, the beam was expanded by setting the condensor to the previously marked low-dose position, and a photographic plate was moved into place. The shutter was then opened for the appropriate length of time to take the image. The first electrons to strike the specimen form the image, and the total beam dose is kept below 50 electrons/nm^2. This is a more than a hundredfold lower dose than that used in conventional microscopy. The image appears completely featureless, but the transform reveals information to a resolution of 0.7 nm, sufficient to identify secondary structures in the protein. A second image was taken at a higher beam dose to evaluate the phase contrast transfer function, which is not easily seen in the initial low-dose image.

Even when crystals are too small or disordered for unstained work and negative stain must be used to increase contrast, control of beam dose is important in achieving the highest possible resolution. Under the impact of the beam, negative stains crystallize and migrate, no longer accurately reflecting the protein surface (Unwin, 1975). This effect can be minimized and the structure of the protein preserved by limiting preirradiation of the specimen (Williams and Fisher,

1970). Beam doses of roughly 1000 electrons/nm^2 seem to affect the crystal only slightly within the resolution afforded by the stain (~2.0 nm) and yet provide adequate contrast for small, negatively stained crystals. Steven and Navia (1980) have shown that negative stain faithfully represents immunoglobulin structure in crystals to this resolution when averaging is employed. This is called minimum-dose microscopy.

2. Specimen Preservation

The environment of the crystal on the carbon film affects its order. In unstained work, crystals are laid on the grid in a 1% glucose solution. This sugar dries into a hydrated shell, protecting the crystal from dehydration in the vacuum. Negative stains serve the same function, although less effectively. The carbon film itself can be a potent disordering influence, particularly if it has been glow-discharged. This can be seen by processing images of crystals that lie atop others. The crystal that is away from the grid is usually the better ordered (Unwin and Henderson, 1975). Uneven staining of the two sides of the crystal often increases when a glow-discharged grid is used (Fuller *et al.*, 1979). Using freshly prepared carbon films or pretreating grids with an ovalbumin or cytochrome *c* solution to produce a thin layer of dried protein reduces these effects (Henderson *et al.*, 1978).

Negative stains differ widely in their disordering effects on crystals, and several staining conditions should be explored with the help of an optical diffractometer. Images of the $p12_1$ cytochrome oxidase crystals negatively stained with phosphotungstic acid are always limited to resolution coarser than 3.0 nm, whereas uranyl acetate often gives information to 2.0 nm. Misleadingly, the phosphotungstic acid picture is often more contrasty than the uranyl acetate picture and hence looks better to the eye. The transform reveals the loss of high-resolution information (Fuller *et al.*, 1979).

3. Optical Effects—Electron

Electron micrographs of biological specimens are usually taken slightly underfocused to compensate for the weak scattering of the material. Underfocusing enhances the contrast of the image by a mechanism analogous to optical phase contrast microscopy. Different degrees of defocus enhance the contrast in different resolution ranges of the image, altering the phases and amplitudes of the image transform, as shown in Fig. 4. Again, resolution is traded for contrast. In an optimally underfocused image (Fig. 4C), the effect can be ignored at resolution coarser than 2.0 nm because no phases are changed within this position of the transform. Phases are reversed at higher resolutions, and, particularly near the nodes of the function, the amplitudes are reduced (Erickson and Klug, 1971).

To reconstruct a high-resolution image accurately, these distortions must be corrected. Unwin and Henderson (1975), in their high-resolution purple membrane work, obtained amplitudes from low-dose electron diffraction patterns, which are unaffected by phase contrast effects. The phases were taken from a low-dose image and corrected by finding the positions of the nodes and reversing

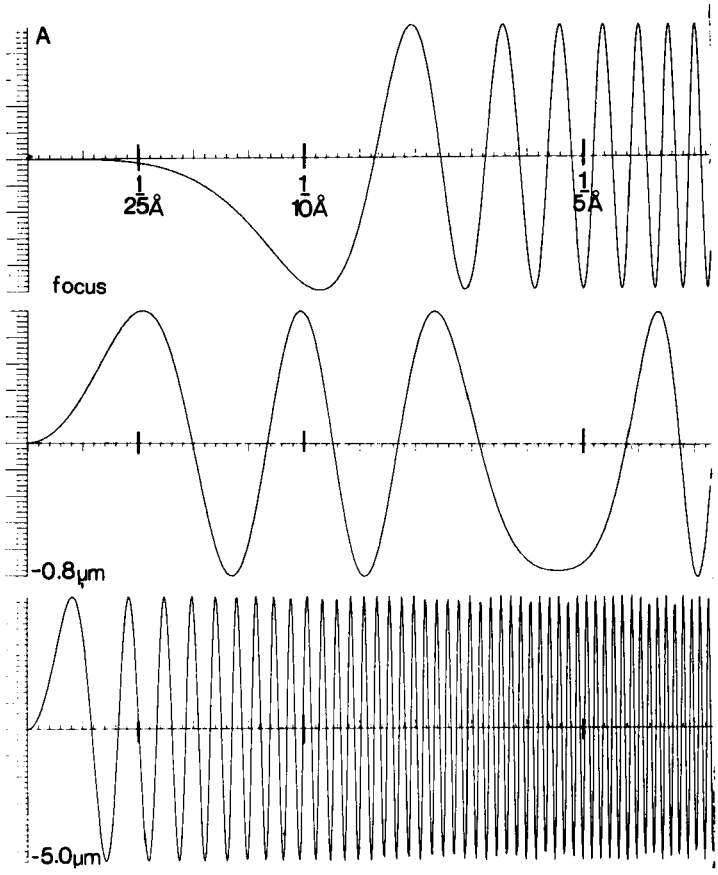


FIG. 4. The phase contrast transfer function. (A) The effect of phase contrast for a specimen whose potential field affects the electrons only slightly, a weak phase object, can be approximated by a factor, $\exp(i\chi)$, where $\chi = (2\pi/\lambda)(\delta f\theta^2/2 - C_s\theta^4/4)$ (Erickson and Klug, 1971). C_s is the spherical aberration coefficient, λ is the wavelength of the electrons, δf is the degree of underfocus, and θ is the scattering angle. The function is shown for a Phillips EM301 (C_s is 1.6 cm) and 100-kV electrons (λ = 0.037 Å). The abscissa is in reciprocal angstroms. The function is shown for focus, 8000 Å underfocused, and 5 μm underfocused. (B) The transform of the density in (C) and the product of that transform with the transfer function plotted in (A). (C) The density plot of the original object, two sharp peaks separated by 100 Å, and the images calculated from (B) for different defocus values. All plots are on the same scale. The best compromise between contrast and resolution is given by 8000 Å underfocus. (1 μm = 1000 nm = 10000 Å.)

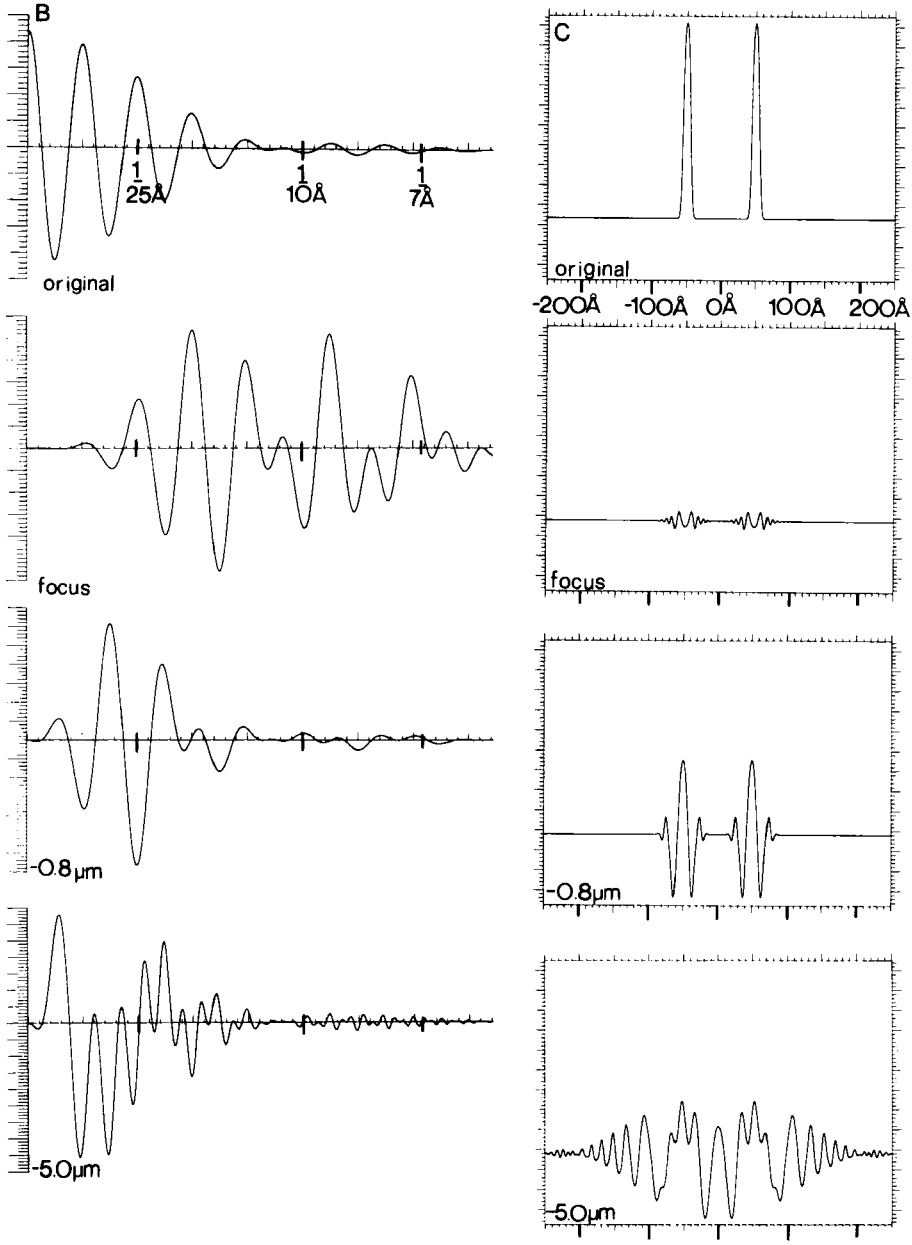


FIG. 4B and C. See p. 269 for legend.

the phases accordingly. The transform of a high-dose image taken at a degree of defocus identical to that of the low-dose one was used to locate the nodes. This combination of imaging and diffraction reliably determined the transform to 0.7-nm resolution.

B. Projection Analysis

The projection is the view of the structure from a single direction. Conclusions drawn about the three-dimensional structure from this image alone rest on assumptions about the packing of molecules in the crystal. Information about the packing in the crystal from other techniques, combined with the projection data, leads to more reliable and far-reaching structural conclusions.

1. Symmetry of the Projection

A micrograph shows the entire thickness of a thin crystal in focus because the depth of field of the electron microscope is so large (Crowther *et al.*, 1970). The image, rather than showing the surface of the specimen, shows the superposition of all the density in the crystal seen from a particular direction, the projection. Because it is a superposition, many three-dimensional structures can show the same projection. The interpretation of a projection in terms of the three-dimensional structure is difficult for this reason. The projection of a slightly tilted crystal, particularly a thick one, or one that has been unevenly stained, can differ enormously from that of an untilted, evenly stained one. These differences can often be understood by examining the three-dimensional data, but they confound the interpretation of projection images.

The symmetry of a crystal has two components: the lattice symmetry, or the arrangement of the unit cells; and the point group symmetry, the symmetry of the unit cell itself (Stout and Jensen, 1968). The symmetry of a three-dimensional crystal is described by one of 230 space groups. These are tabulated in the first volume of the "International Tables for X-ray Crystallography" with their symmetry relations (Henry and Londsdale, 1967). For a two-dimensional crystal, the nomenclature of two-sided plane groups should be used. In this nomenclature, the z axis is always chosen to be perpendicular to the plane of the crystal, and its symmetry is given by the symbol immediately following the cell-type symbol. Hence, p622 has a sixfold axis perpendicular to the plane and twofold axes in the plane. Because proteins are chiral (possessing handedness), some symmetry elements cannot occur, and only 17 of the 80 two-sided groups are possible for protein crystals; the projection symmetry, looking down the z direction, determines the plane group for these crystals. The 17 two-sided plane groups possible for protein crystals, with the associated projection symmetry given in parentheses, are: p1 (p1), p21 (p2), p12 (pm), p12 (pg), c12 (cm), p222 (pmm),

p222 (pmg), p222 (pggg), c222 (cmm), p4 (p4), p422 (p4m), p422 (p4g), p3 (p3), p312 (p3m1), p321 (p31m), p6 (p6), and p622 (p6m). Those used in this chapter are pictured in Fig. 1. The meaning of other symbols can be found in any standard crystallography text (Stout and Jensen, 1968; Woolfson, 1970).

Some authors refer to the symmetry of a two-dimensional crystal by the space group symbol of the three-dimensional crystal formed by stacking two-dimensional crystals. More than one space group can be formed in this way for most projection symmetries. To look up information in the "International Tables for X-ray Crystallography" (Henry and Londsdale, 1967), this associated space group must be used.

The symmetry of the image is revealed by relations between the phases and amplitudes of its transform. Table II shows the phases and amplitudes from a transform of a micrograph of a negatively stained cytochrome *c* oxidase crystal. Examining the amplitudes first, one quickly sees that the $(0, k)$ reflections with k odd are all essentially absent. The weakness of these reflections, called systematic absences, results from the presence of two identical molecules in opposite orientations in the unit cell (Fig. 1H). Further, all the amplitudes have mirror symmetry about a vertical line through the center of the transform. The phases also show a pattern. Idealizing the trends shown in the transform, the relations

$$\begin{aligned} \text{Amplitudes:}\quad & F(h, k) = F(h, -k) \\ & F(0, k) = 0 \text{ for } k \text{ odd} \\ \text{Phases:}\quad & \alpha(-h, k) = k\,180^\circ + \alpha(h, k) \\ & \alpha(h, k) = k\,180^\circ - \alpha(h, -k) \end{aligned}$$

are approximately obeyed by the projections. These relations describe a pg projection symmetry, which is the symmetry shown by a $p12_1$ crystal viewed perpendicularly to the plane of the crystal. They would be exactly obeyed if the image showed exact pg symmetry, but artifacts such as uneven staining cause departures from the true crystal symmetry. Averaging the phases and amplitudes so that they exactly obey these relations (Table II) and back-transforming them yields the part of the image that obeys the pg symmetry (see Fig. 10A).

2. Conclusions from the Projection Image

Reasonable conclusions can be drawn about the packing of the molecules in the crystal from the projection data. The unit cell volume and the projection symmetry reveal the number of molecules in the unit cell. The unit cell shown in projection (Table II) is 6.8×17.4 nm, or 118.32 nm^2. Thin sectioning and shadowing give a thickness of 11.0 nm for this crystal form, yielding a cell volume of 1.3×10^3 nm^3. This is roughly half the volume filled by two dimers of the oxidase in the $p22_12_1$ crystal form (Henderson *et al.*, 1978). This suggests that the unit cell contains at least two monomers, since this crystal form contains

less lipid than the $p22_12_1$ form. This is consistent with the density of soluble proteins in crystals that average 2.5×10^{-3} nm^3/dalton (Matthews, 1968), taking a molecular weight of 140,000 for the monomer. The observation of pg projection symmetry strongly suggests a $p12_1$ three-dimensional symmetry. The "International Tables for X-ray Crystallography" (Henry and Lonsdale, 1967) reveal that a $p12_1$ unit cell must contain a multiple of two molecules unless the molecule itself is symmetric. Internal symmetry is unlikely here, because the 140,000-dalton monomer contains single copies of at least seven distinct polypeptides (Downer *et al.*, 1976). Thus, the unit cell contains exactly two monomers. Further, the $p12_1$ symmetry can be satisfied only if these monomers face in opposite directions in the unit cell. These conclusions define the packing of the molecule in this crystal quite well (Fig. 1H). They are supported by the completed three-dimensional structure (Fuller *et al.*, 1979).

The approximate shape of the protein can be determined by comparison of the projected area with that expected from the molecular weight when this is known. In their work on the $p22_12_1$ crystal of ubiquinone-cytochrome *c* reductase, Wingfield *et al.* (1979) found the dimensions of a projected dimer to be 9.0×7.0 nm. Since these dimensions are about half the Stokes diameter (17.2 nm) measured by gel filtration for the dimeric enzyme-Triton X-100 complex, they conclude that the dimer is rod-shaped. Its elongated axis is perpendicular to the membrane.

3. Artifactual Loss of Symmetry

Artifacts cause the apparent symmetry of the projection to differ from that of the crystal. By imposing symmetry on the transform, the averaging process described above compensates for these artifacts when the departure from symmetry is small. When the symmetry is badly distorted, the image cannot be processed in this way. One alternative is to process the image using the apparent symmetry, and examine the results to determine the nature of the artifact (Unwin and Zampighi, 1980).

a. Uneven Staining. Uneven staining of the crystal changes the contribution of its two sides to the projection, altering the symmetry. For example, when $p12_1$ cytochrome *c* oxidase crystals are negatively stained on a glow-discharged grid, the transform of the image shows strong (0,1), (0,3), and (0,5) reflections. These are very weak or absent in transforms of images taken on non-glow-discharged grids. Further, the phase and amplitude relations are not obeyed, and alternate rows of the crystal are blurred in the image (Fuller *et al.*, 1979). This effect results from an interaction between the grid and the crystal, which causes the two sides of the structure to be outlined differently by the stain (Figs. 5D and 5E). The symmetry collapses because the two oppositely oriented monomers in the unit cell are unequally stained.

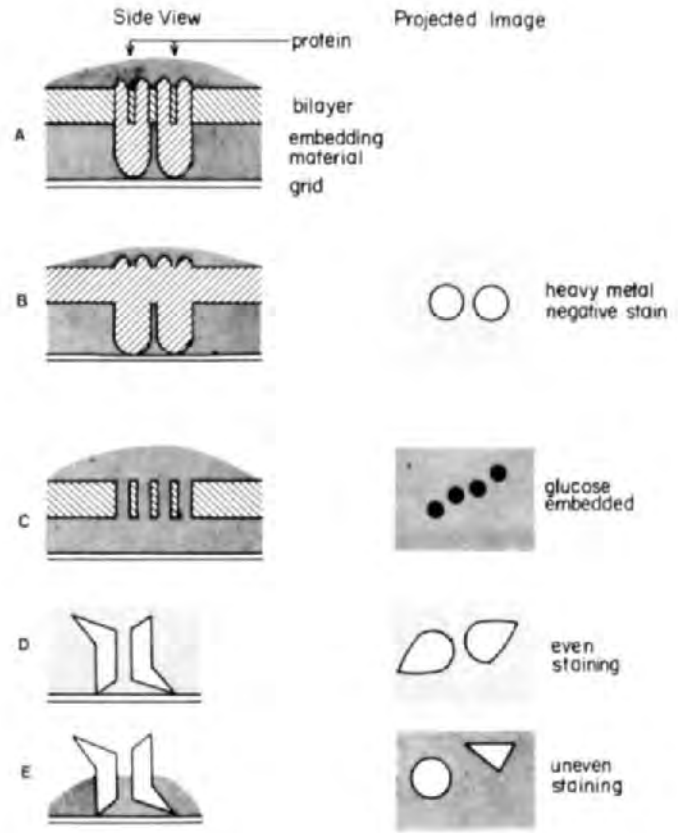


FIG. 5. Origin of contrast in projection. (A–C) Seen from above, the projected image of a protein containing membrane varies with the density of the embedding material. When embedded in a heavy metal negative stain, such as uranyl acetate ($\rho > 5.0$ gm/cc) both the protein ($\rho \simeq 1.4$ gm/cc) and the lipid ($\rho \simeq 1.0$ gm/cc) show up as light. In projection the extramembranous protein is seen. Dried glucose ($\rho = 1.4$ gm/cc) matches the density of the protein so that the protein–lipid boundary is seen. The lipid appears light in projection. (D,E) Uneven staining can cause the loss of projection symmetry. The two oppositely oriented but identical objects show a twofold symmetry in projection when evenly embedded (D) but appear completely dissimilar when unevenly embedded (E). Any relation between the structures depicted here and a particular protein is coincidental.

b. Dose Effects. High electron doses can change the symmetry of the crystal. This occurs when the features that give the molecule asymmetry are lost as the molecule disintegrates under the impact of the electron beam. Mg^{2+}-induced tubulin crystals provide an example. The unit cell of these $p12_1$ crystals contains two molecules that should appear different in projection because they differ slightly in orientation. Images taken with a dose of 10^4 electrons/nm^2 or greater do not show this difference, and the unit cell appears half as large as in minimum-dose images in which these differences are preserved (Baker and Amos, 1978).

c. Crystal Disorder. Disorder in the crystal not only diminishes the resolution seen in the transform but also changes its apparent symmetry. An extreme example is an image of close-packed molecules in random orientations on the surface of a membrane. The transform of this image would contain low-resolution reflections, but the filtered image would show an artificially symmetric molecule because different orientations are averaged by the filtering process. Several membrane proteins form mosaic crystals (Caspar *et al.*, 1977; Fuller *et al.*, 1979; Ross *et al.*, 1977), made up from small, well-ordered domains with slightly differing orientations. The transform of an image area containing more than one domain gives a distorted view of the molecule. To process such an image by this Fourier technique, the area transformed must be restricted to a single domain of the mosaic.

4. Origin of Contrast

The relationship between contrast in the image and molecular features changes with resolution. At high resolution, the internal structure of the protein contributes to the image. This is untrue at resolutions coarser than roughly 1.5 nm, where contrast results primarily from the difference in density between the protein and the surrounding material. Classical negative staining embeds the structure in a dense metal salt. The features of the structure in contact with the stain are seen because the image is dominated by stain-lipid or stain-protein contrast (Fig. 5B). Density variation within the specimen can be visualized by embedding it within a low-density material. The contrast will be much lower than that produced by heavy metal negative staining and must be enhanced by averaging over the crystal to be useful. Dried glucose and protein have roughly the same density, so that the image of a protein containing membrane embedded in glucose shows contrast only between the lipid bilayer and the protein. It reveals the portion of the protein buried in the membrane (Fig. 5).

Comparing the projection images of the $p22_12_1$ form of cytochrome *c* oxidase in uranyl acetate with that in glucose indicates the shape of the protein. The filtered projections perpendicular to the membrane surface are shown in Figs. 6 and 10A. The uranyl image shows the structure in contact with the stain, the portion of the enzyme that emerges from the membrane. The glucose image reflects lipid-protein contrast, showing the membrane-buried protein. The oxidase is a dimer in this crystal. It extends from the membrane as two domains, one domain per monomer. Four domains per dimer compose the membranous part of the protein revealed by glucose. Thus, the enzyme must branch as it crosses the membrane.

The relationship between the membranous and the extramembranous portions is not obvious because they are completely independent structures. Images of crystals embedded in a medium of intermediate density, such as gold-glucose or metrizamide, show a combination of the two structures. Comparing these with

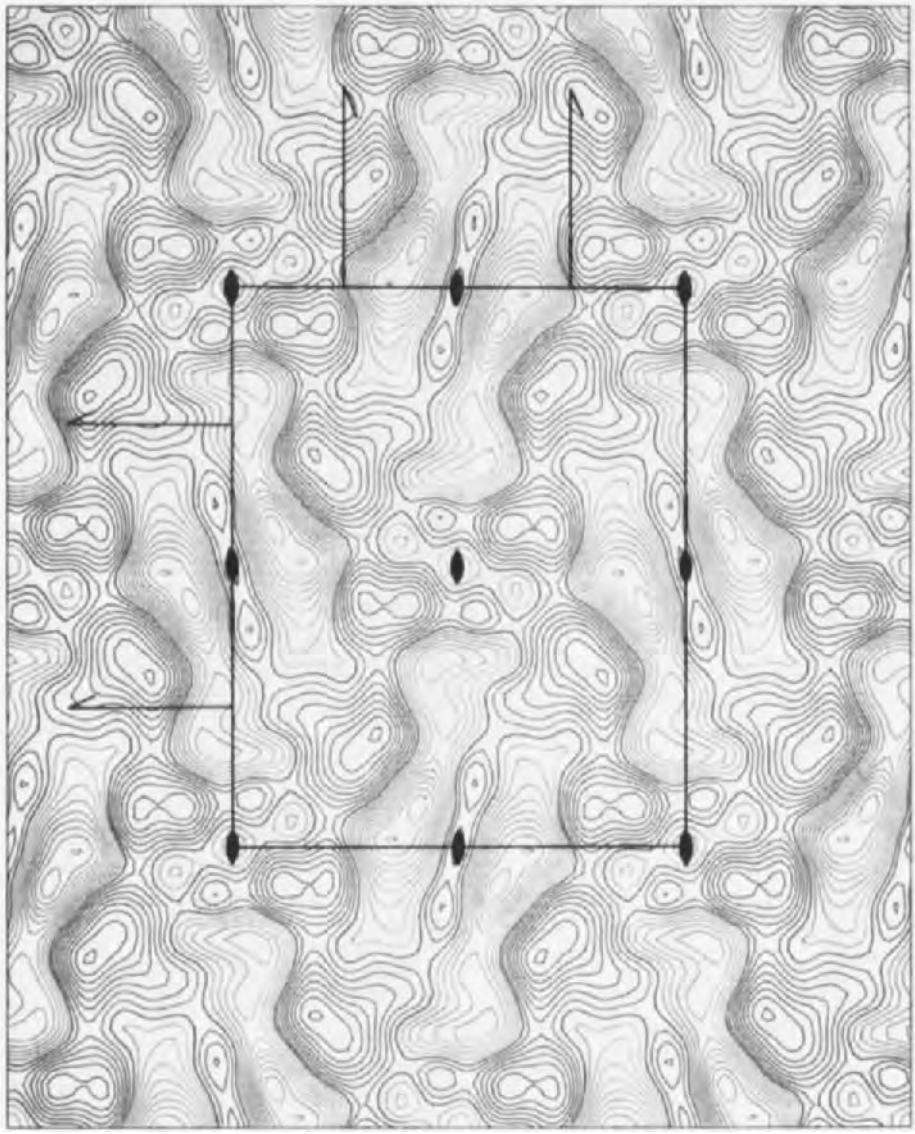


FIG. 6. Unstained $p22_12_1$ cytochrome *c* oxidase. Structure of glucose-embedded $p22_12_1$ cytochrome *c* oxidase crystals in projection. The map includes all data to 1.5 nm and partial data to 1.0 nm. The rectangle outlines the 10.0 × 12.5-nm unit cell. The positions of the twofold axes (⬬) perpendicular to the membrane and the twofold screw axes (→) in the plane of the membrane are marked. From Henderson *et al.* (1977), used with permission.

the glucose and uranyl acetate images reveals the relationship between the segments of the protein (J. F. Deatherage, R. A. Capaldi, and R. Henderson, unpublished).

C. Three-Dimensional Analysis

In principle, the three-dimensional reconstruction is no different from the projection analysis (Fig. 7). Micrographs of tilted crystals are taken. These images are transformed, and their orientations within the three-dimensional transform are determined from the tilt angle and the orientation of the tilt axis to the crystal axes. Next, the transforms of the individual images are combined to yield the three-dimensional transform and symmetry relations imposed. Finally,

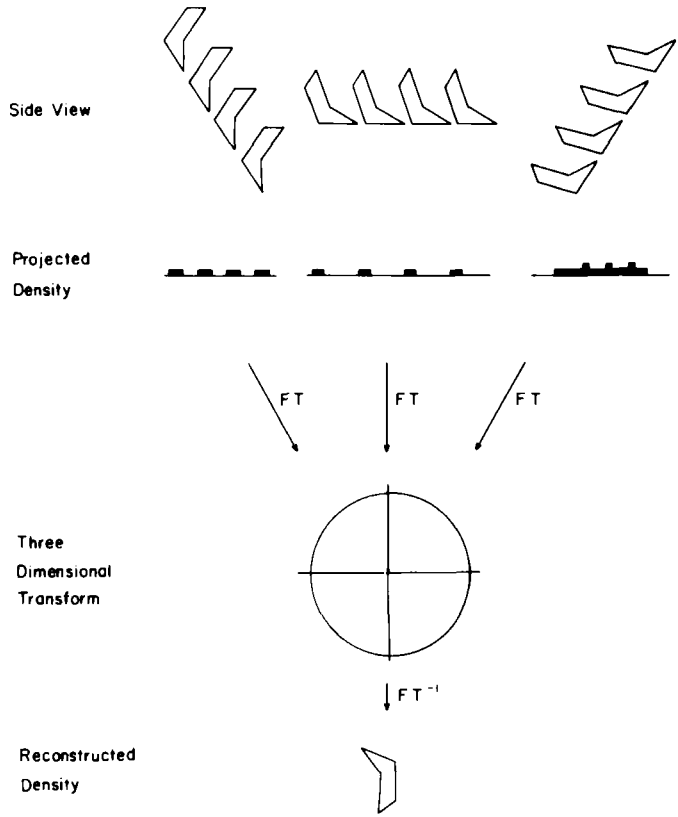


FIG. 7. Process of three-dimensional reconstruction. As described in the text, three-dimensional reconstruction involves the combination of a set of two-dimensional transforms of images of tilted crystals to fill out the three-dimensional transform. The three-dimensional map is obtained by back-transforming the three-dimensional transform.

this three-dimensional transform is back-transformed to obtain the three-dimensional structure.

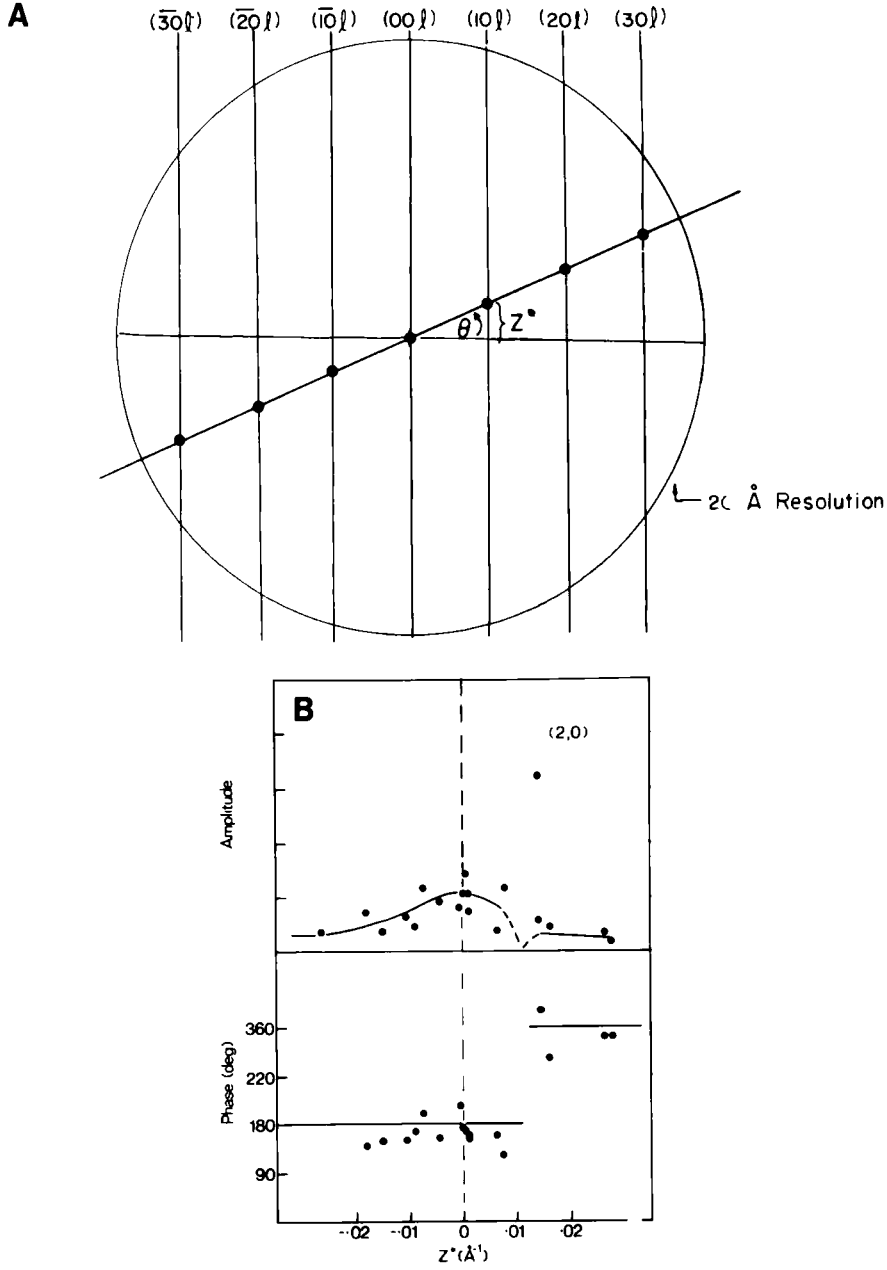
1. Taking Images of Tilted Specimens

A specimen holder with a fixed tilt angle or a tilting stage, which allows continuous variation of the tilt angle, can be used to take micrographs of tilted crystals. The resolution desired and the beam sensitivity dictate this choice. With a tilting stage, a series of images can be taken of the same crystal at different tilt angles. Processing is simplified because the angle of tilt is known and the orientation of the crystal axes relative to the tilt axis can be easily determined. This orientation is the same throughout the series. A typical tilt series might contain tilts of 0°, 15°, 30°, 45°, 60°, −15°, −30°, −45°, −60°, and 0°. The two 0° micrographs serve as a check for information loss due to beam damage during the series. For high-resolution work with a beam-sensitive specimen, only a single micrograph can be taken of each crystal. A fixed-tilt specimen holder is preferable for these specimens because a tilting stage offers no advantage for a single image and is generally less stable than a fixed one. The change in the geometry of the projected unit cell gives the tilt angle and the direction of the tilt axis relative to the crystal axes. These must be determined separately for each image.

2. Building up the Transform

The transform of an image of a tilted crystal is a slice through the three-dimensional transform. As the tilt angle changes, the height at which this slice cuts each reflection of the transform changes (Fig. 8). Plotting the phase and amplitude of each reflection against Z^* (calculated from the tilt axis–crystal axis angle and the angle of tilt) produces a set of curves like the one shown for the (2,0) reflection of $p12_1$ cytochrome *c* oxidase in Fig. 8. The thicker the structure, the more rapidly its image, and hence its transform, changes upon tilting. Roughly, the phase and amplitude should change slightly over the interval $Z^* = 1/2 \cdot \text{thickness}$ (Sayre, 1952). As a result, it takes more image transforms to describe a thick object than a thin one to the same resolution.

FIG. 8. Lattice lines. (A) Relation between θ and Z^*. The crystal has been tilted about an axis perpendicular to *a*. The transform of the image of a tilted crystal is a slice through the three-dimensional transform. Z^* is the position at which the lattice line is cut by this slice. The transform of the image in the figure would give the phase and amplitude values of the $(1, 0, Z_0^*)$, $(2,0,2Z_0^*)$, $(3, 0, 3Z_0^*)$, $(1, 0, -Z_0^*)$, etc. To achieve a uniform resolution of 2.0 nm the three-dimensional transform must be completely determined within the area marked by the circle. (B) Plot of the phase and amplitude of the $(2, 0, l)$ as a function of Z^* for $p12_1$ cytochrome *c* oxidase crystals negatively stained with uranyl acetate. From Fuller *et al.* (1979), used with permission.


A
(3̄0ℓ)
(2̄0ℓ)
(1̄0ℓ)
(00ℓ)
(10ℓ)
(20ℓ)
(30ℓ)
θ°
Z°
20 Å Resolution
B
(2,0)
Amplitude
360
220
180
90
Phase (deg)
-·02
-·01
0
·01
·02
Z°(Å⁻¹)

The image transforms are assembled to generate the three-dimensional transform. An untilted image is used to start the data set. The transform of an orthogonal crystal tilted at a known angle can be put into the three-dimensional transform in four different ways, generated by flipping around the two crystal axes. Image transforms are added to the data set in the orientation that gives the smallest change from the values of nearby points on previous images ($\Delta Z^* = 1/2 \cdot$thickness). The symmetry of the crystal may make some of these orientations appear to be identical. Adding images in order of increasing tilt angle ensures that nearby transform points will be found for comparison.

The three-dimensional transform generated in this way contains no assumptions about the symmetry of the crystal. This transform is examined for relations between the amplitudes and phases that indicate the three-dimensional symmetry. This symmetry can be imposed on the transform by recombining the data using these phase and amplitude relations. For example, a $p12_1$ crystal has only two unique orientations, rather than four. The symmetry relations

$$\begin{aligned} \text{Amplitudes: } & F(h, k, -Z^*) = F(h, -k, Z^*) \\ \text{Phases: } & \alpha(-h, k, Z^*) = k\,180^\circ + \alpha(h, k, -Z^*) \\ & \alpha(h, k, Z^*) = k\,180^\circ + \alpha(h, -k, Z^*) \end{aligned}$$

express this by relating values in the transform. Upon recombination using these relations, the average deviation in phase between nearby points rose from 16° to 22° for the (2, 0). Comparing symmetry-related values in the transform increased the deviation of the phases only slightly. This reflection obeys $p12_1$ symmetry. For all reflections included in the reconstruction, the average deviation in phase is only 30°. This is consistent with $p12_1$ symmetry for this crystal within experimental error (Fuller *et al.*, 1979).

The form of the phase and amplitude curves becomes more clear as more transforms are added. The drop in amplitude with increasing resolution (that is, with Z^* for fixed h, k) determines the number of high-angle tilts needed. Values for each reflection must be obtained to the limit of resolution, or up to a point in Fourier space where its amplitude becomes negligible. Cutting off the reflection too sharply lengthens the three-dimensional structure artificially. When enough transforms have been combined, the values of corresponding reflections are connected by smooth curves. These curves are sampled at even intervals, and the values are back-transformed to give the three-dimensional map.

3. Profile Information

Although the tilted images provide most of the data in the transform, they can never give the values of the central (0, 0, l) line (Fig. 8). These are part of the transform of an image tilted at 90°, the profile of the crystal. Figure 9 shows a side view of the three-dimensional reconstruction of negatively stained $p22_12_1$

cytochrome *c* oxidase without the (0,0,*l*) data (Fig. 9A). Although variation of density in a section perpendicular to *Z* is unaffected by the (0,0,*l*) reflections, the profile determines which contour level on each section corresponds to the edge of the protein. As a result, conclusions drawn from the map about the length of the structure, the molecular volume, and the precise shape all depend critically on the profile information.

When the profile can be measured, conclusions drawn from the map are more reliable. The x-ray profile diffraction from stacked crystals can be used to calculate the (0,0,*l*) for an unstained structure. Henderson and Unwin (1975) did this for their unstained reconstruction of bacteriorhodopsin. For negatively stained structures, sections have been used. Unwin (1977) showed that, to low resolution (~10.0 nm), the negatively stained ribosome structure is the reverse of the positively stained one, and used a positively stained thin section to generate the profile data. This correspondence breaks down at higher resolutions, and the negatively stained structure itself must be used. Amos and Baker (1979) embedded and sectioned a grid containing a negatively stained specimen to obtain

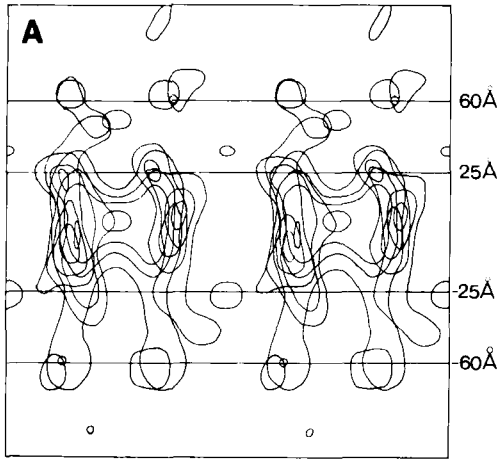


FIG. 9. The structure of $p22_12_1$ cytochrome *c* oxidase crystals. (A) A view of the three-dimensional map of $p22_12_1$ chtochrome c oxidase crystal negatively stained with uranyl acetate. Sections perpendicular to *a* are shown for one quarter of the unit cell ($X = 0$ to $X = 2.5$ nm). *Z* is vertical. From Henderson *et al.* (1977), used with permission. (B) A plot of contrast as a function of *Z*. Here contrast is defined as the difference between the highest and lowest density values on a section perpendicular to *z*. This value will not depend on the values of the (0, 0, *l*) lattice line used to calculate the three-dimensional map. From Henderson *et al.* (1977), used with permission. (C) A diagram showing the model of the $p22_12_1$ cytochrome *c* oxidase crystal derived to explain the variation in contrast in the three-dimensional map. Contrast is high when stain-filled and stain-excluding regions are juxtaposed. This occurs within the vesicle and on its outer surface. The membranes at $Z = +5.0$ nm and $Z = -5.0$ nm exclude all stain, and, as a result, no contrast is seen in those sections.

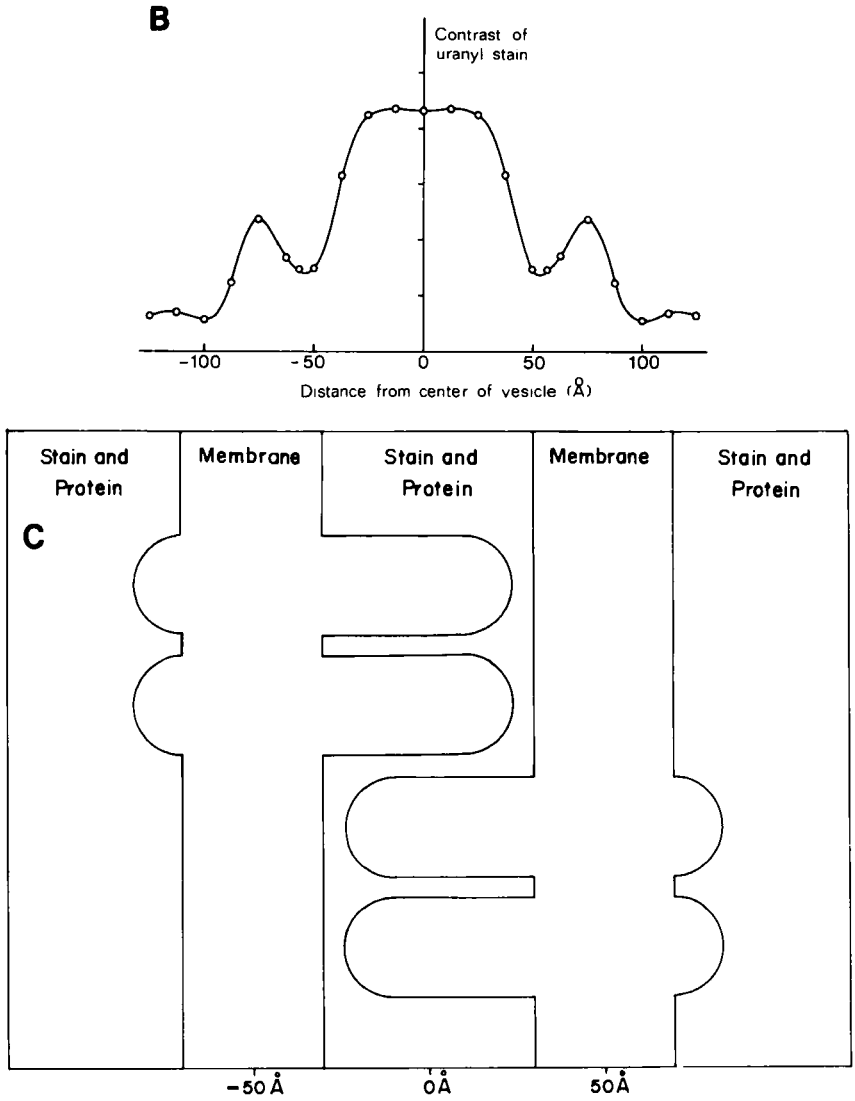


FIG. 9B and C. See p. 281 for legend.

the $(0,0,l)$'s for the $p12_1$ tubulin crystal. The fortuitous occurrence of an upturned edge of a gap junction crystal allowed Unwin and Zampighi (1980) to capture this view without sectioning.

When profile information cannot be measured, the $(0,0,l)$'s must be estimated to interpret the map. The variation of contrast in the map can be combined with

available biochemical and structural information to generate a model for the profile. The $(0, 0, l)$'s are calculated from this model. In the map of the $p22_12_1$ cytochrome oxidase crystals, the contrast is high in the center of the crystal, drops at $Z = \pm 5.0$ nm, and rises to give a second maximum at $Z = \pm 7.0$ nm (Fig. 9B). Contrast will be high when stain and stain-excluding regions are juxtaposed, but low in a completely stain-filled or completely stain-excluding region. Henderson *et al.* (1977) proposed the model in Fig. 9C from the contrast variation, the measured thickness of the structure, and the biochemical data. Contrast is high in the center because the protein sticks out from the membrane and is surrounded by stain within the vesicle. A membrane centered at $Z = \pm 5.0$ nm excludes all stain, lowering the contrast. Protein extending from the outer surface of the membrane contacts stain, raising the contrast outside the vesicle. A map calculated with $(0,0,l)$'s from this model shows these protein boundaries. The coincidence of this protein boundary with the sharpest density change in the map indicates that this is a reasonable result.

V. Biochemical Results

A. Cytochrome *c* Oxidase

Cytochrome *c* oxidase is intrinsic membrane protein that catalyzes the oxidation of cytochrome *c* by molecular oxygen on the inner mitochondrial membrane. Two fundamentally different crystal forms of the oxidase have been prepared from beef heart mitichondria (Sun *et al.*, 1968; Seki *et al.*, 1970). Three-dimensional reconstructions of both forms negatively stained with uranyl acetate have been completed (Henderson *et al.*, 1978; Fuller *et al.*, 1979). Although both reconstructions are complete only to low resolution, the observation of the same domain structure in these two very different crystals shows that the structural conclusions are reliable. The $p22_12_1$ crystal form has a continuous membrane allowing the membranous and nonmembranous parts to be visualized separately (Section II, B,3). The lack of a continuous membrane in the $p12_1$ crystal allows the entire outline of the molecule to be seen in uranyl acetate. This shows the relationship between the membranous portions of the structure. Processing of images of $p22_12_1$ crystal material with density different from that of uranyl acetate or glucose confirms this relationship (J. F. Deatherage and R. Henderson, unpublished observations).

The oxidase is a dimer in the $p22_12_1$ crystal but a monomer in the $p12_1$ crystals. The dimer is observed in the membranous crystal, suggesting that this is the form of the enzyme *in vivo*. Since this structural indication appeared, Bisson *et al.* (1980) have found strong kinetic evidence that the active form of detergent-solubilized enzyme is the dimer.

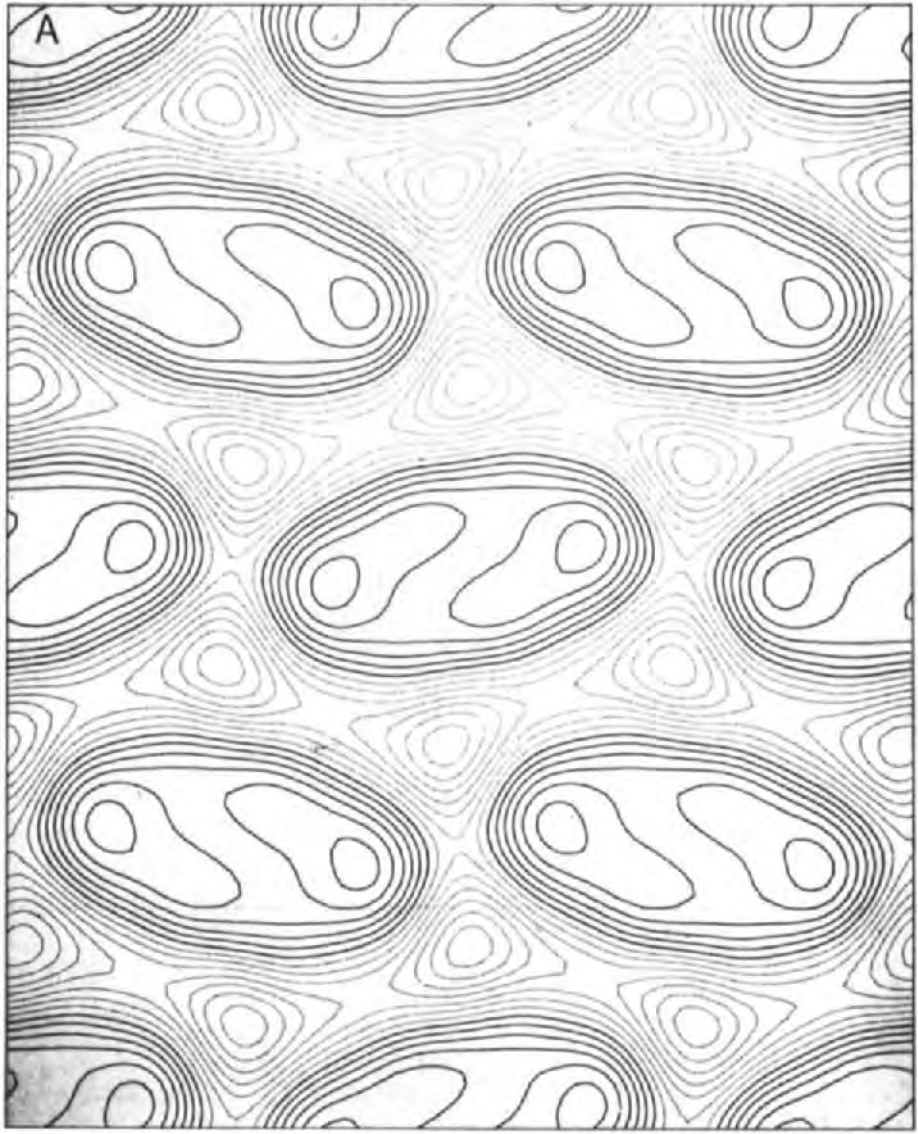


FIG. 10. Projections and three-dimensional structures. (A) Projection, looking down on the surface of the membrane, of $p22_12_1$ cytochrome *c* oxidase. Heavy contours indicate stain exclusion. Each stain-excluding oval is a dimer of the enzyme. Some details of the map, particularly the heights of the peaks within the oval, vary with the negative staining conditions. From J. F. Deatherage and R. Henderson, unpublished observations. Figure 10B-I follow on pp. 285-293.

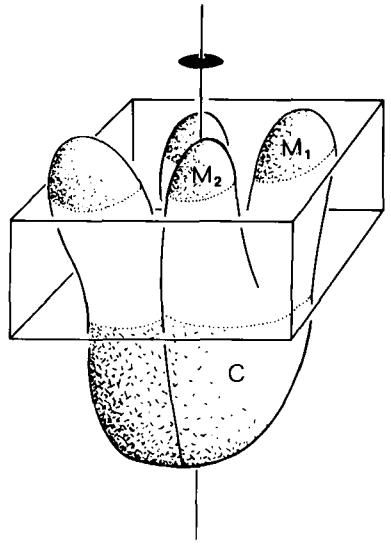


FIG. 10B. A model of the cytochrome *c* oxidase dimer derived by a comparison of the shape seen in the reconstruction of the $p12_1$ crystal form with that seen in the three-dimensional reconstruction of uranyl acetate negatively stained $p22_12_1$ crystals, and the unstained projection of the $p22_12_1$ crystals in glucose. From R. A. Capaldi, J. F. Deatherage, S. D. Fuller, and R. Henderson, manuscript in preparation.

The domain structure and the distribution of mass across the membrane are revealed by the reconstructions (Fig. 10B and 10D). Most of the extramembranous protein extends from the C (cytoplasmic and cytochrome *c* binding) side of the membrane as a single large domain. Roughly half of the protein is buried in the bilayers as two domains, M_1 and M_2, which extend slightly from the matrix side of the membrane. This distribution of density explains the pattern of labeling seen with hydrophobic and hydrophilic chemical probes (Prochaska *et al.*, 1980; Ludwig *et al.*, 1979). The extensions of the M domains are at least 4.0 nm apart, showing that more than a single subunit must be exposed on the matrix side. The chemical labeling results left this unclear. Finally, by comparing the monomer and dimer structures, it is seen that the dimer is formed by the interaction of the M domain (R. A. Capaldi, J. F. Deatherage, S. D. Fuller, and R. Henderson, manuscript in preparation).

The correlation between biochemistry and reconstruction is best drawn by using specific labeling. The first crystalline preparations isolated from mitochondria were impure, and a positive identification of the protein in the crystal was necessary. In both the $p22_12_1$ form (Frey *et al.*, 1978) and the $p12_1$ crystals (Fuller *et al.*, 1979), cytochrome *c* oxidase-specific antibodies proved the identity of the crystalline protein. This was later conformed by the growth of crystals

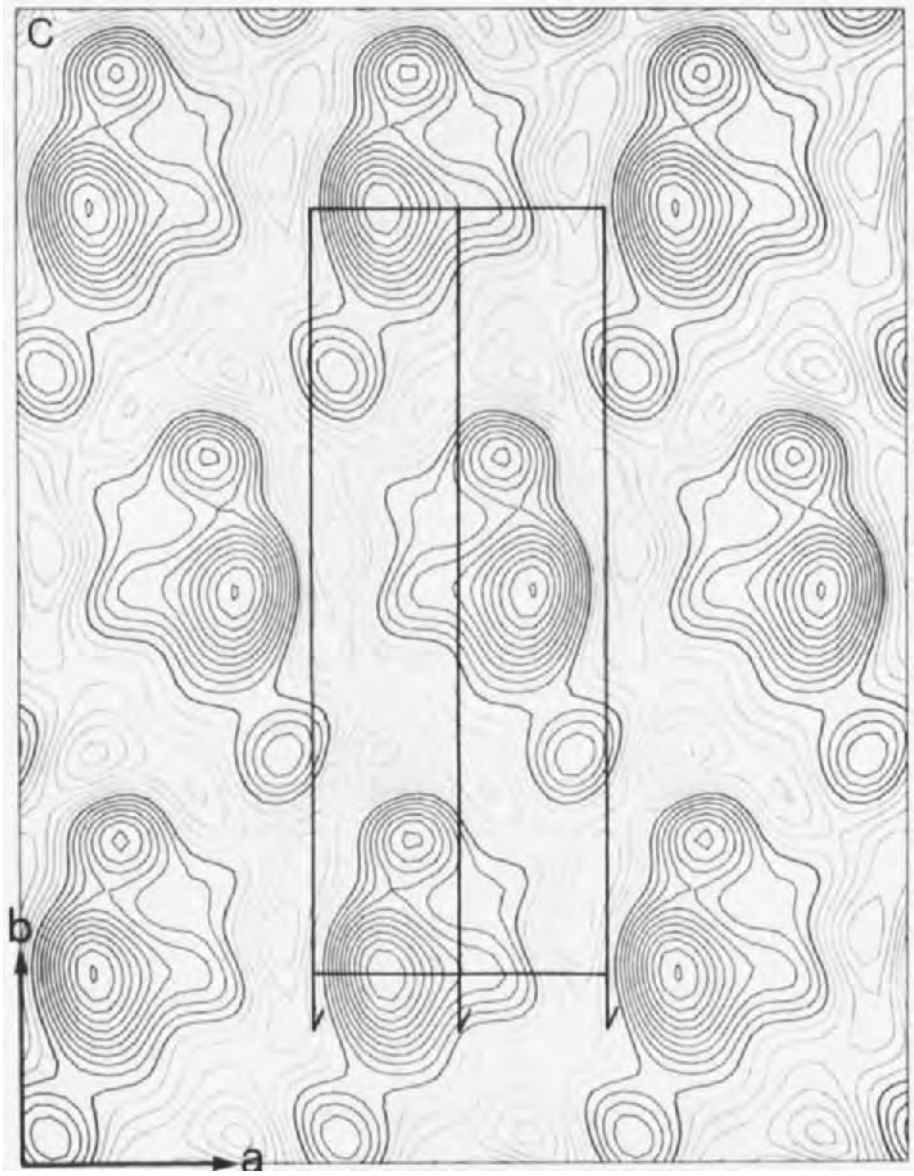


FIG. 10C. Projection, looking down on the surface of the sheet, of $p12_1$ cytochrome *c* oxidase negatively stained with uranyl acetate. Stain-excluding regions are shown by heavy contours. The unit cell and the positions of the screw axes are marked. From Fuller *et al.* (1979), used with permission.

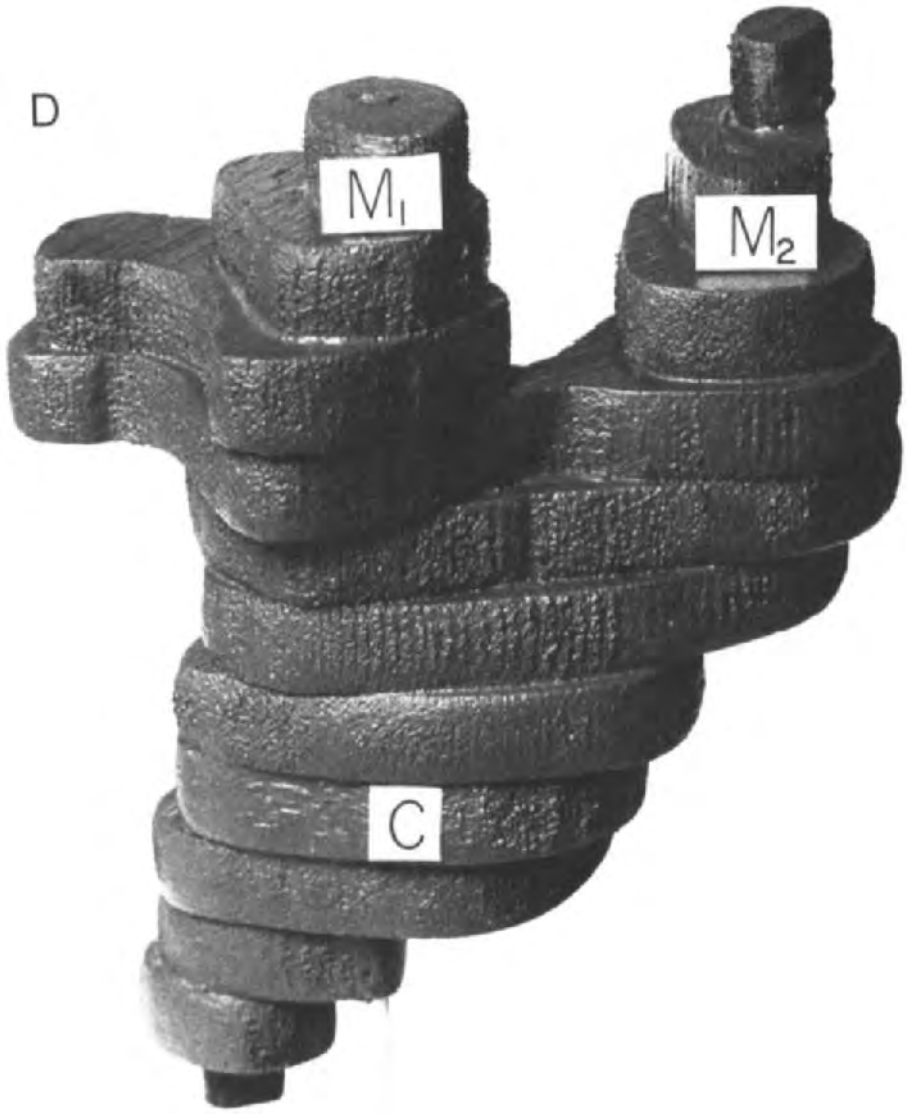


FIG. 10D. Balsa wood model of the density in the three-dimensional map of $p12_1$ cytochrome *c* oxidase negatively stained with uranyl acetate. From Fuller *et al.* (1979), used with permission.

from purified protein (Goldfarb *et al.*, 1979; S. D. Fuller, unpublished results). In the $p22_12_1$ form, only a single side of the protein is exposed (Fig. 1B). Frey *et al.* (1978) showed this to be the M side by using antibodies specific for the M and C sides of the protein. Work now under way aims to localize subunits within the

structures with Fab fragments specific for single subunits. Several laboratories are trying to obtain the high-resolution structure by doing three-dimensional reconstruction of glucose-embedded $p22_12_1$ crystals, which are ordered to at least 1.0 nm.

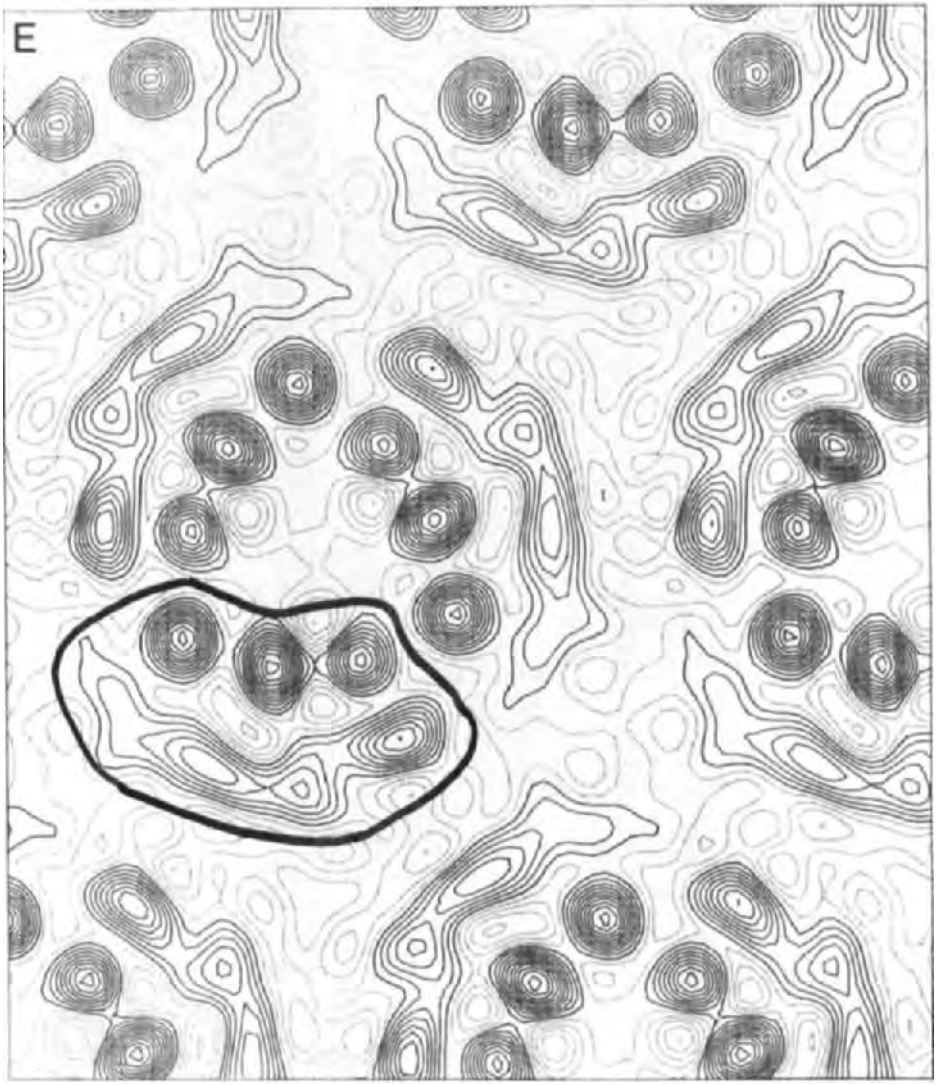


FIG. 10E. Projection, looking down on the cytoplasmic side of the membrane, of the p3 crystal of bacteriorhodopsin embedded in glucose. In this unstained image, protein is high density and is indicated by heavy contours. A monomer of the protein is outlined. From Unwin and Henderson (1975), used with permission.

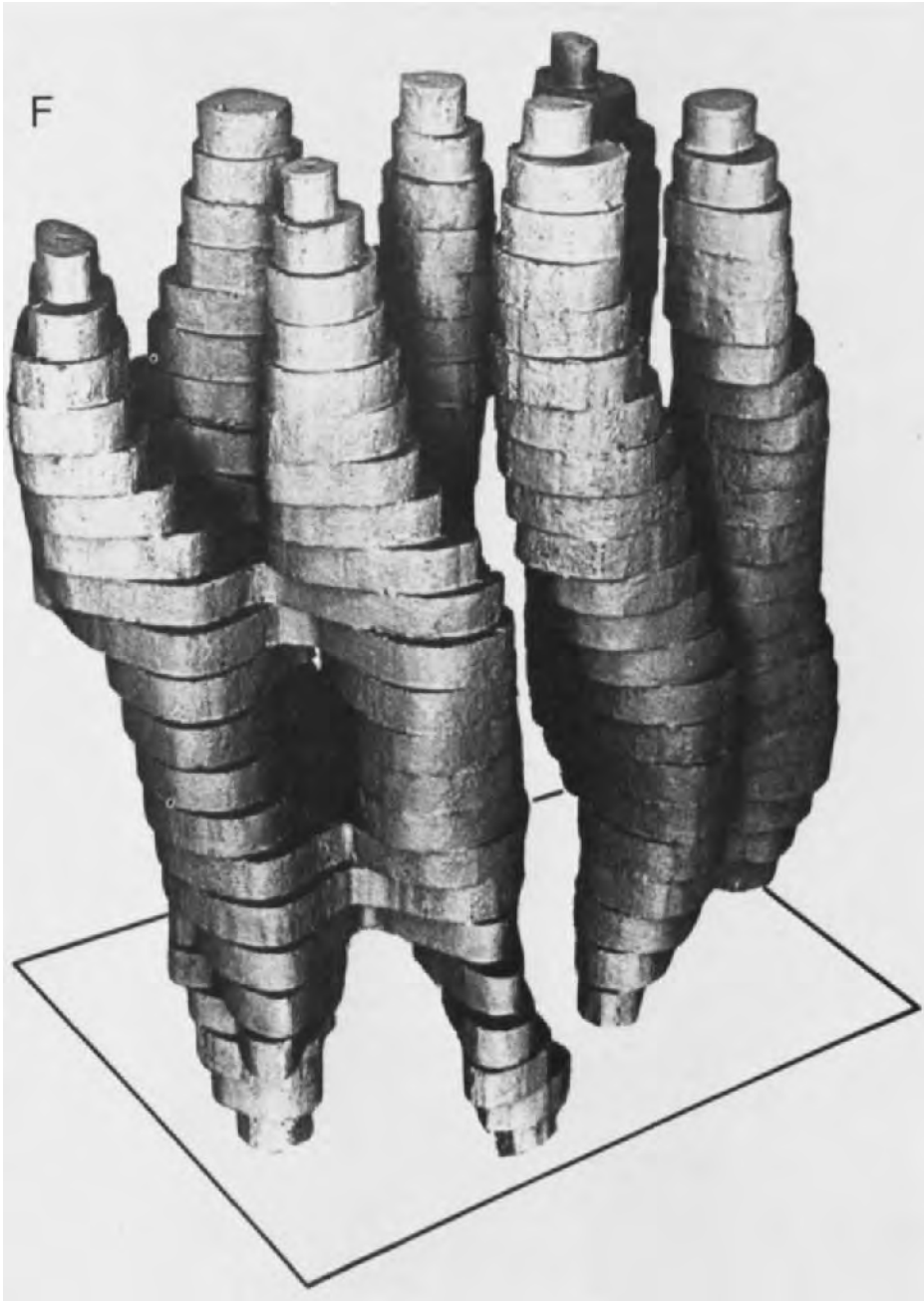


FIG. 10F. A balsa wood model of the three-dimensional density map of a bacteriorhodopsin monomer. The cytoplasmic side is the top. From Henderson and Unwin (1975), used with permission.

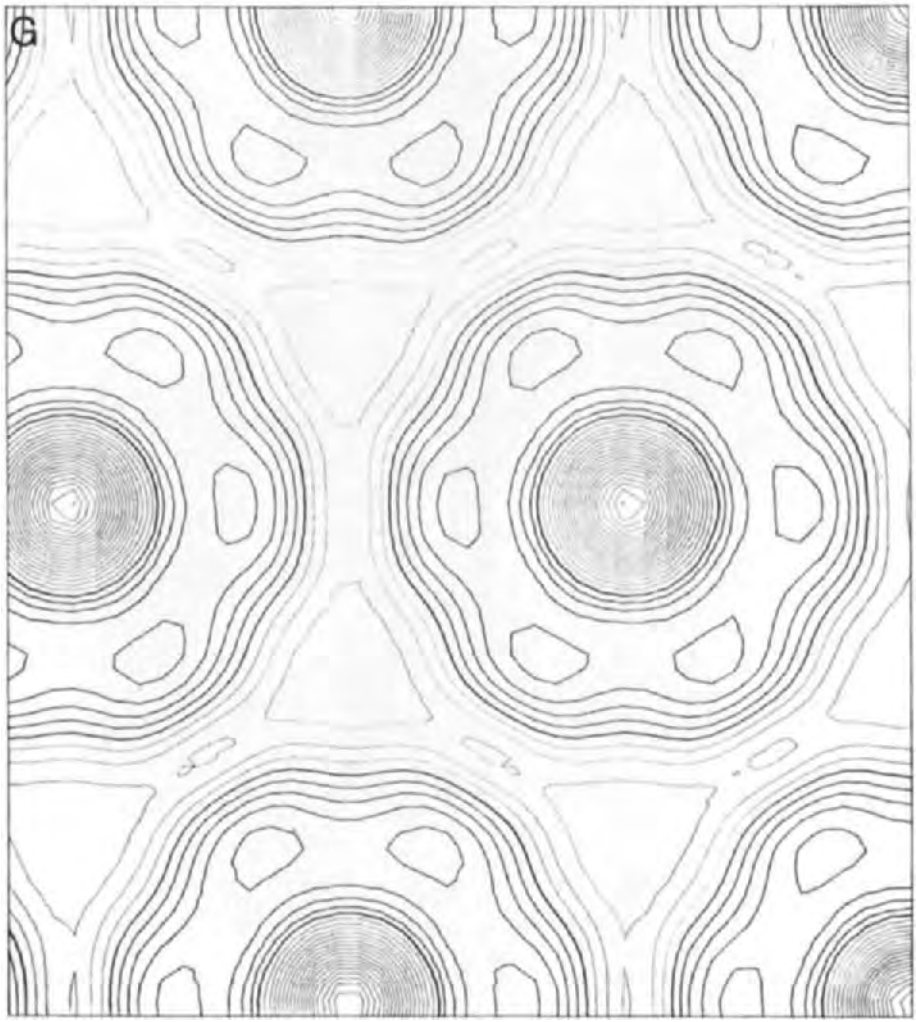


FIG. 10G. Projection, looking down on the membrane, of the A (open) form of p622 gap junction crystals negatively stained with uranyl acetate. Heavy contours indicate stain exclusion. From Zampighi and Unwin (1979), used with permission.

B. Purple Membrane

The purple membrane of *Halobacterium halobium* contains a light-driven proton pump, bacteriorhodopsin, in a very well-ordered p3 crystal (Henderson, 1977). X-ray diffraction from stacked membranes shows a 1.0-nm intensity in the plane of the membrane and a perpendicular 0.5-nm intensity, indicating the presence of α helices. The x-ray results also showed the unit cell axes to be 6.3

nm long and the thickness of the structure to be about 4.5 nm (Henderson, 1975; Blaurock, 1975). Low-dose images were complemented with electron diffraction patterns to yield the 0.7-nm structure of glucose-embedded crystals (Henderson and Unwin, 1975; Unwin and Henderson, 1975). Seven helix-like rods, crossing the membrane with a left-handed twist, compose the monomer. The monomer boundary was drawn arbitrarily because the protein is arranged as trimers in p3 and the connections between the helices are not seen. The boundary shown in Fig. 10E was confirmed by reconstruction of a $p22_12_1$ form of the protein in which the protein is monomeric (Michel *et al.*, 1980).

Labeling has been used to relate the structure of the isolated crystals to the orientation of the protein in the cell. The membrane contains glycolipids only on its extracellular surface. After periodate oxidation, incubation of membranes with biotin hydrazide covalently links biotin to this extracellular side through the glycolipids without disordering the crystal. This biotin label can be visualized by incubating the membranes with avidin-ferritin conjugate (Heitzmann and Richards, 1974). By laying biotin-labeled membranes on the carbon film and washing with avidin-ferritin, crystals that have their extracellular surface away from the film can be identified. Electron diffraction of these membranes reveals that the bottom of the structure in Fig. 10F is the extracellular side of the protein (Henderson *et al.*, 1978).

The original structure was completed only to 0.7-nm resolution, and the detail of the polypeptide chain is not seen. Several groups are attempting to extend the resolution of the structure. One approach is to use frozen hydrated specimens maintained at low temperature to decrease the beam sensitivity of the membrane (Hayward *et al.*, 1978). Electron diffraction alone could be used to solve the structure if the phases of the reflections can be determined. Dumont and Wiggins (1978) have succeeded in producing intensity changes by using a heavy atom reagent on the membrane, opening the possibility of determining phases by isomorphous replacement. Engelman *et al.* (1980) have combined secondary-structure prediction based on the sequence of Ovchinnikov *et al.* (1978) with accessibility data to fit the sequence to the 0.7-nm three-dimensional structure. The model for the folding of the chain that had the shortest links between helices, the fewest unpaired buried charges, and predicted helix densities consistent with the low-resolution structure was chosen as best. This model suggests the existence of a channel of hydrophilic residues forming the path for proton transport.

C. Gap Junction

The gap junction is a specialized region of the cell membrane forming the contact between communicating cells. The junction is believed to allow the passage of ions and small molecules (up to 1000 daltons) between cell interiors.

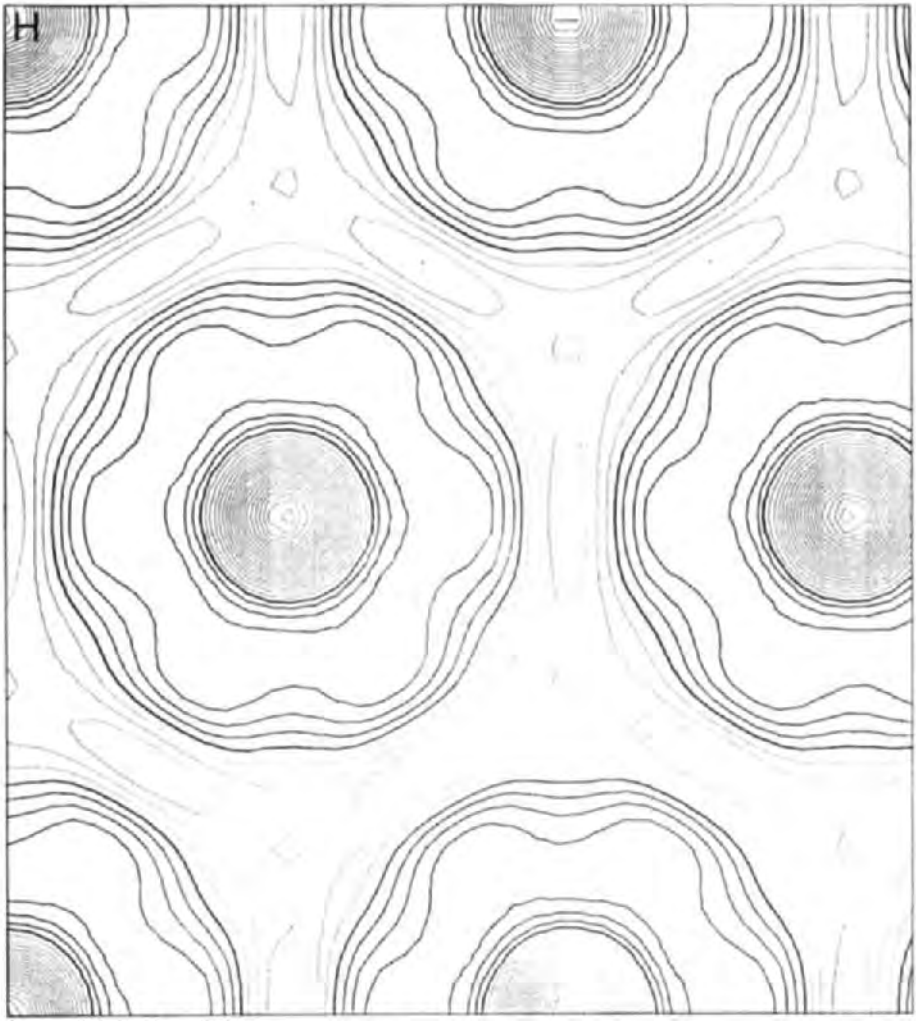


FIG. 10H. Projection, looking down on the membrane, of the B (closed) form of p622 gap junction crystals negatively stained with uranyl acetate. Heavy contours indicate stain exclusion. From Zampighi and Unwin (1979), used with permission.

Loewenstein (1975) has shown that high intracellular Ca^{2+} levels decrease the permeability of the junction. The junction comprises connexons that extend in register from the apposed cell membranes. These connexons are often organized as hexagonal crystals *in vivo* (Robertson, 1963). When isolated by hyaluronidase and collagenase treatment, the junctions maintain their crystallinity and are seen to contain a single major protein of 25,000–20,000 molecular weight (Hertzberg

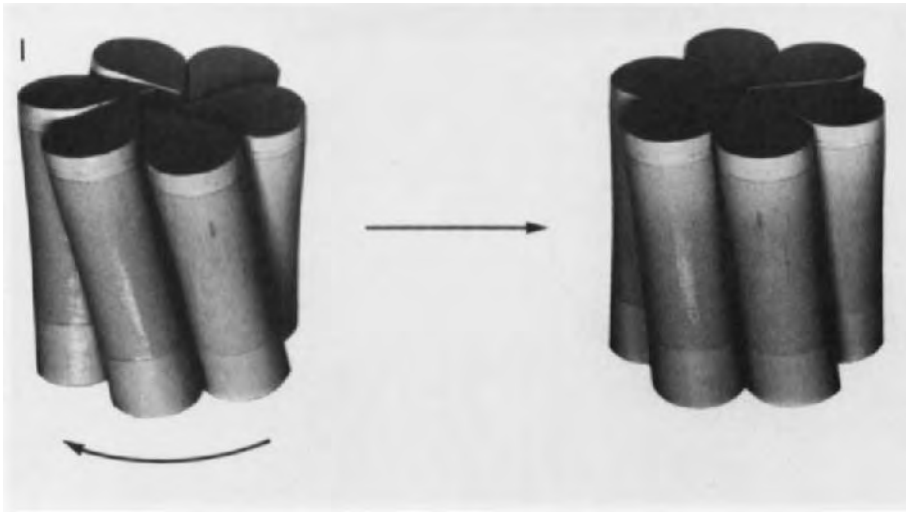


FIG. 10I. Model of the structural change undergone by the connexon between the A and the B forms. From Unwin and Zampighi (1980), used with permission.

and Gulula, 1979). These preparations have been studied extensively by x-ray diffraction and electron microscopy despite their high mosaicity (Caspar *et al.*, 1977; Makowski *et al.*, 1977). These studies show that the thickness of the junction is roughly 15.0 nm and that the spacing between connexon units in the crystal varies between 8.0 nm and 9.0 nm.

A three-dimensional reconstruction of gap junction crystals isolated from rat hepatocytes has been completed (Unwin and Zampighi, 1980). The connexons in these crystals are organized in a hexagonal crystal of spacing 8.5 nm. Dialysis of these preparations against water at 4°C for several days converts them to a second form with the same crystal symmetry. The crystals have p622 symmetry but are unevenly stained and show only p6 symmetry. The three-dimensional data were processed in p6 to bypass this problem. The full three-dimensional reconstruction in p6 shows the different staining of the two sides, which results from contact of one side of the crystal with the grid. The reconstruction shows that the connexon is composed of six apparently identical subunits. The subunits are approximately 7.5 nm in length, of which 0.5–1.0 nm protrudes from the intracellular face and 1.5–2.0 nm from the extracellular space. Each subunit seems to be 2.5–3.0 nm in diameter and inclined relative to the axis of the junction to give the connexon a left-handed, coiled configuration. The hole in the center of the junction is about 2.0 nm across at the extracellular end of the connexon and becomes narrower within the membrane.

The two configurations of the junction are related by a radial movement of the

subunits and a change in their inclination. In the dialyzed form the subunits have moved inward by about 0.6 nm and tilt toward the vertical by about 5° relative to the originally isolated form (Fig. 10H). This motion, a rearrangement of rigid subunits, seems to open and close the channel of the junction. This interpretation may provide the structural basis for the permeability changes seen *in vivo*.

ACKNOWLEDGMENTS

I wish to thank R. Capaldi, R. Henderson, L. Prochaska, K. Ranney, and E. Shabtack for their critical reading of sections of this manuscript. The author is a United States Public Health Service predoctoral trainee (GM-00715). Part of this work was supported by United States Public Health Service grant HL-22050 and PCM-7826258 (to R. Capaldi).

REFERENCES

Aebi, U., Smith, P. R., Dubochet, J., Henry, C., and Kellenberger, E. (1973). *J. Supramol. Struct.* **1,** 498-522.

Aebi, U., ten Heggeler, B., Onarato, L., Kistler, H., and Shove, M. K. (1977). *Proc. Natl. Acad. Sci. U.S.A.* **74,** 5514-5518.

Amos, L. A., and Baker, T. S. (1979). *Nature (London)* **279,** 607-612.

Asai, J. (1978). *Electron Microsc., Proc. Int. Congr., 9th, 1978* Vol. II, pp. 292-293.

Baker, T. S., and Amos, L. A. (1978). *J. Mol Biol.* **123,** 89-106.

Bisson, R., Jacobs, B., and Capaldi, R. (1980). *Biochemistry* **19,** 4173-4178.

Blaise, J. K., Erecinska, M., Samuels, S., and Leigh, J. S. (1978). *Biochim. Biophys. Acta* **501,** 33-52.

Blaurock, A. E. (1975). *J. Mol. Biol.* **93,** 139-158.

Blaurock, A. E., and Stoeckenius, W. (1971). *Nature (London), New Biol.* **233,** 152-155.

Caspar, D. L. D., Goodenough, D. A., Makowski, L., and Phillips, W. C. (1977). *J. Cell Biol.* **74,** 605-628.

Cohen, C., Caspar, D. L. D., Johnson, J. P., Nauss, K., Margossian, S. S., and Parry, D. A. D. (1972). *Cold Spring Harbor Symp. Quant. Biol.* **37,** 287-297.

Crepeau, R. H., McEwen, B., and Edelstein, S. J. (1978). *Proc. Natl. Acad. Sci. U.S.A.* **75,** 5006-5010.

Crowther, R. A., and Klug, A. (1975). *Annu. Rev. Biochem.* **44,** 161-182.

Crowther, R. A., DeRosier, D. J., and Klug, A. (1970). *Proc. R. Soc. London, Ser. A* **317,** 319-340.

DeRosier, D. J., and Klug, A. (1968). *Nature (London)* **217,** 130-134.

Downer, N. W., Robinson, N. C., and Capaldi, R. A. (1976). *Biochemistry* **15,** 2930-2936.

Dumont, M. E., and Wiggins, J. W. (1978). *Biophys. J.* **21,** 74a.

Engelman, D. M., Henderson, R., McLaughlan, A. D., and Wallace, B. A. (1980). *Proc. Natl. Acad. Sci. U.S.A.* **77,** 2023-2027.

Erickson, H. P., and Klug, A. (1971). *Philos. Trans. R. Soc. London, Ser. B* **261,** 105-118.

Finch, J. T., Lutter, L. C., Rhodes, D., Brown, R., Rushton, B., Levitt, M., and Klug, A. (1977). *Nature (London)* **269,** 29-36.

Frey, T. G., Chan, S. H. P., and Schatz, G. (1978). *J. Biol. Chem.* **253,** 4389-4395.
Fuller, S. D., Capaldi, R. A., and Henderson, R. (1979). *J. Mol. Biol.* **134,** 305-307.
Glaeser, R. M. (1973). *Proc. 31st Annu. Meet. Electron Microsc. Soc. Am.* pp. 226-227.
Goldfarb, W., Frank, J., Kessel, M., Hsung, J. C., Kim, C. H., and King, T. E. (1979). *In* "Cytochrome Oxidase" (T. E. King, Y. Orii, B. Chance, and K. Okunuki, eds.), pp. 161-167 Elsevier/North-Holland Biomedical Press, Amsterdam.
Hayashi, H., Vanderkooi, G., and Capaldi, R. A. (1972). *Biochem. Biophys. Res. Commun.* **49,** 92-98.
Hayward, S. B., Grano, D. A., Glaeser, R. M., and Fisher, K. A. (1978). *Proc. Natl. Acad. Sci. U.S.A.* **75,** 4320-4324.
Heitzmann, H., and Richards, F. M. (1974). *Proc. Natl. Acad. Sci. U.S.A.* **71,** 3537-3541.
Henderson, R. (1975). *J. Mol. Biol.* **93,** 123-138.
Henderson, R. (1977). *Annu. Rev. Biophys. Bioeng.* **6,** 87-109.
Henderson, R. (1980). *Nature (London)* **287,** 490.
Henderson, R., and Unwin, P. N. T. (1975). *Nature (London)* **257,** 28-32.
Henderson, R., Capaldi, R. A., and Leigh, J. S. (1977). *J. Mol. Biol.* **112,** 631-648.
Henry, N. F. M., and Lonsdale, K., eds. (1967). "International Tables of X-ray Crystallography," Vol. I. Kynoch Press, Birmingham.
Hertzberg, E. L., and Gulula, N. B. (1979). *J. Biol. Chem.* **254,** 2138-2147.
Holser, W. T. (1958). *Z. Kristallogr., Kristallgeom., Kristallphys., Kristallchem.* **110,** 266-281.
Issacson, M., Johnson, D., and Crewe, A. V. (1973). *Radiat. Res.* **55,** 205-224.
Klug, A., and Berger, L. E. (1964). *J. Mol. Biol.* **10,** 565-569.
Klymkowsky, M. W., and Stroud, R. M. (1979). *J. Mol. Biol.* **128,** 319-334.
Loewenstein, W. R. (1975). *Cold Spring Harbor Symp. Quant. Biol.* **40,** 49-63.
Ludwig, B., Downer, N. W., and Capalid, R. A. (1979). *Biochemistry* **18,** 1410-1417.
Makowski, L., Caspar, D. L. D., Phillips, W. C., and Goodenough, D. A. (1977). *J. Cell Biol.* **74,** 629-645.
Matthews, B. W. (1968). *J. Mol. Biol.* **33,** 491-497.
Michel, H., Oesterhilt, D., and Henderson, R. (1980). *Proc. Natl. Acad. Sci. U.S.A.* 77, 338-342.
Oesterhelt, D., and Stoeckenius, W. (1971). *Nature (London), New Biol.* **233,** 149-152.
Ohlendorf, D. H., Wrenn, R. F., and Banasyak, L. J. (1978). *Nature (London)* **272,** 28-32.
Ovchinnikov, Y. A., Adulaer, N. G., Feigina, M. Y., Kiselev, A. V., Lobanov, N. A., and Nasinov, I. V. (1978). *Bioorg. Khim.* **4,** 1573-1574.
Prochaska, L., Bisson, R., and Capaldi, R. A. (1980). *Biochemistry* **19,** 3174-3179.
Robertson, J. D. (1963). *J. Cell Biol.* **19,** 201-221.
Ross, M. J., Klymkowsky, M. W., Agard, D. A., and Stroud, R. M. (1977). *J. Mol. Biol.* **116,** 635-659.
Sayre, D. (1952). *Acta Crystallogr.* **5,** 843.
Seki, S., Hayachi, H., and Oda, T. (1970). *Arch. Biochem. Biophys.* **138,** 110-121.
Smith, P. R., Aebi, U., Josephs, R., and Kessel, M. (1976). *J. Mol. Biol.* **106,** 243-271.
Stenn, K., and Bahr, G. R. (1970). *J. Ultrastruct. Res.* **31,** 526-550.
Steven, A. C., ten Heggler, B., Muller, L., Kistler, J., and Rosenbusch, J. P. (1977). *J. Cell Biol.* **72,** 292-301.
Steven, A. C., and Navia, M. A. (1980). *Proc. Natl. Acad. Sci. U.S.A.* **77,** 4721-4725.
Stewart, M., and Diakiv, V. (1978). *Nature (London)* **274,** 184-186.
Stout, G. H., and Jensen, L. H. (1968). "X-ray Structure Determination." Macmillan, New York.
Sun, F. F., Preybindowski, K. S., Crane, F. L., and Jacobs, E. E. (1968). *Biochim. Biophys. Acta* **153,** 804-818.
Unwin, P. N. T. (1975). *J. Mol. Biol.* **98,** 235-242.

Unwin, P. N. T. (1977). *Nature (London)* **269,** 118–122.
Unwin, P. N. T., and Henderson, R. (1975). *J. Mol. Biol.* **94,** 425–440.
Unwin, P. N. T., and Zampighi, G. (1980). *Nature (London)* **283,** 545–549.
Weiss, H., and Kolb, H. J. (1979). *Eur. J. Biochem.* **99,** 139–149.
Williams, R. C., and Fisher, H. W. (1970). *J. Mol. Biol.* **52,** 121–123.
Wingfield, P., Anad, T., Leonard, K., and Weiss, H. (1979). *Nature (London)* **280,** 696–697.
Woolfson, M. M. (1970). "An Introduction to X-ray Crystallography." Cambridge Univ. Press, London and New York.
Zampighi, G., and Unwin, P. N. T. (1979). *J. Mol. Biol.* **135,** 451–464.

Chapter 15

Visualization of Virus Structure in Three Dimensions

ALASDAIR C. STEVEN

Laboratory of Physical Biology,
National Institute of Arthritis, Metabolism, and Digestive Diseases,
National Institutes of Health,
Bethesda, Maryland

I. Introduction 298
A. Structural Virology and Cell Biology 298
B. Perspective 298
C. Optical Diffraction and Digital Image Processing 298
D. Regular Virus Structures: Terms of Reference 299
II. Cryomicroscopy of Virus Particles 300
III. Advent and Application of the Scanning Transmission Electron Microscope . . . 300
A. Theoretical Advantages 300
B. STEM Images of Negatively Stained Virions 303
C. Unstained Virions: Molecular Mass Measurements by STEM 303
IV. Three-Dimensional Reconstruction of Virus Particles 304
A. Retrieval of Mass Distributions from Projection Data 304
B. Application to Helical Particles 306
V. Image Processing of Two-Dimensional Surface Lattices 308
A. Extended Tubular Forms 308
B. Conformational Transformations of the T4 Capsid: Structural Expression and Biological Significance 310
C. Antibody Labeling: Insight in the Third Dimension 312
D. Conformational Transformations of Other Viruses 314
VI. Electron Microscopy and Virus Crystallography 316
A. Crystalline Aggregation of Spherical Viruses 316
B. Electron Microscopy of Two-Dimensional Virus Crystals 317
VII. Concluding Discussion 319
A. Resolution and Reproducibility 319
B. Outlook 320
References 321

ISBN 0-12-564122-2

I. Introduction

A. Structural Virology and Cell Biology

The evolutionary origins of viruses are thought to derive (Luria *et al.*, 1978) from mutinous subsets of cellular genes, or from regressive parasitic cells. Dependence on host cell functions remains indispensable to viral propagation, and detailed analogies relate the assembly mechanisms of virus particles to those of such cellular components as organelles and membranes. The development, in recent years, of quantitative methods for three-dimensional analysis of supramolecular assemblies by electron microscopy has contributed to our understanding of both viral and endogenous cellular structures. It is the purpose of this chapter to review the former, with particular attention to how these results may impinge on the latter.

B. Perspective

Certain aspects of virus structure have been reviewed comprehensively in the recent past, notably the tubular viruses (Hull, 1976) and bacteriophages (Eiserling, 1979). Assembly phenomena of viruses in general (Casjens and King, 1975) and bacteriophages in particular (Murialdo and Becker, 1978) have also been covered. This article is intended to survey the most recent work in the field, to evaluate the biological significance of structural findings, and to assess the scope for further development. Three points, in particular, will be elaborated. First, the contribution of image processing methods will be emphasized. In appraising the benefits, limitations, and conditions for profitable applicability of these methods, this discussion will be largely qualitative. For details, the reader will be referred to the original literature. Second, the complementary nature of information derived from different techniques of specimen preparation will be stressed. Third, although electron micrographs are static images, it will be shown that they can afford some insight into the molecular dynamics of coupled assembly reactions between successive states on biochemically defined pathways.

C. Optical Diffraction and Digital Image Processing

Optical diffraction and image processing are covered in detail and with clarity in the monograph of Misell (1978). Optical diffraction analysis of biological electron micrographs was first performed by Klug and Berger (1964). The technique is now widely used both to measure and rationalize periodicities in regular structures, and to provide a rapid, objective, and quantitative means for selecting the most informative images from a collection of micrographs of ostensibly identical specimens. Optical filtering (Klug and DeRosier, 1966; Aebi *et al.*,

1973) is an application of the general technique of spatial frequency filtering in coherent optics (O'Neill, 1956; Goodman, 1968). In the present context, optical filtering is used to reduce noise levels in images of periodic specimens, and to separate the various levels of structure that contribute to a moiré pattern. As shown by Fraser and Millward (1970), optical filtering is formally analogous to the method of image averaging by photographic translation devised by Markham *et al.* (1964). Indeed, the techniques can be combined (Steven *et al.*, 1976a).

Computer image processing of digitized images (see Frank, 1973) may be used in averaging, as well as in performing a much wider repertoire of operations that facilitate retrieval of information from noisy electron micrographs. Computer processing has the additional advantages of being both quantitative and strictly reproducible; it may also be used to perform three-dimensional reconstructions from projection data (Crowther *et al.*, 1970), or topographic reconstructions from shadow casts (Smith and Kistler, 1977). Moreover, the approach is applicable to any situation where an algorithm may be devised to solve an indirect relationship between the micrograph's optical density distribution and the mass density distribution of the specimen.

D. Regular Virus Structures: Terms of Reference

Most, perhaps all, viruses have some regular elements, composed of identical protein subunits, symmetrically arranged. These elements observe *helical* (Crane, 1950) or *icosahedral* symmetries. The basic properties of helical geometry and diffraction are summarized concisely by Fraser and MacRae (1973). An example of a helical projection and the characteristic "layer-lines" of its optical diffraction pattern are given in Figs. 4c and 4d. Caspar and Klug (1962) not only describe pertinent geometric properties of *icosahedra,* but also advance thermodynamic arguments that indicate why this form is appropriate to the design of virus head shells (*capsids*). An icosahedron is a regular closed polyhedron generated by triangulation on twelve points uniformly distributed over the surface of a sphere. Each of these points is a *vertex* common to five equilateral triangles (facets), of which there are twenty in all. In molecular terms, the vertices, with their local fivefold symmetry, may be occupied by *pentamers,* and the remainder of the surface by *hexamers*. The number of hexamers is related to the order of complexity (*triangulation number*) of the icosahedron. A *dimer–trimer* pattern of clustering is also possible. In either case, oligomers that form repeating units are termed *capsomeres*. Alternatively, the icosahedron may be constructed as a *polyhedral folding* of a planar hexagonal lattice. A physical lattice with molecules repetitively arranged over the lattice is called the *surface lattice*. This lattice may be used to generate other foldings such as cylindrical tubes. The family of structures formed by different foldings of the same basic lattice are said to exhibit *polymorphic variation*. Biologically, polymorphism

may be caused either genetically, or by differences in the assembly conditions encountered by the assembling subunits. Cylindrical foldings of hexagonal surface lattices afford a particularly interesting form of polymorphism, since they occupy an intermediate position in relation to icosahedral and helical symmetries. Such tubes may be regarded either in helical terms (the folded lattice lines describe helices) or in terms of the surface lattice of a "failed" icosahedron.

II. Cryomicroscopy of Virus Particles

Although negative staining has been the most widely applied method of preparing virus particles for electron microscopy, in recent years an increasing number of viruses have been studied by shadowing specimens that had been freeze-dried after adsorption to a support film, or freeze-fractured from centrifuged pellets of purified viral particles. Sublimation of ice is thought to constitute a minimally damaging mode of dehydration. The structural information contained in such images is complementary to that conveyed by negative staining. The shadowed image relates to the topography of a single, exposed surface, as opposed to a projected view of all the levels infiltrated in a stained specimen. The resolution attainable by ultrashadowing approaches that of negative stain, as judged by the objective criterion of optical diffractograms of planar, periodic specimens (Kistler *et al.*, 1977). Figure 1 shows images of several different viruses prepared by these methods. The micrographs demonstrate the particular suitability of cryomicroscopy for depicting the capsomere organization of capsids and even capsomeric substructure.

III. Advent and Application of the Scanning Transmission Electron Microscope

A. Theoretical Advantages

A radically novel type of electron microscope, the scanning transmission electron microscope (STEM), has been developed over the past decade, originally by Crewe's group at Chicago (Crewe *et al.*, 1968). A STEM image is formed, element by element, by scanning the specimen with a finely focused electron beam (approximately 0.5 nm in diameter) and recording separately the scattering for each image element. The principles and practice of STEM are discussed

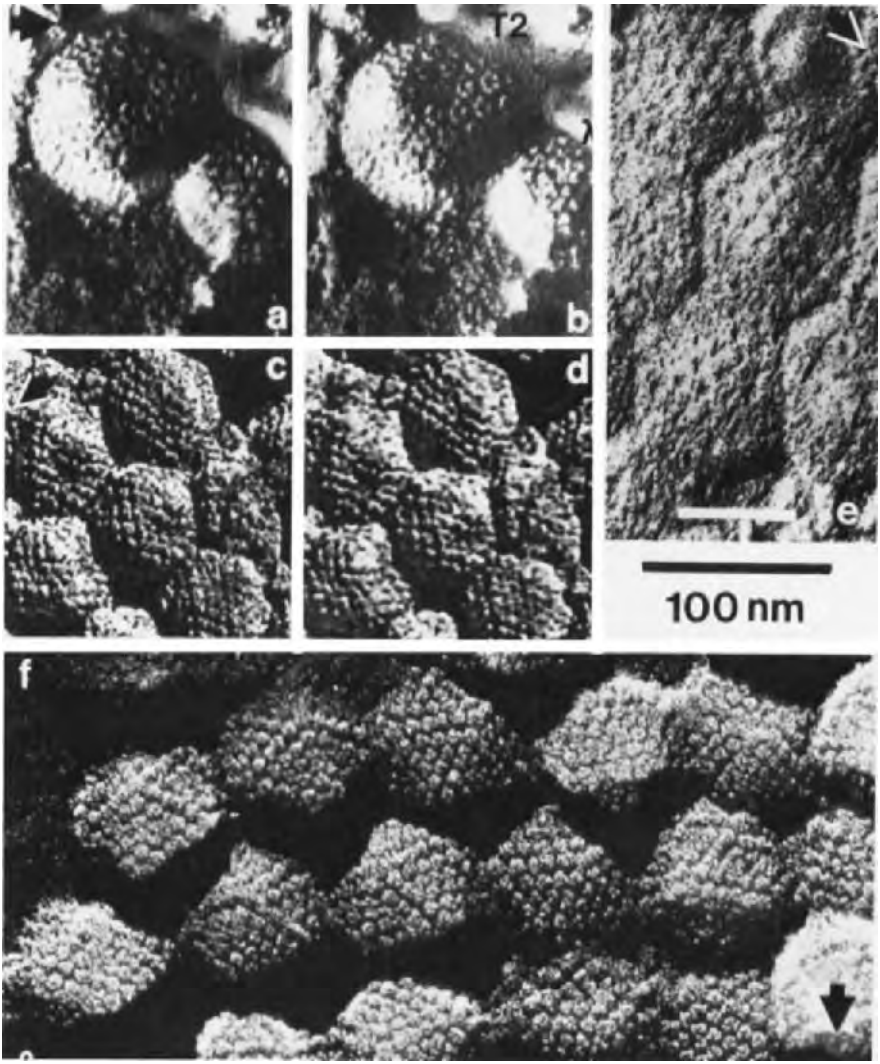


FIG. 1. Cryomicroscopy of virus particles. (a, b) Bacteriophages T2 and lambda (stereo pair), freeze-dried. Reproduced from Bayer and Bocharov (1973), with permission of Academic Press. (c, d) Bacteriophage P22 (stereo pair), freeze-etched. From Casjens (1979), copyright by Academic Press. (e) Mouse mammary tumor virus, freeze-dried. Reproduced from Sarkar and Moore (1974), with permission of Academic Press. (f) Adenovirus, freeze-dried. Reproduced from Nermut (1975), with permission of Academic Press. All micrographs at 250,000×, except (e) at 160,000×. All viruses were shadowed with platinum, shown here as white with black shadows. The shadowing directions are indicated by arrowheads.

elsewhere in greater detail and with much greater authority (Crewe *et al.*, 1975; Wiggins *et al.*, 1979). Here I shall recapitulate briefly the particular features of STEM that commend it as a tool for elucidating structural questions of molecular virology, and then consider the degree to which this promise has been realized in the first few publications to have appeared in this area.

STEM circumvents, at least in part, two long-standing obstacles to biological electron microscopy at high resolution: (1) degradation of fine structure by electron irradiation, and (2) the necessity to augment contrast by applying heavy metal stains or shadows. Total electron dose may be precisely and economically controlled, and STEM microscopy lends itself naturally to the practice of minimizing irradiation by optimizing electron optical parameters (focus, etc.) on portions of the specimen adjacent to those that are to be imaged. Recording of scattered electrons is efficient and can involve the formation of images in different modes simultaneously, if more than one type of detector is used. In particular, the dark-field mode has significant contrast with unstained specimens even at moderate electron dose. Furthermore, images may be recorded directly in digital form for subsequent image processing, bypassing the need for microdensitometry.

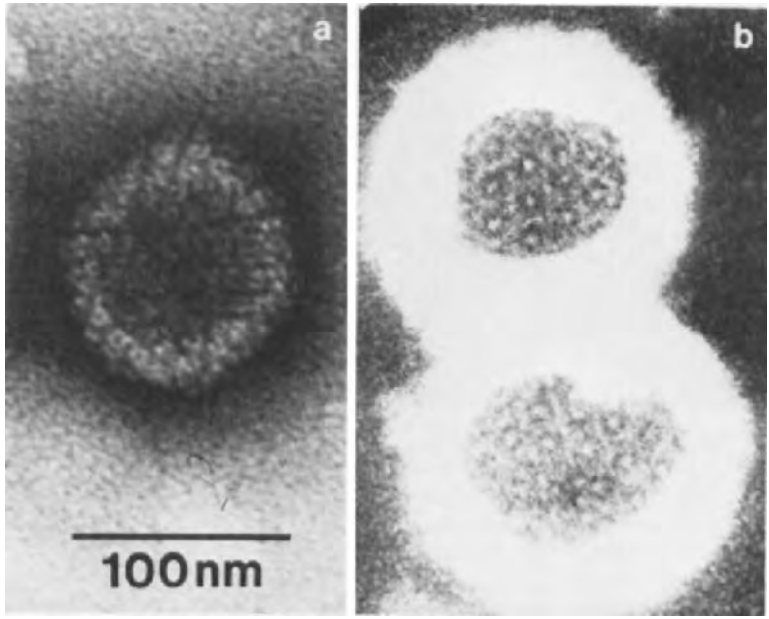


FIG. 2. Nucleocapsids of Herpes virus (Type I) negatively stained with uranyl acetate and imaged by (a) conventional TEM, bright-field mode; (b) STEM, dark-field mode. From Furlong (1978).

B. STEM Images of Negatively Stained Virions

Several viruses have already been observed by STEM microscopists. Ohtsuki *et al.* (1979) examined tobacco mosaic virus (TMV) with particular attention to changes between images recorded in successive scans, which are attributable to the increments in irradiation to which the particles had been subjected. The "stacked disc" form of TMV coat protein was studied by Engel *et al.* (1976), who reported the presence of "triple discs" in addition to the familiar "double disc." Furlong (1978) exploited the differential focusing property of STEM to analyze capsomere structure on a single side of the Herpes virus nucleocapsid (see Fig. 2) and substantiated earlier reports that the capsomere is hexameric.

Although these images certainly convey information comparable to that obtained from conventional micrographs, it is not yet clear whether any decisive advantage is to be derived from using STEM to study stained virus particles at relatively high electron doses.

C. Unstained Virions: Molecular Mass Measurements by STEM

Estimates of molecular mass may be made with the conventional transmission electron microscope (Zeitler and Bahr, 1962; Bahr *et al.*, 1976), but STEM's quantitative control of electron delivery and direct recording of scattered electrons make it uniquely appropriate for this purpose, as first proposed by Lamvik and Langmore (1977). Specific advantages include the following: (1) Only minute quantities of material are required; (2) the material of interest need only be morphologically recognizable, not necessarily pure; and (3) STEM is expected to work effectively in a molecular weight range (10^7–10^{12} daltons) not readily accessible by alternative methods. Encouraging preliminary results have been obtained on test specimens such as fd phage (Engel, 1978; Wall, 1979; see also Fig. 3) and oligomers of gp23, the major precursor protein of the bacteriophage T4 capsid (Engel, 1978). Most recently, the technique has been used to determine the mass per unit length of fibers assembled *in vitro* from the gp22 protein of the T4 prohead core (Engel and Van Driel, 1981). These studies have emphasized the need for extremely clean, thin carbon films as specimen substrates, and the importance of avoiding bias from mass loss during irradiation (typically, 30–50% loss after exposure to 10^4 electrons/nm^2). The early results augur well for profitable applications, both in virology and in other areas of structural biology, such as the organization of myofilaments (Lamvik, 1977) and local measurements of mass density (Halloran *et al.*, 1978), which may contribute to the understanding of membrane organization.

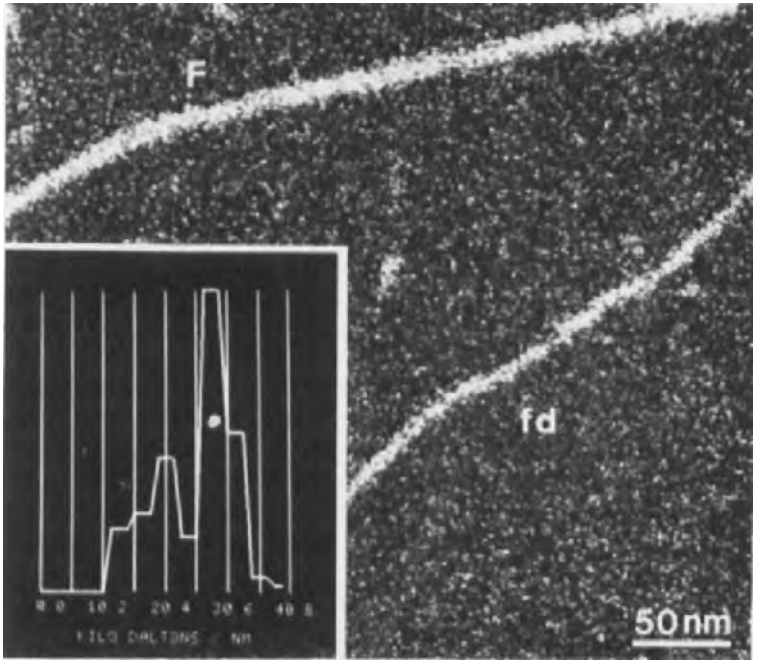


FIG. 3. Filamentous bacteriophage fd, and bacterial F-pilus, unstained, imaged by STEM dark-field. Measurements of mass per unit length from quantitation of electron scattering in STEM are shown in inset. From Engel (1978), reproduced with permission of North-Holland Publishing Company, Amsterdam.

IV. Three-Dimensional Reconstruction of Virus Particles

A. Retrieval of Mass Distributions from Projection Data

The transmission electron micrograph is a two-dimensional image formed by electrons scattered from all levels through the structure it represents. If only a single surface is strongly contrasted, as with shadowed specimens, the fact that one is dealing with a projection does not complicate interpretation of the image, but in the more general case it can be quite difficult to infer the organization even of relatively simple objects from their projections (Figs. 4a and 4b). Several different computational approaches to the problem of reconstructing three-dimensional mass distributions from two-dimensional projections have been developed. These are reviewed by Frank (Chapter 12 in this volume). In biological electron microscopy, the major contributions have been made by algorithms based on the properties of the Fourier transform (Crowther *et al.*, 1970; DeRosier and Moore, 1970) or other integral transforms (Smith *et al.*, 1973). This approach

combines the advantages of utilizing symmetry in a highly efficient manner and of providing a means for discriminating structural information from the noise content of the image.

In practice, three-dimensional reconstruction is often reduced to a number of two-dimensional reconstructions from monodimensional projections by regarding three-dimensional space as sampled on a stack of parallel planes. Nevertheless, an unambiguous solution clearly must incorporate data from several different view angles. How many views are needed? To reconstruct a particle whose greatest dimension is D, to an isotropic resolution of d, Klug and Crowther (1972) have shown that the required number of views, N_v, is stipulated by $N_v \cong \pi D/d$. In this context, "resolution" refers specifically to a capacity for separating coprojected features, and should be distinguished from electron optical resolution and the level to which molecular detail survives microscopy, although these two factors are also important in a final interpretation. In electron microscopy, the different views are acquired either by tilting specimens on a goniometric stage, or by exploiting the equivalent view angles possessed by particles that have internal symmetries, such as the regular viruses. Specialized methods have also been developed for icosahedral virions (Crowther, 1971), but the remainder of this discussion will focus on the treatment of helical particles, which relates to such subcellular assemblies as myofilaments, microtubules, and cilia, in addition to many classes of virus.

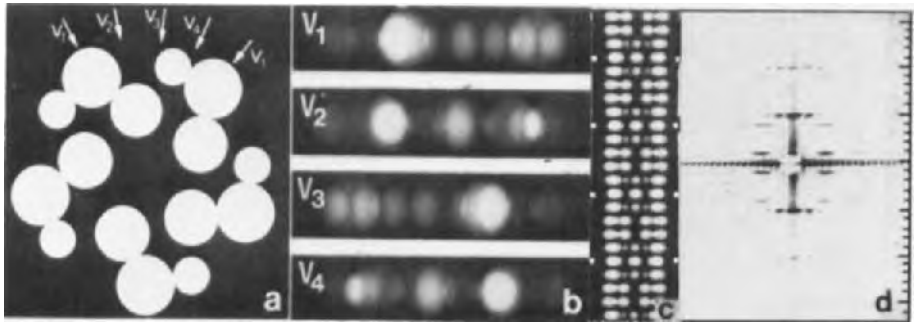


FIG. 4. Projection images and helical diffraction. A "phantom" object with fivefold rotational symmetry seen from above in (a) is viewed in side projection (b) from four different, equally spaced viewing angles (V_{1-4}). In (c) the projection of a computer-generated helix is shown. Each axial layer consists of five solid spheres, symmetrically distributed about the axis. Successive annuli are rotated through 14.4° about the helical axis. In consequence, the nth annulus presents the same projection as the $(n + 5)$th, and there will, in general, be five independent projections of the repeating annulus contained in the projection of such a helix. In this particular case, only three are independent on account of the symmetry of the individual spheres. An optical diffraction pattern (d) of this helix exhibits the characteristic form of horizontal "layer-lines," whose spacing is inversely proportional to that of the total axial repeat of the helix [marked in (c)]. On every fifth layer-line there is a meridional reflection, which corresponds to the axial spacing of annuli.

B. Application to Helical Particles

1. Reconstruction of Helical Particles

The projection of a helix is shown in Fig. 4c; its optical diffractogram (Fig. 4d) illustrates how, for such structures, the structural information is confined to the layer-lines of the Fourier transform. In practice, the information flow runs differently from this illustration (Fig. 4a–d). Starting from the digitized projection image, the Fourier transform is computed. From its layer-lines, the reconstruction algorithm then calculates the three-dimensional mass distribution of the particle and thus of the repeating unit. The parameters of helical symmetry must be predetermined as additional input to the reconstruction algorithm; analysis of the Fourier transform is an important factor in this determination.

Viral components analyzed by these methods include the stacked disc aggregate of TMV (Unwin, 1974), the tail sheaths of bacteriophages Mu (Admiraal and Mellema, 1976) and ϕCbK (Papadopoulos and Smith, 1979), and, in particular depth, the contractile tail sheath of bacteriophage T4 (DeRosier and Moore, 1970; Amos and Klug, 1975; Smith *et al.*, 1976). Reconstructions have also been made of helical fibers of hemocyanin (Mellema and Klug, 1972) and sickle cell hemoglobin (Dykes *et al.*, 1979), thin filaments of vertebrate muscle (Wakabayashi *et al.*, 1975), and bacterial flagellae (Shirakihara and Wakabayashi, 1979).

2. The Contractile Tail Sheath of Bacteriophage T4

Figure 5 shows images that represent various stages in a recent analysis of the T4 tail in its extended conformation (Smith *et al.*, 1976). The contractile tail sheath comprises 24 annuli, each composed of six molecules of gp18 ($M_r \sim 70{,}000$; Tschopp *et al.*, 1979) placed symmetrically around the axis of the tail tube. Successive annuli, spaced at intervals of 4.1 nm along the helical axis, are related by a rotation of about 102.5°, so that, after seven annular steps, two complete rotations nearly restore the original viewing direction. Taking into account the sixfold rotational symmetry of each annulus, we find that a single micrograph contains 21 independent views of the annulus and hence of the whole sheath. The outer diameter is about 22 nm, so a single micrograph should be adequate for reconstruction to about 3.2-nm resolution, according to the prescription given above. In principle, inclusion of other micrographs viewed at different angles should increase the number of independent views, N_p, and hence admit higher resolution. In practice, few optical diffraction reflections are observed beyond 3.0 nm except for a second meridional order at $(2.0\ \text{nm})^{-1}$; the studies of Amos and Klug (1975) and of Smith *et al.* (1976) have concentrated on correlating the information content of different images, rather than extending the resolu-

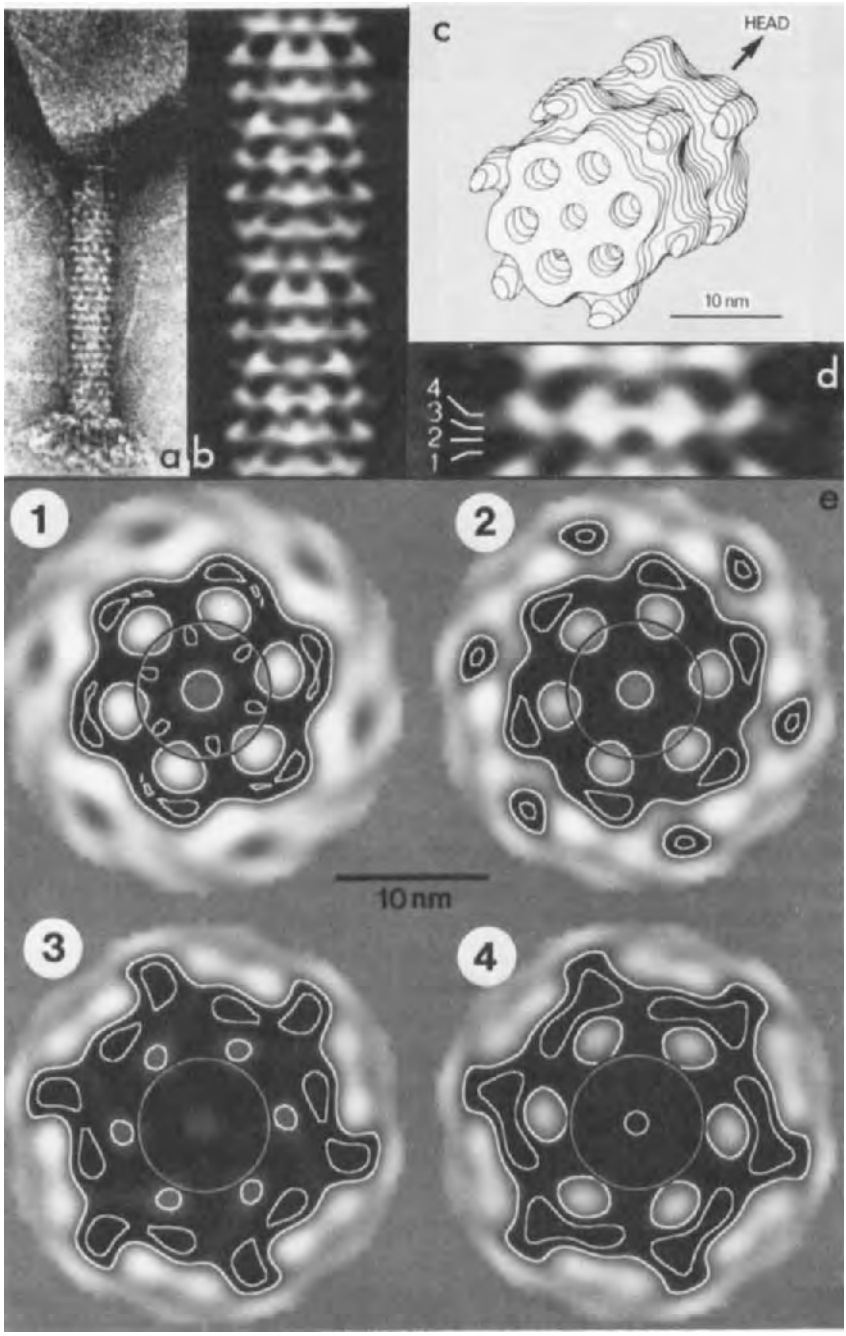


FIG. 5. Three-dimensional reconstruction of the tail of bacteriophage T4. (a) An original micrograph, negatively stained with uranyl acetate. (b) A portion of the tail, processed by averaging two complete helical repeats (fourteen disks) and by low-pass filtering at $(1.9\ \text{nm})^{-1}$. After three-dimensional reconstruction, two reconstructed disks are represented in (c). Panel (e) reveals axial sections through the reconstructed tail at four different levels (1–4), whose positions along the projected disk are indicated in (d). Adapted with permission from Smith *et al.* (1976), copyright by Academic Press.

tion. Here, resolution is constrained by the degree of preservation of fine structural detail in the micrographs rather than the adequacy of the computational methods.

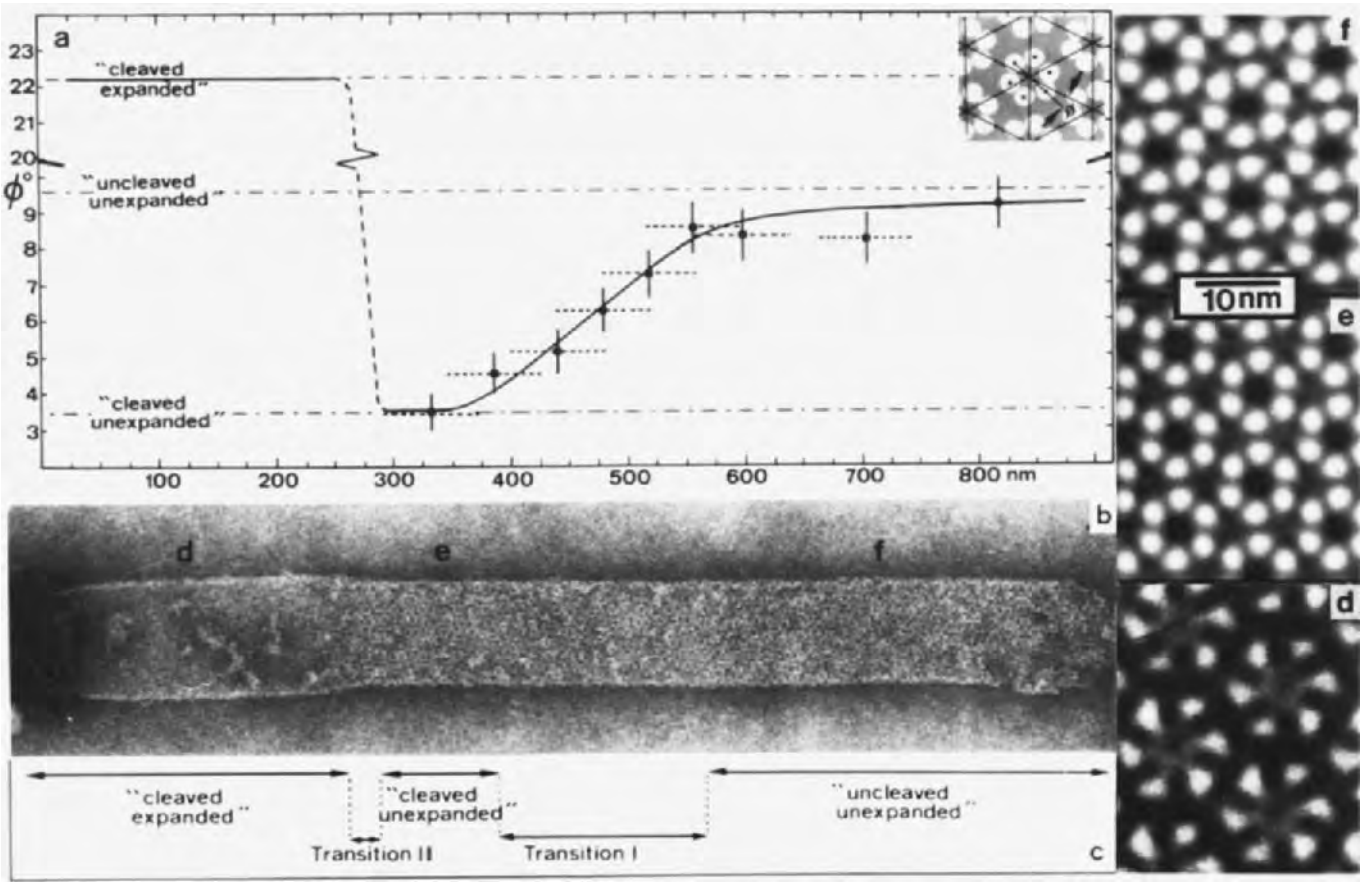
V. Image Processing of Two-Dimensional Surface Lattices

A. Extended Tubular Forms

Fine details of capsomere structure are most easily determined by filtering, optically or digitally, micrographs of uniform expanses of surface lattice. Tubular polymorphs of icosahedral capsids are suitable for this purpose because they flatten uniformly on the electron microscope grid and project an adequate number of well-aligned repeating units. In bacteriophage systems, tubes may be obtained from lysates of certain mutants defective in the regulation of head assembly. Conditions have also been established for assembling tubes *in vitro* from the precursor proteins of T4 (Van Driel, 1977) and lambda (Wurtz *et al.*, 1976). Similar assembly properties were previously determined for coat proteins extracted from mature plant viruses (Bancroft *et al.*, 1967).

The first structural studies of this kind on phage T4 (DeRosier and Klug, 1972; Yanagida *et al.*, 1972) disclosed several different capsomere morphologies, but the basis of these differences was not understood. More recently, it has been possible to extend and refine the structural characterization and, by means of complementary biochemical experiments, to relate the various structural states not only to each other but also to successive stages of the maturation phase of capsid assembly. These analyses will be summarized below for the T4 system, in which two classes of tubular particles have been studied: the open-ended "polyheads," which constitute aberrant cylindrical foldings of the hexagonal surface lattice (Steven *et al.*, 1976a), and "giants" (Doermann *et al.*, 1973), which are abnormally extended but otherwise correctly formed icosahedral capsids. This account will then serve as a point of departure for a discussion of analogous phenomena observed in other viral systems.

FIG. 6. Different conformational states of the gp23 molecules of the bacteriophage T4 capsid are represented on this single, partially transformed "giant" particle (b) negatively stained with sodium phosphotungstate. Filtered images (d–f) represent the capsomere structure on successive parts of this particle. The differences among these morphologies have been established as significant in terms of statistical reproducibility. In (a) the "orientation angle" parameter [cf. inset to (a)] is plotted as a function of distance along the particle. This trajectory indicates which areas of the particle are in the three different, physiologically defined states. The zonal breakdown of the particle is summarized in (c). Adapted from Steven and Carrascosa (1979), with permission of the publisher, Alan R. Liss, Inc., New York.


a
"cleaved expanded"
"uncleaved unexpanded"
"cleaved unexpanded"
ϕ°
23
22
21
20
9
8
7
6
5
4
3
100
200
300
400
500
600
700
800 nm
b
d
e
f
"cleaved expanded"
"cleaved unexpanded"
"uncleaved unexpanded"
Transition II
Transition I
c
f
10nm
e
d

B. Conformational Transformations of the T4 Capsid: Structural Expression and Biological Significance

1. Structural Repercussions of Proteolytic Cleavage

The major protein assembled into the precursor T4 capsoid, gp23, has a monomeric molecular weight of 58,300 (Tsugita *et al.*, 1975). After completion of prohead assembly, these molecules are cleaved proteolytically to the gp23* form ($M_r \sim 47{,}400$) found in the mature capsid. The enzyme responsible for this conversion is phage-specific. It has been purified (Showe *et al.*, 1976) and used to process native (gp23-containing) polyheads *in vitro* (Steven *et al.*, 1976b).

After cleavage, the hexagonal surface lattice is significantly changed in appearance (Laemmli *et al.*, 1976; Carrascosa and Kellenberger, 1978; Steven and Carrascosa, 1979). Moreover, it is susceptible to a subsequent, more radical structural transformation, which expands the lattice repeat from 11.2 to 13.0 nm, profoundly alters the capsomere structure, and greatly strengthens intermolecular bonds. In Fig. 6, the representations of these three conformational states of the surface lattice are shown, as depicted in filtered micrographs of negatively stained specimens.

2. Incorporation of Accessory Proteins

On the expanded surface lattice, sites are exposed that bind two further species of dispensable structural protein called *soc* and *hoc* (Ishii and Yanagida, 1975). The functional role of these "accessory" proteins is to further reinforce the surface lattice (Steven *et al.*, 1976b), already greatly stabilized by the expansion transformation. In this, the mature state, little can be inferred from unprocessed electron micrographs (Fig. 7). However, filtrations reveal a complex distribution of stain-excluding units (Figs. 7 and 8) in the ratio of 6:6:1 per capsomere, which approximates the observed stoichiometry of gp23*:*soc*:*hoc*. The attribution of stain-excluding units to proteins (see Fig. 11), first proposed by Ishii and Yanagida (1975), has been confirmed in three ways, despite the lack of biological specificity in images that represent molecules indirectly as distributions of stain-excluding matter:

1. By titrating the gp23* matrix with the accessory proteins. With fractional occupancy of lattice sites, the corresponding "structure units" appear proportionately intense in the averaged image (Steven *et al.*, 1976b; Aebi *et al.*, 1976; see also Fig. 7).

2. By using the citraconilation reaction to extract the accessory proteins without dismantling the overall structure, and observing the concomitant changes in capsomere morphology (Aebi *et al.*, 1977b).

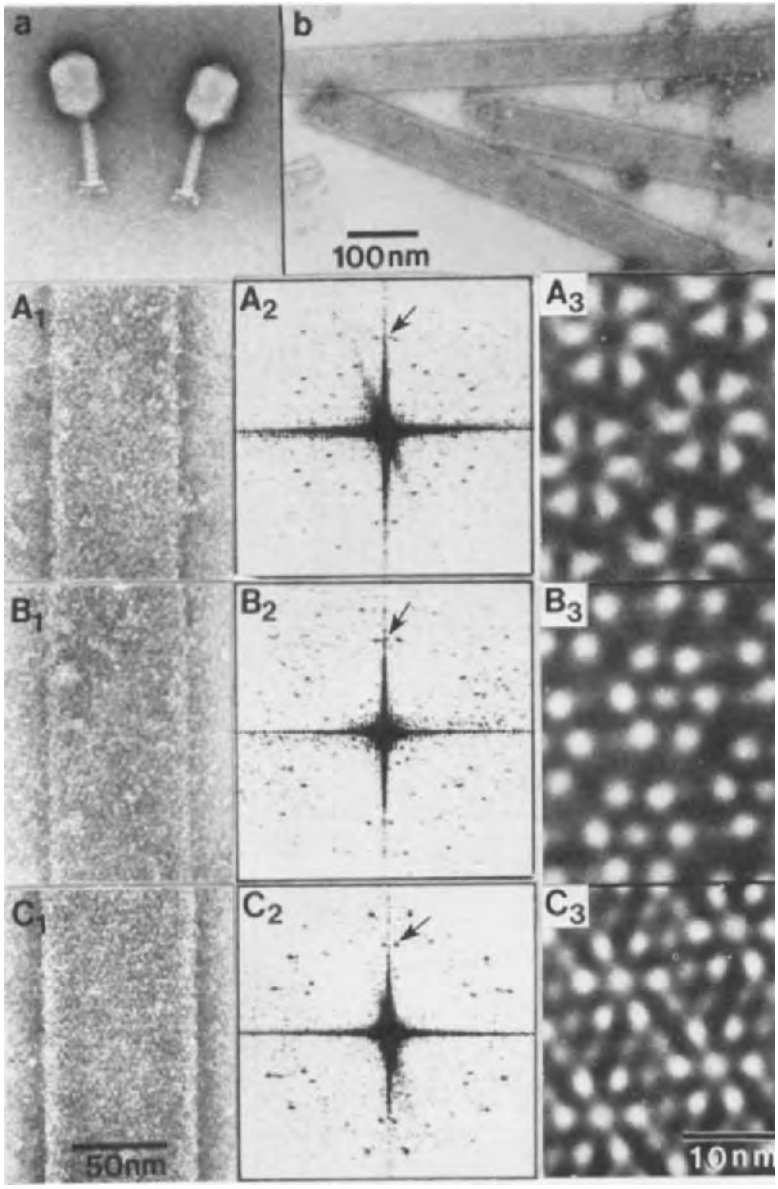


FIG. 7. Surface lattice transformations of bacteriophage T4 capsid maturation—incorporation of accessory proteins. Negatively stained T4 bacteriophage (a) and "polyhead" particles (b) are shown. Three different lattice types are represented at higher magnification by unprocessed micrographs (A_1, B_1, C_1). The lattices have the same hexagonal lattice constant (13 nm), and the differing widths of particles A_1, B_1, and C_1 are due to different lattice foldings. Thus, the corresponding optical diffraction patterns (A_2, B_2, C_2) index on similar reciprocal lattices, but the distribution of intensity over the lattice points is different in the three cases. One set of reflections, visibly intense in all three diffractograms, is marked (arrows). Optical filtrations of single-sided images of these flattened tubes are also shown (A_3, B_3, C_3). Their interpretation is discussed in the text and shown schematically in Fig. 11. Adapted from Steven *et al.* (1976b), copyright by Academic Press.

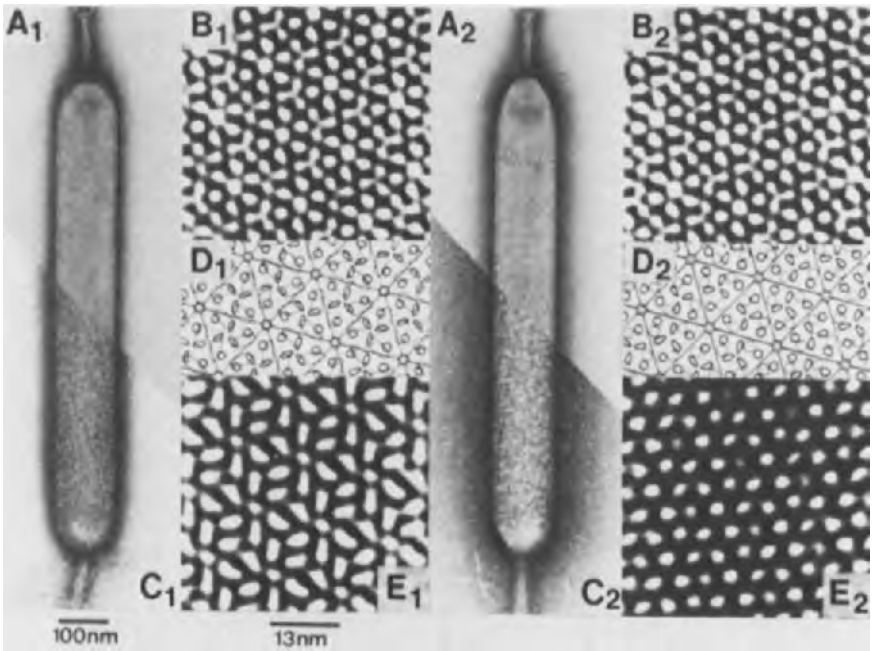


FIG. 8. Antibody (Fab fragment)—labeling patterns of giant T4 capsids treated with Fab fragments derived from two different antisera. In (A_1, A_2) and (B_1, B_2) are shown, respectively, unfiltered images of the "giants" and optical filtrations of single sides of the capsid surface lattice. C_1 and C_2 represent micrographs of giants after reaction with the respective sets of Fab fragments, both of which are rather specific (Aebi *et al.*, 1977a). Filtrations (E_1 and E_2) show the change in stain-exclusion pattern caused by addition of Fabs, and (D_1 and D_2) indicate the respective binding locations that account for the observed changes. Adapted from Aebi *et al.* (1977a).

3. By analyzing the unit cell locations with which certain monospecific Fab fragments, derived from specific antisera, are associated (Aebi *et al.*, 1977a; see also Fig. 8).

C. Antibody Labeling: Insight in the Third Dimension

These and other data demonstrate a sequence of conformational states assumed by the gp23 molecules during capsid maturation. In Fig. 9, the successive positions are mapped, on which the primary (gp23-associated) stain-excluding features are centered, within the unit cell. However, these projection images give little indication of the massive changes that accompany these transformations in the dimension perpendicular to the plane of the surface lattice. Recently, the freeze-drying/shadowing technique has been used in conjunction with both anti-

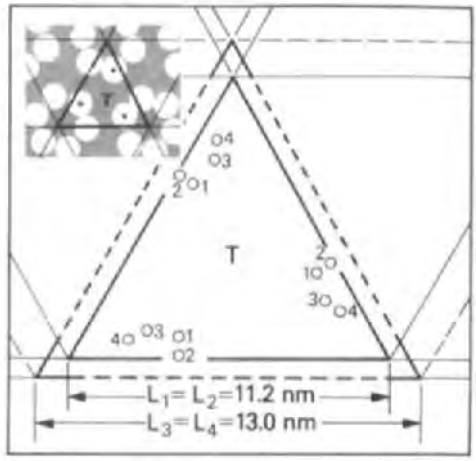


FIG. 9. Successive positions of the centers of major (gp23-associated) stain-excluding features (as defined in insert, upper left) are mapped in the unit cells relative to a threefold symmetry center, T. These positions are characteristic of different conformational states of the surface lattice of bacteriophage T4 capsid. (1) Uncleaved, unexpanded; (2) cleaved, unexpanded; (3) cleaved, expanded, from lattice repeat of 11.2 to 13.0 nm; (4) cleaved, expanded, after incorporation of accessory proteins. The radii of the circles represent the precision to which these locations have been determined (one standard deviation).

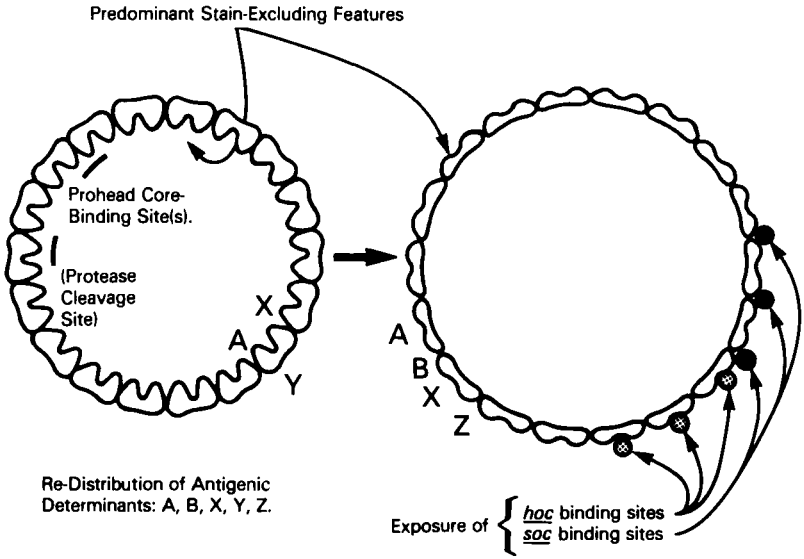


FIG. 10. Surface structure (molecular topography and distribution of binding sites) for two conformational states of the bacteriophage T4 capsid surface lattice. (a) Prohead surface lattice, uncleaved and unexpanded; (b) maturing surface lattice, cleaved and expanded.

body labeling and image processing (Kistler *et al.*, 1979) to compare the surfaces of the structure initially assembled with those of the expanded form. This combination of techniques reveals both surface topography and the locations of specific antigenic determinants. Perhaps the most astonishing finding is the translocation, upon expansion, of a determinant from the interior to the exterior surface. The sets of binding sites (on the inner and outer surfaces), both those involved in physiological interactions and those defined antigenically, change radically between the initial and the expanded states of the surface lattice. Figure 10 collates current information on these aspects of the surface lattice states. It is remarkable how the exposure of physiologically important binding sites is controlled in time, while the structural integrity of the assembly is maintained. Regulation of the pathway thus involves sequentially induced conformational change (Kellenberger, 1972).

D. Conformational Transformations of Other Viruses

Developmental transformations involving an increase in size of 10–20% have been reported for other icosahedral bacteriophages—P22 (Earnshaw *et al.*, 1976), P2 (Gibbs *et al.*, 1973), T7 (Serwer, 1975), and lambda (Zachary and Simon, 1977), although proteolytic cleavage is not the trigger in all cases. These viruses have in common a triangulation number of 7, or greater; it would be interesting to know whether such transformations feature in the maturation of structurally comparable animal viruses.

Nor is T4 unique in its deployment of "accessory" proteins. Phage lambda adds equimolar amounts of gpD ($M_r \sim 10{,}000$) to the capsid matrix of gpE ($M_r \sim 40{,}000$). Again, the functional purpose of gpD addition is to achieve greater capsid stability (Sternberg and Weisberg, 1977). Polyheads as well as disrupted capsids have been used to analyze the capsomere morphologies (Howatson and Kemp, 1975; Wurtz *et al.*, 1976; Katsura, 1978; Williams and Richards, 1974). There is consensus that the subunits pack in pentamer-hexamer-trimer clustering, but not as to which protein forms trimers, and which forms the pentamers and hexamers. The balance of evidence may favor the proposal of trimers of gpD, first advanced by Wurtz *et al.* (1976) (Fig. 11). Phages T2, P22, and T7 do not have accessory structural proteins, at least in stoichiometric amounts, and both T4 and lambda (under certain circumstances) can dispense with them.

The capsid structure of a third phage, ϕCbK, has been analyzed in detail by Lake and Leonard (1974); the proposed distribution of subunits is also shown in Fig. 11. Although no assembly studies have been published on this virus, the precedents discussed above suggest that assembly proceeds by the initial aggregation of the major protein into a prohead, followed by maturation steps that include addition of the smaller subunits, possibly regulated by an expansion transformation.

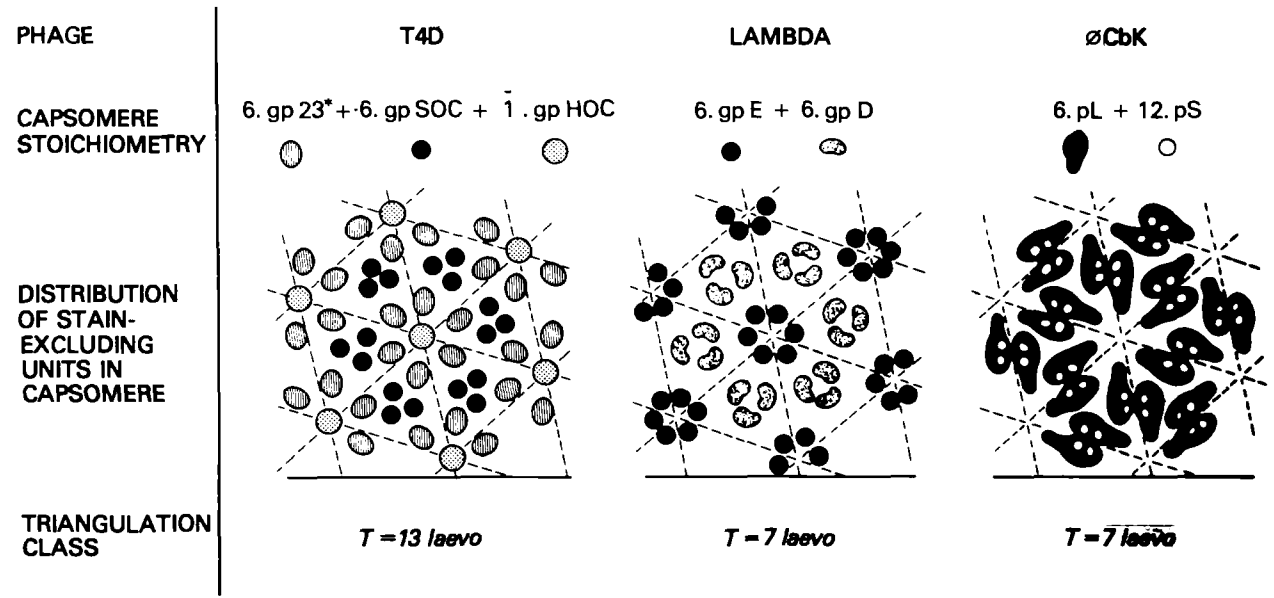


FIG. 11. The capsomere structures of three "complex" bacteriophages, whose capsids contain stoichiometric amounts of more than one protein species, have been analyzed by filtration of negatively stained surface lattices. This diagram summarizes the proposed correlations between visualized "stain-exclusion" units and the corresponding protein subunits.

VI. Electron Microscopy and Virus Crystallography

A. Crystalline Aggregation of Spherical Viruses

Cylindrical polymers are ideal for elucidation of the fine structure of surface lattices, but inappropriate to analysis of the vertex structure of icosahedral capsids. For this latter purpose, if one assumes that image averaging techniques of some sort must again be used to obtain interpretable images, crystals of whole virions (or precursors) are required. Interestingly, many icosahedral viruses have a tendency to crystallize. Thin sections of crystalline aggregates are shown in Fig. 12. The circumstances of crystal formation fall into three categories:

1. The formation of crystalline or quasi-crystalline inclusions of viruses or related particles in infected cells has been observed with numerous animal viruses (e.g., Sindbis—Wagner *et al.*, 1975), bacteriophages (e.g., lambda—

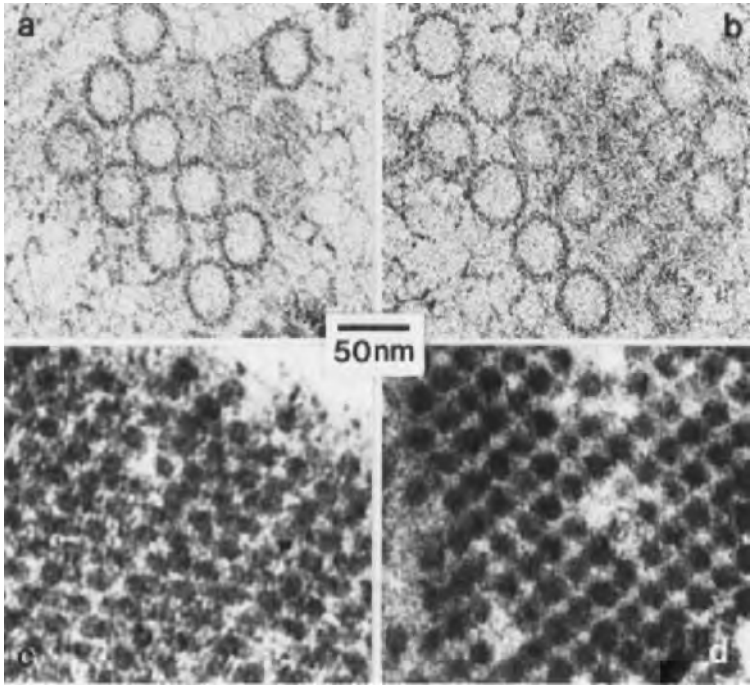


FIG. 12. Regular viral aggregates in thin sections of infected cells. (a, b) Phage lambda proheads in *Escherichia coli*, after induction of A^--lysogen, two serial sections. Reproduced from Lickfeld *et al.* (1977), with permission of Academic Press. (c, d) Sindbis nucleocapsids in cultured L-cells, labeled with ferritin-conjugated antibody. Reproduced from Wagner *et al.* (1975), with permission of S. Karger, AG., Basel.

Lickfeld *et al.*, 1977; fr—Model *et al.*, 1979) and, with exceptional frequency, plant viruses (see Martelli and Russo, 1977).

2. Regular aggregation of purified viral particles compressed into pellets by ultracentrifugation occurs spontaneously in some cases (e.g., P22 —Zorn and Gough, 1976; Semliki forest virus—Wiley and von Bonsdorff, 1978).

3. Some viruses have even been crystallized by conventional techniques [e.g., southern bean mosaic virus (SBMV)—Akimoto *et al.*, 1975; polyoma—Adolph *et al.*, 1979; cowpea chlorotic mottle virus (CCMV)—Rayment *et al.*, 1977].

X-ray crystallography of tomato bushy stunt virus (TBSV) has already been carried to a resolution of 0.28 nm (Harrison *et al.*, 1979). Similar studies of larger, more structurally sophisticated viruses offer compelling prospects for the future, although equivalent resolution on larger virions represents a Herculean proposition in computing. Such long-term studies may well be assisted by electron microscopic analyses at the currently feasible resolution of about 2 nm. Since thick specimens introduce the complication of dynamic scattering (Misell, 1978), the ideal material would be monolayer crystals.

B. Electron Microscopy of Two-Dimensional Virus Crystals

With cowpea chlorotic mottle virus (CCMV), Horne and Pasquali-Ronchetti (1974) discovered regular two-dimensional aggregates (both tetragonal and hexagonal) of virions on electron microscope grids of preparations made according to their "'negative stain-carbon film'' technique. In this method, a drop of virus suspension is spread on a mica surface and air-dried. A thin carbon film is then applied by evaporation, and the dried viruses floated off the mica in a dish of uranyl acetate, collected on a grid, and dried again. These arrays have been studied in detail (Horne *et al.*, 1975). The hexagonal arrays represent spherical close packing of randomly oriented virions, but the tetragonal arrays are crystalline (Steven *et al.*, 1978). Original micrographs and computer-filtered images are compared in Fig. 13. The filtrations of the hexagonal arrays represent a spherically averaged structure, whereas the relative rotation of approximately 90° between the orientations of adjacent virions is apparent in the tetragonal arrays. From detailed scrutiny of Fourier transform phases, Baker (1978) concluded that this angle really alternates between 86° and 94°, and that the space group is $P2_12_12$. Thus, the projected symmetry is pgg, with two virions per unit cell, in a form that closely approximates p4 symmetry, as is evident from Fig. 13. A three-dimensional model derived from these micrographs is shown in Fig. 14.

In consideration of the possibility of extending this approach to other viruses, two possible mechanisms whereby these two-dimensional crystals are formed have been proposed:

1. Epitaxial growth at the mica-solution interface.

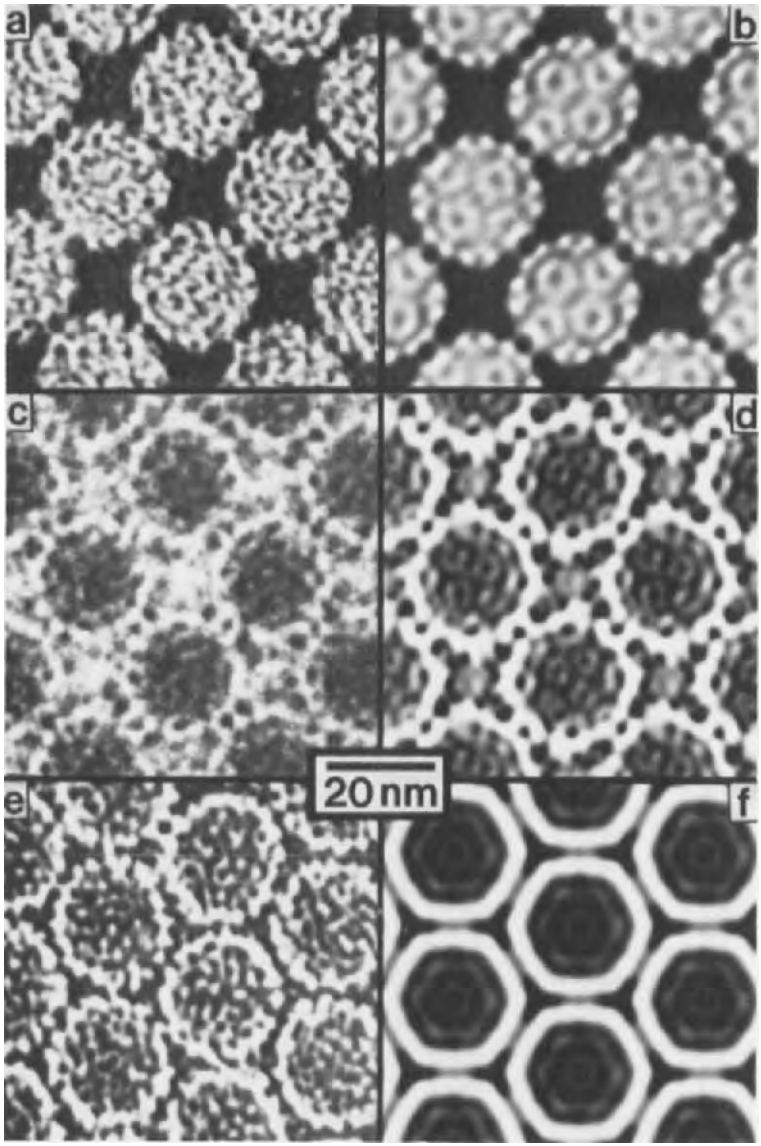


FIG. 13. Regular two-dimensional arrays of cowpea chlorotic mottle virus (CCMV) prepared by the "negative stain-carbon film technique." Two qualitatively different types of array are shown with original micrographs and computer-filtered images. (1) Crystalline quasi-tetragonal packing: the virions not significantly penetrated by negative stain (a, b), and when stain-penetrated (c, d). (2) Hexagonal arrays: (e, f) composed of close-packed virus particles (stain-penetrated) in random orientations. The filtered image (f) consequently represents the spherically averaged capsid structure. Note the alternating orientations of adjacent particles in the square arrays. Adapted from Steven *et al.* (1978), with permission of Academic Press.

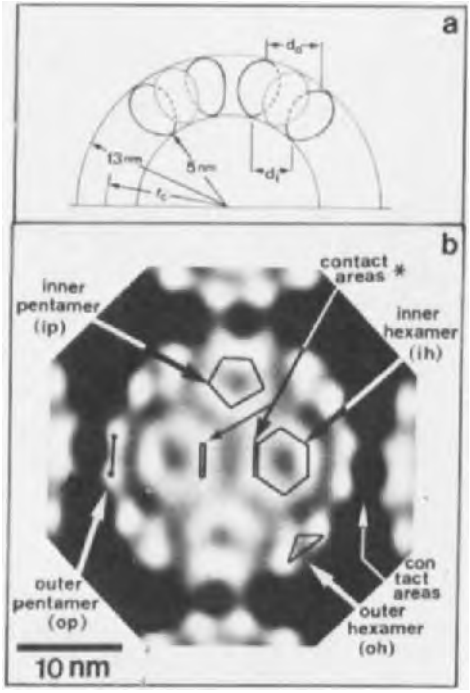


FIG. 14. Three-dimensional structure of the CCMV capsid. The dispositions of the various capsomeres are indicated in (b), and the third dimension is represented in transverse section in (a). Adapted from Steven *et al.* (1978), with permission of Academic Press.

2. The stripping of crystal planes from small three-dimensional crystals salted out during drying and deposited on the mica. Subsequently, the acid stain erodes all but the layer of particles stabilized by the carbon film.

It has not been determined whether either proposal applies to the CCMV monolayers, but the second hypothesis does permit specific suggestions as to how two-dimensional crystals might be obtained with a virus for which conditions for three-dimensional crystal formation had already been established (that is, adjust a viral suspension to crystallization conditions just prior to spreading the drop over the mica surface, or simply crush a macrocrystal and then proceed as outlined above).

VII. Concluding Discussion

A. Resolution and Reproducibility

Although optical diffraction patterns generated by micrographs of periodic objects such as those discussed above seldom show periodic reflections at

spacings beyond $(2.5\ \text{nm})^{-1}$, the filtered images obtained from these micrographs do possess information on a much finer scale. This information does not relate to the resolving of separate structural units, which does conform to this crystallographic criterion, but rather to the precision with which these units can be localized within the unit cell. This precision has been rigorously determined to be within 0.3 nm in terms of statistical reproducibility over a set of micrographs (Steven *et al.*, 1976b; Aebi *et al.*, 1976). After biochemical correlation, these geometric parameters (see Fig. 9) serve as indices of various conformational states (Figs. 7 and 8), although great caution must be exercised in relating them to structural properties of the hydrated molecules prior to microscopy. However, visualized differences must reflect pre-existing differences, although these may well be amplified or otherwise modulated by cumulative effects of specimen preparation.

In their study of the energy-transducing purple membrane of *Halobacter halobium*, Unwin and Henderson (1975) made two major innovations, which ultimately led them to a three-dimensional structure model at 0.7-nm resolution (Henderson and Unwin, 1975). First, they prepared their specimens unstained from dilute sucrose solution. Second, they recorded micrographs of this highly crystalline lipoprotein monolayer at electron doses so low (~ 50 electrons/nm^2), that radiation damage was virtually eliminated. This measure necessitated combining the information content of about 2000 unit cells per image, by image processing, in order to overcome the noise contribution of electron statistics alone. It is of interest to assess the prospects for these methods in extending the resolution of electron microscopy of viral specimens. With helical specimens, whose projections repeat periodically in one dimension only, prospects are remote. However, with flattened tubular structures, the requisite number of unit cells could be obtained by correlating the images of three or four polyheads, each a micron in length. Whether the necessary degree of either short-range or long-range order could be preserved in uniform flattening of these initially cylindrical structures remains an interesting open question.

B. Outlook

The conformational transformations during the expansions of maturing bacteriophage capsids and the contraction of the T4 tail sheath in the initial stages of its infection process are irreversible; they are apparently regulated by protein-protein interactions; and thermodynamically, they are powered by the cooperative release of conformational energy stored in the assembled subunits. In speculating on comparable cellular events where similar mechanisms might be usefully employed, perhaps the most obvious analogy lies in membrane transport phenomena, notably the secretion or assembly of membrane proteins. In any case, many intriguing questions remain unanswered; it is hoped that fruitful interplay,

both methodological and in terms of biological insight, will continue to stimulate further progress in structural virology and neighboring disciplines.

ACKNOWLEDGMENTS

It is a pleasure to thank Drs. U. Aebi, M. Bayer, S. Casjens, A. Engel, D. Furlong, K. Lickfeld, N. Sarkar, P. R. Smith, and M. Wagner for generous provision of their work, and to thank Dr. J. Buck for constructive criticism of the manuscript, Ms. M. Smith for its preparation, and Mr. C. Hanna for his contribution to the photography.

REFERENCES

Admiraal, G., and Mellema, J. (1976). *J. Ultrastruct. Res.* **56,** 48-64.

Adolph, K. W., Caspar, D. L. D., Hollingshead, C. J., Lattman, E. E., Philips, W. C., and Murakami, W. T. (1979). *Science* **203,** 1117-1120.

Aebi, U., Smith, P. R., Dubochet, J., Henry, C., and Kellenberger, E. (1973). *J. Supramol. Struct.* **1,** 498-522.

Aebi, U., Bijlenga, R. K. L., Ten Heggeler, B., Kistler, J., Steven, A. C., and Smith, P. R. (1976). *J. Supramol. Struct.* **5,** 475-495.

Aebi, U., Ten Heggeler, B., Onorato, L., Kistler, J., and Showe, M. K. (1977a). *Proc. Natl. Acad. Sci. U.S.A.* **74,** 5514-5518.

Aebi, U., Van Driel, R., Bijlenga, R. K. L., Ten Heggeler, B., Van den Broek, R., Steven, A. C., and Smith, P. R. (1977b). *J. Mol. Biol.* **110,** 687-698.

Akimoto, T., Wagner, M. A., Johnson, J. E., and Rossmann, M. G. (1975). *J. Ultrastruct. Res.* **53,** 306-318.

Amos, L. A., and Klug, A. (1975). *J. Mol. Biol.* **99,** 51-64.

Bahr, G. R., Engler, W. F., and Mazzone, H. M. (1976). *Q. Rev. Biophys.* **9,** 459-489.

Baker, T. S. (1978). *Electron Microsc., Proc. Int. Congr., 9th, 1978* Vol. II, pp. 24-25.

Bancroft, J. B., Hills, G. J., and Markham, R. (1967). *Virology* **31,** 354-379.

Bayer, M. E., and Bocharov, A. F. (1973). *Virology* **54,** 465-475.

Carrascosa, J. L., and Kellenberger, E. (1978). *J. Virol.* **25,** 831-844.

Casjens, S. (1979). *J. Mol. Biol.* **131,** 1-13.

Casjens, S., and King, J. (1975). *Annu. Rev. Biochem.* **44,** 555-611.

Caspar, D. L. D., and Klug, A. (1962). *Cold Spring Harbor Symp. Quant. Biol.* **27,** 1-24.

Crane, H. R. (1950). *Sci. Mon.* **70,** 376-389.

Crewe, A. V., Eggenberger, D. N., Wall, J., and Welter, L. M. (1968). *Rev. Sci. Instrum.* **39,** 570-583.

Crewe, A. V., Langmore, J., and Isaacson, M. S. (1975). *In* "Physical Aspects of Electron Microscopy and Microbeam Analysis" (B. Siegel and D. Beaman, eds.), pp. 47-62. Wiley, New York.

Crowther, R. A. (1971). *Philos. Trans. R. Soc. London, Ser. B* **261,** 221-230.

Crowther, R. A., DeRosier, D. J., and Klug, A. (1970). *Proc. R. Soc. London, Ser. A* **317,** 319-340.

DeRosier, D. J., and Klug, A. (1968). *Nature (London)* **217,** 130-134.

DeRosier, D. J., and Klug, A. (1972). *J. Mol. Biol.* **65,** 469-488.

DeRosier, D. J., and Moore, P. B. (1970). *J. Mol. Biol.* **52,** 355-369.

Doermann, A. H., Eiserling, F. A., and Boehner, L. (1973). *J. Virol.* **12,** 374–385.
Dykes, G. W., Crepeau, R. H., and Edelstein, S. J. (1979). *J. Mol. Biol.* **130,** 451–472.
Earnshaw, W., Casjens, S., and Harrison, S. C. (1976). *J. Mol. Biol.* **104,** 387–410.
Eiserling, F. A. (1979). *Compr. Virol.* **13,** 543–580.
Engel, A. (1978). *Ultramicroscopy* **3,** 273–281.
Engel, A., and Van Driel, R. (1981). In press.
Engel, A., Dubochet, J., and Kellenberger, E. (1976). *J. Ultrastruct. Res.* **57,** 322–330.
Frank, J. (1973). *In* "Advanced Techniques in Biological Electron Microscopy" (J. K. Koehler, ed.), pp. 213–274. Springer-Verlag, Berlin and New York.
Fraser, R. D. B., and MacRae, T. P. (1973). "Conformation in Fibrous Proteins," pp. 13–31. Academic Press, New York.
Fraser, R. D. B., and Millward, G. R. (1970). *J. Ultrastruct. Res.* **31,** 203–211.
Furlong, D. (1978). *Proc. Natl. Acad. Sci. U.S.A.* **75,** 2764–2766.
Gibbs, W., Goldstein, R. N., Wiener, R., Lindqvist, B., and Calendar, R. (1973). *Virology* **53,** 25–29.
Goodman, J. W. (1968). "Introduction to Fourier Optics." McGraw-Hill, New York.
Halloran, B. P., Kirk, R. G., and Sparr, A. R. (1978). *Ultramicroscopy* **3,** 175–184.
Harrison, S. C., Olson, A. J., Schutt, C. E., Winkler, F. K., and Bricogne, G. (1979). *Nature (London)* **276,** 368–373.
Henderson, R., and Unwin, P. N. T. (1975). *Nature (London)* **257,** 28–32.
Horne, R. W., and Pasquali-Ronchetti, I. (1974). *J. Ultrastruct. Res.* **47,** 361–383.
Horne, R. W., Pasquali-Ronchetti, I., and Hobart, J. M. (1975). *J. Ultrastruct. Res.* **51,** 319–330.
Howatson, A. F., and Kemp, C. L. (1975). *Virology* **67,** 80–84.
Hull, R. (1976). *Adv. Virus Res.* **20,** 1–32.
Ishii, T., and Yanagida, M. (1975). *J. Mol. Biol.* **97,** 655–660.
Katsura, I. (1978). *J. Mol. Biol.* **121,** 71–84.
Kellenberger, E. (1972). *Ciba Found. Symp.* 7 (new ser.), 189–206.
Kistler, J., Aebi, U., and Kellenberger, E. (1977). *J. Ultrastruct. Res.* **59,** 76–86.
Kistler, J., Aebi, U., Onorato, L., Ten Heggeler, B., and Showe, M. K. (1979). *J. Mol. Biol.* **126,** 571–590.
Klug, A., and Berger, J. E. (1964). *J. Mol. Biol.* **10,** 565–569.
Klug, A., and Crowther, R. A. (1972). *Nature (London)* **238,** 435–440.
Klug, A., and DeRosier, D. J. (1966). *Nature (London)* **212,** 29–32.
Laemmli, U. K., Amos, L., and Klug, A. (1976). *Cell* **7,** 191–203.
Lake, J. A., and Leonard, K. R. (1974). *J. Mol. Biol.* **86,** 499–518.
Lamvik, M. K. (1977). *J. Mol. Biol.* **122,** 55–68.
Lamvik, M. K., and Langmore, J. P. (1977). *In* "Scanning Electron Microscopy/1977" (O. Johari, ed.), Vol. I, pp. 401–409. IIT Res. Inst., Chicago, Illinois.
Lickfeld, K. G., Menge, B., Wunderli, H., Van den Broek, J., and Kellenberger, E. (1977). *J. Ultrastruct. Res.* **60,** 148–168.
Luria, S. E., Darnell, J., Baltimore, D., and Campbell, A. (1978). "General Virology," 3rd ed. Wiley, New York.
Markham, R., Hitchborn, J., Hills, G. J., and Frey, S. (1964). *Virology* **22,** 342–359.
Martelli, C. P., and Russo, M. (1977). *Adv. Virus Res.* **21,** 175–266.
Mellema, J. E., and Klug, A. (1972). *Nature (London)* **239,** 146–150.
Misell, D. L. (1978). "Image Analysis, Enhancement, and Interpretation." Elsevier/North-Holland Biomedical Press, Amsterdam.
Model, P., Webster, R. E., and Zinder, N. D. (1979). *Cell* **18,** 235–246.
Murialdo, H., and Becker, A. (1978). *Microbiol. Rev.* **42,** 529–576.
Nermut, M. V. (1975). *Virology* **65,** 480–495.

Ohtsuki, M., Isaacson, M. S., and Crewe, A. V. (1979). *Proc. Natl. Acad. Sci. U.S.A.* **76,** 1228-1232.
O'Neill, E. L. (1956). *IRE Trans. Inf. Theory* **2,** 56-65.
Papadopoulos, S., and Smith, P. R. (1979). *Proc. 37th Annu. Meet. Electron Microsc. Soc. Am.* pp. 54-55.
Rayment, I., Argos, P., and Johnson, J. E. (1977). *J. Ultrastruct. Res.* **61,** 240-242.
Sarkar, N. H., and Moore, D. H. (1974). *Virology* **61,** 38-55.
Serwer, P. (1975). *J. Mol. Biol.* **92,** 433-448.
Shirakihara, Y., and Wakabayashi, T. (1979). *J. Mol. Biol.* **131,** 485-507.
Showe, M. K., Isobe, E., and Onorato, L. (1976). *J. Mol. Biol.* **107,** 35-54.
Smith, P. R., and Kistler, J. (1977). *J. Ultrastruct. Res.* **61,** 124-133.
Smith, P. R., Peters, T. M., and Bates, R. H. T. (1973). *J. Phys. A* **6,** 361-382.
Smith, P. R., Aebi, U., Josephs, R., and Kessel, M. (1976). *J. Mol. Biol.* **106,** 243-275.
Sternberg, N., and Weisberg, R. (1977). *J. Mol. Biol.* **117,** 733-759.
Steven, A. C., and Carrascosa, J. L. (1979). *J. Supramol. Struct.* **10,** 1-11.
Steven, A. C., Aebi, U., and Showe, M. K. (1976a). *J. Mol. Biol.* **102,** 373-407.
Steven, A. C., Couture, E., Aebi, U., and Showe, M. K. (1976b). *J. Mol. Biol.* **106,** 187-221.
Steven, A. C., Smith, P. R., and Horne, R. W. (1978). *J. Ultrastruct. Res.* **64,** 63-73.
Tschopp, J., Arisaka, F., Van Driel, R., and Engel, J. (1979). *J. Mol. Biol.* **128,** 247-258.
Tsugita, A., Black, L. W., and Showe, M. K. (1975). *J. Mol. Biol.* **98,** 271-275.
Unwin, P. N. T. (1974). *J. Mol. Biol.* **87,** 657-670.
Unwin, P. N. T., and Henderson, R. (1975). *J. Mol. Biol.* **94,** 425-440.
Van Driel, R. (1977). *J. Mol. Biol.* **114,** 61-78.
Wagner, B., Veckenstedt, A., and Wagner, M. (1975). *Intervirology* **5,** 103-107.
Wakabayashi, T., Huxley, H. E., Amos, L. A., and Klug, A. (1975). *J. Mol. Biol.* **93,** 477-497.
Wall, J. S. (1979). *In* "Scanning Electron Microscopy/1979" (O. Johari, ed.), Vol. II, pp. 291-302. SEM Inc., AMF O'Hare, Illinois.
Wiggins, J. W., Zubin, J. A., and Beer, M. (1979). *Rev. Sci. Instrum.* **50,** 403-410.
Wiley, D. C., and von Bonsdorff, C. H. (1978). *J. Mol. Biol.* **120,** 375-379.
Williams, R. C., and Richards, K. E. (1974). *J. Mol. Biol.* **88,** 547-550.
Wurtz, M., Kistler, J., and Hohn, T. (1976). *J. Mol. Biol.* **101,** 39-56.
Yanagida, M., DeRosier, D. J., and Klug, A. (1972). *J. Mol. Biol.* **65,** 489-499.
Zachary, A., and Simon, L. D. (1977). *Virology* **81,** 107-116.
Zeitler, E., and Bahr, G. F. (1962). *J. Appl. Phys.* **33,** 837-853.
Zorn, G. A., and Gough, M. A. (1976). *Virology* **71,** 434-443.

This Page Intentionally Left Blank

Chapter 16

Three-Dimensional Reconstruction of Single Molecules

JOACHIM FRANK

Division of Laboratories and Research,
New York State Department of Health,
Albany, New York

I. Introduction 325
A. Rationale for Reconstruction of Single Molecules 325
B. Two Basic Approaches to Single-Molecule Reconstruction 327
II. Some General Problems 329
A. Possibility of Low-Dose Work 329
B. Significance of Projections, and the Use of Correlation Functions 330
III. Reconstruction of Individual Molecules 331
A. Overview 331
B. Fatty Acid Synthetase 332
IV. Reconstruction of Averaged Molecules 335
A. Wrigley's Method 336
B. Frank and Goldfarb's Method 336
C. Kam's Method 338
V. Concluding Remarks 341
References 342

I. Introduction

A. Rationale for the Reconstruction of Single Molecules

Biological macromolecules have defined structures that are uniquely related to their metabolic functions. As was shown in the previous chapters, conventional methods of three-dimensional reconstruction developed for analysis of electron microscopic structure require either a highly ordered arrangement in two dimensions or intrinsic symmetries. The rationale of these methods has been concisely

Copyright © 1981 by Academic Press, Inc.
All rights of reproduction in any form reserved.
ISBN 0-12-564122-2

formulated by Crowther (1976). The presence of order in the arrangement of molecules simplifies the reconstruction of an *averaged* structure that represents the information common to all repeated elements of the crystal or other symmetric arrangement. Noise components, or image details not reproducible from one repeat to another, will not contribute to the reconstruction. In addition, the mathematically defined spatial relationship between different repeats of a structure or between symmetry-related parts of it allows quantitative characterization of how well it has been preserved in the preparation. All present knowledge about the resolution-limiting effects of stain (e.g., Unwin, 1974; Aebi *et al.*, 1973) and electron irradiation (Glaeser, 1971) has been derived on this basis.

This approach to structural investigation, however, restricts the class of molecules amenable to analysis. Except in proteins that form components of cell walls, two-dimensional crystalline order rarely occurs naturally but rather must be induced by appropriate ionic conditions. However, there is no general recipe for crystallizing protein molecules, and, even when such a preparation succeeds, there is no guarantee that the ordering extends to high resolution.

Deviations from the well-ordered arrangement on a regular lattice are frequent, and the search for a good crystalline patch in the optical diffractometer is part of the reconstruction procedure. For example, in Unwin and Taddei's ribosome tetramer crystal (1977) the individual tetramers are well preserved, but they appear rotated and shifted by random amounts with respect to the ideal lattice. This limits the resolution of the computer-filtered average to about 6 nm, which is much poorer than expected for stained specimens. Recently the method of correlation averaging (Saxton, 1980; Frank and Goldfarb, 1980) has revealed a large amount of dislocation of individual repeats from the ideal lattice in a bacterial cell wall (Baumeister and Frank, work in progress). Other crystals reported in the literature appear well ordered in the short range, but with the lattice bent or otherwise distorted in the long range. Again there is a discrepancy between the amount of significant, reproducible detail apparent in the electron micrograph and the amount of detail found in the computer average.

This raises the issue of whether a methodology for quantitative structural investigation could be developed based on projections of single molecules. If such a technique were developed, it could be applied as well to poorly ordered molecules in the crystal. The crystal's function would then be merely to assure the homogeneity of the environment and no longer to establish defined spatial relationships between the molecules. Such a methodology would have to satisfy two requirements: one, to find methods for preserving the three-dimensional structure of single molecules; the other, to develop methods of data collection and analysis suited to aperiodic (that is, nonrepeating) objects. This chapter will address only the second problem.

When the molecule is composed of identical subunits in symmetric or other well-defined arrangements, a single molecule projection may provide sufficient

information for the reconstruction algorithm. For particles containing helical arrangements (DeRosier and Klug, 1968) or highly symmetric arrangements of subunits on a sphere (Crowther, 1971), adequate reconstruction techniques have been developed at the Molecular Biology Laboratory of the Medical Research Council in Cambridge. However, when no such intrinsic symmetries are present, one is forced to collect projection data that show the molecule in different views.

B. Two Basic Approaches to Single-Molecule Reconstruction

Two approaches have been proposed for three-dimensional reconstruction of single molecules. In the approach formulated and pursued by Hoppe *et al.* (1974, 1976a,b,c), a series of views of an individual molecule is picked from micrographs of tilting series.* The molecule is reconstructed from these views by Fourier techniques. Since no averaging is applied in this method, the reconstructed mass-density distribution represents the molecule together with the surrounding stain and the attached support film structure. In practice the stain predominates in the reconstructed volume because of its high relative contrast, so the carbon support structure does not interfere with interpretation. When several molecules have been reconstructed in this way, the resulting three-dimensional density maps can be combined or correlated to distinguish regions with reproducible information from those with no apparent significance.

In the alternative approach, the information on the three-dimensional density distribution in the molecule is extracted from a large number of projections of different molecules. Thus, the three-dimensional map will reflect an average density distribution that no longer contains any random contributions. The support film will be averaged along with the other random components, so the molecule boundary will appear sharply defined in the reconstruction.

We need not examine these two approaches in detail to recognize the dilemma posed by molecules with the variability normally encountered in electron microscopic preparations. A typical electron micrograph of single, stained molecules (Fig. 1) shows a disturbing variety of structural features. The observed variability of the molecule projections is caused largely by dehydration, irregular distribution of the stain, and electron-specimen interaction (radiation damage). Since the image contrast is due mainly to the stain, and since the stain distribution is itself strongly affected by electron irradiation (Unwin, 1974), the latter two factors cannot be clearly distinguished. The relative importance of these effects has been reviewed by Aebi (1978) and Baumeister and Seredynski (1978).

*The term "tilting series" must be understood in a general sense, as a series of projections in different directions with respect to the *particle*. When the goniometer stage is used, the specimen grid is physically tilted with respect to the beam. In the "three-dimensionally imaging electron microscope" of Hoppe (1972), on the other hand, the specimen grid is fixed, and the electron beam is tilted by electron optical means.

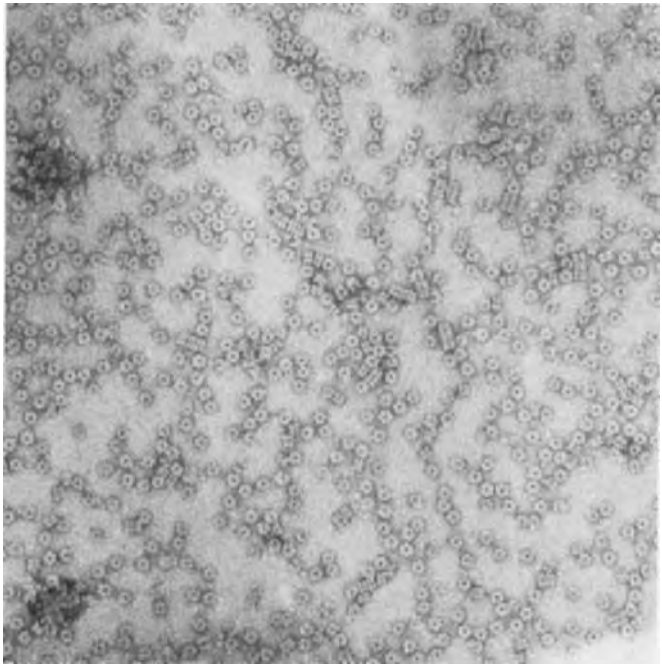


FIG. 1. A field of glutamine synthetase molecules in axial projection. Although chemically identical before preparation, the molecules show a great variety of shapes due to artifacts from staining and electron irradiation.

The dilemma lies in the fact that, in the presence of major structural variations due to the factors cited, the reconstruction of an individual molecule picked from a large population will show only one of the many structures present, with no indication of the extent to which this structure represents the molecules studied or even of the frequency of its occurrence in the total population.

On the other hand, averaging of many molecules picked at random, which is implicit in the second approach, will result in the superposition of many distinctly different structures, leading to a severe loss of resolution in the averaged reconstruction.

As a possible means of resolving this dilemma, the population entering the reconstruction in the second approach could be divided into subpopulations, each with statistically defined characteristics. Instead of a single three-dimensional reconstruction, several reconstructions, one for each subpopulation, would be performed, yielding different averaged structures representing distinct states of the molecule with regard to such factors as stain penetration, binding with substrate molecules, and radiation damage. One way to identify a subpopulation is to rank the particle images by their similarity to a reference image, as measured by

the cross-correlation coefficient (Frank, 1978). Molecules with the highest cross-correlation coefficients are highly similar and thus form a subpopulation that is more homogeneous than the total population. A promising general method for multivariate statistical characterization and identification of subpopulations is now being developed by van Heel and Frank (1980a,b; Frank and van Heel, 1980).

This chapter is more a preview than a review, as the complexity of the problem has prevented a rapid development of the art. Emphasized are methods that utilize information from a large population of particles in a single reconstruction. These methods have not been as thoroughly discussed in the literature as have methods for reconstruction of individual objects (Hoppe *et al.*, 1976a,b,c; Hoppe and Typke, 1979; Hoppe and Hegerl, 1980). Since practical realization is as yet lacking, the treatment necessarily contains some speculative elements.

II. Some General Problems

A. Possibility of Low-Dose Work

Low-dose electron microscopy has been shown to give high-resolution images of the undamaged protein when a suitable embedding medium is used (Unwin and Henderson, 1975). Earlier studies by Williams and Fisher (1970) and Unwin (1974) indicated that the minimum dose also optimizes the information yield from stained specimens. We must examine whether these structure-preserving techniques can be applied in the reconstruction of single particles.

When two-dimensional crystalline sheets are reconstructed from low-dose micrographs (Henderson and Unwin, 1975), averaging over sufficiently many repeats of the unit cell (each containing one or more molecules) guarantees that significant noise-free data are obtained for each projection.

Unwin and Henderson (1975) postulated that the highest order reflection of the image transform to be included in the computation of the image average should be significantly above the noise amplitudes. From this they derived a relationship between maximum dose to be tolerated, relative scattering power at the limiting resolution, and minimum number of unit cells required. For the purple membrane protein at 0.7-nm resolution and 50-e/nm^2 dose level, this minimum number is 1200.* This means that 3600 molecule images (3 per unit cell) were required to make the average of a projection statistically meaningful. Thus, a three-dimensional reconstruction based on 15 statistically meaningful projections (Henderson and Unwin, 1975) requires roughly 50,000 molecule images. Clearly,

*The number actually used by Unwin and Henderson (1975) was 3000, but this does not affect the argument.

it would be nearly impossible to combine a similar number of single-molecule images.

We must first pose the question of whether Unwin and Henderson's (1975) estimate can be applied to single particles. The visualization of details in the presence of quantum noise was investigated by Rose (1948). Rose's formula was adopted by Kuo and Glaeser (1975) for electron microscopic work. When applied to the problem of visualization of single molecules by image averaging (Frank, 1978), this formula specifies a much smaller number of molecules than that estimated by Unwin and Henderson. The ordering and the way the average is formed should, however, be irrelevant to this question. The key to the discrepancy seems to lie in the fact that Rose's formula contains the contrast in a summary fashion, whereas Unwin and Henderson's estimate is based on the significance of a single Fourier coefficient at the limiting resolution (Kessel *et al.*, 1980). A further analysis is necessary to reconcile the two approaches.

Finally, it would be incorrect to assume that three-dimensional reconstruction requires noise-free projection data, because corresponding Fourier coefficients of different projections must obey powerful constraints such as phase continuity. Therefore the estimate of the total number of molecules required for reconstruction should not be based on the requirement of a statistically significant projection measurement at the limiting resolution. For the single molecule the boundedness of the object to be reconstructed introduces additional constraints: Experimental Fourier data within a certain radius of influence are not longer independent of each other but can be considered multiple measurements of the same Fourier coefficient.

The statistical significance of three-dimensional reconstructions in the presence of quantum noise has been investigated by Hegerl and Hoppe (1976). These authors arrived at the surprising conclusion that both a single projection and a complete three-dimensional reconstruction require the same number of electrons to be statistically meaningful at a given resolution [qualitative arguments are given by Hoppe *et al.* (1973) and Hoppe (1978)]. The dose normally employed to obtain a meaningful image of a single projection can therefore be "spread out" into the different projections needed for a three-dimensional reconstruction, without increasing the total dose. The analysis by Hegerl and Hoppe (1976) is limited in that it assumes an ideal reconstruction geometry. Their conclusions, and the relevance of the analysis for practical reconstruction problems, still await general acceptance.

B. Significance of Projections, and the Use of Correlation Functions

Even in normal high-dose work, projections of single molecules and those obtained by averaging images of crystals differ greatly in the noise content of their individual Fourier coefficents. This fact has important consequences for the

reconstruction of single molecules. Crystals, because of the high significance of each Fourier measurement, allow important conclusions to be made regarding symmetry and the degree of preservation, by comparison of individual reflections of projections (which are measured from different preparations).

In contrast, signal and noise remain unseparated in the Fourier transforms of the individual projections of a single molecule. Here the noise is averaged out only at the final stage, where all the Fourier coefficients are used in the interpolation scheme to construct the three-dimensional transform. Great care must be taken, therefore, to prevent noise from interfering with the quantitative analysis. For instance, restoration techniques that are used for defocus correction may lead to noise amplification if improperly applied.

Individual Fourier coefficients of single-particle projections, because of their high noise content, cannot be analyzed and compared individually. The proper way to compare features and assess the reproducibility of projection measurements or their Fourier transforms is to use global measures such as correlation functions. These are obtained by integrating the conjugate product of the two Fourier transforms to be compared (Frank, 1973). Similar measures were used by Unwin and Klug (1974) to assess the consistency among transforms of different particles with helical symmetry.

Because of the lack of fiducial markers on the molecular scale and the small significance of single Fourier coefficients, correlation functions must also be used to find the exact relative positions of different projections with respect to the volume to be reconstructed. Correlation alignment of different projections has been developed as one of the important tools of single-particle reconstruction (Hunsmann *et al.*, 1972; Hoppe, 1974b; Hoppe *et al.*, 1976a).

III: Reconstruction of Individual Molecules

A. Overview

In this section we shall deal with the reconstruction of individual molecules without symmetry from a tilt series. This approach to single-molecule reconstruction, which is being pursued by Hoppe and co-workers at the Max Planck Institute for Biochemistry in Munich (Hoppe, 1969, 1970, 1972, 1974a,b; Hoppe *et al.*, 1974), has culminated in the first reconstruction of a molecule, fatty acid synthetase from yeast (Hoppe *et al.*, 1974). The reconstruction of the 30S ribosome subunit has been reported (Knauer *et al.*, 1978; Hoppe and Typke, 1979; Knauer, 1979; Knauer and Hoppe, 1980), but a detailed account of this work is so far lacking. The most up-to-date accounts on the methods developed by Hoppe's group are found in articles by Hoppe (1979, 1980), Hoppe and Typke (1979), and Hoppe and Hegerl (1980).

For completeness, and before describing Hoppe *et al.*'s procedure in greater detail, we should mention two reconstructions of biological particles in the submicroscopic realm. Bender *et al.* (1970), in a first demonstration of the algebraic reconstruction technique (ART) of Gordon *et al.* (1970), reconstructed a few ribosomes from a series of single-tilt micrographs. The reconstruction is very limited, owing to the small number of views (six), the large size of the angular gap (100°), and the use of a rather coarse alignment procedure.

Subsequently, Baba *et al.* (1979) reported on the three-dimensional reconstruction of the core of the turkey Herpes virus by the ART method. The authors used 25 single-tilt views between −36° and +36°. The effects of the missing angular range are evident in the direction-dependence of resolution in the reconstructed sections. Despite these artifacts, the reconstruction seems to provide some new insights into the core structure not available from the projections alone.

B. Fatty Acid Synthetase

In 1974 Hoppe *et al.* presented a reconstruction of a single molecule of fatty acid synthetase from nine projections, equispaced between −40° and +40°. The projections were obtained by tilting the specimen grid around a single axis. Details of the method were described in a later publication (Hoppe *et al.*, 1976a). The authors point out that three difficulties had to be tackled by the development of new techniques: the variation of the electron-optical focus between molecule images in different projections, the inaccuracy of existing goniometer stages, and the fact that the relative positions of the projections with respect to one another (or with respect to the volume to be reconstructed) are not directly known from the experiment.

Both the method for defocus correction using the computer, and techniques for the alignment of projections, have been mentioned in the previous section and in Chapter 12 of this volume. A high-precision goniometer developed by Hoppe *et al.* (1976a) has sufficient accuracy (0.04°) for high-resolution work.

The authors consider the minimization of radiation damage desirable, but difficult to realize when an individual particle is to be reconstructed from a sequential tilt series. Since radiation damage progresses as the micrographs are being taken, the resulting projections are inconsistent with one another, and with an unchanged three-dimensional object. Solutions to this difficult problem were discussed in an earlier paper (Hoppe, 1972; see also Hoppe and Grill, 1977), and some new electronic techniques for minimum-dose recording of nonsequential tilting series are being developed (Hoppe and Typke, 1979).

The fatty acid synthetase molecule in the reconstruction (Fig. 2) is a hollow ellipsoid with a diameter of 33.0 nm divided by a central membrane. As was pointed out in Chapter 12, the single-tilt reconstruction is conveniently done by

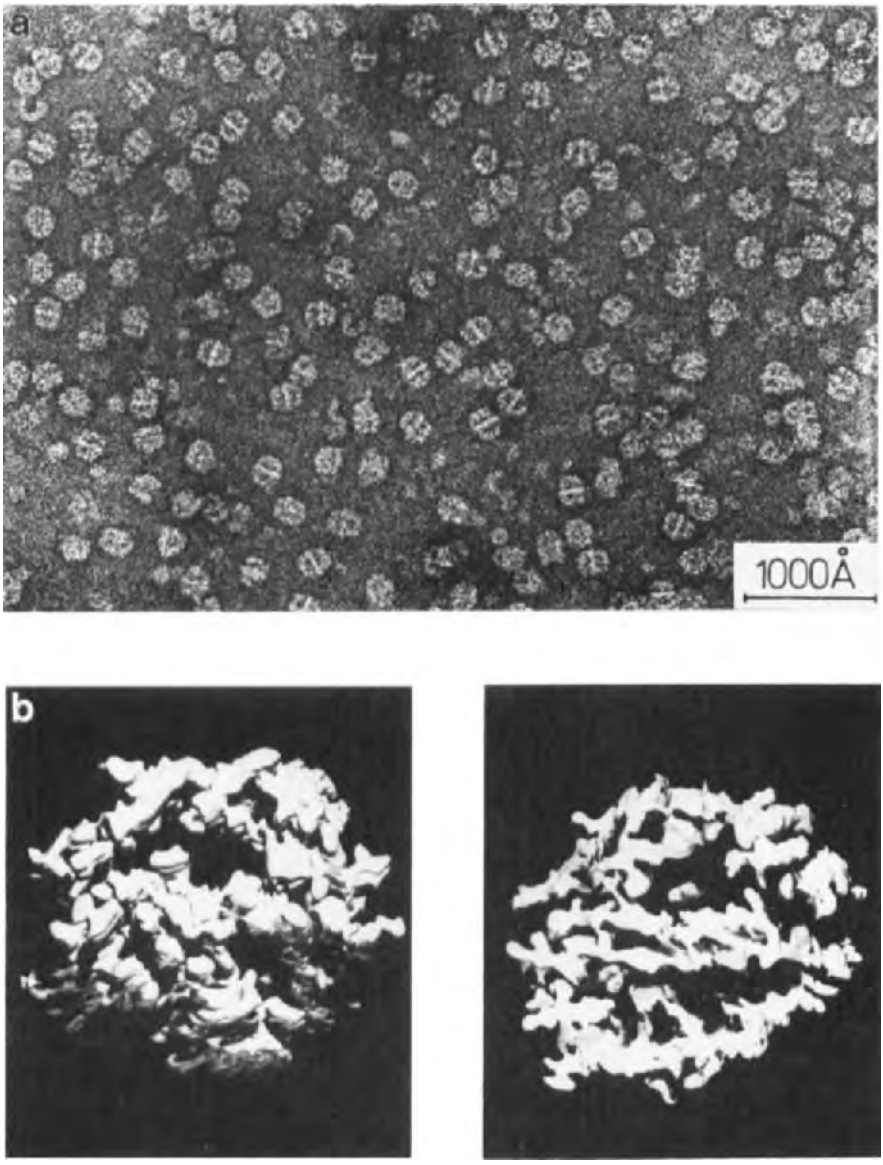


FIG. 2. Three-dimensional reconstruction of two molecules of fatty acid synthetase from yeast. (a) General appearance of molecules in high-dose electron micrographs. (b) Two independently reconstructed molecules represented by styrofoam models, viewed in a direction parallel to the central wall. From Hoppe *et al.* (1976c), courtesy of the authors and Verlag der *Zeitschrift für Naturforschung*, Tübingen, West Germany.

dissecting the two-dimensional projections into parallel strips (perpendicular to the tilt axis), each of whose can be regarded as a one-dimensional projection of a two-dimensional section of the object. The three-dimensional object can thus be constructed by stacking the slices, each of which has the density distribution of a reconstructed section and thickness corresponding to the separation of the strips.

To understand the resolution limitations of the reconstruction, one must realize that, in such a single-axis tilting geometry, the direction of sectioning (that is, selecting parallel strips from the micrographs, which is done in the computer), the direction of the missing angular range, and the direction of the complementary angular range covered with equispaced views are all perpendicular to one another. In the direction of sectioning, the resolution is very good, restricted only by the accuracy of alignment and the imaging limitations. The resolution is poorer in the direction of the missing angular range, with the actual value depending on the size of this range. Finally, in the direction covered with equispaced views the resolution has some intermediate value that depends on the size of the range and on the number of views available.

In the fatty acid synthetase reconstruction the values 0.6 nm, 4.5 nm, and 3.0 nm were given for the resolution in the three directions (Hoppe *et al.*, 1975, 1976c). However, these figures contrast with the estimate by Crowther *et al.* (1970) often quoted in the literature (see, for example, Steven's Chapter 15 in this volume). In the most fortunate situation of equispaced views within the entire $\pm 90°$ range, Crowther *et al.*'s (1970) formula would give a resolution of 10.0 nm when a particle diameter of 33.0 nm and nine views are being considered.

To understand this discrepancy, one must see that Crowther *et al.*'s (1970) resolution concept is very conservative, stipulating uniform resolution in all directions (isotropic resolution), whereas Hoppe *et al.*'s (1975, 1976c) figures relate to a reconstruction with anisotropic resolution. Reconstructions limited according to Crowther *et al.*'s (1970) resolution estimate would be artifact-free and could thus be directly interpreted. However, for a missing angular range of the size found in this experiment the formula gives a totally impractical answer.

Hoppe *et al.*'s (1975, 1976c) use of the resolution figures must be regarded as a pragmatic and legitimate solution to a problem inevitably posed by objects without symmetry. That is, the reconstruction can no longer be directly interpreted as a three-dimensional mass-density distribution with limited resolution; rather, it requires careful analysis using the three-dimensional point-spread function as an aid. It is obvious that the use of a larger tilt range ($\pm 60°$) and a conical instead of a single-tilt geometry (Hoppe and Grill, 1977), both of which are technically feasible, would improve the point-spread function considerably. The fatty acid synthetase work can be expected to advance in this direction.

We now proceed to a more controversial aspect of the individual molecule reconstruction: the fact that a completely reconstructed stain distribution, not-

withstanding the amount of work involved in its computation, is only *one* realization of a multitude of different stain distributions surrounding the molecule and, as such, does not allow a distinction between the significant and the accidental parts of the structure (Baumeister and Hahn, 1975; Crowther, 1976). Investigation of several molecules by these methods, although an admirable feat (Hoppe *et al.*, 1976c), does not seem to solve this difficulty. The result is a large number of details that are easily recognizable in one molecule but not in another. The problem is compounded by the fact that the orientations of the tilt axis and of the molecule on the grid are different for the different molecules studied, so that distortions of the molecule in various directions come into play. Very sophisticated methods of evaluation would have to be developed to provide a quantitative basis for comparing differently distorted models.

Baumeister and Hahn (1975) have summarized the structural alterations of the molecule that occur during fixation, dehydration, staining, and imaging of protein molecules and have cautioned against an interpretation of the three-dimensional structure that fails to take these factors and the variability they introduce into account. They argued further that the resolution of the reconstruction should be matched to the resolution limit created by all these artifacts.

In their reply, Hoppe *et al.* (1975) argued strongly against such a resolution limitation, because it does not allow for the fact that each high-resolution reconstruction represents a structure that is significant as one of the distinct states of the molecule. These two diametrically opposed points of view reflect the dilemma noted in the Introduction. It now appears, on the basis of recent work (van Heel and Frank, 1980a,b; Frank and van Heel, 1980), that for the best extraction of significant detail from a population of molecules with diverse structures both opinions may be equally impractical. Focus on the individual molecule produces a high-resolution model without clearly defined significance, whereas summary characterization of a diverse population of molecules by the features common to all sacrifices useful information of different states of the molecule's structure or its stain surroundings.

Averaging should be extended only over subpopulations that are sufficiently homogeneous. Such subpopulations can be isolated by the application of multivariable statistics to the total set of image data. (van Heel and Frank, 1980a; Frank and van Heel, 1980).

IV. Reconstruction of Averaged Molecules

The shortcomings of the individual-molecule reconstruction have spurred a number of investigators to develop ideas on ways to combine different views of *different* molecules into a single, averaged reconstruction. In the following sec-

tions we shall outline three approaches that have been discussed in the literature. It is not surprising that, as yet, none of these has been put into practice. In Wrigley's (1975) and Frank *et al.*'s (1978a) approaches the task of selecting, sorting, aligning, and combining a two- or three-digit number of projections is enormous, requiring a quite sophisticated software system and a fast computer. In Kam's method (1980a,b), the data collection is straightforward, but the computational steps in the evaluation of the data are quite involved.

A. Wrigley's Method

If the specimen contains many molecules that have random orientation with respect to the supporting grid, all the information needed to build up a three-dimensional reconstruction may be contained in a single micrograph. Wrigley (1975) proposed a scheme by which different particle projections could be identified. A micrograph is taken in the untilted specimen-grid position, using minimal exposure to assure maximum yield of biologically significant information. Two additional micrographs are then taken at different specimen tilts and searched for projections whose outlines (determined by equidensitometry) are identical to those of any projections visible in the micrograph of the untilted specimen. Any such coincidence determines the relative spatial orientation of two particles in the untilted high-quality micrograph. Since there are two micrographs of the specimen at two different tilts, the link with other particles already catalogued can be established. In a large enough population of molecules—Wrigley estimates several hundred to be adequate—a sufficient number of views can be found to cover the entire three-dimensional angular range and so to build up a three-dimensional reconstruction.

This method is intriguing because it overcomes the problem of the missing angular range without requiring more than three relatively low-angle tilts. However, the use of the outline for identification (Bender *et al.*, 1970) is of arguable validity, since the particle periphery is often surrounded by irregular clusters of stain. A more basic problem is particle deformation (Moody, 1967), which occurs in the direction normal to the supporting grid and appears to prevent the combining of data from particles that have different orientations with respect to the grid.

B. Frank and Goldfarb's Method

Restriction of the analysis with a preferential site of attachment to the specimen grid guarantees that all particles suffer the same deformation in the preparation process; hence they form a relatively homogeneous population in terms of their three-dimensional shape. Many molecules have preferential sites of attachment to the grid, owing to their geometry or to the location of electrical charges on their surface. Special examples of molecules with fixed orientation

are those bound to membranes. It may also be possible to artificially induce preferential positions of single macromolecules with respect to the grid by introducing surface charges on the support film (Zingsheim, 1977).

Since particles arranged in this fashion present identical views in the axial projection, they are amenable to a computer procedure that finds the relative in-plane orientations and translations between identical patterns in the presence of noise (Frank *et al.*, 1978a, 1979; Frank, 1980). Theoretical considerations (Saxton and Frank, 1977) and practice (Frank *et al.*, 1978b; Kessel *et al.*, 1981) have shown the algorithm to be stable for low signal-to-noise ratios when the eye fails to recognize the particle outline. For electron microscopic application it is important that both alignment and averaging are still possible when the dose is limited to 100 e/nm^2, a dose that was shown by Unwin and Henderson (1975) to preserve the protein structure to 0.7-nm resolution.

Frank *et al.* (1978a; Frank and Goldfarb, 1980) proposed a three-dimensional reconstruction method that utilizes a fixed-plane geometry (Fig. 3) and composes the three-dimensional structure of the averaged molecule from a large number of independent projections.

As in the single-particle averaging experiment, a specimen grid is prepared that contains molecules preferentially oriented, but with random in-plane rotations and positions. Two images must be taken in the electron microscope, the first image using a low dose with the specimen tilted to the maximum tilting angle, the second one with a normal dose and in untilted position. The first micrograph supplies projections of the undamaged molecules, while the second provides an estimate of the rotation angles and positions of the molecules with respect to one another.

It may not be immediately obvious, but it can be shown by consideration of the

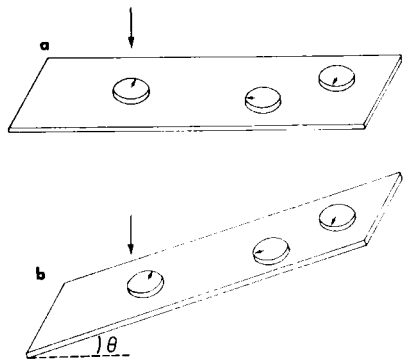


FIG. 3. Geometry of the three-dimensional reconstruction experiment of Frank and Goldfarb (1980). (a) Untilted specimen grid bearing a number of molecules (here symbolized as short cylinders) with differing in-plane orientations. (b) Specimen grid of (a) in a tilted position (tilt angle θ). Owing to the differing in-plane orientations, each molecule now presents a different view to the electron beam (arrow).

geometry of the three-dimensional Fourier transform that a single micrograph of such a specimen in a maximum tilt position carries the same information as a conical tilt series of a single molecule with identical angle limitation. That is, to obtain the same information as is available from a micrograph showing 100 molecules in random in-plane orientations, one would have to take a double tilting series of a single molecule in 100 independent angular positions up to the maximum angle. The experimental advantages of the single-micrograph technique are obvious.

In the evaluation, the second micrograph obtained in the experiment is analyzed first. Molecules are identified and windowed as in the averaging method, and rotation angles and positions are found with respect to a molecule selected as reference using correlation functions. Since at the time of exposure of the second micrograph the molecules are already damaged, the values found for the rotation angles and position vectors must be considered as estimates of the true values for the undamaged molecules. They can nevertheless be used to approximate the relative positions of the projections in the first, low-dose micrograph with respect to the reference molecule.

With these positions known, the Fourier coefficients of the projections can be phased and placed into their proper positions in the three-dimensional Fourier volume. In this step the defocus correction must be applied.

Three-dimensional reconstruction can now be carried out by Fourier methods of reconstruction. After the first model has been reconstructed, the positional parameters of the projection data can be refined by iteration.

Since the micrograph of the untilted specimen shows the molecules in identical projections, one can sort the molecules by using an analysis of proximities (van Heel and Frank, 1980a; Frank and van Heel, 1980) before proceeding with the three-dimensional reconstruction. The purpose of this analysis is twofold. First, it eliminates molecules whose axial projections show extreme deviations in appearance from the "typical" projection. It will also detect the presence of two or more distinct subpopulations with different attributes. If these attributes, as judged from a subpopulation average, are significant in terms of the structural interpretation, each subpopulation will deserve its own three-dimensional reconstruction.

C. Kam's Method

Kam proposes a reconstruction procedure (1980a,b) based on a mathematical analysis of the averaged correlation function of the projections and on its relationship to the three-dimensional structure. Originally developed for investigation of diffraction patterns of macromolecules in solution (Kam, 1977), the method assumes completely random orientations of the molecules on the specimen grid. Kam's method of reconstruction is based on the calculation and ac-

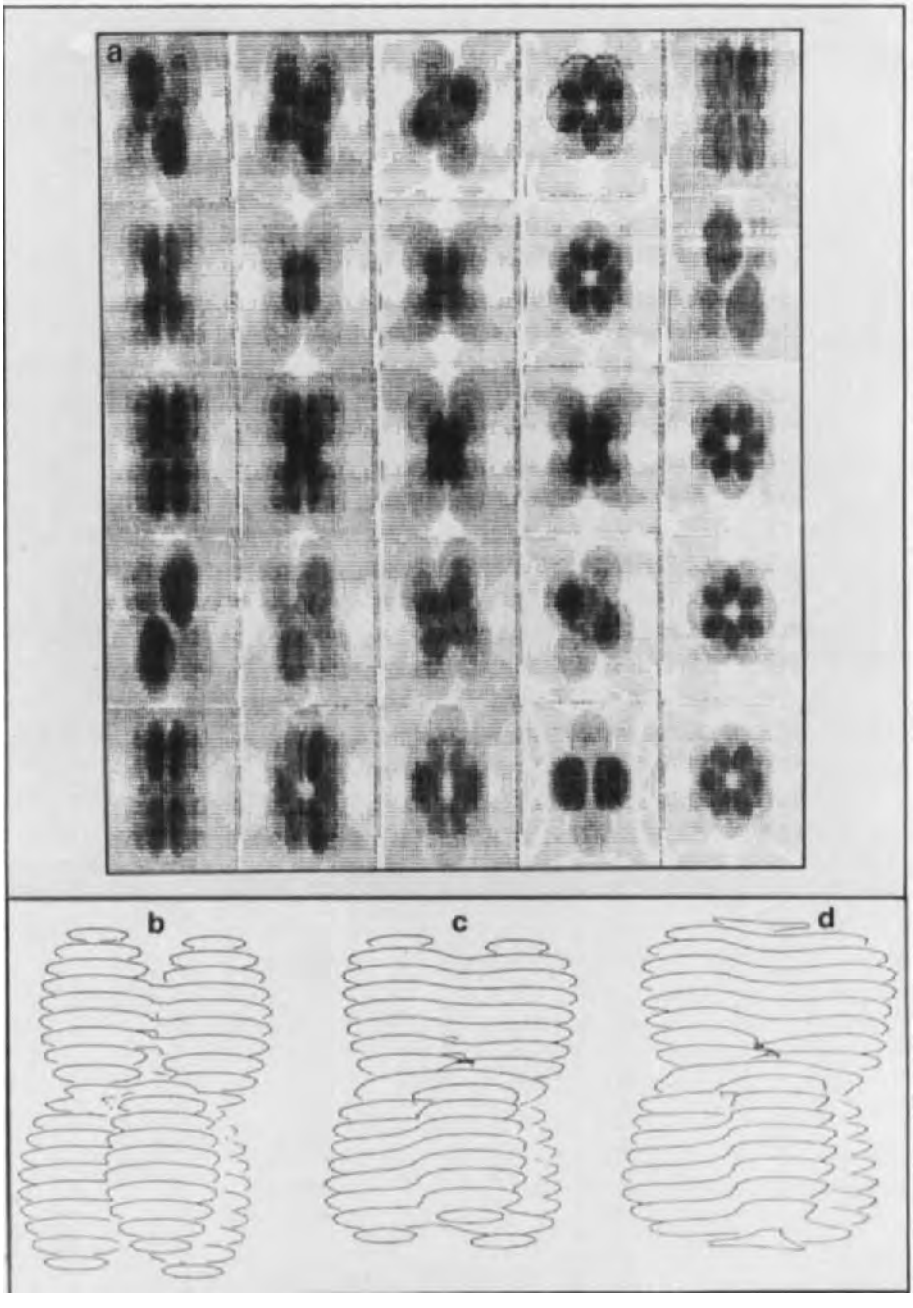
cumulation of the two-dimensional autocorrelation function of the densities in the electron micrographs. From this function the spherical harmonic coefficients of the structure can be calculated.

A detailed description of the reconstruction procedure is beyond the scope of this chapter, but the sequence of steps involved will be outlined. The analysis begins with the calculation of the autocorrelation function of an extended micrograph field containing a large number of particles exhibiting different views with random directions of projection. This method is unique in that the identity of the particles analyzed is entirely lost, in sharp contrast to all other methods reviewed, where each particle view is individually analyzed to form a reconstruction either of one individual particle or of an averaged particle.

Next, the autocorrelation function is analyzed by expansion into spherical harmonics, and a system of equations is derived for the expansion coefficients of the three-dimensional structure. Since the autocorrelation function is the Fourier transform of the diffraction pattern (which would be obtained if the selected area were subjected to electron diffraction), it carries no more information than a "powder pattern" of randomly oriented molecules. It is not surprising that this information is insufficient for three-dimensional reconstruction; Kam's equation system is underdetermined. According to Kam, there are two ways to overcome this problem: specific labeling and the use of triple correlations. A specifically labeled derivative of the molecule is investigated by using the same technique of imaging and analysis as in the heavy-atom replacement method of protein x-ray crystallography. The second set of data resolves the ambiguities, and a complete reconstruction is possible. Correlation expressions containing triple products of image densities at three different image positions also solve the problem of the remaining ambiguities.

A model calculation demonstrated the feasibility of the reconstruction algorithm. A number of simulated projections of the glutamate dehydrogenase molecule are shown in Fig. 4a. The original model, its conventional functional expansion reconstruction (which is an analog to the Fourier method of reconstruction), and the reconstruction from the correlation function of a field containing 100 random views can be compared with one another (Figs. 4b–d). It can be seen from a comparison of Figs. 4b and 4c that Kam's method and the Fourier method yield very similar results.

Without practical results it is too early for a realistic assessment of Kam's method. However, two important aspects should be mentioned here. It was noted earlier that the molecules lose their identity in the first step of the analysis, since the correlation function retains only a statistical characterization of the ensemble of molecules. This is of great advantage compared with all other methods, in which hundreds of projections must be handled individually. Even in individual-particle reconstruction, to obtain statistically meaningful answers, one must reconstruct more than a single particle.


a
b
c
d

Furthermore, the method of data collection implies that there is no theoretical lower bound for the signal-to-noise ratio in the data. Only practical considerations prevent the use of arbitrarily low electron doses. In contrast, Frank *et al.*'s (1978a) method of averaging and three-dimensional reconstruction requires a minimum dose, which depends on particle size, contrast, and resolution (Saxton and Frank, 1977), for alignment of different axial projections.

On the negative side, however, Kam's method makes the unrealistic assumption that the differently oriented molecules are identical. Experimental data prove, as was pointed out earlier in this review, that the molecules flatten as they are dried on the specimen grid, and severe shrinkage has been observed in the direction normal to the grid (Moody, 1967). Since in axial projection the direction of shrinkage coincides with the direction of projection, the observable deviations are less dramatic, but they nevertheless produce inconsistencies in the set of projections, eventually resulting in a loss of resolution.

Another unrealistic supposition is that of completely random orientation. Practice frequently shows the presence of one or more sites of preferential attachment, which may be related to the molecule's functional sites or to its geometry and the influence of forces acting normal to the grid during the drying process.

It is not clear from Kam's analysis how seriously the reconstruction is affected by a mild anisotropy of orientations. However, the lack of an entire angular range can lead to serious errors in the computation.

Finally, there is the dilemma posed by particles with a large variability, as was mentioned in the Introduction. Since in Kam's approach the individual particles lose their identity in the autocorrelation analysis, there is no easy way to distinguish between particle subpopulations (see Section IV,B), and the final averaged reconstruction will suffer the resolution loss caused by both genuine and preparation-induced structural variations among the total population.

V. Concluding Remarks

The efforts involved in three-dimensional reconstruction of single molecules without symmetries are much greater than those for reconstructing ordered

---

FIG. 4. (a) Simulated density projections of the glutamate dehydrogenase molecule as modeled by a hexamer of ellipses (see b). Five rotational positions around the triad axis of symmetry are shown, one for each of five angles between that axis and the plane of projection. (b) Three-dimensional plot of the model. (c) Plot of the three-dimensional density obtained by the conventional method of Fourier reconstruction. This plot presents the highest resolution to be expected for the sampling mesh used in the program. (d) Three-dimensional density reconstructed from the averaged autocorrelation function accumulated from 100 simulated projections of the model. From Kam (1980a), courtesy of the author and Academic Press, New York.

molecules, and it will take some time for standard methods to be recognized and adapted.

There is a certain trade-off between the work involved in growing crystal sheets for electron microscopy (or, in the case of soluble proteins, three-dimensional "bulk crystals" for x-ray crystallography) and the organizational and computational efforts involved in three-dimensional reconstruction from unordered molecules. At present the crystallographic techniques are superior in efficiency and in degree of accuracy, although good-quality crystals are difficult to grow. With the development of new preparation techniques and faster computers and with the implementation of image-sorting algorithms (van Heel and Frank, 1980a,b; Frank and van Heel, 1980), analysis of single molecules may soon be recognized as a valuable alternative to conventional methods.

The new methods will be of particular value when applied to membrane-bound molecules (e.g., Zingsheim *et al.*, 1980a,b), which may alter significantly in structure and appearance when extracted from the membrane.

The list of approaches described here is necessarily incomplete, and it may not include the approach by which the best reconstruction techniques will eventually be developed. The recent proposal by Kam (1980a,b) supports the notion that innovative ideas in a specific field tend to come not only unexpectedly but also from totally unexpected directions.

References

Aebi, U. (1978). *Electron Microsc., Proc. Int. Congr., 9th, 1978* Vol. III, pp. 81-86.

Aebi, U., Smith, P. R., Dubochet, D., Henry, C., and Kellenberger, E. (1973). *J. Supramol. Struct.* **1,** 498-522.

Baba, N., Murata, K., Okada, K., and Fujimoto, Y. (1979). *Optik* **54,** 97-105.

Baumeister, W., and Hahn, M. (1975). *Hoppe-Seyler's Z. Physiol. Chem.* **356,** 1313-1316.

Baumeister, W., and Seredynski, J. (1978). *Electron Microsc., Proc. Int. Congr., 9th, 1978* Vol. III, pp. 40-48.

Bender, R., Bellman, S. H., and Gordon, R. (1970). *J. Theor. Biol.* **29,** 483-487.

Crowther, R. A. (1971). *Philos. Trans. R. Soc. London, Ser. B* **261,** 221-230.

Crowther, R. A. (1976). *In* "The Proceedings of the Third John Innes Symposium" (R. Markham and R. W. Horne, eds.), pp. 15-25. North-Holland Publ., Amsterdam.

Crowther, R. A., DeRosier, D. J., and Klug, A. (1970). *Proc. R. Soc. London, Ser. A* **317,** 319-340.

DeRosier, D. J., and Klug, A. (1968). *Nature (London)* **217,** 130-134.

Frank, J. (1973). *In* "Advanced Techniques in Biological Electron Microscopy" (J. K. Koehler, ed.), pp. 215-274. Springer-Verlag, Berlin and New York.

Frank, J. (1978). *Electron Microsc., Proc. Int. Congr., 9th, 1978* Vol. III, pp. 87-93.

Frank, J. (1980). *In* "Computer Processing of Electron Micrographs" (P. W. Hawkes, ed.), pp. 187-222. Springer-Verlag, Berlin and New York.

Frank, J., and Goldfarb, W. (1980). *In* "Electron Microscopy in Molecular Dimensions: State of the Art and Strategies for the Future" (W. Baumeister, ed.), pp. 261-269. Springer-Verlag, Berlin and New York.

Frank, J., and van Heel, M. (1980). *Proc. Eur. Congr. Electron Microsc., 7th, 1980,* Vol. II, pp. 690-691.

Frank, J., Goldfarb, W., Eisenberg, D., and Baker, T. S. (1978a). *Ultramicroscopy* **3,** 283-290.

Frank, J., Goldfarb, W., and Kessel, M. (1978b). *Electron Microsc., Proc. Int. Congr., 9th, 1978* Vol. II, pp. 8-9.

Frank, J., Goldfarb, W., Eisenberg, D., and Baker, T. S. (1979). *Ultramicroscopy* **4,** 247.

Glaeser, R. M. (1971). *J. Ultrastruct. Res.* **36,** 466-482.

Gordon, R., Bender, R., and Herman, G. T. (1970). *J. Theor. Biol.* **29,** 471-481.

Hegerl, R., and Hoppe, W. (1976). *Z. Naturforsch., Teil A* **31,** 1717-1721.

Henderson, R., and Unwin, P. N. T. (1975). *Nature (London)* **257,** 28-32.

Hoppe, W. (1969). *Optik* **29,** 617-621.

Hoppe, W. (1970). *Acta Crystallogr., Sect. A* **26,** 414-426.

Hoppe, W. (1972). *Z. Naturforsch.* **27,** 919-929.

Hoppe, W. (1974a). *Naturwissenschaften* **61,** 239-249.

Hoppe, W. (1974b). *Naturwissenschaften* **61,** 534-536.

Hoppe, W. (1978). *Ann. N.Y. Acad. Sci.* **306,** 121-144.

Hoppe, W. (1979). *In* "Direct Imaging of Atoms in Crystals and Molecules" (L. Kilbury, ed.), pp. 227-243. Royal Swedish Academy of Sciences.

Hoppe, W. (1980). *In* "Electron Microscopy in Molecular Dimensions. State of the Art and Strategies for the Future" (W. Baumeister, ed.), pp. 278-287. Springer-Verlag, Berlin and New York.

Hoppe, W., and Grill, B. (1977). *Ultramicroscopy* **2,** 153-168.

Hoppe, W., and Hegerl, R. (1980). *In* "Computer Processing of Electron Microscope Images" (P. W. Hawkes, ed.), pp. 127-185. Springer-Verlag, Berlin and New York.

Hoppe, W., and Typke, D. (1979). *In* "Advances in Structure Research by Diffraction Methods" (W. Hoppe and R. Mason, eds.), pp. 137-190. Vieweg, Braunschweig.

Hoppe, W., Bussler, P., Feltynowski, A., Hunsmann, N., and Hirt, A. (1973). *In* "Image Processing and Computer-Aided Design in Electron Optics" (P. W. Hawkes, ed.), pp. 92-126. Academic Press, New York.

Hoppe, W., Gassmann, J., Hunsmann, N., Schramm, H. J., and Sturm, U. (1974). *Hoppe-Seyler's Z. Physiol. Chem.* **355,** 1483-1487.

Hoppe, W., Gassmann, J., Hunsmann, N., Schramm, H. J., and Sturm, M. (1975). *Hoppe-Seyler's Z. Physiol. Chem.* **356,** 1317-1320.

Hoppe, W., Schramm, H. J., Sturm, M., Hunsmann, N., and Gassmann, J. (1976a). *Z. Naturforsch., Teil A* **31,** 645-655.

Hoppe, W., Schramm, H. J., Sturm, M., Hunsmann, N., and Gassmann, J. (1976b). *Z. Naturforsch., Teil A* **31,** 1370-1379.

Hoppe, W., Schramm, H. J., Sturm, M., Hunsmann, N., and Gassmann, J. (1976c). *Z. Naturforsch., Teil A* **31,** 1380-1390.

Hunsmann, N., Bussler, P., and Hoppe, W. (1972). *Inst. Phys. Conf. Ser.* **14,** 654-655.

Kam, Z. (1977). *Macromolecules* **10,** 927-934.

Kam, Z. (1980a). *J. Theor. Biol.* **82,** 15-39.

Kam, Z. (1980b). *In* "Electron Microscopy in Molecular Dimensions. State of the Art and Strategies for the Future" (W. Baumeister, ed.), pp. 270-277. Springer-Verlag, Berlin and New York.

Kessel, M., Frank, J., and Goldfarb, W. (1981). *J. Supramol. Struct.* (in press).

Knauer, V. (1979). Thesis, Technical University, Munich.

Knauer, V., and Hoppe, W. (1980). *Proc. Eur. Congr. Electron Microsc., 7th, 1980,* Vol. II. pp. 702-703.

Knauer, V., Schramm, H. J., and Hoppe, W. (1978). Electron Microsc., *Proc. Int. Congr., 9th, 1978* Vol. II, pp. 4-5.

Kuo, I. A. M., and Glaeser, R. M. (1975). *Ultramicroscopy* **1,** 53-66.

Moody, M. F. (1967). *J. Mol. Biol.* **25,** 167-200.

Rose, A. (1948). *Adv. Electron.* **1,** 131-166.

Saxton, W. O. (1980). *In* "Electron Microscopy in Molecular Dimensions. State of the Art and Strategies for the Future" (W. Baumeister, ed.), pp. 245-255. Springer-Verlag, Berlin and New York.

Saxton, W. O., and Frank, J. (1977). *Ultramicroscopy* **2,** 219-227.

Unwin, P. N. T. (1974). *J. Mol. Biol.* **87,** 657-670.

Unwin, P. N. T., and Henderson, R. (1975). *J. Mol. Biol.* **94,** 425-440.

Unwin, P. N. T., and Klug, A. (1974). *J. Mol. Biol.* **87,** 641-656.

Unwin, P. N. T., and Taddei, C. (1977). *J. Mol. Biol.* **114,** 491-506.

Williams, R. C., and Fisher, H. W. (1970). *J. Mol. Biol.* **52,** 121-123.

van Heel, M., and Frank, J. (1980a). *In* "Pattern Recognition in Practice" (E. S. Gelsema and L. Kanal, eds.), pp. 235-243. North-Holland, Amsterdam.

van Heel, M., and Frank, J. (1980b). *Proc. Eur. Congr. Electron Microsc., 7th, 1980,* Vol. II, pp. 692-693.

Wrigley, N. G. (1975). *In* "Image Processing for 2-D and 3-D Reconstruction from Projections," Dig. Tech. Pap., TuD3-1. Stanford University, California.

Zingsheim, H. P. (1977). *In* "Scanning Electron Microscopy/1977" (O. Johari, ed.), Vol. I, pp. 357-364. IIT Res. Inst., Chicago, Illinois.

Zingsheim, H. P., Neugebauer, D.-C., Barrantes, F. J., and Frank, J. (1980a). *Proc. Natl. Acad. U.S.A.* **77,** 952-956.

Zingsheim, H. P., Neugebauer, D.-C., Barrantes, F. J., and Frank, J. (1980b). *In* "Electron Microscopy in Molecular Dimensions. State of the Art and Strategies for the Future" (W. Baumeister, ed.), pp. 161-169. Springer-Verlag, Berlin and New York.

Index

A

α-Actinin, 13, 58, 68
Acetylcholine receptors, 106, 107
Actin, 58, 66, 67, 70, 71, 112, 113, 114
Algebraic reconstruction techniques (ART), 201, 209, 210, 332
Antibody labeling, 312–314

B

Back projection, 211
Beam damage (*see* Radiation damage)
Binocular rivalry, 15, 22
Biomolecules, 201, 208, 212

C

Capsids, 299, 302, 310–314, 319
Capsomeres, 299, 308, 310, 314, 315
Cell
  antibody labels, 63, 73
  behavior, 59–62, 73
  cation effects, 62, 64
  differentiated, 63, 64, 66
  extracted, 70
  hormone effects, 63
  interior, 106, 108, 112
  surface, 131
  whole mounts, 131
Center of gravity, 212
Centriole, 220
Centromere, 81
Chromatin, 222
  C-bands, 81, 94
  euchromatin, 81, 94
  G-bands, 94
  Giemsa bands, 81
  hetero, 81, 94
  interphase, 78
  nucleosomes, 79
  proteins, 79
  supercoil, 79
  10-nm fiber, 81
  20-nm fiber, 78, 79, 81, 83, 91, 93, 94
Chromosomes, 78, 81, 221
  kinetochore, 80, 81, 90–95, 244
  level of organization, 82–95
  lampbrush, 78
  metaphase, 78, 86
  mitotic, 78–80, 85–90
  polytene, 79, 83–85
  whole mounts, 217
Conical data collection, 202
Correlation alignment, 331
Correlation functions, 330, 331, 338, 339
Critical point drying, 55, 66, 72, 73, 80, 81, 98
Cross-correlation, 212, 329
Crystals, 253–262
  stained, 255, 257, 259, 260, 262
  symmetry, 271, 272, 280
    loss of, 273–275
  thickness, 262
  two-dimensional, 253–261
  unstained and embedded, 252, 268, 275, 277, 288
Cytoplasmic ground substance (CGS), 55, 57, 59, 60, 64, 66, 69, 71
Cytoskeleton, 54, 57, 59, 60, 62, 66, 70, 72, 112–114

D

Depth of field
  HVEM, 4
  relation to specimen thickness, 4

Depth perception, 14, 15, 16, 29 (*see also* Stereo)
accommodation, 6
brightness, 5, 13
color, 5, 14–16
development, 14, 21
light and shade, 5, 7, 22, 23
motion, 3, 5, 6, 15
obscuration, 5
perspective, 5, 11
physchological aspects, 3
position, 5
shape, 5, 7, 10
size, 5
texture, 3, 9, 10, 15
vergence, 6, 11
visual cues, 5–7

E

Endoplasmic reticulum, 130, 131, 133
Extracellular space, 131 (*see also* T-Tubules)

F

Fourier averaging, 267
Fourier transform, 201, 202, 204, 264, 266, 278, 280, 304, 306, 317, 318
coefficients, 330, 331, 338
phases, 211, 212
Freeze drying, 98, 112–119, 121, 300, 312
Freeze etch, 17, 98, 104, 108, 110, 115, 119, 120
Freeze fracture, 29, 36, 97, 98, 104, 108, 115, 300
Friedel symmetry, 263

G

Golgi apparatus, 124, 127–130, 142
Golgi-associated endoplasmic reticulum, 128

H

High-voltage electron microscope, 4, 25, 26, 50, 54, 56, 59, 63, 64, 66, 72, 78, 121, 123, 124, 127, 129, 130, 131, 134, 141, 142, 200, 201, 211, 212, 216, 218, 219, 230

I

Image contrast, 275–277, 282, 302
Intermediate filaments, 114
Interocular distance, 82, 100
Intracellular motion, 59

M

Membrane, 208
crystals, 255–261
proteins, 253, 254
surfaces, 104–108
synaptic, 109, 119
Microfilaments, 58, 62, 66, 70, 218
Microtrabeculae, 57, 59, 60, 62–65, 68, 70
Microtubules, 54, 57, 58, 60, 62, 64, 66, 70, 71, 90, 91, 93–95, 114, 221, 222, 225, 244, 253, 305
Mitochondria, 131, 133
Mitotic spindle, 222, 231, 232
Myofibrils, 58, 66, 67
Myofilaments, 305
Myosin, 58, 66

N

Negative stain, 262, 267, 275, 283, 300, 313, 317–319
Neurons, 142, 143
Nucleosomes, 82, 95

O

Optical diffraction, 298–300, 306, 319
Optical filtering, 312
Optical transform, 266

P

Parallax, 2, 3, 5, 9, 15–21, 25, 27, 29, 33, 34, 37, 46, 47, 49, 147, 150, 179, 238
axis, 8, 42, 45, 46, 49, 50
equation, 5, 6, 34, 35, 37, 43, 46, 47, 49, 193
maximum, 6, 37, 48
recommended amount, 6
Parallel projection, 6, 23, 26, 34, 163–165, 181 (*see also* Photogrammetry)

Perspective projections, 7, 9, 15, 24, 26, 29, 34, 42, 46, 165, 166, 193 (*see also* Photogrammetry)
Phase contrast electron microscopy, 268-271
Photogrammetry, 2, 3, 6, 155-198, 238
  applications, 193-198
  calibration of the electron microscope, 173-176
  coordinate systems, 157-163
  distortions, 166-169
  hardware and methods, 177-192
  stereo models, 169-172
  theory, 155-176
Point-spread function, 206, 208, 334
Polyethylene glycol (PEG) embedding, 66, 72
Polymorphic variation, 299
Projection image, 2 (*see also* Photogrammetry)
Projection theorem, 205-208
Pseudo three-dimensionality, 99, 100, 106

R

Radiation damage, 3, 20, 77, 78, 150-152, 237, 239, 240, 266-268, 274, 291, 302, 303, 327, 328-330, 332, 337
Reciprocal lattice, 211
Replicas, 17, 24, 25, 29, 36, 97-121
Resolution, 78, 208, 209, 262, 265, 266, 269, 302, 305, 306, 319, 320, 330, 334, 335
  computational cutoff, 209
  computer filtered, 326
  disorder limit, 209
  electron optical, 208
  sampling, 209
  stain limit, 326
Retina, 124, 125-127
Rough endoplasmic reticulum, 128, 142

S

Saltatory transport, 59
Sarcoplasmic reticulum (SR), 131-133, 142
Sections
  serial, 78, 123, 127, 200, 216, 218-246
  thick, 4, 78, 123, 124, 126, 127, 129, 131, 134, 136-141, 200, 216, 218-246
  thickness estimate, 236-239
  thin, 4, 53, 54, 64-66, 78, 97, 108, 110, 111, 216-221, 225, 230, 242
Scanning electron microscope, 24, 26, 27, 29, 34, 42-46, 54, 59, 100, 157, 158, 185, 193-195, 197, 198
Scanning transmission electron microscope, 300-304
Selective stains, 4, 17, 24, 54, 64, 123-143, 216, 219
  acid phosphatase, 127, 128
  diaminobenzidine ferrocyanide, 133, 136, 141
  glucose-6-phosphatase, 130
  Golgi method, 124-129, 131
  horseradish peroxidase, 130, 132, 135, 141
  lanthanum, 132, 136
  nucleotide diphosphatase, 127, 128
  periodic acid-silver methenamine, 129
  phosphotungstic acid, 127
  potassium oxalate, 143
  ruthenium red, 130, 133
  thorium oxide, 130
  TPPase, 127, 128, 129
  uranyl acetate, 131
Smooth endoplasmic reticulum, 142
Spatial frequency, 202, 204, 205, 211, 264, 265
Specimen stages, 33-45, 49, 82, 201, 202, 211, 230, 278, 332
  motion analysis, 45, 46
Stages (*see* Specimen stages)
Striated muscle, 131-142
Stereo, 2, 4-7, 17, 20, 21, 23, 24, 26, 29
  angle, 5, 6, 24, 25, 29, 33, 35, 47, 48, 82, 170, 182, 196
  depth reversal, 26
  disparities, 17-22
  display, 7-9, 11, 12, 20-22, 100-104
  fixed tilt and rotation method, 46-49
  mock, 3, 19, 20, 22, 147-153
  orthostereoscopy, 24-28, 30
  pretilt, 35, 41, 45, 49, 78
  quantitative analysis (*see* Photogrammetry)
  specimen tilting methods, 35-45
  tilt angle, 5, 6, 8, 24, 25, 34, 35-37, 44, 49
  viewers, 8, 22, 25, 27, 28, 30, 34, 42, 100
  window, 7-9, 26, 27, 29, 30, 49, 82
Stereopsis, 13-30 (*see also* Depth perception)
Stereoscopic acuity, 20, 21
Stress fibers, 62, 70, 113
Surface lattice, 299, 311-313

T

Three-dimensional information, 17
  collection of, 1, 2, 4
  image overlap, 1, 2, 4, 9
Three-dimensional reconstruction (*see also* Sections, serial)
  cytochrome *c* oxidase, 253, 255, 256, 260, 261, 268, 281, 283–290
  direct space methods, 209–211
  fatty acid synthetase, 332–335
  Fourier methods, 202–209, 252, 275, 327, 338, 339
  Frank and Goldfarb method, 336–338
  gap junction, 253, 257, 282, 294
  graphic methods, 242–246
  Kam's method, 338–341
  projection methods, 271–283, 304–308
  purple membrane, 256, 259, 281, 291
  single molecules, 325–342
  solid models, 246
  Wrigley's method, 336
Triangulation number, 299
T-Tubules, 124, 130–140
Tubulin, 15, 58, 70, 71, 115, 253, 282

V

Viruses
  bacteriophages, 201, 298, 301, 306–308, 314
  helical, 252, 299, 305–308
  spherical, 201, 299, 302, 305, 314
  three-dimensional crystals, 316, 317
  tobacco mosaic, 303
  tubular, 308, 309
  two-dimensional crystals, 317–319

W

Whole mounts, 53, 54, 73 (*see also* Cells and Chromosomes)
  preparation of, 55, 59
  relation to thin sections, 64–66

X

X-ray crystallography, 251, 252, 262, 291, 294, 316, 317, 339, 342

CONTENTS OF RECENT VOLUMES

(Volumes I-XX edited by David M. Prescott)

Volume X

1. Nucleic Acid Hybridization to the DNA of Cytological Preparations
   Mary Lou Pardue and Joseph G. Gall
2. Microanalysis of RNA from Defined Cellular Components
   Bo Lambert and Bertil Daneholt
3. Staining of RNA after Polyacrylamide Gel Electrophoreis
   K. Marcinka
4. Isolation and Fractionation of Mouse Liver Nuclei
   Ph. Chevaillier and M. Phillipe
5. The Separation of Cells and Subcellular Particles by Colloidal Silica Density Gradient Centrifugation
   David A. Wolff
6. Isolation of Subcellular Membrane Components from *Tetrahymena*
   Y. Nozawa
7. Isolation and Experimental Manipulation of Polytene Nuclei in *Drosophila*
   James B. Boyd
8. Methods for Microsurgical Production of Mammalian Somatic Cell Hybrids and Their Analysis and Cloning
   Elaine G. Diacumakos
9. Automated Cell Cycle Analysis
   Robert R. Klevecz
10. Selection of Synchronous Cell Populations from Ehrlich Ascites Tumor Cells by Zonal Centrifugation
    Hans Probst and Jürgen Maisenbacher
11. Methods with Insect Cells in Suspension Culture I. *Aedes albopictus*
    Allan Spradling, Robert H. Singer, Judith Lengyel, and Sheldon Penman
12. Methods with Insect Cells in Suspension Culture II. *Drosophila melanogaster*
    Judith Lengyel, Allan Spradling, and Sheldon Penman
13. Mutagenesis in Cultured Mammalian Cells
    N. I. Shapiro and N. B. Varshaver
14. Measurement of Protein Turnover in Animal Cells
    Darrell Doyle and John Tweto
15. Detection of Mycoplasma Contamination in Cultured Cells: Comparison of Biochemical, Morphological, and Microbiological Techniques
    Edward L. Schneider
16. A Simple Biochemical Technique for the Detection of Mycoplasma Contamination of Cultured Cells
    Edward L. Schneider and E. J. Standbridge
17. Purity and Stability of Radiochemical Tracers in Autoradiography
    E. Anthony Evans
18. ^{125}I in Molecular Hybridization Experiments
    Lewis C. Altenburg, Michael J. Getz, and Grady F. Saunders
19. Radioiodine Labeling of Ribopolymers for Special Applications in Biology
    Neal H. Scherberg and Samuel Refetoff

20. Autoradiographic Analysis of Tritium on Polyacrylamide Gel
Paola Pierandrei Amaldi

21. A Radioautographic Method for Cell Affinity Labeling with Estrogens and Catecholamines
José Uriel

Subject Index—Cumulative Subject Index

Volume XI

1. The Preparation of Yeasts for Light Microscopy
C. F. Robinow

2. Electron Microscopy of Yeasts
Friedrich Kopp

3. Methods in Sporulation and Germination of Yeasts
James E. Haber and Harlyn O. Halvorson

4. Synchoronous Mating in Yeasts
Elissa P. Sena, David N. Radin, Juliet Welch, and Seymour Fogel

5. Synchronous Zygote Formation in Yeasts
T. Biliński, J. Litwińska, J. Zuk, and W. Gajewski

6. Continuous Cultivation of Yeasts
A. Fiechter

7. Methods for Monitoring the Growth of Yeast Cultures and for Dealing with the Clumping Problem
John R. Pringle and Juan-R. Mor

8. Preparation and Growth of Yeast Protoplasts
S.-C. Kuo and S. Yamamoto

9. Dissecting Yeast Asci without a Micromanipulator
P. Munz

10. Use of Micromanipulators in Yeast Studies
Fred Scherman

11. Cell Cycle Analysis
J. M. Mitchison and B. L. A. Carter

12. Genetic Mapping in Yeast
R. K. Mortimer and D. C. Hawthorne

13. The Use of Mutants in Metabolic Studies
F. Lacroute

14. Isolation of Regulatory Mutants in *Saccharomyces cerevisiae*
Helen Greer and G. R. Fink

15. Methods for Selecting Auxotrophic and Temperature-Sensitive Mutants in Yeast
Barbara Shaffer Littlewood

16. Isolation and Characterization of Mutants of *Saccharomyces cerevisiae* Able to Grow after Inhibition of dTMP Synthesis
M. Brendel, W. W. Fäth, and W. Laskowski

17. Mutants of *Saccharomyces cerevisiae* That Incorporate Deosythymidine 5'-Monophosphate into DNA *in Vivo*
Reed B. Wickner

18. Mutants of Meiosis and Ascospore Formation
Michael S. Esposito and Rochelle E. Esposito

Subject Index

Volume XII

1. Growth and Handling of Yeasts
Anthony H. Rose

2. Inhibitors of Macromolecular Synthesis in Yeast
Daniel Schindler and Julian Davies

3. Isolation of Yeast DNA
D. R. Cryer, R. Eccleshall, and J. Marmur

4. Preparation of RNA and Ribosomes from Yeast
Gerald M. Rubin

5. DNA-Dependent RNA Polymerases from Yeasts
H. Ponta, U. Ponta, and E. Wintersberger

6. The Isolation of Yeast Nuclei and Methods to Study Their Properties
John H. Duffus

7. Isolation of Vacuoles from Yeasts
Andres Wiemkein

8. Analytical Methods for Yeasts
P. R. Stewart

9. Methods for Avoiding Proteolytic Artifacts in Studies of Enzymes and Other Proteins from Yeasts
John R. Pringle

10. Induction of Haploid Glyprotein Mating Factors in Diploid Yeasts
Marjorie Crandall and Joan H. Caulton

11. Mutagenesis in Yeast
B. J. Kilbey

12. Induction, Selection, and Experimental Uses of Temperature-Sensitive and Other Conditional Mutants of Yeast
John R. Pringle

13. *In Vivo* and *in Vitro* Synthesis of Yeast Mitochondrial DNA
L. J. Zeman and C. V. Lusena

14. Isolation of Mitochondria and Techniques for Studying Mitochondrial Biogenesis in Yeasts
Anthony W. Linnane and H. B. Lukins

15. Separation and Some Properties of the Inner and Outer Membranes of Yeast Mitochondria
W. Bandlow and P. Bauer

16. The Use of Fluorescent DNA-Binding Agent for Detecting and Separating Yeast Mitochondria DNA
D. H. Williamson and D. J. Fennell

17. Cytoplasmic Inheritance and Mitochondrial Genetics in Yeasts
D. Wilkie

18. Synchronization of the Fission *Schizosaccharomyces pombe* Using Heat Shocks
Birte Kramhøft and Erik Zeuthen

Subject Index

Volume XIII

1. Large-Scale Enucleation of Mammalian Cells
George Veomett, Jerry Shay, Paul V. C. Hough, and David M. Prescott

2. Reconstruction of Cultured Mammalian Cells from Nuclear and Cytoplasmic Parts
George Veomett and David M. Prescott

3. Recording of Clonal Growth of Mammalian Cells through Many Generations
Hiroshi Miyamoto, Leif Rasmussen, and Erik Zeuthen

4. Preparation of Isolated Rat Liver Cells
Per O. Seglen

5. Isolation and Subfractionation of Mammalian Sperm Heads and Tails
Harold I. Calvin

6. On the Measurement of Tritium in DNA and Its Applications to the Assay of DNA Polymerase Activity
Bruce K. Schrier and Samuel H. Wilson

7. The Radioiodination of RNA and DNA to High Specific Activities
Wolf Prensky

8. Density Labeling of Proteins
Aloys Hüttermann and Gertrud Wendlberger

9. Techniques for the Autoradiography of Diffusible Compounds
Walter E. Stumpf

10. Characterization of Estrogen-Binding Proteins in Sex Steroid Target Cells Growing in Long-Term Culture
A. M. Soto, A. L. Rosner, R. Farookhi, and C. Sonnenschein

11. Long-Term Amphibian Organ Culture
Michael Balls, Dennis Brown, and Norman Fleming

12. A Method for the Mass Culturing of Large Free-Living Amebas
Lester Goldstein and Christine Ko

13. Induction and Isolation of Mutants in Tetrahymena
Eduardo Orias and Peter J. Bruns

14. Isolation of Nuclei from Protozoa and Algae
D. E. Buetow

Subject Index

Volume XIV

1. Enhancement of Virus-Induced Cell Fusion by Phytohemagglutinin (PHA)
George Poste, Dennis Alexander, and Peter Reeve

2. Methods of Cell Fusion with Germiston Virus
Lloyd C. Olson

3. Fusion of Mammalian Cells by Lipid Vesicles
George Poste and Demetrios Papahadjopoulos

4. Lipid Vesicles as Carriers for Introducing Biologically Active Materials into Cells
George Poste, Demetrios Papahadjopoulos, and William J. Vail

5. Use of Erythrocyte Ghosts for Injection of Substances into Animal Cells by Cell Fusion
Mitsura Furusawa, Masaru Yamaizumi, Toshikazu Nishimura, Tsuyoshi Uchida, and Yoshio Okada

6. The Production of Binucleate Mammalian Cell Populations
Lois H. Dickerman and Robert D. Goldman

7. Enucleation of Mammalian Cells in Suspension
Michael H. Wigler, Alfred I. Neugut, and I. Bernard Weinstein

8. Cell Culture with Synthetic Capillaries
Paul Schratter

9. Magnesium Acetate Treatment of Glass Roller Bottles to Facilitate Cell Attachment
John J. Monahan

10. Use of Plastics for Suspension Culture Vessels
Roland A. Cook, Frederick T. Counter, and Joyce K. Mc Colley

11. Determination of the Growth Rate in Human Fibroblasts in Cell Culture
Susan Curé and André Boué

12. Cultivation of Mammalian Cell Lines in Serum-Free Chemically Defined Medium
Kiyoshi Higuchi

13. Improved Synthetic Media Suitable for Tissue Culture of Various Mammalian Cells
Hajim Katsuta and Toshiko Takaoka

14. Automatic Collection of Samples from Suspension Cell Cultures for Investigation of Prolonged Metabolic Processes
George Bolcsfoldi and Eva Eliasson

15. A Simple Device and Procedure for Successful Freezing of Cells in Liquid Nitrogen Vapor
Frederick H. Kasten and Dominic K. Yip

16. Long-Term Preservation of the Ehrlich Ascites Tumor
William A. Cassel

17. Rapid Biochemical Screening of Large Numbers of Animal Cell Clones
Michael Brenner, Randall L. Dimond, and William F. Loomis

18. Use of Polyacrylamide for Cloning of Primary Tumors
Tobi L. Jones and J. Stephen Haskill

19. Isolation of Drug-Resistant Clones of Ehrlich Ascites Tumor Cells
Christopher A. Lomax and J. Frank Henderson

20. Separation of Clonogenic Cells from Stationary Phase Cultures and a Murine Fibrosarcoma by Density-Gradient Centrifugation
David J. Grdina

21. Rapid Sreening Assay for Revertants of Murine Sarcoma Virus-Transformed Cells
S. Nomura and P. J. Fischinger

22. Selective Techniques for the Isolation of Morphological Revertants of Sarcoma Virus-Transformed Cells
Joel S. Greenberger, William J. Bensinger, and Stuart A. Aaronson

23. Selection, Screening, and Isolation of Temperature-Sensitive Mutants of Avian Sarcoma Viruses
John A. Wyke

24. Induction and Isolation of Cold-Sensitive Lines of Chinese Hamster Cells
Rosann A. Farber and Paul Unrau

25. Maintenance of Perpetual Synchrony in HeLa S_3 Culture: Theoretical and Empirical Approaches
William G. Thilly

26. A Method for Synchronization of Animal Cells in Culture
Tadamasa Ooka

27. Hypertonicity and the Synchronization of Mammalian Cells in Mitosis
D. N. Wheatley

28. Selection of Synchronized Populations of HeLa Cells
Alison M. Badger and Sydney R. Cooperband

29. The Preparation and Characterization of Intact Isolated Parenchymal Cells from Rat Liver
Douglas R. LaBrecque and Roger B. Howard

30. Selective Cultivation of Mammalian Epithelial Cells
Robert B. Owens

31. Primary and Long-Term Culture of Adult Rat Liver Epithelial Cells
Gary M. Williams

32. Isolation of Rat Peritoneal Mast Cells in High Yield and Purity
P. H. Cooper and D. R. Stanworth

33. Monocyte Preparation from Blood
C. R. W. Rayner

34. Differentiation and Proliferation of Hemopoietic Cells in Culture
T. M. Dexter and N. G. Testa

Subject Index

Volume XV

1. Cell Separations by Counterflow Centrifugation
R. J. Sanderson and Karyn E. Bird

2. Separation of Spermatogenic Cells and Nuclei from Rodent Testes
Marvin L. Meistrich

3. Separation of Mammalian Spermatids
M. Loir and M. Lanneau

4. Isolation of Skeletal Muscle Nuclei
LeRoy Kyehl

5. Isolation of Neuronal Nuclei from Rat Brain Cortex, Rat Cerebellum, and Pigeon Forebrain
Clive C. Kuenzle, Alois Knüsel, and Daniel Schümperli

6. Isolation of Metaphase Chromosomes from Synchronized Chinese Hamster Cells
Masakatsu Horikawa and Takashi Sakamoto

7. Use of Metrizamide for Separation of Chromosomes
Wayne Wray

8. Isolation of Interphase Chromatin Structures from Cultured Cells
R. Hancock, A. J. Faber, and S. Fakan

9. Quantitative Determination of Nonhistone and Histone Proteins in Chromatin
Johann Sonnenbichler, F. Machicao, and I. Zetl

10. Solubilization of Chromatin with Heparin and the Isolation of Nuclear Membranes
Michel Bornens

11. Fractionation of Cell Organelles in Silica Sol Gradients
Jürgen M. Schmitt and Reinhold G. Hermann

12. Preparation of Photosynthetically Active Particles from Synchronized Cultures of Unicellular Algae
Horst Senger and Volker Mell

13. Rapid Isolation of Nucleoli from Detergent-Purified Nuclei of Tumor and Tissue Culture Cells
Masami Muramatsu and Toshio Onishi

14. Isolation of Plasma Membrane Vesicles from Animal Cells
Donald F. H. Wallach and Rupert Schmidt-Ullrich

15. Rapid Isolation of Nuclear Envelopes from Rat Liver
R. R. Kay and I. R. Johnston

16. Isolation of Plasma Membranes from Cultured Muscle Cells
Steven D. Schimmel, Claudia Kent, and P. Roy Vagelos

17. Preparation of Plasma Membranes from Amoebae
J. E. Thompson

18. Induction of Mammalian Somatic Cell Hybridization by Polyethylene Glycol
Richard L. Davidson and Park S. Gerald

19. Preparation of Microcells
T. Ege, N. R. Ringertz, H. Hamberg, and E. Sidebottom

20. Nuclear Transplantation With Mammalian Cells
Joseph J. Lucas and Joseph R. Kates

21. Procedure for Preparation and Characterization of Liver Cells Made Permeable by Treatment with Toluene
Richard H. Hilderman and Peter J. Goldblatt

22. Estimation of Intracellular Fluid Volume
William S. Runyun and Teresa H. Liao

23. Detection of Carbohydrates with Lectin-Peroxidase Conjugates
Nicholas K. Gonatas and Stratis Avrameas

24. Measurement of the Growth of Cell Monolayers *in Situ*
Gerardo Martínez-López and L. M. Black

25. Peptones as Serum Substitutes for Mammalian Cells in Culture
William G. Taylor and Ram Parshad

26. *In Situ* and Embedding for Electron Microscopy
Marlene Sabbath and Barbro Andersson

27. Genetic and Cell Cycle Analysis of a Smut Fungus (*Ustilago Violacea*)
Joseph E. Cummins and Alan W. Day

Subject Index

Volume XVI

Part A. *Isolation of Nuclei and Preparation of Chromatin. I*

1. Methods for Isolation of Nuclei and Nucleoli
Harris Busch and Yerach Daskal

2. NONAQUEOUS ISOLATION OF NUCLEI FROM CULTURED CELLS
Theodore Garney, Jr. and Douglas N. Foster

3. ISOLATION OF NUCLEI USING HEXYLENE GLYCOL
Wayne Wray, P. Michael Conn and Virginia P. Wray

4. ISOLATION OF NUCLEI AND PREPARATION OF CHROMATIN FROM PLANT TISSUES
John T. Stout and Crosby Katovich Harley

5. METHODS FOR THE ISOLATION OF NUCLEI FROM CILIATED PROTOZOANS
Donald J. Cummings

6. THE ISOLATION OF NUCLEI FROM FUNGI
Myrtle Hsiang and R. David Cole

Part B. *Nuclear—Cytoplasmic Exchange.*

7. METHODS FOR NUCLEAR TRANSPLANTATION IN AMPHIBIA
J. B. Gurdon

8. METHODS FOR STUDYING NUCLEOCYTOPLASMIC EXCHANGE OF NONHISTONE PROTEINS IN EMBRYOS
Michael B. Matilsky

9. METHODS FOR STUDYING NUCLEOCYTOPLASMIC EXCHANGE OF MACROMOLECULES
Carl M. Feldherr

Part C. *Fractionation and Characterization of Histones.*

10. HISTONE NOMENCLATURE
E. M. Bradbury

11. THE ISOLATION OF PURIFICATION OF HISTONES
E. W. Johns

12. FRACTIONATION OF HISTONES ON MOLECULAR SIEVE MATRICES
Claus von Holt and Wolf F. Brandt

13. CHROMATOGRAPHIC FRACTIONATION OF HISTONES
Thomas G. Spring and R. David Cole

14. CYTOCHEMICAL QUANTITATION OF HISTONES
Nirmal K. Das and Max Alfert

Part D. *Fractionation and Characterization of Nonhistone Chromosomal Proteins. I*

15. THE ISOLATION AND PURIFICATION OF THE HIGH MOBILITY GROUP (HMG) NONHISTONE CHROMOSOMAL PROTEINS
Graham H. Goodwin and Ernst W. Johns

16. IDENTIFICATION OF CONTRACTILE PROTEINS IN NUCLEAR PROTEIN FRACTIONS
Wallace M. LeStourgeon

17. METHODS FOR SELECTIVE EXTRACTION OF CHROMOSOMAL NONHISTONE PROTEINS
Jen-Fu Chium, Hides Fujitani, and Lubomir S. Hnilica

18. LOW-MOLECULAR-WEIGHT BASIC PROTEINS IN SPERMATIDS
Robert D. Platz, Marvin L. Meistrich, and Sidney R. Grimes, Jr.

19. ISOLATION AND CHARACTERIZATION OF NONHISTONE PHOSPHOPROTEINS
Tung Yue Wang and Nina C. Kostraba

20. FRACTIONATION OF NONHISTONE CHROMOSOMAL PROTEINS UTILIZING HYDROXYAPATITE CHROMATOGRAPHY
A. J. MacGillivray

21. ISOLATION OF NUCLEAR PROTEINS ASSOCIATED WITH THE NUCLEAR PORE COMPLEX AND THE NUCLEAR PERIPHERAL LAMINA OF RAT LIVER
Robert Peter Aaronson

22. POSTTRANSCRIPTIONAL MODIFICATIONS OF NONHISTONE PROTEINS OF SALIVARY GLAND CELLS OF SCIARA COPROPHILA
Reba M. Goodman, Elena C. Schmidt, and William B. Benjamin

23. THE MITOTIC APPARATUS: METHODS FOR ISOLATION
Arthur M. Zimmerman, Selma Zimmerman, and Arthur Forer

24. ISOLATION OF THE MITOTIC APPARATUS
Joseph L. Turner and J. Richard McIntosh

25. Fractionation of Nonhistone Chromosomal Proteins Utilizing Isoelectric Focusing Techniques
A. J. MacMillivray

26. The Rapid Isolation, High-Resolution Electrophoretic Characterization, and Purification of Nuclear Proteins
Wallace M. LeStourgeon and Ann L. Beyer

27. Two-Dimensional Polyacrylamide Gel Electrophoretic Fractionation
Patrick H. O'Farrell and Patricia Z. O'Farrell

Part E. *Chromatin Fractionation. I*

28. Methods for Fractionation of Chromatin into Transcriptionally Active and Inactive Segments
Joel M. Gottesfeld

29. Chromatin Fractionation by Chromatography on ECTHAM-Cellulose
Robert T. Simpson

30. Fractionation of Chromatin in a Two-Phase Aqueous Polymer System
A. J. Faber

31. Biochemical Approaches to Chromatin Assembly
R. Hancock

32. Nuclease Digestion of RNA in Chromatin
Leonard Augenlicht

Subject Index

Volume XVII

Part A. *Isolation of Nuclei and Preparation of Chromatin. II*

1. Procedures for Minimizing Protease Activity during Isolation of Nuclei, Chromatin, and the Histones
Peter Hoffmann and Roger Chalkley

2. Isolation of Nuclei from Animal Cells
G. D. Birnie

3. Prepation of Chromatin from Animal Tissues and Cultured Cells
William T. Garrard and Ronald Hancock

4. Methods for Isolation from Nuclei from Cultured Mammalian Cells: Conditions for Preferential Retention of Selected Histones
Margarida O. Krause

5. Methods for Isolation of Nuclei from Spermatozoa
Yasuko Marushige and Keijji Marushige

6. Manual Enucleation of Xenopus Oocytes
Carl M. Feldherr and Paul A. Richmond

7. Macro and Micro Methods for Isolation and Injection of Cell Components from Polytene Tissues
N. H. Lubsen and A. M. C. Rderker-Kuijpers

8. Isolation of Nuclei and Chromatin from Phycomyces Blakesleenaus
Robert J. Cohen

Part B. *Chromosomes.*

9. Mammalian Metaphase Chromosomes
Joseph J. Maio and Carl. L. Schildkraut

10. Analytical Techniques for Isolated Metaphase Chromosome Fractions
Elton Stubblefield, Shirley Linde, Frances K. Franolich, and L. Y. Lee

11. Methods and Mechanics Chromosome Banding
David E. Comings

12. Cytological Analysis of Crosophila Polytene Chromosomes
J. Derksen

13. Isolation and Purification of Nucleoli and Nucleolar Chromatin from Mammalian Cells
Masami Muramatsu and Toshio Onishi

14. Nucleolar Proteins
Mark O. J. Olson and Harris Busch

Part C. *Fractionation and Characterization of Histones. II*

15. ELECTROPHORETIC FRACTIONATION OF HISTONES UTILIZING STARCH GELS AND SODIUM DODECYL SULFATE-UREA GELS
Lubomir S. Hnilica, Sidney R. Grimes, and Jen-Fu Chiu

16. RESOLUTION OF HISTONES BY POLYACRYLAMIDE GEL ELECTROPHORESIS IN PRESENCE OF NONIONIC DETERGENTS
Alfred Zweidler

17. POLYACRYLAMIDE GEL ELECTROPHORETIC FRACTIONATION OF HISTONES
Ross Hardison and Roger Chalkley

Part D. *Fractionation and Characterization of Nonhistone Chromosomal Proteins.*

18. AFFINITY CHROMATOGRAPHY OF DNA-BINDING PROTEINS ON DNA COLENTLY ATTACHED TO SOLID SUPPORTS
Vincent G. Alfrey and Akira Inoue

19. DNA-BINDING PROTEINS
Gretchen H. Stein

20. FRACTIONATION OF NONHISTONE PROTEINS BY HISTONE-AFFINITY CHROMATOGRAPHY
Alan McClearly, Larry Nooden, and Lewis J. Kleinsmith

21. FRACTIONATION OF NONHISTONE CHROMOSOMAL PROTEINS
Gary S. Stein, William D. Park, and Janet L. Stein

22. FRACTIONATION OF CHROMOSOMAL NONHISTONE PROTEINS USING CHROMATIN-CELLULOSE RESINS: PURIFICATION OF STEROID HORMONE ACCEPTOR PROTEINS
Thomas C. Spesberg, Eric Stake, and David Witzke

23. METHODS FOR ASSESSING THE BINDING OF STEROID HORMONES IN NUCLEI
G. C. Chamness, D. T. Zava, and W. L. McGuire

24. METHODS FOR ASSESSING THE BINDING OF STEROID HORMONES IN NUCLEI AND CHROMATIN
J. H. Clark, J. N. Anderson, A. J. W. Hsueh, H. Eriksson, J. W. Hardin, and E. J. Peck, Jr.

25. PROTEINS OF NUCLEAR RIBONUCLEOPROTEIN SUBCOMPLEXES
Peter B. Billings and Terence E. Martin

26. ISOLATION AND CHARACTERIZATION OF RIBONUCLEOPROTEIN PARTICLES CONTAINING HETEROGENEOUS NUCLEAR RNA
Valerie M. Kish and Thoru Pederson

27. CHROMOSOMAL ASSOCIATION OF AN EPSTEIN-BARR VIRUS-ASSOCIATED NUCLEAR ANTIGEN
Ingemar Emberg

SUBJECT INDEX

Volume XVIII

Part A. *Chromatin Fractionation. II*

1. FRACTIONATION OF CHROMATIN INTO TEMPLATE-ACTIVE AND TEMPLATE-INACTIVE PORTIONS
Michael Savage and James Bonner

2. FRACTIONATION OF CHROMATIN BY BUOYANT DENSITY-GRADIENT SEDIMENTATION IN METRIZAMIDS
G. D. Birnie

3. DISSECTION OF THE EUKARYOTIC CHROMOSOME WITH DEOXYRIBONUCLEASES
Richard Axel

4. ISOLATION OF AMPLIFIED NUCLEOLI FROM XENOPUS OOCYTES
Harvey L. Wahn, Ronald H. Reeder, and Toru Higashinakagawa

5. VISUALIZATION OF CHROMATIN ν-BODIES
Ada L. Olins

6. ISOLATION AND CHARACTERIZATION OF CHROMATIN SUBUNITS
Randolph L. Rill, Babara Ramsay Shaw, and Kensal E. Van Holde

Part B. *Immunochemical Analysis of Chromosomal Properties.*

7. SEROLOGICAL ANALYSES OF HISTONES
B. David Stollar

8. IMMUNOCHEMICAL ANALYSIS OF NONHISTONE PROTEINS
F. Chytil

9. RADIOIMMUNOASSAY OF NONHISTONE PROTEINS
Michael E. Cohen, Lewis J. Kleinsmith, and A. Rees Midgley

10. IMMUNOFLUORESCENT TECHNIQUES IN THE ANALYSIS OF CHROMOSOMAL PROTEINS
L. M. Silver, C. E. C. Wu, and S. C. R. Elgin

Part C. *Sequencing of Histones.*

11. PEPTIDE MAPPING AND AMINO ACIDS SEQUENCING OF HISTONES
Robert J. Delange

12. DETERMINATION OF THE PRIMARY STRUCTURES OF HISTONES
M. W. Hsiang and R. D. Cole

Part D. *Physical Properties of DNA—Nuclear Protein Complexes.*

13. PREPARATION OF CHROMATIN AND CHROMOSOMES FOR ELECTION MICROSCOPY
Hans Ris

14. FLOW-MICROFLUOROMETRIC ANALYSIS OF CHROMATIN
David Bloch, Eugene Chin, and Chi-Tseh Fu

15. THE LASER MICROBEAM AS A PROBE FOR CHROMATIN STRUCTURE AND FUNCTION
Michael W. Berns

16. UTILIZATION OF NEUTRON SCATTERING FOR ANALYSIS OF CHROMATIN AND NUCLEOPROTEIN STRUCTURE
R. P. Hjelm, Jr., J. P. Baldwin, and E. M. Bradbury

17. CIRCULAR DICHROISM ANALYSIS OF CHROMATIN AND DNA-NUCLEAR PROTEIN COMPLEXES
Gerald D. Fasman

18. INTERCALATING AGENTS AS PROBES OF CHROMATIN STRUCTURE
Edmond J. Gabbay and W. David Wilson

19. THERMAL DENATURATION ANALYSIS OF CHROMATIN AND DNA-NUCLEAR PROTEIN COMPLEXES
Hsueh Jei Li

20. THERMAL DENATURATION ANALYSIS OF CHROMATIN AND DNA-NUCLEAR PROTEIN COMPLEXES
Allen T. Ansevin

21. ASSAYING HISTONE INTERACTIONS BY SEDIMENTATION EQUILIBRIUM AND OTHER METHODS
Dennis E. Roark

22. THE STUDY OF HISTONE-HISTONE ASSOCIATIONS BY CHEMICAL CROSS-LINKING
Jean O. Thomas and Roger D. Kronberg

SUBJECT INDEX

Volume XIX

Part A. *Enzymic Components of Nuclear Proteins—Nucleic Acid Substrates.*

1. ISOLATION AND ASSAY OF EUKARYOTIC PROTEINS-NUCLEIC ACID POLYMERASES
Pablo Valenzuela, Graeme J. Bell, Fanyela Wienberg, and William J. Rutter

2. ISOLATION AND CHARACTERIZATION OF DNA POLYMERASES FROM EUKARYOTIC CELLS
Dipak K. Dube, Elizabeth C. Travaglini, and Lawrence A. Loeb

3. METHODS FOR ASSESSMENT OF DNASE ACTIVITY
Muriel A. Lambert and George P. Studzinski

Part B. *Enzymic Components of Nuclear Proteins—Protein Substrates.*

4. ASSESSMENT OF ACETYLATION IN NONHISTONE CHROMOSOMAL PROTEINS
C. C. Liew

5. PURIFICATION AND CHARACTERIZATION OF PROTEIN METHYLASE I (S-

ADENOSYLMETHIONINE: PROTEIN-ARGININE METHYLTRANSFERASE; EC 2.1.1.23) FROM CALF BRAIN
Egon Durban, Hyang Woo Lee, Sangduk Kim, and Woon Ki Paik

6. THE METHYLATION AND DEMETHYLATION OF PROTEIN LYSINE RESIDUES
Samuel Nochumson, Sangduk Kim, and Woon Ki Paik

7. PURIFICATION AND ASSAY OF PROTEIN METHYLASE II (S-ADENOSYLMETHIONINE: PROTEIN-CARBOXYL METHYLTRANSFERASE; EC 2.1.1.24)
Sangduk Kim and Woon Ki Paik

8. ASSESSMENT OF METHYLATION ON NONHISTONE CHROMOSOMAL PROTEINS
C. C. Liew and D. Suria

9. METHOD FOR THE ASSESSMENT OF HISTONE METHYLATION
Paul Byvoet, David F. Sayer, and G. Stuart Baxter

10. PURIFICATION AND ASSAY OF NUCLEAR PROTEIN KINASES
Valerie M. Kish and Lewis J. Kleinsmith

11. PHOSPHORYLATION OF NONHISTONE CHROMOSOMAL PROTEINS BY NUCLEAR PHOSPHOKINASES COVALENTLY LINKED TO AGAROSE
J. A. Thomson, G. S. Stein, and J. L. Stein

12. METHODS FOR THE ASSESSMENT OF NONHISTONE PHOSPHORYLATION (ACID-STABLE, ALKALI-LABILE LINKAGE)
Dorothy E. Pumo and Lewis J. Kleinsmith

13. METHODS FOR THE ASSESSMENT OF SITE-SPECIFIC HISTONE PHOSPHORYLATION
Thomas A. Langan

14. ISOLATION OF HISTONE KINASES
Thomas A. Langan

15. CHROMOSOMAL PROTEIN PHOSPHORYLATION ON BASIC AMINO ACIDS
Roberts A. Smith, Richard M. Halpern, Berndt B. Bruegger, Albert K. Dunlap, and Oscar Fricke

16. ASSAY OF NONHISTONE PHOSPHATE ACTIVITY
Lewis J. Kleinsmith

17. ADP-RIBOSYLATION OF NUCLEAR PROTEINS
Lloyd A. Stocken

18. CHROMATIN-BOUND PROTEASES AND THEIR INHIBITORS
Donald B. Carter, Peggy H. Efird, and Chi-Bom Chae

19. HISTONE HYDROLASE
Woon Ki Paik and Sangduk Kim

Part C. *Histone Messenger RNAs.*

20. TRANSLATION OF HeLa CELL HISTONE MESSENGER RNAs IN CELL-FREE PROTEIN SYNTHESIZING SYSTEMS FROM RABBIT RETICULOCYTES, HeLa CELLS AND WHEAT GERM
Dieter Gallwitz, Ebo Bos, and Hans Stahl

21. ISOLATION OF HISTONE MESSENGER RNA AND ITS TRANSLATION *in Vitro*
Lee. A. Weber, Timothy Nilsen, and Corrado Baglioni

22. *In Vitro* SYNTHESIS OF SINGLE-STRANDED DNA COMPLIMENTARY TO HISTONE MESSENGER RNAs
C. L. Thrall, A. Lichlter, J. L. Stein, and G. S. Stein

23. IMMUNOLOGICAL METHODS FOR THE ISOLATION OF HISTONE H, mRNA FROM CHICKEN RETICULOCYTES
A. C. Scott and J. R. E. Wells

24. ENRICHMENT AND PURIFICATION OF SEA URCHIN HISTONE GENES
Eric S. Weinberg and G. Christian Overton

Part D. *Chromatin Transcription and Characterization of Transcripts.*

25. VISUALIZATION OF GENES BY ELECTRON MICROSCOPY
Babara A. Hamkalo

26. TECHNIQUES OF *in Vitro* RNA SYNTHESIS WITH ISOLATED NUCLEOLI
Toshio Onishi and Masami Muramatsu

27. TRANSCRIPTION OF RNA IN ISOLATED NUCLEI
William R. Marzluff, Jr.

28. TRANSCRIPTION OF CHROMATIN WITH HETEROLOGOUS AND RNA POLYMIRASES
Ronald H. Reeder

29. TRANSCRIPTION OF CHROMATIN WITH PROKARYOTIC AND EUKARYOTIC POLYMERASES
Golder N. Wilson, Alan W. Steggles, W. French Anderson, and Arthur W. Nienhuis

30. TRANSCRIPTION OF CHROMATIN FROM CELLS TRANSFORMED BY SV40 VIRUS
Susan M. Astrin

Part E. *Chromatin Reconstitution.*

31. CHROMATIN RECONSTITUTION
R. S. Gilmour

32. METHODS FOR DISSOCIATION, FRACTIONATION, AND SELECTIVE RECONSTITUTION OF CHROMATIN
G. S. Stein and J. L. Stein

33. TRANSCRIPTION OF GLOBIN GENES IN RECONSTITUTED RETICULOCYTE CHROMATIN
H. J. Gould, D. Maryanka, S. J. Fey, P. Huvos, C. S. M. Tahourdin, and J. J. Shearman

SUBJECT INDEX

Volume XX

1. MEASURING SPONTANEOUS MUTATION RATES IN YEAST
R. C. von Borstel

2. MANGANESE MUTAGENESIS IN YEAST
Aleksandra Putrament, Hanna Baranowska, Anna Eichart, and Wieslawa Prazmo

3. YEAST CELL SELECTION AND SYNCHRONY: DENSITY GRADIENTS AND MATING FACTOR BLOCK
Richard W. Shulman

4. THE RIBOSOMAL PROTEINS OF *Saccharomyces cerevisiae*
Johnathan R. Warner and Charles Gorenstein

5. ISOLATION, CHARACTERIZATION, AND TRANSLATION OF mRNA FROM YEAST
Conjeevaram E. Sripati and Jonathan R. Warner

6. METHOD FOR YEAST PROTEIN SYNTHESIS IN A CELL-FREE SYSTEM
C. H. Sissons

7. PREPARATION OF PROTOPLASTS OF *Schizosaccharomyces pombe*
J. Schwencke and M. Nagy

8. BULK ISOLATION OF YEAST MITOCHONDRIA
Donald Deters, Urs Müller, and Henri Homberger

9. ISOLATION, REGENERATION, AND FUSION OF PROTOPLASTS OF *Phycomyces*
Horst Binding and Hans Jürgen Weber

10. THE NEUROSPORA PLASMA MEMBRANE: A NEW EXPERIMENTAL SYSTEM FOR INVESTIGATING EUKARYOTE SURFACE MEMBRANE STRUCTURE AND FUNCTION
Gene A. Scarborough

11. STAINING FUNGAL NUCLEI WITH MITHRAMYCIN
Martin L. Slater

12. METHODS FOR PROTOPLAST FORMATION IN *Escherichia coli*
Richard L. Weiss

13. FUSION OF BACTERIAL PROTOPLATS
Pierre Schaeffer and Rollin D. Hotchkiss

14. PREPARATION OF PROTOPLASTS OF PLANT CELLS
Craig R. Landgren

15. THE CULTIVATION OF ANIMAL CELLS AND PRODUCTION OF VIRUSES IN SERUM-FREE SYSTEMS
Leonard Keay

16. A RAPID-MIXING TECHNIQUE TO MEASURE TRANSPORT IN SUSPENDED ANIMAL CELLS: APPLICATIONS TO NUCLEOSIDE TRANSPORT IN NOVIKOFF RAT HEPATOMA CELLS

Robert M. Wohlhueter, Richard Marz, Jon C. Graff, and Peter G. W. Plagemann

17. CLONGIN OF NORMAL AND TRANSFORMED CELLS ON PLASTIC FILMS
Lawrence E. Allred

18. A SIMPLE REPLICA-PLATING AND CLONING PROCEDURE FOR MAMMALIAN CELLS USING NYLON CLOTH
L. Karig Holmann

19. HUMAN MINISEGREGANT CELLS
R. T. Johnson, A. M. Mullinger, and C. S. Downes

20. THE USES OF TWEEN-80-PERMEABILIZED MAMMALIAN CELLS IN STUDIES OF NUCLEI ACID METABOLISM
Daniel Billen and Ann C. Olson

21. NUCLEIC ACID SYNTHESIS IN PERMEABILIZED EUKARYOTIC CELLS
Nathan A. Berger

22. RED CELL-MEDIATED MICROINJECTION OF MACROMOLECULES INTO MAMMALIAN CELLS
Robert A. Schlegel and Martin C. Rechsteiner

23. SELECTION OF SOMATIC CELL HYBRIDS BETWEEN HGPRT$^-$ AND APRT$^-$ CELLS
R. Michael Liskay and David Patterson

24. SEQUENTIAL DISSOCIATION OF THE EXOCRINE PANCREAS INTO LOBULES, ACINI, AND INDIVIDUAL CELLS
Abraham Amsterdam, Travis E. Solomon, and James D. Jamieson

25. BROMODEOXYURIDINE DIFFERENTIAL CHROMATID STAINING TECHNIQUE: A NEW APPROACH TO EXAMINING SISTER CHROMATID EXCHANGE AND CELL REPLICATION
Edward L. Schneider, Raymond R. Tice, and David Kram

26. PREPARATION AND CHARACTERIZATION OF MITOCHONDRIA AND SUBMITOCHONDRIAL PARTICLES OF RAT LIVER AND LIVER-DERIVED TISSUES
Peter L. Pedersen, John W. Greenawalt, Baltazar Reynafarje, Joanne Hullihen, Glenn L. Decker, John W. Soper, and Ernesto Bustomente

27. THE USE OF COMPLEMENT-MEDIATED CYTOLYSIS TO ANALYZE SPECIFIC CELL POPULATION OF EUKARYOTE CELLS IN CULTURES
S. M. Clarke, P. F. Kohler, and L. M. Fink

28. MICROELECTROPHORESIS OF ENZYMES IN ANIMAL CELL COLONIES
William C. Wright

SUBJECT INDEX

Volume 21A

Normal Human Tissue and Cell Culture A. Respiratory, Cardiovascular, and Integumentary Systems

1. METHODS OF ORGAN CULTURE FOR HUMAN BRONCHUS
Benjamin F. Trump, James Resau, and Lucy A. Barrett

2. IDENTIFICATION AND CULTURE OR HUMAN BRONCHIAL EPITHELIAL CELLS
Gary D. Stoner, Yoichi Katoh, Jean-Michel Foidart, Gwendolyn A. Myers, and Curtis C. Harris.

3. THE FIBROBLAST OF HUMAN LUNG ALVEOLAR STRUCTURES: A DIFFERENTIATED CELL WITH A MAJOR ROLE IN LUNG STRUCTURE AND FUNCTION
Kathryn H. Bradley, Oichi Kawanami, Victor J. Ferrans, and Ronald G. Crystal

4. EXPLANT CULTURE OF HUMAN PERIPHERAL LUNG
Gary D. Stoner

5. MAINTENANCE OF HUMAN AND RAT PULMONARY TYPE II CELLS IN AN ORGANOTYPIC CULTURE SYSTEM
William H. J. Douglas, Ronald L. Sanders, and Karen R. Hitchcock

6. THE HUMAN ALVEOLAR MACROPHAGE
Gary W. Hunninghake, James E. Gadek, Susan V. Szapiel, Ira J. Strumpf, Oichi Kawanami, Victor J. Ferrans, Brendan A. Koegh, and Ronald G. Crystal

7. CULTURE OF CELLS AND TISSUES FROM HUMAN LUNG—AN OVERVIEW
Curtis C. Harris

8. CULTURE OF AORTA
H. Paul Ehrlich
9. HUMAN ENDOTHELIAL CELLS *in Vitro*
Gary E. Striker, John M. Harlan, and Stephen M. Schwartz
10. HUMAN ARTERIAL WALL CELLS AND TISSUES IN CULTURE
Richard M. Kocan, Ned S. Moss, and Earl P. Benditt
11. THE FETAL MOUSE HEART IN ORGAN CULTURE: MAINTENANCE OF THE DIFFERENTIATED STATE
Joanne S. Ingwall, William R. Roeske, and Kern Wildenthal
12. THE CULTURED HEART CELL: PROBLEMS AND PROSPECTS
Melvyn Lieberman, William J. Adam, and Phyllis N. Bullock
13. ORGAN AND CELL CULTURE APPLIED TO THE CARDIOVASCULAR SYSTEM—AN OVERVIEW
Earl P. Benditt
14. EXPLANT METHODS FOR EPIDERMAL CELL CULTURE
Susan M. Fischer, Aurora Viaje, Gerald D. Mills, and Thomas J. Slaga
15. SERIAL CULTIVATION OF NORMAL HUMAN EPIDERMAL KERATINOCYTES
James G. Rheinwald
16. DERMAL FIBROBLASTS
Richard G. Ham
17. PROSPECTS FOR GROWING NORMAL HUMAN MELANOCYTES *in Vitro*
Sidney N. Klaus
18. INTEGUMENTARY SYSTEM—AN OVERVIEW
Stuart H. Yuspa

SUBJECT INDEX

Volume 21B

Normal Human Tissue and Cell Culture B. Endocrine, Urogenital, and Gastrointestinal Systems

1. STUDIES OF HUMAN ENDOMETRIUM IN ORGAN CULTURE
David G. Kaufman, Thomas A. Adamec, Leslie A. Walton, Charles N. Carney, Susan A. Melin, Valerio M. Genta, Marc J. Mass, B. Hugh Dorman, Nancy T. Rodgers, Guy J. Photopulos, Judith Powell, and Joe W. Grisham
2. TISSUE CULTURE OF THE HUMAN UTERINE CERVIX
George D. Wilbanks, Edmund Leipus, and David Tsurumoto
3. NORMAL HUMAN ENDOMETRIUM IN CELL CULTURE
D. Kirk and J. C. Irwin
4. HUMAN BREAST ORGAN CULTURE STUDIES
E. A. Hillman, M. J. Vocci, J. W. Combs, H. Sanefuji, T. Robbins, D. H. Janss, C. C. Harris, and B. F. Trump
5. METHODS FOR THE ISOLATION AND CULTURE OF NORMAL HUMAN BREAST EPITHELIAL CELLS
Douglas H. Janss, Elizabeth A. Hillman, Louise B. Malan-Shibley, and Theresa L. Ben
6. EXPLANT CULTURE: PANCREATIC ISLETS
Arne Anderson and Claes Hellerström
7. PRIMARY CULTURES OF HUMAN PROSTATE
L. M. Franks
8. LONG-TERM EXPLANT CULTURE OF NORMAL HUMAN PROSTATE
Barry M. Heatfield, Hayato Sanefuji, and Benjamin F. Trump
9. NORMAL HUMAN PROSTATE EPITHELIAL CELL CULTURES
John F. Lechner, Merrill S. Babcock, Maureen Marnell, Shankar Narayan, and M. Edward Kaighn
10. THE HUMAN PLACENTA IN CELL AND ORGAN CULTURE
Kurt Stromberg
11. OVERVIEW: ENDOCRINE SYSTEMS
M. Edward Kaighn
12. ORGAN CULTURE OF NORMAL HUMAN BLADDER: CHOICE OF STARTING MATERIAL AND CULTURE CHARACTERISTICS
M. A. Knowles, R. M. Hicks, R. J. Berry, and E. Milroy

13. HISTOPHYSIOLOGIC GRADIENT CULTURE OF STRATIFIED EPITHELIUM
Joseph Leighton, Ruy Tchao, Robert Stein, and Nabil Abaza

14. CELL AND EXPLANT CULTURES OF KIDNEY TUBULAR EPITHELIUM
B. F. Trump, T. Sato, A. Trifillis, M. Hall-Craggs, M. W. Kahng, and M. W. Smith

15. SUMMARY—URINARY TRACT
Benjamin F. Trump

16. HUMAN ESOPHAGEAL ORGAN CULTURE STUDIES
E. A. Hillman, M. J. Vocci, W. Schürch, C. C. Harris, and B. F. Trump

17. ORGAN CULTURE OF GASTRIC MUCOSA: ADVANTAGES AND LIMITATIONS
Robert M. Donaldson, Jr. and Cyrus R. Kapadia

18. ORGAN CULTURE OF THE MUCOSA OF HUMAN SMALL INTESTINE
Jerry S. Trier

19. EXPLANT CULTURE OF HUMAN COLON
Herman Autrup

20. ESTABLISHMENT AND CHARACTERIZATION OF INTESTINAL EPITHELIAL CELL CULTURES
Andrea Quaroni and Roger J. May

21. CULTURE OF HUMAN PANCREATIC DUCTS
Raymond T. Jones, Benjamin F. Trump, and Gary D. Stoner

22. METHODOLOGY AND UTILITY OF PRIMARY CULTURES OF HEPATOCYTES FROM EXPERIMENTAL ANIMALS
Henry C. Pitot and Alphonse E. Sirica

23. HUMAN LIVER CELLS IN CULTURE
Warren I. Schaeffer and Dana J. Kessler

24. OVERVIEW
Jerry S. Trier

INDEX

This Page Intentionally Left Blank